ISSN 1411-9420 (print) 2460-1578 (online)

Indonesian Journal of Chemistry

Vol. 21, No. 4, August 2021

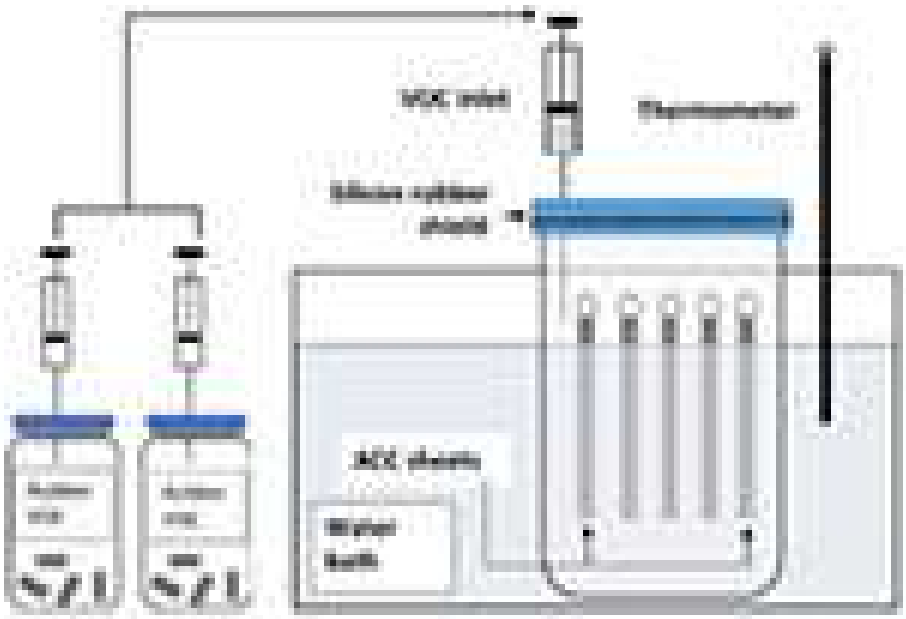

Accredited by RISTEK-DIKTI
No. 30/E/KPT/2019

Hydrochloric Acid and/or Sodium Hydroxide-modified Zeolite Y for Catalytic Hydrotreating of α-Cellulose Bio-Oil

Jason Mandela[1], Wega Trisunaryanti[1*], Triyono[1], Mamoru Koketsu[2], and Dyah Ayu Fatmawati[1***]**

[1]*Department of Chemistry, Faculty of Mathematics and Natural Sciences, Universitas Gadjah Mada, Sekip Utara, Yogyakarta 55281, Indonesia*

[2]*Department of Chemistry and Biomolecular Science, Faculty of Engineering, Gifu University, 1-1 Yanagido, Gifu 501-1193 Japan*

Corresponding author:

email: wegats@ugm.ac.id[*]; triyn102@ugm.ac.id[**]; dyah.ayu.fatmawati@mail.ugm.ac.id[***]

Received: April 24, 2020
Accepted: July 28, 2020

DOI: 10.22146/ijc.55645

Abstract: *The zeolite Y had been successfully modified by HCl and/or NaOH treatment. The modification of zeolite Y was performed by leaching the protonated zeolite Y (HY) in HCl solution (0.1 and 0.5 M) at 70 °C for 3 h resulting in $DY_{0.1}$ and $DY_{0.5}$. Subsequently, HY, $DY_{0.1}$, and $DY_{0.5}$ zeolites were immersed in 0.1 M NaOH for 15 min at room temperature resulting in AHY, $ADY_{0.1}$, and $ADY_{0.5}$. All samples were analyzed for acidity, crystallinity, Si/Al ratio, morphology, and textural properties. The catalytic performance of all samples was investigated in hydrotreating of α-cellulose bio-oil with a catalyst/feed weight ratio of 1/30. The HCl and NaOH treatment led to the decrease of the zeolite Y crystallinity and the increase of the zeolite Y average pore diameter (i.e., the mesopore distribution). The $ADY_{0.5}$ gave the highest mesopore distribution, which was 43.7%, with an average pore diameter of 4.59 nm. Moreover, both of the treatments were found to increase the Si/Al ratio that caused the decrease of zeolites Y acidity. All the zeolite Y samples gave better catalytic activity to produce liquid products after being treated by NaOH. The sample $ADY_{0.5}$ managed to produce 6.12% of 1-isopropyl-2,4-dimethylbenzene that has good potential to be processed into fuel.*

Keywords: *HCl treatment; mesoporous structure; NaOH treatment; pyrolyzed α-cellulose hydrotreatment*

■ INTRODUCTION

Zeolite Y is crystalline microporous aluminosilicate material that widely used as a catalyst, especially in the petroleum industry [1]. However, in a reaction involving large molecules, these microporous structures reduce the catalytic activity due to the limited diffusion of the large molecules [2]. Si/Al ratio of zeolite is one of the many important factors that determine the zeolite properties, especially its catalytic properties. The higher the Si/Al ratio of zeolite, the higher the thermal stability. On the other hand, higher Si/Al decreases zeolite acidity due to the removal of aluminum from its framework [3]. Consequently, the Si/Al ratio should be optimal to get suitable catalytic properties.

Zeolite Y is only possible to be directly synthesized with a maximum Si/Al ratio of 3 [4]. Therefore, post-synthetic treatment must be performed to increase its Si/Al ratio. Acid leaching is one of many treatments that are capable of increasing the Si/Al ratio of the zeolites. A weak acid, such as oxalate acid, has been proved to effectively increase the Si/Al ratio of zeolite [5-6]. However, it is not sufficient to increase the Si/Al ratio of zeolite Y due to the low Si/Al ratio; thus, a strong acid is required [7-8].

A mesoporous structure should be introduced to enhance the performance of zeolite Y as a catalyst. The mesoporous structure was generated using a surfactant as a soft template or polymer composite as a hard template [2,9]. However, this method is not suitable for mass production due to its complicated synthesis procedure and the hydrophobicity of the template [6]. On the other hand, post-synthetic treatments such as acid leaching and alkaline treatment were proven to be simpler and more effective. Alkaline treatment was

found to be a promising procedure to generate a mesoporous structure on the zeolite surface [5-6,10-12].

Mesoporous zeolite Y was found to be an effective catalyst because of its acidity and high conversion percentage due to its mesoporous structure [2]. Therefore, mesoporous zeolite Y is highly possible to be used as a catalyst in the hydrotreatment process to enhance the quality of α-cellulose bio-oil. In the hydrotreatment process, numbers of reactions occur, such as hydrocracking, hydrodeoxygenation, hydrogenation, etc. Cellulose is the most promising biomass to be used to generate biofuel due to its availability on the earth [13]. Cellulose can be converted into bio-oil by using the pyrolysis method [14-16]. However, cellulose bio-oil contains a significant amount of oxidized products that are not suitable enough to be used as a fuel [17]. Consequently, catalytic hydrotreatment should be performed to enhance the quality of cellulose bio-oil.

In this work, the effect of HCl and/or NaOH treatments toward zeolite Y characters were investigated. The concentration of HCl and NaOH solution used in this work was according to the previous study to maintain the crystallinity of the zeolite Y [8,11]. Those treatments were carried out to increase the mesopore distribution of zeolite Y. Then, the catalytic activities and selectivities of the modified zeolites Y were investigated in the hydrotreating of α-cellulose bio-oil.

■ EXPERIMENTAL SECTION

Materials

Zeolite Y, in the form of NH_4-Y (TSZ-310NHA), was supplied by Tosoh Corporation Japan. Meanwhile, NH_4Cl, HCl 37%, NaOH, NH_3 25%, and $AgNO_3$ were purchased from Merck, α-cellulose was provided by Sigma-Aldrich, and demineralized water was purchased from a local supplier. All of the chemicals were analytical grade. The N_2 and H_2 gas were supplied by Samator Ltd.

Instrumentation

Si/Al ratio of all samples was analyzed by inductively coupled plasma atomic emission spectrometer (ICP-AES) Shimadzu ICPE-9820. The functional group of all samples was recorded on the Shimadzu Prestige-21 FT-IR spectrometer with a data station in the range of 400–4000 cm^{-1} with the KBr disc technique. The sample acidity was calculated gravimetrically based on ammonia vapor adsorbed. Acidity calculation was conducted using the formula:

$$\text{Acidity} = \frac{W_{NH3}}{W_Y \times M_{NH3}} \times 1000 \frac{\text{mmol}}{\text{g}}$$

where W_{NH3} is the weight of ammonia vapor adsorbed (g), W_Y is the weight of zeolite Y, and M_{NH3} is the molecular weight of ammonia (17.03 g/mol). Pore size and volume were analyzed using N_2 gas sorption analysis, which was carried out by Quantachrome NOVAtouch. Adsorption and desorption isotherm were measured by the multipoint method. The total surface areas were calculated by the BET method. BJH desorption model was used to provide mesoporous size distribution. The micropore surface areas were obtained using the t-plot method. X-ray diffraction (XRD) analysis was performed using Rigaku Miniflex 600 with Cu Kα monochromatized radiation source (λ = 0.154 nm), operated at 40 kV, 15 mA, at a scan rate of 10°/min between 2–80°. The pore image was taken by transmission electron microscope (TEM) JEOL JEM-1400 with 120 kV acceleration voltage.

Procedure

Acid treatment of zeolite Y

First, NH_4-Y was transformed into a protonated form. In this experiment, 12 g of NH_4-Y was calcined at 10 °C/min rate to 550 °C and kept at this temperature for 5 h. This protonated zeolite Y was designated as HY. Acid treatment of zeolite Y was carried out using HCl solution. In this experiment, 4 g of HY were immersed into 80 mL of 0.1 M HCl solution at 70 °C stirring for 3 h. The slurry was filtered, washed with demineralized water until it was free of chlorine ion then dried at 110 °C overnight. The product was then calcined at a 10 °C/min rate to 550 °C and kept at this temperature for 5 h. The consequent sample was designated as $DY_{0.1}$. Sample $DY_{0.5}$ was acquired by the same procedures except for the concentration of HCl solution, which is 0.5 M.

Alkaline treatment of zeolite Y

The protonated zeolite Y (HY) and the dealuminated

zeolite Y ($DY_{0.1}$ and $DY_{0.5}$) were treated by NaOH solution. In this experiment, 2 g of zeolite Y was immersed into 60 mL of 0.1 M NaOH solution at room temperature under stirring for 15 min. Then, the slurry was filtered, washed with demineralized water, and dried at 110 °C. Subsequently, the product was transformed into protonated form by an ion-exchange process in 40 mL of 1 M NH_4Cl solution at 70 °C for 2 h and then calcined at 10 °C/min rate to 550 °C and kept on this temperature for 5 h. The consequent samples were designated as AHY, $ADY_{0.1}$, and $ADY_{0.5}$.

Zeolite Y catalytic test in hydrotreating of α-cellulose bio-oil

The α-cellulose bio-oil was produced by the pyrolysis method. Solid α-cellulose was heated at 600 °C for 3 h under the N_2 gas stream with a 20 mL/min flow rate to produce α-cellulose bio-oil. The resulting bio-oil was analyzed for its content using gas chromatography-mass spectrometer (GC-MS) Shimadzu QP2010S with a column length of 30 m, a diameter of 0.25 mm, the thickness of 0.25 μm, temperature 50–300 °C, and helium as a carrier gas with an acceleration voltage of 70 eV. The catalytic hydrotreatment of α-cellulose bio-oil was then carried out in a semi-batch stainless steel reactor at 450 °C under the H_2 gas stream with a 20 mL/min flow rate for 2 h using the obtained zeolite Y catalysts (HY, $DY_{0.1}$, $DY_{0.5}$, AHY, $ADY_{0.1}$, and $ADY_{0.5}$). The catalyst and the α-cellulose bio-oil were placed into the reactor with a ratio of 1:30. Subsequently, the liquid product from the catalytic hydrotreatment was analyzed by GC–MS.

■ RESULTS AND DISCUSSION

Effect of HCl and/or NaOH Treatments towards Zeolite Y Characters

Si/Al ratio and acidity analysis

The effect of different HCl concentration treatments toward the Si/Al ratio of zeolites Y is displayed in Table 1. As can be seen, the Si/Al ratio of the consequent zeolite Y increases along with the increase of HCl concentration, giving the values of 6.71 and 8.59 for $DY_{0.1}$ and $DY_{0.5}$, respectively. The increase of the Si/Al ratio indicated the removal of the aluminum atom from the zeolite Y framework. Moreover, this phenomenon resulted in a decrease in the acidity of zeolite Y since the aluminum atoms act as acid sites on the zeolites. As shown in Table 1, $DY_{0.1}$ and $DY_{0.5}$ had lower acidity value than HY.

The effect of NaOH treatment towards the Si/Al ratio of zeolites Y is summarized in Table 1. The NaOH treated samples, which are AHY and $ADY_{0.5}$, show a higher Si/Al ratio compared to the untreated one. The increase of the Si/Al ratio was caused by the removal of extra-framework aluminum (EFAL) throughout the NaOH treatment [18]. Moreover, this can occur because the initial Si/Al ratio of the zeolites (before NaOH treatment) was lower than 15, which led to the inhibition of the desilication process [10]. As a result, the acidity of the NaOH treated zeolites Y decreased. On the other hand, the Si/Al ratio of $DY_{0.1}$ remained the same after NaOH treatment, possibly due to the simultaneous process of the EFAL removal and desilication.

The skeletal IR vibration of the samples is shown in Fig. 1. The wavenumber between 1040–1100 cm^{-1} represents the asymmetric O–T–O (T = Si or Al) stretching shifts linearly with the amount of aluminum framework in the zeolite. The wavenumber increases along with the decrease of the aluminum framework content [6]. As shown in Fig. 1, the higher Si/Al ratio of the samples, the higher the asymmetric O–T–O stretching wavenumbers. The asymmetric O–T–O stretching vibration of the HY sample (1042 cm^{-1}) was found to be lower than those observed on AHY, $DY_{0.1}$, $ADY_{0.1}$, $DY_{0.5}$, and $ADY_{0.5}$, which are 1049, 1065, 1080, 1088, and 1096 cm^{-1}, respectively.

Crystallinity analysis

The XRD patterns of zeolites Y before and after treatments are shown in Fig. 2. As can be seen, the HCl

Table 1. Si/Al ratio and acidity of zeolite Y with various Si/Al ratio before and after treatments

Catalyst	Si/Al[a]	Acidity (mmol NH_3/g)
HY	5.00	10.10
AHY	6.00	10.80
$DY_{0.1}$	6.71	7.70
$ADY_{0.1}$	6.70	6.80
$DY_{0.5}$	8.59	4.90
$ADY_{0.5}$	14.5	4.80

[a] Measured by ICP-AES

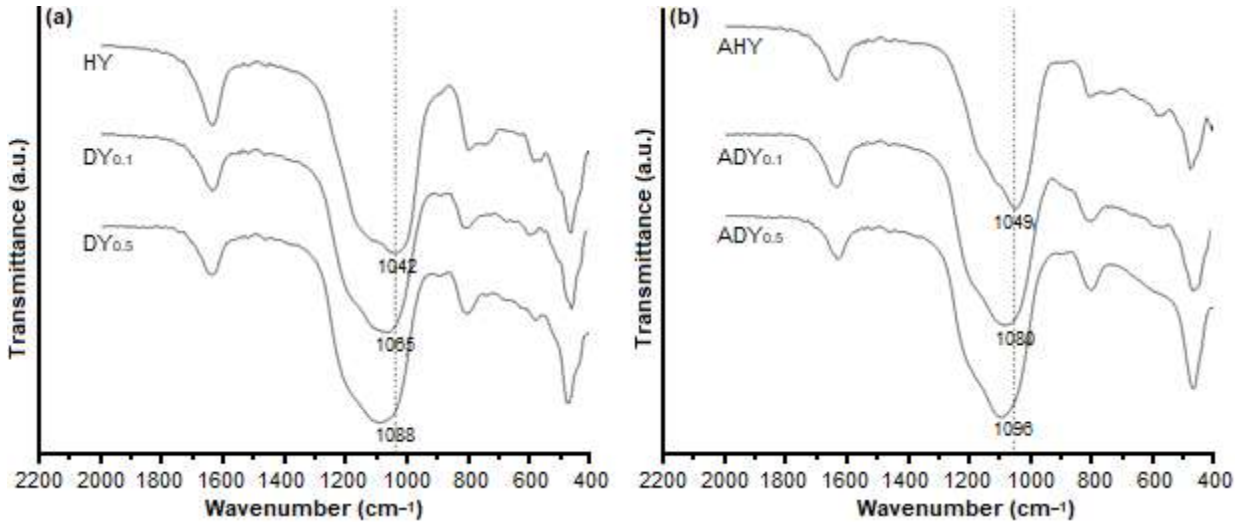

Fig 1. FT-IR spectra of zeolites Y with various Si/Al ratio (a) before and (b) after NaOH treatment

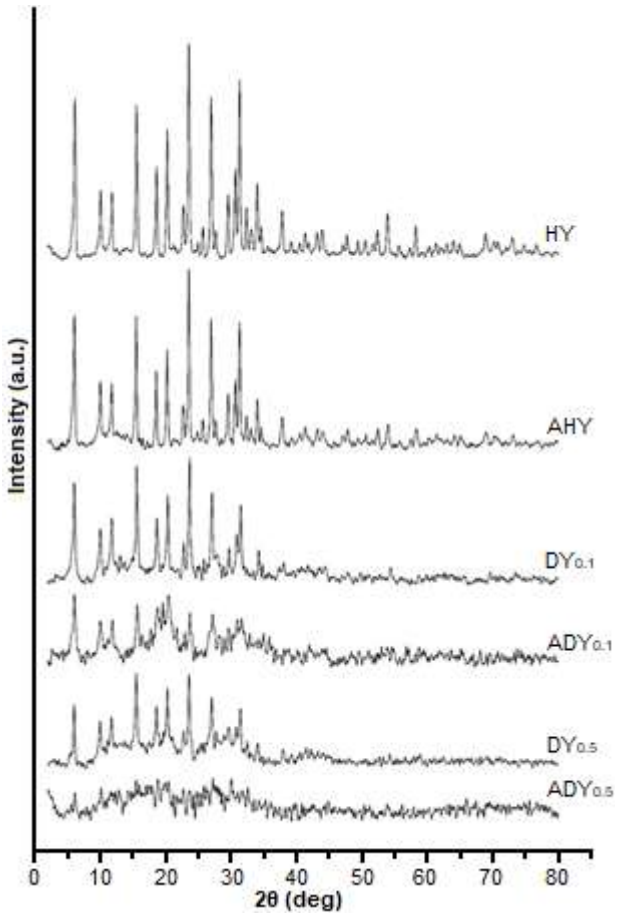

Fig 2. Powder XRD pattern of zeolites Y with various Si/Al ratio before and after treatments

and/or NaOH treatments reduced the crystallinity of zeolite Y. The XRD pattern of AHY showed that NaOH treatment without HCl treatment only slightly reduced the crystallinity of zeolite Y, but insufficient to generate enough mesoporous structure (as shown in Table 2, the composition of the mesoporous surface area in AHY samples was only 7.08%). On the other hand, the zeolite Y managed to maintain its crystallinity after being treated with 0.5 M HCl, as indicated by the XRD pattern of $DY_{0.5}$. However, after treated with NaOH, the $DY_{0.5}$ completely lost its crystallinity (see XRD pattern of $ADY_{0.5}$). The $ADY_{0.5}$ had the highest percentage of the mesoporous structure (as shown in Table 2). The loss of crystallinity was caused by the removal of aluminum and silicon framework throughout the HCl and NaOH treatments. Higher Al and Si atoms removal from the zeolite Y framework resulted in more pores as a defect in the zeolite structure. Therefore, the higher the concentration of HCl used, which is further treated with NaOH, will increase the Si/Al ratio, decrease the crystallinity of zeolites, and increase the mesoporous region.

Morphology analysis

The morphology of HY and NaOH treated samples (AHY, $ADY_{0.1}$, and $ADY_{0.5}$) was investigated by TEM analysis (Fig. 3). According to TEM analysis, the particle size of HY was around 400 nm. The TEM image of AHY, $ADY_{0.1}$, and $ADY_{0.5}$ showed that NaOH treated sample had a smaller particle size, which was around 200 nm. This indicates that NaOH treatment decreased the particle size of zeolite Y. The TEM image of AHY did not

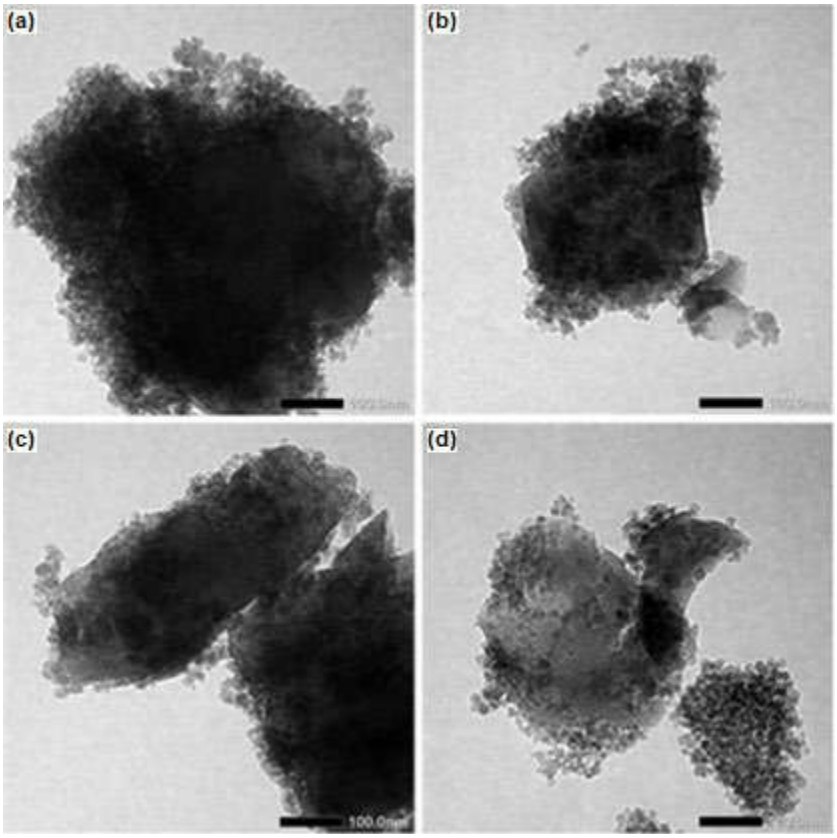

Fig 3. TEM images of (a) HY, (b) AHY, (c) $ADY_{0.1}$, (d) $ADY_{0.5}$

Table 2. Textural properties of zeolites Y before and after treatments

Catalyst	Average Pore Diameter (nm)	S_{BET} (m^2/g)	S_{micro}[a] (m^2/g)	S_{meso}[b] (m^2/g)	S_{micro} (%)	S_{meso} (%)	V_{total} (cc/g)	V_{micro}[a] (cc/g)	V_{meso}[c] (cc/g)	V_{micro} (%)	V_{meso} (%)
HY	2.52	549	517	32.0	94.3	5.75	0.35	0.27	0.07	78.5	21.5
AHY	2.63	414	385	29.0	92.9	7.08	0.27	0.20	0.07	73.9	26.1
$DY_{0.1}$	3.03	278	249	29.0	89.6	10.4	0.21	0.14	0.07	67.5	32.5
$ADY_{0.1}$	3.62	157	137	20.0	87.5	12.5	0.14	0.09	0.05	66.5	33.5
$DY_{0.5}$	3.42	182	156	26.0	85.5	14.6	0.16	0.09	0.06	59.9	40.1
$ADY_{0.5}$	4.60	119	95.0	24.0	79.7	20.3	0.14	0.08	0.06	56.3	43.7

[a] t-plot method; [b] $S_{meso} = S_{BET} - S_{micro}$; [c] $V_{meso} = V_{total} - V_{micro}$

reveal any mesoporosity. On the other hand, the TEM image of $ADY_{0.1}$ and $ADY_{0.5}$ revealed a significant mesoporosity that was shown by the lighter zone on the zeolite Y particles.

Textural properties analysis

The N_2 adsorption-desorption isotherms of zeolite Y samples are shown in Fig. 4, and the corresponding textural properties are summarized in Table 2. All the samples showed the adsorption isotherm type IV with hysteresis loops at $P/P_0 > 0.4$. This indicates that all the zeolite Y samples already had a mesoporous structure in their framework. The hysteresis loops, which became wider after the HCl and/or NaOH treatments, were introduced to the zeolite Y. This confirms that HCl and/or NaOH treatment increased the composition of the mesoporous structure of zeolite Y by removing aluminum and silicon atom from its framework.

As can be seen in Table 2, the reduction of total specific surface area (S_{BET}) and total pore volume (V_{total}) occurred because of the formation of mesoporous

structure in the zeolites Y structure. Therefore, the discussion with pore size composition (in percentage) became more convenient. The mesoporous percentage (whether the specific surface area or the pore volume) of samples increased along with the increase of the Si/Al ratio before NaOH treatment. After NaOH treatment, the percentage of mesoporous volume (V_{meso}) of HY increased from 21.51% to 26.14%, which gave a higher increase than $DY_{0.1}$ (from 32.54% to 33.52%) and $DY_{0.5}$ (from 40.07% to 43.68%). This indicates that HCl treatment was more effective in increasing the pore volume of zeolite Y with a lower Si/Al ratio and higher crystallinity.

On the other hand, the percentage of mesoporous specific surface area (S_{meso}) of HY only slightly increased from 5.75% to 7.08% after treated by NaOH, which was lower than the increasing value of S_{meso} of $DY_{0.1}$ (from 10.40% to 12.49%) and $DY_{0.5}$ (from 14.55% to 20.32%). This phenomenon showed that a combination of HCl and NaOH treatment was more effective in increasing the percentage of the mesoporous surface area of zeolite Y with higher Si/Al ratio and lower crystallinity. The highest increase of S_{meso} occurred in $DY_{0.5}$ because its framework had already been destroyed by the 0.5 M HCl treatment; thus, the removal of aluminum and silicon from the framework throughout NaOH treatment became easier.

The results of the textural properties of zeolites Y were then confirmed by the BJH pore size distribution analysis shown in Fig. 5. It indicates that the mesoporous

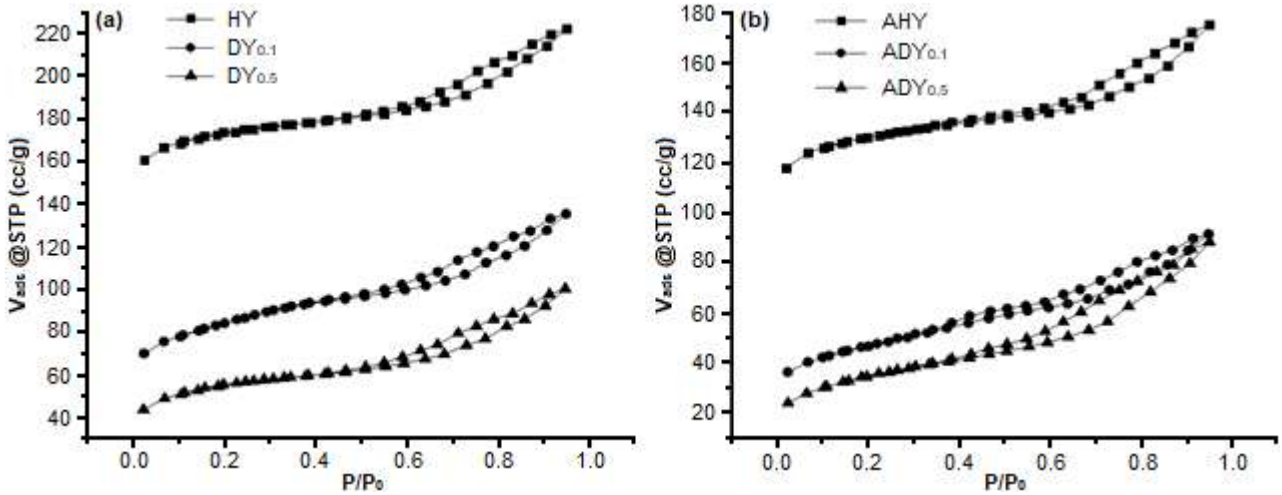

Fig 4. Isotherm adsorption-desorption of zeolites Y with various Si/Al ratio (a) before and (b) after NaOH treatment

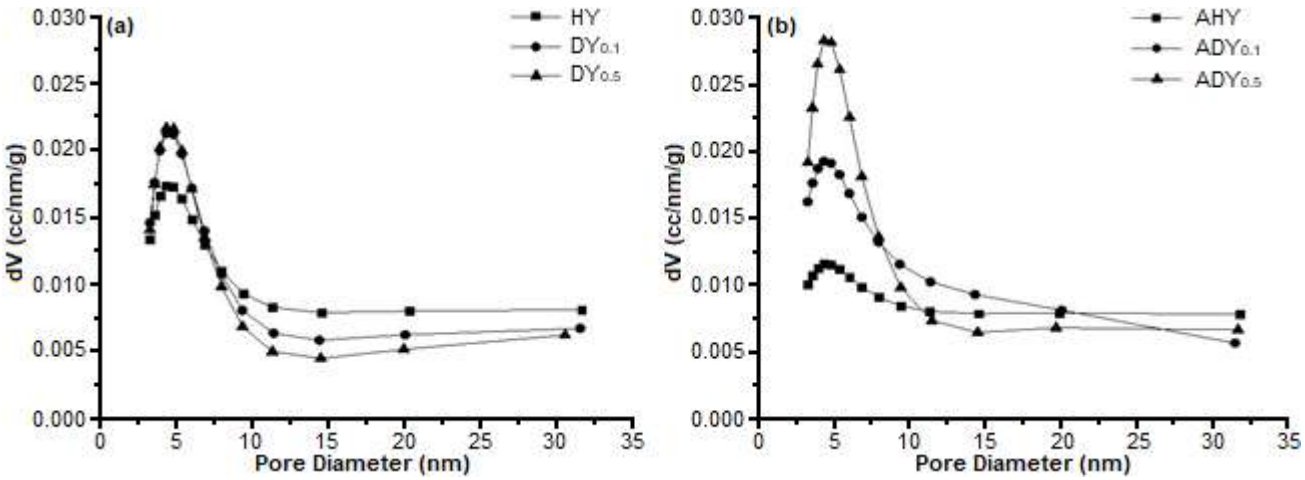

Fig 5. BJH pore distribution with various Si/Al ratio (a) before and (b) after NaOH treatment

distribution of all samples was mainly obtained at 4 nm. As indicated in Fig. 5, there was an increase in mesoporous distribution on $DY_{0.1}$ and $DY_{0.5}$ after NaOH treatment. Such a phenomenon was not observed on HY. This indicated that NaOH treatment was more effective for increasing the mesoporous distribution of the HCl-treated zeolite Y, as also supported by the TEM images of NaOH treated samples in Fig. 3.

Catalytic Performance in Hydrotreating α-Cellulose Bio-Oil

The α-cellulose bio-oil appearance was yellowish and thick liquid. The α-cellulose bio-oil easily changed its appearance into a dark brownish and thick liquid when exposed into the open air at room temperature due to its chemical instability, oxidation, and a strong tendency to re-polymerize. This phenomenon was caused by the high oxygen content in the bio-oil [19]. The pyrolysis process in this work managed to convert solid α-cellulose into α-cellulose bio-oil with 40–45% of the conversion value. The α-cellulose bio-oil mainly contains furans, ketones, aldehydes, carboxylic acid, etc. The major contents of the α-cellulose bio-oil are listed in Table 3.

The hydrotreatment of the α-cellulose bio-oil resulted in a yellowish liquid that clearer and thinner than the α-cellulose bio-oil. Moreover, the hydrotreated α-cellulose bio-oil did not change its appearance if it was exposed to open air and room temperature. This phenomenon suggests that hydrotreated α-cellulose bio-oil was more stable than the untreated α-cellulose bio-oil.

In this work, the hydrotreatment was conducted with HCl and/or NaOH treated zeolites Y to investigate the zeolites Y catalytic performance. The distribution of hydrotreated α-cellulose bio-oil products is shown in Fig. 6. The liquid product in the thermal hydrotreatment of α-cellulose bio-oil (i.e., hydrotreatment without catalyst) was lower than the catalytic hydrotreatment. This is caused by the radical mechanism reaction in thermal hydrotreatment resulted in excess of the gas product [20]. Sample $ADY_{0.1}$ had the best activity as a catalyst due to the highest liquid product yield (74.1%). This indicated that $ADY_{0.1}$ had the most optimal state between a combination of acidity, pore size, pore volume, and surface area to yield liquid products among the other samples effectively. The liquid product increase

Table 3. Major product contents of untreated α-cellulose bio-oil

Contents (%[a])	Product Description	Molecular Formula
9.77	1,3-Dioxolane-4,5-dione	C_2H_4O
7.15	Acetone	C_3H_6O
4.12	Acetaldehyde	$C_2H_4O_2$
6.48	2,3-Butanedione	$C_4H_6O_2$
15.13	Acetic acid	$C_2H_4O_2$
19.28	2-Propanone-1-hydroxy	$C_3H_6O_2$
1.28	3-Buten-2-one	C_5H_8O
1.01	2-Butanone	$C_5H_{10}O$
2.66	2,3-Pentanedione	$C_5H_8O_2$
1.94	Propanoic acid	$C_3H_6O_2$
1.14	1,4-Dioxin	$C_4H_6O_2$
3.74	1-Hydroxy-2-butanone	$C_4H_8O_2$
1.26	Propanal	C_3H_6O
1.91	2-Propanone	$C_3H_6O_2$
11.41	2-Furancarboxaldehyde	$C_5H_4O_2$
3.18	2-Furanmethanol	$C_5H_6O_2$
1.21	Vinyl acetate	$C_4H_6O_2$
2.20	Vinyl propionate 1-Hydroxy-2-butanone	$C_5H_8O_2$
1.23	acetate	$C_6H_{10}O_3$

[a] % area of GC-MS

of HY to AHY was 6.3%, $DY_{0.1}$ to $ADY_{0.1}$ was 24.4%, and $DY_{0.5}$ to $ADY_{0.5}$ was 15.3%. In most of the results, after being treated with NaOH, the catalysts produced the more liquid product, indicating that the increase in average pore size, pore volume, and surface area improve the catalyst performance to give better activities in producing a liquid product.

The major composition of hydrotreated α-cellulose bio-oil is shown in Table 4. The composition distribution of hydrotreated α-cellulose bio-oil was slightly different than the untreated α-cellulose bio-oil (Table 3). The hydrotreated α-cellulose bio-oil mainly contained furans, ketones, aldehydes, and carboxylic acid, which was remained the same as the untreated α-cellulose bio-oil. However, in catalytic hydrotreatment using $ADY_{0.5}$ as the catalyst, there was 6.12% of 1-isopropyl-2,4-dimethylbenzene that managed to be produced. This compound is a deoxygenated branched aromatic that has

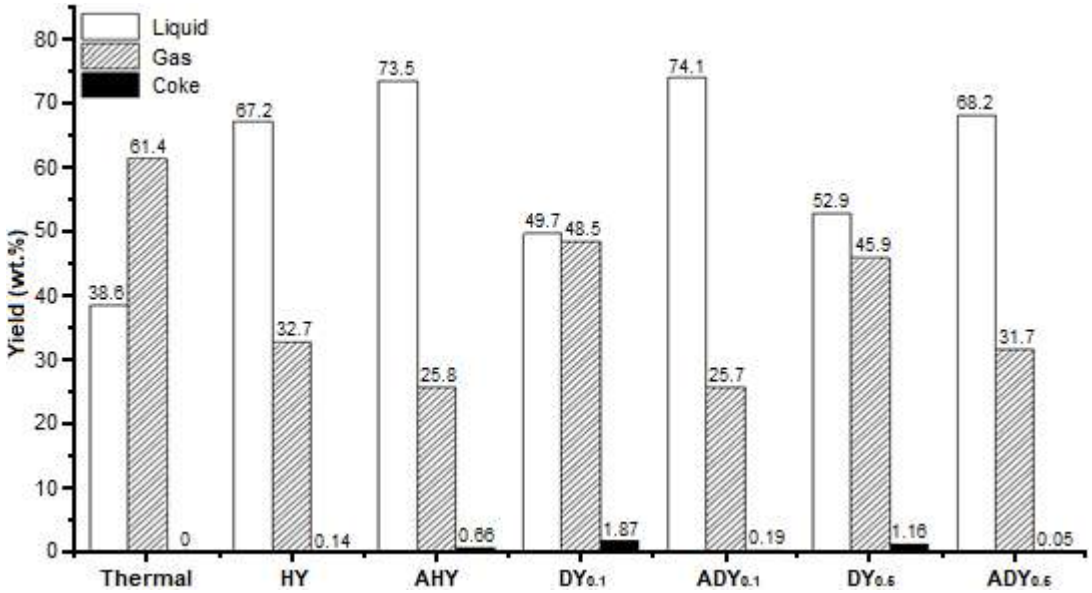

Fig 6. Product distribution of hydrotreated α-cellulose bio-oil

Table 4. Major product of hydrotreated α-cellulose bio-oil

Group	Product Description	Contents (% area of GC-MS)						
		Thermal	HY	$DY_{0.1}$	$DY_{0.5}$	AHY	$ADY_{0.1}$	$ADY_{0.5}$
Carboxylic Acid	Formic acid			6.34	7.72			
	Acetic acid	16.4	12.6	28.4	29.3	19.9	25.4	
	Propionic acid	5.47				6.78	7.17	7.16
	Hexadecanoic acid		6.76					
	Linoleic acid		5.81					
Ketone	1-Hydroxy-2-propanone	29.2	13.2	22.7	18.9	14.0	23.0	16.7
	2-Methyl-3-pentanone			3.95				
	4-Octen-3-one	13.9						
	1-Hydroxy-2-butanone	8.03					5.30	
	Acetone		28.6		7.45	21.9	10.7	6.56
Aldehyde	2-Furancarboxaldehyde	5.27		14.2	7.15	15.3		
	Acetaldehyde		7.91	12.5	16.2	7.97	11.2	17.2
Ester	Vinyl propionate							22.9
Aromatic	1-Isopropyl-2,4-dimethylbenzene							6.12

good potential to be processed into fuel. This indicated that $ADY_{0.5}$ had the best selectivity and properties in producing gasoline-potential compounds among the other samples.

■ CONCLUSION

The HCl and NaOH treatment of zeolites Y managed to increase the mesopore distribution of all zeolites Y. On the other hand, the acidity and crystallinity of zeolite Y samples decreased after the treatments. The sample $ADY_{0.5}$ gave the highest mesopore distribution at 43.7% and the highest average pore diameter at 4.59 nm. The initial Si/Al ratio that was proven to be the most crucial parameter to generate a mesopore structure in zeolite Y. The higher the Si/Al ratio before NaOH treatment, the higher mesopore managed to be generated on the zeolite Y surface. Catalytic performance in hydrotreating α-cellulose bio-oil showed that HY, AHY, $DY_{0.1}$, $ADY_{0.1}$, $DY_{0.5}$, and $ADY_{0.5}$ gave a similar result of product selectivity. However, $ADY_{0.5}$ managed to generate 6.12% of 1-isopropyl-2,4-dimethylbenzene that had the potential to be processed into fuel because it has the largest pore size of 4.6 nm, which allows large molecules to diffuse. The higher the chance of reactants to enter the pore, the higher also the chance of a catalytic reaction between reactant with the catalyst surface.

■ ACKNOWLEDGMENTS

This work was funded by the research grant of PTUPT 2020 (Contract Number: 2876/UN1.DITLIT/DIT-LIT/PT/2020). The authors thank the Indonesian Ministry of Research, Technology, and Higher Education, the Republic of Indonesia, for financial support.

■ REFERENCES

[1] Khowatimy, F.A., Priastomo, Y., Febriyanti, E., Riyantoko, H., and Trisunaryanti, W., 2014, Study of waste lubricant hydrocracking into fuel fraction over the combination of Y-zeolite and ZnO catalyst, *Procedia Environ. Sci.*, 20, 225–234.

[2] Zhao, J., Wang, G., Qin, L., Li, H., Chen, Y., and Liu, B., 2016, Synthesis and catalytic cracking performance of mesoporous zeolite Y, *Catal. Commun.*, 73, 98–102.

[3] Verboekend, D., Nuttens, N., Locus, R., Van Aelst, J., Verolme, P., Groen, J.C., Pérez-Ramírez, J., and Sels, B.F., 2016, Synthesis, characterisation, and catalytic evaluation of hierarchical faujasite zeolites: Milestones, challenges, and future directions, *Chem. Soc. Rev.*, 45 (12), 3331–3352.

[4] Lutz, W., 2014, Zeolite Y: Synthesis, modification, and properties–A case revisited, *Adv. Mater. Sci. Eng.*, 2014, 724248.

[5] Tian, F., Wu, Y., Shen, Q., Li, X., Chen, Y., and Meng, C., 2013, Effect of Si/Al ratio on mesopore formation for zeolite beta via NaOH treatment and the catalytic performance in α-pinene isomerization and benzoylation of naphthalene, *Microporous Mesoporous Mater.*, 173, 129–138.

[6] Wu, Y., Tian, F., Liu, J., Song, D., Jia, C., and Chen, Y., 2012, Enhanced catalytic isomerization of α-pinene over mesoporous zeolite beta of low Si/Al ratio by NaOH treatment, *Microporous Mesoporous Mater.*, 162, 168–174.

[7] Hernawan, Wahono, S.K., Maryana, R., and Pratiwi, D., 2015, Modification of Gunungkidul natural zeolite as bioethanol dehydrating agents, *Energy Procedia*, 65, 116–120.

[8] Mara, A., Wijaya, K., Trisunaryanti, W., and Mudasir, 2016, Effect of sulfuric acid treatment and calcination on natural zeolites of Indonesia, *Asian J. Chem.*, 28, 11–14.

[9] Pongsendana, M., Trisunaryanti, W., Artanti, F.W., Falah, I.I., and Sutarno, 2017, Hydrocracking of waste lubricant into gasoline fraction over CoMo catalyst supported on mesoporous carbon from bovine bone gelatin, *Korean J. Chem. Eng.*, 34 (10), 2591–2596.

[10] Silaghi, M.C., Chizallet, C., and Raybaud, P., 2014, Challenges on molecular aspects of dealumination and desilication of zeolites, *Microporous Mesoporous Mater.*, 191, 82–96.

[11] García, J.R., Falco, M., and Sedran, U., 2016, Impact of the desilication treatment of Y zeolite on the catalytic cracking of bulky hydrocarbon molecules, *Top. Catal.*, 59 (2), 268–277.

[12] Groen, J.C., Sano, T., Moulijn, J.A., and Pérez-Ramírez, J., 2007, Alkaline-mediated mesoporous mordenite zeolites for acid-catalyzed conversions, *J. Catal.*, 251 (1), 21–27.

[13] Chu, S., Yang, L., Guo, X., Dong, L., Chen, X., Li, L., and Mu, X., 2018, The influence of pore structure and Si/Al ratio of HZSM-5 zeolites on the product distributions of α-cellulose hydrolysis, *Mol. Catal.*, 445, 240–247.

[14] Bartoli, M., Rosi, L., Giovannelli, A., Frediani, P., and Frediani, M., 2016, Pyrolysis of α-cellulose using a multimode microwave oven, *J. Anal. Appl. Pyrolysis.*, 120, 284–296.

[15] Lin, Y.C., Cho, J., Tompsett, G.A., Westmoreland, P.R., and Huber, G.W., 2009, Kinetics and mechanism of cellulose pyrolysis, *J. Phys. Chem. C*, 113 (46), 20097–20107.

[16] Zhao, C., Jiang, E., and Chen, A., 2017, Volatile production from pyrolysis of cellulose, hemicellulose, and lignin, *J. Energy Inst.*, 90 (6), 902–913.

[17] Marsuki, M.F., Trisunaryanti, W., Falah, I.I., and Wijaya, K., 2018, Synthesis of Co, Mo, Co-Mo, and Mo-Co catalysts, supported on mesoporous silica-alumina for hydrocracking of a-cellulose pyrolysis oil, *Orient. J. Chem.*, 34 (2), 955–962.

[18] Groen, J.C., Peffer, L.A.A., Moulijn, J.A., and Pérez-Ramírez, J., 2005, Mechanism of hierarchical porosity development in MFI zeolites by desilication: The role of aluminium as a pore-directing agent, *Chemistry*, 11 (17), 4983–4994.

[19] Si, Z., Zhang, X., Wang, C., Ma, L., and Dong, R., 2017, An overview on catalytic hydrodeoxygenation of pyrolysis oil and its model compounds, *Catalysts*, 7 (6), 169.

[20] Vogt, E.T.C., and Weckhuysen, B.M., 2015, Fluid catalytic cracking: Recent developments on the grand old lady of zeolite catalysis, *Chem. Soc. Rev.*, 44 (20), 7342–7370.

Optimizing Natural Deep Eutectic Solvent Citric Acid-Glucose Based Microwave-Assisted Extraction of Total Polyphenols Content from *Eleutherine bulbosa* (Mill.) Bulb

Bohari Yusuf[1], Selvi Jumiatul Astati[2], Mirhansyah Ardana[2], Herman[3], Arsyik Ibrahim[3], Laode Rijai[3], Firzan Nainu[4], and Islamudin Ahmad[2,3*]

[1]*Department of Chemistry, Faculty of Mathematics and Natural Sciences, Universitas Mulawarman, Samarinda 75119, East Kalimantan, Indonesia*

[2]*Department of Pharmaceutical Sciences, Faculty of Pharmacy, Universitas Mulawarman, Samarinda 75119, East Kalimantan, Indonesia*

[3]*Pharmaceutical Research and Development Laboratory of FARMAKA TROPIS, Faculty of Pharmacy, Universitas Mulawarman, Samarinda 75119, East Kalimantan, Indonesia*

[4]*Faculty of Pharmacy, Hasanuddin University, Makassar 90245, South Sulawesi, Indonesia*

* ***Corresponding author:***

tel: +62-81342205060
email: islamudinahmad@farmasi.unmul.ac.id

Received: August 9, 2020
Accepted: December 18, 2020

DOI: 10.22146/ijc.58467

Abstract: *Application of natural deep eutectic solvent (NADES) citric acid-glucose-based microwave-assisted extraction (MAE) method for total polyphenol content (TPC) enriches the use of* Eleutherine bulbosa *(Mill.) bulb more widely and commercially. Therefore, this study aims to optimize NADES citric acid-glucose-based MAE on the TPC from* E. bulbosa *bulbs using response surface methodology (RSM). In the present study, the dried sample of* E. bulbosa *bulb was extracted using the NADES based MAE. Determination of TPC was conducted using Folin-Ciocalteau reagent and standard gallic acid, then measured using a UV-Vis spectrophotometer at 761 nm. Extraction condition optimization of the NADES based MAE method was performed using RSM with Box Behnken Design (four-factors-three-levels and 29 runs) on Design Expert v12. Based on the results study, the optimum condition extraction on the TPC enrichment was obtained at the NADES ratio (citric acid: glucose) 1:1 g/g; solid-liquid ratio 1:8 g/mL; extraction time of 15 min; and 270 Watt microwave power. The confirmation test and scale-up (50 g samples) were obtained with a 61.63 ± 2.23 mg GA/g sample.*

Keywords: Eleutherine bulbosa *Mill; microwave-assisted extraction; natural deep eutectic solvent; response surface methodology; total polyphenols content*

■ INTRODUCTION

Eleutherine bulbosa (*E. bulbosa*), known as Bawang Dayak, is a type of onion that grows wild in Kalimantan's tropical forests that has the potential to be developed and identified compounds that are efficacious [1]. *E. bulbosa* bulbs' chemical content includes tannin, flavonoids, quinones, and triterpenoid compound [2]. Besides, some compounds have been successfully isolated, including anthraquinone, naphthoquinone groups (such as elecanacine, eleutherine, elutherole, eleutherine), and eleuthosides A, B, C [3]. *E. bulbosa* bulbs are known to overcome various diseases such as cancer/cysts (breast/uterus), prostate, diabetes, gout, hypertension, gastrointestinal disturbances, cholesterol, goiter, bronchitis, stamina, and sexual disorders [4]. *E. bulbosa* bulb has enormous potential as a source of raw materials for natural-based medicines. This plant is abundant and easy to grow on Kalimantan island, but so far, commercial use is limited. Therefore, it is necessary to innovate for increasing the commercial use of this plant through the development of natural products with a green extraction approach.

On the other hand, some studies on *E. bulbosa* have been widely reported, including the effect extraction method of this plant against oral glucose tolerance activity [5], sunscreen activity, and TLC profile [6], heat-assisted extraction of phenolic compound [7], and effect of ethanolic extraction of *E. palmifolia* tuber on blood glucose and insulin level [8]. However, the extraction of target secondary metabolites from *E. bulbosa* using a green solvent approach based on non-conventional extraction methods has not been reported.

The development of non-conventional extraction methods is recently increasing, such as the microwave-assisted extraction method (MAE). This method has advantages over other conventional methods because it is expected to shorten the extraction process, minimize the use of solvents, and save energy use through microwave energy in the irradiation process [9].

The choice of solvent and extraction method are the main factors that must be considered to obtain the extraction efficiency of the target compound from natural products. The utilization of Natural Deep Eutectic Solvent (NADES) has increased in recent years. NADES has many advantages as a solvent, such as requires low cost, chemically inert, adjustable viscosity, readily biodegradable, acceptable toxicity, and sustainability [10-12]. NADES is a type of natural solvent in the form of a deep eutectic solvent, composed of a mixture component of primary metabolites (for example, sugar, amino acids, and organic acids). The right constituent of NADES will form a clear and stable liquid. In contrast, the inappropriate constituent components cause the liquid to be unstable, precipitable, and can return to solid form.

In this study, the selection of the composition of NADES in the form of citric acid and glucose is the right combination where glucose has hydrogen bonding acceptor (HBA) properties. Citric acid has hydrogen bonding donor (HBD) properties. Suppose both materials are fused at a specific temperature, forming a stable solution and ready to be used as a green solvent [13]. On the other hand, these two ingredients are pharmaceutical excipients that are safe for consumption, so it is hoped that the extract obtained can be readily consumed because not containing harmful organic solvents.

The combination of NADES with the non-conventional extraction method effectively extracts the desired target compound and minimizes the compound's undesirable extraction. Several studies have reported the success of NADES as an alternative solvent to replace conventional organic solvents, namely the experiment about extraction of flavonoid from *Radix Scutellariae* [14], extraction of phenol compounds from *Cajanus cajan* leaves [15], and extraction of polyphenols and caffeine from robusta coffee beans [16-17]. The optimization process of various factors that influence non-conventional extraction based on NADES is carried out using response surface methodology (RSM).

RSM is a mathematical and statistical tool that has a crucial role in designing, formulating, developing, and analyzing natural product research, mainly in the extraction method optimization process [18]. RSM has the advantage of studying the interaction between various factors on response [19-20]. In this study, box-Behnken design (BBD) with three-level fractional factorial was used to optimize the extraction condition of total polyphenol content (TPC) enrichment. The BBD is more economical and efficient than other factorial designs due to its ability to select points from a three-level factorial arrangement without center point or factorial points. This design requires fewer points than different methods. The BBD has been used extensively to optimize some extraction conditions such as extraction time, extraction temperature, solvent types, solvent concentration, sample-solvent ratio, etc. [20].

Therefore, this study aims to optimize the condition of the NADES citric-glucose acid-based MAE method for the enrichment of TPC from *E. bulbosa* bulbs using RSM.

■ EXPERIMENTAL SECTION

Materials

The samples of *E. bulbosa* bulb was collected from Samarinda, East Kalimantan, Indonesia. The specimen was authenticated and identified at Laboratory of Dendrology, Faculty of Forestry, Universitas Mulawarman, Samarinda, Indonesia. The fresh bulb was washed and cut into small pieces and dried using a dryer

cabinet at 50–60 °C. The citric acid (100% pure food grade non-GMO) and glucose (food grade) were obtained from CV. Chlorogreen, Bandung, Indonesia. Gallic acid (analytical purity), Folin-Ciocalteau reagent, and sodium carbonate were purchased from Merck, Germany (through Elokarsa LLC, Indonesia). The quality test of the chemical purity was carried out before the experiment to ensure that the chemical quality was up to the specifications.

Procedure

The procedure of NADES based MAE method

The extraction process was carried out using NADES based MAE by referring to some previous studies [16,21-22], with some modifications adjusting the extraction conditions. Firstly, the composition of NADES (citric acid and glucose) was melted at 50–80 °C until forming a concentrated solution. The NADES solution slowly added distilled water in a ratio of 1:1, 3:1, and 5:1 g/g. Next, 5 g of *E. bulbosa* bulbs were mixed with NADES in a round bottom flask. Secondly, the extraction process was conducted using the MAE method, operated under various conditions, as shown in Table 1. The extract solution and the residue were separated using a Buchner filter; The extract solution was kept in the refrigerator in a closed container until ready to analyze.

Determination of total polyphenols content

Determination of total polyphenols content (TPC) was done by spectrophotometry using the Folin-Ciocalteau reagent regarding some literature [23-24], with slight modification. Briefly, a 1 mL of sample and standard solution was put into a test tube, added with 5 mL of distilled water and 0.5 mL of Folin-Ciocalteu reagent. After 5 min of incubation, the other reagents such as 2 mL sodium carbonate and 1.5 mL distilled water was added. Absorbance was measured using a UV-Vis spectrophotometer at 761 nm (in this study, 761 nm was the maximum wavelength) after incubating the mixture of sample for 1 h at room temperature. The TPC in mg GAE/g samples were calculated using a linear regression equation obtained from gallic acid standard solutions at various concentrations (from 12.5 up to 200 µg/mL), namely, Y = 0.015 + 0.001559X, with an R^2 value of 0.9977, where Y is absorbance, and X is TPC value.

Design experimental of NADES based MAE optimization

Optimization of the NADES based MAE condition for the TPC enrichment was optimized by response surface methodology (RSM). The optimization process was estimated the interaction between variables and factors (independent parameters) on the TPC value (dependent variable). Box Behnken Design (with four-factor-three-level) was used for experimental design and requiring 29 experiments (with 1 block and 5 center points per block) for optimization extraction condition (in Table 1). A multilinear quadratic regression model was estimated according to the experimental data from different extraction conditions and TPC values using Design Expert v12 software licensed (Statease Inc. Minneapolis, MN, USA).

■ RESULTS AND DISCUSSION

The study results from 29 runs obtained extraction conditions with the highest TPC of 85.251 mg GAE/g (NADES ratio of 5:1 g/g, the solid-liquid ratio of 1:12 g/mL, extraction time of 10 min and microwave power of 270 Watt) and the lowest TPC of 27.091 mg GAE/g (NADES ratio 3:1 g/g, a solid-liquid ratio of 1:8, extraction time of 5 min and 270 Watt of microwave power), as shown in Table 2. The determination of TPC

Table 1. Experimental design of response surface methodology with box Behnken design using NADES citric acid-glucose as a green solvent

No.	Independent Variables	Unit	Symbol	Factor Levels		
				Low (-1)	Medium (0)	High (+1)
1	NADES (citric acid-glucose) ratio	g/g	X_1	1:1	3:1	5:1
2	Liquid-Solid Ratio	mL/g	X_2	8:1	10:1	12:1
3	Extraction Time	min	X_3	5	10	15
4	Microwave Power	Watts	X_4	90	270	450

Table 2. Experimental values of TPC of the *E. bulbosa* bulb extract obtained by NADES-MAE at various conditions

Run	NADES Ratio (g/mL)	Liquid-Solid ratio (g/g)	Extraction Time (min)	Microwave Power (Watt)	TPC (mg GAE/g sample)	
	X_1	X_2	X_3	X_4	Actual	Predicted
1	3:1 (0)	12:1 (+1)	10 (0)	450 (+1)	38.70	43.37
2	5:1 (+1)	10:1 (0)	5 (-1)	270 (0)	68.42	69.69
3	1:1 (-1)	12:1 (+1)	10 (0)	270 (0)	46.71	43.17
4	3:1 (0)	8:1 (-1)	15 (+1)	270 (0)	38.58	40.39
5	3:1 (0)	10:1 (0)	5 (-1)	450 (+1)	41.93	38.33
6	5:1 (+1)	10:1 (0)	15 (+1)	270 (0)	77.24	77.82
7	3:1 (0)	10:1 (0)	10 (0)	270 (0)	39.77	41.61
8	3:1 (0)	8:1 (-1)	10 (0)	450 (+1)	37.68	35.63
9	3:1 (0)	12:1 (+1)	5 (-1)	270 (0)	35.64	38.86
10	1:1 (-1)	10:1 (0)	15 (+1)	270 (0)	51.13	49.27
11	3:1 (0)	8:1 (-1)	10 (0)	90 (-1)	32.75	27.49
12	3:1 (0)	10:1 (0)	10 (0)	270 (+1)	32.86	41.61
13	3:1 (0)	10:1 (0)	15 (+1)	450 (+1)	41.28	42.62
14	5:1 (+1)	10:1 (0)	10 (0)	450 (+1)	75.67	74.91
15	3:1 (0)	10:1 (0)	10 (0)	270 (0)	49.50	41.61
16	1:1 (-1)	10:1 (0)	10 (0)	90 (-1)	31.28	37.08
17	1:1 (-1)	8:1 (-1)	10 (0)	270 (0)	48.18	48.54
18	3:1 (0)	10:1 (0)	5 (-1)	90 (-1)	31.00	25.21
19	3:1 (0)	12:1 (+1)	10 (0)	90 (-1)	28.22	29.69
20	3:1 (0)	8:1 (-1)	5 (-1)	270 (0)	27.09	33.15
21	3:1 (0)	12:1 (+1)	15 (+1)	270 (0)	45.63	44.62
22	5:1 (+1)	10:1 (0)	10 (0)	10 (-1)	57.54	62.18
23	1:1 (-1)	10:1 (0)	5 (-1)	270 (0)	45.55	44.39
24	5:1 (+1)	8:1 (-1)	10 (0)	270 (0)	66.04	65.12
25	3:1 (0)	10:1 (0)	15 (+1)	90 (-1)	34.77	33.92
26	1:1 (-1)	10:1 (0)	10 (0)	450 (+1)	45.76	46.16
27	5:1 (+1)	12:1 (+1)	10 (0)	270 (0)	85.25	80.25
28	3:1 (0)	10:1 (0)	10 (0)	270 (0)	44.62	41.61
29	3:1 (0)	10:1 (0)	10 (0)	270 (0)	41.31	41.61

in extracts was carried out based on the standard gallic acid obtained. Gallic acid acts as a standard because it is a derivative of hydroxybenzoic acid, which is a simple phenol acid that is pure and stable [16,23-24]. The concentration of gallic acid used was at 12.5 to 200 ppm. Gallic acid analysis was performed using a UV-Vis spectrophotometer, which produced the equation Y = 0.015 + 0.001559X with a correlation coefficient (R^2) of 0.997, where Y is the absorbance. At the same time, the X value is the TPC value. The equation used to calculate sample levels with various pre-determined factor conditions using RSM.

The absorbance data was measured using a spectrophotometer at 761 nm. The TPC values were calculated using a regression equation formula from a standard calibration curve, then the TPC value obtained in mg GAE/g samples. All data were analyzed using the Design Expert 12 licensed software to determine the optimum conditions for the enrichment of TPC in this study. In Table 3, the standard quadratic model was

suitable for TPC's response with a value of $p < 0.0001$ (< 0.01%), which shows the probability of a model error of less than 5% or means the quadratic model has a significant effect response to the TPC. Next, an ANOVA analysis was performed on the chosen model. If the value of "prob> F" is lower than 0.05, then the relationship becomes significant, while for the value of "prob> F" higher than 0.1, then the relationship becomes not significant.

The suggested standard quadratic model was based on the insignificant value in the lack of fit with the predicted R^2 value lower than the adjusted R^2 value. However, with a predictive R^2 of 0.7353, this is still in reasonable agreement with the adjusted R^2 of 0.9051. The predicted R^2 and the adjusted R^2 should be within 0.20 of each other. Otherwise, there may be a problem with either the data or the model. The regular R^2 can be artificially inflated by merely adding terms to the model, even if the terms are not statistically significant. The adjusted R^2 plateaus when insignificant terms are added to the model, and the predicted R^2 will decrease when there are too many insignificant terms. A rule of thumb is that the adjusted and predicted R^2 values should be within 0.2 of each other. For the optimal designs, the mixture polynomials can be reduced before point selection. Reducing the number of coefficients reduces the number of model points required and changes the variable's selection criterion [25-27].

Table 4 shows the best reduced quadratic model based on the results of the analysis of variance. The model F-value of 34.39 and p-value of < 0.0001 less than 0.050 indicate the model terms are significant. There is only a 0.01% chance of an F-value occurring due to interference. In this case, X_1, X_3, X_4, X_1X_2, X_1^2, X_4^2 are significant model terms. The "Lack of Fit" F-value of 0.47 implies the "Lack of Fit" is not significant relative to the pure error. There is an 87.43% chance that a "Lack of Fit" F-value this large could occur due to noise. Non-significant "Lack of Fit" is right. This value indicates that all four factor have a significant relationship with the

Table 3. The selection of mathematical model analysis for optimization

Source	Sequential p-value	Lack of Fit p-value	Adjusted R-Squared	Predicted R-Squared	Recommendation
Linear	0.0082	0.0714	0.3274	0.1163	
Two-Factor Interaction	0.9948	0.0420	0.1335	-0.7595	
Quadratic	< 0.0001	0.7209	0.8739	0.7353	Suggested
Cubic	0.8152	0.3899	0.8246	-1.0697	Aliased

Table 4. Analysis of variance

Source	Sum of Squares	df	Mean Square	F-value	p-value	
Model	6016.31	8	752.04	34.39	< 0.0001	Significant
X_1	2174.97	1	2174.97	99.46	< 0.0001	
X_2	74.18	1	74.18	3.39	0.0804	
X_3	126.69	1	126.69	5.79	0.0259	
X_4	357.00	1	357.00	16.33	0.0006	
X_1X_2	106.98	1	106.98	4.89	0.0388	
X_2X_4	7.69	1	7.69	0.3516	0.5598	
X_1^2	2691.64	1	2691.64	123.09	< 0.0001	
X_4^2	210.73	1	210.73	9.64	0.0056	
Residual	437.36	20	21.87			
Lack of Fit	285.90	16	17.87	0.4719	0.8743	not significant
Pure Error	151.46	4	37.86			
Cor Total	6453.67	28				

response [28-29]. The independent variable of X_1 and X_4 was less than 0.05, indicating statistically significant extraction results. Meanwhile, the independent variables X_2 and X_3 were greater than 0.05, indicating that the variable was not significant to the extraction results. But overall, the interaction between variables influences response.

In Table 5, the coefficient estimates represent the expected change in response per unit change in factor value when all remaining factors are held constant. The intercept in an orthogonal design is the overall average response of all the runs. The coefficients are adjustments around that average based on the factor settings. When the factors are orthogonal, the VIFs are 1; VIFs greater than 1 indicate multi-collinearity. The higher the VIF, the more severe the correlation of factors. As a rough rule, VIFs less than 10 are tolerable.

The equation formula obtained was $Y = 40.32 + 13.46X_1 + 2.49X_2 + 3.25X_3 + 5.45X_3 + 5.17X_1X_2 + 1.39X_2X_4 + 19.75X_1^2 - 5.90X_4^2$ with R^2 value of 0.9322 with the predicted R^2 of 0.8580 was in reasonable agreement with the adjusted R^2 of 0.9051, the difference was less than 0.2. Adequate precision measures the signal to noise ratio. Greater than four ratios were desirable. The ratio of 21,150 indicates an adequate signal. This model can be used to navigate the design space. In this equation, Y is the TPC value, where X_1 is the NADES ratio (g/g), X_2 is the solid-liquid ratio (g/mL), X_3 is extraction time (min), and D is microwave power (Watt). The equation in terms of actual factors can be used to make predictions about each factor that has given levels' response. Here, the levels should be specified in the original units for each factor. This equation should not determine each factor's relative impact because the coefficients are scaled to accommodate the units of each factor, and the intercept is not at the center of the design space [28-29].

From this equation, the optimum conditions were obtained according to the results of RSM analysis, including 1:1 g/g NADES ratio (citric acid: glucose), 1:8 g/mL solid-liquid ratio, extraction time of 15 min, and 270 Watt microwave power with predicted the TPC of 51.09 ± 4.68 mg GAE/g sample. The confirmation test and scale-up using ten times the number of samples (50 g) were obtained with a 61.63 ± 2.23 mg GAE/g sample, which showed that the TPC produced was within the tolerance interval (TI) range with 95% TI low and 95 % IT high. The TI means that the extraction process to obtain TPC's response compared to the extraction conditions predicted by the program is entirely consistent. Each parameter's value is determined by considering the efficiency of the results obtained in the extraction process using time, energy, and solvent consumption.

Based on the above findings, the use of NADES with the composition of citric acid and glucose is more effective than conventional methods. Munaeni et al. reported a TPC of 2.5 mg GAE/g from *E. bulbosa* bulbs extracted by maceration using 96% ethanol [30]. At the

Table 5. Coefficient estimate, standard error, confidence interval, and VIF of the reduced quadratic model

Factor	Coefficient Estimate	df	Standard Error	95% Confidence Interval (CI) Low	95% Confidence Interval (CI) High	Variance Inflation Factor (VIF)
Intercept	40.32	1	1.41	37.38	43.27	
X_1	13.46	1	1.35	10.65	16.28	1.0000
X_2	2.49	1	1.35	-0.3296	5.30	1.0000
X_3	3.25	1	1.35	0.4332	6.07	1.0000
X_4	5.45	1	1.35	2.64	8.27	1.0000
X_1X_2	5.17	1	2.34	0.2942	10.05	1.0000
X_2X_4	1.39	1	2.34	-3.49	6.26	1.0000
X_1^2	19.75	1	1.78	16.03	23.46	1.02
X_4^2	-5.53	1	1.78	-9.24	-1.81	1.02

same time, Shi et al. reported a TPC of 1.4 mg GAE/g of *E. bulbosa* bulbs [34]. Those previous extraction studies show that NADES (citric acid-glucose) combined with the MAE method can be an alternative solvent to replace conventional solvents and extraction methods in certain conditions effectively, quickly, and efficiently environmentally friendly.

■ CONCLUSION

The application of the green extraction approach in separating target secondary metabolites from natural products (mainly from plants) continues to experience a significant increase. The use of NADES combined with the MAE method has been successfully optimized using RSM for TPC enrichment. Optimum conditions obtained were 1:1 g/g NADES ratio (citric acid: glucose), 1:8 g/mL solid-liquid ratio, extraction time of 15 min, and 270 Watt microwave power, with the confirmed TPC value of 61.63 ± 2.23 mg GAE/g sample.

■ ACKNOWLEDGMENTS

The authors wish to acknowledge the support Rector of Universitas Mulawarman and Head Laboratory of Pharmaceutical Science and Technology, Faculty of Pharmacy, Universitas Mulawarman for providing facilities for the study.

■ AUTHOR CONTRIBUTIONS

All author was involved in this study. BY, I.A, SJA, and MA conducted the experiment, He, AI, LR, and FN conducted the DFT calculations, BY, I.A and FN wrote and revised the manuscript. All authors agreed to the final version of this manuscript.

■ REFERENCES

[1] Kuntorini, E.M., Dewi, M., and Misrina, 2016, Anatomical structure and antioxidant activity of red bulb plant (*Eleutherine americana*) on different plant age, *Biodiversitas*, 17 (1), 229–233.

[2] Insanu, M., Kusmardiyani, S., and Hartati, R., 2014, Recent studies on phytochemicals and pharmacological effects of *Eleutherine americana* Merr., *Procedia Chem.*, 13, 221–228.

[3] Singab, A.N.B., Ayoub, I.M., El-Shazly, M., Korinek, M., Wu, T.Y., Cheng, Y.B., Chang, F.R., and Wu, Y.C., 2016, Shedding the light on Iridaceae: Ethnobotany, phytochemistry and biological activity, *Ind. Crops Prod.*, 92, 308–335.

[4] Naspiah, N., Iskandar, Y., and Moektiwardoyo, M., 2014, Artikel ulasan: Bawang tiwai (*Eleutherine americana* Merr.), tanaman multiguna, *Indones. J. Appl. Sci.*, 4 (2), 18–30.

[5] Ahmad, I., Ambarwati, N.S.S., Indriyanti, N., Sastyarina, Y., Rijai, L., and Mun'im, A., 2018, Oral glucose tolerance activity of Bawang Dayak (*Eleutherine palmifolia* L. Merr.) bulbs extract based on the use of different extraction method, *Pharmacogn. J.*, 10 (1), 49–54.

[6] Ahmad, I., Arifuddin, M., and Rijai, L., 2016, The effect of extraction methods of bawang Dayak (*Eleutherine palmifolia* (L.) Merr) against TLC profiles and sunscreen activities, *Int. J. PharmTech Res.*, 9 (9), 428–436.

[7] Kamarudin, A.A., Mohd. Esa, N., Saad, N., Sayuti, N.H., and Ab. Razak, N.A., 2019, Heat assisted extraction of phenolic compounds from *Eleutherine bulbosa* (Mill.) bulb and its bioactive profiles using response surface methodology, *Ind. Crops Prod.*, 144, 112064.

[8] Hasni, Y., Aminah, D., and Tri, W., 2019, The effect of ethanolic extract of Dayak onion (*Eleutherine palmifolia* (L) Merr) tuber on blood glucose and insulin level of strepzotocin-induced diabetic wistar rat, *Asian J. Pharm. Res. Dev.*, 7 (4), 38–42.

[9] Ahmad, I., Yanuar, A., Mulia, K., and Mun'im, A., 2018, Ionic liquid-based microwave-assisted extraction: Fast and green extraction method of secondary metabolites on medicinal plant, *Pharmacogn. Rev.*, 12 (23), 20–26.

[10] Dai, Y., Witkamp, G.J., Verpoorte, R., and Choi, Y.H., 2013, Natural deep eutectic solvents as a new extraction media for phenolic metabolites in *Carthamus tinctorius* L., *Anal. Chem.*, 85 (13), 6272–6278.

[11] Dai, Y., Jin, R., Verpoorte, R., Lam, W., Cheng, Y.C., Xiao, Y., Xu, J., Zhang, L., Qin, X.M., and Chen, S., 2020, Natural deep eutectic characteristics of honey

improve the bioactivity and safety of traditional medicines, *J. Ethnopharmacol.*, 250, 112460.

[12] Vanda, H., Dai, Y., Wilson, E.G., Verpoorte, R., and Choi, Y.H., 2018, Green solvents from ionic liquids and deep eutectic solvents to natural deep eutectic solvents, *Comptes Rendus Chim.*, 21 (6), 628–638.

[13] Mulia, K., Fauzia, F., and Krisanti, E.A., 2019, Polyalcohols as hydrogen-bonding donors in choline chloride-based deep eutectic solvents for extraction of xanthones from the pericarp of *Garcinia mangostana* L., *Molecules*, 24 (3), 636.

[14] Wei, Z.F., Wang, X.Q., Peng, X., Wang, W., Zhao, C.J., Zu, Y.G., and Fu, Y., 2015, Fast and green extraction and separation of main bioactive flavonoids from *Radix Scutellariae*, *Ind. Crops Prod.*, 63, 175–181.

[15] Wei, Z., Qi, X., Li, T., Luo, M., Wang, W., Zu, Y., and Fu, Y., 2015, Application of natural deep eutectic solvents for extraction and determination of phenolics in *Cajanus cajan* leaves by ultra-performance liquid chromatography, *Sep. Purif. Technol.*, 149, 237–244.

[16] Ahmad, I., Pertiwi, A.S., Kembaren, Y.H., Rahman, A., and Mun'im, A., 2018, Application of natural deep eutectic solvent-based ultrasonic assisted extraction of total polyphenolic and caffeine content from coffe beans (*Coffea beans* L.) for instant food products, *J. Appl. Pharm. Sci.*, 8 (8),138–143.

[17] Yuniarti, E., Saputri, F.C., and Mun'im, A., 2019, Application of the natural deep eutectic solvent choline chloride-sorbitol to extract chlorogenic acid and caffeine from green coffee beans (*Coffea canephora*), *J. Appl. Pharm. Sci.*, 9 (3), 82–90.

[18] Dean, A., Voss, D., and Draguljic, D., 2017, "Response surface methodology" in *Design and Analysis of Experiments*, Springer, Cham, 565–614.

[19] Yolmeh, M., and Jafari, S.M., 2017, Applications of response surface methodology in the food industry processes, *Food Bioprocess Technol.*, 10 (3), 413–433.

[20] Riswanto, F.D.O., Rohman, A., Pramono, S., and Martono, S., 2019, Application of response surface methodology as mathematical and statistical tools in natural product research, *J. Appl. Pharm. Sci.*, 9 (10), 125–133.

[21] Gomez, F.J.V., Espino, M., Fernández, M.A., and Silva, M.F., 2018, A greener approach to prepare natural deep eutectic solvents, *ChemistrySelect*, 3 (22), 6122–6125.

[22] González, C.G., Mustafa, N.R., Wilson, E.G., Verpoorte, R., and Choi, Y.H., 2018, Application of natural deep eutectic solvents for the "green" extraction of vanillin from vanilla pods, *Flavour Fragrance J.*, 33 (1), 91–96.

[23] Sánchez-Rangel, J., Benavides, J., Heredia, J.B., Cisneros-Zevallos, L., and Jacobo-Velázquez, D.A., 2013, The Folin-Ciocalteu assay revisited: Improvement of its specificity for total phenolic content determination, *Anal. Methods*, 5 (21), 5990–5999.

[24] Bobo-García, G., Davidov-Pardo, G., Arroqui, C., Vírseda, P., Marín-Arroyo, M., and Navarro, M., 2014, Intra-laboratory validation of microplate methods for total phenolic content and antioxidant activity on polyphenolic extracts, and comparison with conventional spectrophotometric methods, *J. Sci. Food Agric.*, 95 (1), 204–209.

[25] Brusco, M.J., Voorhees, C.M., Calantone, R.J., Brady, M.K., and Steinley, D., 2019, Integrating linear discriminant analysis, polynomial basis expansion, and genetic search for two-group classification, *Commun. Stat.- Simul. Comput.*, 48 (6), 1623–1636.

[26] Chelladuai, S.J.S., Murugan, K., Ray, A.P., Upadhyaya, M., Narasimharaj, V., and Gnanasekaran, S., 2021, Optimization of process parameters using response surface methodology: A review, *Mater. Today: Proc.*, 37 (2), 1301–1304.

[27] Salim, N., Santhiagu, A., and Joji, K., 2019, Process modeling and optimization of high yielding L-methioninase from a newly isolated *Trichoderma harzianum* using response surface methodology and artificial neural network coupled genetic algorithm, *Biocatal. Agric. Biotechnol.*, 17, 299–308.

[28] Mäkelä, M., 2017, Experimental design and

response surface methodology in energy applications: A tutorial review, *Energy Convers. Manage.*, 151, 630–640.

[29] Alam, S.T., and Amin, M.A., 2020, Determining optimum design parameters of foldadble product using response surface and genetic algorithm, *Engineering*, 12, 839–850.

[30] Shi, P., Du, W., Wang, Y., Teng, X., Chen, X., and Ye, L., 2019, Total phenolic, flavanoid content, and antioxidant activity of bulbs, leaves, and flowers made form *Eleutherine bulbosa* (Mill.) Urb., *Food Sci. Nutr.*, 7 (1), 148–154.

Purification of Curcuminoids from Natural Deep Eutectic Solvents (NADES) Matrices Using Chromatography-Based Separation Methods

Orchidea Rachmaniah*, Muhammad Rifqy Muhsin, Angga Widya Putra, and Muhammad Rachimoellah

Department of Chemical Engineering, Faculty of Industrial Technology and System Engineering, Institut Teknologi Sepuluh Nopember, Kampus ITS Sukolilo, Surabaya 60111, Indonesia

* ***Corresponding author:***

tel: +62-81233777793
email: orchidea@chem-eng.its.ac.id

Received: August 21, 2020
Accepted: April 7, 2021

DOI: 10.22146/ijc.58935

Abstract: *Curcuminoids can be successfully extracted from* Curcuma zedoaria *using natural deep eutectic solvents (NADES) as extraction solvents. However, a mixture of extracted curcuminoids, NADES, and impurities from* C. zedoaria *was obtained as a slurry at the end of the extraction process. Therefore, further separation and purification were required to obtain the extracted compound in high purity. Herein, two purification methods based on classical column chromatography (CCC) and solid-phase extraction (SPE), were evaluated for the purification of curcuminoids from NADES matrices after extraction. Choline chloride–malic acid–water (CCMA–H_2O) and choline chloride–citric acid–water (CCCA–H_2O) in the molar ratio of 1:1:18 were selected as NADES matrices due to their high solubility and stabilization capability for curcuminoids. Ethanol-conditioned silica gel (60–200 μm) was applied as the bed resin for CCC, and a C_{18} cartridge was used for SPE. Acetonitrile/0.1% acetic acid, water/0.1% acetic acid, and isopropanol/0.1% acetic acid were used as mobile phases for CCC. For SPE, methanol/0.05% acetic acid and water/0.05% acetic acid were applied in the conditioning step, water/0.05% acetic acid in the washing step, and methanol/acetonitrile (1:1) in the eluting step. The SPE method produced higher recovery of curcuminoids from the CCCA–H_2O and CCMA–H_2O matrices (75.27% and 73.40%, respectively) compared to CCC (51.9% and 61.0%, respectively). After removing the NADES constituents from the crude extract of curcuminoids, recrystallization was attempted.*

Keywords: *curcumin; chromatography; recrystallization; separation; solid phase extraction*

■ INTRODUCTION

Natural deep eutectic solvents (NADES) have attracted a great deal of attention since their first introduction in the third quarter of 2011 [1]. The NADES consist of a solution mixture of primary metabolites of hydrogen-bond acceptor (HBA) and hydrogen-bond donor (HBD) compounds such as sugars, organic acids, amino acids, and polyalcohol, which, in certain proportions, can act as a solvent for solubilizing, storing, or even transporting non-water-soluble compounds in organisms [1].

The concept of NADES is similar to that of ionic liquids (ILs) and deep eutectic solvents (DES). Ionic liquids are made of high purity synthetic organic chemicals containing organic cations and either organic or inorganic anions. Meanwhile, DES are mixtures of salts and/or organic compounds that, in certain proportions, can result in the formation of a liquid with entirely new properties that differ completely from those of the pure constituents. The DES can be readily prepared by mixing an HBA and an HBD compounds such as choline chloride and an organic acid, respectively, in eutectic proportion. For instance, mixtures of choline chloride and organic acids such as oxalic, malonic, and succinic acids were introduced in 2001 by Abbot [2]. The same group also reported other combinations of chemical compounds for DES in 2003 [2]. Another DES was prepared by combining choline chloride with alcohol

[3]. As environmentally friendly solvents, NADES offer various advantageous over DES, especially for food, cosmetic, and pharmaceutical applications.

The solubilizing capacity of various NADES including proline/malic acid (PMH), sucrose–choline chloride, glucose–choline chloride, sorbitol–choline chloride, 1,2-propanediol–choline chloride, fructose–glucose–sucrose, and glucose–acid lactate (LGH) for a wide range of compounds was explored by Dai [4]. The non-water-soluble compounds such as gluten, starch, DNA, cinnamic acid, carthamin, quercetin, and rutin proved to be soluble in NADES as well as in macromolecules including proteins and polysaccharides. Their solubility in NADES was substantially higher than that in water. Apart from carthamin, NADES also showed high solubilizing power for other phenolic metabolites in *Carthamus tinctorius* L., i.e., cartormin [5]. Cartormin and carthamin exhibited the highest solubility in PMH and LGH, and both metabolites were highly stable in sugar-based NADES when exposed to light, high temperatures, and long storage times [3-4]. The extraction of other phenolic compounds using NADES as a solvent was also reported, e.g., curcuminoids from *Curcuma longa* [6] and from *C. zedoaria* [7-8], polyphenolics from food by-products such as olive [9] and grape pomace [10], hydroxycinnamic acid and flavonoids from *Moringa oleifera* [11], phenylpropanoids and flavonoids from *Lippia citriodora* [12], and other polyphenolic compounds from peppermint (*Mentha piperita*) leaves and dried lemon balm (*Melissa officinalis*) leaves [13]. The nature and chemical structure of the phenolic compounds were found to affect the extraction parameters. Most phenolic compounds are extracted in high yields when using acidic NADES containing organic acids, since the extraction in aqueous solution is quantitative at pH < pK_a for neutral phenolic compounds.

Curcuminoids in *Curcuma* sp., which include curcumin (CUR), desmethoxycurcumin (DMC), and bisdemethoxycurcumin (BDMC), have numerous bioactive applications such as anti-inflammatory [14], antioxidant [14], anticarcinogenic [14-15], antibacterial [14], and antiinfection [14]. Curcuminoids can be extracted from *C. longa*, *C. xanthorrhiza*, and *C. zedoaria*. In particular, the curcuminoid content in *C. longa* and *C. zedoaria,* which belongs to the Zingiberaceae or ginger family, is 3–5 wt.% and 6–16 wt.%, respectively [14]. Unfortunately, to date, the use of curcuminoids as a medicinal compound is still quite limited, even though CUR has been reported to be safe for consumption up to the dose of 8 g/day [14]. It should be noted that the solubility of curcuminoids in water is low, *i.e.* 4 ppb (4 μg/L) at pH = 7.3 [14] or only 3.10^{-8} M as reported by Tonnensen [16], which limits their bioavailability. In this regard, the use of NADES as water-based environmentally friendly solvents constitutes an interesting alternative for overcoming the low solubility of CUR in water [7-8]. The application of NADES in the extraction of curcuminoids from *C. zedoaria* has been reported [7]. Eleven different types of NADES were evaluated, and all of them showed a high solubilizing capacity for CUR at 40 °C within 24 h of extraction time. Their capacity was higher than that of common organic solvents such as methanol (MeOH), ethanol (EtOH), and water [7]. The curcuminoid yields were 0.269, 0.163, 0.124, 0.131, and 0.14 mg/g for fructose–glucose–water (FG–H_2O, 1:1:7), citric acid–sucrose–water (CAS–H_2O, 1:2:15 and 1:2:79), and malic acid–sucrose–water (MAS–H_2O, 1: 1:11 and 1:1:18), respectively. The solubility of curcuminoids in NADES was further enhanced by lowering the viscosity of NADES, which was achieved by varying the water content (up to 70 wt.%) in CAS–H_2O and MAS–H_2O [8]. It was shown that the solubility of curcuminoids in these NADES was not affected by the water content but by the constituents of NADES [6,8].

For the extraction of polyphenolics and curcuminoids from *Curcuma* sp., a batch stirrer extractor is commonly used [6-8,18]. In these systems, at the end of the extraction process, mixtures of extracted curcuminoids, NADES, and powder materials are obtained in the form of a slurry. This is also the case when using nonconventional methods of extraction such as microwave-assisted extraction, ultrasound-assisted extraction [18-19], and high pressurized liquid extraction [20-21]. Hence, separation and purification processes are required after the extraction, especially to obtain a high purity grade of the extracted compounds.

Despite the extensive research on the application of NADES as solvents for the extraction of bioactive compounds, the development of an efficient separation method to purify the desired compounds, such as curcuminoids, from the NADES matrix after extraction is still required. Generally, the obtained extract is directly analyzed by either high-performance liquid chromatography or UV–vis spectrophotometry. Herein, two purification methods based on classical column chromatography (CCC) and solid-phase extraction (SPE) are developed for the purification of curcuminoids from the NADES matrix after extraction. Choline chloride–malic acid–water (CCMA–H_2O) or choline chloride–citric acid–water (CCCA–H_2O) in the ratio of 1:1:18 were selected as NADES models due to their high solubility and stabilization capability for curcuminoids [7-8]. Moreover, NADES based on choline chloride and organic acids are reported to be less toxic and biodegradable [2].

■ EXPERIMENTAL SECTION

Materials

Synthetic curcuminoids and analytical grade solvents of high purity such as glacial acetic acid (HOAc), *n*-hexane, dichloromethane (DCM), chloroform ($CHCl_3$), acetonitrile (MeCN), ethanol (EtOH), *iso*-propanol (IPA), and methanol (MeOH) were commercially purchased from Merck (Darmstadt, Germany). The synthetic curcuminoids were used as the standard for quantitative analysis. The individual component of NADES that consists of choline chloride (CC) and malic acid (MA), were purchased from Sigma Aldrich (St. Louis, MO, USA). Food-grade citric acid (CA) was purchased from the Surabaya local market (Gajah, Jakarta, Indonesia) while buffer solution (pH = 2.0) was purchased from Mediss (India). Filter paper (no. 589/2) with a pore size of 4–12 μm was purchased from Whatman (Germany). For the column chromatography, silica gel 60 Å (52–73 Å), 70–230 mesh, with a particle size of 63–200 μm was purchased from Merck (Darmstadt, Germany). A silica gel plate 60 F 254 with a size of 20 × 20 cm (Merck, Darmstadt, Germany) was used for qualitative analysis by thin layer chromatography (TLC), and the cartridge for SPE, Hypersep C_{18} 500 mg/2.8 mL, was purchased from Thermo Fisher Scientific (USA).

Instrumentation

The instruments used were spectrophotometer UV–vis T-60 (PG Instrument, Leicestershire, UK), analytical balance (OHAUSS), and vacuum pump (Chem-Tech, USA).

Procedure

Sample preparation

All the NADES used in this study were prepared according to a previously reported method [8]. To mimic a CUR extract, an artificial sample was prepared by dissolving curcuminoids in NADES with a solvent per feed ratio (S/F) of 5/10 mL NADES/mg curcuminoids. As much as 10 ± 0.1 mg of curcuminoids was used for the CCC purification method, whereas 3 ± 0.1 mg curcuminoids was used for the SPE method because the maximum loading capacity of the SPE cartridge is 2.8 mL. The mixture was magnetically stirred at 40 °C until all the curcuminoids were well dissolved. The standard sample of curcuminoids was used in both the CCMA–H_2O and CCCA–H_2O at a molar ratio of 1:1:18.

Quantitative analysis of curcuminoids by UV–vis spectrophotometry

The curcuminoids were quantitatively analyzed using UV–vis spectrophotometer. Briefly, 100 μL of sample was accurately diluted into MeOH/3% HOAc to obtain a volume of 2 mL. The pH was adjusted at 1.8–2.0 using a pH = 2 buffer solution. Then, the sample was subjected to UV–vis analysis at 420 nm (λ_{max}). The obtained values of absorbance were then converted to curcuminoids concentration via a previously prepared calibration curve. The recovery of curcuminoids was calculated as the amount of obtained curcuminoids divided by the initial weight of the powder of *C. zedoaria*.

Prior to the quantitative calculation of curcuminoids, a calibration curve of curcuminoids was prepared. Seven solutions of curcuminoids with concentrations of 1, 2, 3, 4, 5, 6, and 7 ppm were prepared in serial dilutions [22]. A mixture of MeOH/HOAc

(99:1, v/v) was used as a dilution solvent. Each sample was kept at pH = 1.8–2.0 using the buffer solution. As much as 1 mg of curcuminoid standard was precisely weighed and dissolved into 10 mL NADES of CCMA–H_2O (1:1:18) or CCCA–H_2O (1:1:18), in a volumetric flask. The concentration was set at 100 ppm (100 mg/L), and the absorbance of each sample was subsequently measured in triplicates. The limit of detection (LOD) and the limit of quantification (LOQ) were also calculated for each calibration curve [22].

Curcuminoids purification using the classical column chromatography method

The silica gel used as the stationary phase was poured into a glass column of 2 cm in diameter. At first, the column was conditioned by eluting MeOH through the silica bed, followed by closing the top of the column using cotton wetted with MeOH and allowing the system to stand for hours. The polarity of the silica was increased in the presence of MeOH. Thus, the polar constituents of NADES (CC, CA, and MA) were easily separated from the sample.

An artificial curcuminoids sample containing 10 mg of curcuminoids in 5 mL NADES (S/F ratio = 5/10) was then loaded into the column. The NADES constituents were retained in the silica. Initially, 25 mL of MeCN/0.1% HOAc (v/v) was eluted four times, obtaining four fractions for each solvent mixture. By adding HOAc in the mobile phase, an acidic eluent was generated. Afterwards, H_2O/0.1% HOAc (v/v), and IPA/0.1% HOAc (v/v) were sequentially eluted. Each mobile phase mixture was eluted four times, producing a total volume of 100 mL. The process was repeated twice for each NADES, namely, CCMA–H_2O (1:1:18) and CCCA–H_2O (1:1:18).

Curcuminoids purification using the solid-phase extraction method

The SPE method was selected to enhance the recovery of curcuminoids. A less polar cartridge type (C_{18}) was used to separate the NADES matrix from the sample. The hydrophilic tail of the silica backbone in the SPE cartridge was modified using C_8–C_{18} cartridges. The SPE cartridge polarity was relatively lower than that of the silica gel in the CCC method. A reverse approach of separation was applied in the SPE method compared with the CCC method.

The purification of curcuminoids by SPE comprised of four steps which include conditioning, loading, washing, and eluting, using different mobile phase mixtures in each step. For the elution process, 1.5 mL of mobile phase was used. A mixture of MeOH/0.05% HOAc (v/v) and H_2O/0.05% HOAc (v/v) was subsequently eluted using an SPE Hypersep C_{18} cartridge during the conditioning step. At the loading stage, 1.5 mL of the sample containing NADES and curcuminoids (solid/fluids ratio of 5 g/10 mL) was poured into the cartridge. Then, a mixture of H_2O/0.05% HOAc (v/v) was used during the washing stage, and 1 mL of an MeOH/MeCN (1:1, v/v) solution was subsequently eluted to extract the remaining curcuminoids in the cartridge. In the eluting step, 3 mL of the MeOH/MeCN (1:1, v/v) solution was eluted. The obtained purified extract from the successive solvent extraction was evaporated using N_2. The dried curcuminoids residue was precisely weighed, and the recoveries were calculated. This process was performed in triplicates for each NADES.

Qualitative analysis of curcuminoids by TLC

To monitor the progress of curcuminoids purification by CCC, the TLC analysis was performed. The qualitative analysis was conducted using DCM/MeOH (95:5, v/v) as the mobile phase [23]. The spots were observed under UV light at 365 nm. The visualized spots were marked, and the retardation factor (Rf) was calculated.

■ RESULTS AND DISCUSSION

Prior to conducting purification processes of curcuminoids from NADES matrices; for quantitative purposes, the following calibration curves were produced: $y = 0.125x - 0.058$ ($R^2 = 0.99$) and $y = 0.108x - 0.056$ ($R^2 = 0.99$) for CCMA–H_2O (1:1:18) and CCCA–H_2O (1:1:18), respectively (Fig. 1). The LOD and LOQ were also calculated, and the results are shown in Table 1.

In CUR, the keto–enol tautomeric equilibrium occurs due to the presence of a hydroxyl (–OH) groups in

Table 1. Limit of detection (LOD) and limit of quantification (LOQ) for the NADES CCMA–H_2O (1:1:18) and CCCA–H_2O (1:1:18)

Type of NADES	Limit of detection (LOD, ppm)	Limit of quantification (LOQ, ppm)
CCMA-H_2O (1:1:18)	0.862	2.613
CCCA-H_2O (1:1:18)	2.719	8.239

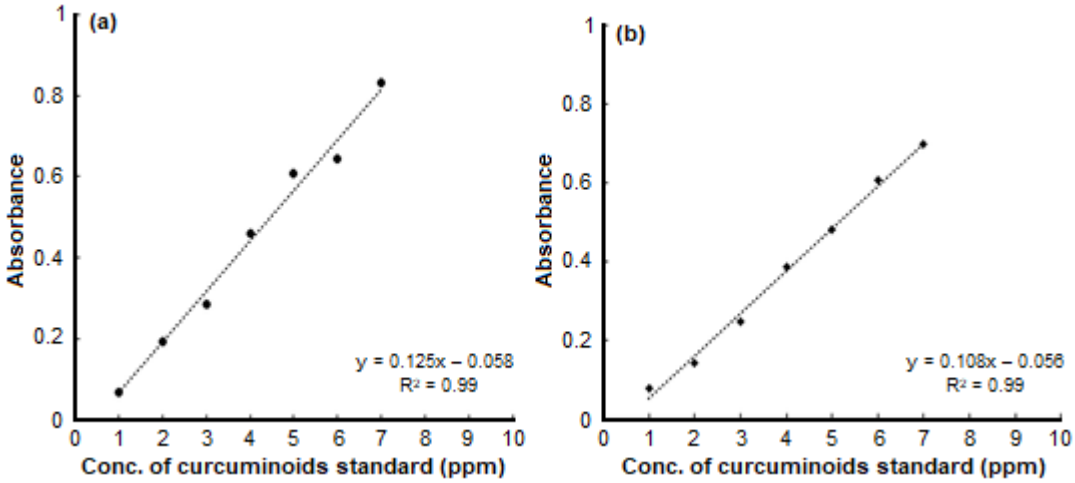

Fig 1. Calibration curves of curcuminoids in NADES matrices: (a) CCMA–H_2O (1:1:18) and (b) CCCA–H_2O (1:1:18)

the alkene moiety (C=C) of CUR. The keto form of CUR is more frequently found in the solid phase than the liquid phase, whereas the enol form is predominantly observed in the liquid phase or in solution [24]. The keto form is thermodynamically more stable than the enol form by 48 kJ/mol due to the presence of C–H, C–C, and C=O bonds [25], whereas the enol structure has C=C, C–O, and O–H bonds [25]. However, the enol tautomer can be stabilized by hydrogen bonds. Moreover, the keto form of CUR is barely influenced by changes in the pH or the temperature. Thus, CUR in the solid phase is more stable and can be stored for a longer time than in the liquid phase. Consequently, it is more convenient to store the extracted curcuminoids from the NADES matrix in the solid phase.

Recrystallization has been previously attempted to extract curcuminoids directly from the NADES matrix (CCMA–H_2O = 1:1:18 or CCCA–H_2O = 1:1:18), by using different volumes or molar ratios of *iso*-propanol/*n*-hexane (1:1, 1:1.5, 1:2, 2:1, or 2.5:1) as recrystallization solvents [26]. *Iso*-propanol (IPA) was used due to its solubilization capability for curcuminoids, and *n*-hexane was used as an antisolvent to induce precipitation [26-27]. However, due to the presence of NADES constituents (CC, CA, and MA), a homogenous mixture of curcuminoids, NADES, and IPA was observed, and attempts to perform the recrystallization failed [26]. Since CC–1,2-propanediol was reported to form a NADES [5], a CC–CA–IPA–H_2O mixture could be expected to form a new NADES mixture. Yadav [29] successfully recrystallized CUR using an artificial sample of a CUR crystalline standard dissolved in EtOH from IPA–*n*-hexane (1:5, v/v) at 30 °C, obtaining amorphous CUR. Consequently, NADES constituents should be removed first before the crystallization step of curcuminoids to eliminate the compounds that interfere with the crystallization process. To achieve this, we used the CCC and SPE methods, in which the flexibility in selecting both stationary and mobile phases of eluent mixtures enables an easy tuning of the polarity of the purification method for different types of NADES.

Purification Using the CCC Method

We started our investigation by evaluating the CCC method for the separation of curcuminoids from

the NADES constituents, namely, CC, CA, and MA. The stationary phase was highly polar due to the presence of oxygen atoms in the silica gel. By adding HOAc to the mobile phase of CCC, an acidic eluent was generated. Curcuminoids are in the keto form at pH = 3–7 [16,24] and have relatively low polarity [23]. In acidic condition, the polarity of curcuminoids is low, and their solubility in MeCN is greater. Accordingly, curcuminoids were quantitively detected to be present in the first four extracts, i.e. 1st–4th fractions (Table 2), indicating that curcuminoids were successfully eluted with MeCN/0.1% HOAc (v/v) as the first mobile phase in acidic condition.

When the second mobile phase of H_2O/0.1% HOAc (v/v) was eluted, some curcuminoids were observed in the 5th–8th fractions for CCCA–H_2O (1:1:18). However, for CCMA–H_2O (1:1:18), no curcuminoids were observed in the 8th fraction, and relatively low curcuminoid content was found in the 7th fraction (Table 2). This is presumably because CA has three carbonyl groups (pKa_1 = 3.13, pKa_2 = 4.76, and pKa_3 = 6.39), whereas MA only has two carbonyl groups (pKa_1 = 3.40 and pKa_2 = 5.20); consequently, curcuminoids would form more hydrogen bonds with CCCA–H_2O than with CCMA-H_2O. Therefore, more volume of the mobile phase was required to disrupt the hydrogen bonds and to remove the curcuminoids from the NADES matrix.

When IPA/0.1% HOAc (v/v) was eluted, no curcuminoids were obtained. All the curcuminoids were, presumably, already eluted out, or the content of purified curcuminoids was below both the LOD and the LOQ. From the CCCA–H_2O and CCMA–H_2O matrices, 5.19 ± 0.054 mg and 6.10 ± 0.242 mg of curcuminoids

Table 2. Amount of curcuminoids in each fraction of column chromatography purification method

Type of NADES	Fraction	Retardation Factor (R_f)*			Curcuminoids (mg)
		C	DMC	BDMC	
		0.89	0.71	0.53	
CCCA-H_2O (1:1:18)	1*	-	-	-	-
	2*	+	++	++	1.21 ± 0.004
	3*	++	++	+	1.67 ± 0.021
	4*	++	+	+	1.00 ± 0.013
	5**	+	+	-	0.17 ± 0.003
	6**	+	+	-	0.97 ± 0.011
	7**	+	-	-	0.11 ± 0.001
	8**	+	-	-	0.06 ± 0.001
	9–12***	-	-	-	-
				Total Curcuminoids (recovery)	5.19 ± 0.054 (51.9%)
CCMA-H_2O (1:1:18)	1*	-	-	-	-
	2*	+	++	++	1.40 ± 0.045
	3*	++	++	++	1.27 ± 0.031
	4*	++	++	+	1.05 ± 0.088
	5**	++	++	+	1.38 ± 0.020
	6**	+	+	-	0.95 ± 0.057
	7**	+	-	-	0.05 ± 0.001
	8**	-	-	-	-
	9–12***	-	-	-	-
				Total Curcuminoids (recovery)	6.10 ± 0.242 (61.0%)

*Eluent: MeCN/0.1% HOAc (v/v); **Eluent: H_2O/0.1% HOAc (v/v); and ***Eluent: IPA/0.1% HOAc (v/v)

were recovered, respectively, indicating that 51.9% and 61.0% of curcuminoids were recovered by the CCC purification method.

The obtained recovery of curcuminoids was higher than that reported by Kulkarni [28], in which a CCC with silica gel as a bed resin was used to purify an extract of crude curcuminoids from turmeric, *C. longa* L. A mixture of $CHCl_3$/MeOH was used as an eluent, starting with a 95:5 ratio and increasing the MeOH content to increase the polarity. The recovery of 5.6% (from 0.34 g of purified extract) was achieved.

The CCC method was previously used by Revathy to purify a crude extract of curcuminoids that was obtained after precipitating with petroleum ether in an acetone extract [29]. Silica gel was also used as a bed resin, producing 95 fractions of 40 mL each. The recovery of CUR was 84%, which was mostly purified at the initial fractions (ca. 1–31). The $CHCl_3$/MeOH mixture with different volume compositions was applied to enhance the polarity. The obtained recovery of CUR was higher because the initial extract was relatively pure and soluble in acetone, a less polar solvent. The CUR is less polar than BDMC and DMC (the two other curcuminoids in *Curcuma*) [16,23], with BDMC being the most polar [23,29]. Therefore, a high proportion of $CHCl_3$ was used at the initial stage of elution, i.e., $CHCl_3$/MeOH (19:1, v/v). In the work of Revathy [29], no polar compounds accompanied the crude extract of curcuminoids as impurities. Hence, a different separation approach based on CCC was applied, reaching higher recovery of CUR.

Heffernan [30] also applied the CCC method for the purification of curcuminoids from the remaining mother liquor of crystallization. The mixture of $CHCl_3$/MeOH was also used as a mobile phase. The pure CUR was successfully obtained when chloroform was eluted into the CCC. Upon increasing the methanol ratio in the eluent, DMC was identified in the purified extract. Finally, BDMC was obtained when the $CHCl_3$/MeOH mixture with the ratio of 7:8 (v/v) was applied [28], which further confirms the higher polarity of BDMC compared with CUR and DMC. In the reports by Revathy [29] and Heffernan [30], CUR was eluted first using a less polar solvent, and the polarity of the mobile phase was subsequently increased to elute DMC and BDMC consecutively. As in the case of Revathy [29] and Heffernan [30], in the present study, curcuminoids were first eluted using MeCN/0.1% HOAc. By increasing the polarity of the mobile phase using water and isopropanol instead of MeCN, impurities such as the NADES constituents that were retained in the column were then washed out.

Purification Using the SPE Method

Curcuminoids are expected to be retained on the C_{18} SPE cartridge because of their low polarity. In the contrary, water and the NADES constituents (CC, CA, and MA) can be expected to elute first. Therefore, the mobile phase was first used to wash out all the NADES constituents from the cartridge. Subsequently, another eluent was used to elute the target curcuminoids, which were then separated from NADES.

Initially, the cartridge was conditioned using 1.5 mL MeOH/0.05% HOAc (v/v) and 1.5 mL H_2O/0.05% HOAc (v/v) (Fig. 2(C)). Thus, the resin was in acidic condition. After 1.5 mL of sample containing 2 mg/mL of curcuminoids (S/F = 5/10, mg/mL) was loaded, curcuminoids were retained in the cartridge (Fig. 2(L)) and remained separated from the NADES impurities owing to the acidic condition. Subsequently, the washing stage was started by eluting H_2O/0.05% HOAc (v/v). As can be seen in Fig. 2(W), a partial elution of curcuminoids through the cartridge occurred (but they were not washed out) since the acidic condition of the SPE cartridge resin caused the curcuminoids to strongly bind with the cartridge. Therefore, the NADES constituents and water were eluted, whereas the less polar compounds, the curcuminoids, were retained. The hydrogen bonds between NADES and the curcuminoids were cleaved due to the dilution effect of water in the eluent.

The eluting step was then conducted by passing MeOH/MeCN (1:1, v/v). First, 1 mL of eluent was used (Fig. 2 (1^{st} E)), and the curcuminoids eluted from the SPE cartridge were collected in a vial. Then, the second and the third eluent were passed, making a total of 3 mL. All the curcuminoids were recovered when the SPE cartridge turned white (Fig. 2 (3^{rd} E)). The results of this

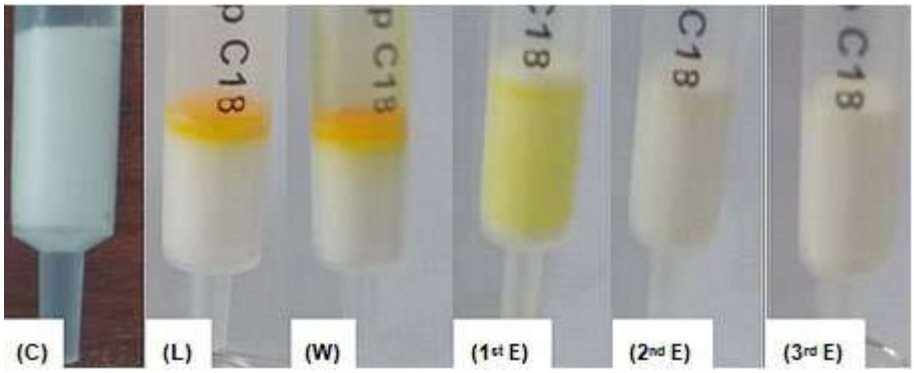

Fig 2. Images of the cartridges used in the solid phase extraction method: conditioning (C), loading (L), washing (W), and eluting (E) steps

procedure are summarized in Table 3. The first elution at the eluting step gave the highest recovery of curcuminoids. Then, the remaining curcuminoids retained in the cartridge were eluted in the other two elution steps. All the curcuminoids were thereby recovered. As can be seen from Table 3, only a small amount of curcuminoids was recovered in the third elution. The TLC chromatogram of the recovery of curcuminoids from the NADES matrices by SPE is shown in Fig. 3.

The purified curcuminoid solutions that were collected in vials were subsequently dried by passing N_2 gas. Using the present SPE method, 2.258 ± 0.017 and 2.202 ± 0.021 mg of curcuminoids were successfully recovered from CCCA–H_2O and CCMA–H_2O, respectively (Table 3). Hence, 75.27% and 73.40% recoveries of curcuminoids were obtained, which were

Table 3. The purified curcuminoids from NADES matrices using solid phase extraction (SPE)

NADES Type	Eluent	Curcuminoids (mg)[λ]
CCCA-H_2O (1:1:18)	1st	2.190 ± 0.01700
	2nd	0.060 ± 0.00040
	3rd	0.004 ± 0.00002
	Total (mg)	2.258 ± 0.01700
	(recovery)	75.27%
CCMA-H_2O (1:1:18)	1st	2.140 ± 0.0090
	2nd	0.060 ± 0.0030
	3rd	0.005 ± 0.0027
	Total (mg)	2.202 ± 0.0210
	(recovery)	73.40%

[λ] Each purification was conducted in triplicate

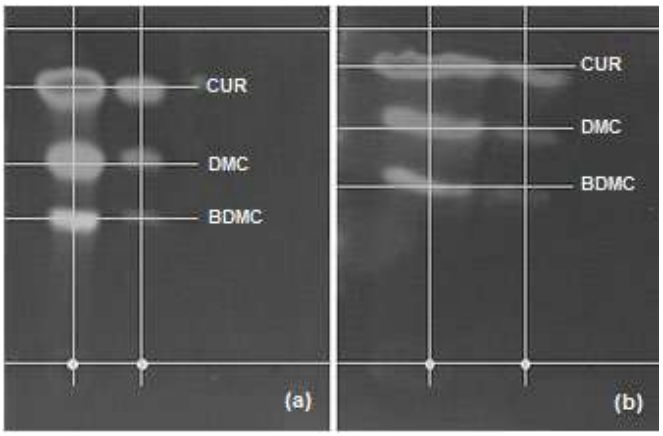

Fig 3. The TLC chromatogram of the recovered curcuminoids from NADES matrices by solid phase extraction: (a) CCCA–H_2O (1:1:18) and (b) CCMA–H_2O (1:1:18)

relatively higher than those of the CCC method. Pushpakumari et al. [31] used Diaion HP 20 resin to purify an enriched sample of curcuminoids from spent turmeric oleoresin by chromatography [31]. When 80 wt.% of MeOH was used as the eluent, CUR, DMC, and BDMC were successfully obtained in the purity of 98.4%, 97.1%, and 97.3%, respectively. Despite the high recovery and purity of curcuminoids reported by Revathy [29], Haffernan [30], and Pushpakumari [31], it should be noted that relatively pure extracts of curcuminoids were used in these experiments. Therefore, it should be mentioned that curcuminoids were able to be separated from NADES matrices for the first time in the present work.

■ CONCLUSION

The purification of the curcuminoids from NADES matrices of CCCA–H_2O (1:1:18) and CCMA–H_2O (1:1:18) was successfully conducted by CCC and SPE methods. The addition of glacial acetic acid in the mobile phase afforded a slightly acidic condition, which was conducive to enhance the curcuminoids recovery. The CCC method only yielded a recovery of curcuminoids of 51.9% and 61.0% for CCCA–H_2O and CCMA–H_2O, respectively, and higher recoveries of 75.27% and 73.40% were obtained with the SPE method. Both methods were effectively applied in laboratory scale. For large-scale application, other methods would be required.

■ REFERENCES

[1] Choi, Y.H., van Spronsen, J., Dai, Y., Verberne, M., Hollmann, F., Arends, I.W.C.E., Witkamp, G.J., and Verpoorte, R., 2011, Are natural deep eutectic solvents the missing link in understanding cellular metabolism and physiology?, *Plant Physiol.*, 156 (4), 1701–1705.

[2] Paiva, A., Craveiro, R., Aroso, I., Martins, M., Reis, R.L., and Duarte, A.R.C., 2014, Natural deep eutectic solvents – Solvents for the 21st century, *ACS Sustainable Chem. Eng.*, 2 (5), 1063–1071.

[3] Gorke, J.T., Srienc, F., and Kazlauskas, R.J., 2008, Hydrolase-catalyzed biotransformations in deep eutectic solvents, *Chem. Commun.*, 10, 1235–1237.

[4] Dai, Y., van Spronsen, J., Witkamp, G.J., Verpoorte, R., and Choi, Y.H., 2013, Natural deep eutectic solvents as new potential media for green technology, *Anal. Chim. Acta*, 766, 61–68.

[5] Dai, Y., Witkamp, G.J., Verpoorte, R., and Choi, Y.H., 2013, Natural deep eutectic solvents as new potential media for phenolic metabolites in *Carthamus tinctorius* L., *Anal. Chem.*, 85 (13), 6272–6278.

[6] Liu, Y., Li, J., Fu, R., Zhang, L., Wang, D., and Wang, S., 2019, Enhanced extraction of natural pigments from *Curcuma longa* L. using natural deep eutectic solvents, *Ind. Crops Prod.*, 140, 111620.

[7] Zullaikah, S., Rachmaniah, O., Utomo A.T., Niawati, H., and Ju, Y.H., 2018, "Green Separation of Bioactive Natural Products using Liquefied Mixture of Solids" in *Green Chemistry*, Eds. Saleh, H.E.D.M. and Koller, M., InTechOpen, London, UK.

[8] Rachmaniah, O., Fazriyah, L.J., Seftiyani, N.H., and Rachimoellah, M., 2018, Tailoring properties of acidic types of Natural Deep Eutectics Solvents (NADES): Enhanced solubility of curcuminoids from *Curcuma zedoaria*, *MATEC Web Conf.*, 156, 01011.

[9] Chanioti, S., and Tzia, C., 2018, Extraction of phenolic compounds from olive pomace by using natural deep eutectic solvents and innovative extraction techniques, *Innovative Food Sci. Emerging Technol.*, 48, 228–239.

[10] Panić, M., Radić Stojković, M., Kraljić, K., Škevin, D., Radojčić Redovniković, I., Gaurina Srček, V., and Radošević, K., 2019, Ready-to-use green polyphenolic extracts from food by-products, *Food Chem.*, 283, 628–636.

[11] Hamany, D.C.Y., Piater, L.A., Steenkamp, P.A., Madala, N.E., and Dubery, I.A., 2018, Differential extraction of phytochemicals from the multipurpose tree, *Moringa oleifera*, using green extraction solvents, *S. Afr. J. Bot.*, 115, 81–89.

[12] Ivanović, M., Alañón, M.E., Arráez-Román, D., and Segura-Carretero, A., 2018, Enhanced and green extraction of bioactive compounds from *Lippia citriodora* by tailor-made natural deep eutectic solvents, *Food Res. Int.*, 111, 67–76.

[13] Miličević, N., Panić, M., Valinger, D., Cvjetko Bubalo, M., Benković, M., Jurina, T., Gajdoš Kljusurić, J., Radojčić Redovniković, I., and Jurinjak Tušek, A., 2020, Development of continuously operated aqueous two-phase microextraction process using natural deep eutectic solvents, *Sep. Purif. Technol.*, 244, 116746.

[14] Kocaadam, B., and Şanlier, N., 2017, Curcumin, an active component of turmeric (*Curcuma longa*), and its effects on health, *Crit. Rev. Food Sci. Nutr.*, 57 (13), 2889–2895.

[15] Patra, D., and Sleem, F., 2013, A new method for pH triggered curcumin release by applying poly(L-lysine) mediated nanoparticle-congregation, *Anal. Chim. Acta*, 795, 60–68.

[16] Tønnesen, H.H., and Karlsen, J., 1985, Studies on curcumin and curcuminoids, *Z. Lebensm. Unters. Forsch.*, 180 (5), 402–404.

[17] Patil, S.S., Bhasarkar, S., and Rathod, V.K., 2019, Extraction of curcuminoids from *Curcuma longa*: Comparative study between batch extraction and novel three phase partitioning, *Prep. Biochem. Biotechnol.*, 49 (4), 407–418.

[18] Patil, S.S., Pathak, A., and Rathod, V.K., 2021, Optimization and kinetic study of ultrasound assisted deep eutectic solvent based extraction: A greener route for extraction of curcuminoids from *Curcuma longa*, *Ultrason. Sonochem.*, 70, 105267.

[19] Neves, M.I.L., Strieder, M.M., Vardanega, R., Silva, E.K., and Meireles, M.A.A., 2020, Biorefinery of turmeric (*Curcuma longa* L.) using non-thermal and clean emerging technologies: An update on the curcumin recovery step, *RSC Adv.*, 10 (1), 112–121.

[20] Kiamahalleh, M.V., Najafpour-Darzi, G., Rahimnejad, M., Moghadamnia, A.A., and Kiamahalleh, M.V., 2016, High performance curcumin subcritical water extraction from turmeric (*Curcuma longa* L.), *J. Chromatogr. B*, 1022, 191–198.

[21] Osorio-Tobón, J.F., Carvalho, P.I.N., Rostagno, M.A., and Meireles, M.A.A., 2016, Process integration for turmeric products extraction using supercritical fluids and pressurized liquids: Economic evaluation, *Food Bioprod. Process.*, 98, 227–235.

[22] Yuwono, M., and Indrayanto, G., 2005, Validation of chromatographic methods of analysis. In profiles of drug substances, *Profiles Drug Subst., Excipients, Relat. Method.*, 32, 243–259.

[23] Fagundes, T.S.F., Dutra, K.D.B., Ribeiro, C.M.R., Epifanio, R.A., and Valverde, A.L., 2015, Using a Sequence of experiments with turmeric pigments from food to teach extraction, distillation, and thin layer chromatography to introductory organic chemistry students, *J. Chem. Educ.*, 93 (2), 326–329.

[24] Nugroho, A.E., Yuniarti, N., Istyastono, E.P., Supardjan, S., and Hakim, L., 2006, Determination of antioxidant activity of dehydro-zingerone through hydroxyl radical scavengers using deoxyribose method, *Indones. J. Pharm.*, 17 (3), 116–122.

[25] Istyastono, E.P., Martono, S., Pranowo, H.D., and Tahir, I., 2003, Quantitative structure activity relationship analysis of curcumin and its derivate as GST inhibitors bases on computational chemistry calculation, *Indones. J. Chem.*, 3 (3), 179–186.

[26] Rachmaniah, O., Muhsin, M.R., Widya, A.P., and Rachimoellah, M., 2020, Process development for the enrichment of curcuminoids in the extract of ionic type of NADES, *IOP Conf. Ser.: Mater. Sci. Eng.*, 732, 012005.

[27] Yadav, D., and Kumar, N., 2014, Nanonization of curcumin by antisolvent precipitation: Process development, characterization, freeze drying and stability performance, *Int. J. Pharm.*, 477 (1-2), 564–577.

[28] Kulkarni, S.J., Maske, K.N., Budre, M.P., and Mahajan, R.P., 2017, Extraction and purification of curcuminoids from turmeric (*Curcuma longa* L.), *Int. J. Pharmacol. Pharm. Technol.*, 1 (2), 81–84.

[29] Revathy, S., Elumalai, S., Benny, M., and Antony, B., 2011, Isolation, purification and identification of curcuminoids from turmeric (*Curcuma longa* L.) by column chromatography, *J. Exp. Sci.*, 2 (7), 21–25.

[30] Heffernan, C., Ukrainczyk, M., Gamidi, R.K., Hodnett, B.K., and Rasmuson, Å.C., 2017, Extraction and purification of curcuminoids from crude curcumin by a combination of crystallization and chromatography, *Org. Process Res. Dev.*, 21 (6), 821–826.

[31] Pushpakumari, K.N., Varghese, N., and Kottol, K., 2014, Purification and separation of individual curcuminoids from spent turmeric oleoresin, a by-product from curcumin production industry, *Int. J. Pharm. Sci. Res.*, 5 (8), 3246–3254.

Synthesis of Graphite Paste/Molecularly Imprinted Polymer (MIP) Electrodes Based on Polyeugenol as a Glucose Sensor with Potentiometric Method

Muhammad Cholid Djunaidi[1*], Mei Dian Risda Afriani[1], Gunawan[1], and Miratul Khasanah[2]

[1]*Department of Chemistry, Faculty of Science and Mathematics, Diponegoro University, Jl. Prof. Soedharto SH, Tembalang, Semarang 50275, Indonesia*

[2]*Department of Chemistry, Faculty of Science and Technology, Universitas Airlangga, Campus C, Jl. Dr. Ir. H. Soekarno (MERR), Surabaya 60115, Indonesia*

* ***Corresponding author:***

email: choliddjunaidi@live.undip.ac.id

Received: August 23, 2020
Accepted: April 4, 2021

DOI: 10.22146/ijc.58964

Abstract: *Diabetes mellitus is a chronic disease in which the body is unable to metabolize carbohydrates, fats, and proteins. In this study, eugenol was polymerized and then contacted with glucose and crosslinked using polyethylene glycol diglycidyl ether (PEGDE). The resulted PE-Glucose-PEGDE was eluted using ethanol to form MIP-Glucose. It was then characterized by FTIR, SEM, electrodes using the Eutech 510 potentiostat and UV-Vis spectrophotometer. The result of polyeugenol synthesis is a reddish-brown powder with a yield of 99.90% and a molecular weight of 6318.033 g/mol. UV-Vis spectrophotometer analysis showed that the contacted glucose was 2152.505 ppm. SEM results showed differences in the surface morphology of the material, indicating the formation of cavities in MIP and ESM, while no cavities are found in NIP and ESN. The electrode optimization resulted in the best composition ratio of MIP 1 mol: paraffin: graphite, respectively of 20:35:45. The resulting electrode has a Nernst factor of 20.24 mV/decade with a measurement range of 10^{-5}–10^{-1} M, a limit of detection value of 8.363 × 10^{-5} M, and the value of the selectivity coefficient (K_{ij}) of the electrodes in a (10^{-5}–10^{-1}) M fructose solution was 0.3733; 0.23048; 0.17864; 0.12359; 0.1073.*

Keywords: *polyeugenol; imprinted polymer; electrode; glucose; potentiometry*

■ INTRODUCTION

Diabetes mellitus is a chronic disease in which the body is not able to metabolize carbohydrates, fats, and proteins. This is caused by the increase of the glucose level in the blood due to a very progressive decrease in insulin secretion. Blood glucose is the simplest form of carbohydrates that is adsorbed into the blood fluids through digestion. Blood glucose levels are monitored by the pancreas and regulated directly by insulin with normal limits of 70–140 mg/dl.

Determination of glucose levels has been carried out, including the Nelson-Somogyi method with spectrophotometry which is based on the formation of brick-red complex compounds from the reaction between glucose and complex reagents [1]. However, this method has a weakness; it is less selective because reagents can give a positive response to reducing other compounds than glucose, such as fructose and galactose. In 2018, Ratnayani et al. [2] analyzed glucose and fructose in cottonwood honey samples using the HPLC method. This method shows more specific results and has higher selectivity than other methods in determining glucose and fructose, but the operational costs are also quite high.

An alternative method that can be used is the potentiometric electrode. Potentiometry is a sample analysis based on the measurement of cell potential at zero current [3]. Previous research has used the potentiometric method to analyze urea and creatinine [4-5]. In potentiometry, there are two types of electrodes, the working electrodes and reference electrodes. The working electrode has a function as a sensor for the compound that is being analyzed [6]. Making the working electrodes in determining the type of sample is very important because it can produce

sensor components as an accurate and selective analysis instrument. This electrode is based on molecularly imprinted polymer (MIP), where this polymerization technique is formed from functional monomers, templates, solvents, initiators, and crosslinker agents that react around the template molecules [7-8]. MIP has high selectivity, good mechanical strength, and good resistance to acids, alkalis, organic solvents, high pressure, and temperature.

Eugenol is a nonpolar organic compound and is found in almost 80% of all plants in Indonesia. Eugenol has three functional groups that are bound to its structure, namely allyl, hydroxyl, and methoxy groups. Allyl groups can be polymerized into polyeugenol, and hydroxyl groups can be synthesized into new compounds that have groups with a greater reactivity level, such as carboxylates and esters [9]. Research conducted by Djunaidi and Astuti regarding MIP-glucose using polyeugenol as a polymer and PEGDE as a MIP crosslink showed good resistance to organic solvents and inorganic acids [10]. The resulting MIP also showed good selectivity to glucose compared to non-imprinted polymer (NIP) by not absorbing fructose even in simultaneous solutions.

The advantage of using the potentiometric analysis method is the existence of a working electrode that is simple and easy to operate because it uses relatively cheap equipment that is a potentiometer (mV meter). The purpose of this study was to synthesize glucose sensor electrodes and determine the optimum composition of the electrode synthesized polyeugenol-based graphite paste/MIP as a potentiometric glucose sensor and determine the Nernst factor, measurement range, detection limit, and coefficient of selectivity on the glucose sensor.

In this study, the synthesis of MIP was done with eugenol as a monomer, polyethylene glycol diglycidyl ether (PEGDE) as a crosslinking agent, 1 M NaOH as a catalyst, and a graphite electrode which has the ability to conduct current. The MIP modified graphite electrode is expected to improve the performance of the potentiometric sensor in determining glucose, including the Nernst factor, measurement range, detection limit, and selectivity coefficient, so that the formed electrode could provide excellence in glucose analysis.

■ EXPERIMENTAL SECTION

Materials

The materials used in this research were eugenol p.a, $BF_3O(C_2H_5)$, polyethylene glycol diglycidyl ether (PEGDE), D-Glucose, and L-Fructose from SIGMA Aldrich, chloroform p.a, Methanol p.a, anhydrous Na_2SO_4, paraffin, graphite, NaOH, KNa-tartrate, 3,5-dinitrosalcylic acid, phenol, Na_2SO_3, ethanol, Na_2HPO_4, NaH_2PO_4, CH_3COOH, CH_3COONa from Merck, Germany, aquabidest from Bratachem, and Ag wire.

Instrumentation

The tools and instruments used in this research were laboratory glass equipment (Herma and Pyrex), reflux Set, 100 mesh sieve, pestle and mortar, analytical scales (Ohaus), magnetic bar, hotplate stirrer (LabTech CO.LTD), pH paper, micropipette tip, oven (Kirin), FTIR (Shimadzu Prestige 21), potentiostats (Eutech 510), UV-Vis spectrophotometer (LW-V- 200-RS), Ubbelohde viscometer, and SEM-EDX (Phenom Pro X Desktop with EDX).

Procedure

Synthesis of polyeugenol

A total of 5.8 g of eugenol in a three-neck flask was added with 0.25 mL of BF_3-diethyl ether for every 1 h until 1 mL was added, while the mixture was stirred. After 16 h, the polymerization reaction was stopped by adding 1 mL of methanol. The gel formed was dissolved with 30 mL of chloroform and washed with aquabidest until it reached neutral pH. The solution was dried by adding anhydrous Na_2SO_4 and then evaporated at room temperature. The precipitate formed was dried, weighed, and analyzed by FTIR.

Polyeugenol contacting with glucose

The synthesized polyeugenol was contacted with glucose to make glucose imprinted polymer (glucose template). It was carried out by adding 0.5 g of polyeugenol to 10 mL of glucose solution with a concentration of 7500 ppm and then stirred for 6 h. It was then filtered, dried, and characterized using FTIR.

Synthesis of molecularly imprinted polymer (MIP)-glucose

As much as 0.3 g of polyeugenol-glucose in a three-neck flask were added with 0.96 g of PEGDE and 20 mL of 1 M NaOH, then refluxed to a temperature of 80–90 °C for 15 min, and dried in an oven at 115 °C for 6 h. Then, it was sieved with a 100 Mesh pass sieve. 0.2 g of polyeugenol-glucose-PEGDE was washed with ethanol for 24 h and then characterized by FTIR and SEM-EDX [10].

Synthesis of non-imprinted polymer (NIP)

In a three-neck flask, as much as 0.3 g of polyeugenol were added with 0.96 g of PEGDE, 20 mL of 1 M NaOH. The mixture was refluxed to a temperature of 80–90 °C for 15 min and dried in an oven at 115 °C for 6 h. It was then sieved through a 100 mesh sieve. Then, 0.2 g of polyeugenol-glucose-PEGDE was washed with ethanol for 24 h and characterized by FTIR and SEM-EDX.

Synthesis of active graphite

Active graphite is prepared chemically using NaOH as an activator. Graphite was immersed in 0.5% NaOH and then let still at room temperature for 24 h. After that, it was filtered and heated in an oven at 105 °C for 3 h. This active graphite is used as a carbon paste electrode material.

Synthesis of graphite paste/MIP-glucose electrode

The working electrode for glucose analysis was prepared by filling ¾ of the micropipette tube with molten solid paraffin. Previously, the silver wire that was used to connect the electrodes with the potentiometer was sanded and then inserted into the micropipette tube. Next, the remaining part of the micropipette tube is filled with a mixture of solid paraffin, graphite, and MIP that has been heated to form a paste. Tube filling was carried out by pressing so that the tube is completely filled with material, then the end of the electrode surface is rubbed using HVS paper. This process is summarized as in Fig. 1.

Characterization of graphite paste/MIP electrode

The characterization carried out included functional group analysis using FTIR, surface morphology analysis using SEM, calculating the potential value using the Eutech 510 potentiostat and the reference electrode, Ag/AgCl.

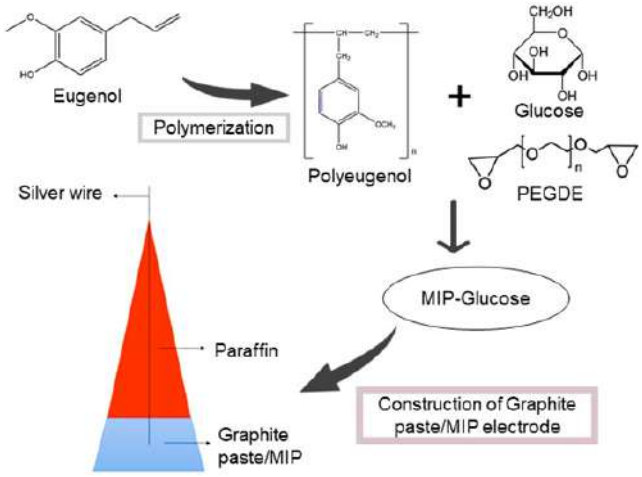

Fig 1. Graphite paste/MIP electrode synthesis

■ RESULTS AND DISCUSSION

Preliminary analysis studies prior to electrode selectivity included analysis of eugenol polymerization result using FTIR, polyeugenol molecular weight measurements, and UV-Vis spectrophotometry analysis. The result of polymerization of eugenol is in the form of orange polyeugenol powder with a yield of 99.90% and a molecular weight of 6318.033 g/mol, which was determined by the viscosity method using the Ubbelohde viscometer. Furthermore, FTIR analysis was carried out to determine the differences in groups between eugenol and the synthesized polyeugenol; the result can be seen in Fig. 2 and Table 1.

Furthermore, the resulting polyeugenol was subjected to contact with glucose and crosslinked with polyethylene glycol diglycidyl ether, and the results of MIP-Glucose were analyzed using a UV-VIS spectrophotometer, and the results from the duplo test showed that the glucose adsorbed on the polyeugenol was 34.70%. After that, the MIP that had been eluted with ethanol solvent was removed, filtered then the residue was analyzed using a UV-Vis spectrophotometer, and the results from the duplo test showed that the glucose released in MIP was 96.94%. The results of the FTIR analysis were aimed at seeing the differences in groups and peaks that appeared on polyeugenol-glucose-PEGDE, MIP, NIP, ESM, and ESN. The FTIR result can be seen in Fig. 3.

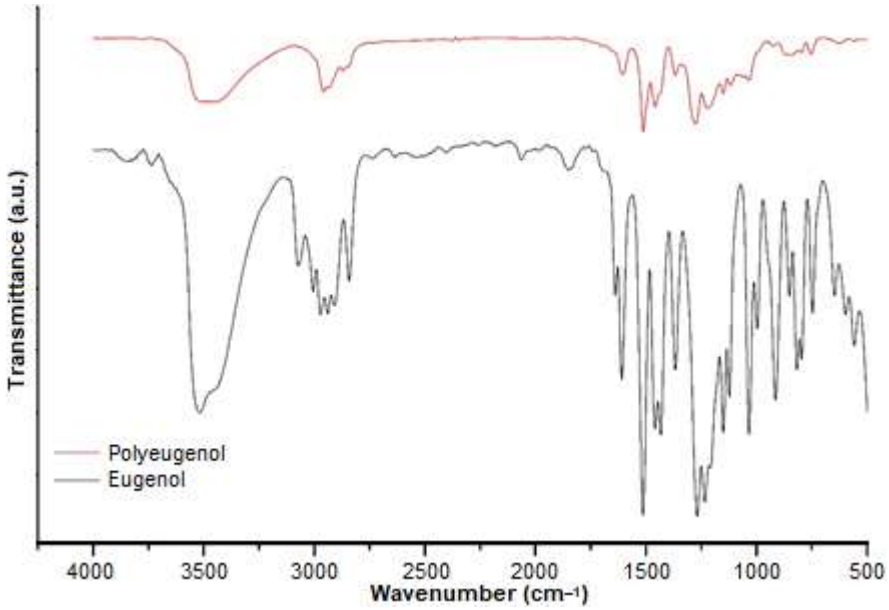

Fig 2. Graph of FTIR comparisons of eugenol and polyeugenol

Table 1. FTIR comparisons of eugenol and polyeugenol

Absorbance (cm^{-1})	Functional groups characteristic	Eugenol	Polyeugenol
3514.7	Hydroxyl (O–H)	Presence	Presence
2932	Saturated Carbon (C–C)	Presence	Presence
1509 and 1603.08	Aromatic (C=C)	Presence	Presence
1432.53	Methylene (–CH_2–)	Presence	Presence
1620 and 1630	Allyl (C=C)	Presence	Not presence
995 and 910	Vinyl (CH=CH_2)	Presence	Not presence
873.74	Substituted Aromatic	Presence	Presence

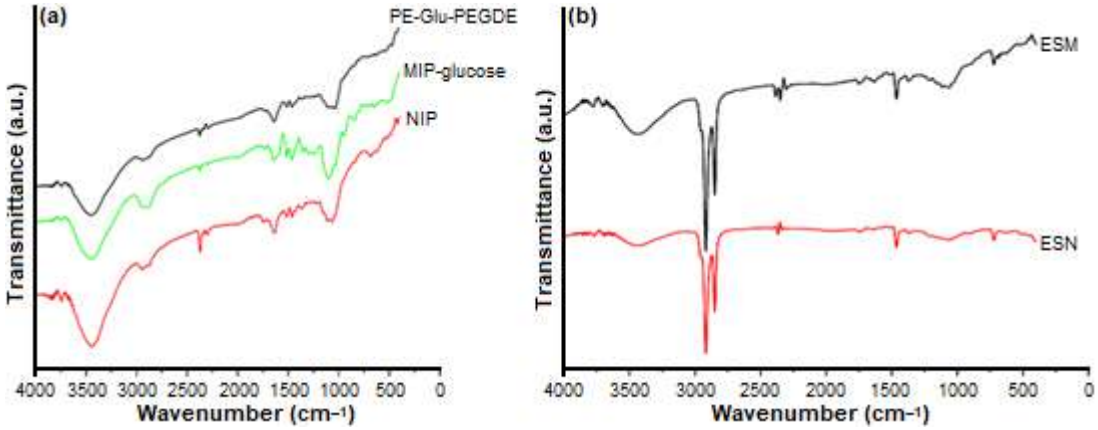

Fig 3. FTIR comparisons of (a) MIP and NIP (b) ESM and ESN

SEM-EDX analysis in Fig. 4 showed the morphological differences between MIP and NIP. In MIP, a cavity which is the template of glucose compounds are formed, while in NIP, the surface tends to be flat, no cavities are visible, and no template of glucose compounds is formed. The EDX analysis results were used to determine the elemental composition of C and O from MIP and NIP (Table 2), where the mass composition of

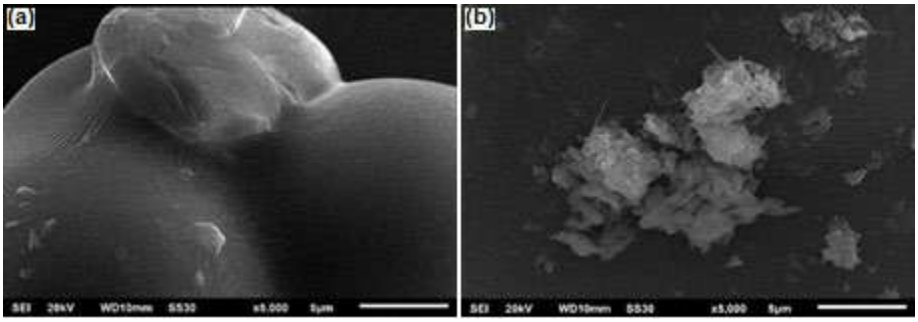

Fig 4. SEM results of (a) NIP (b) IP

C and O in MIP and NIP showed different results. In MIP, the mass of element O is greater than that of NIP. This is possible because there is no real difference because the glucose in MIP has been released.

Synthesis of the electrode was done by mixing MIP, active graphite, and paraffin with composition variation (% mass) and pH variation. Based on Tables 3, 4, and 5, the electrodes that produce a good Nernst factor are the E5 electrodes, and the optimum pH is pH 7 with a Nernst factor of 20.24 mV/decade. E5 also shows a linearity value that is close to 1, which is 0.9996. So, E5 is suitable for use in glucose analysis in this study.

The standard curve of glucose is obtained from measuring glucose solution 10^{-8} M to 10^{-1} M at the optimum pH of 7 using a graphite-MIP paste electrode. Measurements were done potentiometrically with an Ag/AgCl comparison electrode. The potential data obtained can be seen in Table 6.

Table 2. Element mass percentage in MIP and NIP

Element	Mass (%)	
	MIP	NIP
C	63.51	65.31
O	35.02	29.46
Cl	1.24	1.31
Ca	0.23	0.22
Al	-	0.90
Cu	-	2.79

Table 3. Factor Nernst data and measurement range in pH 3

Electrode Code	Composition (wt.%)			Nernst Factor	Measurement	Linearity
	MIP	Carbon	Paraffin	(mV/decade)	Range (M)	(r)
E1	0	65	35	-14.3	10^{-8}–10^{-5}	0.9531
E2	5	60	35	-11	10^{-6}–10^{-3}	0.9853
E3	10	55	35	-8.62	10^{-6}–10^{-2}	0.9866
E4	15	50	35	-5.17	10^{-4}–10^{-1}	0.9887
E5	20	45	35	-2.9	10^{-7}–10^{-4}	0.9397
E6	25	40	35	-3.9171	10^{-7}–10^{-2}	0.9606

Table 4. Factor Nernst data and measurement range in pH 5

Electrode Code	Composition (wt.%)			Nernst Factor	Measurement	Linearity
	MIP	Carbon	Paraffin	(mV/decade)	Range (M)	(r)
E1	0	65	35	-19.7	10^{-4}–10^{-1}	0.7741
E2	5	60	35	-4.7	10^{-5}–10^{-2}	0.9625
E3	10	55	35	-4.7143	10^{-6}–10^{-1}	0.9198
E4	15	50	35	-4.75	10^{-7}–10^{-1}	0.9784
E5	20	45	35	-3.4	10^{-4}–10^{-1}	0.9966
E6	25	40	35	-6.8	10^{-6}–10^{-2}	0.9739

Table 5. Factor Nernst data and measurement range in pH 7

Electrode Code	Composition (wt%)			Nernst Factor	Measurement	Linearity
	MIP	Carbon	Paraffin	(mV/decade)	Range (M)	(r)
E1	0	65	35	9.49	10^{-5}–10^{-1}	0.8143
E2	5	60	35	2.9393	10^{-8}–10^{-2}	0.6572
E3	10	55	35	13.09	10^{-8}–10^{-4}	0.9668
E4	15	50	35	4.1	10^{-7}–10^{-4}	0.9689
E5	20	45	35	20.24	10^{-5}–10^{-1}	0.9996
E6	25	40	35	9.0357	10^{-7}–10^{-1}	0.9404

Based on the potential data obtained, a standard glucose curve was made with the log glucose concentration as the x-axis and the potential as the y-axis. The curve of the relationship between the log of glucose concentration and potential (mV) can be seen in Fig. 5. Furthermore, the concentration range curve that gives a linear line is called the standard curve of glucose solutions that were used to find out the equation of the line that shows the value of the Nernst factor as in Fig. 6.

Result of Determination of Measurement Range

The measurement range is the concentration range that produces a linear potential response, and the value of the Nernst factor is close to theoretical. Determination of the measurement range is carried out on all electrodes, namely E1-E6. From the measurement results of the measurement range of the graphite-MIP paste electrode, which can be seen in Table 5, the electrode that has a Nernst factor close to the theoretical value is E5, namely 20.24 mV/decade, and the measurement range is (10^{-5}–10^{-1}) M.

Result of Determination of Detection Limits

The detection limit is the lowest concentration limit that an electrode can respond to [11]. The detection limit is determined from the intersection of linear lines with non-linear lines on the glucose standard curve [12]. The linear line equation is y = 20.24x + 252.86 while the non-linear line y = $8.3x^2$ + 96.3x + 425. The results of the detection limit measurement on the graphite-MIP paste electrode are shown in Fig. 7.

Table 6. The results of the measurement of the graphite-MIP paste electrode potential at pH 7

Log [Glucose]	Potential (mV)
-8	140
-7	142
-6	146
-5	151
-4	172.6
-3	192.1
-2	213
-1	232

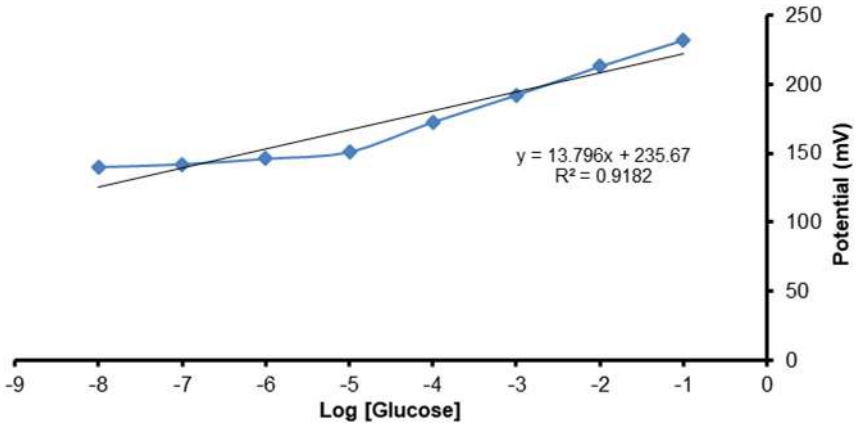

Fig 5. The correlation curve between log [Glucose] and potential (mV)

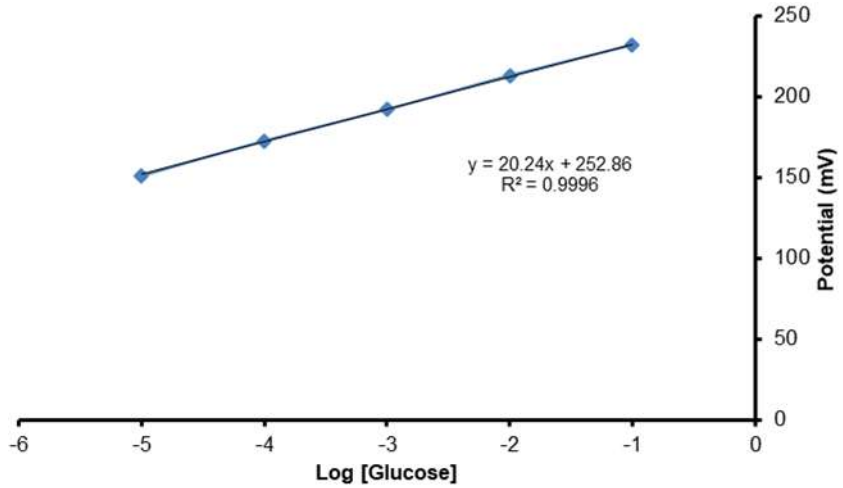

Fig 6. Standard curve of Glucose solution

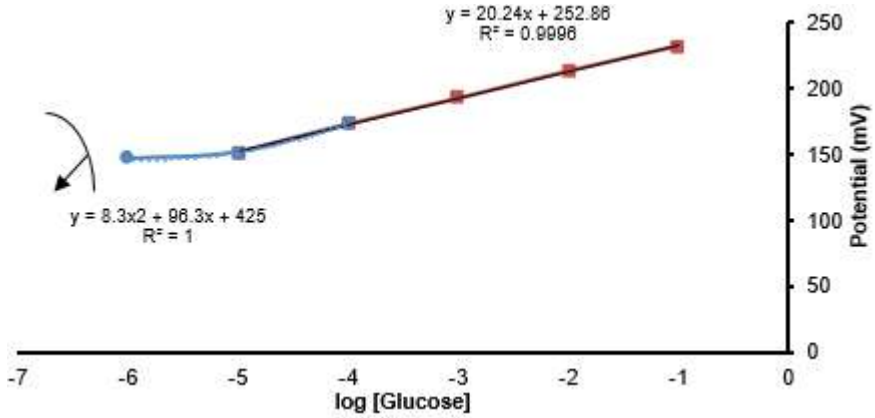

Fig 7. Detection limit measurement curve

The detection limit on the graphite-MIP paste electrode is 8.363×10^{-5} M, which means that the electrode is theoretically able to detect the presence of glucose up to a concentration of 8.363×10^{-5} M with the Nernst factor, which still meets the theoretical value. The detection limit produced by the graphite-MIP paste electrode can be used for glucose analysis in blood serum with a normal concentration of 70–110 mg/dL or the equivalent of 3.88×10^{-3}–6.10×10^{-3} M, while the glucose concentration of patients with diabetes mellitus exceeds 200 mg/dL or equivalent to 1.11×10^{-2} M. The calculation of detection limits is determined from the intersection of the linear lines with the non-linear lines on the glucose standard curve [12]. The linear line equation is y = 20.24x + 252.86 while the non-linear line is $y = 8.3x^2 + 96.3x + 425$, produces a limit of detection (LOD) capable of detecting the presence of glucose up to a concentration of 8.363×10^{-5} M. Some comparisons of the LOD result by our work and previous research is reported in Table 7.

The glucose sensor works because of a redox reaction in the electrode system where the detected glucose undergoes a half-redox reaction. At the electrode, a potential difference appears because there is a redox reaction in glucose, namely the oxidation of glucose, while the reduction occurs at the electrode. Glucose oxidation will release H^+ which is then captured as a sensor because the electrode functions as an H^+ (acid) sensor.

Electrode selectivity for glucose analysis in this study was studied using the match potential method (MPM). The value of the selectivity coefficient (K_{ij}) of the electrodes in a 10^{-5}–10^{-1} M fructose solution was 0.3733; 0.23048; 0.17864; 0.12359; 0.1073. A selectivity test was carried out with fructose because fructose has the

Table 7. Comparison data of the LOD of our work with the previous reports

Method	Electrode Material	Linear range (M)	LOD (M)	Reference
Amperometry	Carbon paste/GOx silica	5×10^{-4}–9×10^{-3}	1.5×10^{-4}	[13]
Amperometry	Carbon paste/selenium nanoparticle-mesoporous silica composite (MCM-41)	1×10^{-5}–2×10^{-3}	1×10^{-4}	[14]
Potentiometry	Poly (terthiophene benzoic acid) (pTBA) layered-AuZn alloy oxide (AuZnOx)	1.6×10^{-3}–2.7×10^{-2}	9.6×10^{-4}	[15]
Potentiometry	Poly (3-aminophenyl boronic acid-co-3-octylthiophene)	5×10^{-3}–5×10^{-2}	5×10^{-4}	[16]
Potentiometry	Carbon nanotube on gold printed	10^{-3}–10^{-1}	1×10^{-4}	[17]
Potentiometry	Carbon paste/IZ	10^{-4}–10^{-2}	5.6×10^{-5}	[18]
Potentiometry	Carbon paste/MIP (Polyeugenol)	10^{-5}–10^{-1}	8.363×10^{-5}	This work

most similar structure to glucose. If the sugars have structures that are so different from glucose, they are not detected by the glucose sensor. Based on the K_{ij} value data, it can be concluded that the presence of fructose does not interfere with the potentiometric analysis of glucose using a graphite-MIP paste electrode because the resulting selectivity coefficient is less than one. If the K_{ij} value is less than 1 then, the electrode is selective to the analyte being measured rather than the disruptor compound, and if the K_{ij} value is bigger than 1, the electrode is selective to the disruptor compound than the measured analyte. If $K_{ij} = 0$, then the foreign compound does not interfere [19-20].

■ CONCLUSION

The optimum composition of graphite, MIP on the electrode using the mass ratio of graphite, paraffin, MIP is 45:35:20 (wt.%) with the optimum pH of the solution is pH 7 (with buffer settings). Potentiometric analysis of glucose using graphite-MIP paste electrodes resulted in a measurement range of 10^{-5}–10^{-1} M, and the Nernst factor of 20.24 mV/decade. The optimum electrode produced has a detection limit of 8.363×10^{-5} M. This electrode has a fairly good selectivity value, which is less than 1.

■ REFERENCES

[1] Shao, Y., and Lin, A.H.M., 2018, Improvement in the quantification of reducing sugars by miniaturizing the Somogyi-Nelson assay using a microtiter plate, *Food Chem.*, 240, 898–903.

[2] Ratnayani, K. Dwi Adhi S., N.M.A., and Gitadewi, I. G.A.M.A.S., 2008, Penentuan kadar glukosa dan fruktosa pada madu randu dan madu kelengkeng dengan metode kromatografi cair kinerja tinggi, *Jurnal Kimia,* 2 (2), 77–86.

[3] Skoog, D.A., West, D.M., Holler, F.J., and Crouch, S.R., 2013, *Fundamentals of Analytical Chemistry*, 9th Ed., Cengage Learning, Boston, MA.

[4] Liu, Y., Cánovas, R., Crespo, G.A., and Cuartero, M., 2020, Thin-layer potentiometry for creatinine detection in undiluted human urine using ion-exchange membranes as barriers for charged interferences, *Anal. Chem.*, 92 (4), 3315–3323.

[5] Lai, C.Y., Foot, P.J.S., Brown, J.W., and Spearman, P., 2017, Urea potentiometric biosensor based on a thiophene copolymer, *Biosensors*, 7 (1), 13.

[6] Kawahara, R., Sahatiya, P., Badhulika, S., and Uno, S., 2018, Paper-based potentiometric pH sensor using carbon electrode drawn by pencil, *Jpn. J. Appl. Phys.*, 57 (4S), 04FM08.

[7] BelBruno, J.J., 2018, Molecularly imprinted polymers, *Chem. Rev.*, 119, 94–119.

[8] Saylan, Y., Akgönüllü, S., Yavuz, H., Ünal, S., and Denizli, A., 2019, Molecularly imprinted polymer based sensors for medical applications, *Sensors*, 19 (6), 1279.

[9] Djunaidi, M.C., Khabibi, and Ulumuddin, I., 2017, Separation of Cu^{2+}, Cd^{2+}, and Cr^{3+} in a mixture solution using a novel carrier poly(methyl thiazoleethyl eugenoxy acetate) with BLM (bulk liquid membrane), *IOP Conf. Ser.: Mater. Sci. Eng.*, 172, 012032.

[10] Djunaidi, M.C., and Astuti, Y., 2019, Synthesis, characterization and selectivity of molecularly

imprinted polymer (MIP) glucose using polyeugenol as a functional polymer, *Rasayan J. Chem.*, 12 (2), 809–821.

[11] Dinh, T.V., Choi, I.Y., Son, Y.S., and Kim, J.C., 2016, A review on non-dispersive infrared gas sensors: Improvement of sensor detection limit and interference correction, *Sens. Actuators, B*, 231, 529–538.

[12] Puspitasari, H.I., 2012, Pembuatan dan karakterisasi elektroda selektif berbasis karbon nanopori/molecularly imprinted polymer untuk analisis glukosa dalam madu, *Undergraduate Thesis*, Department of Chemistry, Universitas Airlangga, Surabaya.

[13] Jędrzak, A., Rębiś, T., Klapiszewski, L., Zdarta, J., Milczarek, G., and Jesionowski, T., 2018, Carbon paste electrode based on functional GOx/silica-lignin system to prepare an amperometric glucose biosensor, *Sens. Actuators, B*, 256, 176–185.

[14] Yusan, S., Rahman, M.M., Mohamad, N., Arrif, T.M., Latif, A.Z.A., Mohd Aznan, M.A., and Wan Nik, W.S.B., 2018, Development of an amperometric glucose biosensor based on the immobilization of glucose oxidase on the Se-MCM-41 mesoporous composite, *J. Anal. Methods Chem.*, 2018, 2687341.

[15] Kim, D.M., Cho, S.J., Cho, C.H., Kim, K.B., Kim, M.Y., and Shim, Y.B., 2016, Disposable all-solid-state pH and glucose sensors based on conductive polymer covered hierarchical AuZn oxide, *Biosens. Bioelectron.*, 79, 165–172.

[16] Çiftçi, H., Tamer, U., Teker, M.Ş., and Pekmez, N.Ö., 2013, An enzyme free potentiometric detection of glucose based on a conducting polymer poly (3-aminophenyl boronic acid-co-3-octylthiophene), *Electrochim. Acta*, 90, 358–365.

[17] Alhans, R.A., Singh, A., Singhal, C., Narang, J., Wadhwa, S., and Mathur, A., 2018, Comparative analysis of single-walled and multi-walled carbon nanotubes for electrochemical sensing of glucose on gold printed circuit boards, *Mater. Sci. Eng., C*, 90, 273–279.

[18] Khasanah, M., Widati, A.A., Handajani, U.S., Harsini, M., Ilmiah, B., and Oktavia, I.D., 2020, Imprinted zeolite modified carbon paste electrode as a selective sensor for blood glucose analysis by potentiometry, *Indones. J. Chem.*, 20 (6), 1301–1310.

[19] Cattrall, R.W., 1997, *Chemical Sensors,* Oxford University Press, New York.

[20] Aulia, M.S., Abdurrahman, M., and Putrada, A.G., 2019, Pendeteksian kadar glukosa dalam darah pada gejala diabetes tipe 1 menggunakan algoritma K-Nearest Neighbor dengan metode nafas, *SMARTICS*, 5 (1), 14–21.

Ionic Surfactant Enhancement of Clay Properties for Heavy Metals Adsorption: Kinetics and Isotherms

Adekeye Damilola Kayode[1*], Asaolu Samuel Sunday[1], Adefemi Samuel Oluyemi[1], Ibigbami Olayinka Abidemi[1], Akinsola Abiodun Folasade[2], Awoniyi Marcus Gbolahan[3], and Popoola Olugbenga Kayode[1]

[1]*Department of Chemistry, Ekiti State University, Ado-Ekiti, Nigeria*

[2]*Department of Industrial Chemistry, Ekiti State University, Ado-Ekiti, Nigeria*

[3]*Department of Biosciences, University of Nottingham, Nottingham, United Kingdom*

Corresponding author:

email: damilola293@gmail.com

Received: September 4, 2020
Accepted: March 19, 2021

DOI: 10.22146/ijc.59480

Abstract: *The global health problems arising from ingesting toxic metals necessitate the quest for developing efficient materials for their remediation. Surface properties of raw kaolinite clay collected from Ire-Ekiti, South-western Nigeria, were improved by modification using sodium dodecyl sulphate (SDS) for the adsorptive removal of Pb, Cr, Ni and Cu from their respective aqueous solution. The raw and modified clays were characterized by X-ray fluorescence, Fourier transformed infrared spectrometry, Scanning electron microscope coupled with EDX and Particle induced x-ray emission technique. A batch adsorption study was used to examine the performance efficiency of the modified clay. Optimization of adsorption conditions like temperature, particle size, concentration, agitation time and pH was performed. The clay after modification showed improved surface properties such as increased pore diameter and number. Freundlich, Langmuir and Temkin isotherm models were applied to explicate the adsorption processes, while Pseudo-First order, Pseudo-Second order and the Elovich kinetic models were used to predict possible mechanisms driving the adsorption processes. The adsorption processes driven by chemical mechanisms involved series of complex mechanisms that include ion exchange, direct bonding and surface complexation other than precipitation. The percentage removal of the metals by the modified clay soil reached the values of 98.53, 94.50, 73.82, and 80.40 for Pb, Cu, Ni and Cr.*

Keywords: *kaolinite clay; heavy metals; clay modification; adsorption kinetics; adsorption isotherms*

■ INTRODUCTION

Environmental pollutants and their toxicity cause a major problem in the world. Water pollution is one of the biggest environmental issues causing serious problems to aquatic organisms and humans. Water bodies are majorly polluted by different industrial activities, including agrochemical production, dyeing, battery production, printing, mining, metallurgical engineering, electroplating, paint and pigment production, nuclear power operations, and electric appliances manufacturing, semiconductor production, cosmetics etc. [1-2]. The industries carrying out these operations generate various types of heavy metal pollutants in wastewater effluent. Heavy metals like chromium, nickel, cobalt, lead, arsenate and cadmium etc., in the aquatic environment, have been known to cause various health problems like chronic bronchitis, kidney problems, high blood pressure, reduced lung function, cancer of the lungs, intestinal cancer and fetal mortality [3-5].

To regulate the uncontrollable discharge of these heavy metals in wastewater, novel and recent water treatment technologies are being proposed globally. Several techniques like chemical precipitation, biological method, electrodialysis, ion exchange, electrochemical treatment and membrane filtration technologies, etc.,

have been used to remove hazardous pollutants [6-11]. The adsorption process is another suitable technique for heavy metal remediation in wastewater because of its significant advantages like low-cost, availability, profitability, ease of operation, high efficiency, and effectiveness over the other techniques [11-12].

Clays proposed as adsorption materials fulfill all requirements for low-cost chemical precursors for industrial applications [13-16]. Clays contain exchangeable cations and anions held to the surface [17-18]. The uptake of heavy metals by clay minerals involves a series of complex adsorption mechanisms such as direct bonding between metal cations with the surface of clay minerals, surface complexation, and ion exchange etc. [19]. In many studies, surface modification is required to enhance the adsorption capacity of clays in order to increase metal uptake [20]. Surface modification enhances the surface area, pore diameter, and the number of present active sites on the surface [21]. Several researches have shown that modified clay is a promising low-cost technology for efficient and effective removal of metals like Pb, Ni, Cr and Cu contaminated water [21-24].

Researches have also shown that both raw and modified clays from Nigeria could find application for the de-metallization of wastewater containing heavy metals [21,25]. A previous study by Adekeye et al. [26] showed low removal efficiency by the clay for metals like chromium and nickel. The authors recommended the improvement of the surface properties of the clay for enhanced performance efficiency. The low removal efficiency of the clay for metals like chromium and nickel immensely necessitates and motivates the quest for modification. The present study is tailored towards the surface modification of the Ire-Ekiti clay for improved heavy metals adsorption properties. It is also aimed at elucidating the kinetics to show the kind of reaction between the adsorbates and adsorbent and the isotherm to explicate the processes to which the adsorbates were adsorbed. This would be the study that showed the kinetics and isotherm of the modified form of Ire-Ekiti clay for heavy metals adsorption.

■ EXPERIMENTAL SECTION

Materials

Chemical and reagents used include copper(II) nitrate trihydrate ($Cu(NO_3)_2.3H_2O$), nickel(II) sulphate heptahydrate ($NiSO_4.7H_2O$), potassium chromate K_2CrO_4, lead nitrate $Pb(NO_3)_2$, sodium dodecyl sulphate ($CH_3(CH_2)_{11}SO_4Na$), sodium hydroxide solution (NaOH), Hydrochloric acid solution (HCl). All reagents used were of analytical grade; hence, no further purification was carried out before use.

Instrumentation

Instrumentations applied in adsorption experiment and for the characterization of clay samples include Scanning Electron Microscope coupled with Energy Dispersive X-ray Spectrophotometer (JEOL JSM-7600F), pH meter (Jenway pH meter 3520), rotary orbital shaker with incubator (Biosan environmental shaker-incubator ES-20/60), laboratory oven, Flame Atomic Absorption Spectrophotometer (Agilent AAS 55AA), X-ray fluorescence (XRF), Fourier Transformed Infrared spectrophotometer (SHIMADZU FTIR-8400S) and Particle Induced X-ray Emission (PIXE) technique.

Study Area

The study area and trial (sample collection) site 'Ire-Ekiti' is a town in Oye local government area of Ekiti State, Southwestern Nigeria, located between latitude 7°47'N to 7°53'N and longitude 5°18'E to 5°24'E. The geological map is shown in Fig. 1. The town is known to have been the home of Ogun Onire, whom the Yoruba ethnic group of Nigeria recognizes as the "god of iron". Ire-Ekiti has naturally abundant clay deposits located within different settings of the town, which are mined both locally and industrially for different applications. The geological settings of Ekiti State are between latitude 7°20'N to 8°00'N and longitude 4°50'E to 5°50'E. The trial site showing the effects of mining activities (a depression filled with water) is shown in Fig. 2. The town possesses the most abundant clay deposits in Ekiti state, and the quality of the clay for making various industrial products

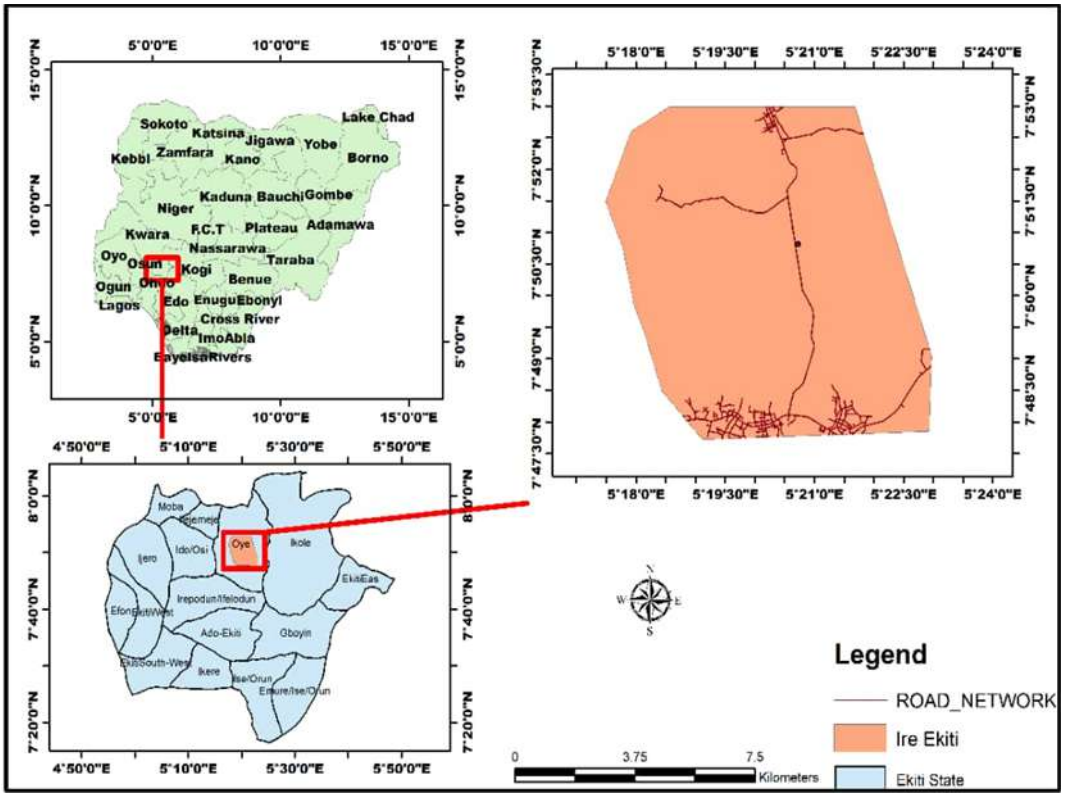

Fig 1. Geological map of Nigeria, Ekiti State, Oye local government area and Ire-Ekiti

Fig 2. Figure of the trial site showing effects of mining activities

such as bricks, tiles and ceramics have drawn the attention of different miners and establishment of a clay processing industry in the town.

Procedure

Collection and preparation of raw clay soil

The clay soil was collected from Ire-Ekiti, Southwestern Nigeria. An adequate amount for use was crushed and dispersed in deionized water; then, floating debris from plants was removed by handpicking and also by decantation. The suspension was thoroughly stirred in order to allow none clay materials to be separated from the clay; the clay soil was recovered from the water by centrifuging the suspension at 3000 rpm. The recovered clay soil was dried at 110 °C for about 12 h and cooled in a desiccator. After cooling, the dried clay

soil was pulverized and sieved using sieves of different mesh sizes based on the experimental requirement. The sieved clay soils were stored in a black polyethylene bag prior to modification.

Modification of clay soil sample

An adequate amount of the raw clay sample to be used was modified with 100 mL of 0.01 M SDS in 100 mL 0.01 M NaCl solution at pH 5 by shaking for 90 min at 200 rpm on a rotary orbital shaker. The pH of the solution was adjusted using HCl and NaOH. After shaking, the mixture was centrifuged in order to collect the residue. The residue was collected and washed until the pH of leachate reached pH of 6.0, then dried in an oven at 105 °C for 12 h. The sample was crushed and sieved into the required particle sizes. The modified sample is called the surfactant (SDS) modified clay.

Preparation of metal solution

The stock solutions (1000 mg L^{-1}) of the adsorbates (Ni, Pb, Cu, and Cr) were prepared by dissolving known quantities of their metal salts (potassium chromate, lead nitrate, copper nitrate, and hydrated nickel sulfate) in deionized water and serially diluted to required concentration upon experimental requirement. The reagents used to prepare metal solutions were all extra pure analytical grades. The initial and equilibrium concentrations of metals were determined by Flame Atomic Absorption Spectrophotometer (Agilent AAS 55AA).

Characterization

Different characterizations were carried out for both the raw and modified clay to ascertain surface modification and enhanced adsorption properties of the clay material. The chemical compositions of the clay samples were determined by X-ray Fluorescence (XRF). Fourier Transformed Infrared spectrometry (FTIR) was used for functional group elucidation and to confirm the surface modification. Scanning Electron Microscopy (SEM) was used to show the surface morphology of both the natural and modified clay soil samples. The elemental make-up of the clay samples was determined by Particle Induced X-ray Emission (PIXE), while the relative abundance (%w) of some important ionic compositions as well as the carbon content of the raw and modified clay materials, were determined by Energy Dispersive X-ray Emission (EDX) technique.

Batch adsorption experiments

An adsorption experiment for the modified clay was carried out in batch by adding 50 mL of adsorbate solution 10 mg L^{-1} into conical flasks containing 0.50 g of the adsorbent [26]. Each adsorbent and adsorbate mixture was equilibrated at pH 5.0 by shaking at 200 rpm at a temperature of 298 K, using a rotary orbital shaker until equilibrium. The pH of each solution was adjusted using drops of HCl and NaOH when necessary. After equilibration, the mixtures were centrifuged for 15 min at 3000 rpm. Thereafter, the supernatants were collected and analyzed for equilibrium concentrations of the Cu, Ni, Pb, and Cr by an Atomic Absorption Spectrophotometer. The effect of pH on adsorption processes was studied at pH 3, 4, 5, 7, and 8 with an equilibration time of 90 min. The effect of agitation time on the adsorption process was investigated at the time varied between 10 and 80 min at a pH value of 5. Also, the adsorption of Cu, Ni, Pb, and Cr on the modified clay material was optimized at different concentrations (20, 40, 60, 80, and 100 ppm) with an equilibration time of 90 min at pH 5.

Data treatment

The percentage metal removal was calculated according to Eq. (1)

$$\% \text{ Metal removal} = \frac{C_0 - C_e}{C_0} \times 100\% \quad (1)$$

where C_0 (mg L^{-1}) and C_e (mg L^{-1}) are the initial and equilibrium adsorbate concentration, respectively.

■ RESULTS AND DISCUSSION

Surface Morphology

A scanning electron microscope image showing the morphology of the raw Ire-Ekiti clay soil is presented in Fig. 3(a). The image of the natural clay presents a very rough surface arising from a dense stacking and piling of particles upon one another and resulting in small-size inter-aggregate pores (10 μm). In this structure, the piling of the particles is in a consistent order, forming a tangled network with a highly dense arrangement of the

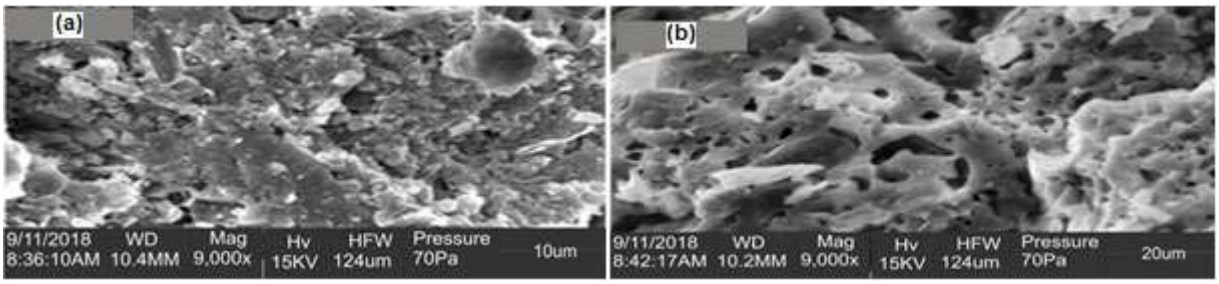

Fig 3. (a) Scanning electron microscope image of the raw clay; (b) Scanning electron microscope image of the modified clay

particles resulting in a reduced number of pores. The small pore size may hinder the permeability of adsorbates and result in low diffusion and reduced adsorption [26]. The SEM image of the modified clay is shown in Fig. 3(b). Modification of the raw clay changed its structure and surface morphology. The modified clay showed a honeycomb-like structure and surface morphology with improved surface adsorptive properties like increased pore number and size. The most notable improved properties are the pore diameter (20 μm) and number. The pore diameter increased from10 to 20 μm. Also, the pores are more numerous compared to those of the raw clay, as shown in Fig. 3(a) and 3(b). These properties make the modified clay more porous. The numerous pores and improved pore diameter have the potency to enhance permeation of the adsorbates during adsorption experiments. The highly porous structure of the SDS modified clay could improve intraparticle diffusion and permeation, resulting in higher adsorption of the adsorbate by enhancing the inner-sphere complexation reaction between the adsorbates and adsorbent.

FTIR Adsorption Spectroscopy Bands

The results of the FTIR analysis of the modified and raw clay are shown in Fig. 4(a) and 4(b), respectively.

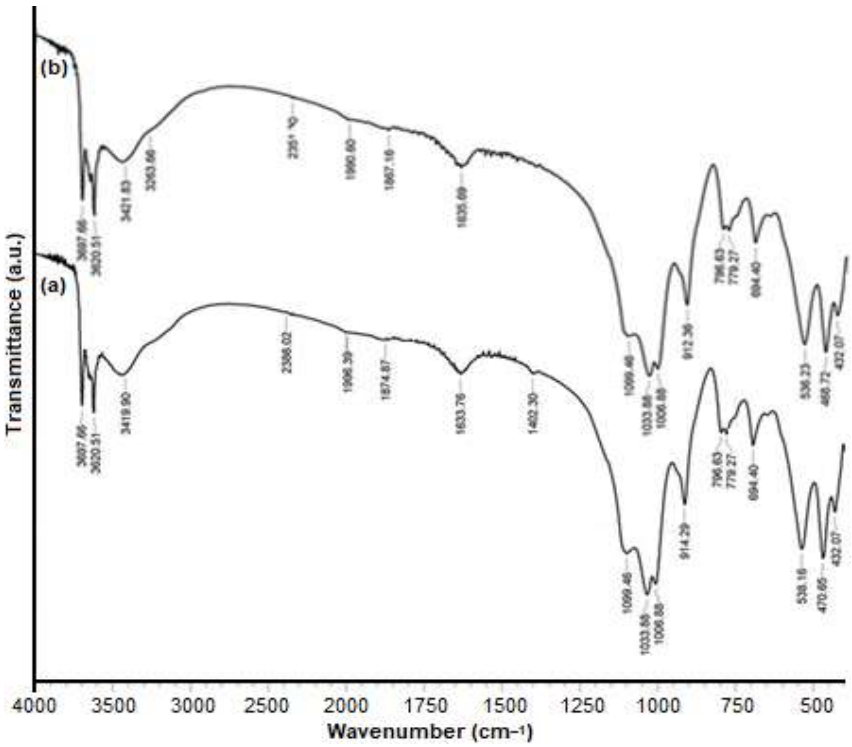

Fig 4. Fourier transform infrared spectra of (a) the SDS modified clay soil, and (b) the raw clay soil

The FTIR results showed absorption bands at 3620, 3421, 3263, 3697, 3620, and 3419 cm^{-1}, which are due to the hydroxyl group of the inner surface of the clays. The bands at 1099 and 1006 cm^{-1} correspond to the Si–O–Si group present in the clays; the band at 694 cm^{-1} is due to the bending mode of the same group. The absorption bands at 1633 and 1402 cm^{-1} are due to the presence of C=O and C=C of the organic components of the clay soils. The bands at 536 and 538 cm^{-1} showed the presence of the Si-O-Al group in the raw and modified clay. The presence of metallic oxide in the clay soil is indicated by the intensity bands at 468 and 432 cm^{-1} [27-28]. The appearance of a new intensity band at 1402 cm^{-1} assigned to the C=C in the modified clay soil, which is not present in the raw clay soil, is due to surface modification of the soil. The presence of the band 3263 cm^{-1} in the raw clay and its disappearance in the modified clay soil is a result of surface modification of the soil. Shifts in the adsorption bands from 2351, 1990, 1867, 912, and 468 cm^{-1} of the raw clay to higher intensity bands of 2386, 1996 1874, 914, and 470 cm^{-1} in the modified clay also confirm the surface modification. The changes in the FTIR results of the raw clay upon modification showed that modification with SDS might have possibly improved the negative charges of the clay surfaces and created more active sites for metal binding. The Si–O–Al and Si–O–Si structures of the soil were not affected by the modification.

Chemical Composition

The chemical composition presented in Table 1 showed that silica and alumina are the major constituents of the raw and modified clay with a percentage composition of 55.80 and 24.28; 56.31 and 27.07, respectively. The XRF results also showed that the metals are present in their oxide form rather than hydroxide. Silica (SiO_2) and alumina (Al_2O_3), being the major constituents of the clay soil, suggest that the clay soil is an alumino-silicate (kaolinite). The percentage of metal oxide compositions of the raw clay increased upon modification except for MnO. This showed that modification could also affect the chemical composition of clay soil. The results of this study are consistent and agreed with the result obtained from a study reported by Akinola et al. [29] and Awokunmi and Asaolu [30] on the modification of clay soil from Ekiti State for fluoride adsorption in an aqueous medium.

Table 1. Chemical composition of SDS modified Ire-Ekiti clay soil

Oxide	Chemical composition of the raw clay (%)	Chemical composition of the modified clay (%)
SiO_2	55.80	56.31
Al_2O_3	24.28	27.07
Fe_2O_3	4.16	4.89
Na_2O	2.91	2.92
K_2O	0.32	0.32
MgO	1.54	1.70
CaO	0.27	0.50
TiO_2	0.2	0.26
ZrO_2	0.06	0.07
MnO	0.03	0.03
LOI	10.30	5.65
Total	99.87	99.65

Elemental Composition

The result from the Proton Induced X-ray Emission technique (Table 2) showed that silicon (Si, 558138 ppm) and Aluminum (Al, 242444 ppm) are the major elemental composition with the highest concentration in the raw clay soil matrix. Al (271498 ppm) and Si (564580 ppm) are also the major elemental composition with the highest concentration in the modified clay soil matrix. These results corroborate the results of the XRF, which showed that silica and alumina are the major chemical composition of both the raw and SDS modified clay soils. The elemental composition of the raw and modified clays also showed that the clay soil samples contained a high concentration of some important exchangeable cations. The exchangeable cations for the modified clay include Na^+ (29473 ppm), Mg^{2+} (17018 ppm), Ca^{2+} (5056 ppm) and Fe^{2+} (49888 ppm). The presence of these exchangeable cations in the soil could bring about a cation exchange mechanism for removing the adsorbates from their respective solution. The concentration of each exchangeable cation of the modified clay is higher than those of the raw clay (Na^+ (28810 ppm), Mg^{2+} (15311 ppm), Ca^{2+} (2723 ppm), and Fe^{2+} (41320 ppm).

Table 2. Elemental composition and concentration of SDS modified Ire-Ekiti clay soil

Z	Symbol	Elemental concentration of the raw clay (ppm)	Elemental concentration of the modified clay (ppm)
11	Na	28810	29473
12	Mg	15311	17018
13	Al	242444	271498
14	Si	558138	564580
15	P	329	400
17	Cl	281	386
19	Kf	3101	3154
20	Ca	2723	5056
22	Ti	2097	2687
24	Cr	261	309
25	Mn	312	318
26	Fe	41320	49888
29	Cu	381	452
30	Zn	138	180
38	Sr	35.8	187
40	Zr	562	690
46	Pd	20.5	35.7
47	Ag	217	273
48	Cd	91.6	107
50	Sn	218	283
82	Pb	13.8	13.2
83	Bi	-	45.9

Where Z is the atomic number

The metals were assumed to have undergone chemical multiplication or amplification reactions during the modification process, which resulted in their respective concentration increase. This improvement in the exchangeable cation concentrations could consequently increase the cation exchange capacity of the soil and enhance the adsorption of the adsorbates through an improved cation exchange mechanism. Bismuth (Bi) was present in the raw clay soil but absent in the modified clay soil. The absence of bismuth in the modified clay is probably due to the effect of modification of the raw clay soil.

Carbon and Ionic Composition of the Raw and Modified Soil Sample

Results of the EDX analysis of both the raw and modified clay soil samples (Fig. 5(a) and 5(b)) showed that aluminum, silicon, and oxygen are the most abundant ionic compositions of the soil matrixes and possessing the highest percentage by weight (%w). The value of Al, Si and O of the raw clay soil are 10.10, 49.30, and 13.0 %w, while that of the modified clay soil are 13.00, 50.00, and 20.70 %w, respectively. The absence of hydrogen and the presence of oxygen is an indication that the elements could be present in the form of oxides rather than hydroxide. This supports the results of the FTIR, PIXE, and XRF analysis obtained for the samples. In agreement with other techniques that have been applied for probing the properties and compositional characteristics of both the raw and modified clay samples in the present study, the EDX results of the raw clay sample also showed the presence of some important exchangeable cations such as K (3.17 %w), Ca (5.47 %w)

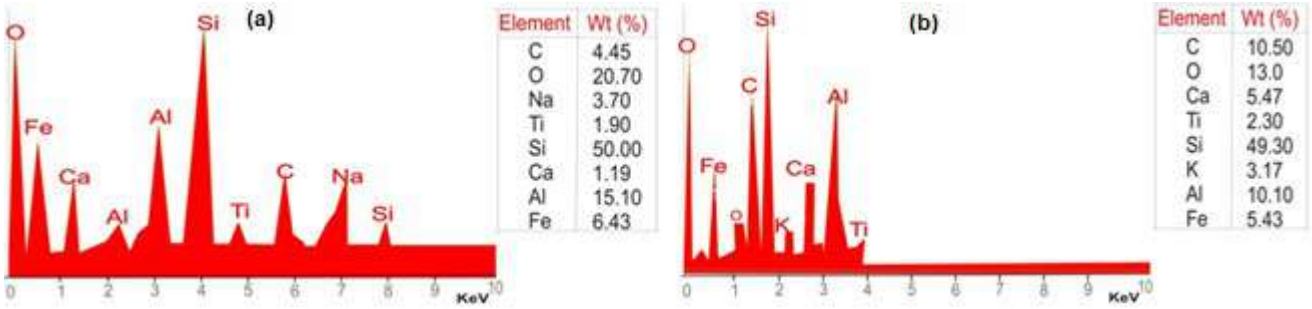

Fig 5. EDX analytical results of (a) the raw clay soil, (b) the modified clay soil

and Fe (5.43 %w) while the modified clay showed the presence of Na (3.70 %w), Ca (1.19 %w) and Fe (6.43 %w). It was observed that modification has a significant influence on the ionic composition of the clay soil. For instance, K was present in the raw clay and absent in the modified clay. The absence of K in the modified clay may be due to the leaching of K from the clay during the modification process. The percentage composition of the elemental composition of the raw clay is different from that of the modified clay, as shown in Fig. 5(a) and 5(b). The carbon content of the raw and modified has the value of 10.50% and 4.45%, respectively. The relative abundance (percentage by weight) of Si and Al compared to other elements showed that the clay soil is typically kaolin confirming the results of the PIXE and XRF analysis.

Effect of pH

The pH of a solution determines the degree of ionization and speciation of metal ions and also affects the surface charge of an adsorbent in the process of metal uptake [31]. From the results in Fig. 6, it is shown that the optimum adsorption of Ni, Pb, and Cu was obtained at pH 4.0, while that of Cr was obtained at pH 5.0. This showed that optimum adsorption could be achieved at an acidic medium (usually, at pH greater than 2.0) without chemical precipitation of the hydroxide form of the metal adsorbates. This is in agreement with previously reported works by Erdemoglu et al. [32] and Chaari et al. [33]. The results obtained for the adsorption trend with increased pH showed that the adsorption process involved series of complex mechanisms, which include ion exchange, direct bonding, and surface complexation other than precipitation.

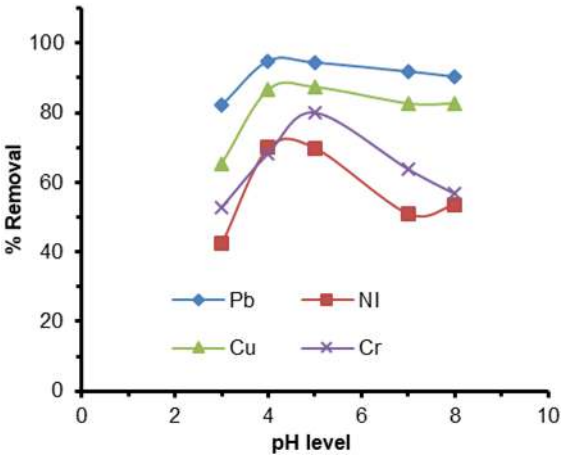

Fig 6. Adsorption trend with increase pH of the metals' solution

Effect of Agitation Time

The effect of agitation time on the adsorption potential of the modified clay material was investigated to show the suitability of the clay material for industrial applications. A good adsorbent suitable for industrial applications usually possesses a high adsorption capacity as well as a fast rate of removal. Equilibration time for adsorption of Cu and Pb was fast and achieved within 30 and 40 min respectively; then tended to be constant for 80 min. The fast adsorption rate of the adsorption process is probably due to the increased concentration gradient between the adsorbate in the solution and adsorbate in the adsorbent. This difference in concentration determined the number of vacant and available sites for metal binding and enhanced the increased uptake of the metals at the initial stages of the adsorption processes. This also implies that the nature of an adsorbent and its active sites determine the rate at

which equilibrium is attained, as suggested by Dal Bosco et al. [34]. Similar results were observed in a study conducted by Jaiswal et al. [35]. Equilibration of Ni (50 min) and Cr (60 min) was achieved at a slower rate, as shown in Fig. 7. The slower rate of adsorption of Ni and Cr implies that the nature of adsorbates also plays a significant role in the rate at which equilibrium is attained or the rate of uptake. The progressive increase in adsorption and, consequently, the attainment of equilibrium adsorption may be due to limited mass transfer of the adsorbate particles from the adsorbate solution to the external surface of the clay material, initially and subsequently by slower internal mass transfer within the clay particles [36].

Effect of Adsorbate Concentration

The equilibrium adsorption trend for Ni, Pb, Cr and Cu by the modified clay material is shown in Fig. 8. Adsorptions of Ni, Pb, and Cu tend to increase as the concentration of the metals in the solution increased. It was observed that increasing the concentration of the metals in the solution resulted in higher uptake of the metal until equilibrium was achieved. This trend was attributed to the fact that when the transport of metals between the adsorbent's internal pores and external surface films tends to be equal, the transboundary movement of metals will not be significantly permissible; however, increasing concentration will re-initiate the movement, and for this reason, the adsorption process will be dependent [37]. Similar findings have been reported in the literature for similar and other pollutants' adsorption [38-39]. The effect of initial concentration on Cr adsorption by the modified clay showed that the percentage of Cr adsorbed decreased with increasing concentration. This decrease was a result of saturation of the active sites of the adsorbents at higher metal concentrations leading to less removal of chromium ions from the solution. This implies that at low concentrations, more chromium ions would be removed by the abundant active sites on the adsorbents. This result is in accordance with the findings by Akpomie et al. [21] in their study of the enhanced sorption of trivalent chromium unto novel cassava peel modified kaolinite clay.

Effect of Temperature

Temperature is one of the most important parameters of adsorption, and its effect on the metals uptake was investigated. The result of the study is shown in Fig. 9. The result showed that the adsorption process for all the metals increases with the increased temperature of the solution and suggesting endothermicity of the adsorption process. The adsorption trend is due to the ability of the metals in solution (lead, copper, chromium, and nickel) to overcome resistance to mass transfer with an increase in kinetic energy as they undergo interactions with active sites of the clay material. Increased temperature has been reported to favour the uptake of

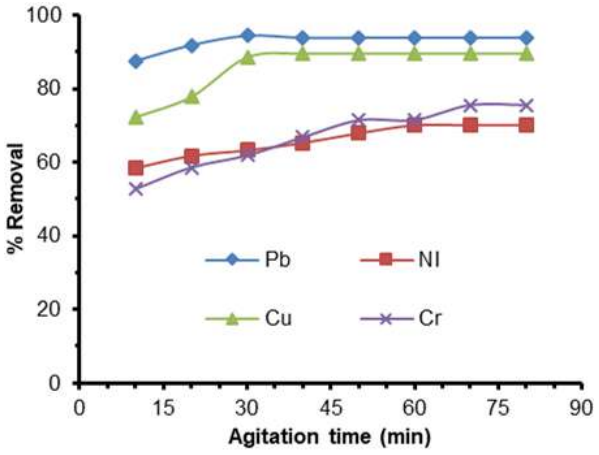

Fig 7. Adsorption trend with increase contact time for the metals

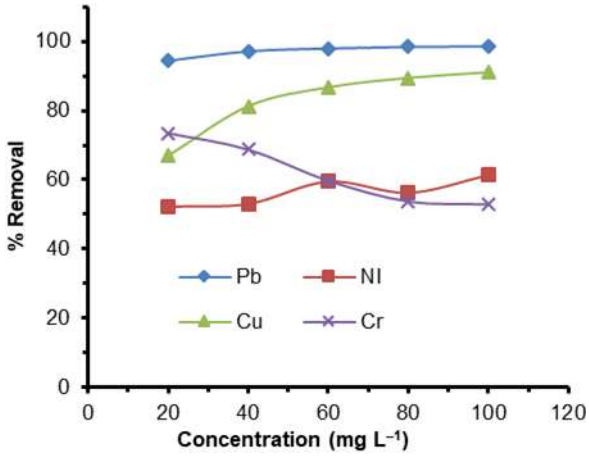

Fig 8. Adsorption trend with increase concentration for the metals

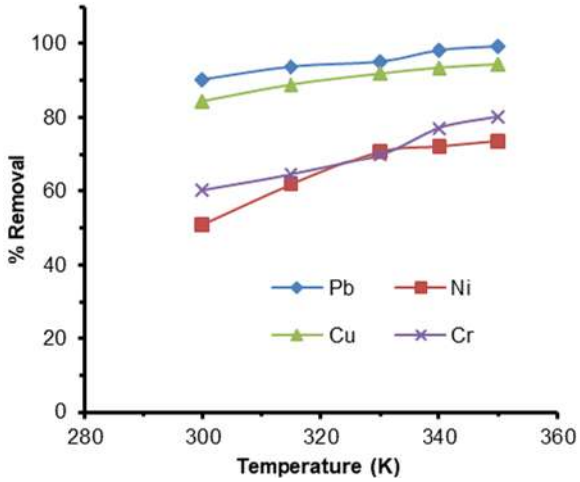

Fig 9. Adsorption trend with increase temperature for the metals

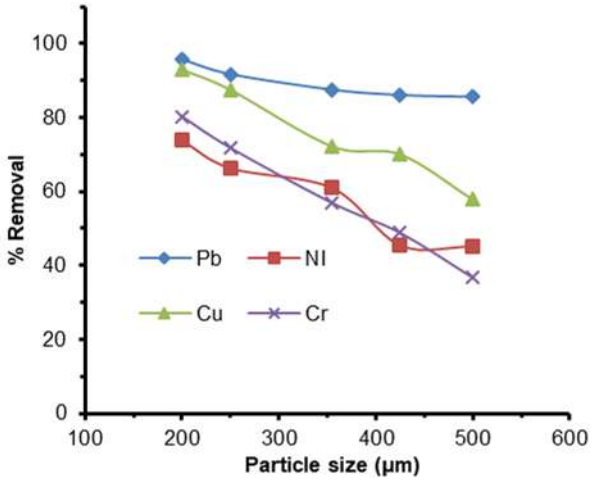

Fig 10. Adsorption trend with increase particle size for the metals

dyes and pigments Rattanaphani et al. [40] while the adsorption of metals was equally favored by increased temperature, as reported by Zouraibi et al. [41].

Effect of Adsorbate Particle Size

Adsorption processes have been known to be particle dependent. Results from this study showed that adsorption of Ni, Pb, Cu, and Cr by the modified clay material increased with decreased particle size (Fig. 10). This is due to the fact that a decrease in particle size of an adsorbent would yield larger surface areas and make available more active sites for metal binding [42].

Langmuir Adsorption Isotherm

The linearized Langmuir equation Kinniburgh [43] was used to show the surface binding properties of the metals on the modified clay soils.

$$\frac{1}{q} = \frac{1}{Q_o} + \frac{1}{Q_o K_L C_e} \quad (2)$$

where q_e (mg g^{-1}) represents the amount of ion adsorbed, C_e (mg L^{-1}) is the equilibrium concentration, Q_o (q_{max}) maximum is monolayer coverage capacity (mg g^{-1}), and K_L (L mg^{-1}) represents the Langmuir adsorption equilibrium constant. The values of K_L and q_{max} were determined from the slope and intercept of the Langmuir plot of $^1/q_e$ against $^1/C_e$. An essential feature of the Langmuir isotherm was also expressed in terms of equilibrium parameter R_L, known as the separation factor, which is a dimensionless constant and represented by Eq. (3).

$$R_L = \frac{1}{1+(1+K_L C_o)} \quad (3)$$

where C_0 represents the initial concentration and K_L is a constant related to the energy of adsorption. If the value of K_L is less than (<) 0, it implies that the adsorption process does not correlate to Langmuir isotherm. The adsorption nature is unfavorable if R_L is greater than 1, it is linear if $R_L = 1$, irreversible if $R_L = 0$, and favorable if $0 < R_L < 1$. A negative R_L value indicates that the adsorption process does not fit the Langmuir isotherm, and hence, it cannot be explained by the Langmuir isotherm.

The data presented in Table 3 shows that the K_L and R_L values for adsorption of Pb, Ni, and Cu on the modified clay are < 0. This showed that the adsorption processes do not fit the Langmuir isotherm. On the other hand, the K_L value for Cr on the modified clays is 26.88 L mg^{-1}. Also, an R_L value in the range of 3.7×10^{-5}–1.9×10^{-4} was also obtained for Cr adsorption on the modified clay material. The R_L value for chromium adsorption on and modified clay is greater than 0 but less than 1, which implies a favored Langmuir isotherm; the positive K_L values indicate that the adsorption processes correlate to the Langmuir isotherm. The R^2 values for the Cr, Pb, Cu, and Ni adsorption onto the modified clay are 0.9538, 0.5119, 0.9215, and 0.9864, respectively. The positive K_L values of Cr and other data obtained from all isotherms showed that chromium adsorption on the modified clay is in best compliance and correlates to the Langmuir

Table 3. Langmuir isotherm parameters for the modified clay material

Parameters	Ni	Pb	Cu	Cr
R^2	0.9864	0.5119	0.9215	0.9538
q_{max}	0.097	0.715	0.058	0.3378
K_L	-87.34	-1.517	-9.007	26.882
R_L	$-(1.15 \times 10^{-6}\text{-}3 \times 10^{-4})$	$-(6.64 \times 10^{-5}\text{-}3.41 \times 10^{-4})$	$-(5.6 \times 10^{-3}\text{-} 1 \times 10^{-3})$	$(3.7 \times 10^{-5}\text{-}1.9 \times 10^{-4})$

isotherm as the negative K_L values (Table 3) of other metals showed their unfitness to the isotherm. These results imply monolayer adsorption of Cr on the clays' flat surfaces. The correlation was not only determined by the (coefficient of determination) linear regression coefficient parameter but also the K_L value as the R^2 value is not enough to describe the fitness and correlation of an adsorption process to Langmuir isotherm.

Freundlich Isotherm

Freundlich isotherm was used to predict a possible multi-layer adsorption of the metals on the clays' rough surfaces. The Freundlich isotherm was elucidated using Eq. (4) and (5) [44].

$$q_e = K_F C_e^{1/n} \quad (4)$$

where n is adsorption intensity, K_F is Freundlich isotherm constant (mg g^{-1}), and C_e represents the equilibrium concentration of adsorbate (mg L^{-1}). Hence,

$$\log q_e = \log K_F + \frac{1}{n}\log C_e \quad (5)$$

where K_F and $^1/n$ are empirical constants, indicating the adsorption capacity and the strength of adsorption in an adsorption process, respectively. Parameters for the constants were obtained by plotting log q_e versus log C_e [45]. If the obtained value for $^1/n$ is below 1, it indicates normal adsorption. On the other hand, if the value of $^1/n$ is above 1, it implies cooperative adsorption [46].

Linear regression parameter is used to determine the fitness of kinetics and isotherm models [47]. From the data presented in Table 4, the values of $^1/n$ are greater than 1 for Cr, Pb and Cu adsorption by the modified clay material. This indicates that the adsorption processes are cooperative while the adsorption of Ni is more favored. The R^2 values of 0.9895 and 0.9806 were obtained for the Cu and Ni, respectively, from the Freundlich adsorption isotherm plot. The adsorption processes of the Cu and Ni on the modified clay fits best to the Freundlich isotherm than other tested adsorption isotherms. This implies that the adsorption process describes a heterogeneous system characterized by multi-layer adsorption on the rough surfaces of the clay material.

The Temkin Isotherm

The Temkin isotherm, which contains factors (Table 5) that explicitly takes into account 'adsorbent–adsorbate interactions', was used to show that heat of adsorption of Pb molecules in layers would decrease linearly rather than logarithmic with coverage by ignoring the extremely low and large value of the concentrations. The isotherm was computed using Eq. (6) and (7) [48].

$$q_e = \frac{RT}{b}\ln\left(A_T C_e\right)$$

$$q_e = \frac{RT}{b}\ln A_T + \left(\frac{RT}{b}\right)\ln C_e \quad (6)$$

$$B = \frac{RT}{b_T}$$

$$q_e = B\ln A_T + B\ln C_e \quad (7)$$

Table 4. Freundlich isotherm parameters for the modified clay material

Parameters	Cu	Ni	Cr	Pb
R^2	0.9895	0.9806	0.0452	0.8956
K_f	4.19×10^{-6}	9.56	1.778	7.863
n	0.149	1.25	0.131	0.097
$^1/n$	6.729	0.799	7.663	10.29

where A_T is Temkin isotherm equilibrium binding constant (L g^{-1}), b_T is Temkin isotherm constant, R is the universal gas constant (8.314 J mol^{-1} K^{-1}), T is Temperature at 298 K, and B is Constant related to the heat of adsorption (J/mol). A_T and B were determined by plotting the quantity adsorbed q_e against ln C_e and the constants were determined from the slope and intercept [48].

The following values shown in Table 5 were estimated for the adsorption of Pb on the modified clay: A_T = 0.943 L g^{-1}, b_T = 47.87 and B = 52.11 J mol^{-1}. The parameters obtained from all the tested isotherms showed that the Temkin plot is the best fitting isotherm for the adsorption of Pb onto the modified clay with an R^2 value of 0.9655. This implies monolayer adsorption of the Pb particles in layers on the modified clay, whereas the heat of adsorption decreased linearly rather than logarithmic with coverage.

Pseudo-First-Order Kinetics

The adsorption data were modeled using the Lagergren pseudo-first-order kinetics given by:

$$\log (q_e - q_t) = \frac{K_1}{2.303} t + \log q_e \quad (8)$$

The model was used to show that the physical adsorption mechanism was responsible for the metals' adsorption on the modified clay material. Where q_e represents the amount of metal adsorbed at equilibrium, q_t (mg g^{-1} min) represents the amount of metal adsorbed on the surface of the adsorbent at any time t (min), and K_1 min^{-1} represents the equilibrium rate constant of pseudo-first-order adsorption kinetics as given by Lagergren [49]. The rate constant K_1 was determined from the slope of log (q_e–q_t) versus time t for plots in which straight lines were obtained. An obtained straight-line graph of the plot of log (q_e–q_t) versus time t obtained, as well as closeness in values of q_{eCal} to q_{eExp}, suggests the applicability of the model.

The results of this study showed that straight line graphs were obtained for metals' adsorption on the modified clay material as shown in Fig. 11, but the values of q_{eCal} were not close to those of q_{eExp} as shown in Table 6. This suggests that the adsorption processes cannot be explained by the pseudo-first-order kinetic model.

Table 5. Temkin isotherm parameters for the modified clay soils

Parameters	Pb	Ni	Cu	Cr
R^2	0.9655	0.8927	0.9695	0.8648
B	52.11	3.53	26.90	1.546
b_T	47.87	7.44×10^2	92.72	1.6×10^3
A_T	0.943	1.231	0.1551	0.591

Table 6. Pseudo-first-order Kinetics parameters for the modified clay

Parameters	Pb	Ni	Cu	Cr
R^2	0.9033	0.5736	0.933	0.9078
K_1	0.1566	0.0836	0.0083	0.0299
q_{eExp}	0.4193	1.3424	0.2125	0.3334
q_{eCal}	0.988	0.680	0.790	0.699

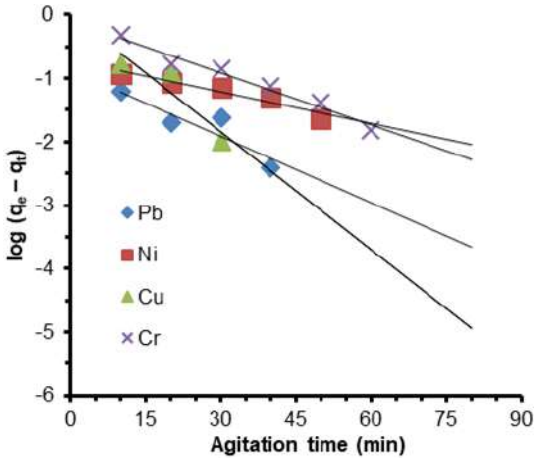

Fig 11. Plot of log (q_e–q_t) vs. agitation time (min) for modified clay

Pseudo-Second-Order Kinetics

The linearized form of the Pseudo-second-order kinetics was applied to explain the adsorption processes of the metals on the modified clay material. It is given by:

$$\frac{t}{q_t} = \frac{1}{h} + \frac{t}{q_e} \quad (9)$$

where $h = kq^2_e$ (mg/(g min)) [46].

Thus, the pseudo-second-order equation can be written as:

$$\frac{t}{q_t} = \frac{1}{K_2 q_e^2} + \frac{t}{q_e} \quad (10)$$

where k (g/(mg min)) represents the pseudo-second-order rate constant, q_t (mg g^{-1} min) represents the amount of metal adsorbed on the surface of the

adsorbent at any time t, while q_e (mg g^{-1}) represents the amount of metal adsorbed at equilibrium [46].

The values of q_e, k, and h were determined experimentally by plotting $^t/q_t$ against t. The Pseudo-second-order kinetic plot of the modified clay is shown in Fig. 12. The values of q_{eCal} for the adsorption process of all the metals onto the modified clay correlate to those of q_{eExp}, as shown in Table 7. This implies that the adsorption process can be explained and represented by pseudo-second-order kinetics. The linear regression R^2 values of the pseudo-second-order kinetics for all the metals' adsorption processes are closer to unity than those of the pseudo-first-order plot. This showed that the adsorption processes best fit the pseudo-second-order kinetics. This fitting implies that there is a possible chemical interaction between the adsorbates and adsorbents during the adsorption processes. Hence, the adsorption process is driven by a chemical mechanism.

Elovich Kinetics

The Elovich equation was applied to test the suitability of the model. Elovich kinetic model shows the extent surface coverage and activation energy of chemisorptions of adsorbates on heterogeneous adsorbing surfaces. The Elovich kinetics was modeled using the linear form of the equation as represented in Eq. (11) [50].

$$q_t = \frac{1}{\beta}\ln(\alpha\beta) + \frac{1}{\beta}\ln(t) \qquad (11)$$

where α represents the initial adsorption rate (mg g^{-1} min), and β is related to the extent of surface coverage and the activation energy for chemisorption (g mg^{-1}). The constants α and β were obtained from the slope ($\frac{1}{\beta}$) and an intercept [$\frac{1}{\beta}\ln(\alpha\beta)$] of the linear plot of q_t versus ln T. Elovich kinetic plots are represented by Fig. 13.

Generally, the R^2 value is used to show the suitability and applicability of the model. The results from Table 8 showed that the R^2 values obtained for adsorption processes are less close to unity than the pseudo-first-order and pseudo-second-order kinetics. This implies that the adsorption processes cannot be explained by the Elovich kinetic model.

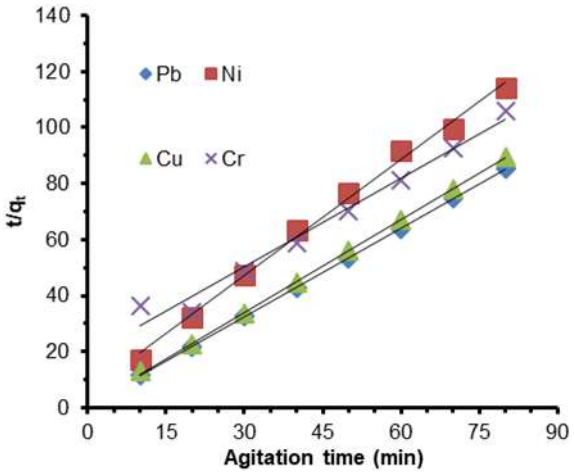

Fig 12. Plot of $^t/q_t$ vs. agitation time (min) for the modified clay material

Table 7. Pseudo-second-order kinetics parameters for the raw and modified clay soils

Parameters	Pb	Ni	Cu	Cr
R^2	0.9999	0.9952	0.9997	0.9786
K	1.4286	0.3615	1.2253	0.0950
q_{eExp}	0.948	0.7235	0.9089	0.9067
q_{eCal}	0.938	0.702	0.895	0.755

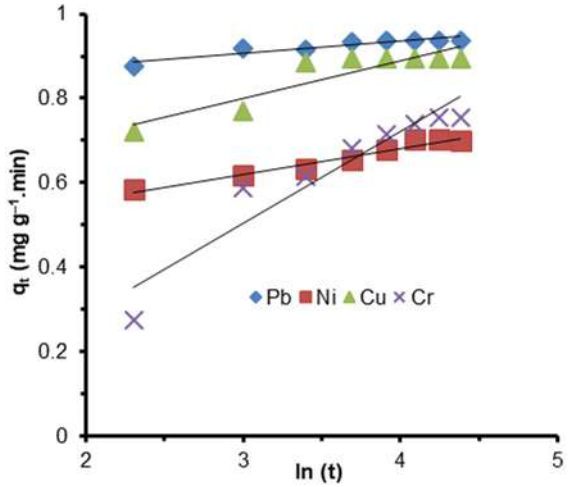

Fig 13. Plot of q_t (mg g^{-1} min) vs. ln (t) for the modified clay

Table 8. Elovich isotherm parameters for the modified clay material

Parameter	Pb	Ni	Cu	Cr
R^2	0.8697	0.9684	0.8249	0.9048

■ CONCLUSION

This study has investigated the enhancement of the adsorptive properties of Nigerian clay (Ire-Ekiti clay) for its potential application for the remediation of lead, chromium, nickel, and copper in their respective contaminated aqueous solution. Findings from this study showed that modification of the clay by anionic surfactant sodium dodecyl sulfate improved its heavy metals adsorption properties. The improved properties include pore diameter, pore numbers, exchangeable cations, surface morphology, and available active sites for metal binding. The instrumentations employed for the materials' characterization were able to give sufficient information on the subject matter. The results from the adsorption study showed a fast rate of the metals' removal by the modified clay material, and a very good percentage of the metals were adsorbed. Adsorption efficiency of the modified clay measured in the form of a percentage of metal removed reached the values of 98.5%, 94.5%, 80.3%, and 73.8% for the Pb, Cu, Cr, and Ni, respectively. The outcome of this research and information contained in this study showed that SDS modified clay is a promising material for remediation of heavy metal contaminated water and laden solution beyond an acceptable level. We recommend that other modification techniques be employed for surface modification of the clay for improved adsorptive properties and efficiency.

■ REFERENCES

[1] Awaleh, M.O., and Soubaneh, Y.D., 2014, Waste water treatment in chemical industries: The concept and current technologies, *Hydrol.: Curr. Res.*, 5 (1), 1000164.

[2] Saxena, G., Chandra, R., and Bharagava, R.N., 2016, Environmental pollution, toxicity profile and treatment approaches for tannery wastewater and its chemical pollutants, *Rev. Environ. Contam. Toxicol.*, 240, 31–69.

[3] Wen, J., Fang, Y., and Zeng, G. 2018, Progress and prospect of adsorptive removal of heavy metal ions from aqueous solution using metal-organic frameworks: A review of studies from the last decade, *Chemosphere*, 201, 627–643.

[4] Chen, C.W., Chen, C.F., and Dong, C.D., 2012, Distribution and accumulation of mercury in sediments of Kaohsiung River mouth, Taiwan, *APCBEE Procedia*, 1, 153–158.

[5] Ahmaruzzaman, M., 2011, Industrial wastes as low-cost potential adsorbents for the treatment of wastewater laden with heavy metals, *Adv. Colloid Interface Sci.*, 166 (1), 36–59.

[6] Guillaume, P.L.A., Chelaru, A.M., Visa, M., and Lassine, O., 2018, "Titanium oxide-clay" as adsorbent and photocatalysts for wastewater treatment, *J. Membrane Sci. Technol.*, 8 (1), 1000176.

[7] Pinto, A.C.S., Grossi, L., de Melo, R.A.C, de Assis, T.M., Ribeiro, V.M., Amaral, M.S.C., and Figueiredo, K.C.S, 2017, Carwash wastewater treatment by micro and ultrafiltration mem-branes: Effects of geometry, pore size, pressure difference and feed flow rate in transport properties, *J. Water Process Eng.*, 17, 143–148.

[8] Tan, J., Huang, Y., Wu, Z., and Chen, X., 2017, Ion exchange resin on treatment of copper and nickel wastewater, *IOP Conf. Ser.: Earth Environ. Sci.*, 94, 012122.

[9] Akhter, M., Habib, G., and Qama, S.U., 2018, Application of electrodialysis in waste water treatment and impact of fouling on process performance, *J. Membr. Sci. Technol.*, 8 (2), 1000182.

[10] Jaishankar, M., Mathew, B.B., Shah, M.S., Murthy, K.T.P., and Gowda, S.K.R., 2014, Biosorption of few heavy metal ions using agricultural wastes, *J. Environ. Pollut. Hum. Health*, 2, 1–6.

[11] Adekeye, D.K., Popoola, O.K., Asaolu, S.S., Adebawore, A.A., Aremu, O.I., and Olabode, K.O., 2019, Adsorption and conventional technologies for environmental remediation and decontamination of heavy metals: an overview, *Int. J. Res. Rev.*, 6 (8), 505–516.

[12] Uddin, M.K., 2016, A review on the adsorption of heavy metals by clay minerals, with special focus on the past decade, *Chem. Eng. J.*, 308, 438–462.

[13] Mustapha, S., Ndamitso, M.M., Abdulkareem, A.S.,

Tijani, J.O., Mohammed, A.K., and Shuaib, D.T., 2019, Potential of using kaolin as a natural adsorbent for the removal of pollutants from tannery wastewater, *Heliyon*, 5 (11), e02923.

[14] Kumrić, K.R., Đukić, A.B., Trtić-Petrović, T.M., Vukelić, N.S., Stojanović, Z., Novaković, J.D.G., Matović, L., 2013, Simultaneous removal of divalent heavy metals from aqueous solutions using raw and mechanochemically treated interstratified montmorillonite/kaolinite clay, *Ind. Eng. Chem. Res.*, 52 (23), 7930–7939.

[15] Iannicelli-Zubiani, E.M., Cristiani, C., Dotelli, G., and Stampino, G.P. 2017, Recovery of valuable metals from electronic scraps by clays and organo-clays: Study on bi-ionic model solutions, *Waste Manage.*, 60, 582.

[16] Fu, F., and Wang, Q., 2011, Removal of heavy metal ions from wastewaters: A review, *J. Environ. Manage.*, 92 (3), 407–418.

[17] Srinivasan, R., 2011, Advances in application of natural clay and its composites in removal of biological, organic, and inorganic contaminants from drinking water, *Adv. Mater. Sci. Eng.*, 2011, 872531.

[18] Adekeye, D.K., Asaolu, S.S., Adefemi, S.O., Ibigbami, O.A., Adebawore, A.A., Osundare, O.S., and Olumide, A.H., 2019, Clay soil modification techniques for the adsorption of heavy metals in aqueous medium: A review, *Int. J. Adv. Re. Chem. Sci.*, 6 (6), 14–31.

[19] Yuan, G.D., Theng, B.K.G., Churchman, G.J., and Gates, W.P., 2013, "Chapter 5.1 – Clays and clay minerals for pollution control" in *Development in Clay Science Series: Handbook of Clay Science*, 2nd Ed., Eds. Bergaya, F., and Lagaly, G., 2nd Ed., Elsevier, 587–644.

[20] Al-Essa, K., and Khalili, F., 2018, Heavy metals adsorption from aqueous solutions onto unmodified and modified Jordanian kaolinite clay: batch and column techniques, *Am. J. Appl. Chem.*, 6 (1), 25–34.

[21] Akpomie, K.G., Odewole, O.A., Ibeji, C.U., Okagu, O.D., and Agboola., I.I., 2017, Enhanced sorption of trivalent chromium unto novel cassava peel modified kaolinite clay, *Der Pharma Chem.*, 9 (5), 48–55.

[22] Zen, S., El Berrichi, F.Z., Abidi, N., Duplay, J., Jada, A., and Gasmi, B., 2018, Activated kaolin's potential adsorbents for the removal of Derma Blue R67 acid dye: kinetic and thermodynamic studies, *Desalin. Water Treat.*, 112, 196–206.

[23] Marino, T., Russo, F., Rezzouk, L., Bouzid, A., and Figoli, A., 2017, PES-kaolin mixed matrix membranes for arsenic removal from water, *Membranes*, 7, 57.

[24] Zhu, J., Cozzolino, V., Pigna, M., Huang, Q., Caporale, A.G., and Violante, A., 2011, Sorption of Cu, Pb and Cr on Na-montmorillonite: Competition and effect of major elements, *Chemosphere*, 84 (4), 484–489.

[25] Olu-Owolabi, B.I., Alabi, A.H., Unuabonah, E.I., Diagboya, P.N., Böhm, L. and Düring, R., 2016, Calcined biomass-modified bentonite clay for removal of aqueous metal ions, *J. Environ. Chem. Eng.*, 4 (1), 1376–1382.

[26] Adekeye, D.K., Asaolu, S.S., Adefemi, S.O., and Ibigbami, O.A., 2019, Heavy metal adsorption properties of the basement complex of clay deposit in Ire-Ekiti Southwestern Nigeria, *IOSR J. Environ. Sci. Toxicol. Food Technol.*, 13 (2), 1–8.

[27] Mbaye, C.A.K., Diop, J.M., Miehe-Brendle, J., Senocq, F., and Maury, F., 2014, Characterization of natural and chemically modified kaolinite from Mako (Senegal) to remove lead from aqueous solutions, *Clay Miner.*, 49 (4), 527–539.

[28] Olagboye, S.A., Ejelonu, B.C., Oyeneyin, O.E., Adekeye, D.K., and Gbolagade, Y.A., 2018, Synthesis, characterization and antimicrobial activities of metal complexes of Cu(II) and Zn(II) with prednisolone in water-isopropyl alcohol medium, *Int. J. Adv. Res. Chem. Sci.*, 5(12), 16–23.

[29] Akinola, Oluwatoyin, O., Ademilua, and Oladimeji, L., 2014, Compositional features and functional industrial applications of the lateritic clay deposits in Oye-Ekiti and Environs, Southwestern Nigeria, *IJST*, 2 (9), 6–12.

[30] Awokunmi, E.E., and Asaolu, S.S., 2017, Physicochemical and performance evaluation of natural and modified Ire-Ekiti clay: Emerging substrate in the de-fluoridation of drinking water, *J. Phys. Chem. Sci.*, 5 (4), 1–5.

[31] Cristiani, C., Iannicelli-Zubiani, E.M., Bellotto, M., Dotelli, G., Stampino, P.G., Latorrata, S., Ramis, G., and Finocchio, E, 2021, Capture mechanism of La and Cu ions in mixed solutions by clay and organoclay, *Ind. Eng. Chem. Res.*, 60 (18), 6803–6813.

[32] Erdemoğlu, M., Erdemoğlu, S., Sayilkan, F., Akarsu, M., Şener, S., and Sayilkan, H., 2004, Organo-functional modified pyrophyllite: Preparation, characterization and Pb(II) ion adsorption property, *Appl. Clay Sci.*, 27 (1), 41–52.

[33] Chaari, I., Medhioub, M., and Jamaoussi, F., 2011, Use of clay to remove heavy metals from Jebel Chakir landfill leachate, *J. Appl. Sci. Environ. Sanit.*, 6 (2), 143–148.

[34] Dal Bosco, S.M., Jimenez R.S., Vignado, C., Fontana, J., Geraldo, B. Figueiredo, F.C.A., Mandelli, D., and Carvalho, W.A., 2006, Removal of Mn(II) and Cd(II) from wastewaters by natural and modified clays, *Adsorption*, 12 (2), 133–146.

[35] Jaiswal, A., Banerjee, S., Mani, R., and Chattopadhyaya, M.C., 2013, Synthesis, characterization and application of goethite mineral as an adsorbent, *J. Environ. Chem. Eng.*, 1 (3), 281–289.

[36] Senthil, K.P., Vincent, C.K., Kirthika, K., and Sathish, K.K., 2010, Kinetics and equilibrium studies of Pb^{2+} ion removal from aqueous solutions by use of nano-silversol-coated activated carbon, *Braz. J. Chem. Eng.*, 27 (2), 339–346.

[37] Teixeira, S.C.G., Ziolli, R.L., Marques, M.R.C., and Pérez, D.V., 2011, Study of pyrene adsorption on two Brazilian soils, *Water Air Soil Pollut.*, 219 (1), 297–301.

[38] An, C., Huang, G., Yu, H., Wei, J., Chen, W., and Li, G., 2010, Effect of short-chain organic acidsn and pH on the behaviors of pyrene in soil–water system, *Chemosphere*, 81, 1423–1429.

[39] Olu-Owolabi, B.I., Diagboya, P.N., and Adebowale, K.O., 2014, Evaluation of pyrene sorption–desorption on tropical soils, *J. Environ. Manage.*, 137, 1–9.

[40] Rattanaphani, S., Chairat, M., Bremner, J.B., and Rattanaphani, V., 2007, An adsorption and thermodynamic study of lac dyeing on cotton pretreated with chitosan, *Dyes Pigm.*, 72 (1), 88–96.

[41] Zouraibi, M., Ammuri, A., Khadija, Z., and Saidi, M., 2016, Adsorption of Cu(II) onto natural clay: Equilibrium and thermodynamic studies, *J. Mater. Environ. Sci.*, 7 (2), 566–570.

[42] Kara, S., Aydiner, C., Demirbas, E., Kobya, M., and Dizge, N., 2007, Modeling the effects of adsorbent dose and particle size on the adsorption of reactive textile dyes by fly ash, *Desalination*, 212 (1), 282–293.

[43] Langmuir, I., 1918, The adsorption of gases on plane surfaces of glass, mica and platinum, *J. Am. Chem. Soc.*, 40 (9), 1361–1403.

[44] Freundlich, H.M.F., 1906, Over the adsorption in solution, *J. Phys. Chem.*, 57, 385–471.

[45] Ramachandran, P., Vairamuthu, R., and Ponnusamy, S., 2011, Adsorption isotherms, kinetics, thermodynamics and desorption studies of Reactive Orange 16 on activated carbon derived from A*nanas Comosus* (L.) carbon, *ARPN J. Eng. Appl. Sci.*, 6 (11), 15–26.

[46] Asaolu, S.S., Adefemi, S.O., Ibigbami, O.A., and Adekeye, D.K., 2020, Kinetics, isotherm and thermodynamic properties of the basement complex of clay deposit in Ire-Ekiti Southwestern Nigeria for heavy metals removal, *Nat. Environ. Pollut. Technol.*, 19 (3), 897–907.

[47] De la Rosa, G., Reynel-Avila, H.E., Bonilla-Petriciolet, A., Cano-Rodríguez, I., Velasco-Santos, C., and Martínez-Hernández, A.L., 2008, Recycling poultry feathers for Pb removal from wastewater: Kinetic and equilibrium studies, *Int. J. Chem. Mol. Eng.*, 2 (11), 338–346.

[48] Temkin, M.I., and Pyzhev, V., 1940, Kinetics of ammonia synthesis on promoted iron catalyst, *Acta Physicochim. URSS*, 12, 327–356.

[49] Lagergren, S., 1898, Zur theorie der sogenannten adsorption gelöster stoffe (About the theory of so-called adsorption of soluble substances), *K. Sven. Vetensk.Akad. Handl.*, 24, 1–39.

[50] Roginsky, S.Z., and Zeldovich, J., 1934, An equation for the kinetics of activated adsorption, *Acta Physicochim. URSS*, 1, 554–559.

Synthesis of Low TENORM Zirconium Sulfate from $ZrO(OH)_2$ with Sulfuric Acid

Rahmatika Alfia Amiliana* **and Muzakky**

Center for Accelerator Science and Technology (CAST), National Nuclear Energy Agency,
Jl. Babarsari POB 6101 Yk bb, Yogyakarta 55281, Indonesia

** **Corresponding author:***

tel: +62-85888914339
email: rahmatika.alfia@batan.go.id

Received: October 2, 2020
Accepted: March 18, 2021

DOI: 10.22146/ijc.60298

Abstract: *Zirconium sulfate (ZS) has become one of the alternative chemical compounds for substituting traditional tannery substances using chromium(III) which was not environmentally friendly. The purpose of this research was to synthesize ZS from $ZrO(OH)_2$ using H_2SO_4 with low Technologically Naturally Occurring Radioactive Material (TENORM) content. This ZS synthesis process shortened the old processing flow at which plenty of chemical reactors were used. The results showed that with 300 mg of feed, 600 mL of 95% H_2SO_4, at a temperature of 250 °C, the contact time of 150 min, the obtained conversion was 77.76%. Furthermore, in this 95% acid leaching reactor, the SiO_2 content was still 2.79% and it was not TENORM free yet, but the FTIR and XRD images were in accordance with BDH standards. Moreover, the quenching process results had been free of SiO_2 and TENORM content, but they still contained 1.48% HfO_2. The surface of the TEM images from the quenching results had been in the form of elongated and transparent crystals. The result of the economic feasibility analysis showed that the new ZS synthesis process was more economical or profitable when it was compared to the old ZS synthesis process, with a BCR value of 1.258.*

Keywords: *TENORM; acid leaching; quenching process; FTIR; XRD; XRF; TEM; BCR*

■ INTRODUCTION

Green chemistry has appeared as an area of research interest for environmental chemists. This has encouraged many researchers to create environmentally friendly methods, particularly in the tannery field [1]. Tannery products are the largest export commodities from Indonesia, but the traditional tannery products still use chromium(III). This may threaten the export of tannery products where they will not be accepted as an export commodity since it is less environmentally friendly and does not meet the current regulations that prioritize eco-labeling [1-2]. To address this problem, several researchers have developed the tanning of leather using zirconium sulfate (ZS) substances instead of chromium(III) [1-3]. Therefore, research on the synthesis of ZS compounds as new tannery substances is very interesting while simultaneously addressing the ideals of green chemistry.

In this report, the researchers will synthesize ZS from $ZrO(OH)_2$ using H_2SO_4, which is also naturally low in Technologically Naturally Occurring Radioactive Material (TENORM). Based on the regulation of the head of Bapeten number 9 in 2009 on the intervention of radiation exposure from TENORM, the level of contamination from the products derived from zirconium minerals, such as zirconium sulfate, is not more than 1 Bq/cm^2 or 1 Bq/g of product which is equivalent to 500 ppm [4]. The purpose of this study was to shorten the process flow in the previous synthesis of ZS which was carried out through the old zirconium oxychloride (ZOC) process [5-7]. The old flow process contained many chemical reactors, which would be less economical from the commercial point of view. Both new and old ZS synthetic flow diagrams were compared in Fig. 1.

There are differences in the quenching process in the old and new ZS synthetic process, as seen in Fig. 1. In the old process, the quenching was repeated only twice leading to the sole formation of Na_2ZrO_3, while in the new process, the quenching process was carried out

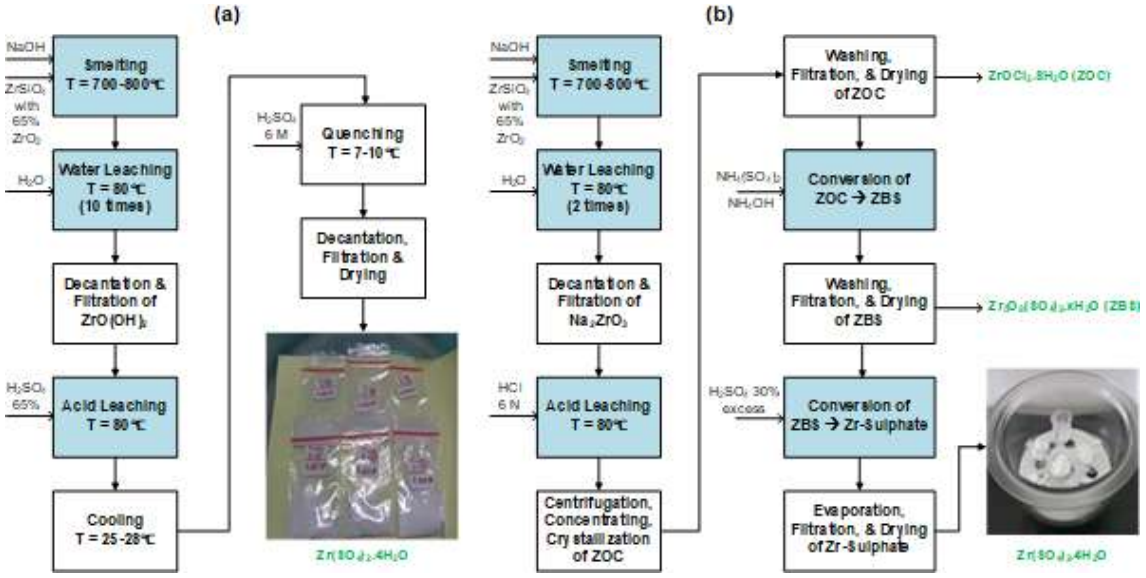

Fig 1. ZS synthesis based on (a) new and (b) old process flow diagram

Table 1. Major oxides (%) in $ZrO(OH)_2$ feed

SiO_2	P_2O_5	SO_3	TiO_2	Fe_2O_3	Y_2O_3	ZrO_2	SnO_2	HfO_2	ThO_2	U_2O_8
4.167	2.142	n.d.	0.648	0.326	0.272	88.021	0.618	2.588	0.0519	0.0651

10 times so that sodium zirconte (Na_2ZrO_3) would be hydrolyzed to $ZrO(OH)_2$. According to Beyer et al., zirconium sulfate could be synthesized from the hydrolysis of sodium zirconate, which was then reacted with 85% sulfuric acid, and the basis of this ZS synthesis was from a simple chemical reaction in an acid leaching reactor as follow [6,8],

$$ZrO(OH)_2 + 2H_2SO_4 \rightarrow Zr(SO_4)_2 + 3H_2O \quad (1)$$

With the ultimate goal to commercialize the ZS products, we report, herein the elimination of the TENORM content (U_3O_8 and ThO_2) apart from conducting the economic feasibility analysis. To qualitatively and quantitatively produce the ZS products, a comparison of major oxide concentrations between the feed, the product, and the standard of BDH was carried out. Meanwhile, the final product would be characterized by XRF, FTIR, XRD, and TEM.

■ EXPERIMENTAL SECTION

Materials

The materials used were $ZrO(OH)_2$ feed from the water leaching process [5]. Table 1 shows the results of the major oxide analysis of $ZrO(OH)_2$ feed with XRF. KBr salts, H_2SO4 95% was obtained from E-Merck. The distilled water was locally prepared by PSTA-BATAN laboratory. $Zr(SO_4)_2$ standard was purchased from BDH Reagents and Chemicals.

Instrumentation

The equipment used in this study included a unit of acid leaching reactors in the form of a three-neck flask (with a capacity of 1 L, equipped with stirrer, temperature regulator and vertical cooling), drying ovens, 4-digit sartorius scales, Fourier Transform Infrared spectroscometer (FTIR, ALPHA II MODULE ATR ZnSe), X-Ray Diffractometer (XRD, PANanalytical Aeris type DY844 equipped with 161039 databases) and X-ray Fluorescence spectrometer (XRF, Malvern PANanalytical type High-Performance ED-XRF Epsilon 4), and Transmission Electron Microscope (TEM, JEOL JEM-1400).

Procedure

Acid leaching reactor calibration

The calibration of the acid leaching reactor was done in a 1 L three-neck flask equipped with a heating mantle, temperature controller, and an adjustable stirrer

with a maximum speed of up to 30 rpm. As much as 400 mL of 95% H_2SO_4 was introduced into the reactor, and then heated with constant stirring at 15 rpm at the 200 °C for 120 min. The process was repeated with temperature variations at 250 °C and 300 °C, then repeated with addition 300 g of feed at 250 °C. Then, the change of the temperature was recorded every 5 min, and the rate of temperature change every 5 min (°C/min) was calculated with the following equation.

$$\text{Rate}\left(\frac{°C}{\text{min}}\right)=\left(\frac{T_n - T_1}{W_n - W_1}\right) \quad (2)$$

where T_n is the temperature at the time of n^{th} (°C), T_1 is the initial temperature (°C), W_n is the time to reach temperature T_n, and W_1 is the initial time.

Optimization of acid leaching reactor

Into the acid leaching reactor, 300 g of feed and 600 mL H_2SO_4 (95%) were introduced. The mixture was heated to 200 °C with constant stirring at 15 rpm for 120 min. After the temperature reaching 200 °C, the reaction was left for 60 min; then, the temperature controller was turned off and the mixture was allowed to stand to ± 30 °C. Then, 300 mL of distilled water was added into the acid leaching reactor. It was then reheated up to a temperature of 100 °C, with a stirring speed of 15 rpm for 60 min. Next, the reaction was allowed to cool to ± 30 °C. The mixture was separated into the filtrate (water phase) and residue (paste). As much as 100 g of paste was dried in the oven at 110 °C, and the dried paste was analyzed with XRF. Similar procedure was then repeated using H_2SO_4 (65%). The conversion was calculated with Eq. 3.

$$\text{Conversion}\ (\%)=\frac{\text{Zr}(SO_4)\ \text{formed(g)}}{\text{ZrO(OH)}_2\ \text{in feed(g)}}\times 100\% \quad (3)$$

Quenching process

As much as 500 mL of paste was sampled from the acid leaching reactor, pipetted dropwise into 2 pieces of beaker glass, where the first beaker (outer) already contained liquid ice and the second beaker (inner) contained 6 M of H_2SO_4 solution. After the quenching process completed, the H_2SO_4 solution was separated with the formed ZS solid. To remove the remaining H_2SO_4, the ZS solid was washed with 0.01 M H_2SO_4. Then, the ZS solid was dried in the oven at 110 °C for 2–3 h. Next, the obtained white ZS solid was crushed and sieved at 100 mesh and sampled 50 g to be analyzed with XRF, XRD, and FTIR.

■ RESULTS AND DISCUSSION

Acid Leaching Reactor Calibration

Based on Fig. 1(a) on the new process of ZS synthesis, the main indicator of success lies in the operational process of the acid leaching reactor and the quenching. Therefore, we performed the calibration followed by taking a closer look at the performance of the acid leaching reactor. The results of the acid leaching reactor calibration can be seen in Fig. 2. At the 200 °C calibration point using H_2SO_4 95%, the maximum heating rate 2.28 °C/min was obtained at the temperature of 203 °C. At 200 °C of the calibration condition, it was proven that the temperature drop rate curve was shorter. When the calibration was done at 300 °C, the maximum rate was achieved at 3.3 °C/min.

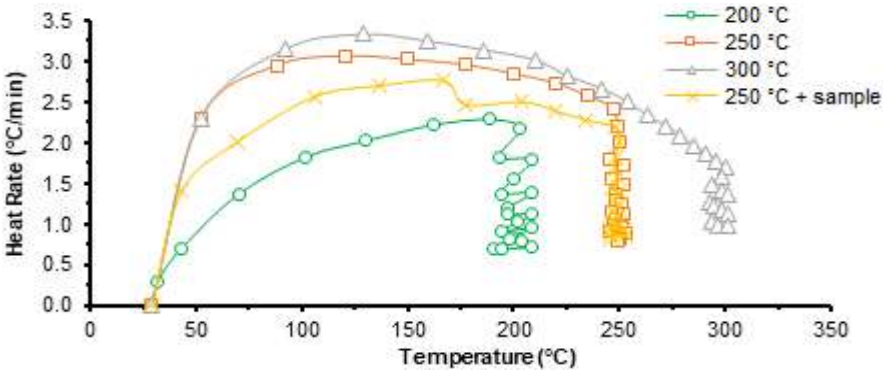

Fig 2. Curve between temperature vs. heat rate on the calibration of the acid leaching reactor

However, the rate curve at 300 °C was longer than that at 200 °C. Therefore, the shorter temperature curve rate was calibrated at 200 °C.

Furthermore, for the calibration at 250 °C, the maximum rate was achieved is at 3.08 °C/min, with a fairly long temperature curve. Based on Levenspiel [9], the length of the temperature rate curve will ensure that the chemical reaction goes would proceed to the side of product. Thus, the calibration was continued at the temperature of 250 °C, in which the feed as much as 300 g was added and hereinafter referred to as calibration 250 °C (+) feed. The results showed that the calibration of 250 °C (+) feeds gave quite long temperature rate curve but lower than 250 °C without feeding. Therefore, the operation of the temporary sulfate leaching reactor was carried out at the optimum temperature condition of 250 °C (+) feed, where the temperature rate curve was quite long.

Optimization of Acid Leaching Reactor

With the optimum temperature at the calibration at 250 °C (+) feed, we performed the synthesis of ZS with various temperatures and contact times. The optimization of the acid leaching process was then done using 65% of sulfuric acid solution (Fig. 3). It can be seen from Fig. 3 that the highest conversion of ZS synthesis (57.2%) was achieved at 250 °C with a contact time of 200 min. The results turned out to be in accordance with the calibration temperature of the acid leaching reactor in Fig. 2, where the temperature curve at the temperature calibration under 200 °C was not long enough leading to the low conversion (Fig. 2). The results showed that the optimization conditions were in accordance with the reports by Beyer et al. [8] and Houchin et al. [10] on the production of zirconium sulfate tetrahydrate (ZS).

The acid leaching process was carried out using 95% of H_2SO_4 solution with the same amount feed of 300 g. Based of Fig. 4, the best conversion of 77.76% was obtained at a temperature of 250 °C with a time of 150 min. The results of this experiment are not contrary to the results in Fig. 2 and 3. Based on Fig. 2 and 3, we know that the acid leaching operating conditions carried out under 200 °C are less stable and the reaction is less than perfect. In Fig. 4, it has been confirmed that the optimization of acid leaching should be carried out at 250 °C for 150 min to obtain high conversion. The optimized conditions were in line reports by Beyer et al. [8] and Houchin et al. [10] on the production of zirconium sulfate tetrahydrate (ZS).

The optimal acid leaching reactor operation (Fig. 2, 3, and 4) was taken at the temperature of 250 °C (+) feed for 150 min. Then, each product was analyzed using XRF to determine the contents of major oxides. The content was then compared with feed and BDH standards (Fig 5).

Fig. 5(a) showed the concentration of SiO_2, SO_3, and ZrO_2 in the feed, acid leaching process using 65% and 95% H_2SO_4 solution as well as BDH standard. The results showed that the concentration of SiO_2 in the acid leaching reactor operation using 65% of H_2SO_4 solution was relatively the same with that in the feed due to the low

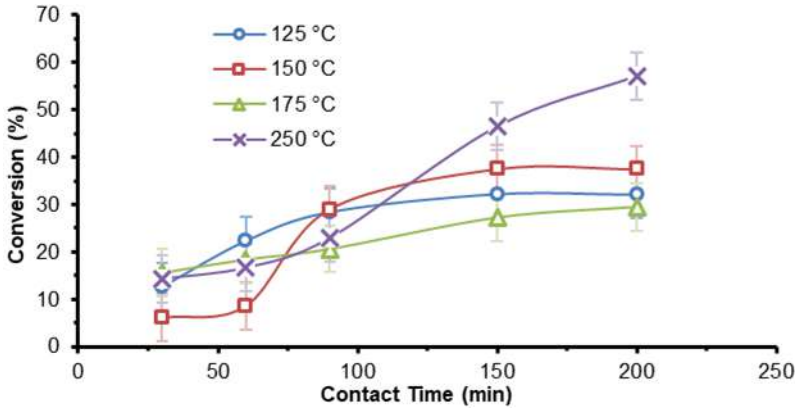

Fig 3. Relationship between conversion (%) and contact time as the function of temperature using 65% of H_2SO_4 solution

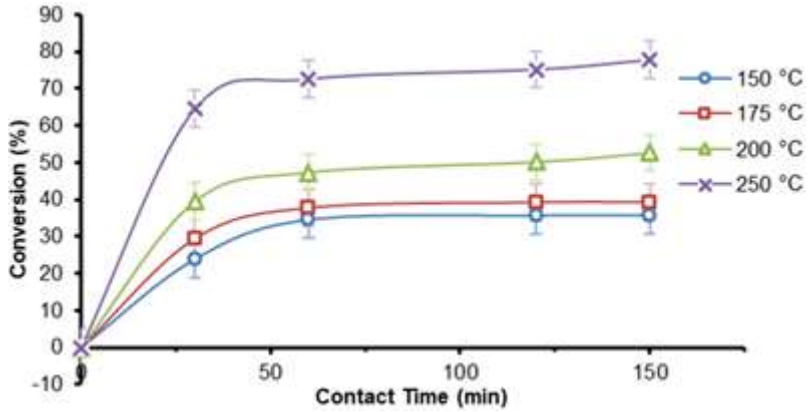

Fig 4. Relationship between conversion (%) and contact time as the function of temperature using 95% of H_2SO_4 solution

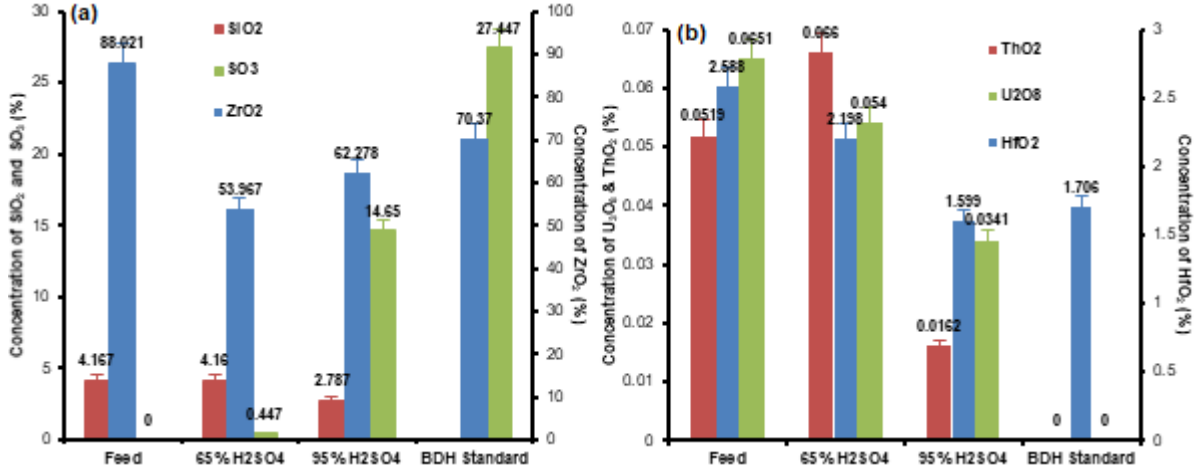

Fig 5. Concentration (%) of major oxides (a) SiO_2, SO_3, ZrO_2 and (b) ThO_2, U_2O_8, HfO_2, after the acid leaching process

solubility of SiO_2 in 65% of H_2SO_4 solution. Comparing to the previous condition, a decrease on SiO_2 concentration (from 4.16% to 2.78%) was observed in the reactor operation using 95% of H_2SO_4 solution. However, when compared to ZS from BDH standard, the concentration of SiO_2 has reached 0.00%.

The concentration of SO_3 is equivalent to that of SO_4^{2-}, which is bound as ZS compound. As displayed in Fig. 5(a), the concentration of SO_3 in the feed, in the leaching reactor operation using 65% and 95% of H_2SO_4 solution were 0%, 0.45% and 14.65, respectively. It indicated the ZS formation is more optimal in the operation using 95% of H_2SO_4 solution. However, when compared to the BDH standard, the concentration has reached 27.45%.

It could be seen from Fig. 5(a) that the concentration of ZrO_2 bound as $ZrO(OH)_2$ in the feed was 88.02%. An insignificant increase of ZrO_2 concentration was observed in acid leaching reactor operations, from 53.97% (using 65% of H_2SO_4) to 66.28% (using 95% of H_2SO_4). However, when compared to BDH standards, the concentration of ZrO_2 has reached 70.37%, which still small.

As depicted in Fig. 5(b), the concentration of ThO_2 in the feed was 0.0529%. The concentration was slightly increased to 0.066% in the 65% acid leaching reactor. While the concentration of ThO_2 in the 95% acid leaching reactor has dropped to 0.0162%, this oxide was not detected in the BDH standard. The concentration of U_3O_8 in the feed was 0.651% and has dropped to 0.054% (in the 65% acid leaching reactor) and 0.0341% (in the 95% acid leaching reactor). Similar with ThO_2, U_3O_8 was

not detected in the BDH standard. Likewise, the HfO_2 concentration in the feed (2.588%) slightly decreased to 2.198% (in the 65% acid leaching reactor) and 1.599% (in the 95% acid leaching reactor). When compared with the BDH standard, the value was smaller.

From Fig. 5, it can be concluded that the concentration of H_2SO_4 affected the concentration of oxides contained in the feed. The addition of H_2SO_4 concentration could reduce the concentration of oxide impurity, namely SiO_2, ThO_2, U_2O_8, and HfO_2. As expected, the addition of H_2SO_4 concentration increased the concentration of both ZrO_2 and SO_3.

The FTIR spectrum of the feed (Fig. 6(a), no. 1) showed the absence of band at 3424 cm^{-1} belong to the hydroxyl group bound to water molecules, indicating that the feed state was quite dry. The band at 1635 cm^{-1} appeared as the asymmetric stretching of the hydroxyl group in the $ZrO(OH)_2$ molecule [11]. However, the appearance of the band at 1635.64 cm^{-1} in FTIR spectrum of the product reactor 65% (no. 2), reactor 95% (no. 3), and BDH standard (no. 4), is a sign of the H_3O^+ compounds, which is the asymmetric OH stretching of H_2O adsorption by sulfate ion compounds with models $(SO_3)_{ads}$ [11-12]. It turned out that H_2O adsorption was supported by the appearance of bands at 3424 cm^{-1} representing the hydroxyl group (Fig. 6(a), no. 2, 3 and 4).

The presence of the H_3O^+ was strengthened by the appearance of band at 964 cm^{-1} from SO_3 sulfite ion. Furthermore, the band at 1095 cm^{-1} represented sulfate species $(SO_4^{2-})_{ads}$ that played an important role in the formation of zirconium sulfate compounds [13]. These peaks have been observed in the FTIR spectra (Fig. 6(a), no. 2, 3 and 4) but for feed (no. 1), the band 1002.42 cm^{-1} may be an impurity (see Table 1). Furthermore, the appearance of the bands at 794, 594, and 549 cm^{-1} came from symmetry and asymmetry stretching of Zr-O bonding in the form of Zr-O-Zr and O-Zr-O [13-16].

Fig. 6(b) no. 1 was the XRD diffractogram of the feed) which still displayed the amorphous structure because the crystallization process was incomplete [17]. Furthermore, the intensity of peaks at 2θ = 28° and 30° increased in the 65% and 95% aid leaching reactors (Fig. 6(b) no. 2 and 3), Then, the peaks at 2θ = 50.2° and 60.1°, even with small intensity, had been seen in both 65% and

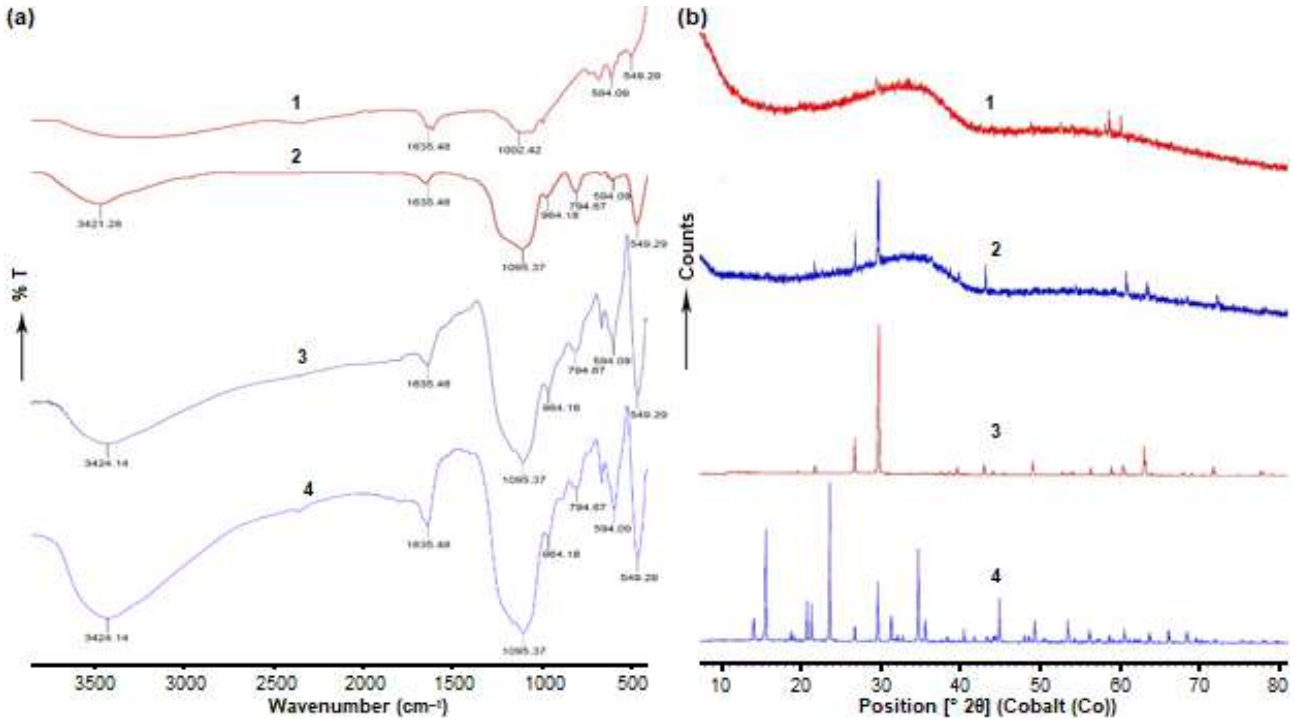

Fig 6. Comparison of (a) FTIR spectra and (b) XRD diffractogram: (1) feed, (2) the product of 65% reactor, (3) the product of 95% reactor, and (4) BDH standard

95% of the reactor product. The appearance of peaks at 2θ = 28°, 30°, 50.2°, and 60.1°, was in a good agreement with the previous reports that showed there is a zirconium sulfate compound [17-21].

Quenching Process

In addition to the acid leaching reactor, the quenching process will also determine the success of ZS synthesis Fig. 1(a). The quenching process is the process of settling the solution, which is quickly carried out and slowly added with 6 M of H_2SO_4 solution at 0.0–1.0 °C. The quenching process in ZS synthesis is carried out to remove or reduce the concentration of oxide impurities, particularly U_3O_8 and ThO_2. The impurities of the TENORM nuclear in the ZS products such as U_3O_8 and ThO_2 are undesirable for commercial purposes, especially in leather tannery applications (< 500 ppm).

Based on the XRF analysis (Fig. 7(a)), the concentration of SiO_2 in the feed was 4.17%. While the concentration of SiO_2 increased (26.03%) in the process without the quenching, the use of the quenching process might eliminate the impurity of SiO_2, as in the BDH standard. The concentration of ZrO_2 in the feed was 88.02% and decreased to 57.11% without the quenching process. When the quenching process was applied, the concentration of ZrO_2 increased to 68.88%, but was still lower than the BDH standard (70.37%). The results showed that the feed did not contain SO_3. Furthermore, the concentration of SO_3 increased to 8.30% when the process was carried out without the quenching. With the quenching process, the concentration of SO_3 will dramatically increase to 40.95%, which was even higher than the BDH standard, which is 27.45%.

According to Fig. 7(b), it could be seen that the concentration of ThO_2 was 0.052% in the feed and decrease to 0.020% when the synthesis was carried out without the quenching process. It should be noted that the quenching process might reduce the concentration of ThO_2 to 0.0%. The same concentration was also found in the BDH standard. Then, the concentration of U_3O_8 in the feed reached 0.0651% and decreased to 0.0371% when the synthesis was conducted without quenching. Similar with ThO_2, U_3O_8 was not detected in the quenching process and in the BDH standard, as well. It is interesting to note that the quenching process might reduce the concentration of HfO_2 contained in the feed, from 2.59% to 1.48%. Although this process could reduce the concentration of HfO_2, the resulting ZS compound was not reached the nuclear grade.

TEM images of the ZS products (Fig. 8, focused on 200 nm) showed a real difference between the products obtained with or without the quenching process. It has been proven that after the quenching process, there were transparent crystals that have elongated, whereas, before the quenching process, the product was still in the form of

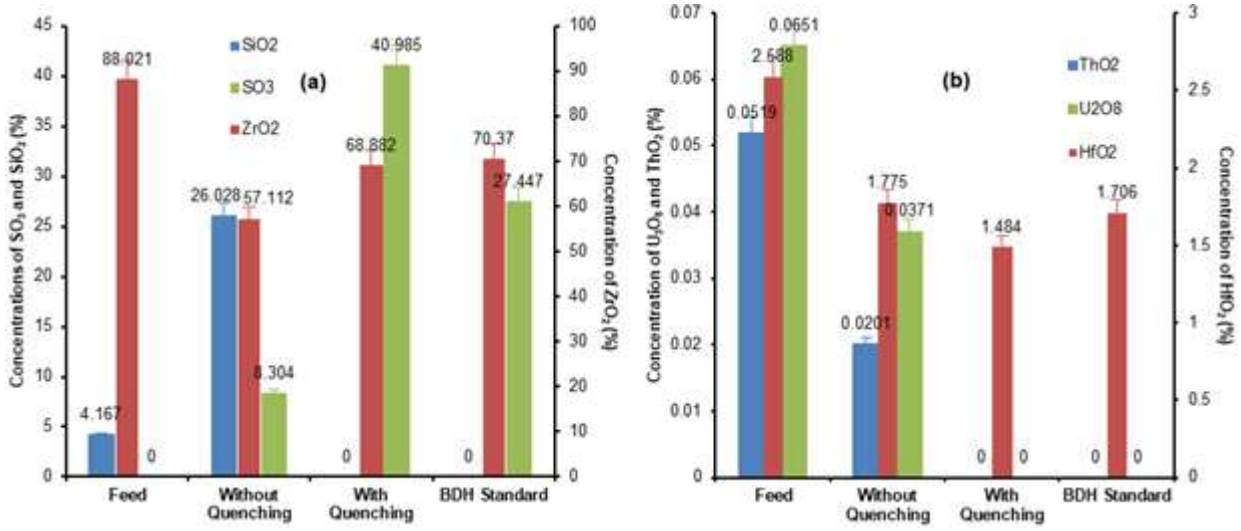

Fig 7. Concentration (%) of major oxides (a) SiO_2, SO_3, ZrO_2 and (b) ThO_2, U_2O_8, HfO_2, after the quenching process

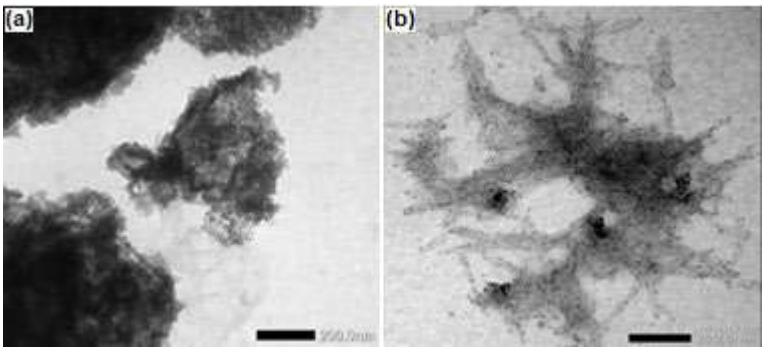

Fig 8. TEM images of ZS product (a) before and (b) after quenching process

particles clumps with a transparent agglomeration form [16-17].

Economic Feasibility Analysis

In this paper, a simple economic feasibility analysis was carried out to compare the economic value of the chemical processes in managing zircon sand into zirconium sulfate products. The economic value of a chemical process can be seen from the value of the Benefit-Cost Ratio (BCR), which is a comparison between the benefits obtained against the costs required for the process [21-22]. The eligibility criteria for the process are considered to be economical if the value of BCR is more than 1, indicating that the profit gained is greater than the production costs incurred [23]. The production costs for the new and old synthesis process were calculated based on the type and amount of raw materials used, while the large profits derived from the total value of zirconium sulfate produced based on market prices. Based on calculations, the BCR value of the new process flow is 1.258 (more than 1), and the BCR value of the old process flow is 0.437. This value becomes the parameter showing that the new zirconium sulfate synthetic process is a financially feasible process to be developed and be considered for investment on a larger scale.

■ CONCLUSION

The new ZS synthetic process has been able to replace the old process which required many chemical reactors. The new process was carried out in the acid leaching reactor and quenching reactor. The optimal results of the acid leaching reactor were obtained using 300 g of feed, 600 mL of 95% of H_2SO_4 solution, at the temperature of 250 °C, and the contact time of 150 min and gave the conversion of 77.76%. Furthermore, the acid leaching reactor with 95% of H_2SO_4 solution still gave SiO_2 content as much as 2.79% and was not free from TENORM. Even though the FTIR spectra of the product of 95% reactor were in accordance with the BDH standards, it turned out that the XRD diffractogram were only suitable at the $2\theta = 30°$ and 28°. Then, the ZS products in the quenching process were free from SiO_2 and TENORM-free but still contained 1.48% of HfO_2. The TEM images from the quenching showed the surfaces of zirconium sulfate forming the elongated and transparent crystals. Based on the economic feasibility calculations, the new zirconium sulfate synthetic process was more profitable than the old one. This was proven by the BCR value (more than 1), indicating that it is financially feasible to be further developed to a larger scale.

■ ACKNOWLEDGMENTS

With the completion of this paper, the authors would like to thank Dr. Susilo Widodo, Suyanti S.ST, and Ir. Herry Poernomo, who helped a lot in terms of funding through DIPA 2018 with SP number 080.01.1.017290/2018. The author was also very grateful to Ali Akrom and Triyono ST, who have helped a lot for the laboratory work.

■ REFERENCES

[1] Sah, N.K., 2013, Greener Approach to Leather Techniques, *Thesis*, Centria University of Applied Sciences, Finland.

[2] Crudu, M., Deselnicu, V., Mutlu, M.M., Gulumser, G., Bitlisli, B.O., Basaran, B., and Zengin, A.C.A., 2010, New tanning agents based on titanium and zirconium, *Int. Conf. Adv. Mater. Syst.*, 1, 27–32.

[3] Castiello, D., Calvanese, G., Puccin, M., Salvadori, M., Seggiani, M., and Vitolo, S., 2011, A technical feasibility study on titanium tanning to obtain upper quality versatile leather, *XXXI IULTCS Congress*, 1–9.

[4] BAPETEN, 2009, *Intervensi terhadap paparan yang berasal dari technologically enhanced naturally occurring radioactive material*, Peraturan Kepala Badan Pengawas Tenaga Nuklir Nomor 9 Tahun 2009, Jakarta.

[5] Liu, R., Xue, T., Song, J., Wang, Y., Qi, T., Qu, J., and Du, A., 2014, Removal of silicon in acid leaching and flocculation processes during zirconium oxychloride octahydrate production, *Ceram. Int.*, 40 (6), 8801–8808.

[6] Liu, J., Song, J., Qi, T., Zhang, C., and Qu, J., 2016, Controlling the formation of Na_2ZrSiO_5 in alkali fusion process for zirconium oxychloride production, *Adv. Powder Technol.*, 27 (1), 1–8.

[7] Perks, C., and Mudd, G., 2019, Titanium, zirconium resources and production: A state of the art literature review, *Ore Geol. Rev.*, 107, 629–646.

[8] Beyer, G.H., Koerner, E.L., and Olson, E.H., 1955, Conversion of zirconium sulfates to anhydrous zirconium tetrafluoride, *Ames Laboratory ISC Technical Reports, 102*, U.S. Department of Energy, Iowa, USA.

[9] Levenspiel, O., 1999, *Chemical Reaction Engineering*, 3rd Ed., John Wiley & Sons, Inc., New York.

[10] Houchin, M.R., and Sinha, H.N., 1987, *Process for the production of zirconium sulphate*, Eur. Patent EP0289537A1.

[11] Miao, Z., Zhou, J., Zhao, J., Liu, D., Bi, X., Chou, L., and Zhuo, S., 2017, A novel mesoporous sulfated zirconium solid acid catalyst for Friedel-Crafts benzylation reaction, *Appl. Surf. Sci.*, 411, 419–430.

[12] Heshmatpour, F., and Aghakhanpour, R.B., 2012, Synthesis and characterization of superfine pure tetragonal nanocrystalline sulfated zirconia powder by a non-alkoxide sol-gel route, *Adv. Powder Technol.*, 23 (1), 80–87.

[13] Rabee, A.I.M., Mekhemer, G.A.H., Osatiashtiani, A., Isaacs, M.A., Lee, A.F., Wilson, K., and Zaki, M.I., 2017, Acidity-reactivity relationships in catalytic esterification over ammonium sulfate-derived sulfated zirconia, *Catalysts*, 7 (7), 204.

[14] Shi, G., Yu, F., Yan, X., and Li, R., 2017, Synthesis of tetragonal sulfated zirconia via a novel route for biodiesel production, *J. Fuel Chem. Technol.*, 45 (3), 311–316.

[15] Ma, L., Lv, E., Du, L., Han, Y., Lu, J., and Ding, J., 2017, A flow-through tubular catalytic membrane reactor using zirconium sulfate tetrahydrate-impregnated carbon membranes for acidified oil esterification, *J. Energy Inst.*, 90 (6), 875–883.

[16] Hauli, L., Wijaya, K., and Armunanto, R., 2018, Preparation and characterization of sulfated zirconia from a commercial zirconia nanopowder, *Orient. J. Chem.*, 34 (3), 1559–1564.

[17] Rachmat, A., Trisunaryanti, W., Sutarno, and Wijaya, K., 2017, Synthesis and characterization of sulfated zirconia mesopore and its application on lauric acid esterification, *Mater. Renewable Sustainable Energy*, 6 (3), 13.

[18] Mftah, A., Alhassan, F.H., Al-Qubaisi, M.S., El Zowalaty, M.E., Webster, T.J., Sh-eldin, M., Rasedee, A., Taufiq-Yap, Y.H., and Rashid, S.S., 2015, Physicochemical properties, cytotoxity, and antimicrobial activity of sulphated zirconia nanoparticles, *Int. J. Nanomed.*, 10 (1), 765–774.

[19] Mossayebi, Z., Saririchi, T., Rowshanzamir, S., and Parnian, M.J., 2016, Investigation and optimization of physicochemical properties of sulfated zirconia/sulfonated poly (ether ether ketone) nanocomposite membranes for medium temperature proton exchange membrane fuel cells, *Int. J. Hydrogen Energy*, 41 (28), 12293–12306.

[20] Ibrahim, A.A., Salama, R.S., El-Hakam, S.A., Khder, A.S., and Ahmed, A.I., 2021, Synthesis of sulfated zirconium supported MCM-41 composite with high rate adsorption of methylene blue and

excellent heterogeneous catalyst, *Colloids Surf., A*, 616, 126361.

[21] Imelda, Marsudi, and Yoga, 2019, Analisis biaya pengolahan pasir zirkon ($ZrSiO_4$) menjadi pasir zirkon berkadar $ZrO_2 \geq 65{,}5\%$ di PT. Sinar Hasil Alam, *JeLAST*, 6 (1), 1–6.

[22] Sasmitaloka, K., Jusnita, N., and Andayani, A., 2015, Analisis kelayakan finansial pendirian industri vanilin dengan bahan baku vanili basah (*Vanilli* spp), *JSEP*, 8 (3), 1–8.

[23] Frej, E.A., Ekel, P., and de Almeida, A.T., 2021, A benefit-to-cost ratio based approach for portfolio selection under multiple criteria with incomplete preference information, *Inf. Sci.*, 545, 487–498.

The Employment of Real-Time Polymerase Chain Reaction Using Species-Specific Primer Targeting on D-Loop Mitochondria for Identification of Porcine Gelatin in Soft Candy

Nina Salamah[1,2,3], Yuny Erwanto[4,5], Sudibyo Martono[1], and Abdul Rohman[1,5*]

[1]*Department of Pharmaceutical Chemistry, Faculty of Pharmacy, Universitas Gadjah Mada, Yogyakarta, 55281, Indonesia*

[2]*Department of Analytical Chemistry, Faculty of Pharmacy, Universitas Ahmad Dahlan, Jl. Prof Soepomo, Janturan Yogyakarta 55164, Indonesia*

[3]*Ahmad Dahlan Halal Center, Universitas Ahmad Dahlan, Jl. Prof Soepomo, Janturan Yogyakarta 55164, Indonesia*

[4]*Division of Animal Products Technology, Faculty of Animal Science, Universitas Gadjah Mada, Jl. Fauna No. 3, Bulaksumur, Yogyakarta 55281, Indonesia*

[5]*Research Centre of Halal Products, Universitas Gadjah Mada, Jl. Kaliurang Km 4, Sekip, Yogyakarta 55281, Indonesia*

Corresponding author:

tel: +62-87838445216
email: abdul_kimfar@ugm.ac.id

Received: October 6, 2020
Accepted: June 10, 2021

DOI: 10.22146/ijc.60413

Abstract: *Analysis of non-halal components, such as pork and porcine gelatin, in food and pharmaceutical products is a need for halal authentication study. This research was aimed to develop a species-specific primer (SSP) to analyze DNA in porcine gelatin in soft candy using real-time PCR. The SSP to porcine DNA primer is designed using NCBI and Primer-BLAST software. The designed primer was subjected to a validation by assessing some parameters, including specificity, sensitivity, repeatability test, and linearity. The results showed that the real-time PCR with SSP targeting on mitochondrial D-loop specifically able to identify the presence of porcine DNA at an optimum annealing temperature of 50.5 °C. The coefficient of variation (CV) on repeatability analysis of Cq was 0.53%, and the efficiency value (E) for DNA amplification was 100%. Real-time PCR using D-LOOP porcine primer (forward: ACTTCATGGAACTCATGATCCG; reverse ATGTACGTTATGTCCCGTAACC) can also be successfully used for the identification of porcine gelatin DNA in soft candy.*

Keywords: *primer D-loop; porcine DNA; real-time PCR; halal authentication*

■ INTRODUCTION

All products, including pharmaceutical, food, personal care, chemical, biotechnology, and cosmetic products declared as halal and commercially available in Indonesia, must be halal certified, according to Indonesian Act No. 33 (2014). Consequently, the authentication analysis of products from the presence of non-halal components is highly required [1]. Along with increasing public awareness to consume halal food, the markets of halal products are believed to increase exponentially [2]. Analysis of non-halal components such as pork and porcine gelatin in food products presents a certain complexity to be carried out because these non-halal components are added in a matrix having a similar composition to halal components. For example, bovine gelatin was substituted with porcine gelatin in soft candy.

Various analytical methods have been developed for the analysis of porcine gelatin and pork, such as infrared spectroscopy combined with chemometrics [3], analytical method of lard extracted from pork in meatballs, and lard in meatball broth [4], liquid chromatography through amino acid analysis in gelatin [5], liquid chromatography-mass spectrometry for analysis of porcine gelatin and bovine gelatin [6], ELISA for analysis of porcine and bovine gelatin in food products [7]. However, these methods are lack of

selectivity. Therefore, DNA-based methods like real-time polymerase chain reaction have been developed.

The real-time PCR method is a method of choice for DNA analysis from certain species because DNA is found in almost all organisms and is not easily damaged even though it is subjected to food processing at high temperatures. DNA sequences are specific to certain types of organisms so that the PCR method can be used to detect a variety of non-halal components and can be applied to processed products [8]. Real-time PCR is capable of producing the amplification curve, which can be directly observed and analyzed quantitatively using fluorescent compounds such as SYBR Green. Real-time PCR using a species-specific primer (SSP) targeting the specific genes on mitochondrial displacement loop686 (D-loop) has been successful for the analysis of non-halal components such as pork in food products such as shredded and jerky [9]. Real-time PCR using SSP CYTBWB2-wb targeting on cytochrome-b has also been used for the detection of wild boar meat [10], pork [11], and dog meat [12] in meatballs. The SSP combined with real-time PCR has also been successfully used to detect porcine gelatin in shell capsules [13]. However, there is limited study on the detection of porcine gelatin in soft candy. In this study, the new designed SSP targeting on D-loop mitochondrial was developed for identification of porcine gelatin in soft candy

■ EXPERIMENTAL SECTION

Materials

The gelatin coming from bovine and porcine were obtained from Sigma (Aldrich, USA). Beef, pork, dog meat, goat meat, chicken meat, and rabbit meat were obtained from the traditional markets in Yogyakarta. The species-specific primers were designed and tested with software from the NCBI website and were subsequently ordered from Genetika Science Company (Jakarta, Indonesia). The other solvents and chemical reagents including sodium acetate, Tris-EDTA buffer, chloroform and *iso*-amyl alcohol were bought from E. Merck (Darmstadt, Germany). The market sample used in this study was soft candy sold in supermarkets in Indonesia.

Instrumentation

The primary tool used in this study is a set of real-time polymerase chain reaction (Biorad type CFX 96, USA).

Procedure

Primers design

The software of Primerquest from Integrated DNA Technologies was used to assist in designing the primers either Forward (F) or Reversed (R) specific to the DNA of wild boar. The DNA sequences of mitochondrial Cyt-b with an accession number of AF034253 was retrieved from GenBank (NCBI). BLAST was used to *in silico* test of designed primer. The selected F and R primers were:
Forward: ACTTCATGGAACTCATGATCCG;
Reverse: ATGTACGTTATGTCCCGTAACC
The melting temperatures of the F and R primers were 63 and 62 °C, respectively, and Guanine-Cytosine (GC) contents were 50% (F) and 45.5% (R) with amplicon product of 130 base pair (bp).

Preparation of soft candy

Preparation of candy samples was carried out as previously described [14]. Briefly, 20.0 g of gelatin were weighed and then soaked with 100 mL of water for 15 min. Next, 150 g of sugar and 5 mL of mango flavoring agent were dissolved in 100 mL of water. Gelatin that has been soaked was poured into a pan sugar and flavoring agent and then cooked while stirring. After thickening, the mixture was poured into a 10 × 20 cm baking pan and was left for 4 h until it solidified. After that, the candy was cut into pieces and sprinkled with sugar.

Isolation of DNA

The DNA was isolated from raw meats, porcine and bovine gelatin, and soft candy containing gelatins in its formulation. For isolation of DNA from raw meats, six types of meat, namely bovine (*Bos taurus*), Pigs (*Sus scrofa*), Goats (*Capra hircus*), chickens (*Gallus gallus*), rabbits (*Lepus curpaeums*), and dogs (*Canis lupus familiaris*) were used. This isolated DNA from raw meats was used for specificity testing of the designed primer. The crushed meat (approximately 200 mg) was weighed, added with 700 µL of buffer lysis, heated for

15 min at 65 °C, then added with 10 µL of proteinase K (2%), and homogenized using a vortex. The mixture was then incubated at a water temperature of 65 °C for 55 min, vortexed every 10 min, and then incubated in the water bath at a temperature of 38 °C for 30 min, and followed by centrifuging the supernatant at 13,000 rpm for 15 min. The supernatant was placed into a new Eppendorf tube, added with 0.5× volume of phenol and 0.5× volume of chloroform-*iso*-amyl alcohol. The mixture was shaken with a shaker for 30 min, followed by a centrifugation process at 13,000 rpm for 15 min. The supernatant was then removed, followed by addition of 1× volume of chloroform, homogenized, and subsequently centrifuged at 13,000 rpm for 15 min. The supernatant was moved and followed by the addition of 0.1× volume of 3 M sodium acetate pH 5.2 and 2× volume of absolute ethanol, and then incubated at -80 °C overnight. The mixture was centrifuged (at 4 °C) for 5 min at 13,000 rpm, and the supernatant was immediately discarded. The remaining ethanol was dried in laminar airflow for approximately 10 min, and each sample was followed by the addition of 40 µL of Tris-EDTA buffer and stored in the refrigerator -20 °C for subsequent analysis [15].

For isolation of gelatin and candy, samples containing gelatin were prepared by weighing approximately 100 mg (standard gelatin) or 200 mg of reference candies. Then, the gelatin and candy samples were incubated at a water temperature of 65 °C until dissolved with vortex every 15 min. Then, the mixture was added with 1 mL of absolute ethanol and followed by a centrifugation process at 13,000 rpm for 3 min at room temperature. The supernatant is then removed, and the obtained precipitate was subjected to the addition of 800 µL of heated buffer lysis and 20 µL of proteinase K (2%) and shaken manually until homogeneous. The mixture was incubated in a water bath at 65 °C for 75 min, vortexed every 15 min. Each sample was then added with 0.5x volume of phenol and 0.5× volume of chloroform-*iso*-amyl alcohol and shaken for 40 min. Then, the mixture was centrifuged for 30 min at 14,500 rpm at room temperature. The supernatant was subjected to the addition of 1× volume of chloroform and shaken for 15 min. The mixture was subsequently subjected to centrifugation process at 14000 rpm for 10 min. Furthermore, the supernatant was subjected to the addition of 3× volume of Na-acetate 3 M, 2× volume of ethanol, and incubated at -80 °C overnight, followed by centrifugation at 14,500 rpm for 5 min at 4 °C. Finally, the supernatant was immediately discarded, and the obtained DNAs were used for real-time PCR analysis.

Determination of purity and concentration of isolated DNA

The purity index of DNAs was analyzed using an ultraviolet spectrophotometer at a wavelength λ of 260 and 280 nm. The levels of analytes (concentration) of DNA were calculated based on the absorbance values at λ of 260 nm multiplied by 50 µg/mL and the dilution factor.

Real-time PCR analysis

The annealing temperature of the primer was optimized by applying the temperature range of 46–52 °C based on the prediction of the melting temperature of the primer. Some temperatures were subjected to optimization, at 49.5, 50.5, and 59.5 °C.

The real-time PCR analysis was performed in reaction tube (total volume of 20 µL) consisting of 10 µL of SYBR Green® universal PCR master mix, 1 µL of forward and reverse primer (10µm/µL), 2 µL of template DNA (50 ng) and 6 µL of free nuclease water. The temperature program used was 95 °C for 30 sec followed by 40 cycles at 95 °C for 5 sec for the denaturation stage. The next stage was the annealing of primer at 50.5 °C that has been previously optimized for 30 sec and 72 °C for 10 sec for the extension (elongation) stage. The melting curve of the PCR reaction was performed at 65–95 °C with a slope of 0.5 °C/5 sec.

Validation of the real-time PCR method

The real time-PCR using designed primer was validated to meet its purpose according to Codex Alimentarius Commission [16]. Some parameters, namely specificity, amplification efficiency, the limit of detection, and repeatability, were evaluated. The primer specificity was confirmed by amplifying DNAs extracted from raw meats and negative control called no template control (NTC). The standard curves for linearity tests

were made based on the amplification of reference candies with various concentrations. Linear regression equation made by comparing the value of Quantification circle (Cq) in *y-axis* to the log value of DNA concentration in *x-axis* was used to determine the efficiency value (E) and limit of detection. The repeatability of the real-time PCR method was assessed based on the coefficient of variation (CV) Cq values during amplification.

Analysis of commercial samples

The validated real time-PCR using species-specific primer was then applied for analysis of porcine gelatin in various candy products commercially available in markets around Yogyakarta, Indonesia.

Data analysis

The data analysis for real-time PCR was done with a standard curve created by comparing the value of Quantification circle (Cq) against the log value of DNA concentration. Efficiency (E) real-time PCR is calculated according to Eq. 1 [17]:

$$\%E = \left(10^{-1/\text{slope}} - 1\right) \times 100\% \quad (1)$$

■ RESULTS AND DISCUSSION

The primary design was carried out using the Primary Quest Tool online software with access code AF034253 targeting on mitochondrial D-loop of *Sus scrofa* (Table 1). The primers were selected by considering several primary design parameters, such as 15–30 bp in length, 40–60% GC content, G and C nucleotides evenly distributed, and the primer and melting temperature (Tm) range at 50–60 °C [18]. The Tm in primers was used to determine the optimization of the annealing temperature of target DNA. Too high or too low of Tm causes the target DNA amplicon to not specifically attach. The GC content in a pair of primers is almost the same. Inadequate GC content can cause the presence of polypurine and polypyrimidine, which will affect the primer not specifically attached [19].

The purity of isolated DNA from fresh meat showed high purity with A260/A280 ratio values obtained close to 1.8. The results of DNA purity from the standard pork gelatin and reference candy samples have ratio values below 1.8. The DNA isolates have experienced degradation during gelatin production from the original material. The DNA purity results of the gelatin are shown in Table 2. The designed primers were then used to optimize the temperature of the porcine DNA attachment to DNA isolates from other meats (beef, pig, chicken, goat, dog, and rabbit).

The primer optimization was carried out on meat DNA isolates because they were easier to obtain variations of animal species likely used as a basis for gelatin than gelatin variations from different species sources. The results of primer optimization can be seen in Fig. 1(a). The observations on the melt peak curve indicated one peak produced at a temperature of 78.0 °C, shown in Fig. 1(b). The annealing temperature optimization is based on several parameters, namely the

Table 1. Results of primary and reverse forward primary designs

Sequence (5'-3')	Nucleotide bases (bp)	Tm (°C)	GC (%)
F: ACTTCATGGAACTCATGATCCG	22	58.20	45.45
R: ATGTACGTTATGTCCCGTAACC	22	57.95	45.45

Table 2. Quantitative results of gelatin DNA and DNA candy references with a nanodrop

No.	Sample Type	A_{260}	A_{280}	Concentration (ng/µL)	Purity index
1	Porcine Gelatin	2.8837	1.3757	1883.74	1.37
2	Bovine Gelatin	2.6668	1.1788	1666.81	1.41
3	Soft candy reference	1.1177	0.8502	1117.74	1.31

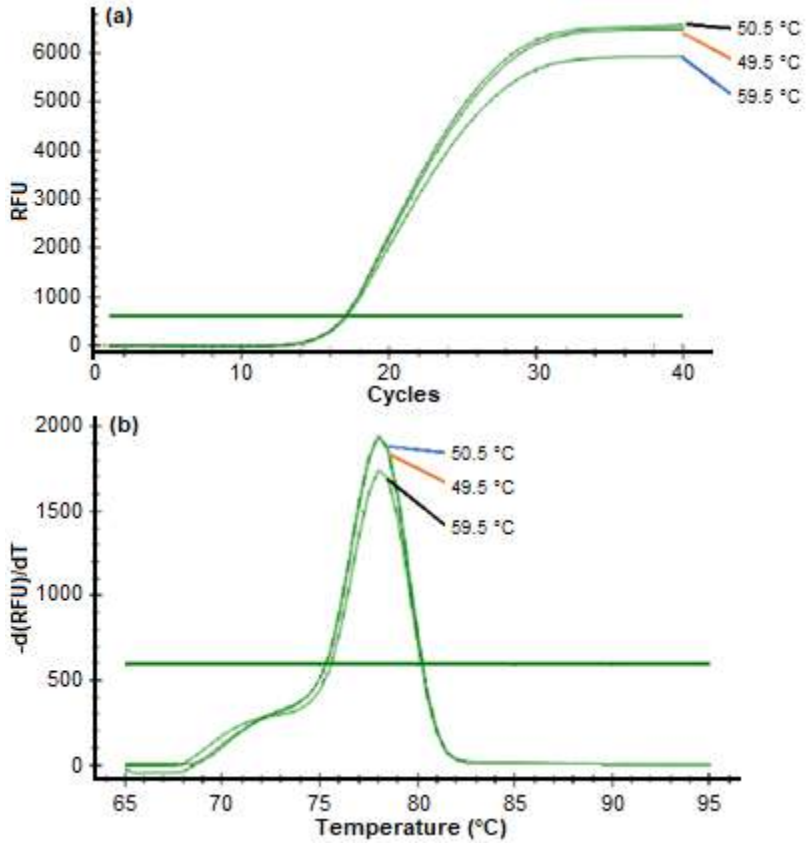

Fig 1. The results of the optimization of D-loop primary attachment temperature in 40-cycle pig DNA, using real-time PCR, (a) amplification, and (b) melting curve

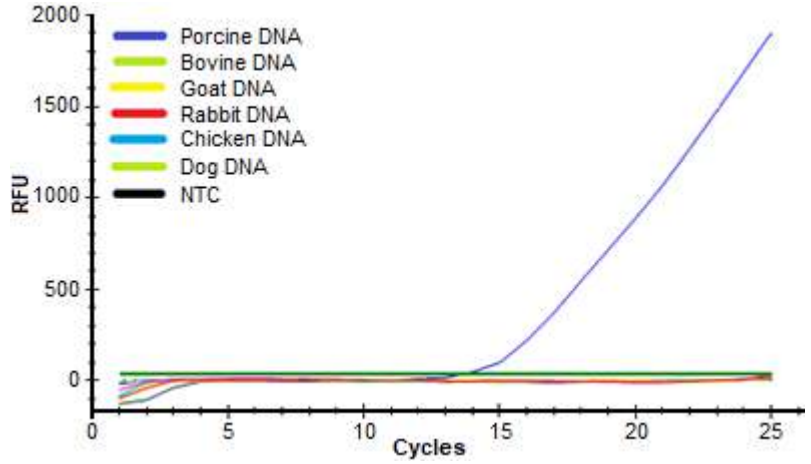

Fig 2. Amplification of the results of the porcine primary specifications against the DNA of other animals

lowest cycle quantification (Cq) value, the minimum non-specific product, and the minimum dimer primary products [20-21]. The optimization of the primary annealing temperature of porcine DNA in this study was 50.5 °C, with a value of Cq of 17.16. Furthermore, the specificity of the primer was tested at the optimum annealing temperature. Based on Fig. 2, it can be seen that the designed primer is specific, in which porcine DNA is amplified while other DNAs along with the negative template control (NTC) are not amplified.

The specific primer was subjected to validation by performing several performance characteristics, including linearity and repeatability tests using the reference DNA samples made from porcine gelatin. Fig. 3 shows a linear regression curve with an R^2 value of 0.971 and an efficiency value of 100.0%. The obtained efficiency values meet the acceptance requirements in the range of 90–110%, but the R^2 value obtained does not meet the qPCR method qualitative and quantitative testing criteria, namely $R^2 = 0.980$ [17]. The lower R^2 values obtained than the required acceptance criteria are probably due to the inhomogeneity of the reference candy products.

The repeatability test to measure the precision of the amplification results from the reference DNA samples containing porcine gelatin was performed by calculating the standard deviation (SD) and the coefficient of variation (CV). The repeatability expresses the closeness of results between a series of measurements obtained from homogeneous samples under predetermined conditions in a short time [22]. The amplification data obtained during precision studies can be seen in Fig. 4. The DNA repeatability test of the reference candy containing pigs resulted in CV = 0.53% (Table 3), which is acceptable for q-PCR, namely CV ≤ 25% [19].

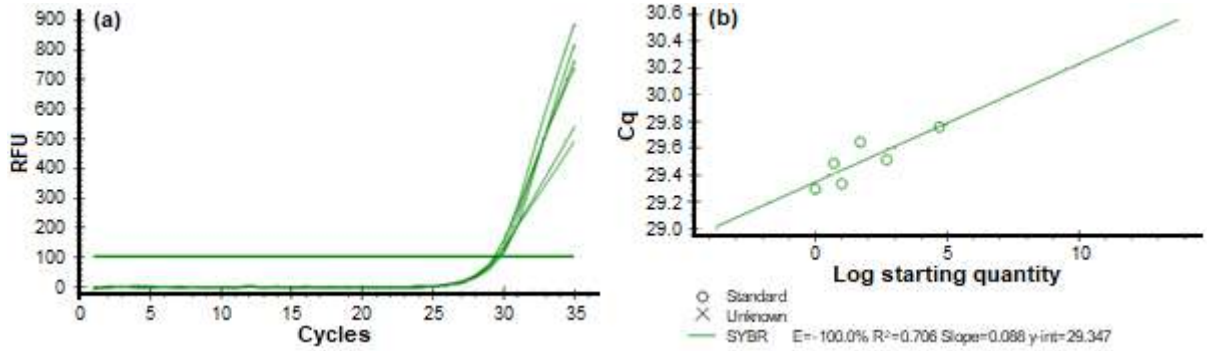

Fig 3. The reference of candy DNA dilution series made from porcine gelatin, (a) amplification and (b) standard curve

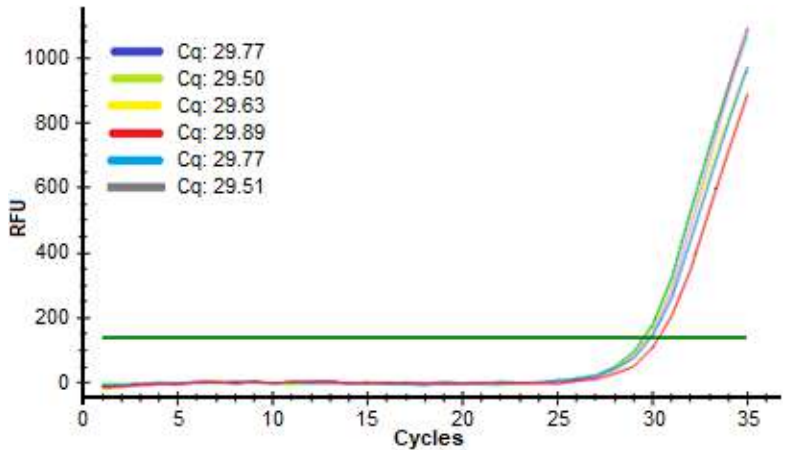

Fig 4. DNA test results of reference candy stability containing porcine gelatin

Table 3. DNA test results for reference candy containing pig gelatin

Sample	Cq	average Cq	SD	CV (%)
Porcine DNA gelatin concentration 50 (ng/µL)	29.77 29.50 29.63 29.89 29.77 29.51	29.68	0.1575	0.53

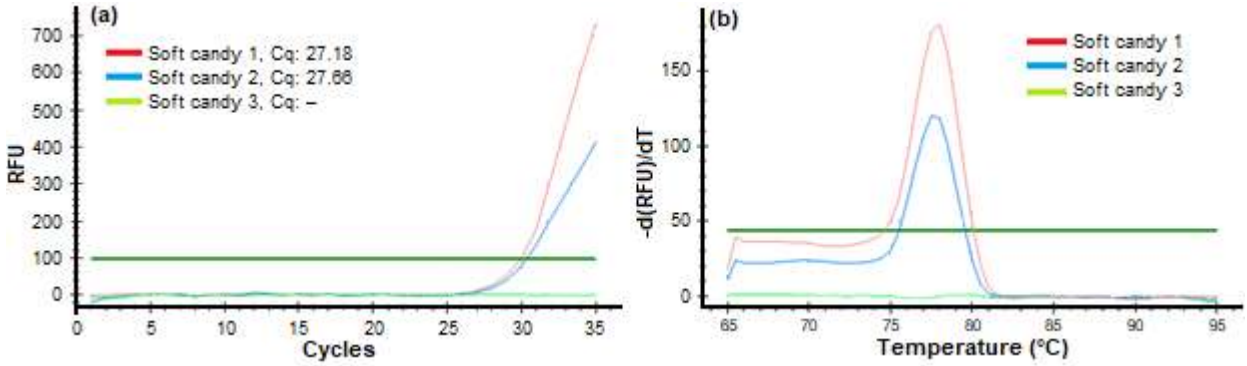

Fig 5. The results of DNA isolates from candy market samples, (a) amplification and (b) melting curve analysis

Therefore, this method is quite precise and precise for analysis candy containing pork gelatin.

The validated method was then applied to commercial samples, and the results can be seen in Fig. 5. There are three market samples tested with third specifications that do not have a halal label, and it turns out that two samples were amplified using primers that have been validated, which means that the sample is likely to contain pig DNA. The results of the melt curve show that both samples have the same Tm at 78 °C. Meanwhile, one sample was not amplified with the designed primer, so that it is most likely that the sample does not contain pig DNA.

■ CONCLUSION

The real-time PCR method with the D-loop primer (forward: ACTTCATGGAACTCATGATCCG; reverse ATGTACGTTATGTCCCGTAACC) can be applied to detect porcine gelatin in soft candy. The optimum annealing temperature was 50.5 °C. The coefficient of variation (CV) on repeatability analysis of Cq was 0.53%, and the efficiency value (E) for DNA amplification was 100%. The developed method is successfully used for the analysis of actual samples with acceptable precision and accuracy. This method can be used as a standard method for the detection of non-halal components (porcine gelatin) for halal authentication study.

■ ACKNOWLEDGMENTS

The authors thank the Ministry of Research and Higher Education, the Republic of Indonesia, through the scheme "*Hibah Penelitian Doktor*" for the year 2020.

■ AUTHOR CONTRIBUTIONS

Nina Salamah and Yuny Erwanto conducted the experiment, Sudibyo Martono and Abdul Rohman conducted the data analysis calculations, Nina Salamah, Yuny Erwanto, Sudibyo Martono, and Abdul Rohman wrote and revised the manuscript. All authors agreed to the final version of this manuscript.

■ REFERENCES

[1] Ali, M.E., Kashif, M., Uddin, K., Hashim, U., Mustafa, S., and Che Man, Y.B., 2012, Species authentication methods in foods and feeds: The present, past, and future of halal forensics, *Food Anal. Methods,* 5 (5), 935–955.

[2] Rahman, M.M., Ali, M.E., Abd Hamid, S.B., Mustafa, S., Hashim, U., and Hanapi, U.K., 2014, Polymerase chain reaction assay targeting cytochrome b gene for the detection of dog meat adulteration in meatball formulation, *Meat Sci.*, 97 (4), 404–409.

[3] Cebi, N., Durak, M.Z., Toker, O.S., Sagdic, O., and Arici, M., 2016, An evaluation of Fourier transforms infrared spectroscopy method for the classification and discrimination of bovine, porcine and fish gelatins, *Food Chem.*, 190, 1109–1115.

[4] Kurniati, E., Rohman, A., and Triyana, K., 2014, Analysis of lard in meatball broth using Fourier transform infrared spectroscopy and chemometrics, *Meat Sci.*, 96 (1), 94–98.

[5] Nemati, M., Oveisi, M., Abdollahi, H., and Sabzevari, O., 2004, Differentiation of bovine and

porcine gelatins using principal component analysis, *J. Pharm. Biomed. Anal.*, 34 (3), 485–492.

[6] Zang, G.F., Liu, T., Wang, Q., Lei, J.D., Ma, G.H., and Su, Z.G., 2008, Identification of marker peptides in digested gelatins by high performance liquid chromatography/mass spectrometry, *Chin. J. Anal. Chem.*, 36 (11), 1499–1504.

[7] Doi, H., Watanabe, E., Shibata, H., and Tanabe, S., 2009, A reliable enzyme linked immunosorbent assay for the determination of bovine and porcine gelatin in processed foods, *J. Agr. Food. Chem.*, 57 (5), 1721–1726.

[8] Pereira, F., Carneiro, J., and Amorim, A., 2008, Identification of species with DNA-based technology: Current progress and challenges, *Recent Pat. DNA Gene Sequences*, 2 (3), 187–199.

[9] Maryam, S., Sismindari, Raharjo, T.J., Sudjadi, and Rohman, A., 2016, Analysis of porcine contamination in laboratory prepared *dendeng* using mitochondrial D-loop686 and *cytb* gene primers by real time polymerase chain reaction, *Int. J. Food Prop.*, 19 (1), 187–195.

[10] Arini, R.L., Ramadhani, D., Pebriyanti, N.W., Sismindari, and Rohman, A., 2018, The use of species-specific primer targeting on D-loop mitochondrial for identification of wild boar meat in meatball formulation, *J. Adv. Vet. Anim. Res.*, 5 (3), 361–368.

[11] Aina, G.Q., Erwanto, Y., Hossain, M., Johan, M.R., Ali, M.E., and Rohman, A., 2019, The employment of q-PCR using specific primer targeting on mitochondrial cytochrome-b gene for identification of wild boar meat in meatball samples, *J. Adv. Vet. Anim. Res.*, 6 (3), 300–307.

[12] Ali, M.E., Razzak, M.A., Hamid, S.B.A., Rahman, M.M., Rashid, N.R.A., and Asing, 2015, Multiplex PCR assay for the detection of five meat species forbidden in Islamic foods, *Food. Chem.*, 177, 214–224.

[13] Sudjadi, Wardani, S., Sepminarti, T., and Rohman, A., 2016, Analysis of porcine gelatin DNA in commercial capsule shell using real-time polymerase chain reaction for halal authentication, *Int. J. Food Prop.*, 19 (9), 2127–2134.

[14] Raraswati, M.A., Triyana, K., and Rohman, A., 2014, Differentiation of bovine and porcine gelatins in food products based on amino acid profiles and chemometrics, *J. Food Pharm. Sci.*, 2 (1), 23–26.

[15] Sambrook, J., Fritsch, E.F., and Maniatis, T.A., 1989, *Molecular Cloning: A Laboratory Manual*, 2nd Ed., Cold Spring Harbor Laboratory Press, Cold Spring Harbor, NY, USA.

[16] Codes Alimentarius, 2010, CAC/GL 74-2010 *Guidelines on Performance Criteria and Validation of Methods for Detection, Identification and Quantification of Specific DNA Sequences and Specific Proteins in Foods*, http://www.codex alimentarius.org/standards/list-of-standards/.

[17] Bio-Rad, 2006, *Real Time PCR Application Guide*, Bio-Rad Laboratories, Inc., USA.

[18] Borah, P., 2011, Primer designing for PCR, *Sci. Vis.*, 11 (3), 134–136.

[19] Fajardo, V., Gonzalez, I., Rojas, M., Garcia, T., and Martin, R., 2010, A review of current PCR-based methodologies for authentication of meats from game animal species, *Trends Food Sci. Technol.*, 21 (8), 408–421.

[20] Nadeau, J., 2011, *Introduction to Experimental Biophysics: Biological Methods for Physical Scientists*, 1st Ed., CRC Press, Boca Raton, FL.

[21] Stanta, G., 2011, *Guidelines for Molecular Analysis in Archive Tissues*, Springer-Verlag Berlin Heidelberg.

[22] ICH, 2005, Q 2 (R1) *Validation of Analytical Procedures, Text and Methodology 15*, European Medicines Agency, London, UK.

Formulation of Blush Preparations by Using Natural Coloring from Red Beetroot Extract *(Beta vulgaris* L.)

Suci Wulan Sari[1*], Ratna Djamil[2], and Faizatun[3]

[1]*Master of Pharmacy, Pancasila University, Jl. Srengseng Sawah, Jagakarsa, South Jakarta 12640, Indonesia*

[2]*Department of Biological Pharmacy, Faculty of Pharmacy, Pancasila University, Jl. Srengseng Sawah, Jagakarsa, South Jakarta 12640, Indonesia*

[3]*Department of Pharmaceutical Technology, Faculty of Pharmacy, Pancasila University, Jl. Srengseng Sawah, Jagakarsa, South Jakarta 12640, Indonesia*

* ***Corresponding author:***

email: suciwulans92@gmail.com

Received: October 6, 2020
Accepted: May 2, 2021

DOI: 10.22146/ijc.60414

Abstract: *Beetroot (*Beta vulgaris *L.) has compounds that can be used for body health, beauty skincare, food additives, and much more. This research was aimed to prepare the dry extract of beetroot and formulate it into a loose powder, compact powder, and cream. The preparation was started by adding 2, 4, or 6% of dry extract, then blending the pulp and drying the resultant residue using a freeze dryer. Testing on color homogeneity, polishing, breakage, pH stability, color stability, and the hedonic test was carried out to determine the product quality. The initial result of phytochemical screening showed it might contain flavonoids, alkaloids, saponins, tannins, triterpenoids, steroids, and quinones. The color stability test performed at 30 °C showed that the cream was unstable while other forms showed fair stability at 8 °C. All dosage forms were homogeneous and could be applied easily. The breakage test showed no fractures. The pH remained stable for all formulas (between 3–5) after 28 days of storage. The color stability test showed that the significant discoloration only happened to the loose powder and cream. The hedonic test showed that the compact powder with a concentration of 6% was the most preferred formula by users.*

Keywords: *beetroot;* Beta vulgaris *L.; blush on; loose powder; compact powder; cream*

■ INTRODUCTION

A research on the consumer buying behaviour towards cosmetic products in 2015 in Pune city showed that of 200 consumers of cosmetic products, 60% preferred to buy organic cosmetics and 42.5% used the cosmetic products for the beauty [1]. Similarly, a research regarding the consumers behavior towards the cosmetic products in Delhi [2] stated that the factors that motivate consumers to buy the cosmetic products were influenced by the culture and social life of consumers as well as their psychological condition that might be affected by the advertisement they saw about cosmetic products [2].

Cosmetics are any substances or unit doses intended to be applied on the entire exterior of the human body including teeth and the mucous membranes around the mouth [3]. Previous research showed that 73% consumers used cosmetics as protection to their skin and others used it as fashion (37%) and to attract people (19%) [4]. Another reason why consumers use cosmetics is to treat disease on their skins [5].

Based on their characteristics, the cosmetic powders can be classified into 2 types, namely loose powder, and compact powder. The particle size of the compact powder is generally greater than that of the loose powder. The dust cloud may be formed during the handling or the use of loose powder so that the safe inhalation should be anticipated. The compact powder is expected to be safer than loose powder, due to the compressed format and the more practical application to the skin [6-7].

Herbal cosmetics are plant-derived-cosmetics which refer to products formulated using several types of cosmetic ingredients that are permitted to form a

basis on which one or more herbal ingredients are used [8]. Previous research showed that some herbal plants were the right choice in treating various disorders on the skin such as inflammation, aging, eczema as well as irritation [9].

Beetroot (*Beta vulgaris* L.) not also can be used as a herbal treatment and a source of antioxidant but it also serves as a natural colorant in food due to the presence of betalain in the extract derived from the root and stem parts of this plant [10-12]. A betalain is a water-soluble flavonoid compound, which has two groups, namely red betacyanin and yellow betaxanthin [13-14]. Previous research [15] successfully used betalain from the beetroot extract to deliver red color in Indian sweet food. However, the instability under heating conditions is one of the shortcomings of betacyanin which is affected by pH, temperature, and oxidation. Elevated temperatures and long heating time can cause decomposition and structural changes in pigment and lead to discoloration [13].

In general, natural colorants have no toxic or allergic properties and show fewer side effects. Their biodegradable properties make them safer to use than the synthetic dyes which sometimes may damage health and environment [16-17]. Natural colorants serve as antimicrobial, UV protection, deodorizing finishing, moth resistant, and food coloration. It has been classified into six classes based on application methods which are mordant dyes, vat dyes, direct dyes, acid dyes, basic dyes, and disperse dyes [18]. Anthocyanins, ones of the important compounds contained in natural colorants, are abundantly available in nature and have many biological activities such as fostering the health of eyes and improving the stability of capillary [19].

This research was aimed to prepare the dry extract of beetroot and to formulate the extract as blushes in the forms of loose powder, compact powder, and cream. The freeze-drying method was done to obtain dry extracts while maintaining the color stability of betacyanin [13]. The beetroot extract was obtained by blending and filtering it to get the filtrate, then drying it using a freeze dryer. The content of betacyanin in the beetroot can be used as a dye in dosage forms. The formulation of blushes in the form of loose powder, compact powder, and cream was aimed to enhance the potency of the natural color by adding 2, 4, or 6% of dry extract into each formula. This research was aimed to explore the potential of beetroot (*Beta vulgaris* L.) as a natural colorant agent, especially for red color, and the application when it formed as compact powder.

■ EXPERIMENTAL SECTION

Materials

The materials used in this study included: fresh beetroot (*Beta vulgaris* L.) obtained from Pasir Mulya organic Indonesia farm, talcum (90% purity, Pingdu Talc Mine, Shandong), oleum ricini (87.4% purity, Fagron, Rotterdam), acidum ascorbicum (99.8% purity, CSPC Weisheng Pharmaceutical), magnesium stearate (Faci Asia Pacific, Singapore), methylparaben (100.3%), vaseline album, oleum cacao (Bumi Tangerang Mesindotama, Tangerang), adeps lanae (Fagron, Rotterdam), 99.9% propylene glycol, cera alba (Caesar Loretz, Germany), cetyl alcohol (Ecogreen Oleochemicals, Jakarta), iron(III) chloride solution (Merck, Germany), formaldehyde 30% (Merck, Germany), HCl (Merck, Germany), NaOH (Merck, Germany), Mg_2SO_4 (Merck, Germany), *n*-amyl alcohol (Merck, Germany), acetic acid (Merck, Germany), sulfuric acid (Merck, Germany), chloroform (Merck, Germany), sodium acetate (Merck, Germany), Dragendorff reagent, Mayer reagent and distilled water (Brataco).

Instrumentation

pH stability was measured at 25 °C and 8 °C using the Delta 320 pH meter (Mettler-Toledo, Schwerzenbach, Switzerland. Color stability was measured at 25 °C and 8 °C using skin color probe (dermalab combo, Denmark).

Procedure

Preparation of the dosage forms from beetroot extract

The fresh beetroot (1 kg) was washed using running water to remove the dust and dirt. The clean material was cut into small pieces then blended and filtered to separate it from the residue. The pH of the

filtrate was determined. The pH should be in the range of 4–6 to produce stability [20]. The filtrate with a stable pH was then dried using a freeze dryer to obtain the dry extract. The next process was phytochemical screening to identify the compounds contained in the extract [21-22].

Phytochemical screening

Identification of tannin. In a beaker glass, 40 mg of extract was added into 100 mL of boiled water for 15 min and the mixture was left for a while so that it could be filtered using filter paper. The filtrate obtained was divided into two parts, each of 5 mL, and put into a test tube.

On tube 1:

A few drops of 1% iron(III) chloride solution was appended to form a blue-green violet precipitate indicating the presence of tannin compounds.

On tube 2:

The filtrate was added with 15 mL of Stiasny's reagent (formaldehyde 30%:concentrated HCl = 2:1) then heated on a water bath to form a pink precipitate which indicated the presence of condensed tannins. Having filtered, it was saturated with sodium acetate powder and then added a few drops of 1% iron(III) chloride solution to show the presence of hydrolyzed tannins.

Identification of flavonoid. As much as 40 mg of extract was added to 100 mL of hot water, the mixture was boiled for 5 min, then filtered to be used as the test solution. The solution (5 mL) was put into a test tube and then added 0.1 mg of powder or magnesium plate and 1 mL of concentrated HCl, and 5 mL of *n*-amyl alcohol. Having vigorously shaken, the mixture was allowed to separate. The formation of red, yellow or orange color in the amyl alcohol solution indicated the presence of flavonoids.

Identification of saponin. The extract (40 mg) was diluted with 20 mL of water, put into a test tube, shaken vertically for 10 sec and left for 10 min. The results showed a formation of a stable foam in the test tube. As an indication of the presence of the saponin group, the foam remained stable when 1% of HCl solution was added into the test tube.

Identification of steroid and triterpenoid. The extract (20 mg) was macerated with 20 mL ether for 2 h (in a container with a tight lid), and then filtered. The filtrate (5 mL) was evaporated in the evaporator cup until a residue was obtained. The residue was then added with two drops of anhydrous acetic acid and a drop of concentrated sulfuric acid (Liebermann-Burchard reagent). While the formation of green color indicated the presence of steroid, the formation of red color indicated the presence of triterpenoid.

Identification of alkaloid. The extract (40 mg) was added to 5 mL of the concentrated ammonia solution (30%). The mixture was then grinded in a mortar, then added with 20 mL of chloroform and grinded again strongly. The mixture was filtered with filter paper to obtain a filtrate in the form of an organic solution (as solution A). Solution A (10 mL) was extracted with 10 mL of HCl solution 2 M in a ratio of 1:10 by shaking in a test tube and then the upper layer was taken (as solution B). The filter paper was dripped with a few drops of solution A then sprayed and then dripped with Dragendorff reagent. The formation of red-orange color on the filter paper showed the presence of alkaloids. Solution B was divided into two test tubes, each was added with Dragendorff and Mayer reagents. The formation of brick-red sediment on the Dragendorff reagent and white precipitate on the Mayer reagent, showed the presence of alkaloids.

Preparation of compact powder

The comparison of each composition of the blush formula in the form of compact powder can be seen in table 1. The blush was made into 10 g dosage form. The ingredients including dry extract of beetroot CP2; CP4; CP6 (0.2; 0.4; 0.6 g) oleum ricini (0.25 g); ascorbic acid (0.2 g); magnesium stearate (0.5 g); methylparaben (0.1 g) and talcum CP2; CP4; CP6 (8.75; 8.55; 8.35 g) were weighed. The weighted extract was then mixed and grinded with a portion of talcum in a clean mortar until it became homogeneous and dry. The next step was to mix the other ingredients and grinded again until it became homogeneous and soft for about 15–20 min to disperse it completely, and then print it in a container to make it dry. The powder was then placed in a tightly closed container.

Table 1. The formulas of beetroot extract into blushes dosage forms

Material	Formula (%)								
	Compact Powder			Loose Powder			Cream		
	CP2%	CP4%	CP6%	LP2%	LP4%	LP6%	C2%	C4%	C6%
Extract (Coloring agent)	2	4	6	2	4	6	2	4	6
Mg Stearate (Adhesive to skin)	5	5	5	5	5	5	-	-	-
Metil Paraben(Antimicrobic)	1	1	1	1	1	1	1	1	1
Ascorbic Acid (Antioxidant)	2	2	2	2	2	2	2	2	2
Oleum ricini (Binding)	2.5	2.5	2.5	1.5	1.5	1.5	20	20	20
Adeps lanae (Emulsifying agent)	-	-	-	-	-	-	5	5	5
Cetyl alcohol (Emulsifying agent)	-	-	-	-	-	-	2	2	2
Oleum cacao (Basis cream)	-	-	-	-	-	-	15	15	15
Cera alba (Basis cream)	-	-	-	-	-	-	10	10	10
Propylene glycol (Humectant)	-	-	-	-	-	-	10	10	10
Vaselin album (Basis cream)	-	-	-	-	-	-	20	20	20
Talcum (Basis powder and compact powder)	Ad 100	Ad 100	Ad 100	Ad 100	Ad 100	Ad 100	-	-	-
Aquadest (Solvent)	-	-	-	-	-	-	Ad 100	Ad 100	Ad 100

Notes : *) LP2% = Loose powder with beetroot extract 2%
LP4% = Loose powder with beetroot extract 4%
LP6% = Loose powder with beetroot extract 6%
CP2% = Compact powder with beetroot extract 2%
CP4% = Compact powder with beetroot extract 4%
CP6% = Compact powder with beetroot extract 6%
C2% = Cream with beetroot extract 2%
C4% = Cream with beetroot extract 4%
C6% = Cream with beetroot extract 6%

Preparation of loose powder

The comparison of each composition in the blush formula in the form of loose powder can be seen in Table 1. The procedure has no difference with the compact powder except at the last stage. The blush was made into 10 g dosage. The ingredients including the dry extract of beetroot LP2; LP4; LP6 (0.2; 0.4; 0.6 g); oleum ricini (0.15); ascorbic acid (0.2 g); magnesium stearate (0.5 g); methyl paraben (0.1 g) and talcum LP2; LP4; LP6 (8.85; 8.65; 8.45 g) were weighed. The weighed extract was then mixed and grinded with a portion of talcum in a clean mortar until it became homogeneous and dry. The next step was to mix the other ingredients and then grinded again until homogeneous and soft for about 15–20 min to disperse completely it, and then sieved using a sieve (100 mesh). The powder was then placed in a tightly closed container.

Preparation of cream

The comparison of each composition in the blush formula in the form of cream can be seen in Table 1. The blush was made into 10 g dosage. The ingredients including dry extract of beetroot C2%; C4%; C6% (0.2; 0.4; 0.6 g) oleum ricini (2 g); ascorbic acid (0.2 g); methyl paraben (0.1g); vaseline album (2 g); oleum cacao (1.5 g); adeps lanae (0.5 g); propylene glycol (1 g); cera alba (1 g) and cetyl alcohol (0.2 g) were weighed. The results were then processed into two phases.

Phase A. Oleum ricini (2 g); oleum cacao (1.5 g); adeps lanae (0.5 g); cera alba (1 g); vaseline album (2 g) and cetyl alcohol (0.2 g) were melted in a water bath and then stirred until they became homogeneous.

Phase B. The extract was dissolved with propylene glycol (1 g) and distilled water (1.3; 1.1; 0.9 mL) then stirred until dissolved. Then, phase A and phase B were

inserted into the mortar and grinded until homogeneous and a cream mass was formed. The mass was then added with ascorbic acid (0.2 g); methyl paraben (0.1 g) and dry extract of beetroot C2%; C4%; C6% (0.2; 0.4; 0.6 g) and the mixture was grinded again until homogeneous.

Evaluation Tests

Color homogeneity test

Homogeneity test was done by applying the sample on a piece of glass or other suitable transparent material [23]. The blushes should show a homogeneous arrangement and show no coarse grains.

Polishing test

The polishing test was carried out on all dosage forms in each formula. Each formula was applied to the inner arm three times to observe the color [24].

Breakage test

This test was only performed for the compact powder by dropping the powder on the wooden surface three times at a height of 0.2–0.25 m [24].

pH stability test

The measurements were made on the 1st, 7th, 14th, 21st, 28th days using a pH meter.

Color stability test

The dosage forms stored at 8 °C and 30 °C were tested for the color stability on the 1st, 7th, 14th, 21st, 28th days using the Dermalab Combo by observing the *a value [25].

Hedonic test

The hedonic test was carried out visually on 20 panelists who had knowledge regarding the assessment method [23]. Each panelist was requested to observe the appearance, texture, smell and color when applied to the skin. The panelists were requested to fill out the questionnaire column that had been given and gave a score as displayed in Table 2.

■ RESULTS AND DISCUSSION

Phytochemical Screening

The initial phytochemical screening showed that the beetroot (*Beta vulgaris* L.) extract might contain flavonoids, alkaloids, saponin, tannin, triterpenoids, steroids (Table 3). The phytochemical screening was carried out to identify flavonoids in the extract of beetroot (*Beta vulgaris*). Betacyanin, which is the red pigment of the beetroot (*Beta vulgaris* L.), is an example of flavonoids. The presence of flavonoids was indicated by the color change from pink to brownish orange due to the addition of reagents of Mg metal and concentrated HCl to the extract. The treatment was aimed to reduce the benzopyrone moiety in the structure of flavonoids to generate red or orange flavylium salts [26]. The saponins tests showed positive results to all beetroot extracts, which was indicated by the formation of stable foam [26]. Saponins are compounds in plants included in the terpenoid group containing the isoprene framework $CH_2=C(CH_3)–CH=CH_2$. The presence of saponins can be detected based on their ability to form foam due to their soap-like properties [27]. The tannin test was carried out using the solution of 1% $FeCl_3$ reagent. The positive result was marked by changes in color to blackish green which indicated the presence of tannins that reacted with Fe^{3+} ions to form complex compounds [26-27]. The results showed that all beetroot extract positively contains alkaloids, which was indicated by the formation of the orange-red precipitate [28] when using

Table 2. The preference point used in hedonic scale

Score	Explanation
9	Extremely Like
8	Really Like
7	Like
6	Fairly Like
5	Neutral
4	Fairly dislike
3	Dislike
2	Really Dislike
1	Extremely Dislike

Table 3. Phytochemical screening results of *Beta vulgaris* L. extract

Secondary Metabolites	Test results
Flavonoids	+
Alkaloids	+
Steroids	+
Tanin	+
Saponin	+
Steroids and Triterpenoids	+

the Dragendorff reagent and the white precipitate when using the Mayer reagent containing mercuric chloride and potassium iodide. The precipitation occurred since the nitrogen atom in the alkaloids can replace the iodide ion to form the coordination bond with metal ions. In addition, the triterpenoid and steroid tests showed positive results by adding acetic acid and sulfuric acid which might bind to a terpenoid/steroid compound to produce a color change reaction [29].

Color Homogeneity Test

The homogeneity test is important because it can determine whether the resulting blush preparation meets the aesthetic requirements or not. A good color homogeneity is indicated by the distribution of dyes evenly among the news carriers [25].

The color homogeneity test was carried out on the blushes to determine whether the carrier particles or the dye could mix well to create color when applied to the skin. The homogeneity test results (Table 4) showed a homogeneous structure, and no coarse grains were found.

Polishing Test

The polishing test was performed to figure out how easy the application of blushes to apply on the skin. Based on the polishing test (Fig. 1), the loose and compact powder produced a soft texture when applied, while the cream had a slightly oily texture. The loose and compact powder showed good results with the pink color at a concentration of 4% and 6% after being applied three times, while the concentration of 2% did not produce a pink color since the level of the extract added was very small. All cream formulas produced a good color by showing red when applied to the inner arm for the first time. The water and oil content of the cream formulation produced a sharper and more pigmented color.

Breakage Test

In this test, compact powder was dropped to a wooden surface from a height of about 0.2–0.25 m several times to see whether any breakage had occurred on compact powder. The results described in Fig. 2 showed that the compact powder for all formulas remained

Table 4. Color homogeneity test results

	Formulas								
	LP2%	LP4%	LP6%	CP2%	CP4%	CP6%	C2%	C4%	C6%
Homogeneity	Good	Good	Good	Good	Good	Good	Good	Good	Good

Notes: LP = Loose powder; CP = Compact powder; C = Cream

Fig 1. Polishing test results

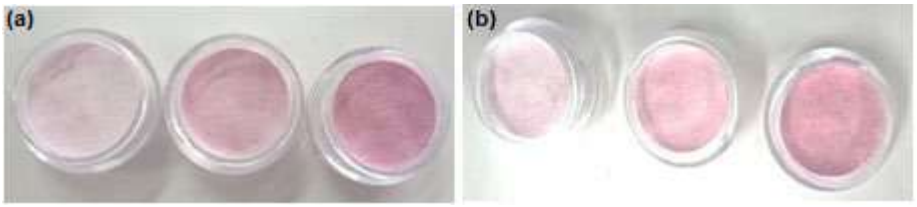

Fig 2. Breakage test results of the blushes compact powder (a) before testing, (b) after testing

compact and unbreakable, indicating that the compactness had passed the test and it was safe in any condition [24].

pH Stability Test

The pH of human skin is usually acidic, in the range of 4–6, which has historically acted as a defence mechanism against organisms. This steep pH gradient of 2–3 units between the stratum corneum and the epidermis and dermis occur due to the influence of the body internal environment which is close to pH 7–9 (neutral). The physiological role of the skin properties has historically been regarded as a defence mechanism against organisms that attack. Age, skin site, and pigmented skin are some factors that influence the pH of the skin [29].

The pH test was performed at 8 and 30 °C to observe the safety on the skin and also the stability of the dosage so that the difference in the temperature will indicate whether there has been a change of pH during the preparation. The temperatures of 8 and 30 °C are the proper temperatures to observe whether the dosages remain stable in this research. The proper pH of skin plays an important role in maintaining the skin because it creates a skin barrier and skin resistance to the external physical and chemical agents [30]. After the testing, the loose and the compact powder had average pH of ± 5, while the cream had average pH of ± 4 (Fig. 3 and 4). Therefore, it can be concluded that the loose and compact powder dosage forms met the skin pH requirements and are safe to use on the skin [31]. The pH value of the cream was around ± 4, which is lower than the requirements, due to the content of the acidic ingredients of ascorbic acid, oleum, cetyl alcohol, and propylene glycol. It should be noted that the low pH may irritate the skin.

Color Stability Test

Stable cosmetic preparation is preparation in which the properties and characteristics are the same as at the first time of manufacture during storage and use [33]. The color stability can be represented by the *a value, which is the value that shows the red color. The higher the *a value, the redder the test sample will be. The color stability test at 30 °C (Fig. 5) showed that the cream was the most unstable. On the 7th day of storage, the cream already showed a color change from dark red

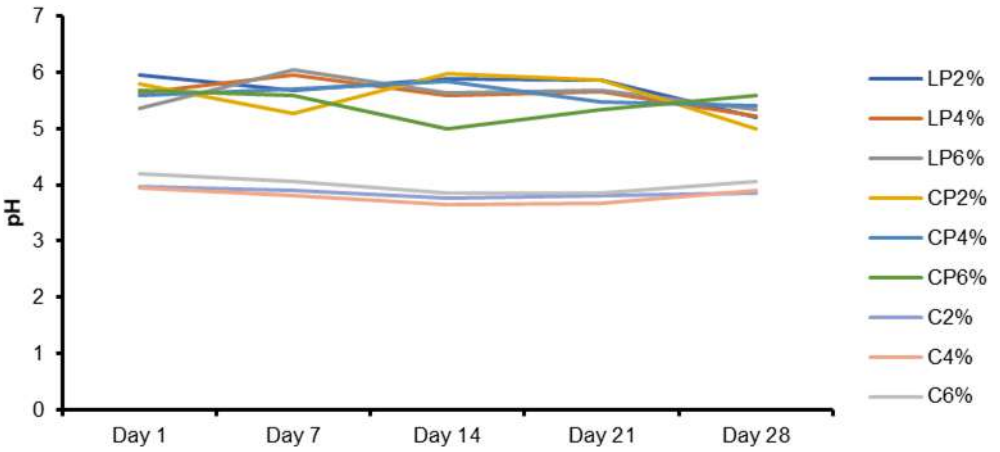

Fig 3. The pH value of the blushes at 8 °C

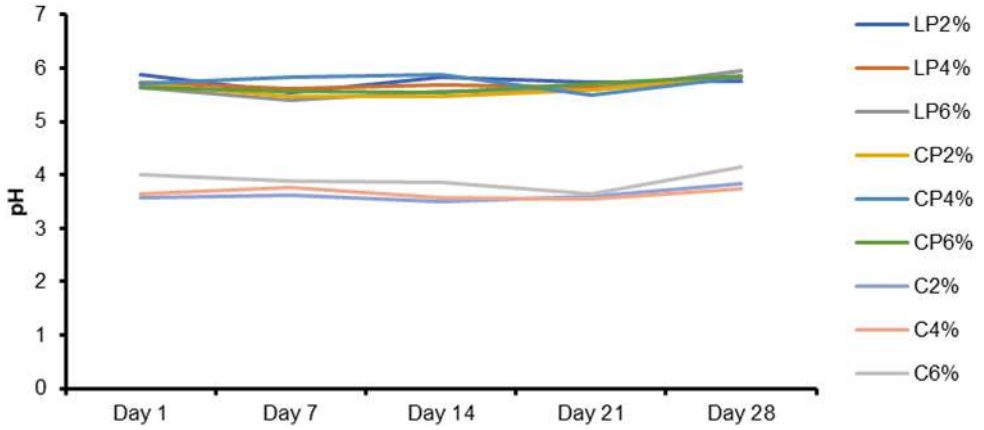

Fig 4. The pH value of the blushes at 30 °C

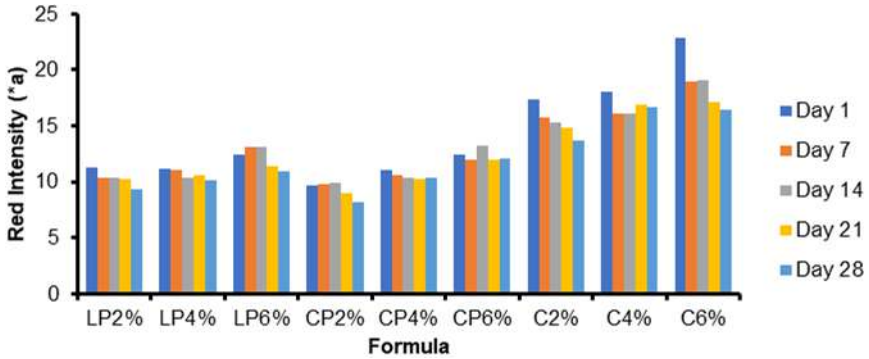

Fig 5. The stability of the blushes at 8 °C

to yellowish-red. This change might occur due to the breaking of bonds in betacyanin which causes a reduction in red color to pale red or turns bright yellow [34]. The color change could be caused by the pH change. Decreasing of pH would result in a change of pigment color from red to purple, whereas increasing of pH will turn it to yellow-brown [32]. As for the loose and compact powder preparation, discoloration occurred on the 14th and 21st day, respectively.

The discoloration occurred because the beetroot extract was easily oxidized [35] and the ascorbic acid content added in it as an antioxidant was not strong enough to protect the dosage forms. The addition of ascorbic acid was used to maintain the color stability of the extract from the influence of air because the ascorbic acid will be oxidized first so that the oxidation of the extract can be avoided [36]. The cream was oxidized earliest because of the water content. Water content could accelerate the oxidation process so that the dosage form was not stable enough. The compact powder was oxidized longer because the surface area was smaller than the loose powder. The compact powder stuck together to form a compact solid powder and reduced the air which came into contact with the dosage form.

At 8 °C (Fig. 6), the three dosage forms (compact powder, loose powder, and cream) showed fair stability. It was evident that on the 28th day, each dosage form still had red color. Therefore, the color stability was greatly influenced by the storage temperature. According to the previous study [36], betacyanin which acts as a dye in beetroot extract was stable at temperatures under 40 °C.

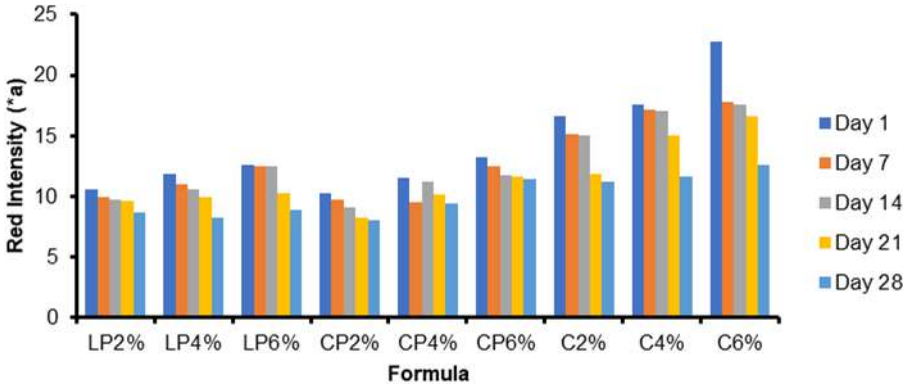

Fig 6. The stability test of the blushes at 30 °C

Hedonic Test

The hedonic test was only performed on compact powder because it was the most stable dosage compared to the cream and loose powder. The sensory analysis has been used because it can guide the process of research and development of a cosmetic product. This analysis allows researchers to identify the acceptance level of users about the product [37]. This analysis method is subjective and is used to evaluate a product using human senses. This method was used in this research to determine whether the preparation of a cosmetic formula in compact powder form was considered pleasurable based on a hedonic scale using a preference scale points of 9 indicating "extremely like" and 1 "extremely dislike" [37]. The hedonic test on this study was approved by The Ethics Committee of the Faculty of Medicine, University of Indonesia (Reg. number: KET.847/UN2.FI/ETIK/PPM.00.02/2019). The hedonic test for the color and appearance of the compact powder (Fig. 7) showed that the extract concentration of 2% had lower value with an average value of 6 (fairly like) compared to the concentration of 4% with an average value of 7 (like) and the concentration of 6% with an average value of 8 (really like). In the case of taste/sensation and odor, the average value of the three concentrations were the same indicating that all panellists liked it. The hedonic test performed on all formulas of the compact powder dosage form showed that the most preferred blush was in the formula with a concentration of 6%.

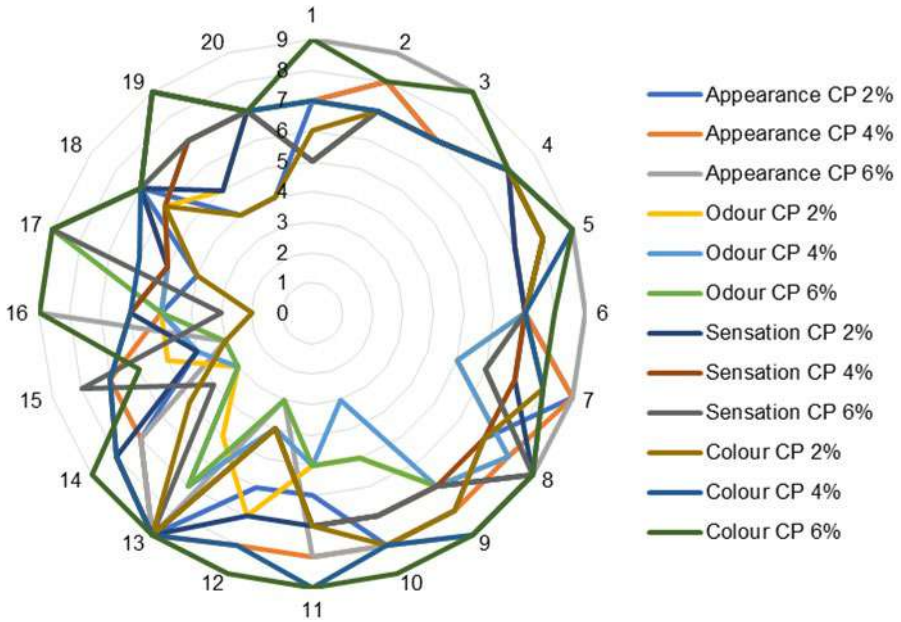

Fig 7. The hedonic test results, see Table 2 for the hedonic scale

■ CONCLUSION

Beetroot (*Beta vulgaris* L.) extract might contain flavonoids, alkaloids, saponins, tannins, triterpenoids, steroids. The dry extract of beetroot (*Beta vulgaris* L.) can be formulated into blush dosage forms. The color stability (*a) value of each dosage form decreased during 28 days of storage. However, discoloration of *a that occurred in the compact powder was insignificant, which indicated that the compact powder was quite stable compared to loose powder and cream dosage forms. Therefore, we conclude that the compact powder was the most stable dosage form. All dosage forms were homogeneous and could be easily applied, and especially for the compact powder, there were no fractures that occurred after the breakage testing, and the pH remained stable for all formulas (between 3–5) after 28 days of storage. The most favored formula of the compact powder was the formula of 6% because it produced color when applied to the skin.

■ ACKNOWLEDGMENTS

The authors are grateful to all staff of Q-Lab Laboratory of Faculty of Pharmacy for providing necessary facilities to do this research work.

■ REFERENCES

[1] Anute, N.B., Deshmukh, A., and Khandagale, A., 2015, Consumer buying behavior towards cosmetic products, *IJMSS*, 3 (07), 25–34.

[2] Oberoi, P., and Oberoi, P., 2018, Consumer behaviour towards cosmetic products: a case of Delhi NCR, *J. Emerg. Technol. Innov. Res.*, 5 (11), 10–31.

[3] National Pharmaceutical Regulatory Agency, 2017, *Guidelines for control of cosmetic products in Malaysia*, Ministry of Health, Malaysia, 1–13.

[4] Tejal, P., Nishan, D., Amisha, J., Umesh, G., Desai, K.T., and Bansal, R.K., 2013, Cosmetics and health: Usage, perceptions and awareness, *Bangladesh J. Med. Sci.*, 12 (4), 392–397.

[5] Mukul, S., Surabhi, K., and Atul, N., 2011, Cosmeceuticals for the skin: An overview, *Asian J. Pharm. Clin. Res.*, 4 (2), 1–6.

[6] Steiling, W., Almeida, J.F., Vandecasteele, H.A., Gilpin, S., Kawamoto, T., O'Keeffe, L., Pappa, G., Rettinger, K., Rothe, H., and Bowden, A.M., 2018, Principles for the safety evaluation of cosmetic powders, *Toxicol. Lett.*, 297, 8–18.

[7] Bennett, J., 2021, *Loose face powders – Cosmetics and skin*, http://cosmeticsandskin.com/aba/loose-face-powders.php.

[8] Kumar, D., Rajora, G., Parkash, O., Antil, M., and Kumar, V., 2016, Herbal cosmetics: An overview, *Int. J. Adv. Sci. Res.*, 1 (4), 36–41.

[9] Arora, R., Aggarwal, G., Dhingra, G.A., and Nagpal, M., 2019, Herbal active ingredients used in skin cosmetics, *Asian J. Pharm. Clin. Res.*, 12 (9), 7–15.

[10] Bahadoran, Z., Mirmiran, P., Kabir, A., Azizi, F., and Ghasemi, A., 2017, The nitrate-independent blood pressure-lowering effect of beetroot juice: A systematic review and meta-analysis, *Adv. Nutr.*, 8 (6), 830–838.

[11] Masih, D., Singh, N., and Singh, A., 2019, Red beetroot: A source of natural colourant and antioxidants: A review, *J. Pharmacogn. Phytochem.*, 8 (4), 162–166.

[12] Koubaier, H.B.H., Snoussi, A., Essaidi, I., Chaabouni, M.M., Thonart, P., and Bouzouita, N., 2014, Betalain and phenolic compositions, antioxidant activity of Tunisian red beet (*Beta vulgaris* L. *conditiva*) roots and stems extracts, *Int. J. Food Prop.*, 17 (9), 1934–1945.

[13] Antigo, J.L.D., Bergamasco, R.C., and Madrona, G.S., 2018, Effect of pH on the stability of red beet extract (*Beta vulgaris* L.) microcapsules produced by spray drying or freeze drying, *Food Sci. Technol.*, 38 (1), 72–77.

[14] Kezi, J., and Sumathi, J.H., 2014, Betalain – a boon to the food industry, *Discovery*, 20 (63), 51–58.

[15] Singh, R., and Srivastava, S., 2017, A critical review on extraction of natural dyes from leaves, *Int. J. Home Sci.*, 3 (2), 100–103.

[16] Verma, S., and Gupta, G., 2017, Natural dyes and its applications: A brief review, *Int. J. Res. Anal. Rev.*, 4 (4), 57–60.

[17] Miraj, S., 2016, Chemistry and pharmacological effect of *Beta vulgaris*: A systematic review, *Pharm. Lett.*, 8, (19), 404–409.

[18] Yusuf, M., Shabbir, M., and Mohammad, F., 2017, Natural colorants: Historical, processing and sustainable prospects, *Nat. Prod. Bioprospect.*, 7 (1), 123–145.

[19] Mansour, R., 2018, Natural dyes and pigments: Extraction and applications, in *Handbook of Renewable Materials for Coloration and Finishing*, Eds. Yusuf, M., John Wiley & Sons, Hoboken, USA, 75–102.

[20] Sabarudin, N.A., Abdul Munaim, M.S., and Ab. Wahid, Z., 2016, Effect of pH on natural pigment betacyanin extraction from *Bougainvillea* Bracts, *The Proceeding of National Conference for Postgraduate Research*, University Malaysia Pahang, 559–563.

[21] Djamil, R., and Anelia, T., 2009, Penapisan fitokimia uji BSLT dan uji antioksidan ekstrak metanol beberapa spesies Papilionaceae, *JIFI*, 7 (2), 65–71.

[22] Banu, K.S., and Cathrine, L., 2015, General Techniques Involved in Phytochemical Analysis, *Int. J. Adv. Res. Chem. Sci.*, 2 (4), 25–32.

[23] Butler, H., 2000, *Poucher's Perfumes, Cosmetics, and Soaps*, 10th Ed., Springer, Netherlands.

[24] Sharma, G., Gadhiya, J., and Dhanawat, M., 2018, "Creams" in *Textbook of Cosmetic Formulations*, Pothi.com, India, 51–66.

[25] Yuliana, A., Nurdianti, L., Fitriani, F., and Amin, S., 2020, Formulasi dan evaluasi kosmetik dekoratif perona pipi dari ekstrak angkak (*Monascus purpureus*) sebagai pewarna dengan menggunakan lesitin sebagai pelembab kulit, *Fitofarmaka Jurnal Ilmiah Farmasi*, 10 (1), 1–11.

[26] Lembong, E., Utama, G.L., and Saputra, R.A., 2019, Phytochemical test, vitamin C content and antioxidant activities beet root (*Beta vulgaris* Linn.) extracts as food coloring agent from some areas in Java Island, *IOP Conf. Ser.: Earth Environ. Sci.*, 306, 012010.

[27] Ekwueme, F.N., Nwodo O.F.C., Joshua, P.E., Nkwocha, C., and Eluka, P.E., 2015, Qualitative and quantitative phytochemical screening of the squeous leaf extract of *Senna mimosoides*: Its effect in in vivo Leukocyte mobilization induced by inflammatory stimulus, *Int. J. Curr. Microbiol. Appl. Sci.*, 4 (5), 1176–1188.

[28] Onuminya, T.O., Shodiya, O.E., and Olubiyi, O.O., 2017, Comparative proximate and phytochemical analyses of leafy vegetables in Lagos state, *Niger. J. Pure Appl. Sci.*, 30 (3), 3097–3103.

[29] Ali, S.M., and Yosipovitch, G., 2013, Skin pH: From basic science to basic skin care, *Acta Derm. Venereol.*, 93 (3), 261–267.

[30] Nieradko-Iwanicka, B., Chrobok, K., Skolarczyk, J., and Pekar, J., 2018, What is the pH, Fe and Cl_2 content of cosmetics we use? – A pilot study on safety of skin care products, *Pol. J. Public Health*, 127 (2), 78–81.

[31] Alamsyah, N., Djamil, R., and Rahmat, D., 2016, Antioxidant activity of combination banana peel (*Musa paradisiaca*) and watermelon rind (*Citrullus vulgaris*) extract in lotion dosage form, *Asian J. Pharm. Clin. Res.*, 9 (Suppl. 3), 300–304.

[32] Suket, N., Srisook, E., and Hrimpeng, K., 2014, Antimicrobial activity of the anthocyanins isolated from purple field corn (*Zea mays* L.) cob against *Candida* spp., *IOSR J. Pharm. Biol. Sci.*, 9 (4), 40–44.

[33] Setyawaty, R., Dwiyanti, M., and Dewanto, D., 2020, Production of compact powder blush on from secang wood (*Caesalpinia sappan* L.) extract, *Majalah Farmaseutik*, 16 (2), 125–130.

[34] Sari, Y., 2018 Pengaruh pemanasan terhadap kestabilan pigmen betalain dari buah naga merah (*Hylocereus polyrhizus*), *Orbital: Jurnal Pendidikan Kimia*, 2 (1), 37–42.

[35] Azeredo, H.M.C., 2009, Betalains: Properties, sources, applications, and stability - A review, *Int. J. Food Sci. Technol.*, 44 (12), 2365–2376.

[36] Agne, E.B.P., Hastuti, R., and Khabibi, K., 2010, Ekstraksi dan uji kestabilan zat warna betasianin dari kulit buah naga (*Hylocereus polyrhizus*) serta aplikasinya sebagai pewarna alami pangan, *J. Kim. Sains Apl.*, 13 (2), 51–56.

[37] Mosquera Tayupanta, T.Á., Espadero, M., Mancheno, M., Peña, S., Uguña, A., Álvarez, S., and Vega, M.A., 2018, Sensory analysis of cosmetic formulations made with essential oils of *Aristeguietia glutinosa* (matico) and *Ocotea quixos* (ishpingo), *Int. J. Phytocos. Nat. Ingred.*, 5, 5.

Synthesis of Fe(II)/Co(II)-Fused Triphenyl Porphyrin Dimer as Candidate for Oxygen Reduction Reaction Catalyst

Atmanto Heru Wibowo[1*], Anggit Pradifta[1], Abu Masykur[1], Ken-ichi Yamashita[2], Yosuke Tani[2], Ari Yustisia Akbar[2], and Takuji Ogawa[2]

[1]*Research Group of Synthesis and Material Functionalization, Department of Chemistry, Universitas Sebelas Maret, Jl. Ir. Sutami 36A, Surakarta, Indonesia*

[2]*Department of Chemistry, Graduate School of Science, Osaka University, Machikaneyama-cho 1-1, Toyonaka-city, Osaka, 560-0043, Japan*

* ***Corresponding author:***

tel: +62-85878677541
email: aheruwibowo@staff.uns.ac.id

Received: November 26, 2020
Accepted: April 20, 2021

DOI: 10.22146/ijc.61671

Abstract: *This paper reports the synthesis of Fe(II)/Co(II) fused triphenyl porphyrin dimers as candidate of hybrid organic metal electrocatalyst. The synthesis was conducted in five-step reactions using the starting materials pyrrole and benzaldehyde. The fuse oxidative reaction was done via free-base form of triphenyl porphyrin to omit metal insertions/removals of intermediate products. This strategy is very beneficial for the synthesis of metal fused triphenyl porphyrin that needs less reactions where phenyliodine(III) bis(trifluoroacetate) (PIFA) was successfully deployed in the oxidative reaction of two free-base triphenyl porphyrins. Here, the comparisons of NMR spectra were presented to see the changes of the starting material to the product. Initial electrochemical tests showed that reduction current of planar structure of Fe/Co fused triphenyl porphyrin dimer was on the potential range at -1.10 V to 0.45 V vs Au. Fe-fused triphenyl porphyrin dimer with 7.58 × 10^{-4} A (-1.05 V) showed slightly better performance than Co-fused triphenyl porphyrin dimer with 5.67 × 10^{-4} A (-0.97 V).*

Keywords: *fused triphenyl porphyrin; metal insertion; oxidative reaction; planar structure*

■ INTRODUCTION

In recent years, synthesis of porphyrin compounds has been developed in various fields focusing mostly on determining organic methods for new structures and gaining the benefit of its functionalization of these materials. Porphyrin consists of four methine carbons and four pyrroles with 18π aromatic macrocycle. Until now, synthesis and structure modification of porphyrin macromolecules have been performed to extend its π system in some way from simple to complicated reactions to gain the benefits of electronic system properties in specific applications. Altering the π system in the molecule porphyrin is done by the addition of substituent groups owing also π system through connection of *meso* and β position carbon atom on main porphyrin structure. Therefore, hundreds of new porphyrin molecules with π system extension and a longer conjugation system than the original porphyrin have been reported up to now. However, extended porphyrins with planar structure of macromolecules have gained more attentions than the non-planar ones due to their effectiveness in the extension of the electronic π system of molecules. Fused porphyrins are of interest in developing new planar structures because of their unique physical properties derived from the narrow HOMO-LUMO gap and supramolecular assemblies based on the intermolecular π-π stacking interaction facilitated by the expanded and planar π conjugation [1]. Therefore, fused porphyrins and metal complexes thereof have attracted considerable interest recently as functional materials for sensor devices, catalysts including photocatalysts and electrocatalysts, nanowires, solar cells, photodynamic therapy, etc., including investigation on magnetic

properties [2-3], absorption spectroscopy [4-12], electrochemistry [3,7-8,10-11,13-14], conductivity [15-17] and photovoltaics [18].

In the year 2000, Osuka and coworkers [19] have reported oxidative transformation of *meso-meso* linked diphorphyrins into triply linked fused porphyrins owing a planar-structure form. Since then, reports on fuse synthesis from porphyrin monomer to porphyrin dimers and porphyrin arrays via *meso-meso* or/and β-β connections have been increasingly published. Ouyang et al. [14] has synthesized symmetrically fused triply porphyrin using oxidant of phenyliodine(III) bis(trifluoroacetate) (PIFA) directly on the position of β-β and *meso-meso* of carbon atoms. Fused asymmetrically porphyrin has also been then synthesized by Ryan et al. [20] with triply C–C connections to fused porphyrins bearing different substituents on each porphyrin monomer. This strategy was done by firstly singly fuse synthesis of *meso* position of C atoms via Suzuki coupling of porphyrin priors to oxidation of each 2β positions of two porphyrins. Up to now, various synthesis of fused porphyrins to extend π electron conjugation by porphyrin dimerization [10,21-23] have been reported. Besides, the presence of supporting materials or in combination with bulky functional groups such as triphenylene and polycyclic aromatic hydrocarbons (PAHs) on porphyrins has been synthesized.

In this study, the synthesis of a fused porphyrin dimers with 2D planar structure of two triphenyl porphyrin is performed. The electrochemical properties of this dimer porphyrin for oxygen reduction are also investigated. Fused porphyrin dimers were synthesized with the procedure modification by Ouyang et al. [14], Lee et al. [24] and Ryan et al. [20] where a fair amount of PIFA is used as an oxidation agent. Fuse synthesis is done without the presence of zinc metal in the porphyrin cavity to cut the procedures that are commonly done in the form of zinc porphyrin complex as its intermediate product. The planar structure of Fe(II)/Co(II) porphyrin dimer synthesized with more rigid form is supposed to support the effectivity for oxygen reduction reaction.

■ EXPERIMENTAL SECTION

Materials

All reagents and solvents used were of high purity grade. Pyrrole and pyridine were from Sigma-Aldrich Chemicals. Benzaldehyde, toluene, chloroform, methanol, sodium borohydride ($NaBH_4$), catalyst of trifluoroacetic acid (TFA) and trichloroacetic acid (TCA), trimethyl orthoformate, ferro chloride tetrahydrate ($FeCl_2{\cdot}4H_2O$), cobalt(II) chloride hexahydrate ($CoCl_2{\cdot}6H_2O$), dimethylformamide (DMF), sodium carbonate (Na_2CO_3), dichloromethane (CH_2Cl_2), silica gel 60 (230–400 mesh) were all from Merck. Phenyllithium solution was from Tokyo Chemical Industries (TCI), Japan. Phenyliodine(III) bis(trifluoroacetate) (PIFA) and 2,3-dichloro-5,6-dicyano-1,4-benzoquinone (DDQ) were from Shanghai Industries. Silica gel used for the separation was from Merck. All solvents were purchased from Sigma-Aldrich without any further purification.

Instrumentation

^1H and ^{13}C-NMR spectra were taken from AGILENT VNMR 400 Hz instrument. Infrared spectra (IR) were obtained from Shimadzu model Prestige 21. MALDI-TOF was from Kratos PCAxima CFR V2.3.5. Cyclic Voltammetry was from Metrohm μ Autolab type III.

Procedure

Synthesis of 5-phenyl dipyrromethane/PDP (2)

PDP was synthesized based on the report from Lee and Lindsay [25]. Necessary modification was made to fit the apparatus in our laboratory. 150 mL Pyrrole (**1**) (2.16×10^3 mmol) and benzaldehyde (6 mL, 59 mmol) were put into a 250 mL three neck flask equipped with magnetic-stirrer bar and connected with nitrogen-gas pipe. The flask was flown with nitrogen for 15 min prior to the addition of TFA (0.45 mL, 5.80 mmol). Stirring of the mixture was done for 15 min at room temperature. The crude product yielded from the reaction was checked with silica TLC with an eluent of DCM:*n*-hexane (70:30)

at Rf = 0.82, whereas the pyrrole and unidentified product were checked at Rf = 0.55 and Rf = 0.88, respectively. After the reaction was accomplished, the excess pyrrole was removed with a vacuum rotary evaporator at 60 °C until a viscous brownish black liquid was obtained. Purification of DPP was done by column chromatography with silica (50 g, 230–400 mesh) and eluted with gradient method (DCM:*n*-hexane 60:40, 70:30, 80:20, and DCM). Solvent was then collected and evaporated with vacuum until white crystals of the product were obtained.

Synthesis of 5,15-diphenylporphyrin/DPP (3)

DPP was synthesized and modified as reported by Baldwin et al. [26]. PDP (**2**) (0.5 g, 2.30 mmol) was put in 300 mL DCM in a 500 mL flask and added to trimethyl orthoformate (18 mL, 1.65×10^2 mmol). The flask was covered with aluminum foil to protect from the sun light before the stirring was started. Trichloroacetic acid/TCA (8.83 g, 54 mmol) in 55 mL DCM was added little by little, followed by a 4 h reaction with stirring. Pyridine (15.6 mL) was then added into the mixture. Stirring at room temperature for 17 h was continued. The crude product was controlled using silica TLC with eluent of DCM:*n*-hexane (70:30) at Rf =0.90 (DPP product) and at Rf = 0.82 (PDP). The reaction was stopped after no PDP spot on TLC was seen. The aluminum foil was then discovered and the mixture was exposed to the air for 10 min followed by stirring underneath the sun light and in contact with air for 4 h. Solvent was evaporated in vacuum at 30 °C and the rest of the solid form was put in the vacuum desiccator for 17 h. The purification was done on a column using silica gel and eluent DCM:*n*-hexane (70:30). The eluate was removed with a vacuum evaporator until the purple solid was obtained. Recrystallization was performed using toluene and pyridine.

Synthesis of 5,10,15-triphenylporphyrin/TPP (4)

About 0.1 g (1 equivalent) of DPP (**3**) was put in a 100 mL flask and dissolved in THF. Before in use, the flask was vacuumed and flown with nitrogen for 15 min. Some preliminary synthesizes have been done to investigate the duration time of the reaction at 0 °C. In this study, the lower initial temperature was taken up to -25 °C to avoid too fast oxidation using self-designed cooler. After the temperature was set to -25 °C, phenyllithium (0.16 mL, 6 equivalent) was added slowly into the solution. The temperature was increased up to room temperature prior to stirring for 2 h. Crude product was monitored with silica TLC using eluent DCM:*n*-hexane (70:30) until only one product at Rf=0.93 as the target product was seen and the starting material at Rf = 0.90 disappeared. Quenching was performed with water and THF (1:4, v/v). The solution was then oxidized with 2,3-dichloro-5,6-dicyano-1,4-benzoquinone 1.04 mL (DDQ) (3 equivalent, in 10 mL DCM) for about 30 min. The solvent was removed with a vacuum rotary evaporator. Purification was done with column chromatography using silica gel and DCM eluent. The solvent was then removed with a vacuum evaporator until a light purple solid was obtained. Recrystallization was done with chloroform and methanol.

Synthesis of fused 5,10,15-triphenylporphyrin dimer/FP (5)

Synthesis of the fused porphyrin dimers was done through the reaction of oxidative coupling with 2.5 equivalents of phenyliodine(III) bis(trifluoroacetate) (PIFA). This procedure is modified from the previously reported from [14] and Lee et al. [24], where no zinc metal or metal center was involved in the reaction. About 0.03 g (1 equivalent) TPP (**4**) was dissolved in 50 mL DCM at -25 °C with self-designed cooler. Phenyliodine(III) bis(trifluoroacetate) (PIFA) (2.5 eq) was then added into the solution. The mixture was stirred while the temperature was slowly increased until room temperature. The crude product was identified on silica TLC using DCM:*n*-hexane (70:30) until only one spot of FP product (Rf = 0.98) and no other spots seen. The reaction was quenched with the addition of $NaBH_4$ and CH_3OH. Purification was done with column chromatography using silica gel and DCM eluent. After removal of the solvent, a dark purple solid of FP was obtained.

Insertion of Fe(II) and Co(II) into fused porphyrin dimer (FP)

Synthesis of Fe(II) and Co(II) FP was done by insertion of Fe(II) and Co(II) into the free-base FP (**5**).

Firstly, FP was dissolved in 70 mL DMF. To the solution, $FeCl_2{\cdot}4H_2O$ (1.5 equivalent) was added at room temperature and refluxed for about 1 h. This reaction was controlled with TLC until no FP spot was seen on the plate. The reaction was stopped at the time where only spot was detected (Rf = 0.97). The solution was then added to 80 mL HCl solution (6 M). The precipitate was then filtered and washed with a little amount of 3 M HCl and dried. Similar procedure was also applied for the insertion on free-base FP with $CoCl_2{\cdot}6H_2O$.

Oxygen reduction test with voltammetry cyclic

Fe(II)-FP was dissolved in 50 mL DMF. The solution was then added to 1 M H_2SO_4. Bubbling with N_2 for 2 h was done to remove O_2 dissolved in the solvent. After no dissolved O_2 into the solution, the solution was bubbled with O_2 for 5 min. A certain volume of the solution (15 mL) was tested using cyclic voltammetry at room temperature with scan rate 100 mV/s, voltage range from -5 to 5 volt with a reference electrode of gold (Au). Similar procedure was applied also to the measurement of Co(II) FP.

■ RESULTS AND DISCUSSION

In the general procedure, the critical stage of the reaction was in the third and fourth stage of the reaction, where the fit and controlled condition were required. Therefore, a cooler equipped with an automatic cooler and thermostat up to -25 °C was made to stabilize the temperature during the oxidation reaction with phenyllithium (stage **iii**) and PIFA (stage **iv**). The synthesis method was modified from Lee et al. [24] where the metal center of zinc in the fuse dimer reaction was used. The role of zinc metal was to help in withdrawing electron on the *meso* carbon in the oxidation reaction. This method is beneficial to the *meso-meso* linking of two porphyrins. However, this zinc insertion was not preferred in this fuse reaction, where the target products are Fe/Co-FP. In the common procedure, zinc should be inserted and then removed if the Fe or Co ion would be inserted. This caused inefficiency and time consuming for the whole reactions. To compensate the absence of zinc, careful reaction is

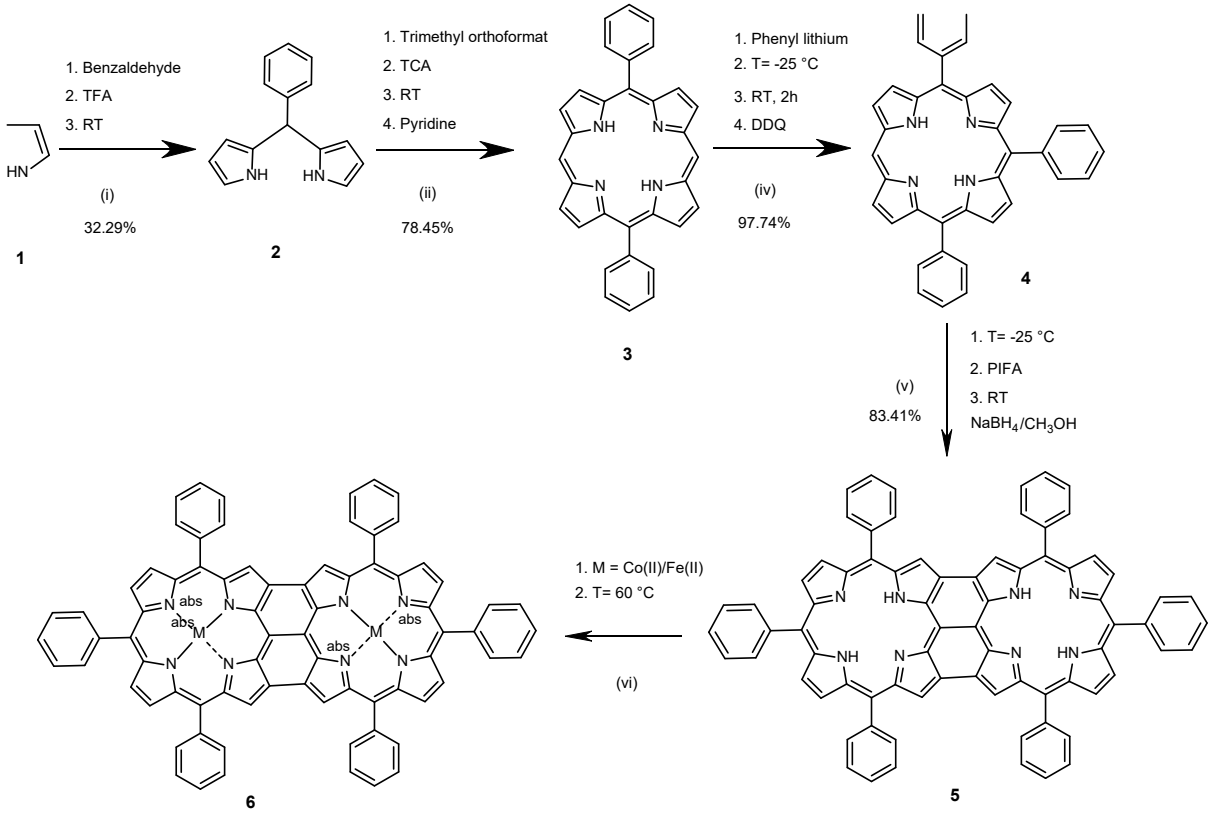

Fig 1. Reaction scheme of the general synthesis of fused triphenyl porphyrin dimer

is done by controlling the temperature with thermostat and to keep the temperature stable in the oxidation reaction. In the dimerization, the initial temperature of the cooler was also adjusted only at -25 °C instead of -75 °C. Ouyang et al. reported that the amount of PIFA added into the fuse reaction influenced the yield of the product. Addition of 2.5 eq PIFA produced the highest yields of only triply linked porphyrins, but increasing the amount of PIFA (up to 5 eq) could depress the dimer yield. Besides, the use of $NaBH_4$ and CH_3OH was also reported well for quenching the oxidation reaction. The following result is of synthesis from the PDP to the target product of Fe/Co-FP. Some NMR spectra comparisons are presented to convince the reaction products.

Synthesis of 5-Phenyl Dipyrromethane/PDP (2)

After purification, PDP product obtained was in the form of white solid about 0.860 g (32.92%), melting point = 101 °C. ^{1}H-NMR spectra of PDP in $CDCl_3$ showed that 7 proton-environment peaks of PDP was found with δH = 7.91 ppm (s, 2H), δH = 7.20–7.33 ppm (m, 5H), δH = 6.68 ppm (d, *J* = 2.4 Hz, 2H), δH = 6.15 ppm (t, 2H), δH = 5.91 ppm (s, 2H), and δH = 5.46 ppm (s, 2H). ^{13}C-NMR spectra in $CDCl_3$ showed that 9 carbons have been identified. Carbons on PDP were identified at δC = 107.18, 108.36, 117.19, 117.23, 126.96, 128.37, 128.63, 132.46 and 142.02 ppm. The yield of the synthesis of PDP was 0.860 g (32.92%)

Synthesis of 5,15-Diphenylporphyrin/DPP (3)

The DPP obtained was about 0.851 g (78.45%) in the form of purple crystal solid, melting point = 302 °C. ^{1}H-NMR spectra of DPP in $CDCl_3$ showed proton groups identified at δH = 10.31 ppm (s, 2H), δH = 9.38 ppm (d, *J* = 2.2 Hz, 4H), δH = 9.08 ppm (d, *J* = 3.4 Hz, 4H), δH = 8.26 ppm (d, *J* = 3.2 Hz, 4H), δH = 7.80–7.36 ppm (m, 6H), and δH = -3.04 ppm (s, 2H). ^{13}C-NMR spectra in $CDCl_3$ showed carbon atom groups at δC = 105.23, 119.10, 126.94, 127.63, 131.02, 131.57, 134.83, 141.37, 145.01, 147.21 ppm. *m/z* = 462.2. The yield of the synthesis of DPP was 0.851 g (78.45%)

The change of NMR spectra from PDP to DPP proved that the reaction of the conversion occurred. The spectra comparison was shown in Fig. 2.

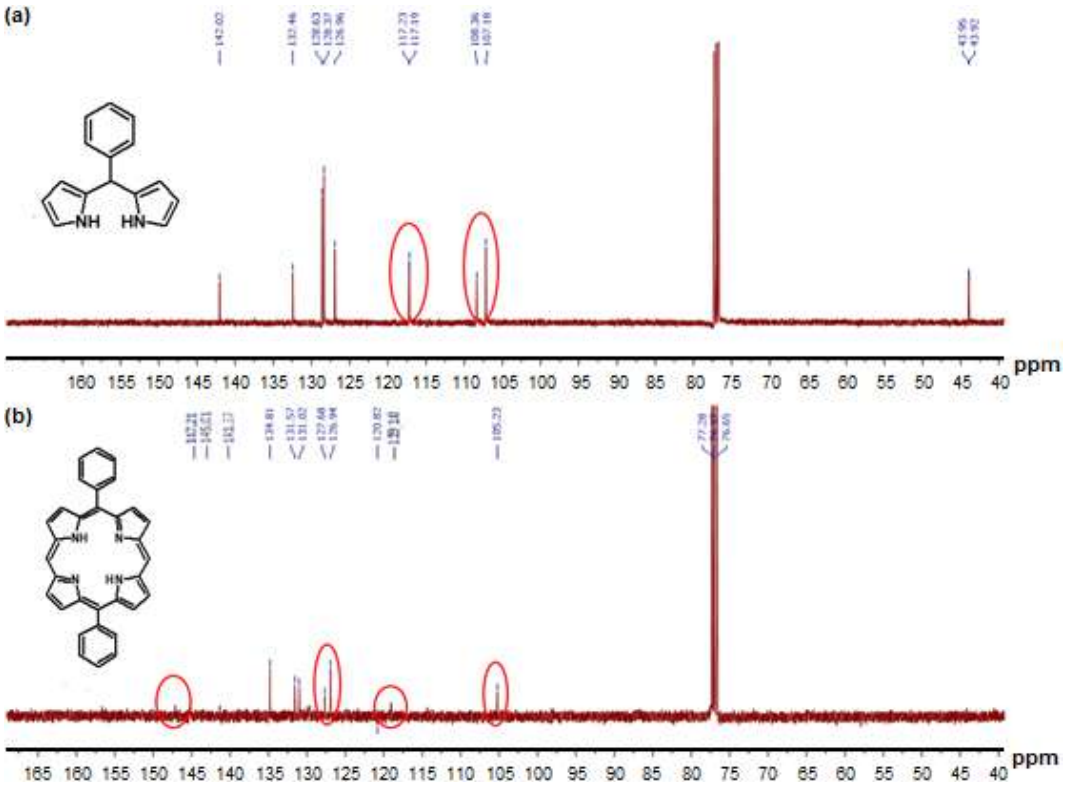

Fig 2. ^{13}C-NMR spectra comparison of (a) 5-phenyl dipyrromethane/PDP and (b) 5,15-diphenyl porphyrin (DPP)

From the Fig. 2, it was clear that the peak number and chemical shift of carbon groups on PDP different from DPP. The carbon groups of pyrrole ring on the PDP was at δ = 106.23, 119.10, 126.94, and 127.63 ppm, whereas DPP showed chemical shift at δ = 107.18, 108.36 and 117.19 ppm. It proved that the condensation of two PDPs with porphyrin was successfully.

Synthesis of 5,10,15-Triphenylporphyrin/TPP (4)

The formation of TPP was an important stage before the fuse reaction. The preliminary investigation of the factors that determine the occurrence of the reaction with phenyllithium has been done. Fig. 3 shows the progress of the reaction of DPP with phenyllithium in different reaction times. From Fig. 3, it was seen that the time reaction was not the main factor in obtaining the TPP product. The mass spectra showed that the 2 h, 14 h, and 17 h reaction times had almost similar mass intensity at *m/z* = 461/462. At initial temperature 0 °C, it was seen that the side products at about *m/z* = 551 appeared. For the further reaction, the lower temperature at -25 °C was chosen to more carefully handle the initial reaction.

The addition of phenyl to DPP with the present of phenyllithium has been successfully carried out with 0.13 g (97.74%) reddish purple powder product (melting point at 295 °C). ^{1}H-NMR spectra of TPP in $CDCl_3$ showed 7 proton groups at δH = -3.04 ppm (s, 2H), 7.76–7.79 ppm (m, 9H), 8.20–8.26 ppm (m, 6H), 8.85–8.90 (d to d, *J* = 13.1–4.8 Hz, 4H,), 9.01–9.02 (d, *J* = 4.4 Hz, 2H), 9.33–9.34 (d, *J* = 4.3 Hz, 2H), 10.21 (s, 1H). ^{13}C-NMR spectra of TPP in $CDCl_3$ showed that 15 carbon atom groups were detected at δC = 104.89, 119.74, 120.67, 126.64, 126.91, 127.48, 127.80, 130.82, 131.57, 134.59, 134.78, 140.46, 140.75, 141.86, 142.65 and 169.36 ppm.

The conversion of the synthesis from the starting material (DPP) into the product of TPP can be proved by the ^{1}H-NMR and ^{13}C-NMR spectra in comparison with DPP and TPP as given in Fig. 4 and 5.

Based on Fig. 5, comparison of ^{1}H-NMR spectra of DPP and TPP showed that new peaks (multiplets) of TPP were seen at δH = 7.77 and 8.23 ppm indicating that one phenyl group from phenyllithium was attached on the DPP. Fig. 5 showed that there were chemical-shifting changes of DPP at 131.02, 131.57, 134.83, and 141.37 ppm to 134.59, 134.78, 140.46 and 140.75 ppm, and carbon of *meso* position on DPP from 147.21 ppm to 169.16 ppm. The yield of the synthesis of TPP was 0.130 g (97.74%).

Synthesis of Fused 5,10,15-Triphenylporphyrin Dimer/FP (5)

The FP after purification was a dark purple crystal about 0.083 g (83.41%) with melting point of 398 °C.

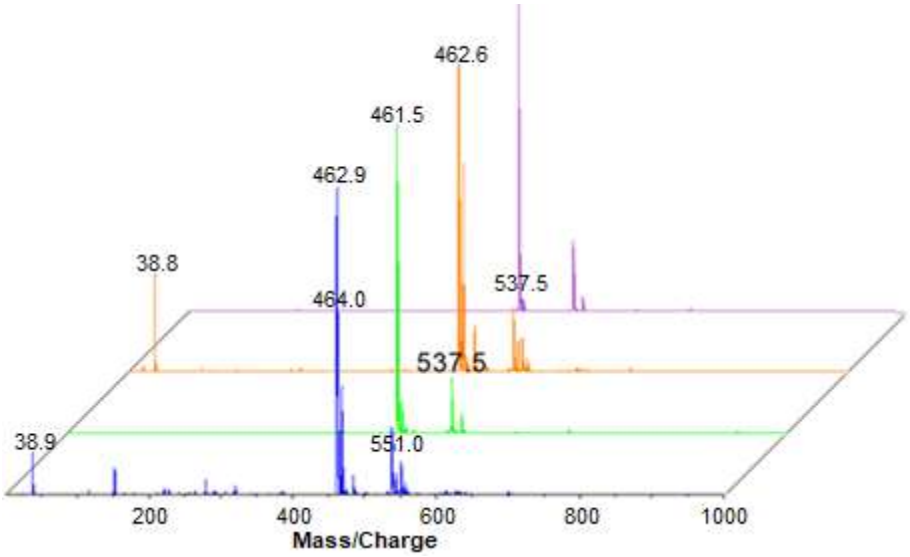

Fig 3. Comparison of mass spectra from MALDI-TOF of the reaction of DPP (1.6 mmol in THF) with phenyllithium after 2 h (blue line), 14 h (green line), 17 h (orange line) reaction and 17 h quenched (purple line) at initial addition temperature 0 °C

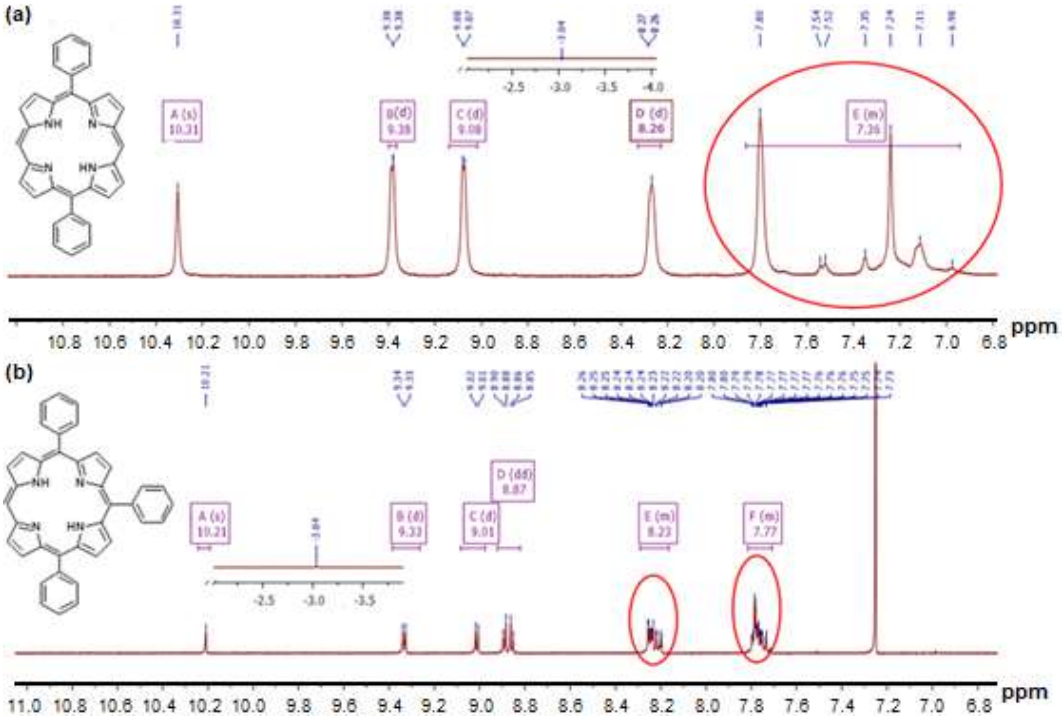

Fig 4. Comparison of ^{1}H-NMR spectra (a) 5,15-diphenylporphyrin/DPP and (b) 5,10,15-triphenylporphyrin/TPP

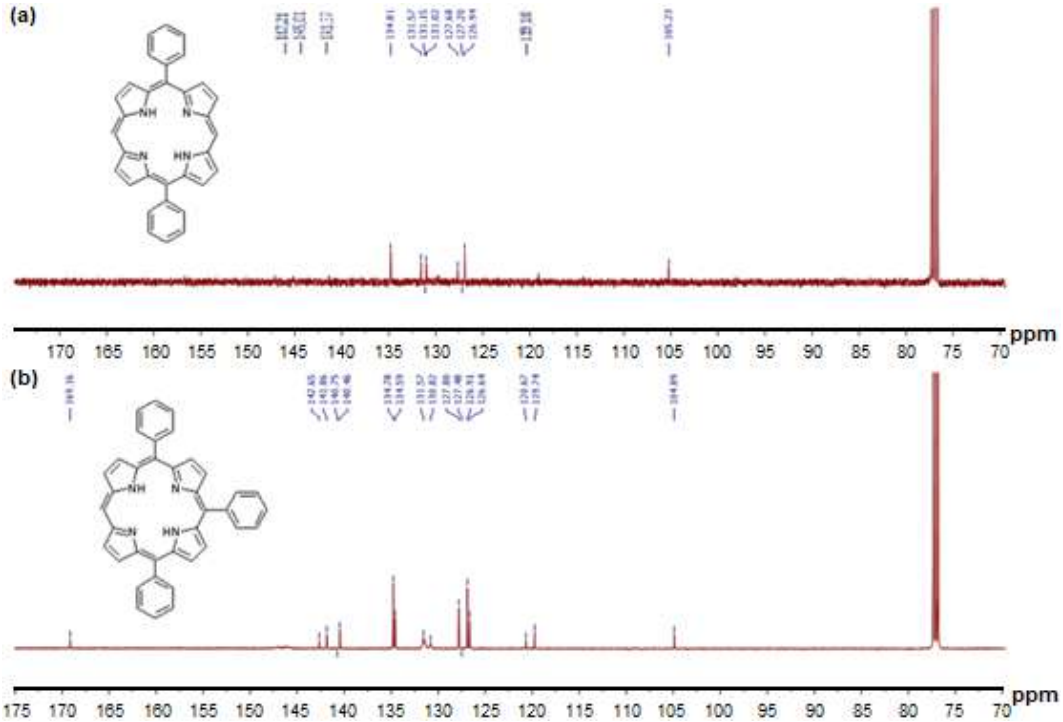

Fig 5. Comparison of ^{13}C-NMR spectra (a) 5,15-diphenylporphyrin/DPP and (b) 5,10,15-triphenylporphyrin/TPP

^{1}H-NMR spectra of FP in $CDCl_3$ showed 6 proton groups with δH = -2.77 ppm (s, 4H), 7.73–7.79 ppm (m, 18H), 8.16–8.21 ppm (m, 12H), 8.77–8.79 ppm (d to d, J = 4.7–3.4 Hz, 4H), 8.90–8.88 ppm (d to d, J = 4.6–3.3 Hz, 4H), 9.63 ppm (s, 4H). Meanwhile, ^{13}C-NMR spectra of FP in $CDCl_3$ showed 23 carbon atoms at δC = 120.73, 120.81,

120.85, 126.64, 126.83, 126.91, 127.54, 127.97, 128.89, 130.96, 131.12, 134.06, 134.53, 134.63, 134.78, 140.77, 141.65, 141.80, 141.99, 169.67, 169.51, 169.36 and *m/z* = 1070.8. The comparison of the spectra of the starting material and the product was done to validate that the reaction was accomplished, as in Fig. 6 and 7.

From the spectra in Fig. 6 and 7, it was seen that there were changes of ^{1}H-NMR and ^{13}C-NMR spectra after reaction. C–H *meso* on the TPP at δ = 10.21 ppm disappeared in the FP spectra. This was caused by the C–H binding to the *meso* position of the two TPPs to form a dimer structure. ^{1}H-NMR spectra of TPP showed a peak (doublet) at δ = 9.33 ppm, whereas the spectra of FP showed a singlet peak at δ = 9.63 ppm. This indicated the change of C–H on the pyrrole ring in TPP. ^{13}C-NMR spectra showed that TPP has peak pattern differences with

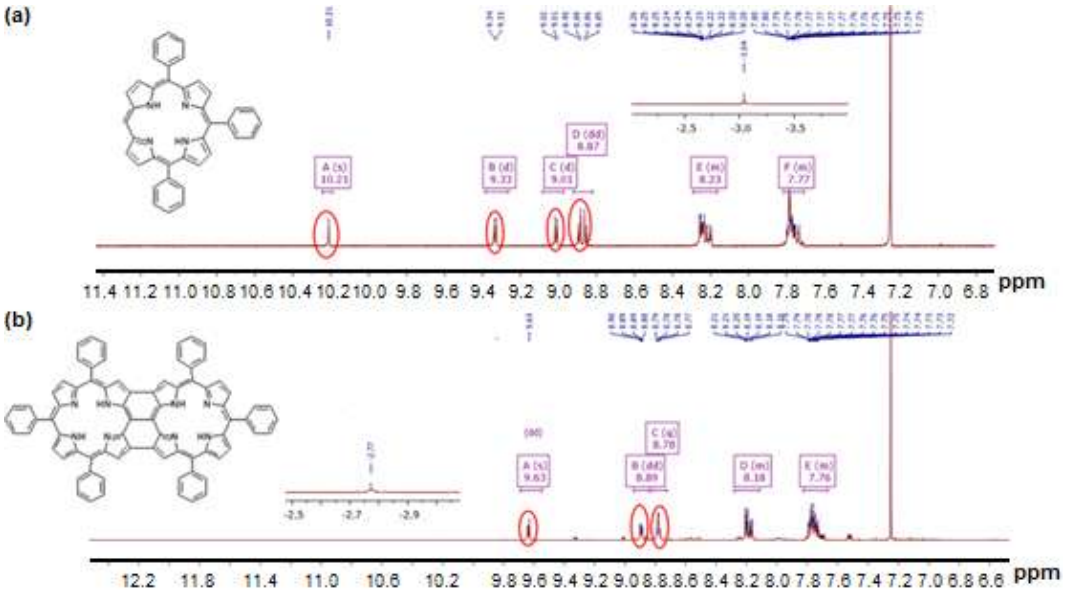

Fig 6. Comparison of ^{1}H-NMR spectra of (a) TPP and (b) FP

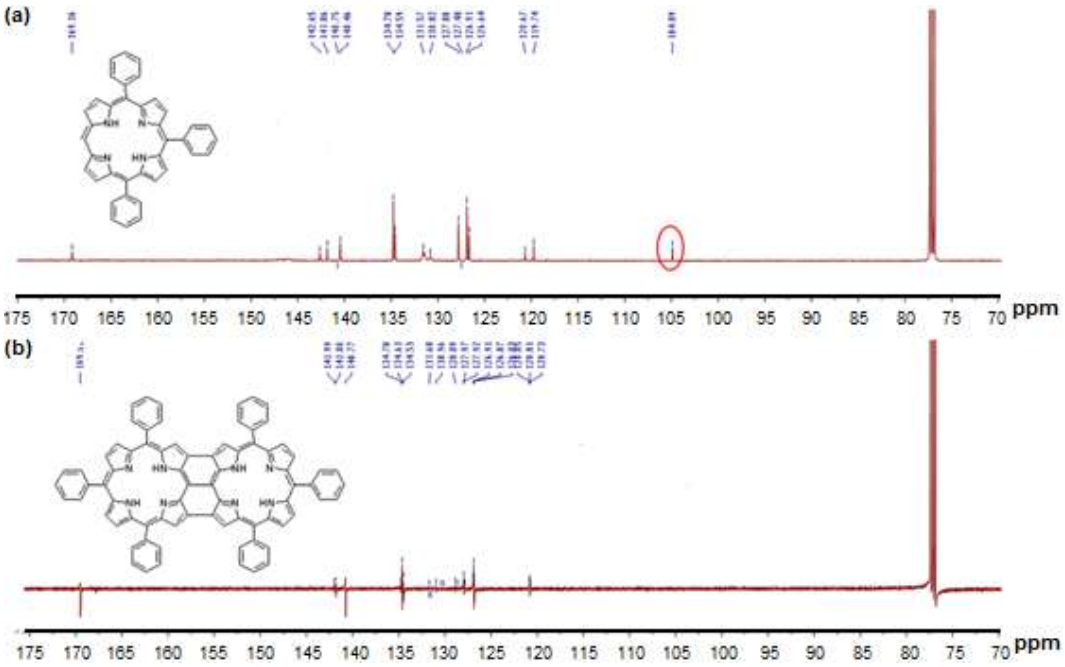

Fig 7. Comparison of ^{13}C-NMR spectra of (a) TPP and (b) FP

FP. A peak at δ = 104.89 ppm was not found on FP spectra, indicating that a dimerization process has already accomplished. The yield of the synthesis of FP was 0.083 g (83.41%)

Insertion of FP with Iron(II) and Cobalt(II) (6)

As the conversion was accomplished, the FTIR data was done to ensure the binding of the N atom to Fe(II) or Co(II) in the cavity of the dimer as seen in Fig. 8.

The metal binding into the porphyrin cavity could be proved from the FTIR spectra (Fig. 8). The absorption peak at about 400–560 cm^{-1} was not found in the FP. Meanwhile, Fe-FP and Co-FP showed absorption peak at 431.11 and 426.29 cm^{-1}, respectively. These absorption peaks indicated that the Fe and Co ions were bonded with the N-atoms in the porphyrin cavities.

Catalytic Test of Fe/Co-FP for Reduction of Oxygen

The result test of Fe/Co FP planar structure (as seen in Fig. 9) using cyclic voltammetry (CV) with voltage scan from -4 to 4 Volt, scan rate = 100 mV/s, T = 25 °C, 1 mm^2 surface area of working electrode and M-FP concentration in DMF = 5 mM was seen in Fig. 10. Voltammogram in the Fe-FP and Co-FP electrodes showed that the reduction current was on the potential range at -1.10 V to 0.45 V vs Au. Reduction potential peak occurred at -1.05 V vs Au. As comparison that the oxygen reduction potential of Pt electrode was reported at 0.40 V vs RHE [27] and the oxygen reduction potential of MOF at 0.60–0.80 V vs RHE [28]. This potential value proved that Fe-FP and Co-FP owe the catalytic activity for oxygen reduction reaction.

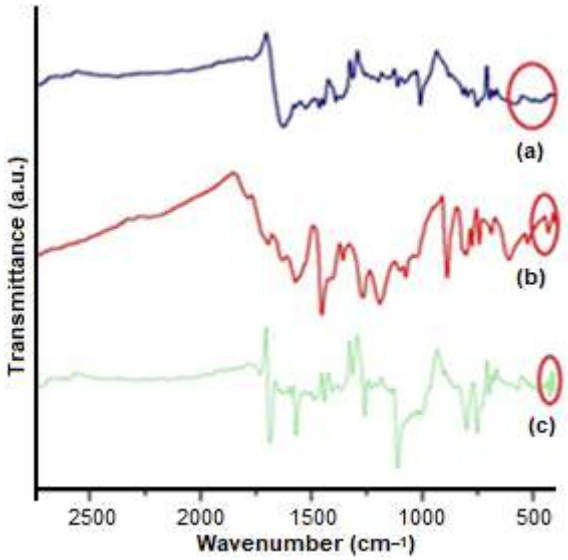

Fig 8. FTIR spectra of FP (a), Co-FP (b) and Fe-FP (c)

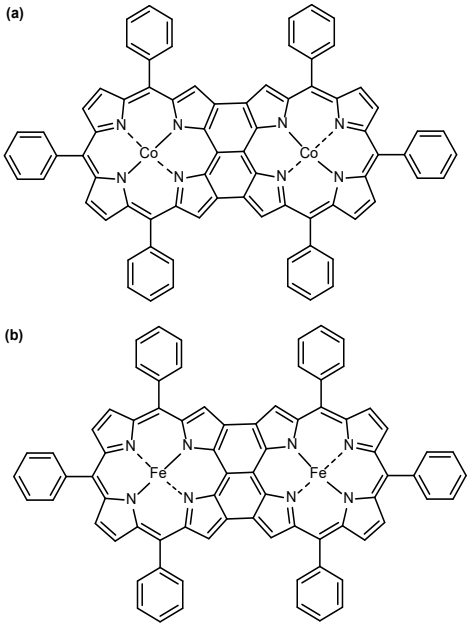

Fig 9. The structure of Co-FP (a) and Fe-FP (b)

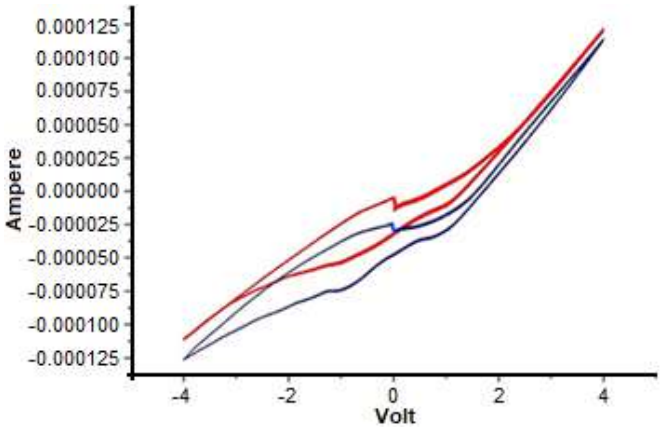

Fig 10. Voltammogram from the Fe FDP (—) and Co-FDP (—) in 1 M H_2SO4, saturated with oxygen and scan rate 100 mV/s

Table 1. Peak current and voltage of CV from Fe/Co FDP in DMF with H_2SO_4 1 M, saturated with oxygen and scan rate 100 mV/s.

M-FDP	Peak current (A)	Voltage (V)
Fe-FDP	7.58×10^{-4}	-1.05
Co-FDP	5.67×10^{-4}	-0.97

■ CONCLUSION

Synthesis of fused triphenyl porphyrin dimer (FP) could be done without the metal presence (zinc) in the porphyrin cavity or via free-base porphyrin oxidation of *meso* and β carbon of the porphyrin using PIFA. Initial electrochemical tests showed that the planar/coplanar structure of Fe/Co-FP dimers was capable to be employed as a catalyst for oxygen reduction, where Fe-FP showed slightly better performance than Co-FP.

■ REFERENCES

[1] Saegusa, Y., Ishizuka, T., Komamura, K., Shimizu, S., Kotani, H., Kobayashi, N., and Kojima, T., 2015, Ring-fused porphyrins: extension of π-conjugation significantly affects the aromaticity and optical properties of the porphyrin π-systems and the Lewis acidity of the central metal ions, *Phys. Chem. Chem. Phys.*, 17 (22), 15001–15011.

[2] Stähler, C., Shimizu, D., Yoshida, K., Furukawa, K., Herges, R., and Osuka, A., 2017, Stable Ni^{II} porphyrin *meso*-oxy radical with a quartet ground state, *Chem. Eur. J.*, 23 (30), 7217–7220.

[3] Fukui, N., Cha, W., Shimizu, D., Oh, J., Furukawa, K., Yorimitsu, H., Kim, D., and Osuka, A., 2017, Highly planar diarylamine-fused porphyrins and their remarkably stable radical cations, *Chem. Sci.*, 8 (1), 189–199.

[4] Fujimoto, K., Oh, J., Yorimitsu, H., Kim, D., and Osuka, A., 2016, Directly diphenylborane-fused porphyrins, *Angew. Chem. Int. Ed.*, 55 (9), 3196–3199.

[5] Fujimoto, K., and Osuka, A., 2018, A 1,5-naphthyridine-fused porphyrin dimer: Intense NIR absorption and facile redox interconversion with its reduced congener, *Chem. Eur. J.*, 24 (25), 6530–6533.

[6] Fujimoto, K., Shimizu, D., Mori, T., Li, Y., Zhou, M., Song, J., and Osuka, A., 2019, Selective formation of helical tetrapyrrin-fused porphyrins by oxidation of β-to-β linked *meso*-aminoporphyrin dimers, *Chem. Eur. J.*, 25 (7), 1711–1715.

[7] Fukui, N., Cha, W.Y., Lee, S., Tokuji, S., Kim, D., Yorimitsu, H., and Osuka, A., 2013, Oxidative fusion reactions of *meso*-(diarylamino)porphyrins, *Angew. Chem.*, 125 (37), 9910–9914.

[8] Fukui, N., Lee, S.K., Kato, K., Shimizu, D., Tanaka, T., Lee, S., Yorimitsu, H., Kim, D., and Osuka, A., 2016, Regioselective phenylene-fusion reactions of Ni(II)-porphyrins controlled by an electron-withdrawing *meso*-substituent, *Chem. Sci.*, 7 (7), 4059–4066.

[9] Banala, S., Fokong, S., Brand, C., Andreou, C., Kräutler, B., Rueping, M., and Kiessling, F., 2017, Quinone-fused porphyrins as contrast agents for photoacoustic imaging, *Chem. Sci.*, 8 (9), 6176–6181.

[10] Brennan, B.J., Arero, J., Liddell, P.A., Moore, T.A., Moore, A.L., and Gust, D., 2013, Selective oxidative synthesis of *meso*-beta fused porphyrin dimers, *J. Porphyrins Phthalocyanines*, 17 (4), 247–251.

[11] Chaudhri, N., Cong, L., Bulbul, A.S., Grover, N., Osterloh, W.R., Fang, Y., Sankar, M., and Kadish, K.M., 2020, Structural, photophysical, and electrochemical properties of doubly fused porphyrins and related fused chlorins, *Inorg. Chem.*, 59 (2), 1481–1495.

[12] Zhang, P., Yu, C., Yin, Y., Droste, J., Klabunde, S., Hansen, M.R., and Mai, Y., 2020, Bis-anthracene fused porphyrin as an efficient photocatalyst: Facile synthesis and visible-light-driven oxidative coupling of amines, *Chem. Eur. J.*, 26 (69) 16497–16503.

[13] Ishizuka, T., Komamura, K., Saegusa, Y., Tanaka, S., Shiota, Y., Yoshizawa, K., and Kojima, T., 2019, Iron complex of a quadruply fused porphyrin: Synthesis, structure and redox properties, *J. Porphyrins Phthalocyanines*, 24 (01n03), 252–258.

[14] Ouyang, Q., Zhu, Y.Z., Zhang, C.H., Yan, K.Q., Li, Y.C., and Zheng, J.Y., 2009, An efficient PIFA-mediated synthesis of fused diporphyrin and triply–singly interlacedly linked porphyrin array, *Org. Lett.*, 11 (22), 5266–5269.

[15] Baba, K., Bengasi, G., El Assad, D., Grysan, P., Lentzen, E., Heinze, K., Frache, G., and Boscher, N.D., 2019, Conductive directly fused poly(porphyrin) coatings by oxidative chemical vapour deposition – From single- to triple-fused, *Eur. J. Org. Chem.*, 2019 (13), 2368–2375.

[16] Bengasi, G., Desport, J.S., Baba, K., Cosas Fernandes, J.P., De Castro, O., Heinze, K., and

Boscher, N.D., 2020, Molecular flattening effect to enhance the conductivity of fused porphyrin tape thin films, *RSC Adv.*, 10 (12), 7048–7057.

[17] Algethami, N., Sadeghi, H., Sangtarash, S., and Lambert, C.J., 2018, The conductance of porphyrin-based molecular nanowires increases with length, *Nano Lett.*, 18 (7), 4482–4486.

[18] Bodedla, G.B., Wang, H., Chang, S., Chen, S., Chen, T., Zhao, J., Wong, W.K., and Zhu, X., 2018, β-Functionalized imidazole-fused porphyrin-donor-based dyes: Effect of π-linker and acceptor on optoelectronic and photovoltaic properties, *ChemistrySelect*, 3 (9), 2558–2564.

[19] Tsuda, A., Furuta, H., and Osuka, A., 2000, Completely fused diporphyrins and triporphyrin, *Angew. Chem. Int. Ed.*, 39 (14), 2549–2552.

[20] Ryan, A.A., and Senge, M.O., 2013, Synthesis and functionalization of triply fused porphyrin dimers, *Eur. J. Org. Chem.*, 2013 (18), 3700–3711.

[21] Fukui, N., Yorimitsu, H., and Osuka, A., 2016, *meso*-*meso*-Linked diarylamine-fused porphyrin dimers, *Chem. Eur. J.*, 22 (51), 18476–18483.

[22] Ryan, A., Tuffy, B., Horn, S., Blau, W.J., and Senge, M.O., 2011, Carbazole-linked porphyrin dimers for organic light emitting diodes: Synthesis and initial photophysical studies, *Tetrahedron*, 67, 8248–8254.

[23] Feng, C.M., Zhu, Y.Z., Zhang, S.C., Zang, Y., and Zheng, J.Y., 2015, Synthesis of directly fused porphyrin dimers through $Fe(OTf)_3$-mediated oxidative coupling, *Org. Biomol. Chem.*, 13 (9), 2566–2569.

[24] Lee, S., Yamashita, K., Sakata, N., Hirao, Y., Ogawa, K., and Ogawa, T., 2019, Stable singlet biradicals of rare-earth-fused diporphyrin-triple-decker complexes with low energy gaps and multi-redox states, *Chem. Eur. J.*, 25 (13), 3240–3243.

[25] Lee, C.H., and Lindsey, J.S., 1994, One-flask synthesis of meso-substituted dipyrromethanes and their application in the synthesis of trans-substituted porphyrin building blocks, *Tetrahedron*, 50 (39), 11427–11440.

[26] Baldwin, J.E., Crossley, M.J., Klose, T., O'Rear, E.A., and Peters, M.K., 1982, Syntheses and oxygenation of iron(II) "strapped" porphyrin complexes, *Tetrahedron*, 38 (1), 27–39.

[27] Maciá, M.D., Campiña, J.M., Herrero, E., and Feliu, J.M., 2004, On the kinetics of oxygen reduction on platinum stepped surfaces in acidic media, *J. Electroanal. Chem.*, 564, 141–150.

[28] Xue, W., Zhou, Q., and Li, F., 2020, The feasibility of typical metal–organic framework derived Fe, Co, N co-doped carbon as a robust electrocatalyst for oxygen reduction reaction in microbial fuel cell, *Electrochim. Acta*, 355, 136775.

The Effects of Manganese Dopant Content and Calcination Temperature on Properties of Titania-Zirconia Composite

Muhamad Imam Muslim[1], Rian Kurniawan[2], Mokhammad Fajar Pradipta[1], Wega Trisunaryanti[1], and Akhmad Syoufian[1*]

[1]*Department of Chemistry, Faculty of Mathematics and Natural Sciences, Universitas Gadjah Mada, Sekip Utara, 55281 Yogyakarta, Indonesia*

[2]*Institute of Chemical Technology, Universität Leipzig, Linnéstr. 3, 04103 Leipzig, Germany*

** **Corresponding author:***

email: akhmadsyoufian@ugm.ac.id

Received: December 5, 2020
Accepted: March 24, 2021

DOI: 10.22146/ijc.61900

Abstract: *The effects of dopant content and calcination temperature on Mn-doped TiO_2-ZrO_2 structure and properties were successfully investigated. Composite of Mn-doped titania-zirconia was synthesized by sol-gel method. Titanium(IV) isopropoxide was used as the precursor of TiO_2, while zirconia powder was used as another semiconductor. $MnCl_2{\cdot}4H_2O$ was used as the source of dopant in this study. Various amounts of manganese were incorporated into TiO_2-ZrO_2 and calcination was performed at temperatures of 500, 700 and 900 °C. Synthesized composites were characterized by Fourier-transform infrared spectroscopy (FTIR), specular reflectance UV-Vis spectroscopy (SR UV-Vis), X-ray diffraction method (XRD) and scanning electron microscopy equipped with X-ray energy dispersive spectroscopy (SEM-EDX). The results showed that Mn-doped TiO_2-ZrO_2 with the lowest bandgap (2.78 eV) was achieved with 5% of Mn dopant and calcined at 900 °C, while Mn-doped TiO_2-ZrO_2 with the highest bandgap (3.12 eV) was achieved with 1% of Mn dopant content calcined at 500 °C.*

Keywords: *Mn-doped TiO_2-ZrO_2; bandgap; manganese; ZrO_2; TiO_2*

■ INTRODUCTION

Titanium dioxide (TiO_2) is a semiconductor that has been widely used as a photocatalyst material because of its interesting properties such as low cost, strong oxidizing power, non-toxicity, and chemical inertness [1]. Another photocatalyst material that has attracted attention is zirconium oxide (ZrO_2) which has good stability and easily produces holes in the valence band, leading to strong interactions with the active component. ZrO_2 is resistant to both alkali and acid conditions as well as oxidation and reduction reactions. Moreover, because of its properties, composites containing ZrO_2 as the main material have pulled much attention in recent years. This is mainly because of the difference in energy levels between ZrO_2 and other semiconductors to efficiently separate the charges, thus decrease the recombination of electrons and holes [2-3].

Previous research reported that coupling ZrO_2 with TiO_2 at Ti:Zr molar ratio of 1:1 had resulted in zirconium titanate hollow sphere with a non-visible-light response (3.31 eV), however, this material has a higher redox potential [1]. Pirzada et al. [2] successfully synthesized nanocomposite TiO_2/ ZrO_2 with the lowest bandgap (3.26 eV, non-visible light response) with an average particle diameter particle of 10.5 nm yielding a higher redox capability. However, the photocatalytic performance of semiconductor can be improved with an approach to broaden the photo-response by doping with various metals [3]. Doping of semiconductor material with transition metals leads to reduction of bandgap and it will provide a good photocatalytic activity [4].

The metallic dopants with 3d orbitals, such as Mn, Fe, Co and Zn, had been studied and reported in recent years [5-9]. Transition metal will reduce the particle size

of photocatalyst and increase its surface area, Table 1 shows the use of dopants with 3d orbitals on the photocatalyst materials that had been studied previously. Doping photocatalyst with transition metals increases the surface defects and optical absorption of light, which can ultimately lead to an increase in the efficiency of the photocatalyst [9]. The lowest bandgap of TiO_2-ZrO_2 doped using Fe (2.83 eV), Co (2.94 eV) and Zn (2.87 eV) were achieved in composites with 7% of iron content calcined at 500 °C, 3% of cobalt content calcined at 500 °C, and 5% of zinc content calcined at 900 °C, respectively [6-8]. The properties of semiconductor are enhanced after manganese doping because Mn^{2+} and Mn^{3+} exist on the surface of photocatalyst and catch the electron in semiconductor. Therefore, Mn should trap electrons and suppress electron–hole recombination. Thus, the lower the electron–hole recombination is, the higher the quantum efficiency of the photons will be and then will reduce bandgap value [10]. Mragui et al. [5] successfully synthesized Mn-TiO_2 with 10% of Mn content and bandgap of 2.95 eV, using $MnCl_2{\cdot}4H_2O$ as a dopant source.

Beside the addition of dopant, the calcination temperature can also affect the bandgap value of the photocatalyst material by changing the structure of the material. TiO_2 which has been synthesized at high calcination (400 °C) could have higher photoactivity compared to the TiO_2 which was synthesized at low temperature (200 °C) [11]. However, photocatalytic activity is related to the combination properties of crystalline phase, particle size, surface area, electron-hole recombinant, bandgap energy, pore volume, and surface chemical state [11-12].

This study was conducted with various Mn dopant contents and calcination temperatures to determine its effects on the properties of Mn-doped TiO_2-ZrO_2 composite. The addition of Mn dopant and increased calcination temperature were expected to produce a TiO_2-ZrO_2 composite with reduced bandgap energy. Mn-doped TiO_2 was developed on the surface of ZrO_2 by the sol-gel process. The sol-gel method was chosen because it has several advantages, such as an easy process, simple equipment, homogeneous phase, the ability to control the crystal size, and low temperature condition [13-14].

Table 1. Bandgap data of Mn-TiO_2, Fe, Co and Zn doped TiO_2-ZrO_2 at the optimum condition

Sample	Eg (eV)
Mn-TiO_2 10% 500 °C	2.95 [5]
Co-ZrO_2-TiO_2 3% 500 °C	2.94 [6]
Fe-ZrO_2-TiO_2 7% 500 °C	2.83 [7]
Zn-ZrO_2-TiO_2 5% 900 °C	2.87 [8]

■ EXPERIMENTAL SECTION

Materials

Titanium(IV) isopropoxide (TTIP, 97%, Sigma-Aldrich) was used as TiO_2 precursor. Manganese(II) chloride tetrahydrate ($MnCl_2{\cdot}4H_2O$, 98%, Merck) was used as source of Mn dopant. Zirconia powder (ZrO_2, Jiaozuo Huasu) was used as the source of coupling semiconductor. Absolute ethanol (Merck) and demineralized water (Jaya Sentosa) were used as solvents.

Instrumentation

Specular reflectance UV-Vis spectrophotometer (SR UV-Vis) UV1700 Pharmaspec was used to measure the ultraviolet and visible (UV-Vis) absorption of the material. Fourier-transform infrared spectroscopy (FTIR) analysis was conducted using Thermo Nicolet iS10. The crystal structures of material were analyzed by using X-ray powder diffractometer (XRD) PANalytical X'Pert PRO MRD instrument with Cu Kα radiation. Surface morphology was observed with scanning electron microscopy equipped with energy dispersive X-ray spectrometer (SEM-EDX) Phenom Desktop ProXL.

Procedure

Mn-doped TiO_2-ZrO_2 was synthesized by the sol-gel method. Firstly, 2.5 mL of TTIP was dissolved in 25 mL of absolute ethanol and then stirred homogeneously. One gram of ZrO_2 powder was dispersed into 25 mL of demineralized water then as much as 14.38, 43.59, 72.66, 101.72, and 130.79 mg of $MnCl_2{\cdot}4H_2O$ was separately added dropwise into the mixture to obtain 1, 3, 5, 7 and 9% Mn wt./Ti wt., respectively. The mixture was stirred for 30 min and separated by centrifugation at 2000 rpm for 1 h. The obtained solid was aged in the open space

for 24 h and then heated at 60 °C for 24 h. Composites with various Mn dopant contents were calcined at 500 °C for 4 h to observe the effect of Mn contents. Additionally, the composite with 5% of Mn content was calcined at 700 and 900 °C to observe the effect of calcination temperature. The variation of dopant percentage and calcination temperature were based on the previous works [6-8]. All samples were characterized by using XRD, FTIR, SR UV-Vis and SEM-EDX.

■ RESULTS AND DISCUSSION

Fig. 1 displays the morphology and its corresponding EDX spectra of 5% Mn-doped TiO_2-ZrO_2 calcined at 500 °C. The morphology of Mn-doped TiO_2-ZrO_2 appears to be rough and its particles appear to be agglomerated with an estimated diameter of 1–5 μm. Table 2 shows the result of EDX spectra analysis. EDX analysis confirms that TiO_2-ZrO_2 was successfully synthesized and 0.33% of Mn was present in the composite.

FTIR spectra of Mn-doped TiO_2-ZrO_2 with various contents of Mn dopant and calcination temperatures are shown together in Fig. 2. FTIR spectra show hydroxyl stretching vibration of H_2O around 3300–3700 cm^{-1} and hydroxyl bending vibration of H_2O around 1650 cm^{-1} [15]. The Zr–O vibration was found around 420 and 744 cm^{-1} correspond to monoclinic structure of ZrO_2 [3]. At low wavenumber region, the absorption belonged to the vibration of Ti–O–Ti, Mn–O–Ti and Mn–O are found around 400–700 cm^{-1} [16]. Spectra of Mn-doped TiO_2-ZrO_2 has combined characteristic vibrations between TiO_2 and ZrO_2, where there are broad stretching vibration

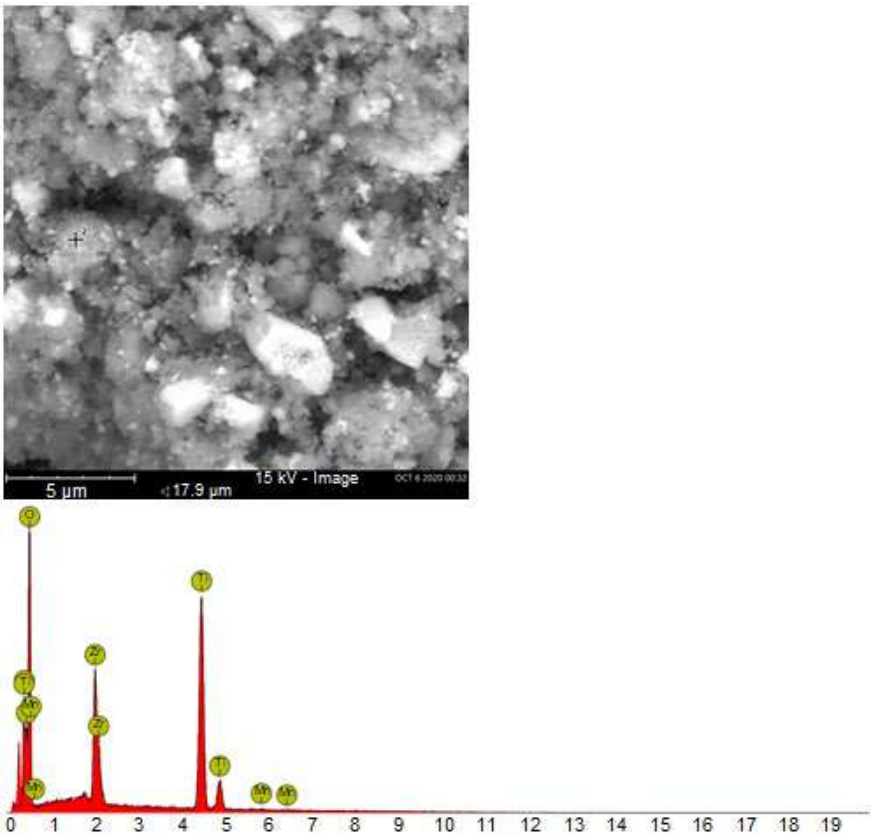

Fig 1. SEM image of TiO_2-ZrO_2 with 5% Mn content calcined at 500 °C and its corresponding EDX spectra

Table 2. EDX analysis of 5% Mn-doped TiO_2-ZrO_2 calcined at 500 °C

Sample	% Weight				
	Zr	Ti	O	Mn	Total
5% Mn-dopedTiO_2-ZrO_2 @ 500 °C	49.09	32.42	18.16	0.33	100

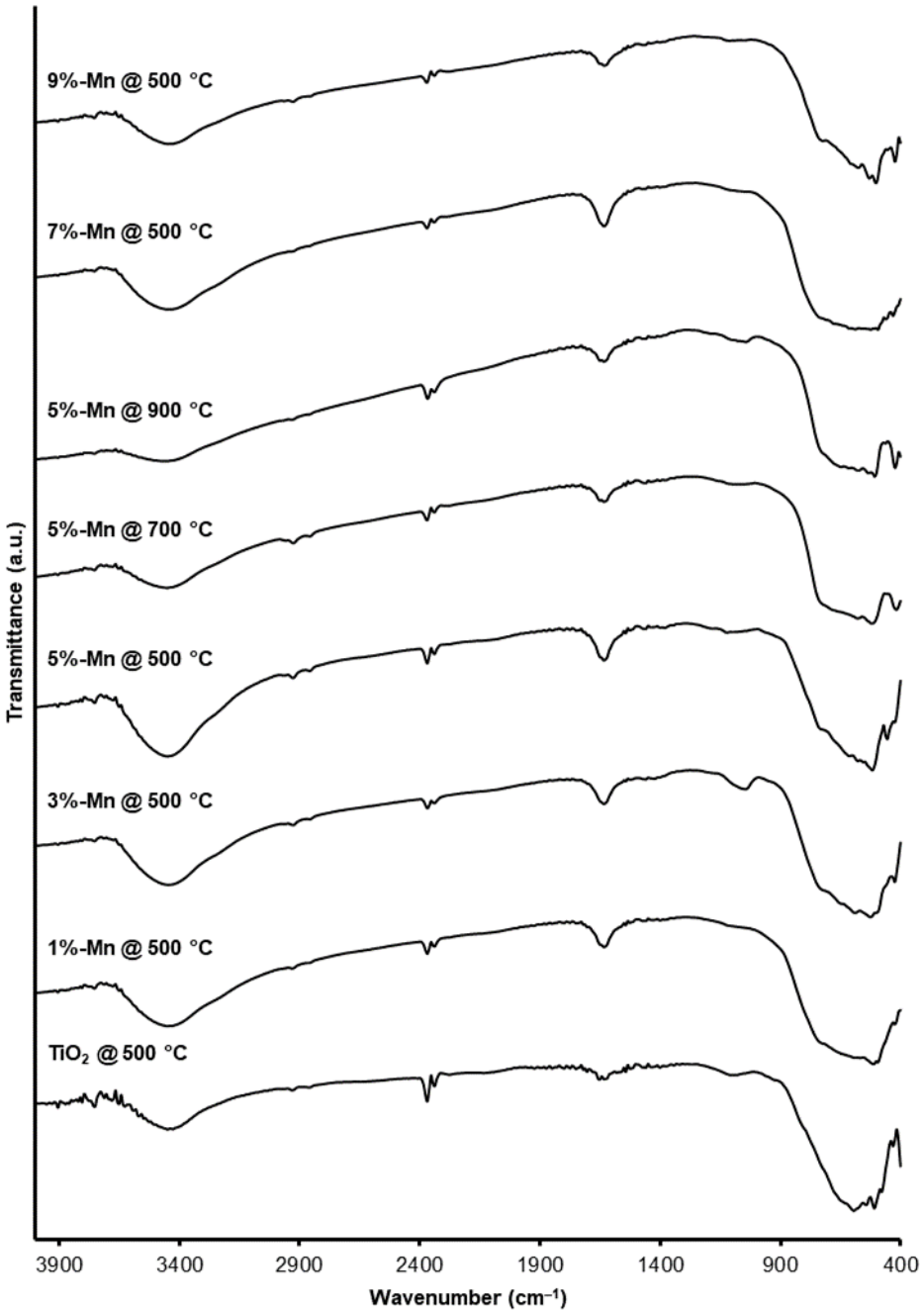

Fig 2. FTIR spectra of Mn-doped TiO_2-ZrO_2 with various dopant contents and calcination temperatures

of OH at 3300–3700 cm^{-1} and also around 400–700 cm^{-1}, which is probably the vibration of Zr–O–Zr, Ti–O–Ti, or Mn–O–Ti. The stretching and bending intensities of H_2O decrease at 9% of Mn-doped TiO_2-ZrO_2, possibly because the number of Mn replacing Ti increases. The hydroxyl bending and stretching intensities of H_2O at 1630 and 3300–3700 cm^{-1}, respectively, decrease with the increase of calcination temperature. This possibly happened because H_2O molecules of synthesized material are released due to the high temperature heating during the calcination process.

Fig. 3 shows diffraction patterns of various Mn-doped TiO_2-ZrO_2 composites, while Table 3 presents their calculated crystallite sizes based on Scherrer's equation [17]. The diffraction patterns confirm the presence of monoclinic ZrO_2 and anatase TiO_2. There are

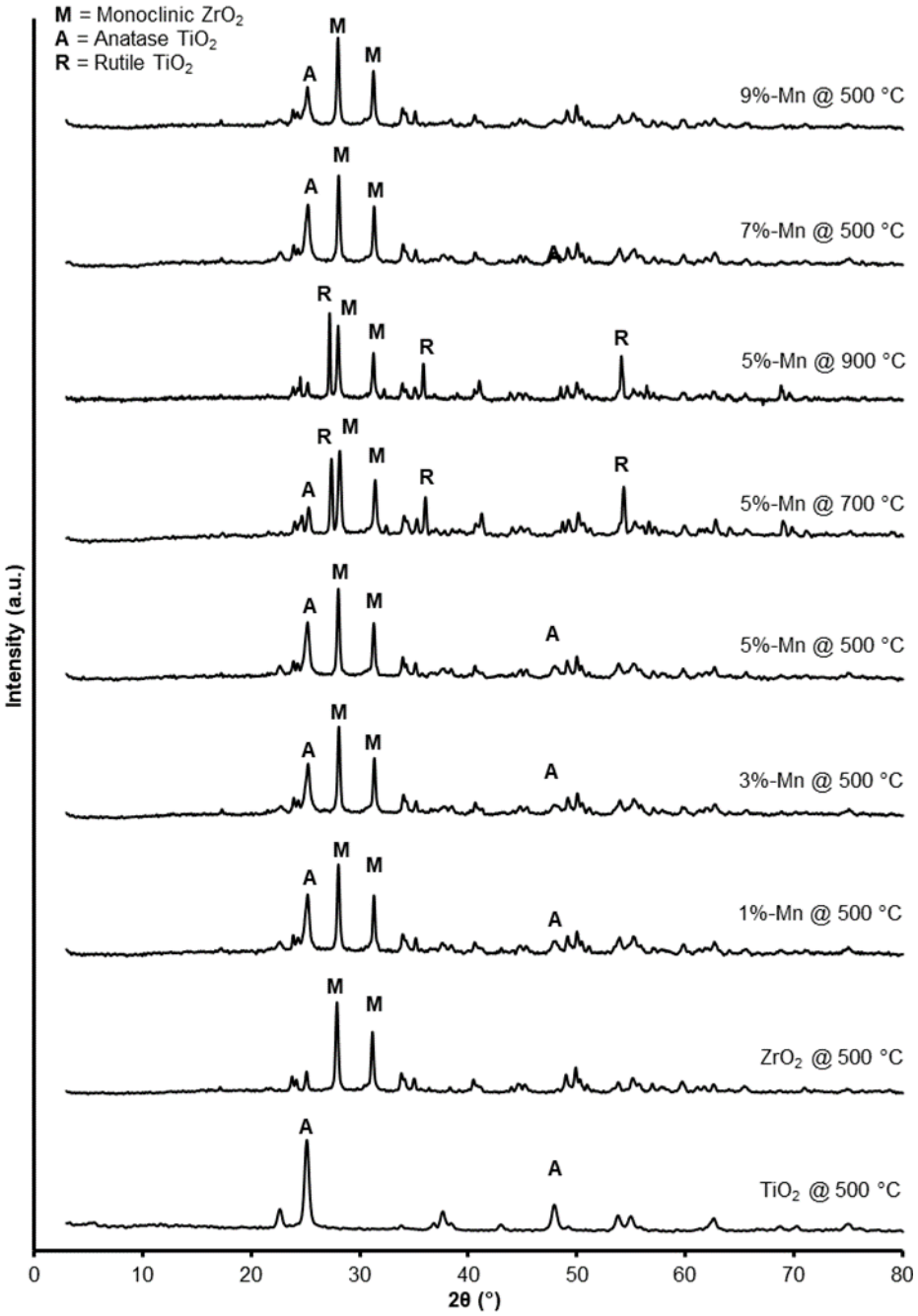

Fig 3. Diffraction patterns of Mn-doped TiO_2-ZrO_2 with various dopant contents and calcination temperatures

no tetragonal and rutile patterns observed at 500 °C. Monoclinic peaks are observed at 28.21° (-111) and 31.50° (111), according to ICDD:01-083-0944, while anatase peaks are observed at 25.28° (101) and 48.05° (200), according to ICDD:00-021-1272. All Mn-doped TiO_2-ZrO_2 had a pattern combination of high monoclinic and anatase intensities at 500 °C, while no Mn pattern was observed. The high intensity of monoclinic peaks shows that ZrO_2 has a greater amount than anatase. The average crystallite sizes of monoclinic and anatase remain unchanged significantly as the content of manganese dopant increases. It indicates that Mn^{2+} (67 pm) has substituted Ti^{4+} (60.5 pm) in the anatase TiO_2 structure, as the ionic radius of both metal ions are similar [18]. Some literature reported that TiO_2 starts to form rutile structure at 500 °C [7,11]. One report found

Table 3. Average crystallite size of various Mn-doped TiO_2-ZrO_2

Sample	Crystal phase	(hkl)	L (nm)
ZrO_2 @ 500 °C	Monoclinic	(-111)	26.36
TiO_2 @ 500 °C	Anatase	(101)	15.72
1%-Mn @ 500 °C	Monoclinic	(-111)	25.10
	Anatase	(101)	15.00
3%-Mn @ 500 °C	Monoclinic	(-111)	27.94
	Anatase	(101)	14.96
5%-Mn @ 500 °C	Monoclinic	(-111)	28.82
	Anatase	(101)	15.60
5%-Mn @ 700 °C	Monoclinic	(-111)	22.88
	Anatase	(101)	18.44
	Rutile	(110)	29.19
5%-Mn @ 900 °C	Monoclinic	(-111)	30.62
	Rutile	(110)	44.64
7%-Mn @ 500 °C	Monoclinic	(-111)	28.28
	Anatase	(101)	15.72
9%-Mn @ 500 °C	Monoclinic	(-111)	29.01
	Anatase	(101)	15.12

that the presence of Mn^{2+} ion promotes anatase-rutile phase transformation [16], while another report suggested that Zr^{4+} prevents phase transformation of anatase [19]. The presence of ZrO_2 is assumed to be responsible for preventing the anatase-to-rutile transformation on Mn-doped TiO_2-ZrO_2 calcined at 500 °C.

The diffraction patterns also confirm the presence of ZrO_2 monoclinic, TiO_2 anatase and TiO_2 rutile at 5% Mn-doped TiO_2-ZrO_2 calcined at 700 and 900 °C. Monoclinic and anatase peaks were observed similar to the previous discussion, but the intensity of anatase decreased while the rutile increased. Rutile peaks are observed at 27.91° (110), 36.43° (101) and 55.11° (211), according to ICDD:01-088-1175 [20]. The intensity of anatase decreased as the calcination temperature increased because of the anatase-to-rutile transformation. The rutile pattern starts to be observed at 700 °C and almost all anatase peaks transform into rutile at 900 °C. The average crystallite size of monoclinic ZrO_2 also remains unchanged at higher calcination temperature. On the other hand, there is an increase in rutile crystallite size, which is possibly due to agglomeration of the rutile phase at 900 °C.

The SR UV-Vis absorption spectra of the Mn-doped TiO_2-ZrO_2 are shown in Fig. 4 with the variation of Mn dopant content and calcination temperature, while Table 4 presents the bandgap energy values. The bandgap energy of the composites was evaluated by using absorption edge cross method. All synthesized materials have lower E_g values than TiO_2 (3.12 eV) and ZrO_2 (3.23 eV) [8,21]. The SR UV-Vis spectra show that all synthesized materials have absorption edge at visible range (above 400 nm). The presence of Mn^{2+} ions forms a new energy orbital under the conduction band and decreases the E_g value of the materials [22]. The increased calcination temperature reduces the E_g values of Mn-doped TiO_2-ZrO_2. This is possibly because the higher calcination temperature would facilitate the phase transformation of anatase to rutile and decrease the E_g value [23].

Based on the obtained results, the synthesized Mn-doped TiO_2-ZrO_2 using the sol-gel method had been successfully carried out. The Mn dopant was proven to reduce the E_g values from 3.12 to 2.78 eV with an optimum content of 5% and calcination temperature of 900 °C. The addition of Mn dopant 1–7% was shown to be able to reduce the E_g value, and it may possibly increase the response of the synthesized material under visible-light range. The E_g values of Mn-doped TiO_2-ZrO_2 increased as the addition of Mn dopant reached above 7%

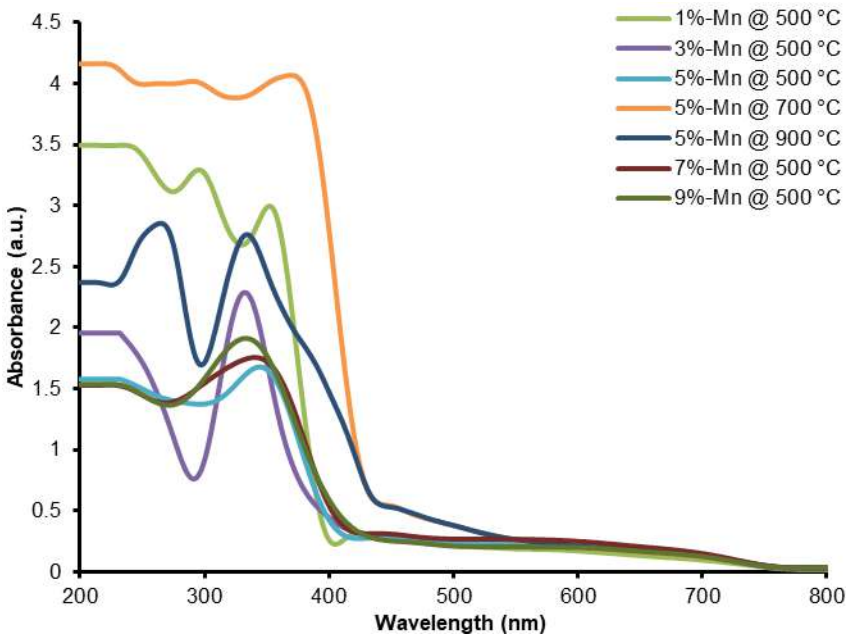

Fig 4. SR UV-Vis absorption spectra of various Mn-doped TiO_2-ZrO_2

Table 4. Bandgap energy data of Mn-doped TiO_2-ZrO_2

Sample	Eg (eV)
1%-Mn @ 500 °C	3.12
3%-Mn @ 500 °C	3.09
5%-Mn @ 500 °C	3.03
5%-Mn @ 700 °C	2.87
5%-Mn @ 900 °C	2.78
7%-Mn @ 500 °C	2.81
9%-Mn @ 500 °C	2.95

due to the heterojunction effect appearing and cancelling the dopant effect [4,6,21]. Furthermore, the higher calcination temperature was proven to enable the material transformations phase of anatase to rutile, which causes the E_g value to be smaller. This result corresponds with other previous works in which the addition of dopant between 1–9% and calcination temperature would show optimum condition of doped composite [4,6-8].

■ CONCLUSION

The investigation of Mn dopant content and calcination temperature affecting the properties of Mn-doped TiO_2-ZrO_2 composite had been successfully conducted. The results of EDX analysis confirm the presence of Zr, Ti, O and Mn. It was confirmed by the XRD analysis that the presence of Zr^{4+} inhibits the anatase-to-rutile transformation at higher calcination temperature. The bandgap of Mn-doped TiO_2-ZrO_2 decreases as the calcination temperature and the dopant content increase until reaching the optimum condition. The composite with the lowest bandgap is Mn-doped TiO_2-ZrO_2 with 5% of Mn content calcined at 900 °C. All of the synthesized composites in this research can be considered as a potential visible-light-responsive photocatalyst.

■ ACKNOWLEDGMENTS

We would like to express our gratitude to The Ministry of Research, Technology and Higher Education of the Republic of Indonesia for their support on this work through PDUPT 2020 Grant (2828/UN1.DITLIT/DIT-LIT/PT/2020).

■ REFERENCES

[1] Syoufian, A., Manako, Y., and Nakashima, K., 2015, Sol-gel preparation of photoactive srilankite-type zirconium titanate hollow spheres by templating sulfonated polystyrene latex particles, *Powder Technol.*, 280, 207–210.

[2] Pirzada, B.M., Mir, N.A., Qutub, N., Mehraj, O., Sabir, S., and Muneer, M., 2015, Synthesis,

characterization and optimization of photocatalytic activity of TiO_2/ZrO_2 nanocomposite heterostructures, *Mater. Sci. Eng., B*, 193, 137–145.

[3] Cheng, Q., Yang, W., Chen, Q., Zhu, J., Li, D., Fu, L., and Zhou, L., 2020, Fe-doped zirconia nanoparticles with highly negative conduction band potential for enhancing visible light photocatalytic performance, *Appl. Surf. Sci.*, 530, 147291.

[4] Deng, Q.R., Xia, X.H., Guo, M.L., Gao, Y., and Shao, G., 2011, Mn-doped TiO_2 nanopowders with remarkable visible light photocatalytic activity, *Mater. Lett.*, 65 (13), 2051–2054.

[5] El Mragui, A., Zegaoui, O., and Daou, I., 2019, Synthesis, characterization and photocatalytic properties under visible light of doped and co-doped TiO_2-based nanoparticles, *Mater. Today: Proc.*, 13, 857–865.

[6] Sulaikhah, E.F., Kurniawan, R., Pradipta, M.F., Trisunaryanti, W., and Syoufian, A., 2020, Cobalt doping on zirconium titanate as a potential photocatalyst with visible-light-response, *Indones. J. Chem.*, 20 (4), 911–918.

[7] Kurniawan, R., Sudiono, S., Trisunaryanti, W., and Syoufian, A., 2019, Synthesis of iron-doped zirconium titanate as a potential visible-light responsive photocatalyst, *Indones. J. Chem.*, 19 (2), 454–460.

[8] Alifi, A., Kurniawan, R., and Syofian, A., 2020, Zinc-doped titania embedded on the surface of zirconia: A potential visible-responsive photocatalyst material, *Indones. J. Chem.*, 20 (6), 1374–1381.

[9] Singh, J., Rathi, A., Rawat, M., Kumar, V., and Kim, K.H., 2019, The effect of manganese doping on structural, optical, and photocatalytic activity of zinc oxide nanoparticles, *Composites, Part B*, 166, 361–370.

[10] Xu, Y., Lei, B., Guo, L., Zhou, W., and Liu, Y., 2008, Preparation, characterization and photocatalytic activity of manganese doped TiO_2 immobilized on silica gel, *J. Hazard. Mater.*, 160 (1), 78–82.

[11] Wu, H., Ma, J., Zhang, C., and He, H., 2014, Effect of TiO_2 calcination temperature on the photocatalytic oxidation of gaseous NH_3, *J. Environ. Sci.*, 26 (3), 673–682.

[12] Lv, K., Xiang, Q., and Yu, J., 2011, Effect of calcination temperature on morphology and photocatalytic activity of anatase TiO_2 nanosheets with exposed {001} facets, *Appl. Catal., B*, 104 (3-4), 275–281.

[13] Tomar, L.J., Bhatt, P.J., Desai, R.k., and Chakrabarty, B.S., 2014, Effect of preparation method on optical and structural properties of TiO_2/ZrO_2 nanocomposite, *J. Nanotechnol. Adv. Mater.*, 2 (1), 27–33.

[14] Wellia, D.V., Xu, Q.C., Sk, M.A., Lim, K.H., Lim, T.M., and Tan, T.T.Y., 2011, Experimental and theoretical studies of Fe-doped TiO_2 films prepared by peroxo sol-gel method, *Appl. Catal., A*, 401 (1-2), 98–105.

[15] Sudrajat, H., Babel, S., Ta, A. T., and Nguyen, T. K., 2020, Mn-doped TiO_2 photocatalysts: Role, chemical identity, and local structure of dopant, *J. Phys. Chem. Solids*, 144, 109517.

[16] Sharotri, N., Sharma, D., and Sud, D., 2019, Experimental and theoretical investigations of Mn-N-co-doped TiO_2 photocatalyst for visible light induced degradation of organic pollutants, *J. Mater. Res. Technol.*, 8 (5), 3995–4009.

[17] Fischer, K., Schulz, P., Atanasov, I., Abdul Latif, A., Thomas, I., Kühnert, M., Prager, A., Griebel, J., and Schulze, A., 2018, Synthesis of high crystalline TiO_2 nanoparticles on a polymer membrane to degrade pollutants from water, *Catalysts*, 8 (9), 376.

[18] Gao, X., Zhou, B., and Yuan, R., 2015, Doping a metal (Ag, Al, Mn, Ni and Zn) on TiO_2 nanotubes and its effect on Rhodamine B photocatalytic oxidation, *Environ. Eng. Res.*, 20 (4), 329–335.

[19] Venkatachalam, N., Palanichamy, M., Arabindoo, B., and Murugesan, V., 2007, Enhanced photocatalytic degradation of 4-chlorophenol by Zr^{4+} doped nano TiO_2, *J. Mol. Catal. A: Chem.*, 266 (1-2), 158–165.

[20] Radić, N., Grbić, B., Petrović, S., Stojadinović, S., Tadić, N., and Stefanov, P., 2020, Effect of cerium oxide doping on the photocatalytic properties of rutile TiO_2 films prepared by spray pyrolysis,

Physica B, 599, 412544.

[21] Andita, K.R., Kurniawan, R., and Syoufian, A., 2019, Synthesis and characterization of Cu-doped zirconium titanate as a potential visible-light responsive photocatalyst, *Indones. J. Chem.*, 19 (3), 761–766.

[22] Abdelouahab Reddam, H., Elmail, R., Lloria, S.C., Monrós Tomás, G., Reddam, Z.A., and Coloma-Pascual, F., 2020, Synthesis of Fe, Mn and Cu modified TiO_2 photocatalysts for photodegradation of Orange II, *Bol. Soc. Esp. Ceram. Vidrio*, 59 (4), 138–148.

[23] Samet, L., Ben Nasseur, J., Chtourou, R., March, K., and Stephan, O., 2013, Heat treatment effect on the physical properties of cobalt doped TiO_2 sol–gel materials, *Mater. Charact.*, 85, 1–12.

Synthesis and Characterization of Ferrofluid-Chitosan-Au Nanoparticles as Brachytherapy Agent Candidate

Muflikhah[1*], Ahmad Marzuki Ramadhan[2], Maria Christina Prihatiningsih[2], Mujamilah[1], and Aloma Karo Karo[1]

[1]*Center for Science and Technology of Advanced Materials, National Nuclear Energy Agency of Indonesia, Kawasan Puspiptek Serpong, Banten 15314, Indonesia*

[2]*Polytechnic Institute of Nuclear Technology, National Nuclear Energy Agency of Indonesia, Jl. Babarsari POB 6101 Ykbb, Yogyakarta 55281, Indonesia*

* ***Corresponding author:***

tel: +62-85640680600
email: muflikhah@batan.go.id

Received: December 13, 2020
Accepted: May 24, 2021

DOI: 10.22146/ijc.62191

Abstract: *Brachytherapy is expected to be a solution to the side effect of other cancer therapy methods. This study aims to synthesize ferrofluids (FF)-Chitosan-Au (so-called cold synthesis) as the initial step before using ^{198}Au that is expected to be a targeted and controllable brachytherapy agent. In this research, the preparation of FF-Chitosan was done by the co-precipitation method. Furthermore, FF-Chitosan-Au was produced via self-assembly by the adsorption method. The adsorption followed the Langmuir model with a maximum capacity of 30.24 mg Au/g FF-Chitosan. The X-Ray Diffractometion (XRD) of FF-Chitosan-Au confirms the existence of Au. Particle Size Analyzer (PSA) indicates FF-Chitosan-Au has an average size of 82.93 nm with a polydispersity index of 0.175. Morphological and distribution analysis of nanoparticles using Scanning Electron Microscope (SEM) shows that nanoparticles have a homogenous spherical shape. Vibrating Sample Magnetometer (VSM) measurement confirms the superparamagnetic properties of FF-Chitosan and FF-Chitosan-Au with a saturated magnetization of 80.48 and 74.52 emu/g, respectively. The overall results are associated with biomedical requirements, such as high saturation magnetization and good polydispersity. The synthesis can also be applied to produce FF-Chitosan-^{198}Au that has great potential as a brachytherapy agent, which will reduce the nuclear waste and potential danger of radiation received by workers during synthesis.*

Keywords: *ferrofluids; magnetic nanoparticle; adsorption; chitosan-gold, brachytherapy*

■ INTRODUCTION

Research of nanomaterials by assembling some nanomaterials components becomes interesting due to having versatile physical and biological properties that have a wide range of applications such as in catalysis and targeting therapeutic drugs [1-2]. For example, nanoparticle magnetic is one of the favorite materials combined with other materials by surface modification, especially in biomedical applications [3]. This modification aims to make magnetic nanoparticles (MNP) being compatible with the bio-system [4].

Recently, research on targeted therapy agents has become the most promising cancer treatment option [5]. Extensive studies on chemically modified polymeric MNP have been done because of their capability of carrying a wide range of drugs to tumor sites [5]. However, for biomedical applications, MNP-mostly magnetite must have high saturation magnetization, stability, biocompatibility, and interactive functions at the surface [6]. On the other hand, MNP has hydrophobic surfaces that tend to agglomerate due to strong magnetic dipole-dipole interaction, which causes different behavior [7]. Moreover, the naked MNP have high chemical activity and are easily oxidized in the air (especially magnetite), resulting in loss of magnetism and dispersibility [8-9]. Therefore, the surface coating

should be done as effective protection strategies to keep the stability of MNP. The MNP surfaces were generally coated by organic molecules (surfactants, polymers, and biomolecules) or an inorganic layer (silica, metal, non-metal elementary substance, metal oxide, or metal sulfide). These coating strategies protect and stabilize the MNP and play a crucial role in improving MNPs specificity; hence, the higher the targeting specificity, the more selective target cancer cells will be achieved [10-12].

Development of MNP coated by organic molecule becomes important in biomedical application due to its wide range of functions such as targeted drug delivery and radiotherapy and diagnostic agents [13]. Chitosan is a polyamine molecule with more advantages as an MNP coating agent than a neutral polymer such as polyethylene glycol (PEG) because of its ability to secondary functionalization [14-15]. Chitosan protects and stabilizes MNP agents and establishes electrostatic interactions with the negatively charged cell membrane in the weakly acidic microenvironment of tumors (pH 6.8–7.2) [14-15]. In addition, Low Molecular Weight (LMW) chitosan as an MNP coating agent increases the hydrophilicity of the polymer and further improves its protective effect at neutral pH [16].

A variety of molecules or elements are able to bind with amine functional groups at chitosan. Gold is a noble metal that widely used in various fields, including health. Over the last decade, researchers have made many efforts to use gold nanoparticles for cancer treatment [4-5]. Gold has become an important material in nanomedicine due to its stability and ease of functionalization [15]. Gold nanoparticles (AuNPs) also have extraordinary tumor retention capabilities because of their natural affinity to leaky tumor vasculature, manifested in tumor angiogenesis [16]. Many research uses gold nanoparticles and their activated phase (^{198}Au) as therapeutic agents by different mechanisms, including thermal therapy, photodynamic therapy, and radiotherapy [14,17]. Gold nanoparticles are also extensively studied in the range of medical diagnostic and therapeutic applications (as theranostic agents) [14,18]. In order to reach the tumor target and avoiding its toxicity, gold combine with other molecules such as chitosan and magnetic material. Iron oxide/gold hybrid coated with chitosan has been studied for diagnostic and targeted drug delivery (theranostic agent) [18]. Pati and co-workers have synthesized chitosan functionalized iron oxide-Au core-shell for targeted drug delivery (TDD) [2]. Irradiated gold (^{198}Au) combined with poly(amidoamine) (PAMAM) for brachytherapy or internal radiotherapy has been inspected by Ritawidya and co-workers [17]. However, synthesis method of composite Au-iron oxide-chitosan that allows for activated Au has not been proposed yet. Many research of Au-iron oxide-chitosan added Au in the first step (before coated with chitosan). This method is quite difficult and not safe when using Au in activated phase. In this research, a more simple synthesis method of Au-iron oxide-chitosan nanocomposite has been studied which allows the using of irradiated Au. The iron oxide-chitosan functionalized with Au in the final step by self-assembly. This method has benefit to reduce the chance of radioactive waste and the potential danger of radiation received by workers when using irradiated gold.

Synthesis of Au-iron oxide-chitosan nanoparticles has been done in two steps. First, magnetite as a magnetic source that will play a role as a controllable therapy agent has been synthesized in chitosan solution to form Ferrofluid-Chitosan (FF-Chitosan) with sodium tripolyphosphate (Na-TPP) as a cross-linker [19]. Then, FF-Chitosan is functionalized with Au by self-assembly through the adsorption method in a batch system [13]. In this research, chloroauric acid tetrahydrate has been used as an Au source, then adsorbed by FF-Chitosan through electrostatic interaction. The influence of the initial pH of the Au was investigated to get the optimum pH of FF-Chitosan-Au synthesis. Langmuir and Freundlich isotherms were used to evaluate the equilibrium adsorption data [13]. This synthesis route will be the reference when using Au in the active phase (^{198}Au).

■ EXPERIMENTAL SECTION

Materials

Chemicals used for the synthesis of FF-Chitosan-Au were $FeCl_2.4H_2O$ and $FeCl_3.6H_2O$ from Sigma

Aldrich as precursors for ferrofluid, chitosan with Low Molecular Weight (Sigma Aldrich), acetic acid (analytical grade, from Merck), sodium tripolyphosphate (Na-TPP) as a cross-linking agent, ammonium hydroxide (NH_4OH) 32%, distilled water with a resistivity of 18.2 MΩ cm, chloroauric acid tetrahydrate ($HAuCl_4$) from Sigma Aldrich. All chemicals in this study were used without further purification.

Instrumentation

Morphology and elemental analysis of nanoparticles Ferrofluid-Chitosan and Ferrofluid-Chitosan-Au were subjected to SEM-EDAX (JEOL-JED-2300). The estimation of the particle size has been done using DLS analysis (Malvern). XRD (PANalytical) was used for structural analysis. FTIR spectra of chitosan, FF-Chitosan, and FF-Chitosan-Au were recorded with Infrared Transmission Spectroscopy (KBr module) in the range of 4000–400 cm^{-1} on FTIR-Bruker Tensor 27. The magnetization behavior of FF-Chitosan and FF-Chitosan-Au were subjected to VSM (OXFORD 1.2H). Au concentrations in the supernatant (un-bounded Au) were calculated using a Flammable Atomic Absorption Spectrophotometer (Perkin Elmer AAS Analyst 400).

Procedure

Synthesis of Ferrofluid-Chitosan

Ferrofluid-Chitosan (FF-Chitosan) nanoparticles were in-situ synthesized by co-precipitation method as described by Unsoy et al., with some modifications [20]. Ferrous chloride salts, Fe(II) and Fe(III), were dissolved in chitosan solution. TPP was used as a cross-linker. The synthesis has been conducted at room temperature by adding a total of 3.40 g of $FeCl_3{\cdot}6H_2O$ and 2.68 g of $FeCl_2{\cdot}4H_2O$ (mol ratio of Fe(II) and Fe(III) is 1:1), in 30 mL of 0.1% w/v chitosan in 1% acetic acid solution. Furthermore, the mixture of Fe(III) and Fe(II) chloride salts in chitosan solution was dispersed with ultrasound irradiation for 1 min. Sodium-TPP (0.00773 g dissolved in 10 mL DI-water) was mixed with 30 mL of 32% NH_4OH and then added vigorously to the Fe-chitosan solution under ultrasonic irradiation for 5 min. The resulting black-colored solution was then stirred using a mechanical mixer for an hour. The colloidal chitosan-coated Fe_3O_4 nanoparticles were extensively washed with deionized water and separated by magnetic decantation several times to remove the impurities. The solids were then added with deionized water and got additional ultrasound irradiation for 5 min, then centrifuged for 30 min at 12000 rpm. The supernatant containing magnetic nanoparticles Fe_3O_4-chitosan was stored in the refrigerator.

Synthesis of Ferrofluid-Chitosan-Au

The synthesis of FF-Chitosan-Au has been carried out by the adsorption method in a batch system. FF-Chitosan were act as adsorbent and $HAuCl_4$ as adsorbate. All the synthesis procedures were done at room temperature. In order to get the optimum condition, synthesis has been done in various pH of Au solution (1 to 6). Variation of FF-Chitosan amount (5, 10, 15, and 20 mg) and concentration of the gold solution (40, 60, 80, 100, and 120 ppm) have been done at optimum pH. In this study, the volume of Au solution used was 5 mL for each batch, and after the FF-Chitosan addition, the mixtures were shaken for 2 h. Then, the adsorbent and supernatant were separated with an external magnet and centrifuge. The concentration of Au that remains in the supernatant was analyzed with Flammable Atomic Absorption Spectroscopy (FAAS). The resulting data of synthesis FF-Chitosan-Au in various gold solution concentrations were evaluated with Langmuir and Freundlich equations to determine the adsorption capacity.

■ RESULTS AND DISCUSSION

This research is the initial research in the manufacture of FF-Chitosan-Au(198), which will be applied as a radiation source agent in brachytherapy. It is crucial to determine the optimum condition of synthesis using non-activated gold. This adsorption method (which Au takes place in the last step of synthesis) aims to reduce radioactive waste and the potential danger of radiation that workers will receive when synthesis using Au(198).

FF-Chitosan-Au has been synthesis in two steps. After FF-Chitosan has been obtained via co-precipitation, it was then bound to gold Au with

adsorption method in a batch system. Magnetite nanoparticles (MNP) in ferrofluid form have been obtained in situ in chitosan solution with TPP as a cross-linker. Schematic interaction between MNP (ferrofluid) and chitosan with crosslinked TPP as a synthesis product is shown in Fig. 1. The amino groups in the chitosan have a positive charge as a result of protonation in an acidic medium that able to bond with the negative charge of hydroxyl groups of magnetite via electrostatic interaction. Similar interactions also occur between –OP groups of TPP with amino groups in chitosan. Thus, the TPP plays a role in the formation of densely packed nanoparticles [20].

Determination of the optimum pH of Au solution is important due to the acidity of the medium affects the charge of the FF-Chitosan surface and its stability. The acidity of Au solution was set at acid condition (pH 1–6), where gold ion (Au(III)) has negative charge as $AuCl_4^-$, $[AuCl_3(OH)]^-$, $[AuCl_2(OH)_2]^-$, and $[AuCl(OH)_3]^-$ species [13,21]. The optimum pH of Au solution for FF-Chitosan-Au synthesized in this research has been achieved at pH 2 (as shown in Fig. 2). It can be explained that at pH 1, Au that binds to the active site of FF-Chitosan was low because of the strong acidity environment leading to ion competition between $[AuCl_4]^-$ with Cl^- of HCl. Au ion and FF-Chitosan surface electrostatic interaction has reached the maximum at pH 2 and decreased slightly until pH 6. This happened due to the H^+ ion in the Au solution that protonates $–NH_2$ and –OH groups in FF-Chitosan was decreased with the increase in pH. Another reason is, at pH 5 and 6, Au ions have a negative charge as $[AuCl_2(OH)_2]^-$ and $[AuCl(OH)_3]^-$, which have lower electrostatic attraction than at lower pH [13]. Since the maximum capacity of Au that binds to the FF-Chitosan surface occurred at pH 2 in the examined pH range, the following synthesis of FF-Chitosan-Au was carried out at pH 2.

The initial concentration of Au solution becomes an important driving force that affects the adsorption capacity of FF-Chitosan to Au ion. The amount of Au ion that binds to FF-Chitosan surface at pH 2 and room temperature is shown in Fig. 3, which informs the correlation of adsorption capacity of FF-Chitosan with

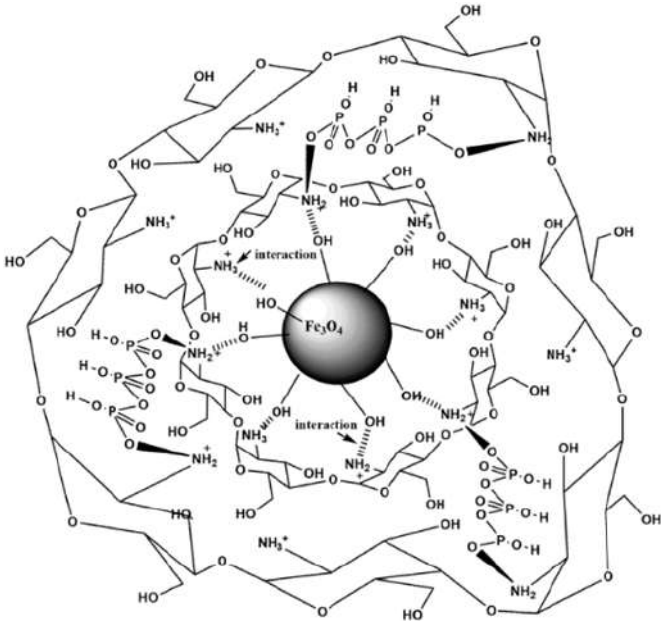

Fig 1. Schematic illustration of the interaction between Fe_3O_4 and chitosan with cross-linker TPP

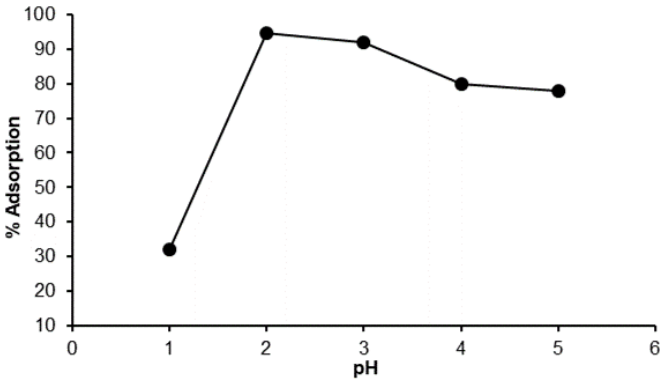

Fig 2. Determination of the optimum pH on the FF-Chitosan-Au synthesis

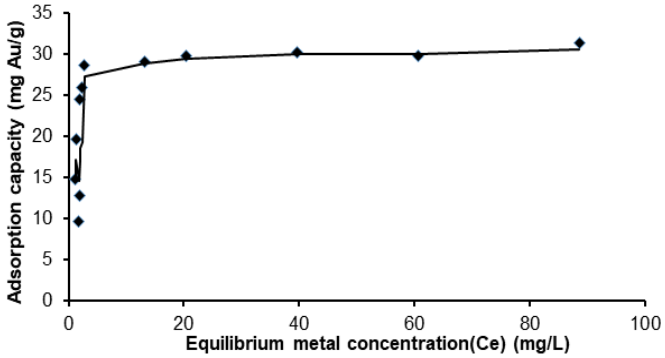

Fig 3. Equilibrium isotherm for the adsorption of Au ions on the FF-Chitosan in the synthesis of FF-Chitosan-Au

Au ion concentration at equilibrium (Ce). As the initial metal ion concentration increases, the percentage of Au that binds to FF-Chitosan decreases, which was in line with the basic concept of mass transfer [22]. At a low concentration of Au ion, the active binding sites of FF-Chitosan remain unsaturated, offering a large surface area for Au ion. At a higher concentration, Au ion leads to a decreasing in the total surface area of the Au ion adsorbent [13]. After the equilibrium has been reached, the increasing concentration in the system caused the distance of particles to narrow and limited the mobility of particles, then made the amount of Au ion that binds to FF-Chitosan decrease. Fig. 3 informs the adsorption capacity of FF-Chitosan to Au is 30 mg Au/g FF-Chitosan.

The adsorption isotherm that informs the correlation between the amount of Au per unit mass of FF-Chitosan at constant temperature and its concentration in the equilibrium solution is important to determine the capacity of Au ion that binds onto FF-Chitosan surface. The calculation was done by fitting the experimental data into the Langmuir and Freundlich isotherm models. Table 1 shows the coefficient correlation of the Langmuir and Freundlich models of FF-Chitosan to Au ion. Mass of FF-Chitosan was varied by 5, 10, and 15 mg to get more accurate information.

Based on the coefficient correlation of Langmuir and Freundlich, the adsorption capacity of the FF-Chitosan-Au synthesis fits the Langmuir model. Langmuir adsorption isotherm is examined based on the adsorbent monolayer surface, and all of the active sites on the adsorbent surface give the same affinity to interact with adsorbate [13]. The calculation result shown in Table 2 confirms the maximum adsorption capacity and Au loading content of 30.24 mg Au/g FF-Chitosan.

Table 1. Coefficient correlation of the Langmuir and Freundlich models of the adsorption FF-Chitosan to Au

Mass of FF-Chitosan	R^2	
(mg)	Langmuir	Freundlich
5	0.969	0.069
10	0.999	0.465
15	0.995	0.449

Table 2. Langmuir parameters of FF-Chitosan-Au synthesis

FF-Chitosan	Langmuir Isotherm		
(mg)	(R^2)	Kl (L/mg)	Qmax (mg/g)
5	0.969	0.219	30.77
10	0.999	1.622	30.21
15	0.995	0.938	29.76
Average			30.24

Characterization of Materials

FTIR spectrophotometric analysis was carried out to verify the functional groups that were present in the synthesized materials. Fig. 4 shows the functional groups of chitosan (a), FF-Chitosan (b), and FF-Chitosan-Au (c). The broad absorption band at wavenumber 3361 cm^{-1} attributed to O–H and N–H vibrations (Fig. 4 a-c). Characteristic of chitosan peak shown at 2926 cm^{-1} (C–H stretching), 1648 cm^{-1} (N–H stretching), 1378 cm^{-1} (C–C bending), 1315 cm^{-1} (C–N stretching), 1071 cm^{-1} (C–O asymmetry), 1035 cm^{-1} (C–O symmetry) and 894 cm^{-1} (C–H ring stretching) [10]. FTIR spectra FF-Chitosan (Fig. 4(b)) also show O–H and N–H absorption peaks at 3363 cm^{-1}. The peak at 1648 cm^{-1} belongs to the stretching vibration of N–H from chitosan. The new peak at 582 cm^{-1} (Fig. 4(b)) can be related to the stretching vibration of Fe-O from Fe_3O_4 in FF-Chitosan [7,22]. The absorption bands at 455 cm^{-1} attributed to tetrahedral and octahedral sites of Fe_3O_4 [23]. The enhanced peak at 582 cm^{-1} at Fig. 4(c) suggested that FF-Chitosan-Au already formed successfully [24].

Diffraction analysis of the samples has been done to confirm the existence of Fe_3O_4 and Au in the FF-Chitosan and FF-Chitosan-Au. Diffractogram of FF-Chitosan in Fig. 5(a) shows the seven characteristic peaks of Fe_3O_4 at 30.26°, 35.49°, 43.24°, 53.63°, 57.14°, 62.81°, 74.38° [25]. The peak of chitosan was observed at $2\theta = 20.0°$ with low intensity and wide bump, indicating the amorphous phase [13]. The XRD result of FF-Chitosan-Au (Fig. 5(b)) shows some characteristic peaks that also appear at the FF-Chitosan diffractogram, which

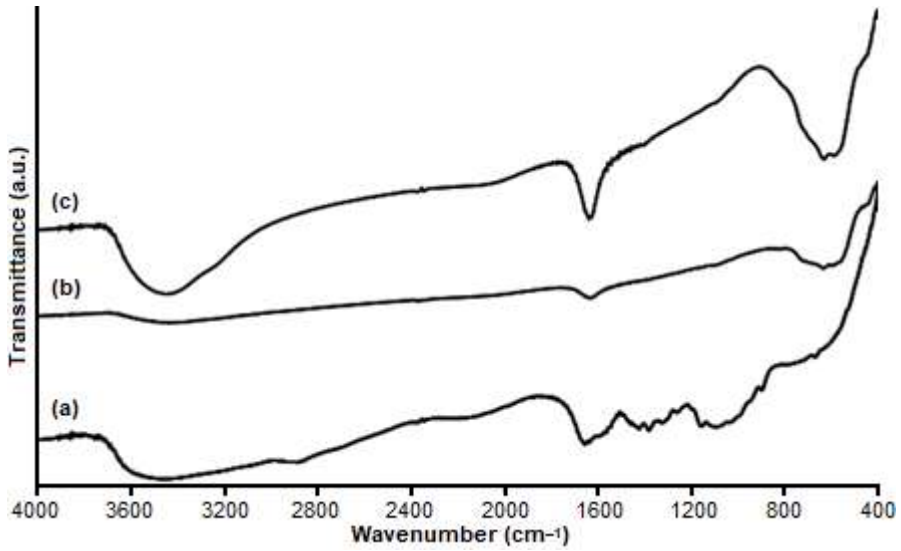

Fig 4. FTIR spectra of (a) Chitosan, (b) FF-Chitosan and (c) FF-Chitosan-Au

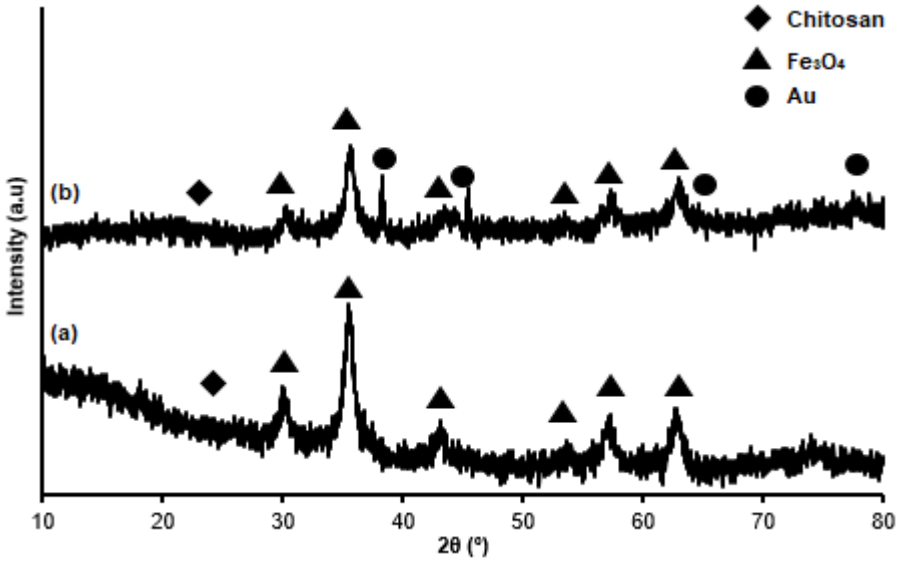

Fig 5. Diffraction pattern of (a) FF-Chitosan and (b) FF-Chitosan-Au

belong to Fe_3O_4 and chitosan. Other peaks also appear that belong to Au at 2θ 37.94°, 44.13°, 64.22°, and 77.03° [26]. Peaks of Au corresponds to COD-Inorg entry number 96-901-3039. It indicates that Au has embedded at FF-Chitosan [23].

Particle size distribution of FF-Chitosan with dynamic light scattering (DLS) method presented in Fig. 6 shows a narrow distribution particle size with an average size of 90.57 nm with a polydispersity index (PDI) of 0.150. The value of the polydispersity index indicates the homogeneity of FF-Chitosan particles is polydisperse (if the PDI < 0.1, the particle distribution is monodispersed). In drug delivery applications, a PDI value of 0.3 or below is acceptable. Previous research on coating magnetic nanoparticles using chitosan has broad particle distribution (20–100 nm) [25]. However, the polydispersity of the samples is low (homogeneity of the sample is high as confirmed with SEM). The particle size distribution of FF-Chitosan-Au also shows narrow distribution particle size in the nanometer range (average size 82.93 nm) with a polydispersity index of 0.175, indicating a good homogeneity. A self-assembly

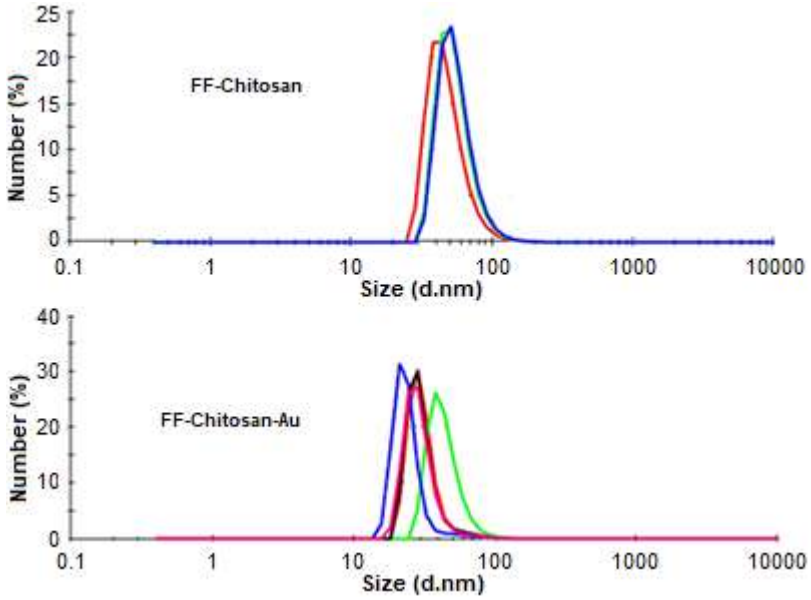

Fig 6. Particle size distribution of FF-Chitosan and FF-Chitosan-Au

process of Au to FF-Chitosan surface may cause a reduction of the tendency of magnetic chitosan to agglomerate (magnetic interaction), making slight changes in the increasing of the polydispersity index, decreasing the average size.

The morphology of the prepared nanoparticles was examined using SEM, as shown in Fig. 7. SEM micrograph of nanoparticles FF-Chitosan indicates that the particles have a spherical shape and good uniformity in size with a diameter less than 100 nm (Fig. 7(a)). This result corresponds to the FF-Chitosan particle size obtained from the DLS method that the polydispersity index of FF-Chitosan is 0.1, which is close to monodisperse (< 0.1). In the FF-Chitosan in SEM micrograph seemed to form clusters, but still in nanometers size, due to intermolecular interactions, such as electrostatic, hydrophobic, magnetic, and van der Waals interactions during sample preparation in SEM analysis. SEM micrograph of FF-Chitosan-Au (Fig. 7(b)) shows that FF-Chitosan-Au has a spherical shape with homogeneous size distribution. There are also several nanoparticles agglomeration but still in the nanometer range.

Magnetic properties of the samples have been characterized using Vibrating Sample Magnetometer (VSM) and presented in a hysteresis curve. Fig. 8 shows

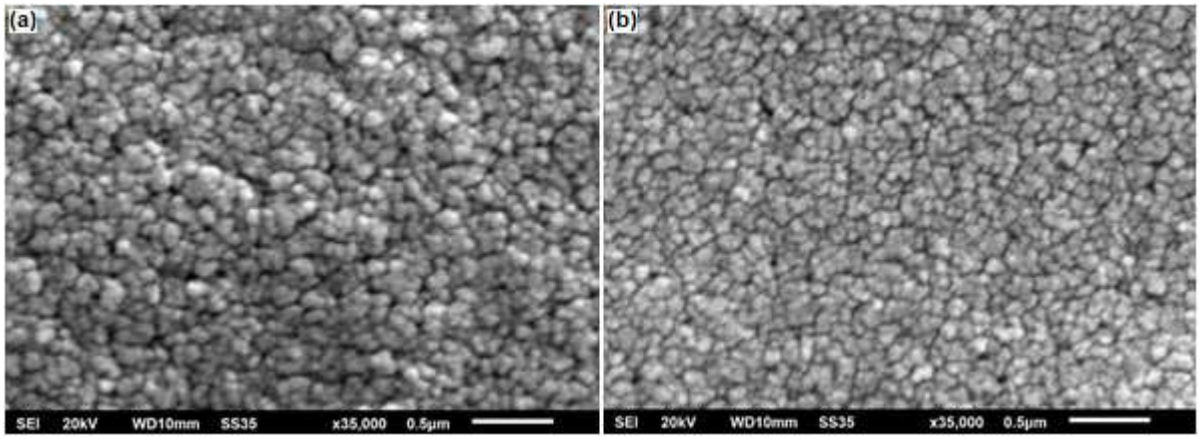

Fig 7. Scanning electron micrograph (SEM) image of FF-Chitosan (a) and FF-Chitosan-Au (b)

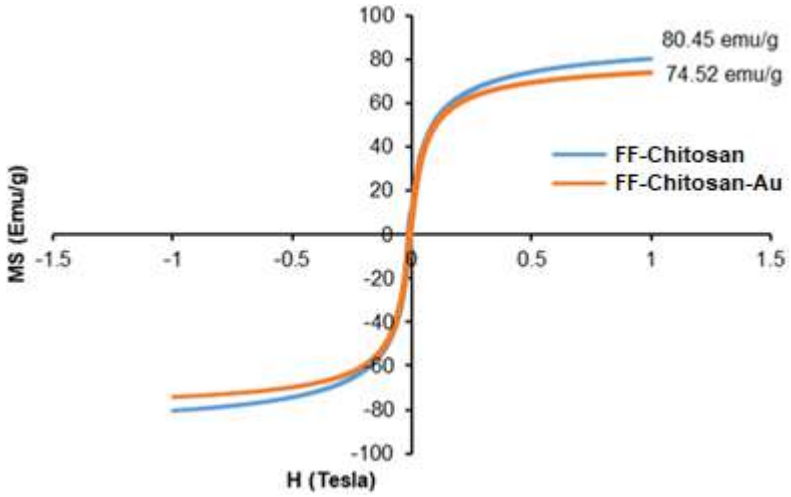

Fig 8. Hysteresis curve of FF-Chitosan and FF-Chitosan-Au

a hysteresis curve of FF-Chitosan and FF-Chitosan-Au, respectively. Base on particle size data from the DLS method and SEM, the size of FF-Chitosan and FF-Chitosan-Au in the tens nanometers show superparamagnetic behavior. The magnetization of superparamagnetic nanoparticles will be zero in the absence of an external magnetic field, while the coercivity and remanence will be nearly zero in its hysteresis curve [6]. Fig. 8 shows that the magnetization saturation (Ms) value of FF-Chitosan is 80.45 emu/g. Compared to another magnetic-chitosan research [22,27], the Ms value in this research is higher. The Ms value of FF-Chitosan-Au is 74.52 emu/g, which lower than FF-Chitosan because Au has diamagnetic properties that hamper magnetic interaction between magnetic nanoparticles. This also indicates that Au has been embedded in FF-Chitosan.

■ CONCLUSION

This study reports the synthesis of Ferrofluid-Chitosan-Au in two steps procedure. FF-Chitosan was synthesized through in-situ co-precipitation, then Au was assembled to FF-Chitosan via adsorption process. The maximum capacity of Au embedded in FF-Chitosan is 30 mg Au/g FF-Chitosan and fits the Langmuir isotherm model. Characterization results from FTIR, SEM, XRD show that FF-Chitosan-Au has been formed in the nanometer range with a Ms value of 74.52 emu/g. Considering its effectiveness and safety synthesis route, this FF-Chitosan-Au synthesis procedure could be employed when using Au in an active phase, promisingly in a biomedical application (brachytherapy agent).

■ ACKNOWLEDGMENTS

We acknowledge the financial support from the research funding DIPA 2018. We also would like to thank Mr. Ajrieh Setyawan from PTLR-BATAN for his assistance with the FAAS analysis.

■ REFERENCES

[1] Pati, S.S., Singh L.H., Oliveira, A.C., and Garg, V.K., 2016, Chitosan functionalized Fe_3O_4@Au core-shell nanomaterials for targeted drug delivery, *Int. J. Chem. Mol. Nucl. Mater. Metall. Eng.*, 9 (6), 643–646.

[2] Pati, S.S., Singh, L.H., Guimar, E.M., Mantilla, J., Coaquira, J.A.H., Oliveira, A.C., Sharma, V.K., and Garg, V.K., 2016, Magnetic chitosan-functionalized Fe_3O_4@Au nanoparticles: Synthesis and characterization, *J. Alloys Compd.*, 684, 68–74.

[3] Sun, S.N., Wei, C., Zhu, Z.Z., Hou, Y.L., Venkatraman, S.S., and Xu, Z.C., 2014, Magnetic iron oxide nanoparticles: Synthesis and surface coating techniques for biomedical applications, *Chin. Phys. B*, 23 (3), 037503.

[4] Leamy, P.J., 2003, Preparation, characterization, and in vitro testing of poly(lactide-co-glycolide) and dextran magnetic microspheres for in vivo applications, *Dissertation*, University of Florida.

[5] Mohammed, L., 2016, Polymeric superparamagnetic nanoparticles for drug delivery applications, *Thesis*, University of Western Ontario.

[6] Sulungbudi, G.T., and Mujamilah, 2016, An effort on homogenizing size distribution of magnetic nanosphere Fe_3O_4-poly-lactic acid for hyperthermia treatment, *MPI*, 19 (1), 68–83.

[7] Ebrahimi, M., 2016, A short review on ferrofluids surface modification by natural and biocompatible polymers, *Nanomed. J.*, 3 (3), 155–158.

[8] Wu, W., He, Q., and Jiang, C., 2008, Magnetic iron oxide nanoparticles: Synthesis and surface functionalization strategies, *Nanoscale Res. Lett.*, 3 (11), 397.

[9] Mahdavi, M., Ahmad, M.B., Haron, J., Namvar, F., Nadi, B., Rahman, M.Z., and Amin, J., 2013, Synthesis, surface modification and characterisation of biocompatible magnetic iron oxide nanoparticles for biomedical applications, *Molecules*, 18 (7), 7533–7548.

[10] Pylypchuk, I.V., Kołodyńska, D., Kozioł, M., and Gorbyk, P.P., 2016, Gd-DTPA adsorption on chitosan/magnetite nanocomposites, *Nanoscale Res. Lett.*, 11 (1), 168.

[11] Qu, H., Ma, H., Riviere, A., Zhou, W., and Connor, C.J.O., 2012, One-pot synthesis in polyamines for preparation of water-soluble magnetite nanoparticles with amine surface reactivity, *J. Mater. Chem.*, 22 (8), 3311–3313.

[12] Abouelmagd, S.A., Ku, Y.J., and Yeo, Y., 2015, Low molecular weight chitosan-coated polymeric nanoparticles for sustained and ph-sensitive delivery of paclitaxel, *J. Drug Targeting*, 23 (7-8), 725–735.

[13] Muflikhah, Rusdiarso, B., Putra, E.G.R., and Nuryono, 2017, Modification of silica coated on iron sand magnetic material with chitosan for adsorption of Au(III), *Indones. J. Chem.*, 17 (2), 264–273.

[14] Yao, C., Zhang, L., Wang, J., He, Y., Xin, J., Wang, S., Xu, H., and Zhang, Z., 2016, Gold nanoparticle mediated phototherapy for cancer, *J. Nanomater.*, 2016, 5497136.

[15] Boyles, M.S.P., Kristl, T., Andosch, A., Zimmermann, M., Tran, N., Casals, E., Himly, M., Puntes, V., Huber, C.G., Lütz-Meindl, U., and Duschl, A., 2015, Chitosan functionalisation of gold nanoparticles encourages particle uptake and induces cytotoxicity and pro-inflammatory conditions in phagocytic cells, as well as enhancing particle interactions with serum components, *J. Nanobiotechnology*, 13 (1), 84.

[16] Chanda, N., Kan, P., Watkinson, L.D., Shukla, R., Zambre, A., Carmack, T.L., Engelbrecht, H., Lever, J.R., Katti, K., Fent, G.M., Casteel, S.W., Smith, C.J., Miller, W.H., Jurisson, S., Boote, E., Robertson, J.D., Cutler, C., Dobrovolskaia, M., Kannan, R., and Katti, K.V., 2010, Radioactive gold nanoparticles in cancer therapy: Therapeutic efficacy studies of Ga-^{198} AuNP nanoconstruct in prostate tumor–bearing mice, *Nanomed. Nanotechnol. Biol. Med.*, 6 (2), 201–209.

[17] Ritawidya, R., Pujiyanto, A., Setiawan, H., Ramli, M., and Kurniasih, D., 2012, Synthesis and characterization of poly(amidoamine) dendrimers encapsulated ^{198}Au nanoparticles, *At. Indones.*, 38 (3), 118–126.

[18] Hemalatha, T., Prabu, P., Gunadharini, D.N., and Gowthaman, M.K., 2018, Fabrication and characterization of dual acting oleyl chitosan functionalised iron oxide/gold hybrid nanoparticles for MRI and CT imaging, *Int. J. Biol. Macromol.*, 112, 250–257.

[19] Nasution, T.I., Asrosa, R., Nainggolan, I., Balyan, M., Indah, R., and Wahyudi, A., 2018, Sodium tripolyphosphate cross-linked chitosan based sensor for enhancing sensing properties towards acetone, *IOP Conf. Ser.: Mater. Sci. Eng.*, 309, 012083.

[20] Unsoy, G., Yalcin, S., Khodadust, R., Gunduz, G., and Gunduz, U., 2012, Synthesis optimization and characterization of chitosan-coated iron oxide nanoparticles produced for biomedical applications, *J. Nanopart. Res.*, 14 (11), 964.

[21] Parisien-La Salle, J.C., 2012, In-situ adsorption of gold(III) chloride on activated carbon under pressure oxidation-leaching conditions, *Thesis*, Mc Gill University.

[22] Zhao, M., Zhao, J., Huang, Z., Wang, S., and Zhang, L., 2019, One pot preparation of magnetic chitosan-cystamine composites for selective recovery of Au (III) from the aqueous solution, *Int. J. Biol. Macromol.*, 137, 721–731.

[23] Liu, X.L., Yang, X., Xin, H.Y., Tang, X.P., Weng, L.J., Han, Y.Y., and Geng, D., 2016, Ecofriendly fabrication of Au/Fe_3O_4-chitosan composites for catalytic reduction of methyl orange, *Dig. J. Nanomater. Biostruct.*, 11 (2), 337–348.

[24] Pham, X.N., Nguyen, T.P., Pham, T.N., Tran, T.T.N., and Tran, T.V.T., 2016, Synthesis and characterization of chitosan- coated magnetite nanoparticles and their application in curcumin drug delivery, *Adv. Nat. Sci.: Nanosci. Nanotechnol.*, 7 (4), 045010.

[25] Shirazi, H., Daneshpour, M., Kashanian, S., and Omidfar, K., 2015, Synthesis, characterization and in vitro biocompatibility study of Au/TMC/Fe_3O_4 nanocomposites as a promising, nontoxic system for biomedical applications, *Beilstein J. Nanotechno*l., 6, 1677–1689.

[26] Pestov, A., Nazirov, A., Modin, E., Mironenko, A., and Bratskaya, S., 2014, Mechanism of Au(III) reduction by chitosan: Comprehensive study with ^{13}C and ^{1}H NMR analysis of chitosan degradation products, *Carbohydr. Polym.*, 117, 70–77.

[27] Podrepšek, G.H., Knez, Ž., and Leitgeb, M., 2020, Development of chitosan functionalized magnetic nanoparticles with bioactive compounds, *Nanomaterials*, 10 (10), 1913.

The Atmospheric Corrosion of Structural Steel after Exposure in the Palm Oil Mill Industry Area of Aceh-Indonesia

Muhammad Zulfri[1,2], Nurdin Ali[1,3*], Husaini[1,3], Sri Mulyati[1,4], and Iskandar Hasanuddin[3]

[1]*Doctoral Program, School of Engineering, Program Pasca Sarjana, Universitas Syiah Kuala, Banda Aceh 23111, Indonesia*

[2]*Department of Mechanical Engineering, Universitas Samudra, Langsa, 24416, Indonesia*

[3]*Department of Mechanical & Industrial Engineering, Universitas Syiah Kuala, Banda Aceh 23111, Indonesia*

[4]*Department of Chemical Engineering, Universitas Syiah Kuala, Banda Aceh 23111, Indonesia*

* ***Corresponding author:***

email: nurdin.ali@unsyiah.ac.id

Received: January 1, 2021
Accepted: March 16, 2021

DOI: 10.22146/ijc.62769

Abstract: *The major cause of early failure in the infrastructures of the palm oil industry in Aceh, Indonesia has been discovered to be the corrosion caused by air pollution from exhaust fumes of the factory plants. Therefore, this research was conducted to analyze the effect of the atmospheric corrosion of the structural steel used in the palm oil mill industry. The five types of structural steel used as samples include strip, l-shape, round bar, plate, and SAPH 610 low carbon steel with a carbon content of 0.18%. These specimens were cleansed from dirt, scaled, and rubbed with sandpaper to achieve a grid of 600, later washed with fresh water and rinsed with alcohol, and subsequently exposed to the environment in PT ASN and PT AKTS palm oil mills for 12 months. Moreover, they were placed on a measuring tray for exposure and the corrosion rate was recorded once a month using the mass loss method in line with the ASTM G50. The results showed the steel construction with a round bar shape was more resistant to atmospheric corrosion and the remaining samples were also observed to be safe and relatively resistant based on their classification as being outstanding (< 1 mpy).*

Keywords: *structural steel; air pollution; weight loss; corrosion rate; atmospheric corrosion*

■ INTRODUCTION

Indonesia was reported to be the highest palm oil-producing country in the world in 2014 with a plantation area of approximately 10.6 million hectares (Mha) [1]. The province of Aceh had 393,270 hectares of palm plantation area in the year 2016 [2]. The growth of oil palm plantations in Aceh provided a positive impact on the surrounding environment in the form of employment but also led to environmental pollution due to the diffusion of exhaust fumes into the atmosphere as a result of industrial activities. The fumes from the palm oil mill industry contain approximately 45.5 mg/Nm^3 of hydrogen sulfide gas [3-4] that can cause atmospheric corrosion.

Industrial fumes have also been proven to decrease the quality of building materials due to the direct and indirect effects of chemical reactions [5-7]. This is observed in the reduction of strength, mass, or aesthetics of metal structures which can further cause a gradual decrease in the mass of the metal material [8-9]. Moreover, thinning of the metal surface caused by corrosion is also the main reason for the premature damage of infrastructures [6,10].

Previous studies have been conducted on the carbon steel corrosion in recycled sour water of 3.5% NaCl using the Inductively Coupled Plasma-Mass Spectrometry (ICP-MS) method dipped in different NaCl solutions [11]. The results showed the corrosion rate decreased when the carbon steel was soaked in recycled sour water due to the passivation effect of the corrosion product [12]. Meanwhile, the NaCl concentration was observed to have a significant effect on the corrosion rate in all the variations of the solution [13-14]. Similar research was conducted [15] on

aluminum matrix composite material AlSi10Mg and Silicon Carbide (SiC) at different variations. The results showed the highest corrosion rate was in the materials dipped in HCl solution with PH 1 while the addition of Silicon Carbide (SiC) was able to reduce the corrosion rate in the aluminum material.

The effect of atmospheric corrosion in the palm oil mill environment was previously researched by Priyotomo et al., and Zulfri et al. [16-17] by determining the corrosion rate of five types of construction steel, classified < 1 mpy [18]. Furthermore, de la Fuente et al. [19] observed carbon steel corrosion under different types of atmosphere such as the industrial, urban, rural, and marine atmosphere [20]. Results showed that marine and industrial atmospheres had significantly worse conditions compared to urban and rural atmospheric conditions [21]. Ridha et al. [22] focused on the atmospheric corrosion mapping of structural metals in the Tsunami area of Aceh in the year 2004 and found a relatively fine resistance for all structural steel exposed in the area which was classified in the outstanding category (< 1 mpy). Furthermore, Castaño et al. [23] evaluated corrosion to determine the effect of the total chloride ion and SO_2 in line with the wet period of different types of atmospheric conditions using X-ray diffraction (XRD) and scanning electron microscopy-energy dispersive X-ray spectroscopy (SEM-EDS) analysis and found the most aggressive atmospheric corrosion to be based on the chloride content in the air.

The content of active substances in the air such as carbon monoxide (CO), NO_x, SO_x, and H_2S obtained from the processing of fresh oil palm fruit bunches through complex chemical reactions has been discovered to be the cause of atmospheric corrosion in the palm oil mill industry [24]. This means there is a need to study the atmospheric corrosion of structural steel infrastructure at the palm oil mill industry in Aceh province.

This research was, therefore, conducted to assess the effect of atmospheric corrosion on different shapes of construction steel that are used in the palm oil mill industry located on the southwest coast of Aceh province. The study was focused on two different locations, PT Agro Sinergi Nusantara (PT ASN), Bates Puteh, Aceh Jaya, and PT Astra Karya Tanah Subur (PT AKTS), West Aceh.

■ EXPERIMENTAL SECTION

Materials

This research used five types of structural steel namely strip, l-shape, round bar, plate, and SAPH 610 low carbon steel with a carbon content of 0.18% as shown in Fig. 1. The mechanical properties and chemical composition of the samples are presented in Tables 1 and 2.

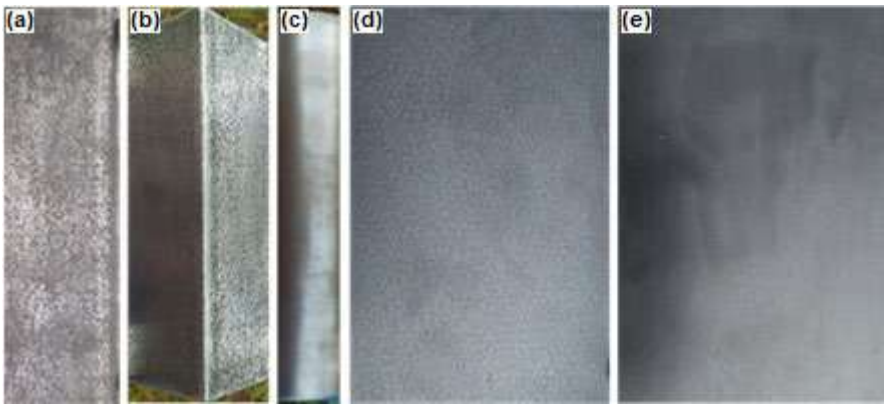

Fig 1. Test Specimen (a) Strip, (b) L-shape, (c) Round bar, (d) Plate, (e) SAPH 610 Low carbon steel

Table 1. Mechanical properties of the samples [14]

Yield Strength (MPa)	Tensile Strength (MPa)	Elongation (%)	Young Modulus (GPa)
356	496.5	22.68	187.8

Table 2. Chemical composition of the samples [14]

C	Si	Mn	P	S	Ni	Al	Fe
0.18	0.19	0.44	0.005	0.017	0.037	0.023	Balance

Procedure

Sample preparation and exposure

A total of 30 samples were used, divided into 2 groups of treatment, and each was exposed to an atmospheric environment near PT Agro Sinergi Nusantara (PT ASN) and Astra Karya Tanah Subur (PT AKTS). Each of the specimens of the materials in the research area had 6 coupons and their sizes were in line with the ASTM G 50 standard [25] as shown in Table 3.

The samples were sectioned and subtracted sequentially using silicon carbide abrasive paper with grit from 180 to 600. They were washed, cleansed with ethyl alcohol, and dried before initially weighed to a precision of 3 decimal places after which an immersion test was conducted to assess the weight loss. The samples were exposed in two locations, PT ASN and PT AKTS, and measurements were obtained monthly for a total of 12 months. In addition to the previous objectives, the corrosion rate of the samples due to weight loss during the immersion test was also analyzed. The test rack for the sample exposure is shown in Fig. 2.

Weight loss measurement

A quantitative analysis method was applied to determine weight loss and calculate the corrosion rate of the samples. This involved the total exposure of the coupon samples to the atmospheric conditions of PT Agro Sinergi Nusantara (PT ASN) and Astra Karya Tanah Subur (PT AKTS) after which the weight loss was measured as a function of exposure time during and after cleaning from 1 to 12 months according to ASTM G50 [25]. The cumulative weight loss data were arranged in the form of a matrix while the logarithmic form of the graph was constructed to elaborate the relationship between weight loss and immersion time for the designed location. Consequently, the corrosion rate was calculated using Eq. (1) [6-7].

$$\text{Corrosion Rate}(CR) = K\frac{W}{(A \times t \times \rho)} \quad (1)$$

where K is the conversion constant for corrosion rate unit, W is the mass loss in grams, A is the surface area in cm^2, t is the exposure period in an hour, and ρ is the density in g/cm^3. Meanwhile, the cross-sectional area was calculated using the following Eq. (2).

$$A = 2\left[(l \times w) + (w \times h) + (h \times l)\right] \quad (2)$$

Fig 2. Test specimens on a test rack with samples exposure

Table 3. Numbers and dimensions of specimens used

No.	Specimens	Size (mm)				Number of samples
		L	W	T	D	
1	Strip	150	50	4	-	6
2	L-shape	150	100	3	-	6
3	Round bar	150	-	-	22	6
4	Plate	150	100	4	-	6
5	Sheet	150	100	4	-	6
Total samples						30

The relative corrosion resistance was determined in Table 4 through the use of the corrosion rate obtained from Eq. (1).

■ RESULTS AND DISCUSSION

The results of the measurements of the 5 types of construction steel metals used as the atmospheric corrosion test specimens are presented in the form of graphs of corrosion rates and morphological tests with Scanning Electron Microscope to determine the formation of corrosion based on the experiments that were conducted for 12 months.

Corrosion Rate

The corrosion rate chart was constructed on 5 types of construction metal steel in the oil palm industry. Regarding PT ASN, after exposure during 12 months of investigation, the results show that the chart had a fluctuating trend regarding corrosion and also tended to be influenced by rainfall around the area. The highest corrosion rate was found at 0.56 mpy by the strip construction metal steel in the sixth month of exposure, while the lowest corrosion rate was obtained by the round bar steel at about 0.05 mpy.

The strip steel was observed to have the highest average corrosion rate except in the twelfth month where it was surpassed by the plate steel with a corrosion rate of 0.18 mpy as presented in Fig. 3. It was also discovered that the round bar shape and low carbon steel from SAPH 610 were more resistant to atmospheric corrosion than the strip, l-shape, or plate shape steel in PT ASN palm oil mill. which was associated with the higher Cu content compared to the carbon element [14].

The corrosion rate chart in PT AKTS had a similar trend with PT ASN but an increment was observed in line with an increment in the rainfall. The highest value of approximately 0.58 mpy was recorded for strip steel in the fourth month, September, with the rainfall estimated to be 105 mm, while the lowest corrosion rate of 0.04 mpy, was obtained by the round bar steel in the

Table 4. Relative corrosion resistance based on corrosion rate [18]

Relative Corrosion Resistance	Approximate Metric Equivalent				
	mpy	mm/year	μm/year	nm/year	pm/sec
Outstanding	< 1	< 0.02	< 25	< 2	< 1
Excellent	1–5	0.02–0.1	25–100	2–10	1–5
Good	5–20	0.1–0.5	100–500	10–50	5–20
Fair	20–50	0.5–1	500–1000	50–100	20–50
Poor	50–200	1–5	1000–5000	150–500	50–200
Unacceptable	200+	5+	5000+	500+	200+

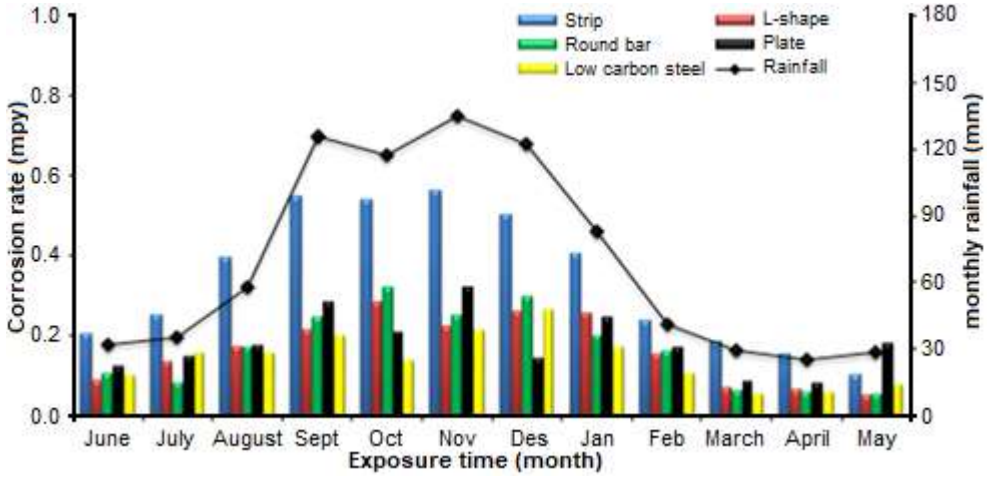

Fig 3. The corrosion rate of construction steel at PT ASN

twelfth month, May, in which the rainfall was recorded to have reduced drastically to 31 mm.

The lowest corrosion rate in PT AKTS was found for the round bar steel followed by the plate steel as illustrated in Fig. 4. This was attributed to the higher proportion of Cu in the round bar and a low percentage of carbon in the plate.

Morphology of the Corrosion Product

The shape of each of the 5 specimens used was evaluated through pre to post sterilization of the products to determine the metal defects or damages due to atmospheric corrosion.

Strip steel

The results of the morphological test conducted on the steel with the strip profile from different locations of the palm oil mill are presented in Fig. 5. The pre and post sterilization conditions of the test specimens from the corrosion products were measured at 200 μm magnification. The samples from the PT ASN area showed the degradation of pitting corrosion in the form of a black color ferrite and pearlite or a black profile on the steel surface. The changes also occurred in the texture of the steel due to the oxidation process during corrosion. The samples in PT AKTS had finer texture on the strip steel shape compared to those in PT ASN with

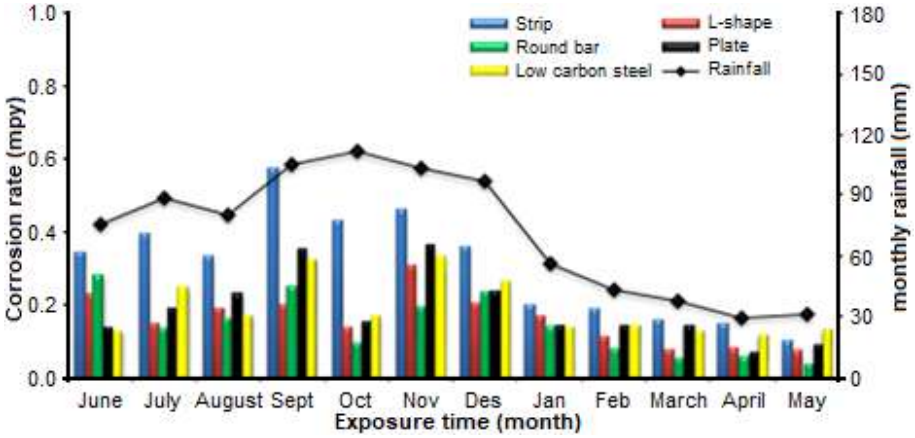

Fig 4. The corrosion rate of construction steel at PT AKTS

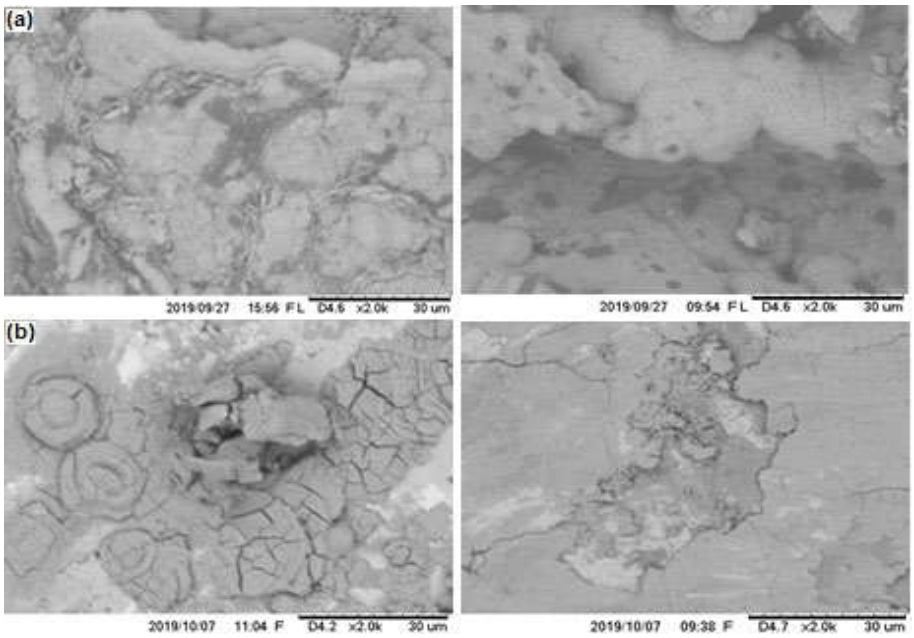

Fig 5. Morphology test for strip steel at PT ASN and PT AKTS using SEM: (a) Pre sterilization, (b) Post sterilization

a similar shape.

The texture of the strip steel specimens in PT ASN showed significant damages and cracks after post-sterilization, thereby, indicating the physical defects due to the atmospheric corrosion while the damage in the specimen from PT AKTS was not too severe, however the surface center was observed to have pitting corrosion.

In conclusion, the strip steel in PT AKTS did not have significant damage on the texture of the surface, however potentially damaging pitting corrosion was observed particularly in the center area of the steel.

L-shape steel

The corrosion degradation of the L-shape steel after the sterilization process was observed to be significantly different in the two locations. The corrosion in PT ASN was in the form of white ferrite granules while the sample in PT AKTS had a black color. The damages caused to the samples are shown in Fig. 6. The samples in PT ASN were partially damaged due to pitting corrosion with cavities texture or sweet or general corrosion which is usually in the form of holes with no sediment [26]. The corrosion was caused by aggressive chemical elements such as chloride with damaging effects on the passive layer or oxide as well as the presence of CO_2, followed by the formation of carbonic acid which lowers the pH. These chemical reactions are presented as $CO_2 + H_2O \leftrightarrow H_2CO_3$ (carbonic acid) and $Fe + H_2CO_3 \rightarrow FeCO_3 + H_2$ [20]. The corrosion formed in PTAKTS tended to be uniform due to the distribution of the chemical reactions or electrochemistry on the metal steel surface, which caused thinning and formation of fine grains as shown in Fig. 6 (b) for the post-sterilization of test specimens from the corrosion products [27].

Round bar steel

The corrosion degradation in the cylindrical steel before the products were cleaned is presented in Fig. 7 and the results showed that it is similar to the cases of the L-shape steel as indicated in Fig. 6. The corrosion profile in PT ASN was ferrite granules while PT AKTS had perlite granules captured at 20 μm by the morphology test as shown in Fig. 7.

The corrosion products were cleaned after the test and the results showed that the metal damages in the two locations were caused by pitting corrosion with the damage in PT ASN being more severe than PT AKTS. It was concluded that the round bar steel was more resistant towards corrosion in comparison with the previous two types of steel.

Plate steel

The corrosion products from the plate steel were indicated by the presence of lumps on the surface of the metal for the samples at PT ASN and PT AKTS, as shown

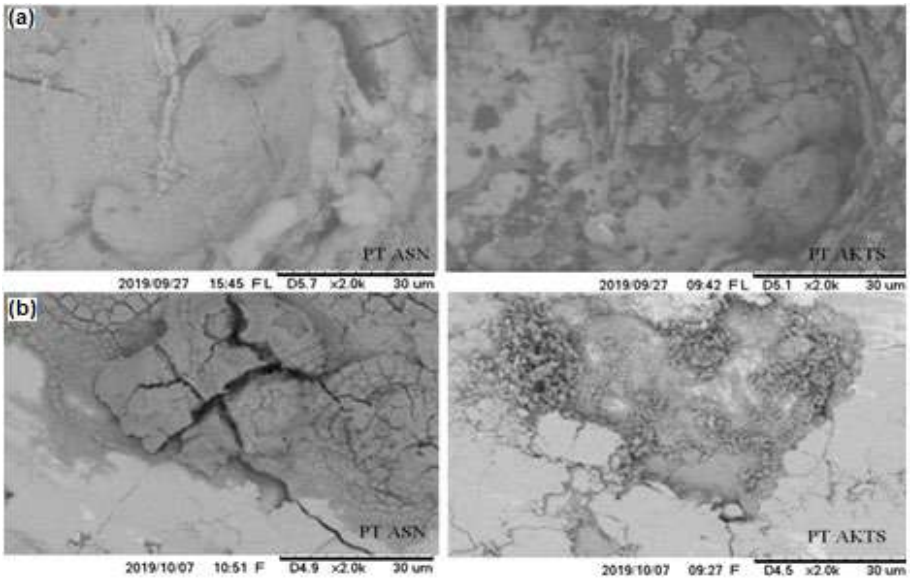

Fig 6. Morphology test for L-shape steel at PT ASN and PT AKTS using SEM: (a) Pre sterilization (b) Post sterilization

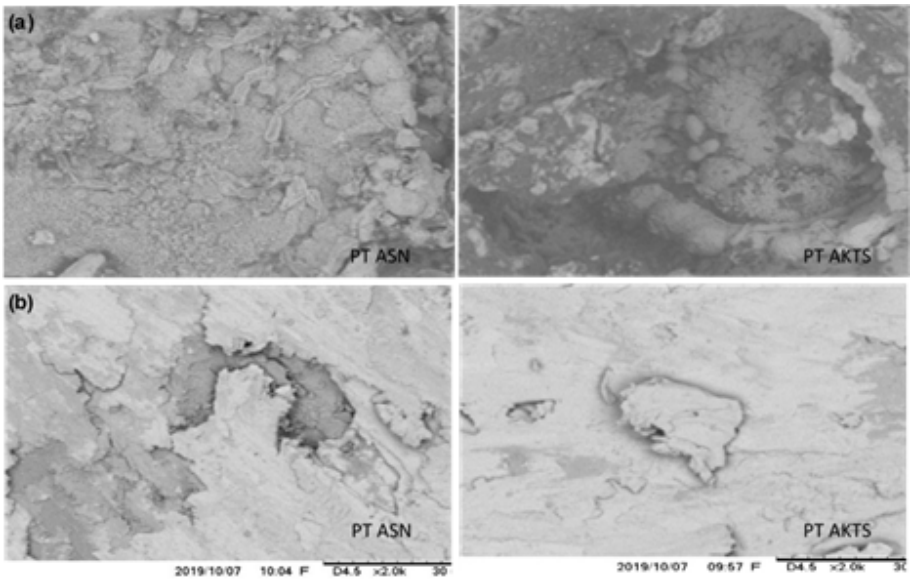

Fig 7. Morphology test for round bar steel at PT ASN & PT AKTS using SEM: (a) Pre sterilization (b) Post sterilization

in Fig. 8. The corrosion was observed to be uniform due to the electrochemical reaction from the surrounding atmosphere of the oil palm industry as well as the reaction of the CO_2 content.

The uniform corrosion had both ferrite and perlite granules formed around the surface of the plate steel in both areas, however, the sample at PT ASN had smaller structures compared to the sample at PT AKTS. In addition, ferrite particles were observed to be partially formed by the granules in PT AKTS. Moreover, post sterilization results showed more severe damages and massive structural cracks in the entire surface of the metal in PT AKTS, while to the metal in PT ASN had finer textural damage with an outside rift.

Sheet steel

The sheet-shaped steel also had uniform corrosion as shown in Fig. 9 which is common with sheet steel due to its massive surface. Moreover, the corrosion products in PT ASN tended to be perlite granules with high uniformity while those in PT AKTS had more equal ferrite and perlite granules.

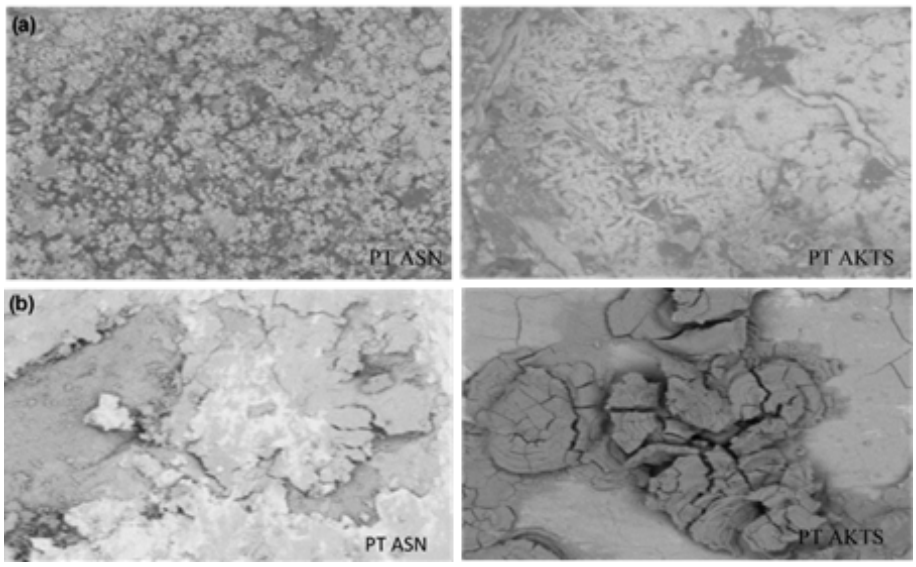

Fig 8. Morphology test for plate steel at PT ASN & PT AKTS using SEM: (a) Pre sterilization (b) Post sterilization

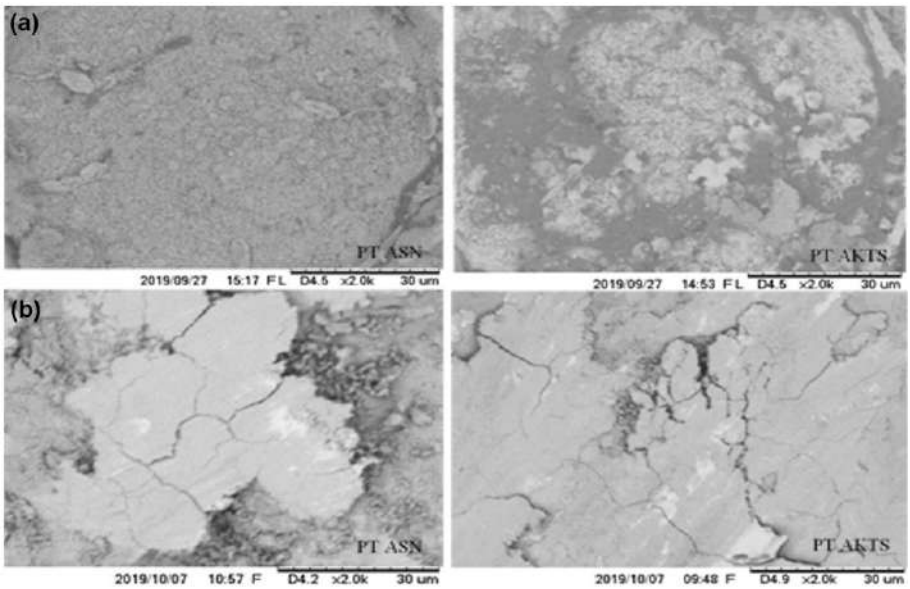

Fig 9. Morphology images of sheet steel at PT ASN & PT AKTS using SEM: (a) Pre sterilization (b) Post sterilization

The morphology test was also conducted after post sterilization to evaluate the surface structure and the cracks on low carbon steel. The results show that the metals in PT ASN were found to be in poorer conditions compared to those in PT AKTS, which was majorly due to the higher rainfall recorded in PT ASN. The scientific cases are shown in Fig. 4 and 5.

X-Ray Diffraction Analysis

The morphological test on the pre-and post-sterilized samples using SEM was not able to comprehensively explain the corrosion products in the 5 specimens at the two research locations. Therefore, XRD (X-Ray Diffraction) analysis was conducted to see the compound formed by the corrosion process.

The data were collected when the x-ray tube was measured using a voltage of 40 kA and a current of 30 mA and the results were in the form of a spectrum which states the intensity or counts as a function of the diffraction angle 2θ (°), as shown in Fig. 10.

The results for PT ASN showed that the low carbon and plate steel metals had higher peaks compared to the others as shown in Fig. 10(a). The highest intensity of the low carbon steel was 650 at an angle of 42° while the plate steel reached 646 at an angle of 37.5°. These peaks indicate the occurrence of corrosion in the test specimens.

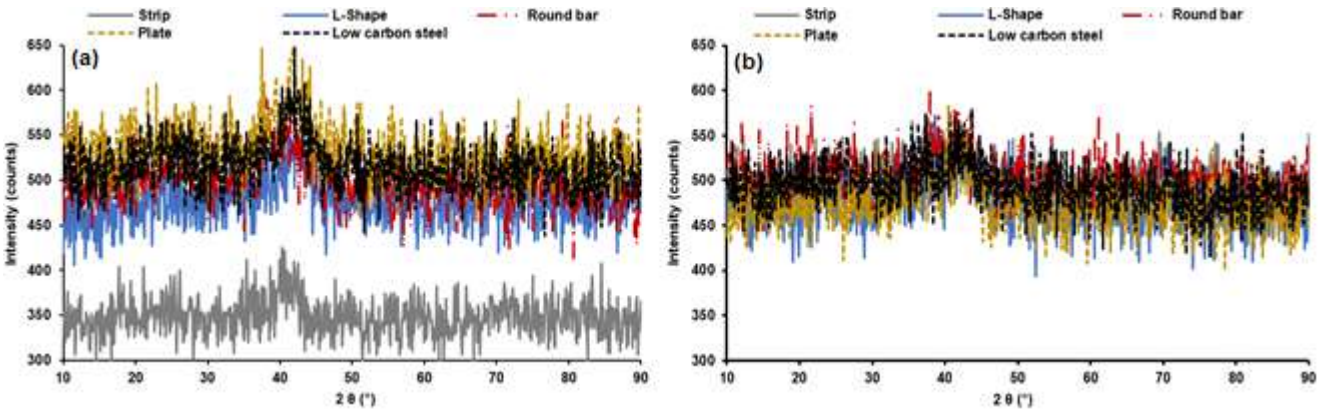

Fig 10. The XRD results of the five types of construction steel metals in the two research locations (a) PT ASN (b) PT AKTS

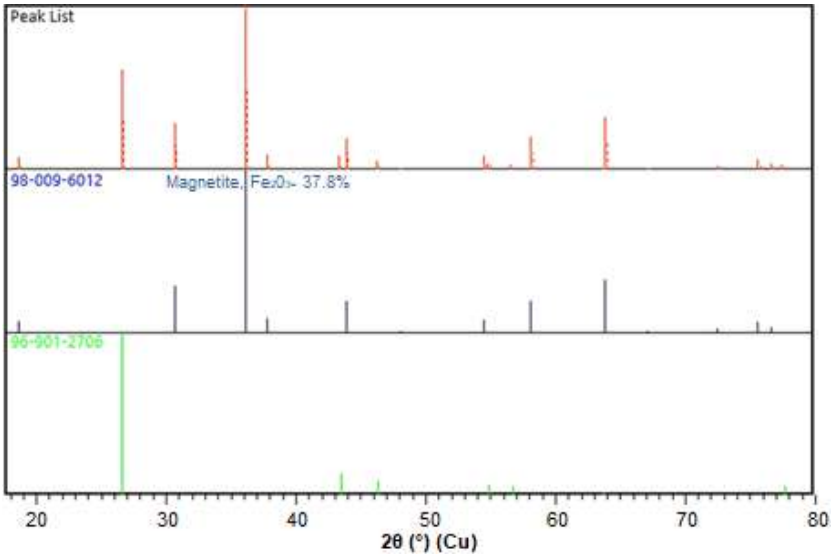

Fig 11. Proving the formation of magnetite (Fe_2O_3) for strip steel with 37.8%

Further analysis was also conducted using JCPDS software and the findings showed a solid corrosion compound of iron oxide including magnetite and Fe_2O_3 at an angle of 2θ = 32.5°, 42°, and 67.8° for carbon steel and 2θ = 23.5° and 37.5° for strip steel. Meanwhile, the intensity of the other types of steel was reported to be smaller and less striking when compared to the low carbon and strip steel [16]. For PT AKTS, the highest peak was recorded by the cylindrical steel as shown in Fig. 10(b) with the intensity recorded to have reached 598 at 37.9° followed by the low carbon steel with 566 at 41.9° and strip steel with 364 at 40.1°. An example of the magnetite (Fe_2O_3) formed on the strip shape steel is presented in Fig. 11.

The high peaks at PT ASN are due to the reaction of the corrosion products such as iron oxide (FeO, Fe_2O_3, and Fe_3O_4), goethite (α-FeOOH), and lepidocrocite (γ-FeOOH) [28-30].

■ CONCLUSION

The analysis of five different construction steel metals in two research locations showed that strip plate steel had the highest corrosion rates of 0.56 on the sixth month and 0.57 mpy on the fourth month of evaluation after the samples were exposed to the atmospheric conditions of PT ASN and PT AKTS areas, respectively. Meanwhile, the lowest corrosion rate was recorded for the round bar steel at a value of 0.04 mpy in PT AKTS and 0.05 mpy in the PT ASN area during the twelfth month. Moreover, both pitting and uniform corrosions were discovered in the products and the variations of the steel metal forms were found to be most affected by the speed of corrosion rate which tended to be higher for the strip plate steel and conventional plate. The results after 1 (one) year of exposure showed that the cylindrical steel was more resistant to atmospheric corrosion and damage while the others tended to be safe, relatively resistant, and classified to be outstanding materials since their corrosion rates were < 1 mpy.

■ ACKNOWLEDGMENTS

The authors express their gratitude to the Directorate of Research and Community Service Kemenristek Dikti Contract No.136/UN54.6/LT/2018 for funding this research through the Higher Education Collaboration Research scheme of 2018. The authors also appreciate Dr.-Eng. Deni Shidqi Khaeruddin of the Indonesian Institute of Sciences, Serpong, Banten 15314, Indonesia for analyzing the XRD data.

■ AUTHOR CONTRIBUTIONS

MZ and NA designed, experimented, and wrote the manuscript, H and SM supervised the experiment and article writing while IH proofread the manuscript. All authors agreed to the final version of this manuscript.

■ REFERENCES

[1] Khatiwada, D., Palmén, C., and Silveira, S., 2021, Evaluating the palm oil demand in Indonesia:

production trends, yields, and emerging issues, *Biofuels*, 12 (2), 135–147.

[2] Hanafiah, J., 2016, *Palm oil expands in Aceh*, Mongabay Series: Indonesian Forests, Indonesian Palm Oil, Leuser Ecosystem, https://news.mongabay.com/2016/01/palm-oil-expands-in-aceh/.

[3] Syahza, A., 2019, The potential of environmental impact as a result of the development of palm oil plantation, *Manage. Environ. Qual.*, 30 (5), 1072–1094.

[4] Badrun, Y., 2010, Emisi udara industry pengolahan kelapa sawit di kabupaten Rokan Hilir, *Photon: Jurnal Sain Dan Kesehatan*, 1 (1), 23–29.

[5] Roberge, P.R., 2000, Handbook of Corrosion Engineering, 2nd Ed, McGraw-Hill, New York.

[6] Revie, R.W., and Uhlig H.H., 2008, *Corrosion and Corrosion Control: An Introduction to Corrosion Science and Engineering*, 4th Ed., John Wiley & Sons, Inc., Canada.

[7] Ali, N., Fulazzaky, M.A., Mustapa, M.S., Ghazali, M.I., Ridha, M., and Sujitno, T., 2014, Assessment of fatigue and corrosion fatigue behaviours of the nitrogen ion implanted Cp Ti, *Int. J. Fatigue*, 61, 184–190.

[8] Ali, N., Putra, T.E., Iskandar, V.Z., and Ramli, M., 2020, A simple empirical model for predicting weight loss of mild steel due to corrosion in NaCl solution, *Int. J. Automot. Mech. Eng.*, 17 (1), 7784–7792.

[9] Martinez, C., Briones, F., Villarroel, M., and Vera, R., 2018, Effect of atmospheric corrosion on the mechanical properties of SAE 1020 structural steel, *Materials*, 11 (4), 591.

[10] Ghahari, M., Rashid-Nadimi, S., and Bemana, H., 2019, Metal-air desalination battery: Concurrent energy generation and water desalination, *J. Power Sources*, 412, 197–203.

[11] Ismail. A., Mahari, S., Shamsuddin, F., Hasan, N., and Ramli N., 2019, Evaluation of corrosion product formed on carbon steel in recycled sour water of overhead system, *Int. J. Integr. Eng.*, 11 (7), 95–101.

[12] Ismail, A., and Adan, N.H., 2014, Effect of Oxygen Concentration on Corrosion Rate of Carbon Steel in Seawater, *Am. J. Eng. Res.*, 03 (1), 64–67.

[13] Möller, H., Boshoff, E.T., and Froneman, H., 2006, The corrosion behaviour of a low carbon steel in natural and synthetic seawaters, *J. South. Afr. Inst. Min. Metall.*, 106 (8), 585–592.

[14] Ali, N., Putra, T.E., Husaini, Iskandar, V.Z., and Thalib, S., 2019, Corrosion rate of mild steel for construction materials in various NaCl concentrations, *IOP Conf. Ser.: Mater. Sci. Eng.*, 536, 012015.

[15] Tjahjanti, P.H., Darminto, Nugroho, W.H., and Ganda, A.N.F., 2019, Study of corrosion penetration rate on composite materials EN AC-43100 (AlSi10Mg (b)) + SiC*, *Int. J. Integr. Eng.*, 11 (6), 1–9.

[16] Priyotomo, G., Nuraini, L., Prifiharni, S., Royani, A., Sundjono, Gunawan, H., and Zheng, M., 2020, Atmospheric corrosion behavior of carbon steel and galvanized steel after exposure in Eretan and Ciwaringin, West Java Province, Indonesia, *Indones. J. Chem.*, 20 (5), 1032–1043.

[17] Zulfri, M., Ali, N., Husaini, Fonna, S., Huzni, S., Mulyati, S., and Cut, B., 2019, Atmospheric corrosion assessment of structural steel exposed in the environment of palm oil processing (PKS) industry around coastal zone, *IOP Conf. Ser.: Mater. Sci. Eng.*, 536, 012016.

[18] Marzorati, S., Verotta, L., and Trasatti, S.P., 2019, Green Corrosion Inhibitors from Natural Sources and Biomass Wastes, *Molecules*, 24 (1), 48.

[19] De la Fuente, D., Alcántara, J., Chico B., Díaz, I., Jiménez, J.A., and Morcillo, M., 2016 Characterisation of rust surfaces formed on mild steel exposed to marine atmospheres using XRD and SEM/Micro-Raman techniques, *Corros. Sci.*, 110, 253–264.

[20] Nuraini, L., Prifiharni, S., Priyotomo, G., Sundjono, Gunawan, H., and Purawiardi, I., 2018, Atmospheric corrosion performance of different steels in early exposure in the coastal area region West Java, Indonesia, *AIP Conf. Proc.*, 1964, 020040.

[21] Shafiei, E., Zeinali, M., Nasiri, A., Charroostaei, H., and Gholamalian, M.A., 2014, A brief review on the atmospheric corrosion of mild steel in Iran, *Cogent Eng.*, 1 (1), 990751.

[22] Ridha, M., Fonna, S., Huzni, S., Supardi, J., and Ariffin, A.K., 2013, Atmospheric corrosion of structural steels exposed in the 2004 tsunami-affected areas of Aceh, *Int. J. Automot. Mech. Eng.*, 7, 1014–1022.

[23] Castaño, J.G., Botero, C.A., Restrepo, A.H., Agudelo, E.A., Correa, E., and Echeverría, F., 2010, Atmospheric corrosion of carbon steel in Colombia, *Corros. Sci.*, 52 (1), 216–223.

[24] Dugstad, A., Halseid, M., and Morland, B., 2013, Effect of SO_2 and NO_2 on corrosion and solid formation in dense phase CO_2 pipelines, *Energy Procedia*, 37, 2877–2887.

[25] ASTM G50-10, 2010, *Standard Practice for Conducting Atmospheric Corrosion Tests on Metal*, ASTM International, Barr Harbor Drive, West Conshohocken, PA, 1–15.

[26] Antunes, R.A., Ichikawa, R.U., Martinez, L.G., and Costa, I., 2014, Characterization of corrosion products on carbon steel exposed to natural weathering and to accelerated corrosion tests, *Int. J. Corros.*, 2014, 419570.

[27] Pessu, F.M, Barker, R., and Neville A., 2016, Understanding pitting corrosion behavior of X-65 carbon steel in CO_2-saturated environments: The temperature effect, *Corrosion*, 72 (1), 78–94.

[28] Montoya, P., Marín, T., Echavarría, A., and Calderón, J.A., 2013, Influence of anion and pH on the electrochemical Co-deposition and transformation of iron oxy-hydroxide, *Int. J. Electrochem. Sci.*, 8, 12566–12579.

[29] Morcillo, M., de la Fuente, D., Díaz, I., and Cano, H., 2011, Atmospheric corrosion of mild steel, *Rev. Metal.*, 47 (5), 426–444.

[30] Thalib, S., Ikhsan, M., Fonna, S., Huzni, S., and Syahrir, 2018, Identification of corrosion product on medium carbon steel under the exposure of Banda Aceh's atmosphere, *IOP Conf. Ser.: Mater. Sci. Eng.*, 352, 012004.

Preparation and Spectroscopic Studies of Cadmium(II), Zinc(II),Mercury(II) and Vanadium(IV) Chelates Azo Ligand Derived from 4-Methyl-7-hydroxycoumarin

Bayader Fathil Abass, Taghreed Mohy Al-Deen Musa, and Mahmoud Najim Abid Al-Jibouri*

Department of Chemistry, College of Science, Mustansiriyah University, Baghdad, Iraq

* ***Corresponding author:***

tel: +964-7713460946
email: mahmou_inor71@uomustansiriyah.edu.iq

Received: January 11, 2021
Accepted: May 18, 2021

DOI: 10.22146/ijc.63032

Abstract: *The present paper demonstrates the synthesis and characterization of some transition elements complexes derived from (E)-7-hydroxy-6-((4-methoxyphenyl)diazenyl)-4-methyl-2H-chromen-2-one. The ligand was prepared in the general route of azo dyes by coupling the diazonium salt of 4-methoxyaniline with 4-methyl-7-hydroxycoumarin in sodium hydroxide 10% (w/v) solution. The azo ligand was identified on the basis of elemental analyses, MS, H-NMR and FT-IR spectra. The products of complexes with the new azo dye were isolated by the direct reactions of the metal chlorides of cadmium(II), zinc(II), vanadium(IV) and mercury(II) ions with the alkaline solution of free ligand to afford the colored in the following formulas, complexes[ML_2]$2H_2O$ formula, M=Cd(II) and Zn(II). However the vanadium(IV) complex was square pyramid in [VOL_2]$SO_4 2H_2O$ chemical formula. As well as the tetrahedral environment was suggested for mercury(II) complex in formula [HgL_2]. The time and mole ratio factors were studied to obtain the optimized conditions of metal complexes formations and the observed data investigated the deprotonation of the azo-dye at pH to range (7–7.5) with 30 min as time of reaction to get pure metal chelates. The TG-DSC study confirmed the thermal stability of complexes at a wide range of average heating in inert gas of analysis and the results observed from loss weight percent investigated the proposed structures of the prepared metal complexes.*

Keywords: *azo ligands; metal complexes of coumarin; spectroscopic studies*

■ INTRODUCTION

The major branch of coordination chemistry has been partially allocated with the azo dyes of 4-hydroxycoumarine and their derivatives [1-2]. The inorganic complexes of chromen-2-one rings mainly could possess applications in catalysis, manufacturing of dyes and pharmaceutical drugs [3-5]. The pentagonal and hexagonal coordination complexes of dyes involving immine and hydroxyl groups have shown a wide range of applications in the diodes and solar cells fields [6-7]. The common coordination compounds derived from azo dyes of chromen-2-one have interested in wide spectrum of applications in the emission studies like fluorescence and phosphorescence [8-10].

Recently the researchers have encouraged enhancing the electronic and geometrical features of complexes of azo dyes that they would have exhibited nonlinear optical elements and printing systems [11-14]. All the above mentioned about the development of coumarin azo dyes with their chelation ability afford us to prepare and characterize new azo dye complexes of Zn(II), Cd(II), V(IV) and Hg(II) derived from (*E*)-7-hydroxy-6-((4-methoxyphenyl)diazenyl)-4-methyl-2*H*-chromen-2-one.

■ EXPERIMENTAL SECTION

Materials

The starting 4-methoxyaniline and 4-methyl-7-hydroxycoumarin and 4-methoxyaniline were supplied

via Merck Company and the metal salts of $VOSO_4 \cdot 5H_2O$, $CdCl_2 \cdot 2H_2O$, $ZnCl_2$, $CdCl_2$ and $HgCl_2$ were supplied from Quaternary Group Merck Chemicals Companies and used as supplied without purification.

Instrumentation

The melting points temperature of the coumarin derivatives and metal complexes were determined on the Stuart melting point apparatus. The molecular weights of the ligand and some selected metal complexes were measured their mass spectra on a Shimadzu model GC MS QP 1000EX at college of science, Mustansiriyah University. The electronic spectra of ligand and its complexes in ethanol and DMSO solvents was determined with UV-1800 Shimadzu spectrometer apparatus. The nuclear magnetic resonance spectroscopy was carried out in *d6*-DMSO solvent on Bruker-500 MHz NMR spectrometer. The main features of vibration frequencies of azo dye ligand and its metal complexes were scanned on Shimadzu FT-IR spectroscopy in the range (4000–200) cm^{-1}. The pH of the solutions was checked using a Jenway 3020 pH meter. Furthermore, the percentages of metal ions were determined with GBC 933 model FAAS at Ministry of Industry, Ibn-Cina company, Baghdad, Iraq.

Procedure

Synthesis of azo ligand

The azo dye was synthesized according to the modified classical procedure established in literature, by dissolving (1.83 g, 0.01 mmol) from 4-methoxyaniline in hot distilled water (10 mL) then followed by an addition of 36% (v/v) HCl (5 mL). To this solution, a cooled aqueous solution of sodium nitrite (0.45 g, 5 mmol) was added by maintaining the temperature of the reaction at 0 °C. The formed diazonium salt was gradually added to an alkaline solution of 4-methyl-7-hydroxycoumarin (0.02 mol, 3.90 g) with stirring for 30 min, after that the resulting solution was neutralized to pH of about 6.5 by addition drops of 10% NaOH. The dark orange crude was then filtered, washed several times with water and ethanol, then dried. The re-crystallization from hot ethanol afforded dark orange crystals of azo dye ligand, L, Scheme (1).

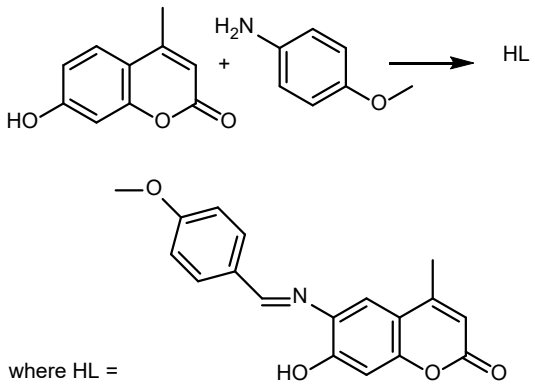

Scheme 1. Synthesis of azo dye, HL

Synthesis of metal complexes

The metal complexes were prepared by dissolving $ZnCl_2$ (10 mmol, 1.45 g) or $CdCl_2.2H_2O$ (1 mmol, 1.118 g) in (15 mL) hot water and ethanolic solution of (20 mmol, 1.44 g) of azo dye, L. The mixture was stirred on water bath for 1 h then red precipitates of ZnL and CdL complexes were separated and filtered off. The Hg(II) complex was prepared by mixing (10 mmol, 1.45 g) of azo dye in (15 mL) hot ethanol with (10 mmol, 0.272 g) in (10 mL) hot water with stirring on a water bath for 2 h, the white off separated precipitate was filtered of and dried in oven at 90 °C. However, the vanadium(IV) complex was isolated in its solid state from oxo-vanadium sulfate penta hydrate after adjusting the mole ratios 1:2 of (M:L) with respect to dissolving $VOSO_4 \cdot 5H_2O$ in (15 mL) hot water with (20 mmol, 1.45 g) of azo dye then refluxed the mixture for 2 h. The brown precipitate was filtered, dried in air then washed several times with hot ethanol and diethyl ether, Table 1.

■ RESULTS AND DISCUSSION

Physical Properties and Elemental Analyses

Table 1 list the main physical properties of ligand and its complexes and show the thermal stability of almost complexes through the elevated their decomposition points. All the complexes are colored and sparingly soluble in most organic solvents except DMSO and DMF. The micro-analyses (C.H.N.) confirm the suggested chemical formula for all complexes beside the structure of azo dye. The calculation of mole ratios was in good agreement of their formation procedure and

Table 1. Some physical properties and elemental analyses of Azo dye and its complexes

Compound	Molecular Weight (g/mol) Formula	Color	M.P. (°C)	%C Found (Calc.)	%H Found (Calc.)	%N Found (Calc.)	%M Found (Calc.)
HL	310.09 $C_{17}H_{14}N_2O_4$	Dark brown	178–180	65.00 (65.81)	4.22 (4.55)	8.88 (9.03)	--
ZnL	683.03 $C_{34}H_{26}ZnN_4O_8$	Red	> 288	57.90 (58.232)	3.49 (3.89)	10.11 (9.36)	7.99 (9.22)
CdL	732.22 $C_{34}H_{28}CdN_4O_{10}$	Orange	> 300	52.21 (53.33)	4.80 (3.90)	9.04 (10.01)	15.38 (16.22)
HgL	820.53 $C_{34}H_{26}HgN_4O_8$	Brown	277–279	55.22 (56.11)	3.22 (3.99)	10.80 (9.82)	
VOL	746.79 $C_{34}H_{30}N_4SO_{14}V$	Dark brown	> 295	55.33 (56.73)	5.33 (5.90)	12.60 (11.99)	15.44 (16.30)

stoichiometric and it is based on flame atomic absorption data. The flame atomic absorption spectroscopy for metal contents (M%) in the solid complexes are experimentally determined through standard addition method and the observed analyses are in good agreement with the calculated data confirming the structures of all the prepared complexes. However the molar conductivity measurements reveals that all complexes do not show electrolytic nature [15], except vanadium(IV) complex solution in DMF that exhibits conductivity motion due to the presence of sulfate counter ion in the structure.

Mass Spectra

The mass spectrum of azo-dye ligand showed peak at molecular ion *m/e* = 310 which indicates the unstable molecular weight of the expected $C_{17}H_{14}N_2O_4$ formula due to losing methoxy and methyl groups in the gas-phase of GC conditions for the MS spectra then confirms formation of the azo dye [13]. The peaks observed at around *m/e* = 116 and 89 would be resulted from cleavage of chromen ring and points of $–CH_3$ and –OH respectively [12]. As well as the mass spectrum of vanadium (II) complex shows weak intensity peak at 747 that is allocated to the molecular ion of complex in the gas phase [14,17].

NMR Spectra

The H and ^{13}C-NMR were displayed only for the azo dye with chemical shifts in (ppm) units and are relative to residual proton solvent signals. The spectrum of the ligand is in a good agreement with the number of protons and their assignments of nuclear spins of Ar-H and methyl protons. The ^{1}H-NMR spectrum of the ligand, Fig. 1 shows a singlet signal at δ (7.9–8.99) ppm corresponding to the –C=C–H of chromen ring. The peak showed at around δ (14.50) ppm was also recorded in the ligand spectrum, due to the –OH proton that is directly attached to C7 of chromen ring. The doublet of doublet peaks at around δ (12.45) ppm reflects mainly the spin coupling of aromatic protons adjacent to each other in aromatic substituted [12-13]. Furthermore, the aliphatic protons of $–CH_3$ groups attached at C-4 were resonated at around 4.43.

The ^{13}C-NMR spectrum of azo ligand showed multiple peaks at 75 ppm related to –CH3 aliphatic carbon atom and 96 ppm related to –C=OH moiety [12-13]. The peaks at 125–135 ppm may be related to resonance of aromatic carbon atoms while the deshielded –C-N=N– and –C=C– of coumarin may be assigned to effect of withdrawing groups and showed at 145–165 ppm, respectively. As well as the H-NMR spectrum of CdL complex displayed remarkable changes in some resonated aromatic protons and disappearance of –OH moiety. These data of NMR confirmed the coordination of Cd(II) ion with the HL azo dye through –C=N– and OH with deprotonation in the chelation reaction. As well as the deshielded protons of –HC=CH– of chromene ring and hydrated water molecules was download shifted due to the electron donation of the active site toward the empty orbitals of Cd(II) ion [16-17].

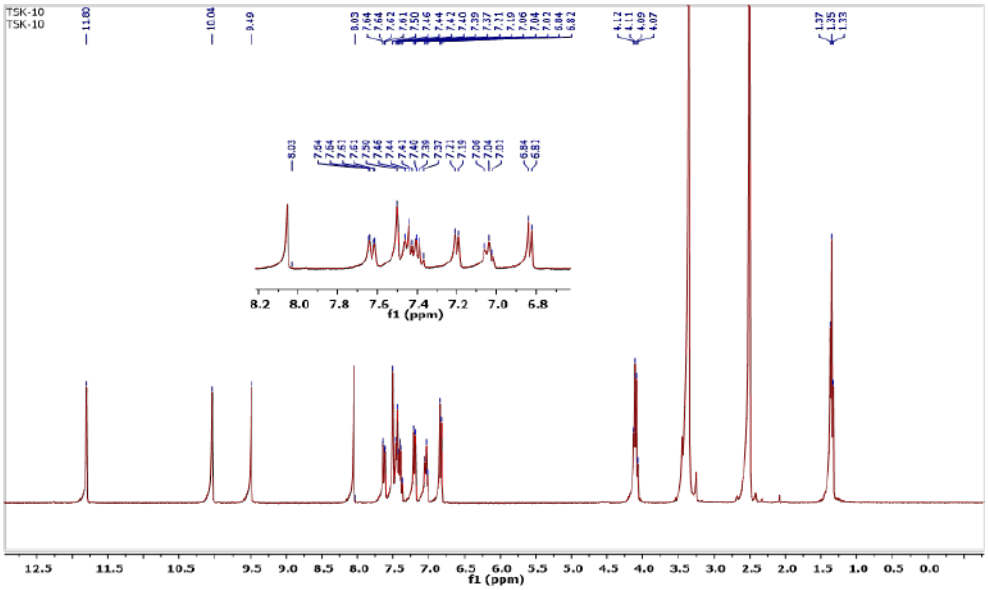

Fig 1. H NMR of azo ligand in DMSO-d_6 solvent

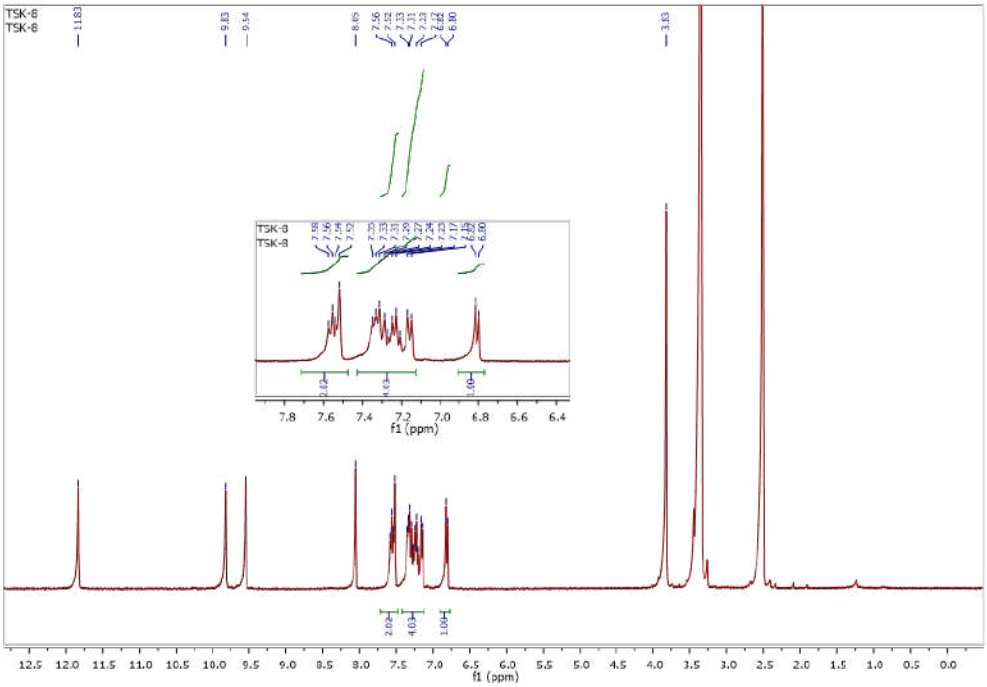

Fig 2. H-NMR of CdL complex in DMSO-d_6 solvent

IR Spectra of the Ligand and Complexes

The IR spectra of the synthesized complexes in CsI were compared with that of the azo dye. The spectra of the complexes showed the absorption bands characteristic of the ligand with some differences ascribed to the formation of respective ion associated, which showed the more characteristic infrared spectral bands of the free ligand and its complexes. The broad absorption at 3500 cm^{-1} is assigned to –OH of coumarin azo ligand. The strong band at 1651 is associated to –C=O of chromene ring while the strong band at 1623 cm^{-1} is associated with –CH=CH– of aromatic and - rings respectively [12,15] as given in Fig. 3. The appearance of new band at 1477 cm^{-1} confirms the formation of azo –N=N– moiety. The remarkable changes

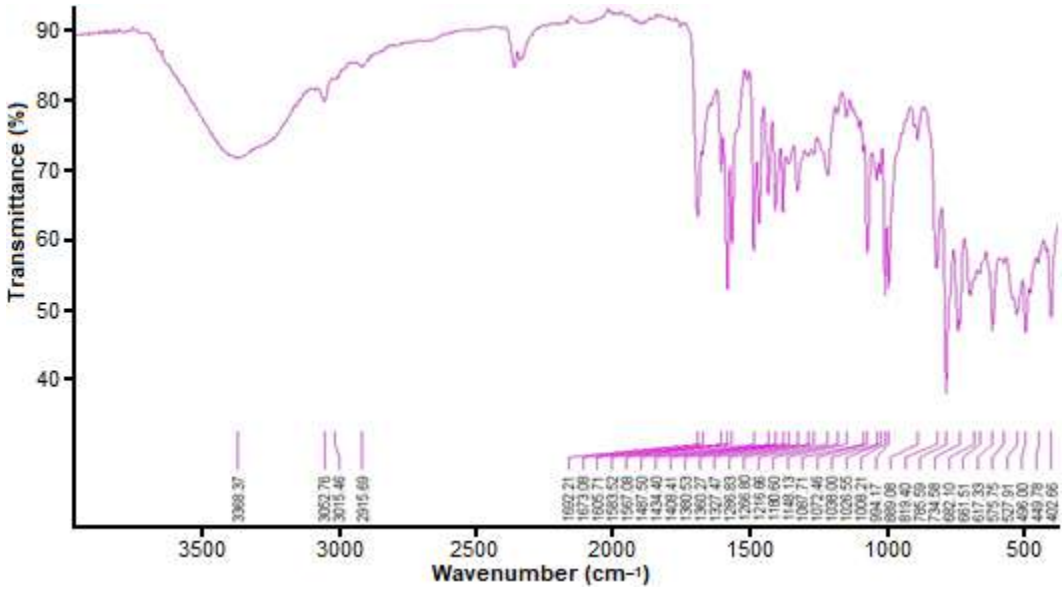

Fig 3. FT-IR spectrum of azo dye, HL in KBr disc

on –N=N– to lower frequencies at 1450–1433 cm^{-1} confirm the coordination of ligand via nitrogen atom with M–N formation beside the –C=O shift and supports the bi dentate neutral ligand behavior as shown in Fig. 3. The vanadyl complex in Fig. 4 exhibits new band at 950.633 and 590 cm^{-1} confirming V=O and V–N bands [14-17].

Electronic Spectra and Magnetic Susceptibility

The azo ligand showed one strong absorption around 379 nm which was assigned to intra-ligand charge transfer of –N=N– moiety, then confirms the formation of azo dye due to the high intensity band located near the visible region. On comparison the UV-Visible spectra of all complexes with the spectrum of the free ligand in DMSO solvent, it is noted that the new weak bands observed at around (490–380) nm are consistent with the chelation of empty orbitals of Hg(II), Zn(II), Cd(II) and V(IV) ions [18-19] with the lone pairs of the donating atoms in the active sites of azo dye. The intra-ligand charge transfer of –N=N– moiety was shifted to longer or shorter wavelengths due to the linkage of lone

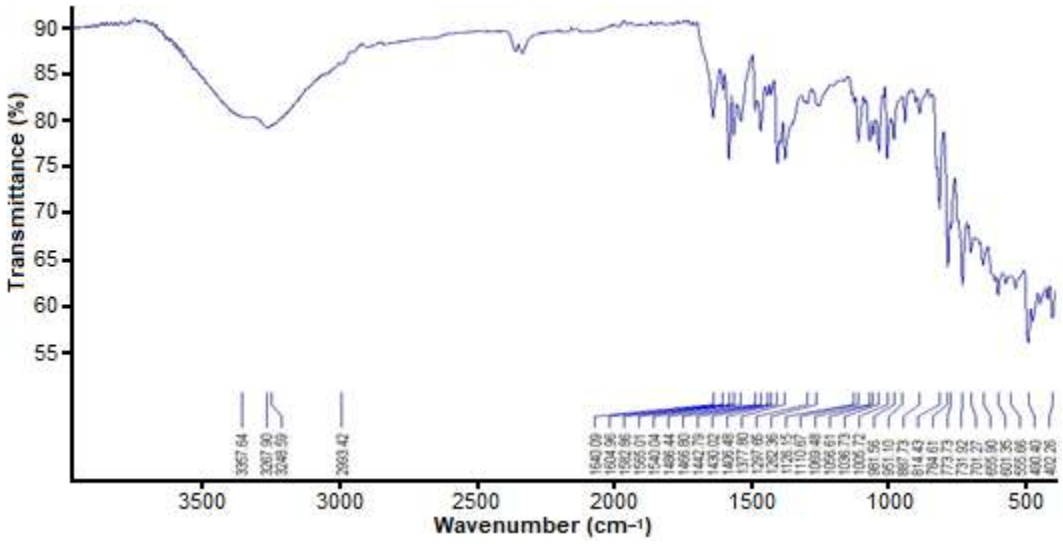

Fig 4. FT-IR spectrum of VOL complex in CsI disc

pair to the empty orbitals of metal ions in the region (380–500) nm, Table 2. The diamagnetic properties of zinc (II), cadmium (II) and mercury(II) complexes with the association of elemental analyses confirm the tetrahedral environment. The red solution of vanadium (IV) complex displayed two spin-allowed peaks at 650 and 490 nm that are attributed to $^2A_1g \rightarrow {}^2B_1g$ and $^2A_1g \rightarrow {}^2B_2g$ transitions respectively [20]. The value of magnetic moment of solid complex of vanadium(II) at 27 °C to 1.80 BM revealed the presence of unpaired electron in its outer level $3d^1$ and make it forms the possibility of five-coordinate complex with a bi dentate azo-dye ligand through two active site –N=N and –OH groups [18-19].

Thermal Analysis of C1 and C2 Complexes

The thermal stability of zinc(II) and cadmium(II) complexes was screened with TG-DTA analyses in the nitrogen atmosphere and presented in Table 3. The losing of weak points like M–Cl and methyl groups were shown in the first stages of analyses at range (190–270) °C temperature while the final stage of analysis for C1 complex was accomplished at (300–450) °C to give the stable phase of zinc(II) oxide [20]. As well as the hydrated cadmium(II) complex showed three stages of thermal analysis with losing of crystalline water at around (160–280) °C. The data observed from weight loss (%w) would be in agreement with the theoretical data

Table 2. Electronic spectra and molar extinction coefficients for complexes

Compounds	Molar Conc.	nmλ	Σ_oL.mol^{-1} cm^{-1}	Assignment	μ (BM)
		655	110	$^2A_1g \rightarrow {}^2B_1g$	
VOL	1×10^{-3}	490	90	$^2A_1g \rightarrow {}^2B_2g$	1.80
		380	2900	LMCT	
		455	8000	MLCT	
ZnL	1×10^{-4}	390	27000	INCT	Dia
		280	13000	$\pi \rightarrow \pi^*$	
		500	20000	INCT	
CdL	1×10^{-5}	470	12700	MLCT	Dia
		250	3000	$\pi \rightarrow \pi^*$	
HgL	1×10^{-5}	455	11700	MLCT	Dia
		300	10000	INCT	

Dia = Diamagnetic, LMCT and MLCT are charge transfer from ligand to metal or vice-versa, and INCT = Intra-ligand charge transfer bands

Table3. Thermo gravimetric analysis (TGA) of the metal complexes

No.	Molecular formula	Temp. range (°C)	Mass loss%		Assignment
			Found	Calc.	
C1	$[ZnL_2]$	190–270	6.43	8.66	Loss of Cl and –OH, $-2OCH_3$
		300–450	33.84	3160	Further dissociation of the organic ligand ($C_8H_6N_2$) with formation of ZnO + Zn_3N_2 as final product
		160–280	16.01	17.08	
C2	$[CdL_2]\cdot 2H_2O$	290–390	10.06	9.14	Loss of 2 hydrated H_2O molecules, $-OCH_3$
		400–560	52.13	52.26	Loss of phenyl, 2Cl anion and decomposition of the organic ($2C_6H_7N_2O$)
		441–541	15.16	14.25	Loss of ($C_6H_5CH_3$)
		541–930	6.16	5.43	Further dissociation of the organic ligand (2C) with formation of CdO as final product

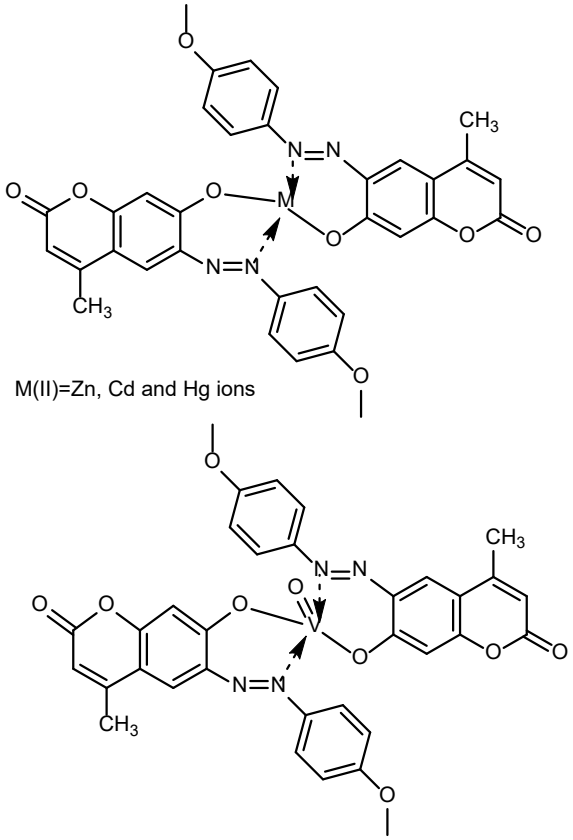

Scheme 2. Structures of metal complexes

and supports their structures [21-22].

■ CONCLUSION

According to the results obtained from elemental analyses, FT-IR, NMR and EI-MS spectra and electronic spectra in ethanol and DMSO solvents, the tetrahedral geometry was identified for zinc(II), cadmium(II) and mercury(II) complexes, while the vanadium(IV) complex was square-pyramid of five coordination number via optimization the mole ratios 2:1 of ligand azo to the metal ion. The thermal analyses and molar conductivity measurements confirmed the square-pyramid around vanadium(IV) ion and tetrahedral environment around zinc(II), cadmium(II) and mercury(II) ions, Scheme 2.

■ ACKNOWLEDGMENTS

Authors are so grateful for service laboratories at Mustansiriyah University, College of Science, Department of Chemistry facilitating of FT-IR, UV-Visible spectra and magnetic moments measurements. As well as the authors appreciated the role of University of Baghdad, Ibn-Haitham Education College for pure sciences for carrying out the thermal analyses.

■ REFERENCES

[1] Gao, P., Tsao, H.N., Yi, C., Grätzel, M., and Nazeeruddin, M.K., 2014, Extended π-bridge in organic dye-sensitized solar cells: The longer, the better?, *Adv. Energy Mater.*, 4 (7), 1301485.

[2] Tsuzuki, K., and Tada, M., 1986, The syntheses of pteridin-2-one derivatives from diaminomaleonitrile (DAMN), *J. Heterocycl. Chem.*, 23 (5), 1299–1301.

[3] Ayare, N.N., Ramugade, S.H., and Sekar, N., 2019, Photostable coumarin containing azo dyes with multifunctional property, *Dyes Pigm.*, 163, 692–699.

[4] Tathe, A.B., and Sekar, N., 2016, Red emitting coumarin–azo dyes: Synthesis, characterization, linear and non-linear optical properties-experimental and computational approach, *J. Fluoresc.*, 26 (4), 1279–1293.

[5] Matsumura, K., Yoshizaki, S., Maitani, M.M., Wada, Y., Ogomi, Y., Hayase, S., Kaiho, T., Fuse, S., Tanaka, H., and Takahashi, T., 2015, Rapid synthesis of thiophene-based, organic dyes for dye-sensitized solar cells (DSSCs) by a one-pot, four-component coupling approach, *Chem. Eur. J.*, 21 (27), 9742–9747.

[6] Sahoo, J., and Paidesetty, S.K., 2015, Biological evaluation and spectral characterization of 4-hydroxy coumarin analogues, *J. Taibah Univ. Med. Sci.*, 10 (3), 306–319.

[7] Cigáň, M., Donovalová, J., Szöcs, V., Gašpar, J., Jakusová, K., and Gáplovský, A., 2013, 7-(Dimethylamino)coumarin-3-carbaldehyde and its phenylsemicarbazone: TICT excited state modulation, fluorescent H-aggregates, and preferential solvation, *J. Phys. Chem. A*, 117, 4870–4883.

[8] Wang, S., Shen, S., and Xu, H., 2000, Synthesis, spectroscopic and thermal properties of a series of azo metal chelate dyes, *Dyes Pigm.*, 44 (3), 195–198.

[9] Refat, M.S., EI-Sayed, M.Y., and Adam, A.M.A., 2013, Cu(II), Co(II) and Ni(II) complexes of new Schiff

base ligand: Synthesis, thermal and spectroscopic characterizations, *J. Mol. Struct.*,1038, 62–72.

[10] Sahoo, J., Mekap, S.K., and Paidesetty, S.K., 2015, Synthesis, spectral characterization of some new 3-heteroaryl azo 4-hydroxy coumarin derivatives and their antimicrobial evaluation, *J. Taibah Univ. Sci.*, 9 (2), 187–195.

[11] Satyanarayana, B., Muralikrishna, P., Kumar, D.R., and Ramachandran, D., 2013, Preparation and biological evaluation of phenothiazine derivatives, *J. Chem. Pharm. Res.*, 5 (5), 262–266.

[12] Chetioui, S., Zouchoune, B., Merazig, H., Bouaoud, S.E., Rouag, D.A., and Djukic, J.P., 2021, Synthesis, spectroscopic characterization, crystal structure and theoretical investigation of two azo-palladium(II) complexes derived from substituted (1-phenylazo)-2-naphtol, *Transition Met. Chem.*, 46, 91–101.

[13] Al-Jibouri, M.N., 2014, Synthesis and characterization of transition metal complexes with Azop ligand derived from 4-hydroxy-6-methyl-2-pyranone, *Eur. Chem. Bull.*, 3 (5), 447–451.

[14] Freedman, D.A., Keresztes, I., and Asbury, A.L., 2002, Metal–coumarin complexes: Synthesis and characterization of 7-isocyanocoumarin ligands and $Mo(CO)_4$(7-isocyanocoumarin)2 complexes. X-ray crystal structure of $Mo(CO)_4$(7-isocyano-4-trifluoromethylcoumarin)$_2$, *J. Organomet. Chem.*, 642 (1), 97–106.

[15] Geary, W.J., 1971, The use of conductivity measurements in inorganic solvents for the characterization of coordination compounds, *Coord. Chem. Rev.*, 7 (1), 81–122.

[16] Nithya, P., Rajamanikandan, R., Simpson, J., Ilanchelian, M., and Govindarajan, S., 2018, Solvent assisted synthesis, structural characterization and biological evaluation of cobalt(II) and nickel(II) complexes of Schiff bases generated from benzyl carbazate and cyclic ketones studies, *Polyhedron*, 145, 200–217.

[17] Al-Hamdani, A.A.S., and Al Zoubi, W., 2015, New metal complexes of N3 tridentate ligand: Synthesis, spectral studies, and biological activity, *Spectrochim. Acta, Part A*, 137, 75–89.

[18] Silverstein, R.M., Webster, X.F., and Kiemle, D.J., 2005, Spectrometric Identification of Organic Compounds, 7th Ed., John Wiley & Son, Inc., Hoboken, New York.

[19] Lu, L., Wang, J., Chen, F., Wei, L.T., Lin, L.M., Li, B.H., Singh, A., and Kumar, A., 2019, Structures and photocatalytic performance of two d^{10} metal-based coordination polymers containing mixed building units, *Transition Met. Chem.*, 44 (2), 107–114.

[20] Esmaeilzadeh, M.A., 2019, Composite prepared from a metal-organic framework of type MIL-101(Fe) and morin-modified magnetite nanoparticles for extraction and speciation of vanadium(IV) and vanadium(V), *Microchim. Acta*, 186, 14.

[21] Kostova, I., Bhatia, S., Grigorov, P., Balkansky, S., Parmar, V.S., Prasad, A.K., and Saso, L., 2011, Coumarins as antioxidants, *Curr. Med. Chem.*, 18 (25), 3929–3951.

[22] Białek, M., Fryga, J., Spaleniak, G., and Żołnowska, M., 2017, Synthesis and olefin homo- and copolymerization behavior of new vanadium complexes bearing [OSSO]-type ligands, *React. Kinet., Mech. Catal.*, 122 (1), 259–273.

Simple Preparations and Characterizations of Activated-Carbon- Clothes from Palm-Kernel-Shell for Ammonia Vapor Adsorption and Skim-Latex-Odor Removal

Muhammad Adlim[1,2*], Ratu Fazlia Inda Rahmayani[2], Fitri Zarlaida[2], Latifah Hanum[2], Maily Rizki[2], Nurul Ummi Manatillah[2], and Omar Muktaridha[1]

[1]*Graduate School of Mathematics and Applied Science, Universitas Syiah Kuala, Banda Aceh 23111, Indonesia*

[2]*Chemistry Department, FKIP Universitas Syiah Kuala, Darussalam, Banda Aceh 23111, Indonesia*

* ***Corresponding author:***

tel: +62-651-7553205
email: adlim@unsyiah.ac.id

Received: January 25, 2021
Accepted: April 4, 2021

DOI: 10.22146/ijc.63570

Abstract: *This study explored a simple preparation and characterization of the activated carbon and cloth from the palm kernel shell and compared it to the commercial-water-filter-carbon specification. A new pyrolysis chamber that is easily scaled up using the palm kernel shell itself as a heat source was tested. Two different steps were compared: the alkaline activation process performed before or after the carbonation process in the palm-kernel-shell carbon preparation. The palm-kernel-shell activated carbons prepared with the current method fulfilled the standard quality of activated charcoal except for the ash content. The sequencing step of the preparation affected the adsorption capacity. Instead of the reverse sequence, the soaking palm kernel shells in NaOH before the carbonation process lead to a higher adsorption capacity. The carbon particle stability on the cloth surface was affected by both the adhesive concentration and its size. The ammonia adsorption capacity of activated carbon cloth (ACC) was between 1–4 mg ammonia per g stuck carbon. The preparation and the carbon type source on ACC affected the adsorption capacity. The ACC absorbed and lessened the skim latex odor vapor, nearly odorless depending on the ACC area and the volume of odor vapor.*

Keywords: *agriculture; adsorption capacity; activation; carbonation*

■ INTRODUCTION

The odor from ammonia is one of the major problems experienced in daily life. It has been discovered to be originating from trash bins and, on a large scale, agricultural industry and municipal organic wastes. The primary source of ammonia emission is cattle farming, as observed with its 49% contribution (244 kT-NH_3) in the United Kingdom in 2016. Other sources include livestock, agriculture, human and vehicle wastes, etc. [1]. However, it is possible to detect the odor in the concentration range of 5–53 ppm and has also been observed to have the ability to spread to other rooms at 50 ppm in 10 min. The poison effect of ammonia depends on its emission concentration level in the air. Inhaling vapor at 570 ppm causes respiratory interferences and sore feelings in the tract [2].

Several other things are causing severe air pollution in Asian countries, including Indonesia. These include lousy odor from rubber processing industries as observed in 2016 by merdeka.com and detik.com to disturb Mojokerto. Other similar cases have also been reported in different places since the country produces > 3 million tons of rubber in 2016, with more than a 1.3% increase in production annually. The air pollution was associated with the focus of these factories on treating liquid wastes [3] even though every step of treating skim latex also produces an unpleasant odor. A new smoke chamber prototype for rubber latex sheets was published previously [4-5], but there is no mention of reducing the smell, especially during the drying process.

One of the solutions to reduce ammonia and skim latex odor is the use of an adsorbent-based treatment. However, despite the reputation of granular activated carbon as an absorbent [6] and odor removal mainly for water and gas, it is barely used to remove the odors in the skim latex vapor [7-10]. The process involves filling

a container with the granular or powder content to make the carbon particles denser and reduce their absorbing capacity. Carbon cloth is suggested to be more compatible than the granular ones but expensive due to its source as well as the carbonization and activation processes [11-12]. This material has several applications, including its use as a chemical protecting blanket or jacket [13]. Anti-odor textile fabricated from palm kernel shells has been reported for onion odor adsorption [14]. However, the carbon cloth prepared with a simpler method has been reported for ammonia vapor adsorption.

In the current study, the activated carbon was prepared from the waste of palm kernel shells using a simple method, which is easy for farmers in rural areas to apply. It is important to note that this specific product has not been comprehensively explored by past studies [15]. For a simple process, palm kernel was used as the fuel for carbonization in two-layer-cylindrical-pyrolysis chambers. At the same time, caustic soda was applied as the activating agent due to its availability in the rural market.

The current study explores the effect of the activation-carbonation sequence, which is crucial to prevent the corrosive chemical loaded into the pyrolysis chamber. The characteristics of the activated carbons were compared with the new and the regenerated commercial activated carbons. The immobilization methods of activated carbon on a fabric, the capacity for ammonia odor adsorption, and skim latex odor removal were unknown. These areas have not been much discussed in previous literature because most of them are focused on the immobilization of active matter on activated carbon [16]. Therefore, the stability of activated carbon cloths, adsorption capacity, and organoleptic studies on odor removal were explored.

■ EXPERIMENTAL SECTION

Materials

Several research materials were bought from several companies. Palm Kernel Shells were from palm plantation (PT. Perkebunan Lembah Sakti). Ethanol (ACS grade), ammonia (25%), hydrochloric acid (35%), Nessler reagent A, and methylene blue were all from Supelco Merck. Commercial caustic soda (flake 98%), water filter commercial activated carbon (Hexagon coconut shells®) and polyvinyl acetate glue were from a local market.

Instrumentation

Some analytical instruments were used for characterization. An analytical instrument of UV-Vis Spekol 2000 spectrophotometer was used for the determination of ammonia concentration. A trinocular Olympus CX41 microscope with camera DP12, a Bellstone stereo microscope with an optical camera was used to observe the ACC surfaces. Brunauer-Emmett-Teller (BET) Sorptomatic 1800 is used to analyze carbon porosity, and scanning electron microscopy (SEM) JEOL JSM-6510LA was for surface characterization of activated carbons.

Procedure

Preparation of activated carbon from palm kernel shell

Dried palm kernel shells (PKS) were obtained from the local (Aceh Selatan) palm oil industry. About 16 kg was washed, sun-dried, and divided into two containers. It was divided into two groups of treatments. In the first treatment, PKS was initially carbonized by pyrolysis methods before alkaline activation. Alkaline activation is done by soaking it into 25% NaOH for 24 h. The charcoal was filtered and washed with deionized water until neutral and then sun-dried. This variation was called “Palm-carb-prior-act-C”. The second treatment involved the initial soaking of the PKS into 25% NaOH for 24 h and sun-dried before it was carbonized within a pyrolysis chamber. The cold charcoals were washed until they have a neutral pH and sun-dried, and the variation was called “Palm-act-prior-carb-C”.

Carbonization was conducted in a pyrolysis chamber; other than PKS filled in a pyrolysis chamber, the heat source was the burning PKS itself. The combustion equipment is made of two different sizes of hollow metal cylinders. The inner (smaller size), the pyrolysis tube, was shielded from the air, and the outer was the combusting chamber, where PKS was continuously added as fuel to produce the heat for pyrolysis. The combustion was adiabatic took 3 h, and the temperature reached around 800–1000 °C, which

was controlled by continuous addition of PKS as the fuel to simulate the actual application in the community. For comparison, both a new commercial-water-filter-carbon (WF-C) and the regenerated ones (RWF-C) were also studies. Each material was included in the characterization and fabrication of the Activated Carbon Cloths (ACC). The new and used WF-C were obtained from the local refill-water depot under a similar trade name, hexagon coconut shell (granular, ASTM American Society for Testing Materials quality). For RWF-C sample preparation, the WF-C that was previously used for three years was regenerated by drying at 105 °C for 2 h, re-activated by soaking in 6 M HCl for 24 h, and then washed and neutralized [17].

Characterization of the activated carbon

All types of activated carbon were characterized in powder with a size of more than 100 mesh. Characterization of the activated carbon was conducted for moisture, ash, iodine number, and volatile compound. The surface area and morphology were analyzed respectively using Brunauer-Emmett-Teller (BET) Sorptomatic 1800 and scanning electron microscopy (SEM) JEOL JSM-6510LA. The characteristic of activated carbon level for each referred to ASTM D-3175-11, ASTM D-3175-02, ASTM D-3174-11, and ASTM D-4607-94 respectively.

Immobilization/supported technique of activated carbon on the cloth

Each type of activated carbon particles (0.3 g) was immobilized on the surface of cotton cloth (4 cm × 7 cm) by using polyvinyl acetate adhesive (PAA), which was prepared in various concentrations of 50, 60, 70, and 80 %-weights-volume in technical-grade ethanol. The adhesive was smeared and flattened on the surface of the cotton cloth by using a roller grinder before the activated carbon particles flattened by a 5-kg-roller-grinder. The experiments were repeated to search for a combination between the adhesive concentration and the particle size of activated carbon (60, 80, and 100 mesh prepared with several layer sieves), which is crucial for the particle stickiness on the cloth. The best combination was determined from the stability of the carbon stickiness measured as the percentage of the mass loss in the immobilized carbon cloth after it was spun in a rotary evaporator for 5 min at 40 rpm. The stability test was run to study the ACC endurance in packaging and friction. The particle dispersion homogeneity was compared based on the microscope images.

Ammonia adsorption test

Approximately 25% of concentrated ammonia (Merck, 105432 Supelco) was transferred in a small baker glass, cooled in an ice bath (~15 °C) for 10 min to avoid excessive evaporation. Later, 0.1 mL of chilly ammonia was transferred using a micropipette into several 250-mL-glass reactors (equipped with electric plastic film cover) in which carbon cloth sheets were hung, as shown in Fig. 1. All glass reactors were airtight-shield and placed in a water batch at 28 $\pm$ 1 °C. The initial pH of ammonia vapor within the closed container was neutral, the pH was not controlled, but there was no significant change during this gas-phase experiment. This also confirmed with the theory that in the gas phase, ammonia does not significantly change pH [18]. The ACC sheets have a dimension (@3.5 cm × 6.5 cm, containing each 0.25 g average weight of activated carbon). The ACCs were attached inside the surface of the glass reactors except for the control. Adsorption experiments were set up in various ACC sheets (0, 1, 2, 3, 4, and 5 sheets). The optimum contact time was determined at the time when the amount of absorbed ammonia reached a constant. For this experiment, four sheets of ACC were hung in the glass reactor. Then, 0.1 mL of cold 25% concentrated ammonia was transferred into each six glass reactors using a micropipette. The initial concentration of ammonia vapor, which was 0.1 mL (13.38 M) within 250 mL container at 28 °C was 0.0052 M. The reactors were kept in a water bath at 28 °C and shielded with silicone rubber sheets to maintain an airtight condition with each was labeled according to the experimental-time, including 0, 60, 90, 105, 120, 135, and 150 min. At the due time, the carbon cloth sheets were quickly transferred into a 250 mL Erlenmeyer, which was covered with a rubber stopper connected to a 50 mL burette containing distilled water to ensure they absorbed the ammonia dissolved into the distilled water. After 10 min of agitation, the filtrate was analyzed using

a UV-Vis Spekol 2000 spectrophotometer with Nessler reagent as the complexing agent for the ammonium. The standard solution used, NH_4Cl, was verified using the previous method [19], which involved determining the ammonia concentration before and after adsorption. The adsorption capacity of the adsorbent in equilibrium isothermal Langmuir adsorption was calculated using Eq. (1) and (2), which is known as the Hannes-Woolf model, as follows [20-21]:

$$\frac{C_e}{q_e} = \frac{1}{q_m K_l} + \frac{C_e}{q_m} \quad (1)$$

or modified into

$$\frac{C_e}{q_e} = \frac{1}{bK} + \frac{C_e}{b} \quad (2)$$

where C_e is the concentration of ammonia vapor at equilibrium (mg g^{-1}), K_l is Langmuir constant related to adsorption capacity (mg g^{-1}), q_e is total ammonia vapor adsorbed per gram of immobilized carbon (mg g^{-1}), b = maximum adsorption capacity per gram of immobilized carbon (mg g^{-1}), K = equilibrium constant (L/mg).

Adsorption of volatile organic compounds (VOCs) from skim latex

The coagulated skim latex was cut into small pieces to a dimension of 1 cm × 1 cm × 5 cm, and the weight was estimated to be 10 g. Every four pieces were kept in 16 of 100 mL-rubber-sealed vials prepared for latex VOC sources for five days to concentrate the VOCs, as shown in Fig. 1(a). Three types of immobilized ACC named (a) Palm-carb-prior act-C, (b) Palm-act-prior carb-C and, (c) commercial water filtration (WF-C) were prepared from four types of carbon sources and hung inside a 250 mL Beaker glass as the reactor as indicated in Fig. 1(b). Meanwhile, the immobilized ACC sheets, each with a dimension of 3.5 cm × 6.5 cm (22.75 cm^2), were varied at 0, 2, 3, 4, and 5 sheets per reactor and combined with having three replications. Each reactor was shielded with an elastic rubber sheet to ensure airtight, as shown in Fig. 1. Furthermore, 10 mL of VOC was transferred from a vial into the reactor using a syringe after adsorption time was initiated, and the experiments were conducted at 0, 60, 120, and 135 min.

Organoleptic test odor

Twenty undergraduate chemistry students, including ten males and ten females within the age range of 21–23 years volunteered to participate in the organoleptic test for skim latex (VOC) odor removal using the method used by a previous study [22]. They were made to smell four shield-caps containing different concentrations of VOCs at 10, 5, and 0 mL during calibration. The level of odor in organoleptic sheets was recorded using a 0–10 level scale with the provision of a space to write an extreme level if they want to grade or respond differently. However, during the experiment, each of the participants separately smelled five caps containing a similar level of VOC but a different number of ACC sheets (0, 2, 3, 4, and 5 sheets) and then recorded the odor level in the organoleptic-observation table.

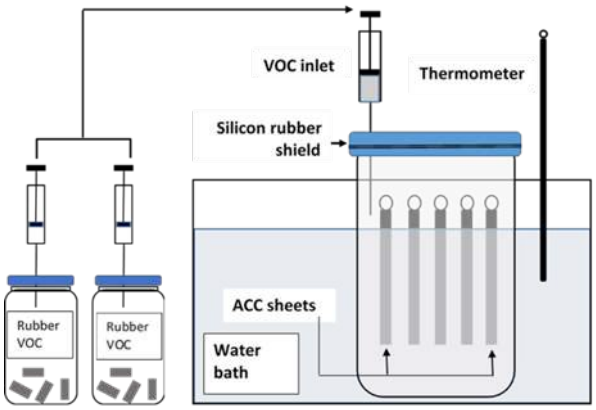

Fig 1. Vapor adsorption experiment. Skim latex VOC source (left) and vapor adsorption reactor equipped with ACC sheets (right)

■ RESULTS AND DISCUSSION

Preparation and Characterization of Activated Carbon from Palm Kernel Shells

The sequence of activation-carbonization was compared, and the treatment initially carbonized before chemical activation (Palm-carb-prior-act-C) was found to have produced hard charcoals and less yield. Still, better characteristics were observed in the reverse treatment, which was initially activated before carbonization (Palm-act-prior-carb-C) as observed from 37.5 and 42.86% yields, respectively. These were, however, considered higher than the results of a previous study [23]. Furthermore, the activated carbon was discovered to have produced more micropore than other raw

materials [24-26], as shown in the surface images obtained from SEM and compared with commercial-grade water filter carbons as presented in Fig. 2. The SEM images with similar 5000 times magnification in Fig. 2 show palm-carb-prior act-C (a) has smaller pores than Palm-act-prior carb-C (b). In comparison, the water filter carbon (c) was discovered to have more pores than those regenerated (d). Therefore, the products shown in Fig. 2(b) and Fig. 2(c) should have higher adsorption capacity.

The physical and chemical parameters fulfilled the minimum Indonesian National Standard (SNI). It is also comparable to ASTM minimum standards except for ash content, which was not preferable, as shown in Table 1. The characteristics correlate with the chemical properties of the activating agent. The chemical reaction produced some insoluble materials that cover the pores of carbon, and then it will subsequently reduce the adsorption capacity [27]. Therefore, more soluble activating chemicals are preferable, but there is a need to consider the toxicity level, cost, and availability in rural areas. Moreover, physical activation was also confirmed to be the better choice but requires a high-pressure reactor, which also has cost consequences.

The stability of the immobilized-activated-carbon on the cotton cloth was deduced from the weight loss percentage after ACC was rotated in a rotary evaporator at 40 rpm for 5 min. The results showed the most stable ACC was prepared with 80 wt.% of the adhesive and 100 mesh activated carbon particles. The smallest percentage of carbon particle loss was produced at this condition, leaving the highest percentage on the cloth. The data were confirmed using light microscope images present in

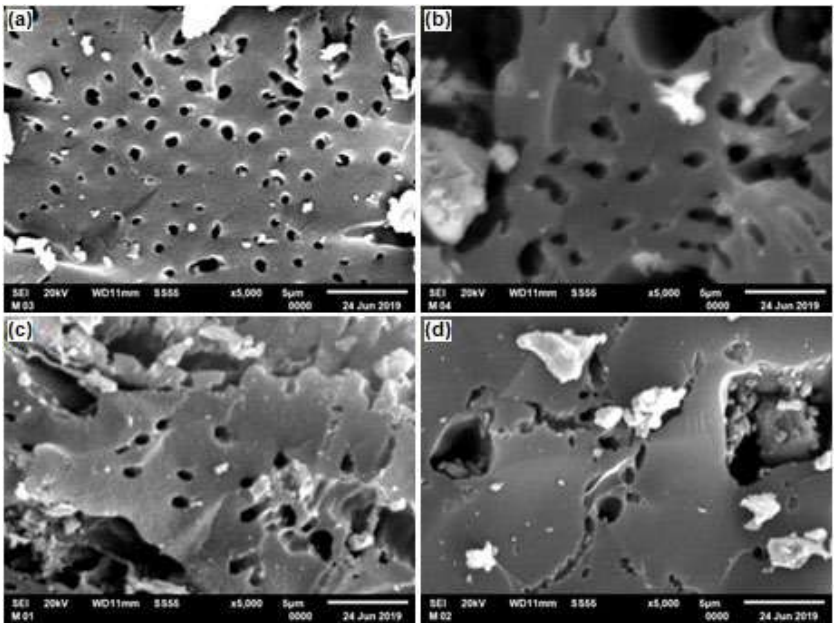

Fig 2. SEM images of the ACC (a) Palm-carb-prior act-C, (b) Palm-act-prior carb-C. (c) water filtration carbon (WF-C), (d) regenerated filtration regeneration (RWF-C)

Table 1. Activated carbon quality standard based on Indonesian National Standard (SNI), and comparable to ASTM

Parameters	Palm-carb-prior-act-C	Palm-act-prior-carb-C	RWF-C	WF-C	SNI
Water content (%)	8.20	5.70	11.80	13.90	≤ 15
Ash content (%)	8.20	13.80	12.70	11.50	≤ 10
Volatile compound (%)	24.00	25.00	23.27	21.50	≤ 25
Iodine number (mg g^{-1})	920.24	1113.81	1132.85	1259.78	≥ 750
Methylene Blue (mg g^{-1})	178.18	203.59	419.73	433.18	≥ 120

Fig. 3 and 4, which showed the most dispersed and homogeneous carbon particles, were observed in ACC prepared with 80 wt.% of the adhesive and 100 mesh carbon particles as indicated in Fig. 3 and Fig. 4. Fig. 3 shows that at a constant of 80% adhesive, the smaller carbon particle gave the more homogeneous carbon stickiness on the cloth. Fig. 3(c) is the dark color indicating the better carbon particle dispersion. Attempting to increase the ACC flexibility using lower adhesive concentration (< 80 wt.%) caused less carbon particle dispersion. As shown in Fig. 4 (a-c), carbon particles did not completely cover the cloth surface.

The results of the Brunauer-Emmett-Teller (BET) analysis for each type of activated carbon are presented in Fig. 5, and the adsorption-desorption plot was essential to elaborate the adsorption layered model, quantity of the pollutant adsorbed, pollutant holding ability, etc. All the curves were found to have exhibited good adsorption points at 1 atm, with the curve pattern observed somewhat similar to type III isotherm with the hysteresis loop, as found in the literature [28].

Alkaline activation after carbonation (the palm-carb-prior act-C in Fig. 5(a)) showed a lower adsorption capacity (50 $cm^3 g^{-1}$) compared to revised step activation (palm-act-prior carb-C in Fig. 5(b)), which was up to 600 $cm^3 g^{-1}$. Fig. 5(a) demonstrated an adsorption capacity despite the fact the adsorbed quantity was relatively low. This desorption trend indicated the gas was strongly held at reduced pressure. The pore volume of the palm-act-prior carb-C was 1.012 g cm^{-3}, higher than

Fig 3. Light microscope images of ACC surfaces prepared with several carbon particle sizes using 80 wt.% adhesive: (a) 60, (b) 80, and (c) 100 mesh

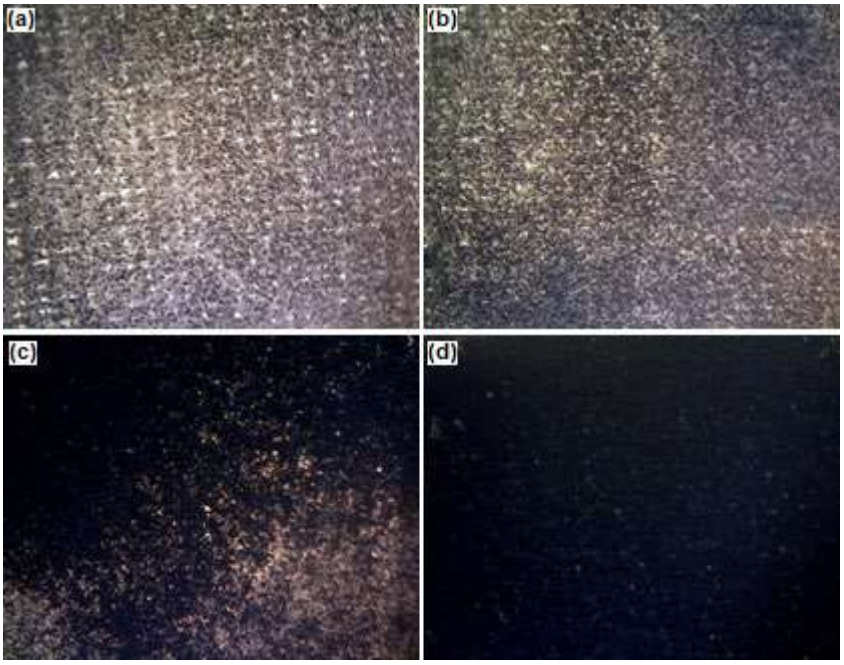

Fig 4. ACC surfaces prepared with various concentrations of adhesive: (a) 50, (b) 60, (c) 70, and (d) 80 wt.%

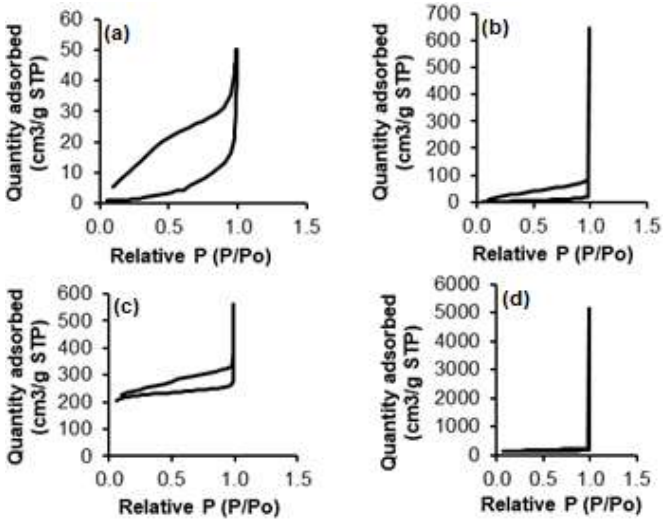

Fig 5. Adsorption-desorption isotherm plots of the activated carbons; (a) Palm-carb-prior act-C, (b) Palm-act-prior carb-C, (c) water filter carbon (WF-C), (d) regenerated filter carbon (RWF-C)

that of the water filter carbon (WF-C) of 0.56 g cm^{-3}. The regenerated filter carbon (RWF-C) has the largest volume (8.00 g cm^{-3}). Probably, trace chemicals during the regenerating process caused the anomaly.

Ammonia Adsorption Test of the Activated Carbon

The mean optimum contact time between 4 sheets of ACC (containing a total of 1.4 g stuck carbon particles) and the initial concentration of ammonia vapor (0.0052 M) was 100 min at 1 atm and 28 $\pm$ 1 °C. The adsorption capacity of ACC with a different type of carbon source is tabulated in Table 2. WF-C and RWF-C have an adsorption capacity of 7.038 $\pm$ 0.2 and 6.246 $\pm$ 0.07 mg ammonia per gram of carbon. The WF-C and RWF-C were made of coconut shells and as commercialized water filter products.

Table 2. Experimental adsorption of ACC toward ammonia vapor at 28 °C and 1 atm

Type of Carbons	Total weight stuck C (g)	Total of ACC sheets	Area (cm^2)	Adsorption capacity (total mg ammonia. g^{-1} carbon)
	0.294	1	22.75	6.681
	0.616	2	45.5	7.123
WF-C	1.048	3	68.25	7.208
(coconut shell carbon)	1.419	4	91	7.140
	1.869	5	113.8	7.038
				7.038 $\pm$ 0.2
	0.302	1	22.75	6.137
	0.613	2	45.5	6.273
RWF-C	1.009	3	68.25	6.290
(coconut shell carbon)	1.323	4	91	6.307
	1.658	5	113.8	6.222
				6.246 $\pm$ 0.07
	0.399	1	22.75	2.771
	0.701	2	45.5	2.873
Palm-act-prior-carb-C	1.125	3	68.25	2.873
(palm kernel shell carbon)	1.409	4	91	2.873
	1.76	5	113.8	2.873
				2.853 $\pm$ 0.05
	0.35	1	22.75	1.275
	0.697	2	45.5	1.428
Palm-carb-prior-act-C	1.146	3	68.25	1.445
(palm kernel shell carbon)	1.456	4	91	1.445
	1.843	5	113.8	1.428
				1.404 $\pm$ 0.07

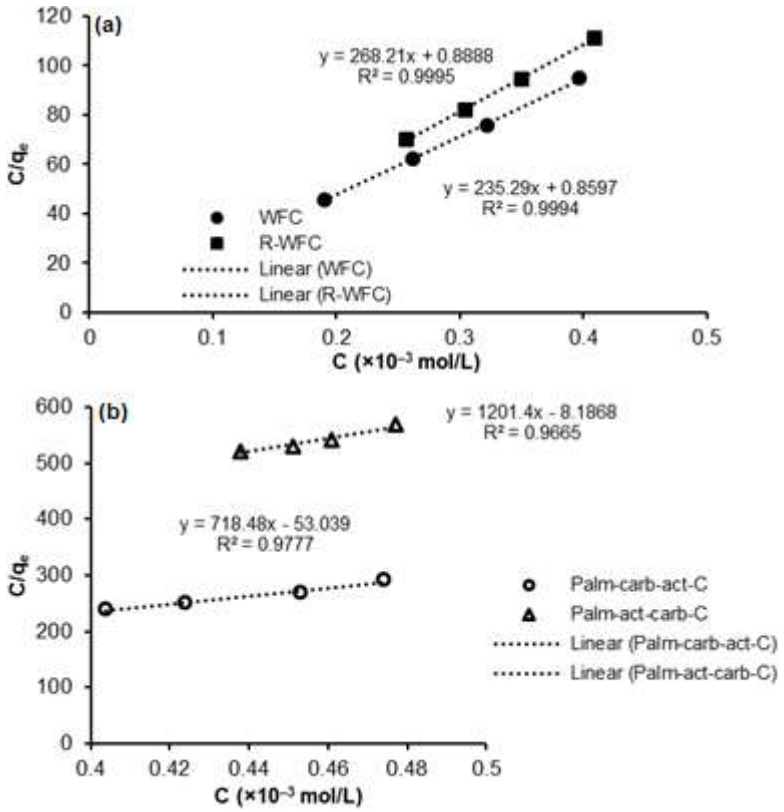

Fig 6. Isothermal Langmuir plot of ammonia vapor adsorption on several types of activated carbon cloth made of (a) commercial water filter carbon and the regenerated one, (b) palm kernel activated carbon prepared with different activation sequences

The adsorption capacity of these sources of carbon is higher than palm kernel carbons.

Since the adsorption occurs between the gas (ammonia vapor) and solid adsorbent (ACC), the Langmuir model was chosen to study the adsorption model verifying literature [20]. We plot (C/q_e) vs. C and found linear graphs with R^2 of 0.9995 and 0.9994. The Freundlich plot gave a smaller R^2 that is the highest with only 0.8667, and other models have not been studied [29]. The ammonia adsorption characteristics of several activated carbons were presented as a plot graph in Fig. 6. They were all found to be linear following the isothermal Langmuir law. Refer to equation (2), the graph plotted in Fig. 6 shows that the b value can be calculated as the reversed gradient and multiply by 1000 as the concentration correction factor. The b for y = 235.29x + 0.86 (WFC), y = 268.21x + 0.88 (R-WFC); y = 1201.1x – 8.1868 (Palm-act-carb) and 718.48x – 53.04 (Palm-carb-act) are 4.25, 3.37, 1.39, and 0.83 mg g^{-1} respectively at operating temperature of 28 °C. These calculated data are much smaller than the experimental adsorption capacities (Table 2) but higher than the adsorption capacity prepared active carbon previously reported, which was 0.6–1.7 mg g^{-1} at 40 °C [30]. The difference in adsorption capacity between experimental and graph data analysis might relate to fewer data plotted and the graph correction factor. The trend was consistent between the SEM and BET data, which showed palm shell activated carbon has comparable adsorption capacity to the commercial water filter carbon made from coconut shell-activated charcoal. The slightly higher adsorption capacity of WF-C is in line with the findings of previous reports that coconut carbon has a higher adsorption capacity than those produced by Palm Kernel Shell (PKS) [31-32]. Still, in the Asian community, PKS has much larger resources and waste than coconut shells.

Adsorption capacity enhancement of Palm-act-prior carb-C might relate to a chemical reaction between

NaOH and PKS cellulose prior to the carbonization process. By soaking palm kernel shells in NaOH before the carbonization process, it causes cellulose to swell and fragment. This effect subsequently made more porous carbon after the carbonation process [33]. The phenomenon no longer worked for the activated carbon prepared in the reverse process (in the case of Palm-carb-prior act-C). The carbon particles were already inert toward NaOH, and thereby the adsorption capacity was lower. Since PKS was activated by NaOH and the trace has been washed until neutral, then ACC active sites for adsorption were plausibly just the carbon porosity. Analog to the previous study that, unlike the KOH activation, the NaOH-activated biochar showed no obvious FTIR spectra between 4000–400 cm^{-1}. It indicated that chemical functional groups on the biochar surface were relatively absent [34]. Refer to this previous report, adsorption in this current study is predicted due to the physical interaction between ammonia and carbon pores in the surface of ACC. The molecular interaction type also confirmed the Langmuir isothermal model (Fig. 6) [35]. This finding verified the previous report that suggested both Langmuir isothermal model and physisorption for the adsorption of ammonia gas onto activated carbon [30]. The experiment was comparable to our work in that it was carried out in the gas phase and at relatively low temperatures. Adsorption studies of carbon-ammonia in aqueous solution were previously reported to follow the Freundlich instead of the Langmuir adsorption model [36]. The BET graph plots (Fig. 5) also showed desorption models representing the physical interaction characteristics.

Skim Latex Odor Removal

The skim latex released some volatile organic compounds (VOCs) with unpleasant odors, especially from the low molecular weight of carboxylic acid components; they are natural compounds and relatively none of the recognized toxic chemicals [37]. The PKS ACC was applied to absorb skim latex odor, which is VOCs. The PKS ACC performance was attempted to compare to WF-ACC. The odor-reducing performance was analyzed based on the panelist's responses during the organoleptic test. From 20 panelists, 100% of respondents agreed that the control sample (skim latex vapor without ACC adsorbent) has the worse smell with a level of 10. They also confirmed that the empty container was odorless with a level of 0. After treating skim latex odor with 45.5 cm^2 of ACC (2 pieces with @ 3.5 × 6.5 cm^2) at optimum contact time in a close container, the majority (55%) respondents smell that odor had been in medium with the level of 5–7, but the rest respondents still feel that the scent remains worse. However, after treating the skim latex vapor with 113.75 cm^2 of ACC (5 pieces), nearly all respondents agreed that the odor had been at a deficient level. About 60% of respondents scored the odor level being reduced to level 2; the rest marked it as level 1. The respondents could not differentiate the effect of different source carbon on the ACCs odor reduction capacity.

■ CONCLUSION

The activation-carbonization sequence of palm kernel shells using NaOH as the activator significantly affects activated carbon quality. The treatment prepared by initially activating palm kernel before carbonization gave better properties than those prepared with the reciprocal sequence. The activated carbon prepared with a new model pyrolysis chamber fulfilled the Indonesian industrial standard, and the quality is comparable with commercial-water- filter-activated carbons. The regenerated WF-C shows high adsorption capacity. The carbon particle stability on the ACC surface was affected by both the adhesive concentration and size. The adsorption capacity of ACC made of palm kernel shell toward ammonia vapor is lower than that of commercial water filter carbon made, which is made of coconut shell carbon, but kernel ACC has the comparable capacity with other work previously published. The ACC also showed a high capacity to reduce the skim-latex-odor level depending on its ACC area and odor quantity.

■ ACKNOWLEDGMENTS

We highly appreciated research funding provided by Universitas Syiah Kuala, Aceh Province Indonesia, in 2019 financial years with Research Grant number:

520/UN11/SPK/PNBP/2019 (February 8, 2019); also the second grant; 268/UN11/SPK/PNBP/2020 (March 17, 2020).

■ AUTHOR CONTRIBUTIONS

M. Adlim is the corresponding author who composed the main manuscript. Ratu F.I. Rahmayani, Fitri Zarlaida, and Latifah Hanum monitored research activities in the laboratory. Maily Rizki, Nurul U. Manatillah, and O. Muktaridha were undergraduate and graduate students who conducted the experiments in the laboratory.

■ REFERENCES

[1] Guthrie, S., Giles, S., Dunkerley, F., Tabaqchali H., Harsfield, A., Loppolo, B., and Manville, C., 2018, *The impact of ammonia emissions from agriculture on biodiversity*, RAND Corporation, Cambridge, UK.

[2] National Research Council (US) Committee on Acute Exposure Guideline Levels, 2008, *Acute Exposure Guideline Levels for Selected Airborne Chemicals: Volume 6*, National Academies Press, Washington, DC.

[3] Mokhtar, N.M., Lau, W.J., Ismail, A.F., and Veerasamy, D., 2015, Membrane distillation technology for treatment of wastewater from rubber industry in Malaysia, *Procedia CIRP*, 26, 792–796.

[4] Dejchanchaiwong, R., Kumar, A., and Tekasakul, P., 2019, Performance and economic analysis of natural convection based rubber smoking room for rubber cooperatives in Thailand, *Renewable Energy*, 132, 233–242.

[5] Dejchanchaiwong, R., Tirawanichakul, Y., Tirawanichakul, S., Kumar, A., and Tekasakul, P., 2017, Techno-economic assessment of forced-convection rubber smoking room for rubber cooperatives, *Energy*, 137, 152–159.

[6] Anisuzzaman, S.M., Bono, A., Krishnaiah, D., and Tan, Y.Z., 2016, A study on dynamic simulation of phenol adsorption in activated carbon packed bed column, *J. King Saud Univ. Eng. Sci.*, 28 (1), 47–55.

[7] Bertone, E., Chang, C., Thiel, P., and O'Halloran, K., 2018, Analysis and modelling of powdered activated carbon dosing for taste and odour removal, *Water Res.*, 139, 321–328.

[8] Otulana, J.O., Oluwole, O.O., and Adeleke, M.B., 2016, A reactor plant for activated carbon production, *Int. J. Novel Res. Eng. Sci.*, 2 (2), 20–26.

[9] Menya, E., Olupot, P.W., Storz, H., Lubwama, M., and Kiros, Y., 2018, Production and performance of activated carbon from rice husks for removal of natural organic matter from water: A review, *Chem. Eng. Res. Des.*, 129, 271–296.

[10] Mohammad Razi, M.A., Al-Gheethi, A., Al-Qaini, M., and Yousef, A., 2018, Efficiency of activated carbon from palm kernel shell for treatment of greywater, *Arab J. Basic Appl. Sci.*, 25 (3), 103–110.

[11] Cukierman, A.L., 2013, Development and environmental applications of activated carbon cloths, *Int. Scholarly Res. Not.*, 2013, 261523.

[12] Attia, N.F., Jung, M., Park, J., Jang, H., Lee, K., and Oh, H., 2020, Flexible nanoporous activated carbon cloth for achieving high H_2, CH_4, and CO_2 storage capacities and selective CO_2/CH_4 separation, *Chem. Eng. J.*, 379, 122367.

[13] Tripathi, N.K., Singh, V.V., Sathe, M., Thakare, V.B., and Singh, B., 2018, Activated carbon fabric: An adsorbent material for chemical protective clothing, *Def. Sci. J.*, 68 (1), 83–90.

[14] Eza, T.S.M., Wan Ahmad, W.Y., Omar, K., and Ahmad, M.N., 2014, Effectiveness of activated carbon produced from coconut and palm shells as anti-odour on textile fabrics, *Indian J. Fibre Text. Res.*, 39, 190–195.

[15] Ayinla, R.T., Dennis, J.O., Zaid, H.M., Sanusi, Y.K., Usman, F., and Adebayo, L.L., 2019, A review of technical advances of recent palm bio-waste conversion to activated carbon for energy storage, *J. Cleaner Prod.*, 229, 1427–1442.

[16] Lelifajri, Nawi, M.A., Sabar, S., Supriatno, and Nawawi, W.I., 2018, Preparation of immobilized activated carbon-polyvinyl alcohol composite for the adsorptive removal of 2, 4-dichlorophenoxyacetic acid, *J. Water Process Eng.*, 25, 269–277.

[17] Da'na, E., and Awad, A., 2017, Regeneration of spent activated carbon obtained from home filtration system and applying it for heavy metals adsorption, *J. Environ. Chem. Eng.*, 5 (4), 3091–3099.

[18] Guo, H., Weber, R.J., and Nenes, A., 2017, High levels of ammonia do not raise fine particle pH sufficiently to yield nitrogen oxide-dominated sulfate production, *Sci. Rep.*, 7 (1), 12109.

[19] Smeets, M.A.M., Bulsing, P.J., van Rooden, S., Steinmann, R., de Ru, J.A., Ogink, N.W.M., van Thriel, C., and Dalton, P.H., 2007, Odor and irritation thresholds for ammonia: A comparison between static and dynamic olfactometry, *Chem. Senses*, 32 (1), 11–20.

[20] Ayawei, N., Ebelegi, A.N., and Wankasi, D., 2017, Modelling and interpretation of adsorption isotherms, *J. Chem.*, 2017, 3039817.

[21] Kul, A.R., and Caliskan, N., 2009, Equilibrium and kinetic studies of the adsorption of Zn(II) ions onto natural and activated kaolinites, *Adsorpt. Sci. Technol.*, 27 (1), 85–105.

[22] Juntarachat, N., Bouvier, N., Lepoutre, J.P., Roland, A., Sainte-Beuve. J., Granet, F., Salmon, J.M., Rigou, P., and Chalier, P., 2013, Identification by GC-O and GC-MS of new odorous compounds in natural rubber, *J. Appl. Polym. Sci.*, 130 (3), 1863–1872.

[23] Dada, A.O., Inyinbor, A.A., and Oluyori, A.P., 2012, Preparation and characterization of activated carbon using coconut and palm kernel shells, *Sci. Focus*, 17 (2), 188–197.

[24] Arami-Niya, A., Wan Daud, W.M.A., Mjalli, F.S., Abnisa, F., and Shafeeyan, M.S., 2012, Production of microporous palm shell-based activated carbon for methane adsorption: Modeling and optimization using response surface methodology, *Chem. Eng. Res. Des.*, 90 (6), 776–784.

[25] Sumathi, S., Bhatia, S., Lee, K.T., and Mohamed, A.R., 2009, Optimization of microporous palm shell activated carbon production for flue gas desulphurization: Experimental and statistical studies, *Bioresour. Technol.*, 100 (4), 614–1621.

[26] Rashidi, N.A., and Yusup, S., 2017, A review on recent technological advancement in the activated carbon production from oil palm wastes, *Chem. Eng. J.*, 314, 277–290.

[27] Wilcox, J., 2012, "Adsorption" in *Carbon Capture*, Springer, New York, 115–176.

[28] Thommes, M., Kaneko, K., Neimark, A.V., Olivier, J.P., Rodriguez-Reinoso, F., Rouquerol, J., and Sing, K.S.W., 2015, Physisorption of gases, with special reference to the evaluation of surface area and pore size distribution (IUPAC Technical Report), *Pure Appl. Chem.*, 87 (9-10), 1051–1069.

[29] Nandiyanto, A.B.N., Girsang, G.C.S., Maryanti, R., Ragadhita, R., Anggraeni, S., Fauzi, F.M., Sakinah, P., Astuti, A.P., Usdiyana, D., Fiandini, M., Dewi, M.W., and Al-Obaidi, A.S.M., 2020, Isotherm adsorption characteristics of carbon microparticles prepared from pineapple peel waste, *Commun. Sci. Technol.*, 5 (1), 31–39.

[30] Rodrigues, C.C., de Moraes, D., da Nóbrega, S.W., and Barboza, M.G., 2007, Ammonia adsorption in a fixed bed of activated carbon, *Bioresour. Technol.*, 98 (4), 886–891.

[31] Hidayu, A.R., and Muda, N., 2016, Preparation and characterization of impregnated activated carbon from palm kernel shell and coconut shell for CO_2 capture, *Procedia Eng.*, 148, 106–113.

[32] Ademiluyi, F.T., and David-West, E.O., 2012, Effect of chemical activation on the adsorption of heavy metals using activated carbons from waste materials, *Int. Scholarly Res. Not.*, 2012, 674209.

[33] Zhang, S., Wang, W.C., Li, F.X., and Yu, J.Y., 2013, Swelling and dissolution of cellulose in NaOH aqueous solvent systems, *Cellul. Chem. Technol.*, 47 (9-10), 671–679.

[34] Hsu, D., Lu, C., Pang, T., Wang, Y., and Wang, G., 2019, Adsorption of ammonium nitrogen from aqueous solution on chemically activated biochar prepared from sorghum distillers grain, *Appl. Sci.*, 9 (23), 5249.

[35] Kecili, R., and Hussain, C.M., 2018, "Mechanism of adsorption on nanomaterials" in *Nanomaterials in Chromatography*, Eds. Hussain, C.M., Elsevier, Amsterdam, 89–115.

[36] Long, X.L., Cheng, H., Xin, Z.L., Xiao, W.D., Li, W., and Yuan, W.K., 2008, Adsorption of ammonia on activated carbon from aqueous solutions, *Environ. Prog.*, 27 (2), 225–233.

[37] Kamarulzaman, N.H., Le-Minh, N., and Stuetz, R.M., 2019, Identification of VOCs from natural rubber by different headspace techniques coupled using GC-MS, *Talanta*, 191, 535–544.

Optimization of Polyurethane Membrane Physical Characteristics of Red Seaweed Biomass Using a Box-Behnken Design

Salfauqi Nurman[1,2,3], Saiful[4*], Binawati Ginting[4], Rahmi[4], and Marlina[4]

[1]*Graduate School of Mathematics and Applied Sciences, Universitas Syiah Kuala, Banda Aceh 23111, Indonesia*

[2]*Department of Agricultural Industrial Engineering, Faculty of Agricultural Technology, Universitas Serambi Mekkah, Banda Aceh 23245, Indonesia*

[3]*Malahayati Merchant Marine Polytechnic, Aceh Besar 23381, Indonesia*

[4]*Department of Chemistry, Faculty of Mathematics and Natural Sciences, Universitas Syiah Kuala, Banda Aceh 23111, Indonesia*

* ***Corresponding author:***

tel: +62-81360581225
email: saiful@unsyiah.ac.id

Received: January 27, 2021
Accepted: April 21, 2021

DOI: 10.22146/ijc.63649

Abstract: *The polyurethane membrane is used as a separator either by filtration or adsorption, and this process is significantly affected by its strength and physical condition. We synthesized polyurethane membranes using red seaweed with* Gracilaria sp *as a hydroxyl source. The Box-Behnken Design of the Response Surface Methodology (RSM) using Software Design Expert Version 10.0.3.0 with three factors (TRL, TDI, and Glycerin). The F-value of 0.42 suggests that the membrane is less fit, while the P-value of 75.10% indicates that the quadratic design model is suitable for data analysis of physical characteristics. The optimal physical characteristics were obtained at a composition of 0.233 g TRL, 2.675 g TDI, and 0.254 g glycerin with a physical point of 6.5 (strong and elastic). Optimal polyurethane membrane has good thermal and mechanical properties at temperatures of Tg 58 °C, Tm 322 °C, and Td 534 °C, as well as stress and nominal strain values of 69.3 MPa and 5.74%. Polyurethane membrane synthesized from red seaweed has good physical properties. The result of this research is the basis for the development of polyurethane membrane applications from red seaweed.*

Keywords: *physical characteristics; response surface methodology; optimization; polyurethane membranes*

■ INTRODUCTION

Membranes are separators used to separate various substances in a gas mixture [1] or liquid [2-3]. This technology continues to develop due to its high selectivity properties [4-5] as well as its ability to be easily synthesized and applied [6-7]. One of the commonly developed membranes is polyurethane [8], which is a type of polymer membrane composed of urethane bonds [9] and formed from the reaction between compounds containing two or more reactive hydroxyl and isocyanate groups [10-12]. Polyurethane membranes can be synthesized using natural materials, such as carrageenan, which has strong and slightly elastic properties with a tensile strength of 340 kgf/mm^2, at a 9% elongation percentage [13]. In this study, we used the *Gracilaria sp* type of red seaweed as a hydroxy source for the synthesis of polyurethane membranes due to its abundant availability in coastal areas and the presence of hydroxy groups from carrageenan, alginate, and agar [14].

The polyurethane membrane is also applied as a separator either by filtration [15-16] or adsorption [2,17]. The strength and physical condition of the membrane significantly affect the success of the separation process, using a large pressure driving force and a concentration gradient during filtration. Therefore, a strong and slightly elastic membrane is required [6] to produce a suitable polyurethane membrane, which is strongly influenced by the composition of the materials used to regulate the formation of hard and soft segments [18-19]. The

research used the Box-Behnken Design from Response Surface Methodology (RSM) due to its ability to combine factorial and incomplete group designs to obtain optimal composition [20-21]. This design uses a Design Expert Software Version 10.0.3.0 with three factors and three levels.

Furthermore, RSM is also used to model and analyze the effect of the quantitative variable to obtain optimized results. The relationship between these variables can be described in the form of an equation [22-24]. Furthermore, the response used is the polyurethane membrane's physical or visual characteristics, which assign points to the characteristic level. These points were used as response variables and linked with other factors to produce 3D graphs to determine the optimal composition for polyurethane membrane synthesis. The physical characteristics can be used as a qualitative analysis of polyurethane membranes.

■ EXPERIMENTAL SECTION

Materials

The materials used were 1,4-dioxane as a solvent, glycerin, castor oil as a plasticizer, and toluene diisocyanate (TDI) as a reagent in Pro's quality Analysis (PA) from Merck (Darmstadt, Germany). The sample used was red seaweed (*Gracilaria verucosa* Greville) from the ponds in Lamnga Village, Mesjid Raya District, Aceh Besar District, Aceh Province. The seaweed used was Seaweed Flour (TRL) with a particle size of 777.3 nm.

Instrumentation

The equipment used includes glassware, namely measuring cups, beakers, Petri dishes, magnetic stirrers, hotplates, analytical scales, ovens, grinders, and other supporting tools. While the instruments used are FTIR (IR-Prestige-21, Shimadzu), DSC (DSC-60, Shimadzu), TGA (DTG-60, Shimadzu), SEM (JEOL - 6510 LA) and MTS EM tensile test with ASTM D638 Plastics Tension 1229.

Procedure

Treatment design

Due to its ability to combine factorial with incomplete blocking design, the Response Surface Methodology with Box-Behnken Design was used to synthesize polyurethane membrane [20]. This research was carried out with the Software Design Expert Version 10.0.3.0 with three factors (TRL, TDI, and Glycerin) and three levels (low, medium, and high). As shown in Table 1, the factors and levels used in this study are based on preliminary investigations. In addition, the combined polyurethane membrane synthesis design using Box-Behnken Design is shown in Table 2.

Polyurethane membrane synthesis

TRL was weighed according to the combination and put in a beaker containing 5 g of 1,4-dioxane and 0.5 g of castor oil. The solution was homogenized for 10 min, followed by the addition of TDI and glycerin. The

Table 1. Design levels of polyurethane membrane synthesis by three factors (x)

Factor	Parameter	Level		
		Low (-)	Medium (0)	High (+)
x_1	TRL (g)	0.1	0.2	0.3
x_2	TDI (g)	2.0	2.5	3.0
x_3	Glycerin (g)	0.2	0.3	0.4

TRL: Seaweed flour
TDI: Toluene diisocyanate

Table 2. Combined polyurethane membrane synthesis design using Box-Behnken Design

Run	TRL (g)	TDI (g)	Glycerin (g)
1	0.2	3.0	0.4
2	0.2	2.5	0.3
3	0.3	2.5	0.4
4	0.2	2.0	0.2
5	0.2	3.0	0.2
6	0.1	2.5	0.4
7	0.2	2.5	0.3
8	0.1	2.0	0.3
9	0.3	2.0	0.3
10	0.1	2.5	0.2
11	0.3	2.5	0.2
12	0.2	2.5	0.3
13	0.2	2.0	0.4
14	0.3	3.0	0.3
15	0.2	2.5	0.3
16	0.2	2.5	0.3
17	0.1	3.0	0.3

mixture was then polymerized at 60 °C for 2 h while stirring using a magnetic stirrer. The dope solution formed was then molded using a petri dish, then placed in a dust-free room at room temperature for 24 h. After forming the membrane sheet, the membrane was removed from the mold by immersing it in warm distilled water for 1–2 h.

Physical characterization

The visible physical characterization of polyurethane membranes is shown in Table 3. According to points 6 to 7 of the physical characteristics, the membrane is elastic, not easily torn, or strong. This characterization is an initial qualitative analysis used to determine the optimal composition comprising functional group, thermal, and tensile strength analysis.

Polyurethane membrane characterization

The optimal polyurethane membrane characterization of functional groups using Fourier Transform Infra-Red (FTIR), samples were made into KBr pellets (ratio 1:20), the spectrum was recorded in the wavenumber range of 4000–400 cm^{-1}. Thermal analysis using the Differential scanning calorimetry (DSC) and Thermogravimetric Analysis (TGA). The observation was carried out under a nitrogen gas flow with a speed of 20 mL/min. The sample with a 10–20 mg weight was heated in an aluminum pan at a temperature of 0–600 °C with a scanning speed of 20 °C/min. For Scanning Electron Microscope (SEM) analysis, the sample was placed on an aluminum plate and coated with palladium gold in a vacuum chamber. The sample was analyzed using Det.BSE and SE at a voltage of 10, 15, and 20 kV. Mechanical analysis using MTS EM tensile test with ASTM D638 Plastics Tension 1229.

■ RESULTS AND DISCUSSION

Physical Characteristics of Polyurethane Membranes

Polyurethane membranes are formed by the presence of urethane bonds that occur between two main groups, namely hydroxyl (–OH) and isocyanates (NCO) [18,25], as shown in Fig. 1. The urethane bonds can affect the physical properties of the polyurethane membrane. Points 5 to 8 in Table 3 show that the resulting polyurethane membrane has good physical properties, namely elastic, and does not tear easily. The results of the physical characterization are then entered into the Box-Behnken design, as shown in Table 4.

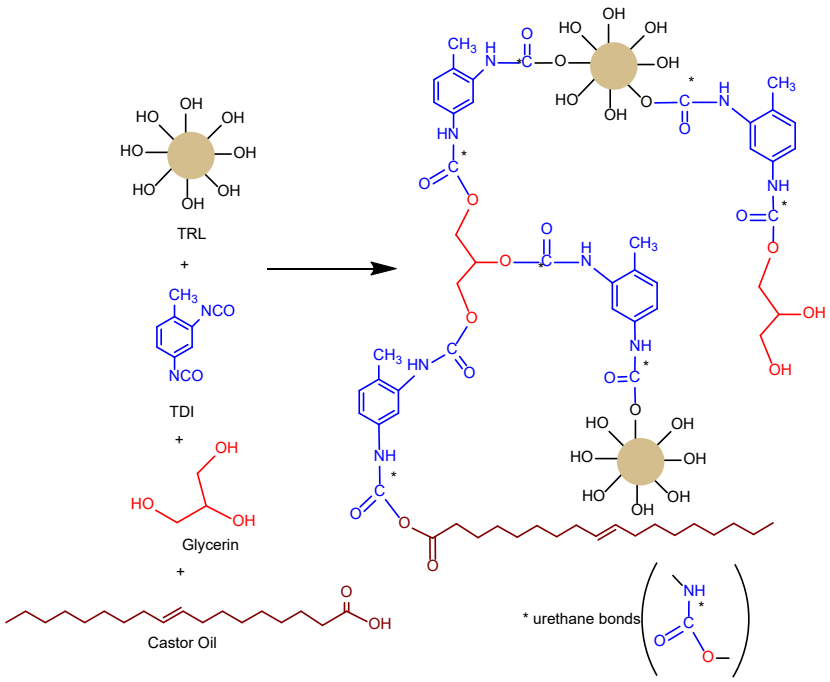

Fig 1. Reaction of polyurethane membrane synthesis

Statistical Design Model

The optimum conditions for synthesizing polyurethane membranes were determined using Box-Behnken Design in Software Design Expert Version 10.0.3.0 with three factors (x) in three levels. This led to 17 runs, as shown in Table 2. The quadratic model design was chosen in this study because it produced high R^2 values and low PRESS values for the response to physical characteristics compared to the 2FI, linear, and cubic models. The greater the R^2 value, the higher the contribution or role of the factor (x) to the response (y). With the value of R^2 above 70%, it is considered to be good enough [20]. Although the cubic model has a high R^2 value, it does not have a Pred-R^2 and a PRESS value. Therefore, the effect of each variable with a different signal is not controlled. The statistical design and variance analysis of the polyurethane membrane synthesis model are shown in Tables 5 and 6, respectively.

Pred R-Squared and Adj R-Squared values are 0.6694 and 0.8489, with a reasonable difference of 0.18, which is less than the expected difference of 0.2. The Adeq Precision value is the signal to noise ratio, which is greater than 4, with a ratio of 10.520, in the quadratic model, which indicates an adequate signal. Therefore, this model can be used to navigate spatial design [24,26-27]. The Model F value is 10.99, and Prob > F less than 0.0500 indicates that the model is significant. The significant factors to the polyurethane membrane characteristics are B, C, BC, and B2, with a p-value less than 0.0500 and greater than 0.100, thereby indicating that the model is insignificant. Furthermore, the insignificance of the F-value of lack of fit at 0.42 and a p-value of 75.10% indicates that the quadratic design model is suitable for

Table 3. Point physical characteristics of polyurethane membranes

No	Physical characteristics	Point
1	Crushed or shapeless	1
2	Brittle or crumbles easily	2
3	Not elastic and breaks easily	3
4	Not elastic and does not break easily	4
5	Elastic and easy to tear	5
6	Elastic does not tear easily	6
7	Elastic and strong	7
8	Stiff and easy to tear	8
9	Stiff and not easily tear	9
10	Rigid and hard	10

Table 4. The physical characteristics results of the polyurethane membrane

Run	Factor 1 A:TRL (g)	Factor 2 B: TDI (g)	Factor 3 C: Glycerin (g)	Response Physical (Point)
1	0.2	3.0	0.4	8
2	0.2	2.5	0.3	7
3	0.3	2.5	0.4	8
4	0.2	2.0	0.2	5
5	0.2	3.0	0.2	5
6	0.1	2.5	0.4	7
7	0.2	2.5	0.3	7
8	0.1	2.0	0.3	5
9	0.3	2.0	0.3	5
10	0.1	2.5	0.2	6
11	0.3	2.5	0.2	6
12	0.2	2.5	0.3	7
13	0.2	2.0	0.4	6
14	0.3	3.0	0.3	7
15	0.2	2.5	0.3	6
16	0.2	2.5	0.3	7
17	0.1	3.0	0.3	6

Table 5. Statistical design model of polyurethane membrane synthesis

Source	Linear	2FI	Quadratic	Cubic
Std.Dev	0.69	0.68	0.39	0.45
R-Square	0.6139	0.7083	0.9339	0.9496
Adj R-Square	0.5248	0.5333	0.8489	0.7985
Pred R-Square	0.3010	-0.0444	0.6694	N/A
Adeq Precision	9.005	6.869	10.520	7.671
PRESS	11.10	16.59	5.25	N/A

Table 6. ANOVA analysis for a quadratic model of the physical characteristics of a polyurethane membrane

Source	Sum of Squares	df	Mean Square	F Value	p-value Prob > F	Characterization
Model	14.83	9	1.65	10.99	0.0023	significant
A-TRL	0.50	1	0.50	3.33	0.1106	
B-TDI	3.13	1	3.13	20.83	0.0026	
C-Glycerin	6.13	1	6.13	40.83	0.0004	
AB	0.25	1	0.25	1.67	0.2377	
AC	0.25	1	0.25	1.67	0.2377	
BC	1.00	1	1.00	6.67	0.0364	
A^2	0.095	1	0.095	0.63	0.4529	
B^2	3.41	1	3.41	22.74	0.0020	
C^2	0.042	1	0.042	0.28	0.6126	
Residual	1.05	7	0.15			
Lack of Fit	0.25	3	0.083	0.42	0.7510	not significant
Pure Error	0.80	4	0.20			
Cor Total	15.88	16				

data analysis of physical characteristics [28]. The relationship between the polyurethane membrane's physical characteristics and the factor (x) based on the coefficient value is seen in Eq. (1) and the 3D plot in Fig. 2.

$$y = 6.80 + 0.25(A) + 0.63(B) + 0.88(C) + 0.25(AB) + 0.25(AC) + 0.50(BC) - 0.15(A)^2 - 0.90(B)^2 + 0.100(C)^2 \quad (1)$$

Polyurethane Membrane Optimization

The optimization results using the Response Surface Methodology with Box-Behnken Design provide five solutions of polyurethane membrane composition from seaweed flour, as shown in Table 7. These five solutions can be used as a reference for the production of polyurethane membranes because they have a Desirability value of 1.0 [29]. The optimization results using the Response Surface Methodology resulted in a predictive physical value of 6.5 with strong and elastic physical characteristics. The experimental results of the optimal composition show the physical values 6 and 7, the results of the predictions and experiments show the appropriate results.

Optimal Polyurethane Membrane Characterization

The FTIR spectrum results in Fig. 3 show the formation of the urethane bonds on the polyurethane membrane, indicated by the absorption attributable to the –NH bond at the wavenumber of1583 and 3348 cm^{-1}. It is also supported by the vibration of the –C=O bond at the wavenumber of 1726 cm^{-1} with an intensity of 63.56%, –CN amine at the wavenumber of 1249 cm^{-1} with an intensity of 63.38%, as well as –CH alkane the wavenumber 2931 cm^{-1} with an intensity of 66.29%. In addition, the weakening of the –NCO uptake of toluene diisocyanate was also observed at the wavenumber 2265 cm^{-1} [30].

Thermal analysis is an important parameter used to determine the membrane's stability against temperature

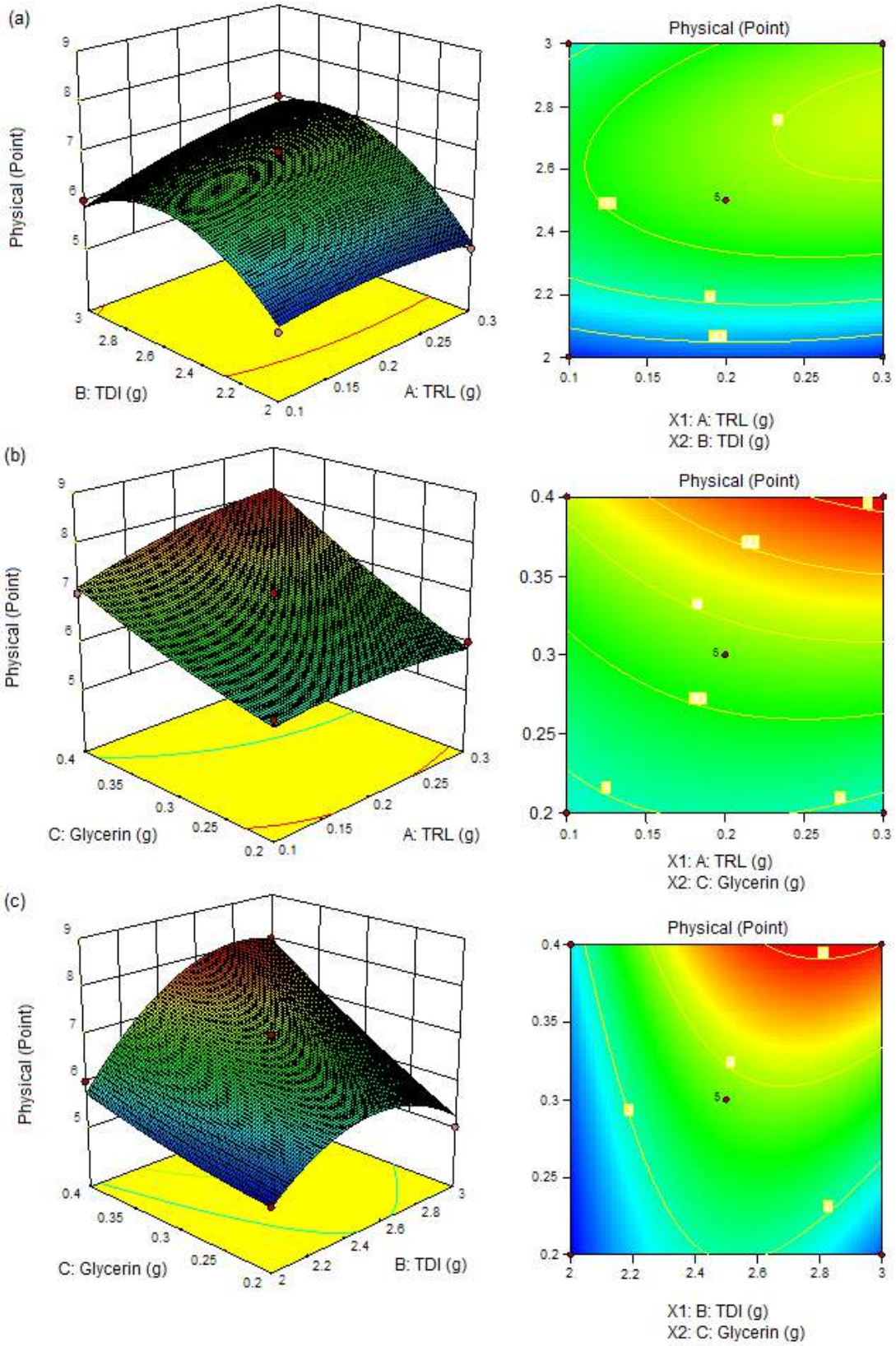

Fig 2. 3D plot and surface plot of the relationship between (a) TRL and TDI to Physical, (b) TRL and Glycerin to Physical (c) TDI and Glycerin to Physical

Table 7. Optimal compositional solution for polyurethane membrane synthesis

No	TRL (g)	TDI (g)	Glycerin (g)	Physical (point) Predictions	Physical (point) Experiment	Desirability
1	0.233	2.675	0.254	6.5	7	1.0
2	0.218	2.546	0.257	6.5	6	1.0
3	0.136	2.849	0.304	6.5	-	1.0
4	0.281	2.197	0.352	6.5	-	1.0
5	0.192	2.156	0.394	6.5	-	1.0

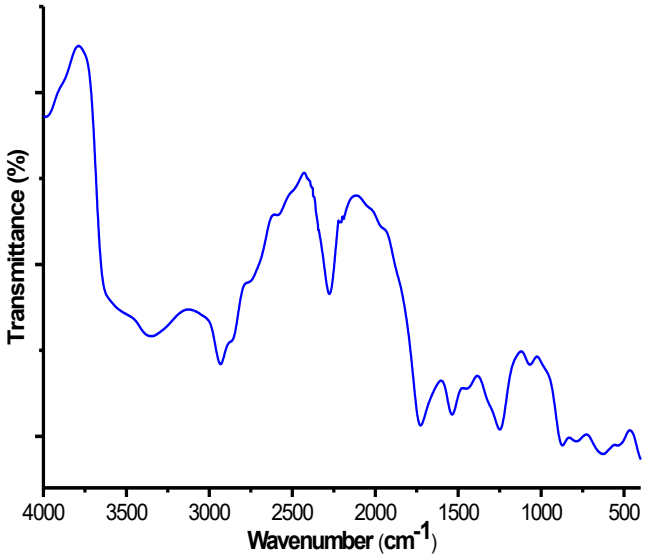

Fig 3. Optimal FTIR spectrum of polyurethane membranes

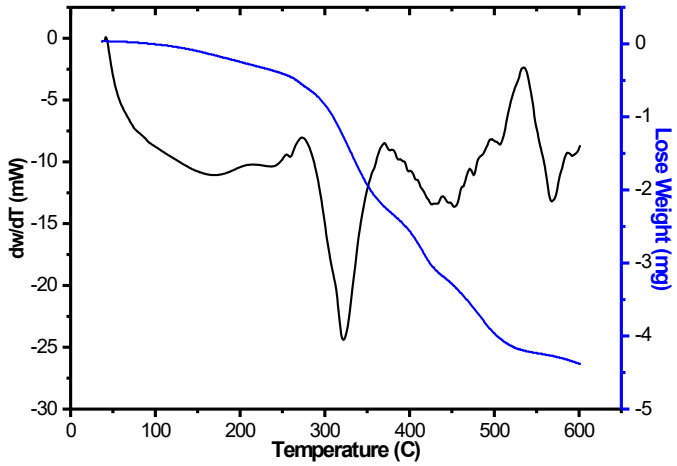

Fig 4. Optimal DSC thermogram and TGA polyurethane membrane

during storage and usage. The DSC thermogram (Fig. 4) shows that the optimal polyurethane membrane has a T_g of 58 °C, T_m of 322 °C, and T_d of 534 °C, while the polyurethane membranes have T_m and T_d values. This high level is caused by the strong urethane bonds and cross-links that form crystal segments or regularities in the hard segments [1,18]. The polyurethane membrane from carrageenan has a T_g of 243 °C and T_m of 423 °C. The difference in value is due to the difference in the base material used and the polymerization conditions [13]. The TGA thermogram shows the change in sample weight to the optimal temperature rise of the polyurethane membrane at an initial degradation temperature ranging from 105.24 to 267.48 °C for water evaporation and cellulose determination. The weakest units in the macromolecular structure of the next degradation temperature are in the range of 267.48–423.17 °C, which is the degradation of urea and urethane bonds from hard segments and other aliphatic bonds. The final degradation value above 423.17 °C is the remaining structures [25,31-33] with a residue of 11.7%.

The SEM results of the optimal polyurethane membrane can be seen in Fig. 5. There is a gap on the inside of the membrane formed from the urethane bonds. The polyurethane membrane produced in this study is

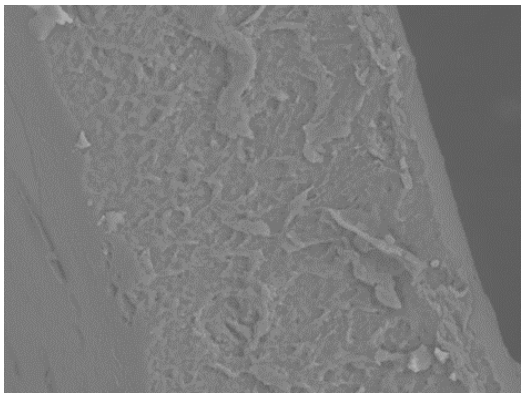

Fig 5. Cross-section of optimal polyurethane membrane

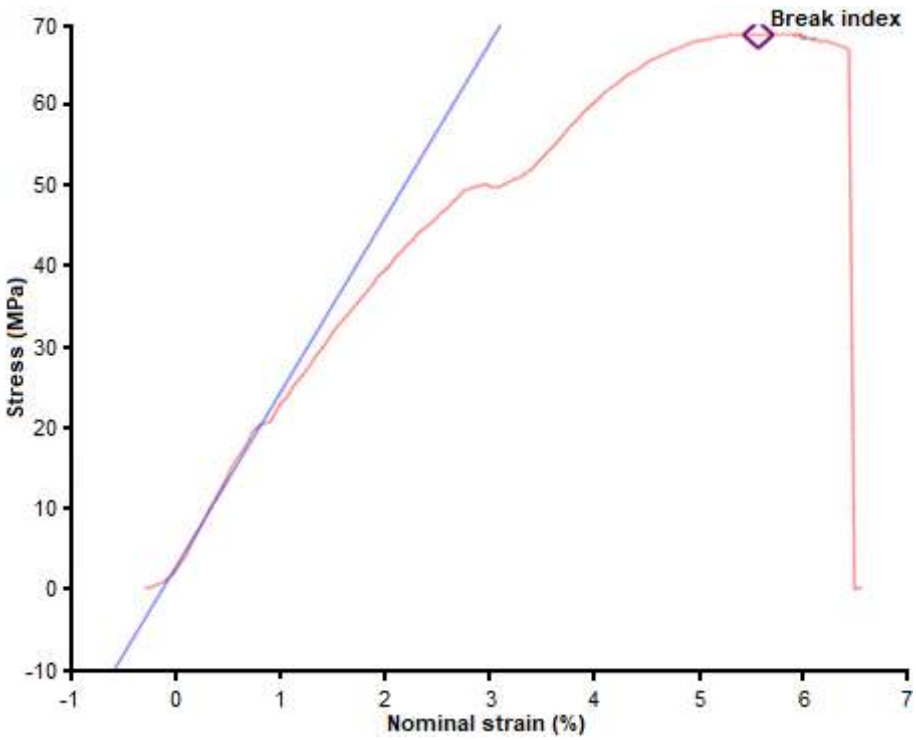

Fig 6. Optimal polyurethane membrane tensile strength curve

applied to the ammonia adsorption and filtration processes. In future studies, it needs to have good mechanical properties with the ability to withstand water pressure. The optimal polyurethane membrane's mechanical properties are good, with a stress value of 69.3 MPa and a nominal strain of 5.74%, as shown in Fig. 6. The expected polyurethane membrane has strong mechanical properties, and it is slightly elastic, with the strength of the membrane related to its ability to withstand water pressure. Meanwhile, the elongation or the level of membrane elasticity is related to the strain of pore size, which can affect the adsorption or filtration process of the analyte.

■ CONCLUSION

The polyurethane membrane's optimal physical characteristics made from red seaweed were obtained at a composition of 0.233 g TRL, 2.675 g TDI, and 0.254 g glycerin with a physical point of 6.5 (strong and elastic). Optimal polyurethane membrane has good thermal and mechanical properties, with a value of T_g of 58 °C, T_m of 322 °C, T_d of 534 °C, a stress value of 69.3 MPa, and a nominal strain of 5.74%. The polyurethane membrane synthesized from red seaweed has good physical characteristics. The results of this study are the basis for the development of polyurethane membrane applications from red seaweed.

■ ACKNOWLEDGMENTS

The authors are grateful to the Universitas Syiah Kuala and Universitas Serambi Mekkah for supporting and facilitating this research.

■ AUTHOR CONTRIBUTIONS

SN conducted the experiment, S, BG, R, and M supervised and revised the manuscript. All authors agreed to the final version of this manuscript.

■ REFERENCES

[1] Karimi, M.B., Khanbabaei, G., Mir, G., and Sadeghi, G.M.M., 2017, Vegetable oil-based polyurethane membrane for gas separation, *J. Membr. Sci.*, 527, 198–206.

[2] Hao, S., Jia, Z., Wen, J., Li, S., Peng, W., Huang, R., and Xu, X., 2021, Progress in adsorptive membranes for separation – A review, *Sep. Purif. Technol.*, 255,

117772.

[3] Kyllönen, H.M., Pirkonen, P., and Nyström, M., 2005, Membrane filtration enhanced by ultrasound: A review, *Desalination*, 181 (1-3), 319–335.

[4] Zhao, D.L., Japip, S., Zhang, Y., Weber, M., Maletzko, C., and Chung, T.S., 2020, Emerging thin-film nanocomposite (TFN) membranes for reverse osmosis: A review, *Water Res.*, 173, 115557.

[5] Joshi, M., Adak, B., and Butola, B.S., 2018, Polyurethane nanocomposite based gas barrier films, membranes and coatings: A review on synthesis, characterization and potential applications, *Prog. Mater Sci.*, 97, 230–282.

[6] Ersahin, M.E., Ozgun, H., Dereli, R.K., Ozturk, I., Roest, K., and van Lier, J.B., 2012, A review on dynamic membrane filtration: Materials, applications and future perspectives, *Bioresour. Technol.*, 122, 196–206.

[7] Singh, I., and Mishra, P.K., 2020, Nano-membrane filtration a novel application of nanotechnology for waste water treatment, *Mater. Today: Proc.*, 29, 327–332.

[8] Marlina, Iqhrammullah, M., Saleha, S., Fathurrahmi, Maulina, F.P., and Idroes, R., 2020, Polyurethane film prepared from ball-milled algal polyol particle and activated carbon filler for NH_3–N removal, *Heliyon*, 6 (8), e04590.

[9] Howard, G.T., 2002, Biodegradation of polyurethane: A review, *Int. Biodeterior. Biodegrad.*, 49 (4), 245–252.

[10] Nurman, S., Marlina, Saiful, and Saleha, S., 2015, Sintesis dan karakterisasi membran poliuretan dari minyak biji karet dan heksametilen-1,6-diisosianat, *JRKL*, 10 (4), 188–195.

[11] Matavos-Aramyan, S., Jazebizadeh, M.H., and Babaei, S., 2020, Investigating CO_2, O_2 and N_2 permeation properties of two new types of nanocomposite membranes: Polyurethane/silica and polyesterurethane/silica, *Nano-Struct. Nano-Objects*, 21, 100414.

[12] Zhang, X.D., Macosko, C.W., and Davis, H.T., 1997, Effect of silicone surfactant on air flow of flexible polyurethane foams, *ACS Symp. Ser.*, 669, 130–142.

[13] Marlina, 2010, Sintesis membran poliuretan dari karagenan dan 2,4 toylulene diisosianat, *JRKL*, 7 (3) 138–148.

[14] Sedayu, B.B., Cran, M.J., and Bigger, S.W., 2019, A review of property enhancement techniques for carrageenan-based films and coatings, *Carbohydr. Polym.*, 216, 287–302.

[15] Hube, S., Eskafi, M., Hrafnkelsdóttir, K.F., Bjarnadóttir, B., Bjarnadóttir, M.A., Axelsdóttir, S., and Wu, B., 2020, Direct membrane filtration for wastewater treatment and resource recovery: A review, *Sci. Total Environ.*, 710, 136375.

[16] Hoslett, J., Massara, T.M., Malamis, S., Ahmad, D., van den Boogaert, I., Katsou, E., Ahmad, B., Ghazal, H., Simons, S., Wrobel, L., and Jouhara, H., 2018, Surface water filtration using granular media and membranes: A review, *Sci. Total Environ.*, 639, 1268–1282.

[17] Dlamini, D.S., Tesha, J.M., Vilakati, G.D., Mamba, B.B., Mishra, A.K., Thwala, J.M., and Li, J., 2020, A critical review of selected membrane- and powder-based adsorbents for water treatment: Sustainability and effectiveness, *J. Cleaner Prod.*, 277, 123497.

[18] Li, R., and Shan, Z., 2020, Study on structure-induced heat transfer capabilities of waterborne polyurethane membranes, *Colloids Surf., A*, 598, 124879.

[19] Melnig, V., Apostu, M.O., Tura, V., and Ciobanu, C., 2005, Optimization of polyurethane membranes: Morphology and structure studies, *J. Membr. Sci.*, 267, 58–67.

[20] Tekindal, M.A., Bayrak, H., Ozkaya, B., and Genc, Y., 2012, Box-Behnken experimental design in factorial experiments: The importance of bread for nutrition and health, *Turk. J. Field Crops*, 17 (2), 115–123.

[21] Khajeh, M., and Gharan, M., 2014, Separation of organic acid compounds from biological samples by zinc oxide nanoparticles–chitosan using genetic algorithm based on response surface methodology and artificial neural network, *J. Chemom.*, 28 (7), 539–547.

[22] Myers, R.H., Montgomery, D.C., and Anderson-Cook, C.M., 2002, *Response Surface Methodology: Process and Product Optimization Using Designed Experiments*, 2nd Ed., John Wiley & Sons, Inc., New York, USA.

[23] Khajeh, M., Kaykhaii, M., and Sharafi, A., 2013, Application of PSO-artificial neural network and response surface methodology for removal of methylene blue using silver nanoparticles from water samples, *J. Ind. Eng. Chem.*, 19 (5), 1624–1630.

[24] Khajeh, M., Moghaddam, M.G., Danesh, A.Z., and Khajeh, B., 2015, Response surface modeling of betulinic acid pre-concentration from medicinal plant samples by miniaturized homogenous liquid-liquid extraction and its determination by high performance liquid chromatography, *Arabian J. Chem.*, 8 (3), 400–406.

[25] Das, B., Konwar, U., Mandal, M., and Karak, N., 2013, Sunflower oil based biodegradable hyperbranched polyurethane as a thin film material, *Ind. Crops Prod.*, 44, 396–404.

[26] Chelladurai, S.J.S., Murugan, K., Ray, A.P., Upadhyaya, M., Narasimharaj, V., and Gnanasekaran, S., 2021, Optimization of process parameters using response surface methodology: A review, *Mater. Today: Proc.*, 37 (2), 1310–1304.

[27] Khajeh, M., Sarafraz-Yazdi, A., and Moghadam, A.F., 2017, Modeling of solid-phase tea waste extraction for the removal of manganese and cobalt from water samples by using PSO-artificial neural network and response surface methodology, *Arabian J. Chem.*, 10 (Suppl. 2), S1663–S1673.

[28] Mäkelä, M., 2017, Experimental design and response surface methodology in energy applications: A tutorial review, *Energy Convers. Manage.*, 151, 630–640.

[29] Zhao, Z., Cuéllar-Bermúdez, S., Ilyas, A., Muylaert, K., and Vankelecom, I.F.J., 2020, Optimization of negatively charged polysulfone membranes for concentration and purification of extracellular polysaccharides from *Arthrospira platensis* using the response surface methodology, *Sep. Purif. Technol.*, 252, 117385.

[30] Zhang, F., Liu, W., Liang, L., Liu, C., Wang, S., Shi, H., Xie, Y., Yang, M., and Pi, K., 2020, Applications of hydrophobic α,ω-bis(amino)-terminated polydimethylsiloxane-graphene oxide in enhancement of anti-corrosion ability of waterborne polyurethane, *Colloids Surf., A*, 600, 124981.

[31] Marlina, Saiful, Saleha, S., and Nurman, S., 2017, 2017, Synthesis and characterization new polyurethane membrane from hydroxylated rubber seed oil, *Orient. J. Chem.*, 33 (1), 199–206.

[32] Ghadimi, A., Gharibi, R., Yeganeh, H., and Sadatnia, B., 2019, Ionic liquid tethered PEG-based polyurethane-siloxane membranes for efficient CO_2/CH_4 separation, *Mater. Sci. Eng. C*, 102, 524–535.

[33] Wu, J., Wang, C., Xiao, Y., Mu, C., and Lin, W., 2020, Fabrication of water-resistance and durable antimicrobial adhesion polyurethane coating containing weakly amphiphilic poly(isobornyl acrylate) side chains, *Prog. Org. Coat.*, 147, 105812.

The Effect of Temperature, Sulfonation, and PEG Addition on Physicochemical Characteristics of PVDF Membranes and Its Application on Hemodialysis Membrane

Retno Ariadi Lusiana[1*], Ayub Indra[1], Nor Basid Adiwibawa Prasetya[1], Nurwarrohman Andre Sasongko[1], Parsaoran Siahaan[1], Choiril Azmiyawati[1], Nanik Wijayanti[2], Anugrah Ricky Wijaya[3], and Mohd Hafiz Dzarfan Othman[4]

[1]*Department of Chemistry, Faculty of Sciences and Mathematics, Diponegoro University, Jl. Prof. H. Soedarto, S.H., Tembalang, Semarang 50275, Indonesia*

[2]*Department of Chemistry, Faculty of Mathematics and Natural Sciences, Semarang State University, Kampus Sekaran, Gunungpati, Semarang 50229, Indonesia*

[3]*Department of Chemistry, Faculty of Mathematics and Natural Sciences, Universitas Negeri Malang, Jl. Semarang No. 5 Malang 65145, East Java, Indonesia*

[4]*Advanced Membrane Technology Research Centre (AMTEC), Faculty of Chemical and Energy Engineering, Universiti Teknologi Malaysia, 81310 Skudai, Johor, Malaysia*

* ***Corresponding author:***

email: retnolusiana@live.undip.ac.id

Received: February 10, 2021
Accepted: June 23, 2021

DOI: 10.22146/ijc.63740

Abstract: *Polyvinylidene fluoride (PVDF) membrane and its derivative have been investigated the permeation ability for creatinine and urea. The membrane was made by an inversion precipitation system in* N,N*-dimethyl acetamide (DMAc) and water as non-solvents. In this study, the modification of PVDF membrane permeability with PEG additives, CBT variations, and sulfonation was successfully carried out. The membrane solidification process was carried out on three variations of the coagulation bath temperature (CBT): 30, 45, and 60 °C. Eight types of membranes were characterized by using FT-IR and TGA/DSC, followed by the analysis of their porosity, hydrophilicity, water uptake, swelling degree, tensile strength, and permeability of creatinine and urea. The FT-IR spectra indicate that PVDF modification has been successfully carried out. The porosity, hydrophilicity, water uptake, and swelling degree values increase with the modification of functional groups. Furthermore, improvements in creatinine and urea permeability and clearances are achieved by increasing CBT and sulfonation in the PVDF/PEG membrane. The presence of sulfonate groups improves the membrane permeability through the interaction of intermolecular hydrogen with water and dialysate compounds. The existence of PEG as a porogen enhanced membrane porosity. Creatinine and urea clearance values increase from 0.29–0.58 and 6.38–20.63 mg/dL, respectively.*

Keywords: *PVDF membrane; inversion phase; CBT; physicochemical; permeation*

■ INTRODUCTION

In recent years, many people suffer chronic kidney disease. One of the methods to help the patient is the hemodialysis process. Currently, Membrane has been widely used as hemodialysis process to treat the patient who suffers a chronic kidney disease [1]. The membrane is a semipermeable thin layer that separates two phases (donor and acceptor). Typically, membranes are made from polymers such as polysulfone (PSF), polyethersulfone (PES), and PVDF, which have good hydrolytic stability, thermal stability, easy to generate, and permeable [2]. However, the permeability and biocompatibility of those materials must be enhanced to get the optimum separation [3].

The ideal hemodialysis membrane has a non-absorbent character protein or cells, but can be permeable

to toxins in the blood, has high mechanical strength and stability in water, and biocompatible. A balance between hydrophilicity and hydrophobicity on the membrane surface dramatically influences the character membrane [4]. PVDF has been widely used as a membrane material due to advantages such as good mechanical strength, high thermal and chemical stability, anti-ultraviolet radiation, smooth surface, and no protein adsorption [5]. However, PVDF has several weaknesses: hydrophobic, low porosity, and less function group [6]. Therefore, it is crucial to enhance the character of PVDF membranes.

Zhang et al. studied the effect of PEG content on PVDF hollow fiber membranes [7]. The increasing PEG content in the membrane increases the porosity, hydrophilicity, tensile strength, and flux values. A study on the effect of coagulation bath temperature (CBT) for PVDF membranes suggested that the membrane with the highest thickness and porosity could be obtained at the temperature of 60 °C [8]. Zhang et al. had created PVDF/PEG hollow fiber membranes in various CBT: 15, 30, 45, and 60 °C [9]. Furthermore, the increase of CBT showed that the membrane has better elongation, porosity, and permeability [9]. In 2014, Fadaei et al. investigated the effect of PEG concentration and CBT variations (25 and 60 °C) on the properties of the PVDF membrane. The increase in PEG and the CBT had enhanced porosity and flux values [10].

On the other hand, non-covalent interactions such as hydrogen bonds play a crucial role in many chemical processes to control the molecular structure, even mass transfer in the case of hemodialysis [2]. One way to enhance the functional group for PVDF membrane is the sulfonation process, giving an SO_3H cluster in the PVDF structure. Furthermore, the sulfonation group helps the membrane make hydrogen bond interaction and improves hydrophilicity and mechanical strength [2,11]. This study aims to modify PVDF through the addition of PEG, sulfonation, and CBT variations in membrane manufacture. The addition of PEG and sulfonation has been known to increase porosity and membrane hydrophilicity. This is possible since the entry of the –OH and $–SO_4$ groups is quite reactive into the PVDF backbone chain. Thus, water as a non-solvent is easy to diffuse into the material. CBT variations aim to control pore size in the mechanism of membrane formation. The pore size of the membrane determines the porosity, and the porosity, together with the hydrophilicity of membranes, could be adjusted to improve the membrane permeability.

■ EXPERIMENTAL SECTION

Materials

Polyvinylidene fluoride (PVDF, Mw = 60,000 g/mol), polyethylene glycol (PEG, Mw = 4,000 g/mol), *N,N*-Dimethyl Acetamide (DMAc), sulfuric acid (95–97%, Mw = 98.079 g/mol), sodium hydroxide (Mw = 39.997 g/mol), creatinine (Mw = 113 g/mol), urea (Mw = 60 g/mol), picric acid (Mw = 229.1 g/mol), 4-dimetylamine benzaldehyde (4-DAB) (Mw = 149.19 g/mol), and ethanol (96%) were purchased from Merck and without purification before being used.

Instrumentation

The functional groups of the membrane were determined using an FT-IR spectrophotometer (Perkin Elmer). Thermal stability membranes were analyzed using TGA Hitachi STA200RV instruments. The surface morphology and cross-section of the PVDF membrane were examined using scanning electron spectroscopy SEM of a JEOL JSM-6510LA instrument. Membrane hydrophilicity was measured by the sessile drop (OCA 25). Mechanical strength of membranes was measured using a tensile strength analyzer. The concentration of the transport sample was measured with a UV-Visible spectrophotometer at wavelengths of 486 nm for creatinine and 430 nm for urea.

Procedure

Membrane preparation

The membrane was prepared by the phase inversion method, with DMAc as a solvent and water as a non-solvent. Before being used, the PVDF crystals were dried at 100 °C for 1 h. The membrane composition is summarized in Table 1. For membranes with the addition of PEG without sulfonation, the PEG powder was first dissolved in the DMAc solvent, followed by the addition of PVDF powder. To prepare the sulfonated membranes,

Table 1. Dope solution composition and CBT condition of prepared membrane

Membrane Code	PVDF (g)	PEG (g)	DMAc (g)	H_2SO_4 (mL)	CBT (°C)
P	3.75	0	21.25	0	30
SP	3.75	0	21.25	1	30
PP30	3.75	0.75	20.125	0	30
PP45	3.75	0.75	20.125	0	45
PP60	3.75	0.75	20.125	0	60
SPP30	3.75	0.75	20.125	1	30
SPP45	3.75	0.75	20.125	1	45
SPP60	3.75	0.75	20.125	1	60

a concentrated H_2SO_4 and catalyst were put into the DMAc solvent. Then, the dried PVDF crystals were poured into a homogeneous mixture for 4 h, followed by the addition of PEG additive powder. Next, all components were mixed in a dope solution at 60 °C until the solution was homogeneous and formed a suspension for a total of 6 h.

Furthermore, the dope solution was homogenized by ultrasonication for 15 min at 60 °C. The casting process was then carried out on a glass plate and soaked in a coagulant tub filled with water to form a thin film. Next, the membrane sheet was washed several times and then soaked for 24 h to vaporize the remaining solvent. Finally, the membrane was dried and stored for further research.

FTIR analysis

Analysis of functional groups membrane was conducted by using FT-IR spectrophotometer (Perkin Elmer). The thin membrane sheet was placed in the sample holder and measured at wavenumbers of 700–4000 cm^{-1}.

TGA/DSC analysis

The temperature was set in the temperature range of 30–900 °C with a heating rate of 5 °C/min. The membranes with a weight of 1.9–3.2 mg were placed in an aluminum crucible during heating rate. Thermal degradation is indicated by a decrease in sample weight that is automatically monitored. DSC data were obtained based on energy differences between the sample and the standard.

Morphology studies

The surface morphology and cross-section of the PVDF membrane were examined using EDX, installed in environmental SEM using the JEOL JSM-6510LA instrument. Thin membrane sheets were cut and glued to the sample holder, coated using platinum metal, then observed at an energy of 20 kV, with 1,000 and 1,500 magnification.

Porosity measurement of membrane

The membrane sample (0.022 g) was immersed in 10 mL of distilled water for 24 h, coated with tissue to absorb water on the surface of the membrane, and weighed as the initial wet weight of the membrane (Ww (g)). Furthermore, the membrane was dried in an oven with a temperature of 100 °C for 6 h, cooled, and re-weighed to measure the Wd (g) as the dry weight of the membrane. All steps are conducted in three repetitions. Percentage of membrane porosity was calculated through Eq. (1), where ρp = polymer density (1.78 g/cm^3); and ρw = water density (1.0 g/cm^3) [1].

$$\varepsilon = \frac{Ww - Wd/\rho w}{(Ww - Wd/\rho w) + Wd/\rho p} \times 100\% \quad (1)$$

Hydrophilicity (Water contact angle)

Membrane hydrophilicity was measured by the sessile drop method, which illustrates the membrane's ability to absorb water that drips on its surface. Contact angles are formed between water droplets and membranes. Low contact angle values indicate the membrane has hydrophilic properties.

Water uptake (WU) and swelling degree (SD)

Water absorption is an important property on membranes to describe the membrane hydrophilicity and hydrophobicity associated with the degree of membrane porosity. To determine the WU and SD,

0.022 g of the membrane was immersed in water for 24 h and measured by weight and diameter both before and after immersion. The percentage values of WU and SD were calculated using Eq. (2) and (3), respectively. Wt represents the membrane weight after immersion (g), while Wo was membrane weight before immersion (g). I_o and I_t represent the diameter before and after immersion (in cm), respectively.

$$WU = \frac{Wt - Wo}{Wo} \times 100\% \quad (2)$$

$$SD = \frac{It}{Io} \times 100\% \quad (3)$$

Tensile strength

Mechanical strength is one of the critical aspects of membrane dialysis. The 15 × 3 cm of the synthesized membrane was immersed in distilled water until it expands, then pulled in a specific force until the membrane is broken (Tensile Strength Analyzer). Tensile strength was determined by the maximum load when the membrane was stretched with a certain force until it is torn, and the percentage of its elongation is based on the elongation of the membrane when it breaks. The tensile strength and percent elongation can be calculated using Eq. (4) and (5), where F represents the tensile strength (N), A represents membrane cross-sectional area (mm^2), while a and b are the initial membrane length (mm) and after breaking up (mm), respectively.

$$\text{Tensile strength(MPa)} = \frac{F}{A} \quad (4)$$

$$\text{Elongation at break} = \frac{b - a}{a} \times 100\% \quad (5)$$

Membrane permeability

Membrane permeability was measured to know the ability of the membrane in transporting creatinine and urea. Permeation test was carried out using a set of tools with a membrane placed in the middle that separates the donor and acceptor parts. The source was filled with creatinine 1.5 mg/dL and urea 50 mg/dL as much as 50 mL in phosphate buffer media. The acceptor was filled with 50 mL phosphate buffer. The transport process was carried out for 6 h at room temperature. Every 1 h, 2 mL samples are taken from the source phase and the acceptor. The sample was complexed with picric acid for creatinine and 4-DAB for urea. It was then measured for its absorbance with a UV-Visible spectrophotometer at 486 nm (creatinine) and 430 nm (urea). The permeability of the membrane to the solute (clearance) is calculated by Eq. (6), where Co and Ct are the concentration of the source solution at t = 0 and t = 6 h.

$$\text{Clearance} = Co - Ct \quad (6)$$

■ RESULTS AND DISCUSSION

Membrane Characterization

Functional groups

The interactions between PVDF with sulfuric acid and chitosan derivatives were performed using FT-IR. The success of the synthesis and modification processes for PVDF can be assessed from the suitability of the resulting functional groups. The FTIR spectra showed changes in the chemical composition of the PVDF membrane before and after the modification Fig. 1. The typical PVDF spectra are presented by the appearance of absorption at 766 cm^{-1} attributed to the bending vibration of $–CF_2$. The absorption at the wavenumbers of 840 and 1374 cm^{-1}, respectively, indicate the stretching and bending vibrations of the $–CH_2$ group. The stretching vibrations of the $–CH_2$ group are observed at 1402 and 2936 cm^{-1}. The symmetrical stretching of the $–CF_2$ group is indicated by the absorption at wavenumbers of 1071 and 1178 cm^{-1}. The asymmetrical stretching vibration of the $–CF_2$ group is observed at 1210 and 1279 cm^{-1}. Furthermore, absorption at 878 cm^{-1} indicates the asymmetrical strain vibrations of the C–C–C group [2]. These data are supported by previous studies [3,12]. There is absorption with a widening peak in an area of about 3400 cm^{-1} which indicates the vibration of the –OH group, which comes from the diffusion of DMAc solvents with water during the solidification process [13]. It can be predicted that the C=O group from the DMAc solvent attracts water molecules; so that there is an intermolecular hydrogen interaction between the O and H atoms. The coagulation process rapidly converts the dope solution into a membrane and causes OH to be trapped in the formed membrane. Sharp peaks in the area of 1739 cm^{-1} on the PVDF, PVDF/PEG, and Sulfonated-PVDF membranes

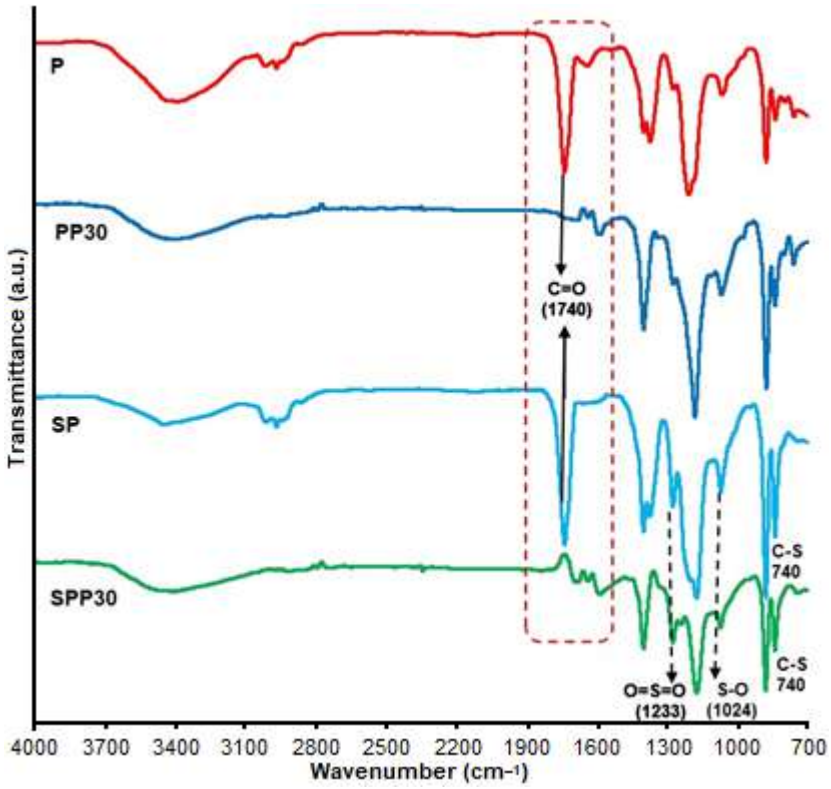

Fig 1. FTIR spectral profiles of (P) PVDF, (PP30) PVDF/PEG, (SP) SPVDF, (SPP30) SPVDF/PEG

show the vibrations of the C=O group originating from the DMAc structure that has not completely evaporated during the membrane solidification process [11].

The addition of PEG in the structure of PVDF causing the emergence of widening absorption at 3440 cm^{-1} associated with the stretching vibration of OH groups originating from PEG [7] that can be seen in the spectra of PVDF/PEG and SPVDF/PEG membranes. The sulfonation process on the PVDF membrane resulted in the presence of O=S=O, which is indicated by the absorption at the wavenumber of 1233 cm^{-1} [14] and symmetrical strain observed at 1040 cm^{-1}. The reaction between PVDF and PEG takes place through the interaction of hydrogen. The electronegative F atoms form dipole interactions with H atoms from the PEG chain. Based on molecular weight stoichiometry calculations, every three PVDF monomers will bind to two PEG monomers. PVDF sulfonation takes place based on the unimolecular electrophilic substitution reaction (SE1) mechanism. The acidic atmosphere in the reaction causes the H atoms in the PVDF to be activated to become H^+ and release. Then a negatively charged carbanion is formed in the PVDF chain, which acts as an intermediate for the reaction. This carbanion formation stage is slow, so it determines the rate of reaction. Furthermore, the negative carbanion group will attack the $–SO_3^-$ group of sulfuric acid that is positively charged at the S atom. Because the reaction takes place in an acidic environment, the –O at the end of the $–SO_3^-$ group can attract free-moving H^+ ions to form a sulfonate ($–SO_3H$) group attached to the carbon atom in the PVDF chain. This stage takes place quickly so that it is not used as a stage determining reaction rate. The pathway of the PVDF modification reaction is presented in Fig. 2.

Thermal stability

TGA provides information related to the degradation of membrane material when the membrane is heated. DSC characterization aims to determine the glass transition temperature (Tg) in various membranes and provide information about the level of hardness and flexibility in the polymer chain. The results of the TGA/DSC test for PVDF membranes before and after

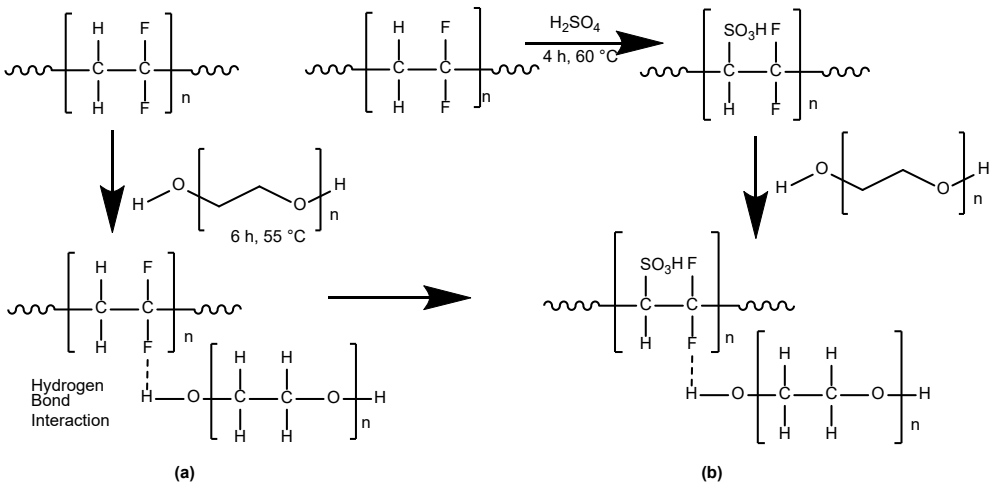

Fig 2. The synthetic pathway of PVDF modification: (a) mixing with PEG and (b) sulfonation reaction

modification are shown in Fig. 3 and Fig. 4. It can be seen that all membranes have thermograms that are similar to each other.

Before experiencing weight loss at the first stage, there was a slight decrease in weight at the temperatures of 150–160 °C by approximately 0.1–0.5%, which is related to the drying of DMAc solvents trapped in the membrane [9]. Weight reduction related to the thermal stability starts in the temperature range 420–470 °C, where the PVDF, PVDF/PEG, and SPVDF membrane decreased by about 61.6, 61.6, and 62.9%, respectively. The membranes are still stable and able to be used at a temperature less than 400 °C. At a temperature higher than 400 °C, the membrane starts to be damaged and melted. The decrease of weight in the temperature range is related to the decomposition process in the main polymer chain. PVDF undergoes CH bond breakdown and shows the presence of hydrogen and fluorine atoms which influence the formation of hydrogen fluoride gas (HF) [15]. The addition of PEG and

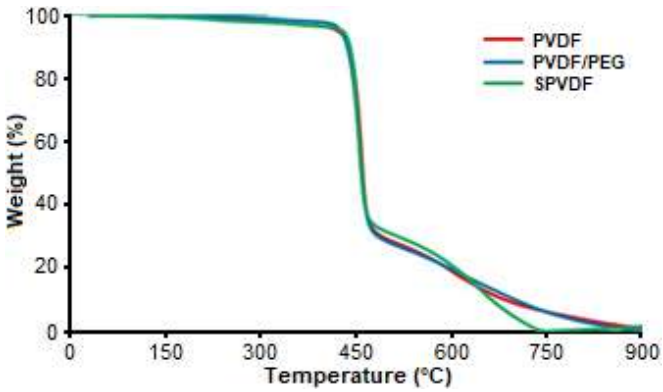

Fig 3. TGA Curve of PVDF and modified PVDF membranes

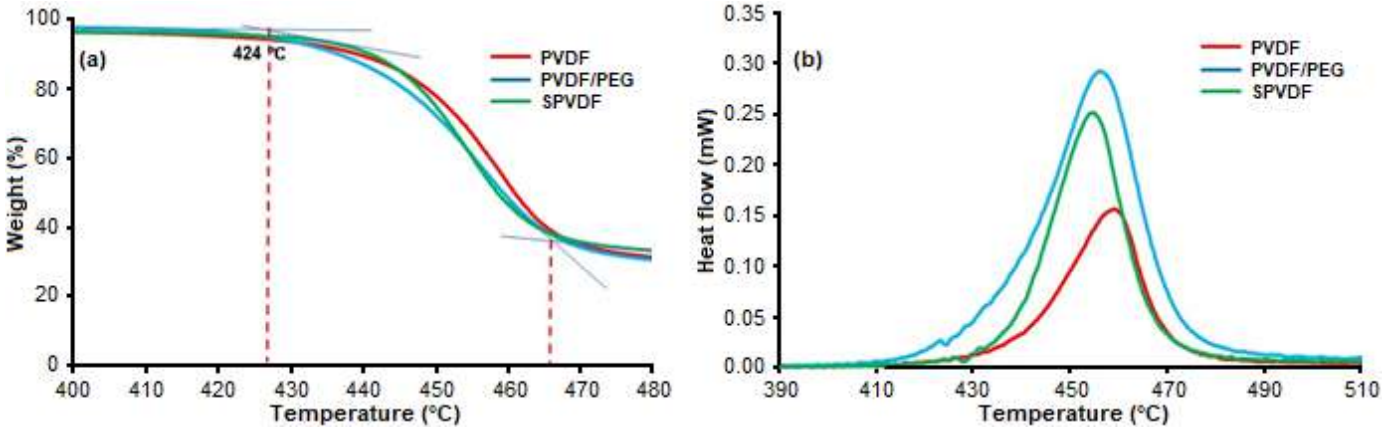

Fig 4. (a) TG curve and (b) DSC curve of PVDF and modified PVDF membranes

sulfonation reactions slightly decrease the thermal stability of the membrane. Meanwhile, the decomposition occurs at a slightly lower temperature compared to pure PVDF membranes. The insertion of ethylene glycol and sulfonate groups causes the conformation of the chain to become softer and the structure to be less orderly, resulting in a decrease in thermal stability [16].

The addition of PEG and sulfonation reactions in the PVDF membrane slightly decreased the thermal stability of the membrane. Exothermic peaks in the temperature range of 400–500 °C indicate that the membrane has melted physically and chemically breaks the bonds in the main polymer chain. The reduction in stability is also related to the membrane structure where the lower Tg is more porous [12]. The entry of the ethylene glycol and sulfate structure into the PVDF binding structure affects the decrease in compacting and crystallinity in the polymer structure, thereby reducing the melting point of the PVDF membrane. The decrease in thermal stability due to the additives is caused by the disruption of hydrogen bonds between the polymer chains of the membrane matrix. The thermal stability of membranes with additives decreases because the additives interfere with hydrogen bonds in the polymer chain. The addition of additive material can reduce thermal stability due to the formation of pores that damage the integrity of the polymer matrix [17].

The TGA/DSC results are similar to the research conducted by H. Farrokhzad et al. and Nasirian et al. [11,18]. Similarly, in this study, PEG was able to enlarge the pore of the membrane. Large pores damage the integrity of the PVDF matrix. Furthermore, the thermal stability of the membrane decreases with the increase of pore size in the membrane. This is caused by the contraction of the polymer chain that occurs in membranes with closer pores.

Morphology properties

The surface morphology and cross-section of the PVDF membrane and its derivatives are shown in Fig. 5 and 6. All membranes have an asymmetrical structure consisting of a dense top layer and a porous sublayer. This is related to the membrane formation mechanism. During the solidification process, there is an interaction between the dope solution (PVDF/NMP) and the non-solvent (water). This meeting causes the immersion of the dope solution into the non-solvent. The NMP solvent penetrates the non-solvent and leaves the polymer solution (dope), and the non-solvent penetrates the polymer solution. This solvent exchange will cause the dope composition to change and then solidify to form a membrane.

The addition of PEG and sulfonation, a hydrophilic functional group, causes the dope solution to be less thermodynamically stable and follows an instantaneous separation mechanism resulting in a membrane with larger pores. In addition, the presence of hydrophilic additives in the dope solution increases the penetration of the non-solvent (water) to the dope solution and consequently an acceleration of the exchange rate between the solvent and non-solvent during the formation of the membrane in the coagulation bath [19]. The rapid exchange between solvent and non-solvent increases the rate of precipitation from the dope solution to the coagulation bath, which facilitates instantaneous separation and the formation of a porous membrane [20].

Increasing the temperature of CBT increases the rate of solvent to non-solvent exchange. As a result, the membrane solidification process takes place rapidly following the instantaneous liquid-liquid demixing

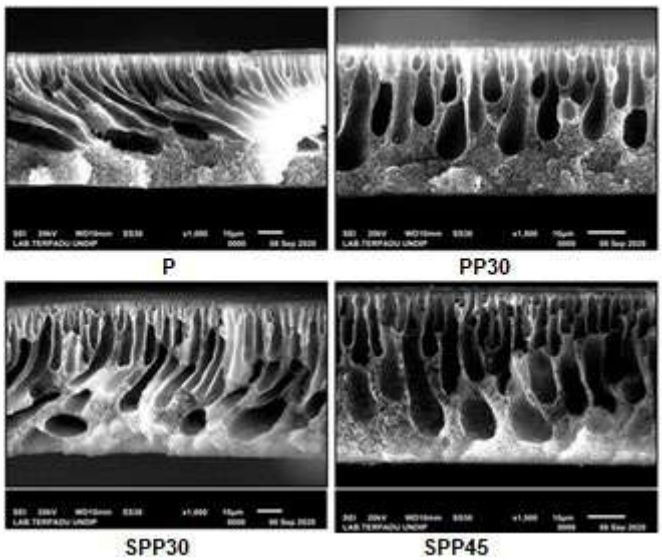

Fig 5. SEM cross-section image of membranes

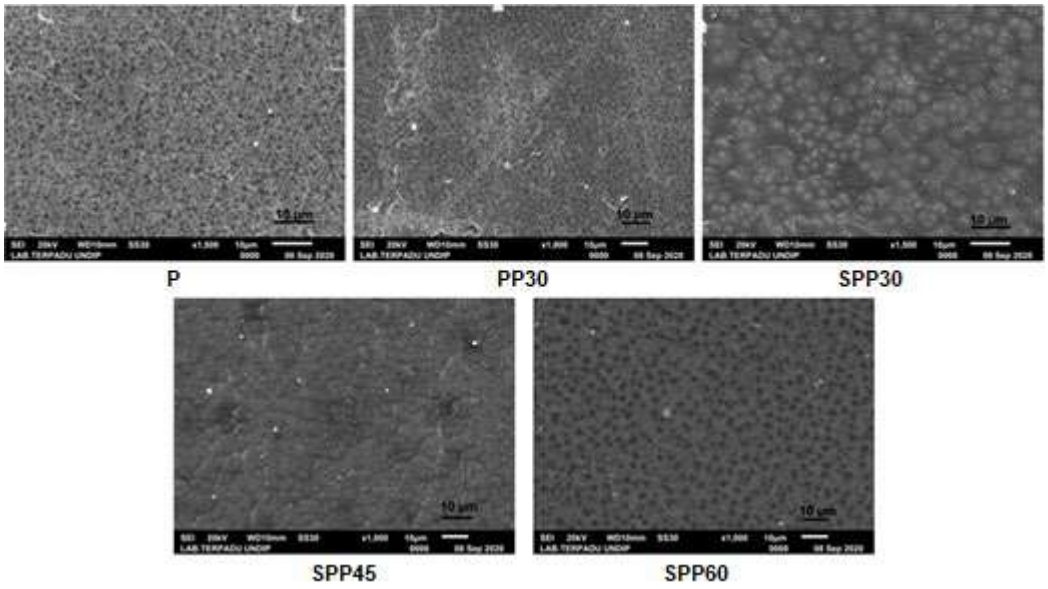

Fig 6. SEM surface image of membranes

mechanism, causing macrovoids growth in the sublayer and thinning in the top-layer membrane (Fig. 5). In general, the formation of macrovoids occurs under the conditions of rapid coagulation at higher temperatures. The effect of increasing CBT temperature is also observed on the membrane surface (Fig. 6). The pore size on the membrane surface increases, and the initially dense membrane structure expands to become wider with increasing temperature in the coagulation bath. The same results were obtained in the research of Zhang et al. [9], Chou et al. [21], and Amirilargani et al. [22] explained that increasing CBT increases diffusion between solvents and non-solvents in the phase inversion process so that the outer surface of the membrane gradually produces more cavities.

Membrane porosity

Modifications to PVDF caused the weight, thickness, and porosity of the membrane to decrease (Table 2). PEG compounds that are partially attached to the surface and pore of the membrane increased the solid content present in the dope solution [23]. Wang et al. explained that the solid phase formed in the coagulation process expands PVDF in the solvent [24]. The casting process makes the solvent evaporating into the air and leaving a shrinking polymer chain network. The coagulation process took place faster at high temperatures, caused fewer solvents evaporation, and decreased a smaller membrane shrinkage ratio. In addition, the fast separation was causing the exchange rate between the solvent and the non-solvent to increase so that the membrane formed becomes thicker. This is due to the outer layer of the membrane having the greatest contact area with the non-solvent. In addition, these phenomena cause the membrane to be thicker [18]. A similar result was also reported by Saljoughi et al. [17], in which the addition of PEG caused the increase of membrane thickness. PEG will fill the formed membrane matrix. Then, the diffusion process occurs between the solvent and the non-solvent. Additives and the solvent will dissolve in the non-solvent cavity to leave pores on the membrane [5]. Increasing CBT can

Table 2. Weight, thickness, and membrane porosity

Membrane Code	Weight (mg)	Thickness (μm)	Porosity (%)
P	7.3	2.54	66.48
SP	12.1	2.86	68.70
PP30	11.8	2.88	63.59
PP45	13.0	3.00	66.43
PP60	15.1	3.16	80.84
SPP30	16.6	3.52	77.04
SPP45	17.3	3.88	79.01
SPP60	19.4	3.94	82.94

increase membrane porosity and cause membranes to have wider pore structures in the upper and lower layers of the membrane. Sulfonation caused an increase of electronegative –OH and O–S=O_2^- groups in the membrane. Note that the functional group is hydrophilic.

The trend of membrane porosity in this research is similar to the work conducted by Zhang et al. in [7], which shows that the increase of porosity caused by the increasing CBT, and the thinning membrane skin structure as well as the widening membrane cellular structure causing the membrane porosity to increase. The increase in CBT produces more cavities on the outer surface of the membrane, which is the effect of PEG as a porogen. A discussion of membrane porosity has been shown in the morphology of the membranes. Membrane porosity refers to the empty space between spaces in the membrane. The high porosity can be interpreted that the membrane has a large empty space and affecting the membrane's ability to retain water increases. Penetration and flow of water will be easier with the increasing membrane porosity [24]. Sulfonation of the membrane can also generate a macrovoid which increases membrane porosity. According to Holda et al. [25], macrovoid growth because the attracting and floating force of the fluid flow during the casting process. Drag force plays a vital role in forming the final pore structure of the asymmetrical membrane. Sulfonation caused stronger polar-polar interactions between dope solutions and coagulants (water). Low drag force in the dope solution makes water easier to flow into the initial macrovoid and grow the macrovoid.

Water contact angle (WCA)

Fig. 7 shows that modification using PEG, sulfonation, and increasing the temperature of CBT decreased the contact angle of the membrane, which means increasing membrane hydrophilicity. When the dope solution is immersed in a coagulant bath in the coagulation process, a small amount of air is trapped in the layer where the solvent meets the non-solvent. Furthermore, this trapped air causes the membrane surface to solidify, resulting in a rough membrane surface. The inclusion of hydrophilic additives such as PEG and sulfates in the dope solution increases the ability to mix

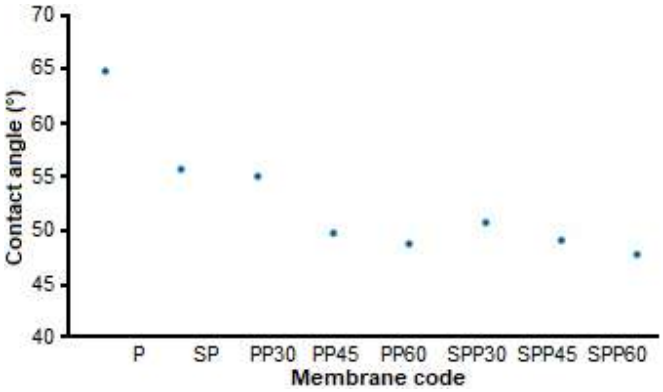

Fig 7. Water contact angle graph of prepared membranes

between polymer and non-solvents in the coagulation process. Additive compounds that can mix with non-solvents in the coagulant bath will immediately diffuse out of the dope solution to produce a solid membrane. As the CBT temperature increases, the solvent diffusion process runs faster, less air is trapped, and the membrane's roughness decreases so that the contact angle decreases [11,22].

The results of the hydrophilicity test and contact angle are in accordance with the research reported by Farrokhzad et al. [11] and Amirilargani et al. [22] that the addition of additives and increasing CBT can increase membrane hydrophilicity and decrease the contact angle of water on the membrane. The larger the macrovoid that is formed causes the water droplets that hit the membrane surface immediately drop into the holes in the macrovoid so that it reduces the water contact angle that occurs on the membrane surface. Based on the concept of polar-polar interactions, sulfonate groups on the membrane affect surface polarity and reduce the contact angle [25]. The increasing polarity on the sulfonated membrane indicates that the adsorption of water on the membrane surface is easier than the adsorption of water on the surface of the pure membrane. In addition, the presence of hydrophilic ionic groups in the PVDF backbone chain increases the hydrophilicity of the membrane surface and consequently decreases the contact angle [2].

Dialysis Performance

In this study, the transport process was carried out

for 6 h with a membrane contact area of 4.96 cm^2. The results of creatinine and urea transport are shown in Fig. 8. Creatinine clearance is increased by twice on the modified PVDF membrane. The clearance of PVDF membrane and SPVDF/PEG-CBT 60 °C are 0.29 mg/dL and 0.58 mg/dL, respectively. Likewise, urea clearance increased from 6.38 mg/dL on pure PVDF membranes to 20.63 mg/dL on the 60 °C SPVDF-PEG-CBT membranes. It can be concluded that the modification of PVDF membrane with PEG, the increasing of CBT, and sulfonation increased the ability of PVDF membrane in the process of creatinine and urea transport.

The PVDF membrane experienced structural changes because of the –OH and $–SO_3^-$ functional groups (Fig. 2). The groups such as –OH and -S=O that bond to the PVDF structure have a functional group with a high electronegativity to help the membrane bind urea and creatinine through hydrogen bonding. In addition, membrane hydrophilicity makes the membrane respond quickly to contact with water as media. According to Amiji [26], membrane permeability for creatinine and urea will increase proportionally with the increase in hydrophilic groups contained in the membrane. On the other hand, the value of membrane porosity also contributes to the membrane permeation ability. A porosity presents a lot of free space in the membrane that can be entered and passed through the donor phase to the acceptor phase. Increasing porosity enhanced the number of open cavities in the membrane. This condition will facilitate the flow of permeate through the membrane. The addition of PEG and the increasing of CBT play an important role in forming wider macrovoid pores. Saljoughi et al. [17] explained that higher CBT intensively increased porosity and resulted in a wider structure in the upper and lower layers of the membrane, thereby increasing membrane permeability. Meanwhile, sulfonation increases the hydrophilic side of the membrane through the addition of the –OH and S=O groups derived from sulfonates [19].

The increase in clearance value and transport percent after modification indicated that modification could increase membrane permeation in carrying out the transport of creatinine and urea molecules. The modification can increase hydrophilicity, porosity, and increase the number of hydrophilic sides on the membrane so that the membrane has a more remarkable ability to transfer dialysate into the acceptor phase. These results were obtained in the transport conditions without the push force. Meanwhile, the dialysis process, which is commonly used in the medical world, such as hemodialysis, is performed using a dialysis machine with a complete set of equipment. So that most patients experience a decrease in creatinine levels by 10–40% and a decrease in urea levels by 30–60% [27]. Based on the mechanical strength, porosity, and permeation ability of toxic compounds like urea and creatinine, it was found that the membrane from the study had a fairly good character [4]. It can be concluded that the modified PVDF membrane in this study has a fairly good ability in dialysis applications for the medical world.

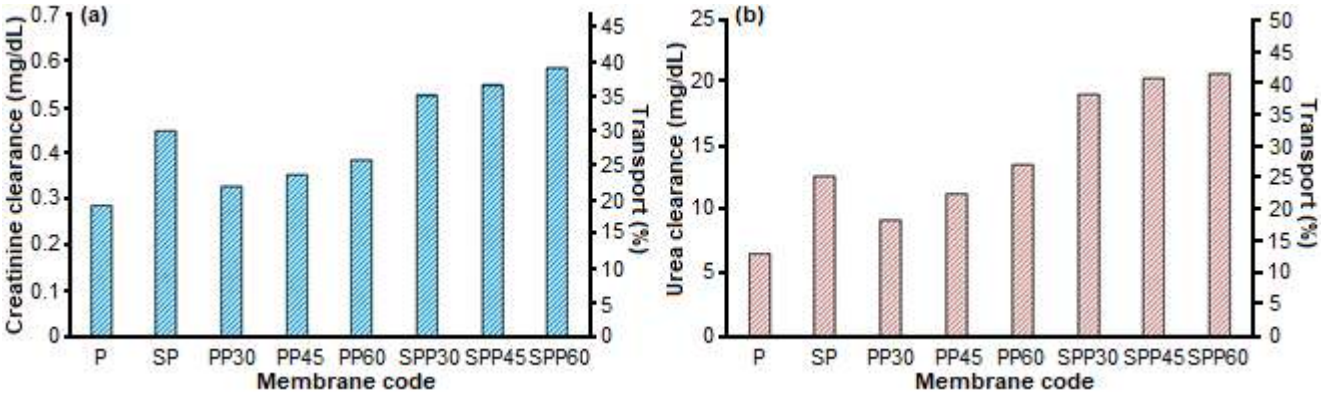

Fig 8. Comparison of permeability membranes towards (a) creatinine (b) urea

CONCLUSION

The modification of PVDF membrane permeability with PEG additives, CBT variations, and sulfonation was successfully carried out. Improvements in creatinine and urea permeability and clearances are achieved by increasing CBT and sulfonation in the PVDF/PEG membrane. The presence of sulfonate groups improves the membrane permeability through the interaction of intermolecular hydrogen with water and dialysate compounds. The existence of PEG as a porogen enhanced membrane porosity. Overall, the results show that the PVDF membrane modified with the addition of PEG, CBT variation, and sulfonation can be promoted as a hemodialysis membrane material.

ACKNOWLEDGMENTS

The author is very thankful to the Directorate General of Higher Education, Government of Indonesia, for the funding through contract number 257-57/UN7.6.1/PP/2020.

REFERENCES

[1] Siahaan, P., Sasongko, N.A., Lusiana, R.A., Prasasty, V.D., and Martoprawiro, M.A., 2021, The Validation of molecular interaction among dimer chitosan with urea and creatinine using density functional theory: In application for hemodialysis membrane, *Int. J. Biol. Macromol.*, 168, 339–349.

[2] Lusiana, R.A., Sangkota, V.D.A., Sasongko, N.A., Gunawan, G., Wijaya, A.R., Santosa, S.J., Siswanta, D., Mudasir, M., Abidin, M.N.Z., Mansur, S., and Othman, M.H.D., 2020, Permeability improvement of polyethersulfone-polyethylene glycol (PEG-PES) flat sheet type membranes by tripolyphosphate-crosslinked chitosan (TPP-CS) coating, *Int. J. Biol. Macromol.*, 152, 633–644.

[3] Afsarian, Z., and Mansourpanah, Y., 2018, Surface and pore modification of tripolyphosphate-crosslinked chitosan/polyethersulfone composite nanofiltration membrane; Characterization and performance evaluation, *Korean J. Chem. Eng.*, 35 (9), 1867–1877.

[4] Kaleekkal, N.J., Thanigaivelan, A., Tarun, M., and Mohan, D., 2015, A functional PES membrane for hemodialysis – Preparation, characterization and biocompatibility, *Chin. J. Chem. Eng.*, 23 (7), 1236–1244.

[5] Matsuda, M., Yamamoto, K., Yakushiji, T., Fukuda, M., Miyasaka, T., and Sakai, K., 2008, Nanotechnological evaluation of protein adsorption on dialysis membrane surface hydrophilized with polyvinylpyrrolidone, *J. Membr. Sci.*, 310 (1), 219–228.

[6] Zhao, X., and Liu, C., 2016, Irreversible fouling control of PVDF ultrafiltration membrane with "fouled surface" for mimetic sewage treatment, *RSC Adv.*, 6 (96), 94184–94192.

[7] Zhang, Q., Lu, X., dan Zhao, L., 2014, Preparation of polyvinylidene fluoride (PVDF) hollow fiber hemodialysis membranes, *Membranes*, 4 (1), 81–95.

[8] Wang, X., Zhang, L., Sun, D., An, Q., and Chen, H., 2008, Effect of coagulation bath temperature on formation mechanism of poly(vinylidene fluoride) membrane, *J. Apply. Polym. Sci.*, 110 (3), 1656–1663.

[9] Zhang, H., Lu, X., Liu, Z., Ma, Z., Wu, S., Li, Z., Kong, X., Liu, J., and Wu, C., 2018, The unidirectional regulatory role of coagulation bath temperature on cross-section radius of the PVDF hollow-fiber membrane, *J. Membr. Sci.*, 550, 9–17.

[10] Fadaei, A., Salimi, A., and Mirzataheri, M, 2014, Structural elucidation of morphology and performance of the PVDF/PEG membrane, *J. Polym. Res.*, 21 (9), 545.

[11] Farrokhzad, H., Kikhavani, T., Monnaie, F., Ashrafizadeh, S.N., Koeckelberghs, G., Van Gerven, T., and Van der Bruggen, B., 2015, Novel composite cation exchange fi lms based on sulfonated PVDF for electromembrane separations, *J. Membr. Sci.*, 474, 167–174.

[12] Nishiyama, T., Sumihara, T., Sato, E., and Horibe, H., 2017, Effect of solvents on the crystal formation of poly (vinylidene fluoride) film prepared by a spin-coating process, *Polym. J.*, 49 (3), 319–325.

[13] Roy, K.J., Anjali, T.V., and Sujith, A., 2017, Asymmetric membranes based on poly(vinyl chloride): Effect of molecular weight of additive and

solvent power on the morphology and performance, *J. Mater. Sci.*, 52 (10), 5708–5725.

[14] Nikooe, N., and Saljoughi, E., 2017, Preparation and characterization of novel PVDF nanofiltration membranes with hydrophilic property for filtration of dye aqueous solution, *Appl. Surf. Sci.*, 413, 41–49.

[15] de Jesus Silva, A.J., Contreras, M.M., Nascimento, C.R., and da Costa, M.F., 2020, Kinetics of thermal degradation and lifetime study of poly(vinylidene fluoride) (PVDF) subjected to bioethanol fuel accelerated aging, *Heliyon*, 6 (7), e04573.

[16] Hu, Y., Yan, L., and Yue, B, 2020, Sulfonation mechanism of polysulfone in concentrated sulfuric acid for proton exchange membrane fuel cell applications, *ACS Omega*, 5 (22), 13219–13223

[17] Saljoughi, Amirilargani, M., and Mohammadi, T., 2010, Effect of PEG additive and coagulation bath temperature on the morphology, permeability and thermal/chemical stability of asymmetric CA membranes, *Desalination*, 262 (1) 72–78.

[18] Nasirian, D., Salahshoori, I., Sadeghi, M., Rashidi, N., and Hassanzadeganroudsari, M., 2019, Investigation of the gas permeability properties from polysulfone/ polyethylene glycol composite membrane, *Polym. Bull.*, 77 (10), 5529–5552.

[19] Mansur, S., Othman, M.H.D., Ismail, A.F., Sheikh Abdul Kadir, S.H., Goh, P.S., Hasbullah, H., Ng, B.C., Abdullah, M.S., Kamal, F., Abidin, M.N.Z., and Lusiana, R.A., 2019, Synthesis and characterisation of composite sulphonated polyurethane/polyether sulphone membrane for blood purification application, *Mater. Sci. Eng., C*, 99, 491–504.

[20] Boubakri, A., Bouchrit, R., Hafiane, A., and Bouguecha, S.A.T., 2015, Fluoride removal from aqueous solution by direct contact membrane distillation: Theoretical and experimental, *Environ. Sci. Pollut. Res.*, 21 (17), 10493–10501.

[21] Syawaliah, Arahman, N., Mukramah, and Mulyati, S., 2017, Effects of PEG molecular weights on PVDF membrane for humic acid-fed ultrafiltration process, *IOP Conf. Ser.: Mater. Sci. Eng.*, 180, 012129.

[22] Amirilargani, M., Saljoughi, E., Mohammadi, T., and Moghbeli, M.R., 2010, Effects of coagulation bath temperature and polyvinylpyrrolidone content on flat sheet asymmetric polyethersulfone membranes, *Polym. Eng. Sci.*, 50 (5), 885–893.

[23] Lusiana, R.A., Sasongko, N.A., Sangkota, V.D.A., Prasetya, N.B.A., Siahaan, P., Kiswandono A.A., and Othman, M.H.D, In-Vitro study of polysulfone-polyethylene glycol/chitosan (PES-PSf/Cs) membrane for urea and creatinine permeation, *J. Kim. Sains Apl.*, 23 (8), 283–289.

[24] Marino, T., Russo, F., and Figoli, A., 2018, The formation of polyvinylidene fluoride membranes with tailored properties via vapour/non-solvent induced phase separation, *Membranes*, 8 (3), 71.

[25] Hołda, A.K., and Vankelecom, I.F.J., 2015, Understanding and guiding the phase inversion process for synthesis of solvent resistant nanofiltration membranes, *J. Appl. Polym. Sci.*, 132 (27), 42130.

[26] Amiji, M.M., 1995, Permeability and blood compatibility properties of chitosan-poly(ethylene oxide) blend membranes for haemodialysis, *Biomaterials*, 16 (8), 593–599.

[27] Amin, N., Mahmood, R., Asad, M.J., Zafar, M., and Raja, A.M., 2014, Evaluating urea and creatinine levels in chronic renal failure pre and post dialysis, *J. Cardiovasc. Dis.*, 2 (2), 182–185.

Performance of *N,O*-Carboxymethyl Chitosan as Corrosion and Scale Inhibitors in CO_2 Saturated Brine Solution

Muhamad Jalil Baari[1*], Bunbun Bundjali[2], and Deana Wahyuningrum[2]

[1]*Department of Chemistry, Universitas Sembilanbelas November Kolaka, Jl. Pemuda, Kolaka, 93511, Indonesia*

[2]*Department of Chemistry, Institut Teknologi Bandung, Jl. Ganesha No. 10, Bandung 40132, Indonesia*

* ***Corresponding author:***

email: jalilbaari@gmail.com

Received: February 22, 2021
Accepted: April 7, 2021

DOI: 10.22146/ijc.64255

Abstract: *The presence of salts and dissolved gas like CO_2 that is carried with natural gas and crude oil along the pipeline is the main reason for corrosion and scale formation. These problems are usually resolved separately by corrosion inhibitors and scale inhibitors or acidification. Meanwhile, utilizing a compound to resolve both corrosion and scale formation has an advantage in the economic side and working time.* N,O-*carboxymethyl chitosan or* N,O-*CMCs is one of the chitosan's derivates. It is water-soluble and has different functional groups. Those properties support its capability as a complexing agent on corrosion and scale inhibitors. Synthesis of* N,O-*CMCs was carried out by chemical reactions between chitosan and chloroacetic acid under alkaline circumstances.* N,O-*CMCs product was characterized using FT-IR and* ^{1}*H-NMR spectroscopy. The inhibition efficiency was analyzed by electrochemical impedance spectroscopy (EIS) and potentiodynamic polarization techniques. The measurements showed that the highest efficiency of corrosion inhibition reached 63.54% when the concentration and temperature were 30 ppm and 35 °C, respectively.* N,O-*CMCs was classified as a mixed-type inhibitor. The adsorption mechanism of the inhibitor followed Langmuir adsorption isotherm. The static scale inhibition test informed that the optimum inhibition efficiency of* N,O-*CMCs reached 60.00%.*

Keywords: N,O-*carboxymethyl chitosan; corrosion inhibitor; carbon steel; scale inhibitor*

■ INTRODUCTION

Corrosion and scale formation are severe problems on pipelines of the petroleum industry. Those correspond to natural gas and crude oil transportation from the oil wells to the processing and storage stages through the pipeline containing corrosive substances such as water, chloride, minerals, and dissolved CO_2 [1-2]. Generally, carbon steel is a primary material for pipeline construction due to its good physical and mechanical properties [3]. Availability and lower price are the other reasons when uses this material [4]. However, carbon steel is rapidly corroded after contacting with corrosive environments.

Meanwhile, deposition of $CaCO_3$ on the inner surface of the pipeline will reduce the stream of fluids and triggers localized corrosion attacks (formed pitting corrosion) [5]. Consequently, pipeline leakage is unavoidable. The utilization of acid solutions can prevent or dissolve scale formation, but the aggressiveness of fluids also increases simultaneously, accelerating the pipeline failure [6]. Besides that, the accumulation of acid solution is very harmful to organisms around the contaminated area.

Corrosion and scale problems are usually treated separately by corrosion and scale inhibitors with different compounds [7-9]. However, the use of a compound that has double functions as the corrosion inhibitor and scale inhibitor is an advantage. Organic corrosion inhibitors have been widely used owing to cost-effective, practical means, and contain oxygen, nitrogen, phosphor, sulphur atoms that have π and lone pair electrons in their molecular structure to be

adsorbed on the metal surface by sticking on active sites [10-11]. Previous studies inform that corrosion inhibitors from polymeric compounds can be adsorbed strongly than monomer units or simple compounds [12-13]. On the other hand, scale inhibitors from polymer compounds are powerful complexing agents toward calcium and magnesium ions, good thermal stability, and better environmental compatibility [6,12]. A potential biopolymer as both corrosion and scale inhibitor is carboxymethyl chitosan (CMCs). It is a chitosan derivative that can be synthesized from the shell of crustaceans, for instance, shrimp, lobster, or crab. CMCs have different functional groups compared to chitosan so that it is easily dispersed into the aqueous solution and adsorbed onto a metal surface and $CaCO_3$ crystal surface [14]. The other characteristics of this polymer include biocompatible, biodegradable, low toxicity, antioxidant, and antibacterial [15-16].

CMCs are classified into several types according to the position of carboxymethyl groups in the glucosamine rings, including *N*-CMCs, *N,N*-CMCs, *O*-CMCs, and *N,O*-CMCs respectively [17]. Each type of CMCs is obtained through different synthesis processes [18]. *N,O*-CMCs is a type of carboxymethyl chitosan in which carboxymethyl groups are bound to amine groups on C-2 atoms and two hydroxyl groups on C-6 and C-3 atoms (Fig. 4). Previous studies had shown that carboxymethyl chitosan could be used as a corrosion inhibitor in several media [19-20]. However, there is no information about the natural source of chitosan, a specific type of CMCs, utilization of CO_2 in the corrosive medium, and its performance as a scale inhibitor. Therefore, this research aims to synthesize *N,O*-CMCs from shrimp shell waste and to study its performance as corrosion and scale inhibitors in the saturated CO_2 solution for metal protection. Adsorption isotherm and adsorption energy are also studied.

■ EXPERIMENTAL SECTION

Materials

Shrimp shell waste was obtained from Makassar, South Sulawesi. Chemicals were analytical grades consisting of sodium hydroxide, hydrogen chloride (37%), sodium chloride, potassium bromide, chloroacetic acid, absolute ethanol (99%), isopropanol, $MgCl_2{\cdot}6H_2O$, $CaCl_2{\cdot}2H_2O$, sodium bicarbonate, ethylene diamine tetraacetate dehydrate, potassium hydroxide, and calcium indicator. All chemicals were procured from Merck.

Instrumentation

The structure characterization of *N,O*-CMCs was conducted by proton nuclear magnetic resonance (^{1}H-NMR) Bruker Avance 500 MHz and Fourier transform infrared (FT-IR) ALPHA Bruker Spectrometers. The effectivity of corrosion inhibition was electrochemically analyzed by Voltalab PGZ 301 potentiostat with three electrodes configuration. All electrodes were immersed in NaCl (1.0%) solution with continuous sparging of CO_2. Composition of carbon steel as the testing metal were C (0.1%), S (0.03%), Mn (0.45%), P (0.025%), and balanced Fe [21].

Procedure

Preparation of chitin and chitosan

NaOH 3.5% (w/v) solution was mixed to shrimp shell powder in a ratio of 1:10 for 2 h at 68 °C for the deproteination stage. Then, demineralization was carried out by adding HCl 1 M solution to protein-free chitin in a ratio of 1:15 for 2 h at room temperature. After that, chitosan was synthesized by the triple deacetylation of chitin. In this stage, the mixture of chitin and NaOH 50% (w/v) solution was refluxed in a ratio of 1:15 for 3 h at 110 °C. The deacetylation degree (DD) of obtained chitosan was determined based on the baseline method from the IR spectra. It was calculated by Eq. (1) [22].

$$DD = 100 - \left(\frac{A_{1655}}{A_{3450}} \times \frac{100}{1.33} \right) \quad (1)$$

where A_{1655} and A_{3450} are vibrational absorbances of carbonyl in amides at 1655 cm^{-1} and amine groups at 3450 cm^{-1}, respectively. Factor 1.33 is a value from the ratio between A_{1655} and A_{3450} through a specific baseline. A viscometric method using the Ostwald viscometer was determined by the average molecular weight (AMW) of chitosan. Specific viscosity was measured by observing the time of flowing fluid with and without chitosan,

respectively, then determined the reduced viscosity and intrinsic viscosity ([η]) of each solution. Furthermore, the average molecular weight of the viscosity $\overline{M_v}$ was calculated by the Mark-Houwink formula like on Eq. (2) [23].

$$[\eta] = K.\overline{M_v}^{\alpha} \quad (2)$$

where value of $K = 1.4 \times 10^{-4}$ mL g^{-1} and $\alpha = 0.83$, $\overline{M_v}$ is the average molecular weight of viscosity.

Synthesis of N,O-CMCs

N,O-CMCs was synthesized by modification Zheng and partner method. NaOH (7.2 g) was dissolved in the mixture of 25 mL demineralized water and 50 mL isopropanol. Then, chitosan (4.0 g) was added to this mixture and reacted at room temperature for 1 h. Afterward, 5.0 g chloroacetic acid that had dissolved in 10 mL demineralized water-isopropanol solution at a ratio of 1:4 was slowly dropped to chitosan suspension. This solution was reacted for 4 h at 50 °C. Furthermore, the solution was acidified by adding HCl 2 M solution, neutralized by 80% of ethanol, washed with ethanol (95%), rinsed with concentrated ethanol, and dried inside of the oven at 65 °C for 24 h [24]. The structure elucidation of *N,O*-CMCs was conducted with ^{1}H-NMR and FT-IR Spectrometers. Modification of chitin to chitosan and *N,O*-CMCs is displayed in Fig. 1.

Performance analysis of corrosion inhibitor

Performance analysis of corrosion inhibitor was conducted by electrochemical impedance spectroscopy (EIS) and potentiodynamic polarization techniques. These experiments used potentiostat with a three-electrodes configuration. Carbon steel was used as a working electrode, platinum as an auxiliary electrode, and saturated calomel electrode (SCE) as a reference electrode. The working electrode was formed to a cylindrical rod (cross-section surface area of 1.13 cm^2) which was embedded in an epoxy resin. Before starting the analysis, the exposed surface of the working electrode was polished with 800, 1200, 2000 grit emery-papers on a Heidolph rotator, washed with demineralized water, and rinsed by ethanol. All electrodes were connected to a potentiostat. The flask was filled with 100 mL NaCl 1% solution and continued by fulfillment CO_2 gas throughout the experiment. The self-assembly of electrochemical measurements in this experiment is displayed in Fig. 2. For the EIS technique, temperature variations were 25, 35, 45, and 55 °C, respectively. The operating frequency was in the range of 10 kHz–100 mHz, and the variations of inhibitor concentration were 6, 12, 18, 24, and 30 ppm, respectively. Meanwhile, corrosion inhibition analysis by potentiodynamic polarization technique was carried out by taking a temperature that generates the highest inhibition efficiency from the EIS technique with several concentrations (18, 24, 30, and 36 ppm). Inhibition efficiency by EIS and potentiodynamic polarization techniques were calculated using Eq. (3) and Eq. (4) [25-26].

$$IE = \frac{Rp_{inh} - Rp}{Rp_{inh}} \times 100\% \quad (3)$$

$$IE = \frac{I_{corr\ o} - I_{corr\ inh}}{I_{corr\ o}} \times 100\% \quad (4)$$

where IE is inhibition efficiency of inhibitor (%), Rp_{inh} is polarization resistance with inhibitor (Ohm cm^2), Rp is polarization resistance without inhibitor (Ohm cm^2), $I_{corr\ o}$ and $I_{corr\ inh}$ (mA cm^{-2}) are corrosion current density of the system without and with inhibitor.

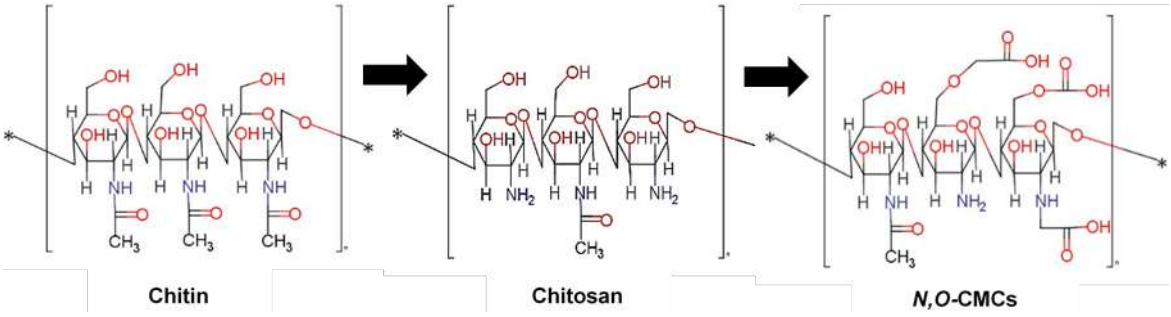

Fig 1. Modification chitin to chitosan and *N,O*-CMCs [15]

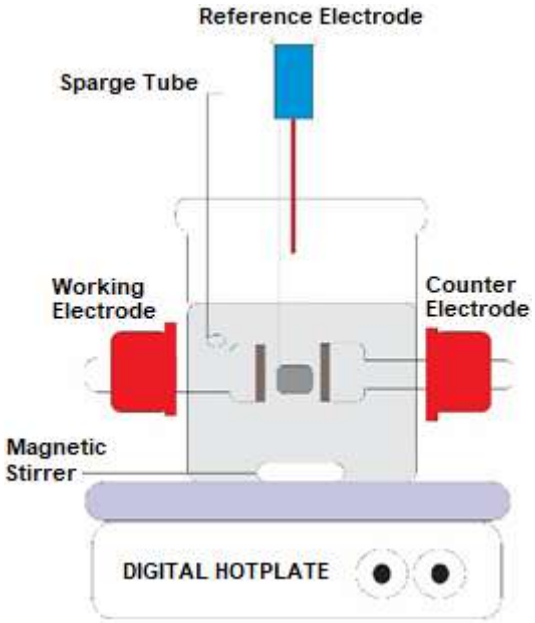

Fig 2. Self-assembly of electrochemical measurements

Study of adsorption isotherm

The surface coverage of the inhibitor (θ) on the metallic surface correlated to the efficiency of corrosion inhibition which is shown in Eq. (5) [27].

$$\theta = \frac{Rp_{inh} - Rp}{Rp_{inh}} \text{ or } \frac{IE(\%)}{100} \quad (5)$$

The adsorption process of *N,O*-CMCs on the metal surface was matched to various adsorption isotherms such as Langmuir, Freundlich, and Temkin isotherms. The adsorption type of inhibitor (physisorption, chemisorption, or physical-chemical adsorption) was determined by the value of the standard Gibbs free energy of adsorption (ΔG^{o}_{ads}) that is displayed in Eq. (6) [26-27].

$$\Delta G^{o}_{ads} = -RT\ln(55.55K_{ads}) \quad (6)$$

where R is the constant (8.314 J mol^{-1} K^{-1}), the value of 55.55 is water concentration in 1000 mL solution (mol L^{-1}), and T is the temperature (K).

Analysis of scale inhibition

This test followed NACE Standard TM0374-2001 about the Standard Test Method Laboratory Screening Test that based on the capability of scale inhibitors to restrain the precipitation of calcium carbonate in a solution. Initially, the mixture of 3.68 g, $MgCl_2{\cdot}6H_2O$, 12.15 g $CaCl_2{\cdot}2H_2O$, and 33.0 g NaCl was dissolved in demineralized water to attain 1.0 L calcium brine solution. Then, 1.0 L carbonic brine solution was obtained by dissolve 7.36 g $NaHCO_3$ and 33 g NaCl into demineralized water [28]. Both brine solutions were mixed into the vessels and were divided for the solution without the addition of inhibitors in various concentrations (6, 12, 18, 24, and 30 ppm). The solution was bubbled with CO_2 to remove O_2. Non-inhibitor solutions were specifically distinguished through heating at 71 °C for 24 h and without going through heating.

Meanwhile, all solutions with inhibitors were heated at 71 °C for 24 h. After cooling in the atmosphere, the next stage was to analyze residual Ca^{2+} concentration and scale inhibition efficiency by titration method with standard ethylene diamine tetraacetate dehydrate (EDTA) solution. This analysis was repeated two times to get accurate results.

■ RESULTS AND DISCUSSION

Isolation of Chitin, Synthesis of Chitosan and Their Characterizations

The deproteination step was intended to cut off atomic interactions, such as Van der Waals forces, covalent bonds, electrostatic forces, and hydrogen bonds among polymer chains of chitin with amino acids. The demineralization step can reduce mineral content on shrimp shells such as $CaCO_3$ and $Ca_3(PO_4)_2$ [23]. Functional group analysis of chitin is displayed on the IR spectra in Fig. 3. The spectra show peaks at wavenumber 3263 cm^{-1} and 3446 cm^{-1}, which relate to stretching vibrations of –OH in alcohol groups by intermolecular and intramolecular hydrogen bonds. Besides that, those peaks also correspond to the stretching vibrations of –NH in acetamide groups. The existence of C–H groups on alkane (–CH_3 and –CH_2) is displayed by absorption peaks in the wavenumber range 2891–2960 cm^{-1} from stretching vibrations in phase and out of phase. Whereas the C–H vibrations of the methine groups only have bending vibration at 1315 cm^{-1}. The presence of the C–O bond in the alkoxy group is confirmed by absorption peaks at wavenumber 1028–1112 cm^{-1}. The typical peak of chitin lies in the wavenumber 1655 cm^{-1} with a very high intensity derived from the carbonyl (C=O) stretching vibrations in the acetamide group.

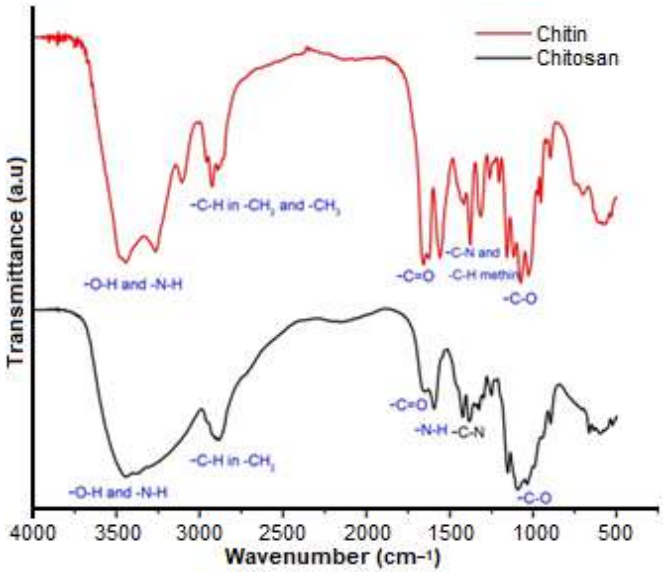

Fig 3. IR spectra of chitin and chitosan

The synthesis of chitosan from chitin was carried out by the deacetylation process. In this stage, chitin was hydrolyzed by a concentrated NaOH solution and high temperature to produce primary amine groups after releasing acetyl groups in glucosamide rings [29]. This stage was carried out three times to get optimization in the hydrolysis chitin. The IR spectra of chitosan are displayed in Fig. 3. Some absorption peaks are similar to the IR spectra of chitin. The differences lie in the reduced intensity of the vibrational peak of C=O from the acetyl group at 1655 cm^{-1} and the appearance of a peak at wavenumber 1596 cm^{-1} resulted from bending vibration of N–H bonds in primary amine groups [16].

Mass of chitin and chitosan after deproteination, demineralization, and deacetylation from 75 g shrimp shell powders, DD, and AMW of chitosan are shown in Table 1.

Table 1 displays that deacetylation of chitosan repeatedly can increase the degree of deacetylation until reaching 81.46%. This is followed by the decrease of molecular weight due to the change of acetyl groups to primary amines and accompanied by the possibility of breaking glycosidic bonds on the several polymer chains. The average molecular weight of chitosan from the first deacetylation cannot be determined by the viscometric method because there are still many acetyl groups in the polymer chains.

Synthesis and Characterization of *N,O*-Carboxymethyl Chitosan

The change of chitosan into carboxymethyl chitosan was intended to improve its solubility and surface-active property [30]. Improvements of these characters depend on the degree of substitution and the possibility of secondary reactions like cross-linking reactions during the synthesis process [31]. IR spectra of *N,O*-CMCs are shown in Fig. 4. The presence of –OH groups from carboxymethyl (–CH_2COOH) and alcohol groups on glucosamine rings (C-6 and C-3) is displayed by the extensive peak of about 3000–3450 cm^{-1}. A new peak at wavenumber 1739 cm^{-1} comes from the vibration of carbonyl bonds in the carboxyl groups [16,22]. Furthermore, the peak at wavenumber 1030 cm^{-1} due to stretching vibration of C–O from –CH_2–OH, which appeared on the chitosan spectra, becomes weaker. While stretching vibrations –C–O– from –CH–OH groups at 1070 cm^{-1} still clearly appear. This indicates carboxymethylation on the chitosan mostly in C-6 [32]. More significant steric obstacles of the –OH group in C-3 lead to fewer carboxymethylation in this site [33]. The

Table 1. Synthesis steps, product, and several characterization results such as percent yield, deacetylation degree (DD), and average molecular weight (AMW)

No	Stages	Product	Mass (g)	Percent yield (%)	DD (%)	AMW (amu)
1	Deproteination	Chitin + minerals	37.5	50.00	-	-
2	Demineralization	Chitin	14.7	39.20	-	
3	Deacetylation 1	Chitosan	10.8	73.47	52.23	u
4	Deacetylation 2	Chitosan	9.8	90.74	62.45	2.00×10^6
5	Deacetylation 3	Chitosan	7.8	79.59	81.46	1.36×10^6

u: cannot be determined because chitosan is not soluble in the used solvent

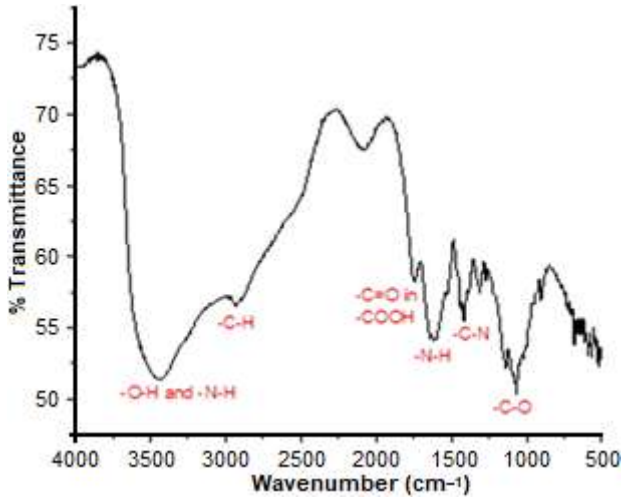

Fig 4. IR spectra of *N,O*-carboxymethyl chitosan (with KBr pellet)

peak intensity at 1383 cm^{-1} from the vibration C–N bond does not increase significantly to indicate that carboxymethyl groups are also not much bound to the amine groups [34]. Bending vibration of N–H bonds generates absorption peak at wavenumber 1596 cm^{-1} to indicate primary amines in the produced *N,O*-CMCs.

The type of protons composing *N,O*-CMCs were determined by ^{1}H-NMR spectroscopy. ^{1}H-NMR spectra in Fig. 5 show proton signals in *N,O*-CMCs compound. The signal intensity is low due to the poor solubility of *N,O*-CMCs in a small amount of D_2O. This corresponds to the lower degree of substitution of *N,O*-CMCs. More deshielding methylene protons from ^{1}H-NMR spectra are due to the environment adjacent to the electronegative groups, such as oxygen ether and oxygen carboxyl. Therefore, these protons have low electron density.

The presence of methyl protons in acetyl groups of *N,O*-CMCs is displayed by a signal at chemical shift 1.95 ppm. It explains that deacetylation processes to primary amines do not occur as a whole when converting chitin to chitosan [31]. Strong signals at 3.95 ppm and 3.97 ppm indicate that carboxymethylation mainly occurs in the hydroxyl groups at C-3 and C-6. Carboxymethylation on primary amines is shown by a signal at a chemical shift of 3.24 ppm [35]. Then, a powerful signal at 4.7 ppm comes from the solvent's undeuterated parts.

Analysis of Corrosion Inhibition

Fig. 6(a) and 6(b) represent a plot of inhibition efficiency (%) and polarization resistance (Ohm cm^2) as a function of *N,O*-CMCs concentration at several temperatures. The increment of polarization resistances describes that inhibitor molecules have covered active sites on the metal surface and form a protective layer on the metal-solution interface [36-37]. A low concentration of *N,O*-CMCs was found to have reduced the corrosion rate. *N,O*-CMCs has too large molecular size, which can be adsorbed and occupies a wider area on the carbon steel surface. Adsorption processes of polymeric inhibitor on metal surface in aqueous solution are via substitution reactions with water molecules [38]. There are many heteroatoms (oxygen and nitrogen) and π electrons of

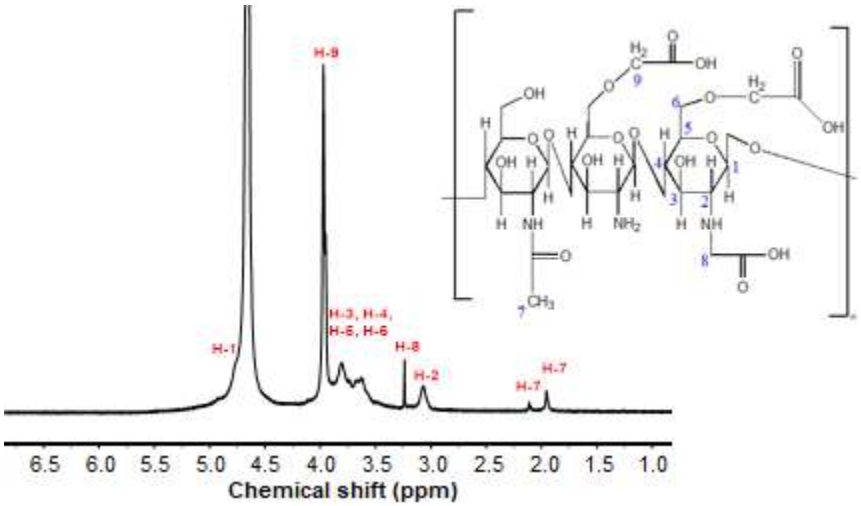

Fig 5. ^{1}H-NMR spectra of *N,O*-CMCs (in D_2O solvent)

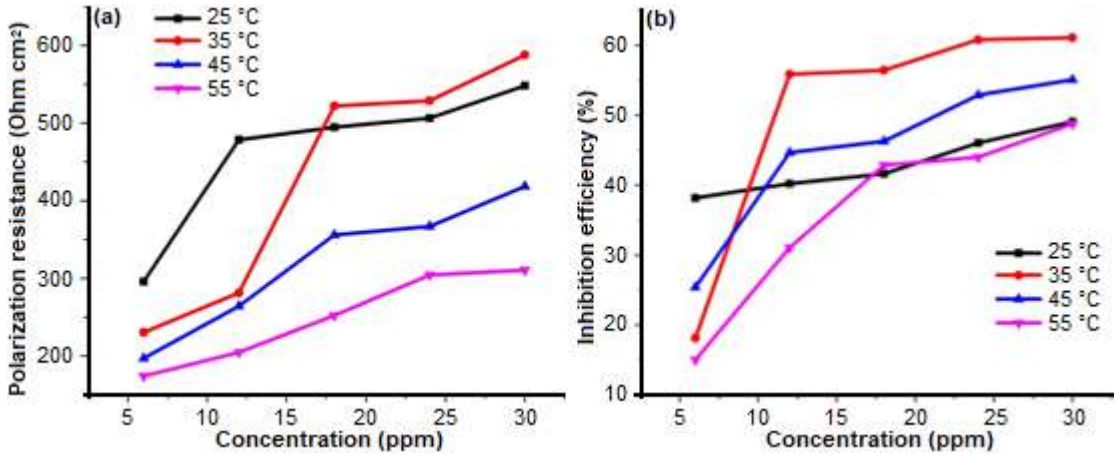

Fig 6. Plots of polarization resistance (a) and inhibition efficiency (b) by the presence of *N,O*-CMCs at various concentrations and temperatures

multiple bonds in *N,O*-CMCs molecular structure to make coordination bonding with ions or vacant *d*-orbitals of iron in the metal surface (chemisorption) [39-40].

Electrostatic and/or dipole-ion interactions can also occur among iron ions and/or iron atoms on the metal surface with carboxylate ions from *N,O*-CMCs compounds (physisorption). Besides that, there are electrostatic interactions between adsorbed chloride ions and positively charged inhibitor molecules from amine groups [41]. Bumby curves can be related to the difference in inhomogeneities and roughness of the working electrode surface during the analysis [42]. The formula of polarization resistance (R_p) is shown in Eq. (7).

$$R_p = Z_{re\,f\ min} - Z_{re\,f\ max} \quad (7)$$

where $Z_{re\,f\,max}$ is real impedance at a maximum frequency (Ohm cm^2), and $Z_{re\,f\,min}$ is actual impedance at a minimum frequency (Ohm cm^2). Values of the corrosion potentials (E_{corr}), solution resistance (R_s), polarization resistance (R_p), and inhibition efficiency (IE) are listed in Table 2. The highest efficiency was obtained at 35 °C when the inhibitor concentration was 30 ppm. This efficiency tends to be stable since the concentration continues to be increased. Then, it decreased again by increasing temperatures because higher temperatures can accelerate metal dissolution and diffusion processes of CO_3^{2-} and H^+ ions in solution to go to the active sites of metal [43]. Besides that, higher temperatures will desorb inhibitor molecules that are physically adsorbed from the metal-solution interface [44]. Structural decomposition and structural rearrangement may also occur [45-46]. However, protection to the metal surface from corrosion attack is still maintained.

The analysis of corrosion inhibition was also carried out by the potentiodynamic polarization technique. This method especially measures some electrochemical quantities such as corrosion current density and corrosion rate at 35 °C, which gives the highest efficiency from EIS.

The type of inhibitor (anodic or cathodic inhibitor) can be accurately determined by this technique from potential shifting trends on the linear polarization curves. The polarization curves for several concentrations of *N,O*-CMCs resulted from this method are shown in Fig. 7.

Corrosion potential values were obtained more positively after raising concentration, but these shifts were not greater than 85 mV. Therefore, *N,O*-CMCs is classified as a mixed inhibitor with a dominant character as an anodic inhibitor [47-48]. As a mixed inhibitor, *N,O*-CMCs can retard metal dissolution in the anodic site as well as reduce reaction in the cathodic site [49]. Table 3 displays the highest efficiency for the potentiodynamic polarization technique when the inhibitor's concentration is 30 ppm. These results have a good agreement with EIS result. The addition of *N,O*-CMCs up to 36 ppm even decreased inhibition efficiency. It can be explained that polymer molecules prefer parallelly adsorbed on the metal surface in a low

Table 2. Electrochemical parameters calculated by EIS technique in 1% NaCl solution

Temperature (°C)	Concentration (ppm)	E_{corr} (mV Vs SCE)	R_s (Ohm cm^2)	R_p (Ohm cm^2)	IE (%)
25	Blank	-710.8	16.71	295.7	-
	6	-716.1	14.22	478.4	38.19
	12	-682.1	13.89	494.7	40.22
	18	-673.9	14.92	506.5	41.62
	24	-671.4	14.28	548.1	46.05
	30	-682.9	13.36	580.7	49.08
35	Blank	-716.4	15.46	230.3	-
	6	-714.3	15.30	281.3	18.13
	12	-686.0	15.81	522.0	55.88
	18	-678.1	15.32	528.8	56.45
	24	-675.9	16.03	587.9	60.83
	30	-671.8	15.77	592.6	61.11
45	Blank	-721.6	14.68	197.0	-
	6	-715.2	11.37	264.1	25.40
	12	-687.5	11.36	356.0	44.66
	18	-687.0	11.85	366.8	46.29
	24	-686.4	11.23	418.4	52.91
	30	-686.0	11.54	438.7	55.09
55	Blank	-730.0	11.35	173.9	-
	6	-728.3	11.16	204.6	15.00
	12	-703.2	10.76	252.2	31.05
	18	-700.1	10.79	304.3	42.85
	24	-699.8	10.69	310.6	44.01
	30	-695.0	10.71	339.6	48.79

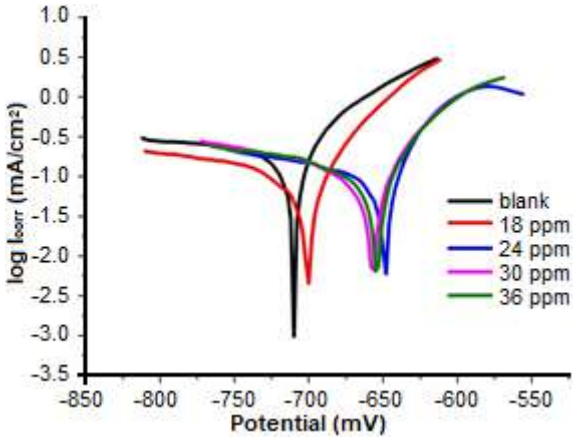

Fig 7. Polarization curves of *N,O*-CMCs at 35 °C

concentration to cover more active sites and accompanied by the expulsion of water molecules from the surface. These events continue until higher concentration that repulsive forces between inhibitor molecules were strong. In that condition, inhibitor molecules tend to be perpendicularly adsorbed on the metal surface to occupy a smaller surface area [50]. Another reason is the intermolecular attraction between the inhibitor molecules on the metal surface and the solution phase that can release adsorbed inhibitors from the carbon steel surface [8].

Study of Adsorption Isotherm and the Energy of Adsorption

Some types of adsorption isotherms (Langmuir, Freundlich, and Temkin isotherms) were matched to know the adsorption mechanism of *N,O*-CMCs on the working electrode surface. The type of adsorption isotherm and the values of parameters in adsorption energy are summarized in Table 4. Linear curves (Fig. 8) display adsorption of *N,O*-CMCs for some concentrations within the range of 25–45 °C on the carbon steel surface obtained from the formula of

Table 3. Electrochemical quantities calculated by potentiodynamic polarization technique with and without *N,O*-CMCs at 35 °C

Concentration (ppm)	Corrosion potential (mV)	Corrosion current density (mA/cm^2)	Corrosion rate (mmPY)	IE (%)
0	-710.0	0.2677	3.131	
18	-700.3	0.1135	1.327	57.60
24	-649.1	0.1068	1.249	60.10
30	-657.4	0.0976	1.141	63.54
36	-654.2	0.1691	1.977	36.83

Table 4. The types of adsorption isotherm, equilibrium constants of adsorption, and standard Gibbs free energies of adsorption (ΔG_{ads}) *N,O*-CMCs at range 25–55 °C

Temperature (°C)	Types of adsorption isotherm	K_{ads} (L/mol)	ΔG_{ads} (kJ/mol)	R_L
25	Langmuir	2.5×10^8	-57.90	0.559
35	Langmuir	5.0×10^8	-61.58	0.240
45	Langmuir	1.43×10^8	-60.26	0.689
55	Langmuir	5.0×10^7	-59.30	0.863

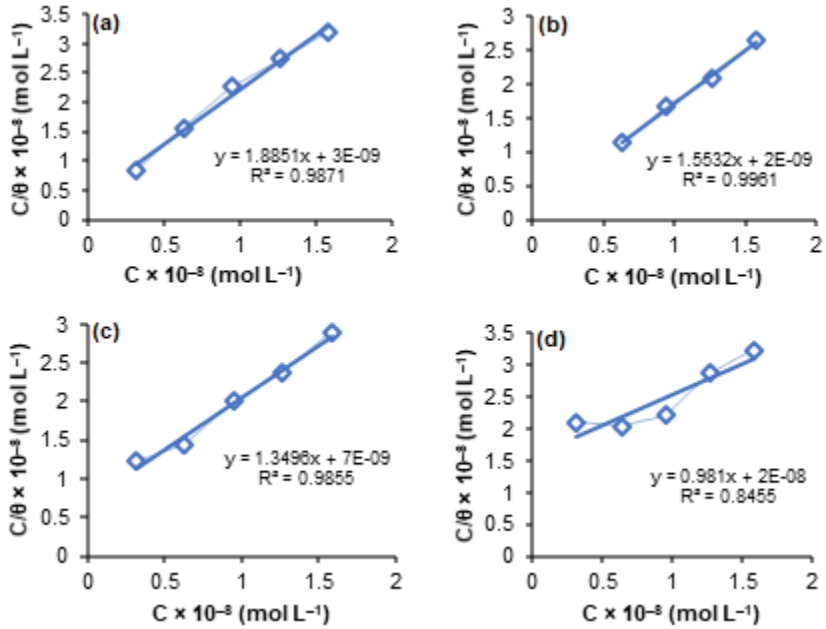

Fig 8. The linear relationship among several concentrations of *N,O*-CMCs (C_{inh}) and C_{inh}/θ, based on Langmuir adsorption isotherm in Eq. (8) at (a) 25, (b) 35, (c) 45, and (d) 55 °C, respectively

Langmuir isotherm adsorption in Eq. (8). It indicates that *N,O*-CMCs molecules have formed a monolayer on the metal surface without interaction between their neighbors [12].

$$\frac{C}{\theta} = \frac{1}{K_{ads}} + C \quad (8)$$

where C is the inhibitor's concentration (mol L^{-1}), θ is surface coverage, and K_{ads} is the equilibrium constant of adsorption-desorption (L mol^{-1}).

Whereas at 55 °C, the linear regression coefficient is relatively low ($R^2 < 0.900$), thus utilizing the first type of Langmuir isotherm is not fitted at this temperature. It was matched by another Langmuir equation and other isotherms like Freundlich and Temkin isotherm equations (Eq. (9)–(11)) to fix this discrepancy. Linear curves are displayed in Fig. 9.

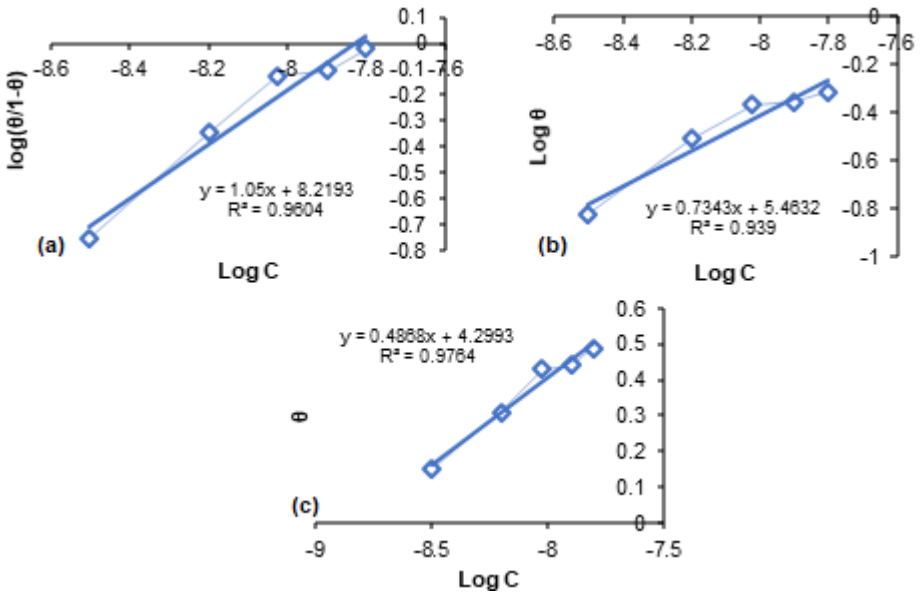

Fig 9. The linear relationship among several concentrations of *N,O*-CMCs and surface coverage (θ) based on (a) modified form of Langmuir adsorption isotherm, (b) Freundlich isotherm, and (c) Temkin isotherm at 55 °C

$$\log\left(\frac{\theta}{1-\theta}\right) = \log K_{ads} + \log C \quad (9)$$

$$\log\theta = \log K_{ads} + \frac{1}{n}\log C \quad (10)$$

$$\theta = \frac{1}{f}\log K_{ads} + \frac{1}{f}\log C \quad (11)$$

where 1/n relates to the adsorption intensity of *N,O*-CMCs onto the metallic surface, factor f is related to adsorbent-adsorbate interactions [51]. The dimensionless constant of the equilibrium parameter (R_L) is based on the utilization of the Langmuir equation to predict the efficiency of adsorption inhibitor on the metal surface. It was calculated by Eq.(12) [52].

$$R_L = \frac{1}{1+K_{ads}\cdot C} \quad (12)$$

The adsorption process is favorable occurred when the values of R_L are in the range 0 to 1, while $R_L > 1$, $R_L = 0$, and $R_L = 1$, indicate that adsorption is irreversible, unfavorable, and linear adsorption processes respectively [52].

The negative values from ΔG_{ads}, high values of K_{ads}, and the values of R_L parameter indicate the adsorption process of inhibitor molecules on to carbon steel surface is spontaneous and favorable [8,47]. Meanwhile, because ΔG_{ads} values are within the range -20 kJ mol^{-1} to -80 kJ mol^{-1}, therefore, adsorption mechanism of *N,O*-CMCs was a combination of physisorption and chemisorption [1].

Study of $CaCO_3$ Scale Inhibition

$CaCO_3$ crystals will be formed when the mixture of calcium and carbonate brine solutions were heated for 24 h. Calcium ion concentrations were obtained from consumed standard EDTA volume to reach the endpoint of the titration. The concentration of calcium ion and efficiency of scale inhibition was calculated using Eq. (13) and Eq. (14) [53].

$$\left[Ca^{2+}\right] = \frac{M_{EDTA}\cdot V_{EDTA}}{V_{system}} \quad (13)$$

$$IE = \frac{\left[Ca^{2+}\right]_{inh} - \left[Ca^{2+}\right]_{blank\ A}}{\left[Ca^{2+}\right]_{blank\ B} - \left[Ca^{2+}\right]_{blank\ A}} x100\% \quad (14)$$

where $[Ca^{2+}]_{blank\ A}$ and $[Ca^{2+}]_{blank\ B}$ are concentrations of calcium ion without inhibitor under heated/after precipitation and unheated/before precipitation respectively, M_{EDTA} is the molarity of EDTA, V_{EDTA} is the volume of EDTA, and $[Ca^{2+}]_{inh}$ is the concentration of calcium with the presence of inhibitor.

A lot of EDTA volumes that were consumed indicate higher content of calcium ions in the solution

Table 5. The average volume of EDTA solution that was needed for an equivalent point in titration, the concentration of calcium ions, and inhibition efficiency of *N,O*-CMCs against $CaCO_3$ scale in the various concentrations at 71 °C for 24 h

Solution	The average volume of EDTA (mL)	$[Ca^{2+}]$ (mol L^{-1})	IE (%)
0 ppm (unheated)	2.325	1.161×10^{-3}	-
0 ppm (heated)	1.700	8.490×10^{-4}	-
6 ppm	1.850	9.240×10^{-4}	24.04
12 ppm	1.925	9.620×10^{-4}	36.22
18 ppm	1.987	9.930×10^{-4}	46.15
24 ppm	2.033	1.015×10^{-3}	53.28
30 ppm	2.075	1.036×10^{-3}	60.00

phase. The action of inhibitor in solution could retard crystal nucleation and crystal growth of $CaCO_3$. Consequently, Ca^{2+} ions were longer dispersed in the solution phase, and the equilibrium concentrations of Ca^{2+} ions in the mixed brine solution increased than the solution without inhibitor. Kelvin equation in Eq. (15) explains the relationship between equilibrium concentration and the critical radius of $CaCO_3$ [14]. It was known that there is a decrease of critical radius from $CaCO_3$ crystal since the equilibrium concentration of ions increased.

$$\frac{\ln C}{C_0} = \frac{2\gamma M}{RT\rho r_c} \quad (15)$$

where C and C_0 are the equilibrium and initial concentrations of ion products (Ca^{2+}, CO_3^{2-}) and $CaCO_3$ respectively, γ is the surface tension of the crystal, M is the molar mass of the crystal, ρ is the density of $CaCO_3$, T is the testing temperature, R is the constant, and r_c is the critical radius of $CaCO_3$ crystal.

The capability of scale inhibition is attributed to hydroxyl, amide, and carboxyl groups, which are contained by inhibitor compound to improve chelating solubilization or complexing calcium ion, and maintain the dispersion effect to form $CaCO_3$ microparticles [14,54]. Table 5 reveals that the increment of *N,O*-CMCs concentration will increase scale inhibition efficiency until it reached 60.00% when the concentration is 30 ppm. It corresponds to the availability of more surface area and sorption sites to increase the metal adsorption capacity [6]. Further increase in concentrations may increase scale inhibition. However, this will decrease the corrosion inhibition effect. Ether groups in the carbon number 6 (C-6) from glucopyranose rings have the lone pair electrons that could also increase the adsorbed *N,O*-CMCs onto $CaCO_3$ crystal surface. Therefore, it has been good performance as a scale inhibitor at lower concentrations [54].

■ CONCLUSION

N,O-CMCs from shrimp shell waste had been synthesized by a chemical reaction between monochloro acetic acid and chitosan in base condition. Its structure was confirmed using FTIR and NMR characterizations. Analysis of corrosion inhibition efficiency toward carbon steel in the saturated CO_2 brine solution indicated that the increase of *N,O*-CMCs concentrations also increases inhibition efficiency. *N,O*-CMCs is effective enough as a green corrosion inhibitor at 35 °C when the concentration was 30 ppm. The optimum inhibition efficiency (*IE*) was 63.54%. However, this *IE* value is still lower than other green corrosion inhibitors like imidazole and its derivatives which *IE* value reaches 90%. *N,O*-CMCs is classified as a mixed-type inhibitor. Adsorption's processes obey Langmuir isotherm, which is dominated by chemical adsorption based on changes in the standard Gibbs free energy of adsorption. *N,O*-CMCs also acts as $CaCO_3$ scale inhibitors because they can improve the solubilization of calcium ions and the dispersion effect of $CaCO_3$ microparticles. The efficiency of scale inhibition reaches 60.0%. Further modifications on *N,O*-CMCs structure, may be considered to improve scale and corrosion inhibitions. Utilization of other

metals as a working electrode and other types of scale, such as $CaSO_4$ and $Ca_3(PO_4)_2$ are also helpful to know their interaction with *N,O*-CMCs.

■ AUTHOR CONTRIBUTIONS

All authors conducted the experiment and calculations. All authors wrote and revised the manuscript. All authors agreed to the final version of this manuscript.

■ REFERENCES

[1] Tawfik, S.M., and Negm, N.A., 2016, Synthesis, characterization and evaluation of some anionic surfactants with phosphate group as a biodegradable corrosion inhibitor for carbon steel in acidic solution, *J. Mol. Liq.*, 215, 185–196.

[2] Usman, B.J., and Ali, S.A., 2018, Carbon dioxide corrosion inhibitors: A review, *Arabian J. Sci. Eng.*, 43 (1), 1–22.

[3] Olivares-Xometl, O., López-Aguilar, C., Herrastí-González, P., Likhanova, N.V., Lijanova, I., Martínez-Palou, R., and Rivera-Márquez, J.A., 2014, Adsorption and corrosion inhibition performance by three new ionic liquids on API 5L X52 steel surface in acid media, *Ind. Eng. Chem. Res.*, 53 (23), 9534–9543.

[4] Salleh, N.I.H., and Abdullah, A., 2019, Corrosion inhibition of carbon steel using palm oil leaves extract, *Indones. J. Chem.*, 19 (3), 747–752.

[5] Kamal, M.S., Hussein, I., Mahmoud, M., Sultan, A.S., and Saad, M.A.S., 2018, Oilfield scale formation and chemical removal: A review, *J. Pet. Sci. Eng.*, 171, 127–139.

[6] Younes, A.A., El-Maghrabi, H.H., and Ali, H.R., 2017, Novel polyacrylamide-based solid scale inhibitor, *J. Hazard. Mater.*, 334, 1–9.

[7] El-Haddad, M.A.M., Radwan, A.B., Sliem, M.H., Hassan, W.M.I., and Abdullah, A.M., 2019, Highly efficient eco-friendly corrosion inhibitor for mild steel in 5 M HCl at elevated temperatures: Experimental & molecular dynamics study, *Sci. Rep.*, 9 (1), 3695.

[8] Baari, M.J., Bundjali, B., and Wahyuningrum, D., 2020, Synthesis of oligosuccinimide and evaluation of its corrosion inhibition performance on carbon steel in CO_2-saturated 1% NaCl solution, *J. Math. Fundam. Sci.*, 52 (2), 202–221.

[9] Li, C., Zhang, C., and Zhang, W., 2019, The inhibition effect mechanisms of four scale inhibitors on the formation and crystal growth of $CaCO_3$ in solution, *Sci. Rep.*, 9 (1), 13366.

[10] Raja, P.B., Qureshi, A.K., Rahim, A.A., Osman, H., and Awang, K., 2013, *Neolamarckia cadamba* alkaloids as eco-friendly corrosion inhibitors for mild steel in 1 M HCl media, *Corros. Sci.*, 69, 292–301.

[11] Saraswat, V., Yadav, M., and Obot, I.B., 2020, Investigations on eco-friendly corrosion inhibitors for mild steel in acid environment: Electrochemical, DFT and Monte Carlo Simulation approach, *Colloids Surf., A*, 599, 124881.

[12] Lv, J., Fu, L., Zeng, B., Tang, M., and Li, J., 2019, Synthesis and acidizing corrosion inhibition performance of N-doped carbon quantum dots, *Russ. J. Appl. Chem.*, 92 (6), 848–856.

[13] Biswas, A., Pal, S., and Udayabhanu, G., 2015, Experimental and theoretical studies of xanthan gum and its graft co-polymer as corrosion inhibitor for mild steel in 15% HCl, *Appl. Surf. Sci.*, 353, 173–183.

[14] Huang, H., Yao, Q., Jiao, Q., Liu, B., and Chen, H., 2019, Polyepoxysuccinic acid with hyper-branched structure as an environmentally friendly scale inhibitor and its scale inhibition mechanism, *J. Saudi Chem. Soc.*, 23 (1), 61–74.

[15] Mourya, V.K., Inamdar, N.N., and Tiwari, A., 2010, Carboxymethyl chitosan and its applications, *Adv. Mater. Lett.*, 1 (1), 11–33.

[16] Macedo, R.G.M.A., Marques, N.N., Paulucci, L.C.S., Cunha, J.V.M., Villetti, M.A., Castro, B.B., and Balaban, R.C., 2019, Water-soluble carboxymethylchitosan as green scale inhibitor in oil wells, *Carbohydr. Polym.*, 215, 137–142.

[17] Shariatinia, Z., 2018, Carboxymethyl chitosan: Properties and biomedical applications, *Int. J. Biol. Macromol.*, 120, 1406–1419.

[18] Upadhyaya, L., Singh, J., Agarwal, V., and Tewari, R.P., 2013, Biomedical applications of carboxymethyl chitosans, *Carbohydr. Polym.*, 91 (1), 452–466.

[19] Darmokoesoemo, H., Suyanto, S., Anggara, L.S., Amenaghawon, A.N., and Kusuma, H.S., 2018, Application of carboxymethyl chitosan-benzaldehyde as anticorrosion agent on steel, *Int. J. Chem. Eng.*, 2018, 4397867.

[20] Sun, H., Wang, H., Wang, H., and Yan, Q., 2018, Enhanced removal of heavy metals from electroplating wastewater through electrocoagulation using carboxymethyl chitosan as corrosion inhibitor for steel anode, *Environ. Sci. Water Res. Technol.*, 4 (8), 1105–1113.

[21] Bundjali, B., Surdia, N.M., Liang, O.B., and Ariwahjoedi, B., 2006, Pelarutan besi selektif pada korosi baja karbon dalam larutan buffer asetat, natrium bikarbonat - CO_2 jenuh, *J. Math. Fundam. Sci.*, 38 (2), 149–161.

[22] Domszy, J.G., and Roberts, G.A.F., 1985, Evaluation of infrared spectroscopic techniques for analysing chitosan, *Makromol. Chem.*, 186 (8), 1671–1677.

[23] Roberts, G.A.F., 1992, *Chitin Chemistry*, 1st Ed., Macmillan, London.

[24] Zheng, X., Zhang, H., She, Y., and Pu, J., 2014, Composite films of N,O-carboxymethyl chitosan and bamboo fiber, *J. Appl. Polym. Sci.*, 131 (3), 1–6.

[25] Qiang, Y., Fu, S., Zhang, S., Chen, S., and Zou, X., 2018, Designing and fabricating of single and double alkyl-chain indazole derivatives self-assembled monolayer for corrosion inhibition of copper, *Corros. Sci.*, 140, 111–121.

[26] Chaudhari, L.P., and Patel, S.N., 2019, Corrosion inhibition study of expired acetazolamide on mild steel in dilute hydrochloric acid solution, *J. Bio-Tribo-Corros.*, 5 (1), 1–13.

[27] Dagdag, O., Safi, Z., Erramli, H., Cherkaoui, O., Wazzan, N., Guo, L., Verma, C., Ebenso, E.E., and El Harfi, A., 2019, adsorption and anticorrosive behavior of aromatic epoxy monomers on carbon steel corrosion in acidic solution: Computational studies and sustained experimental studies, *RSC Adv.*, 9 (26), 14782–14796.

[28] NACE International, 2001, *Standard Test Method Laboratory Screening Tests to Determine the Ability of Scale Inhibitors to Prevent the Precipitation of Calcium Sulfate and Calcium Carbonate from Solution (for Oil and Gas Production Systems)*, NACE International, Houston, Texas.

[29] Jitareerat, P., Paumchai, S., Kanlayanarat, S., and Sangchote, S., 2007, Effect of chitosan on ripening, enzymatic activity, and disease development in mango (*Mangifera indica*) fruit, *N. Z. J. Crop Hortic. Sci.*, 35 (2), 211–218.

[30] Alsabagh, A.M., Elsabee, M.Z., Moustafa, Y.M., Elfky, A., and Morsi, R.E., 2014, Corrosion inhibition efficiency of some hydrophobically modified chitosan surfactants in relation to their surface active properties, *Egypt. J. Pet.*, 23 (4), 349–359.

[31] le Dung, P., Milas, M., Rinaudo, M., and Desbrières, J., 1994, Water soluble derivatives obtained by controlled chemical modifications of chitosan, *Carbohydr. Polym.*, 24 (3), 209–214.

[32] Larkin, P., 2011, *Infrared and Raman Spectroscopy Principles and Spectral Interpretation*, 1st Ed., Elsevier, Oxford, UK.

[33] Kim, C.H., Kim, S.Y., and Choi, K.S., 1997, synthesis and antibacterial activity of water-soluble chitin derivatives, *Polym. Adv. Technol.*, 8 (5), 319–325.

[34] Kong, X., 2012, Simultaneous determination of degree of deacetylation, degree of substitution and distribution fraction of –COONa in carboxymethyl chitosan by potentiometric titration, *Carbohydr. Polym.*, 88 (1), 336–341.

[35] Muzzarelli, R.A.A., Ilari, P., and Petrarulo, M., 1994, solubility and structure of N-carboxymethyl chitosan, *Int. J. Biol. Macromol.*, 16 (4), 177–180.

[36] Arjomandi, J., Moghanni-Bavil-Olyaei, H., Parvin, M.H., Lee, J.Y., Ko, K.C., Joshaghani, M., and Hamidian, K., 2018, Inhibition of corrosion of aluminum in alkaline solution by a novel azo-Schiff base: Experiment and theory, *J. Alloys Compd.*, 746, 185–193.

[37] Verma, C., Quraishi, M.A., and Singh, A., 2016, 5-Substituted 1H-tetrazoles as effective corrosion inhibitors for mild steel in 1 M hydrochloric acid, *J. Taibah Univ. Sci.*, 10 (5), 718–733.

[38] Kasshanna, S., and Rostron, P., 2017, Novel synthesis and characterization of vegetable oil

derived corrosion inhibitors, *J. Mater. Environ. Sci.*, 8 (12), 4292–4300.

[39] Douadi, T., Hamani, H., Daoud, D., Al-Noaimi, M., and Chafaa, S., 2017, Effect of temperature and hydrodynamic conditions on corrosion inhibition of an azomethine compounds for mild steel in 1 M HCl solution, *J. Taiwan Inst. Chem. Eng.*, 71, 388–404.

[40] El Faydy, M., Touir, R., Ebn Touhami, M., Zarrouk, A., Jama, C., Lakhrissi, B., Olasunkanmi, L.O., Ebenso, E.E., and Bentiss, F., 2018, Corrosion inhibition performance of newly synthesized 5-alkoxymethyl-8-hydroxyquinoline derivatives for carbon steel in 1 M HCl solution: Experimental, DFT and Monte Carlo simulation studies, *Phys. Chem. Chem. Phys.*, 20 (30), 20167–20187.

[41] Deng, S., Li, X., and Xie, X., 2014, Hydroxymethyl urea and 1,3-bis(hydroxymethyl) urea as corrosion inhibitors for steel in HCl solution, *Corros. Sci.*, 80, 276–289.

[42] Bentiss, F., Lebrini, M., and Lagrenée, M., 2005, Thermodynamic characterization of metal dissolution and inhibitor adsorption processes in mild steel/2,5-bis(n-thienyl)-1,3,4-thiadiazoles/hydrochloric acid system, *Corros. Sci.*, 47 (12), 2915–2931.

[43] Kahyarian, A., and Nesic, S., 2019, A new narrative for CO_2 corrosion of mild steel, *J. Electrochem. Soc.*, 166 (11), C3048–C3063.

[44] Chakravarthy, M.P., and Mohana, K.N., 2014, Adsorption and corrosion inhibition characteristics of some nicotinamide derivatives on mild steel in hydrochloric acid solution, *Int. Scholarly Res. Not.,* 2014, 687276.

[45] Barmatov, E., Hughes, T., and Nagl, M., 2015, Efficiency of film-forming corrosion inhibitors in strong hydrochloric acid under laminar and turbulent flow conditions, *Corros. Sci.*, 92, 85–94.

[46] Nešić, S., 2007, Key issues related to modelling of internal corrosion of oil and gas pipelines - A review, *Corros. Sci.*, 49 (12), 4308–4338.

[47] Verma, C., Singh, P., and Quraishi, M.A., 2016, A thermodynamical, electrochemical and surface investigation of Bis (indolyl) methanes as green corrosion inhibitors for mild steel in 1 M hydrochloric acid solution, *J. Assoc. Arab Univ. Basic Appl. Sci.*, 21, 24–30.

[48] Anejjar, A., Salghi, R., Zarrouk, A., Benali, O., Zarrok, H., Hammouti, B., and Ebenso, E.E., 2014, Inhibition of carbon steel corrosion in 1 M HCl medium by potassium thiocyanate, *J. Assoc. Arab Univ. Basic Appl. Sci.*, 15 (1), 21–27.

[49] Kaskah, S.E., Pfeiffer, M., Klock, H., Bergen, H., Ehrenhaft, G., Ferreira, P., Gollnick, J., and Fischer, C.B., 2017, Surface protection of low carbon steel with N-acyl sarcosine derivatives as green corrosion inhibitors, *Surf. Interfaces*, 9, 70–78.

[50] Wang, B., Du, M., Zhang, J., and Gao, C.J., 2011, Electrochemical and surface analysis studies on corrosion inhibition of Q235 steel by imidazoline derivative against CO_2 corrosion, *Corros. Sci.*, 53 (1), 353–361.

[51] Saadi, R., Saadi, Z., Fazaeli, R., and Fard, N.E., 2015, Monolayer and multilayer adsorption isotherm models for sorption from aqueous media, *Korean J. Chem. Eng.*, 32 (5), 787–799.

[52] Ayawei, N., Angaye, S., Wankasi, D., and Dikio, E.D., 2015, Synthesis, characterization and application of Mg/Al layered double hydroxide for the degradation of Congo Red in aqueous solution, *Open J. Phys. Chem.*, 5 (3), 56–70.

[53] Huang, H., Yao, Q., Liu, B., Shan, N., and Chen, H., 2017, Synthesis and characterization of scale and corrosion inhibitors with hyper-branched structure and the mechanism, *New J. Chem.*, 41 (20), 12205–12217.

[54] Feng, J., Gao, L., Wen, R., Deng, Y., Wu, X., and Deng, S., 2014, Fluorescent polyaspartic acid with an enhanced inhibition performance against calcium phosphate, *Desalination*, 345, 72–76.

Java Red Rice (*Oryza sativa* L.) Nutritional Value and Anthocyanin Profiles and Its Potential Role as Antioxidant and Anti-Diabetic

Ayu Tri Agustin[1,2], Anna Safitri[2,3], and Fatchiyah Fatchiyah[1,2*]

[1]*Department of Biology, Faculty of Mathematics and Natural Sciences, Brawijaya University, Jl. Veteran, Malang 65145, East Java, Indonesia*

[2]*Research Center of Smart Molecule of Natural Genetics Resource, Brawijaya University, Malang 65145, East Java, Indonesia*

[3]*Department of Chemistry, Faculty of Mathematics and Natural Sciences, Brawijaya University, Jl. Veteran, Malang 65145, East Java, Indonesia*

* ***Corresponding author:***

tel: +62-341-575-841
email: fatchiya@ub.ac.id

Received: March 5, 2021
Accepted: April 20, 2021

DOI: 10.22146/ijc.64509

Abstract: *This study investigates nutritional value, amino acid profile, and total anthocyanin in pigmented rice as an antioxidant and anti-diabetic agent. Six rice varieties were extracted using 0.1% HCl in methanol, namely four red rice, one black rice, and one white rice. Rice extract was used for proximate analysis and amino acid profiling. Total anthocyanin was measured and identified by ultraviolet-visible (UV-Vis) spectrophotometer and thin-layer chromatography (TLC). The antioxidant activity was determined using Ferric-reducing antioxidant power (FRAP) assay, and the α-amylase enzyme-inhibited by anthocyanin extract of red rice as anti-diabetic was measured. The study result showed that the proximate level (carbohydrate, protein, lipid, water, and ash) in pigmented rice was different. Cempo merah red rice is a source of amino acids, both essential and non-essential amino acids that act as good nutrition. The highest total anthocyanin level between red rice varieties of 10.87 mg/g was found in Aek sibundong red rice. High biological function activities as an antioxidant were indicated by Aek sibundong red rice with an IC_{50} value of 6.65 μg/mL. Aek sibundong red rice shows the lowest IC_{50} value of 144.46 μg/mL in anti-diabetic activity. Thus, Aek sibundong red rice may have the potential as α-amylase inhibitor for diabetes prevention.*

Keywords: *anthocyanin; bioactivity; nutrition; pigmented rice*

■ INTRODUCTION

Rice (*Oryza* spp.) consists of 40,000 varieties worldwide and is divided into two widely cultivated types, namely *Oryza sativa* (Asian rice) and *Oryza glaberrima* (African rice) [1]. Based on the pericarp color, rice is divided into several cultivars, including white, red, black, and purple rice. It is determined by the accumulation of proanthocyanidin and anthocyanin pigments in the pericarp, seed coat, and aleurone [2]. Various bioactive compounds in pigmented rice are beneficial for the health and prevention of metabolic diseases [3]. Generally, red rice is rich in nutrients such as calcium, zinc, magnesium, protein, and fiber compared to white rice [4]. Proximate analysis shows that the vitamin B1 content of red rice is higher than black rice [5]. The main phytochemical content of red rice includes phenolics, flavonoids, proanthocyanidins, and anthocyanins. It has biological functions to reduce free radicals, oxidative stress and prevent lipid peroxidation [6].

The dominant phenolic compounds found in red rice varieties include ferulic, vanillic, and proto-catechuic acid [7]. Research by Thitipramote et al. [8] shows that ethanol extract from Brown Red Jasmine (BRJ) red rice contains phenolic compounds and the highest antioxidant activity among Kam Leum Pua (KLP) black rice and Japanese Brown Rice (JBR) white rice. This high antioxidant activity is supported by the presence of proanthocyanidins found only in BRJ red rice. Effective extraction and identification methods are

essential in anthocyanin analysis. Using 0.1% HCl in methanol is an optimum solvent for anthocyanin extraction of rice [9]. The addition of hydrochloric acid is needed to increase solvent polarity and maintain anthocyanin stability [10]. Anthocyanin identification is commonly performed using a spectrophotometric approach based on changes in the structure and absorption of anthocyanins at different pHs (generally pH 1.0 and pH 4.5). It is referred to as a pH differentiation method [11]. The thin-layer chromatography (TLC) method was carried out to identify anthocyanins and organic compounds in pigmented rice [12].

Anthocyanins consist of a benzoyl ring [A], a pyran ring [C], and a phenolic ring [B], as well as a sugar group at position C3 in the heterocyclic [C] ring. These sugar groups include glucose, galactose, xylose, rhamnose, and arabinose. The addition of sugar groups (glycosylation) may increase the anthocyanin stability in water. Anthocyanins commonly found in plants include pelargonidin, peonidin, cyanidin, malvidin, petunidin, and delphinidin [13]. The chemical structure of anthocyanins, such as the position and number of hydroxyl groups or methoxy group as electron donors, has a strong effect on antioxidant activity [14]. Biological function test of cyanidin-3-*O*-glucoside in red rice showed inhibition of Advanced Glycation End-products (AGEs)-Receptor for AGEs (RAGE), which is involved in the chronic inflammatory cascade, diabetes, and its complications [15]. Peonidin-3-*O*-glucoside can inhibit the tumor necrosis factor alpha (TNF-α) signaling pathway so that it has the potential to be anti-inflammatory [16]. A previous study reported that brown rice extract consumed by hyperglycemic rats induced using streptozotocin (STZ) and nicotinamide (NA) could reduce blood glucose up to 50.9% [17]. In vivo study on dyslipidemia mice treated with anthocyanin from pigmented rice showed decreased cholesterol levels, malondialdehyde (MDA), and the expression of genes involved in obesity [18]. The inhibitory activities of α-amylase and α-glucosidase were carried out on red, purple, and brown rice bran extracts to evaluate their anti-diabetic effect in vitro. Among other pigmented rice, red rice bran was able to inhibit the enzymes α-amylase (46.2%) and α-glucosidase (reaching 91.8%) [19]. The potential role of whole grain extracts of red rice in inhibiting glucose digestion enzymes has limited information. The α-amylase enzyme is secreted by the salivary glands and pancreas, which can break the internal bonds of α-1,4-starch glycosides to produce maltose and glucose. When the α-amylase enzyme is inhibited, it will slow down the digestion of carbohydrates [20]. Thus, the glucose absorption rate into the blood will decrease.

Besides genetic factors, the growing environment, such as light, temperature, drought, and soil salinity, can affect variations in the content of bioactive compounds in red rice [21]. In Indonesia, red rice is divided into more than 60 varieties spread across Java, Bali, Sumatra, Sulawesi, and NTT. Research related to physicochemical characterization and antioxidant activity has been carried out on two local red rice varieties of North Buton, Wakawondu, and Wangkakiri varieties [22]. In the current study, four local Javanese red rice varieties were used. Blambangan and Aek sibundong red rice varieties were obtained from East Java, while red rice varieties of Cempo Merah and Inpari 24 were obtained from Central Java. Mentik susu white rice and wojalaka black rice were obtained from East Java as control. We aimed to investigate nutritional value, amino acid profile, total anthocyanin, and antioxidant and anti-diabetic activity in six pigmented rice varieties.

■ EXPERIMENTAL SECTION

Materials

The chemicals used were 1.0 M HCl, methanol (MeOH 99.9%), α-aminobutyric acid (AABA), α-amylase enzyme (334 units/mg from *Aspergillus oryzae*), AccQ•Fluor Borate, fluorine reagent A, potassium chloride buffer, n-butanol, acetic acid, phosphate buffer, potassium ferricyanide, Trichloroacetic Acid (TCA) 10%, ferric chloride, and dinitrosalicylic acid reagent. In addition, various rice varieties were used, including Mentik Susu white rice (WREJms) as a negative control, Wojalaka black rice (BREJwj) as a positive control, Cempo Merah red rice (RRCJcm), Blambangan red rice

(RREJbl), Inpari 24 red rice (RRCJin), and Aek Sibundong red rice (RREJas) (Fig. 1).

Instrumentation

Anthocyanin extraction was optimized using a shaking water bath at 25 °C. Solvent evaporation was performed using a rotary evaporator. The instrument used to determine the proximate components were Kjeltec™ and Soxhlet. The amino acid was determined Ultra-Performance Liquid Chromatography (UPLC), Liquid Chromatography-Mass Spectrometry (LC-MS), and High-Performance Liquid Chromatography (HPLC). UV-Vis spectrophotometer was employed to measure the absorbance of the extract. The identification of anthocyanin compounds was carried out on a silica gel plate F_{254} and visualized under a UV chamber.

Procedure

Extraction of anthocyanin from pigmented rice

Extraction was carried out using the maceration method. The 250 g of sample powder was dissolved with 1000 mL of 0.1% HCl in methanol [9]. Total extracts were then incubated in a shaking water bath at 25 °C overnight. The filtrate was obtained using a 0.45 µm Whatman filter paper and then concentrated in a rotary evaporator. The evaporated extract was stored at 4 °C for further analysis.

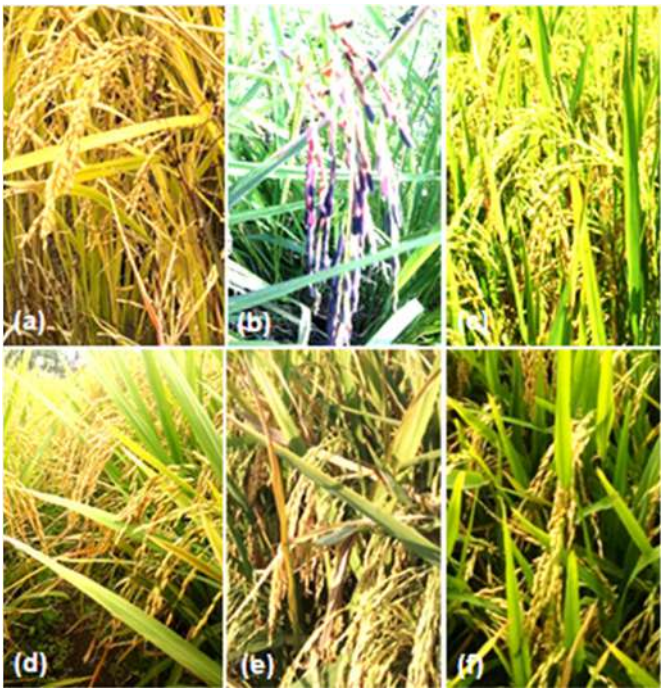

Fig 1. Various pigmented rice. (a) WREJms, (b) BREJwj, (c) RRCJcm, (d) RREJbl, (e) RRCJin, and (f) RREJas

Proximate analysis

Proximate analysis for carbohydrates was carried out according to the standard 18-8-9/MU/SMM-SIG protocol, protein according to the 18-8-31/MU/SMM-SIG (Kjeltec), lipid according to the 18-8-5/MU/SMM-SIG (Soxhlet), water and ash content according to the Indonesian National Standard (SNI 6128:2015 and SNI 01-2891:1992).

Amino acid determination

Characterization of essential and non-essential amino acid profiles was carried out using the Ultra Performance Liquid Chromatography (UPLC) method [23]. Briefly, 0.1 g of pigmented rice were dissolved in 5 mL of 6 N HCl. Then, each solution was vortexed and heated at 110 °C. Distilled water was added to the solution until the final solution volume was 50 mL. The resulted solution was filtered and dissolved in 40 µm AABA and 460 µL distilled water. A 10 µL of the solution was added to the 70 µL of AccQ-Fluor Borate and vortexed. Then, 20 µL of fluorine reagent A was added to the solution and was incubated at 55 °C for 10 min. After incubation, the solution was injected onto the UPLC column (AccQ.Tag Ultra C18 1.7 µm) according to the 8-5-17/MU/SMM protocol-SIG (UPLC), 18-12-38/MU/SMM-SIG (LC-MS/MS) for the amino acids L-Cystine and L-Methionine test, and 18-5-63/MU/SMM-SIG (HPLC) for the amino acid L-Tryptophan test.

Determination of total anthocyanin content

Anthocyanin content in the sample extract was determined based on the pH differentiation method [24]. A 0.1 g of the paste extract was dissolved in 2 mL of potassium chloride buffer pH 1.0 and pH 4.5 separately. Each solution was vortexed, filtered, and centrifuged at 2500 rpm at 25 °C for 10 min. Buffer solution pH 1.0 and pH 4.5 were used as blank solutions. The absorbance was measured at 200–800 nm using a UV-Vis spectrophotometer. Total anthocyanin content was calculated as follows:

$$\text{Anthocyanin content}\left(\text{mg}/\text{g}\right)=\frac{\text{A}\times\text{MW}\times\text{DF}\times 1000}{\text{MA}\times 1}$$

with:
A: The formula determines the absorbance of the sample: $A = (A_{\lambda Vis\text{-}max\ nm} - A_{700\ nm})_{pH\ 1.0} - (A_{\lambda Vis\text{-}max\ nm} - A_{700\ nm})_{pH\ 4.5}$
MW: Molecular weight of cyanidin-3-*O*-glucoside (449.2 g/mol)
DF: Dilution factor
MA: Molar absorbtivity of cyanidin-3-*O*-glucoside

Thin layer chromatography (TLC) analysis

Concisely, 0.1 g paste extract was diluted with 0.4 mL 0.1% HCl in methanol. The solution was vortexed, then centrifuged at 2500 rpm at 25 °C for 10 min. 0.3 mg/mL of supernatant was spotted on the silica gel plate F_{254}. Next, the silica gel plate F_{254} that had been spotted was eluted in the mobile phase with eluent *n*-butanol:acetic acid:distilled water (3:1:1). The spots were observed under UV chamber of 254 nm and 366 nm, then the intensity and density of each spot were determined using ImageJ software, and the retention factor (Rf) was measured [18].

Antioxidant activity assay

Samples were diluted with 0.1% HCl in methanol with concentrations of 0, 2, 4, 6, 8, 10 µg/mL. The solution was mixed with 200 mmol/L phosphate buffer (2.5 mL) pH 6.6 and 1% potassium ferricyanide 2.5 mL. The solution was incubated at 50 °C for 30 min, then 2.5 mL of 10% TCA was added. An aliquot of the solution (5 mL) was transferred to a new test tube. Lastly, 5 mL of distilled water and 0.1% ferric chloride 1 mL were added to each tube. The absorbance was measured at 700 nm using a UV-Vis spectrophotometer. The antioxidant activity was calculated as follows: Percentage of antioxidant = {[(absorbance of control - absorbance of sample)/ absorbance of control] × 100}. The IC_{50} value was determined using a linear regression equation (x and y axes, respectively) of extract concentration and its antioxidant activity [25].

α-Amilase enzyme inhibitory activity

Briefly, 250 µL of pigmented rice extracts (10–100 µg/mL), buffer control and positive control (the acarbose 1–10 µg/mL) were added with 250 µL of α-amylase enzyme (334 units/mg from *Aspergillus oryzae*). Each solution was incubated at 37 °C for 30 min. Next, amylum 1% was added to each tube and incubated at 25 °C for 10 min. Then, 500 µL of dinitrosalicylic acid reagent was added and incubated in boiling water for 5 min. Lastly, each solution was added 5 mL of distilled water. The absorbance was measured at 495 nm, and the IC_{50} value was determined. The inhibitory activity of α-amylase was determined by the percentage of enzyme inhibition against the extract [26].

Data analysis

One-way Analysis of Variance (ANOVA) and Brown-Forsythe using SPSS Statistic v16 software performed statistical analysis of TAC, intensity, and density. The statistically significant test was determined at $p < 0.05$ [27]. Results were expressed as mean ± standard deviation (SD) of triplicate experiments.

■ RESULTS AND DISCUSSION

Nutritional Value and Amino Acid Residue of Pigmented Rice

The nutrition component of pigmented rice was determined by proximate analysis, while the amino acid residues were determined by the UPLC method. Evidence of macro and micronutrient components is very important in the development of functional foods. Pigmented rice is a staple food rich in macronutrients such as carbohydrates, fiber, protein, and fat as an energy source [28]. These studies showed that carbohydrate, protein, lipid, ash, and moisture content among pigmented rice have different values (Table 1). Several factors influence pigmented rice macronutrients variation, including genetic factors, environment, rice milling, and storage [5]. The percentage of carbohydrates in red rice varieties was 71.07%–74.49%. In the human body, carbohydrates are hydrolyzed into monosaccharides, disaccharides, starch, and other smaller components. A high carbohydrate diet can trigger hyperglycemia [5]. However, RREJbl red rice has the lowest carbohydrate content. RRCJcm red rice has a protein content of 11.23%, higher than BREJwj black rice, which has a protein content of 10.14%. The fat level in red rice is around 4.34%–5.81%, whereas the lowest level was RREJas red rice. The previous studies also found similar variations in the nutritional value of rice [5,7].

Table 1. Profile of nutrition and amino acid residues composition in pigmented rice

(a) Constituents	WREJms	BREJwj	RRCJcm	RREJbl	RRCJin	RREJas
Carbohydrate (%)	75.125 ± 0.05*	72.92 ± 0.07	71.94 ± 0.14	71.065 ± 0.045	72.79 ± 0.02	74.49 ± 0.05
Protein (%)	11.82 ± 0.01*	10.135 ± 0.045	11.225 ± 0.095	10.985 ± 0.055	9.445 ± 0.145	10.82 ± 0.06
Lipid (%)	1.16 ± 0.02	4.775 ± 0.065	5.805 ± 0.035*	5.59 ± 0.08	5.25 ± 0.07	4.34 ± 0.03
Moisture content (%)	10.97 ± 0.05*	9.515 ± 0.055	8.655 ± 0.055	9.495 ± 0.055	9.925 ± 0.055*	7.88 ± 0.05
Ash (%)	0.925 ± 0.025	2.655 ± 0.035	2.375 ± 0.025	2.865 ± 0.035*	2.59 ± 0.04	2.47 ± 0.03
(b) Amino acid (mg/Kg)	WREJms	BREJwj	RRCJcm	RREJbl	RRCJin	RREJas
Essential amino acids						
L-Phenylalanine	7041.50 ± 13.20	5671.60 ± 1.93	7194.08 ± 9.41*	6649.84 ± 18.33	4876.60 ± 4.54	5218.72 ± 13.43
L-Isoleucine	4394.41 ± 1.22	4066.33 ± 15.06	4501.66 ± 18.31*	4316.34 ± 1.64	4043.50 ± 9.95	4083.41 ± 9.63
L-Valine	6652.15 ± 51.83	6430.91 ± 10.33	6888.28 ± 24.79*	6589.49 ± 24.40	6159.63 ± 5.27	6054.40 ± 36.77
L-Lysine	4256.26 ± 10.72*	4084.85 ± 8.54	3923.48 ± 23.08	3907.21 ± 4.08	3763.41 ± 4.04	4223.05 ± 18.32*
L-Leucine	8718.39 ± 39.35	7959.40 ± 13.30	8911.00 ± 11.36*	8558.51 ± 2.16	8024.24 ± 1.54	8105.08 ± 28.82
L-Threonine	4872.74 ± 8.76	4661.00 ± 19.63	5386.79 ± 5.26*	5101.63 ± 9.89	4425.68 ± 13.10	4406.68 ± 19.84
L-Histidine	2995.33 ± 12.11	2953.04 ± 8.95	3711.28 ± 7.43*	3405.98 ± 17.43	2667.81 ± 5.68	2608.70 ± 16.77
L-Methionine	2466.04 ± 1.23*	2027.91 ± 1.80	2422.98 ± 0.71	2249.76 ± 1.12	1844.37 ± 0.92	2260.31 ± 0.90
L-Tryptophan	1550.67 ± 0.99*	1181.33 ± 0.67	1209.88 ± 5.79	1229.28 ± 5.43	1209.24 ± 5.33	1188.82 ± 0.34
Non-essentials						
L-Serine	7676.81 ± 57.02*	5755.88 ± 7.96	7530.38 ± 14.29	6432.35 ± 7.12	5708.48 ± 17.52	6247.60 ± 44.45
L-Glutamic acid	19756.37 ± 111.22*	18454.93 ± 35.82	18685.57 ± 69.31	16815.84 ± 72.20	15346.26 ± 38.61	18655.68 ± 123.59
L-Aspartic acid	8922.30 ± 42.33	9282.61 ± 12.65	9383.25 ± 28.80*	7680.57 ± 21.63	7208.30 ± 4.86	8955.61 ± 33.66
L-Tyrosine	4791.15 ± 23.06	3604.19 ± 2.53	5083.72 ± 16.72*	4398.77 ± 0.05	3272.53 ± 4.24	3723.00 ± 23.86
L-Proline	4683.12 ± 13.91	4491.93 ± 47.98	4693.33 ± 13.10*	4496.24 ± 2.01	4160.27 ± 13.65	4384.31 ± 9.58
L-Alanine	5995.01 ± 39.74	6028.48 ± 23.82	6297.38 ± 37.89*	5706.91 ± 29.03	5343.24 ± 17.54	6033.32 ± 18.11
L-Arginine	9393.25 ± 11.01	8480.83 ± 89.45	9596.37 ± 54.24*	8707.33 ± 33.22	7361.11 ± 22.37	7690.07 ± 27.88
Glycine	5202.28 ± 26.17	4942.58 ± 11.75	5932.36 ± 23.87*	5488.05 ± 19.18	5050.48 ± 8.69	4829.40 ± 22.53
L-Cysteine	2561.51 ± 1.28	1970.56 ± 0.88	2422.74 ± 2.45	2615.46 ± 2.18*	1651.06 ± 0.82	2346.79 ± 0.93

Note: An asterisk (*) show the highest value with 5% probability ($P < 0.05$)

Generally, amino acids are classified into essential amino acids and non-essential amino acids. Non-essential amino acids can be synthesized in the body to promote optimal growth and health. Essential amino acids cannot be synthesized in the body but derived from foods [29]. Glutamic acid is the non-essential amino acid most predominantly found in all rice (Table 1(b)). These findings are similar to previous studies, where glutamic acid was dominated in black rice, red rice, and white rice [18]. Our study found that red rice, especially RRCJcm red rice has the highest essential amino acid level (phenylalanine, isoleucine, valine, leucine, threonine, and histidine). The content of non-essential amino acid residues (aspartic acid, tyrosine, proline, alanine, arginine, and glycine) in RRCJcm is also richer than black rice and white rice. Therefore, it indicates that red rice has a great nutritional value for health. An essential amino acid diet is necessary to maintain physiological functions. Non-essential amino acids (glutamate, glutamine, and aspartate) play a crucial role in promoting the digestive process and protect the integrity of the intestinal mucosa [29].

Profile and Total Anthocyanin Content

The UV-Vis spectra profile shows two peaks in all red and black rice varieties, namely in the UV and visible light regions, both at pH 1.0 and pH 4.5 (Fig. 2(b-f)). However, in RREJbl red rice was exhibited the peak

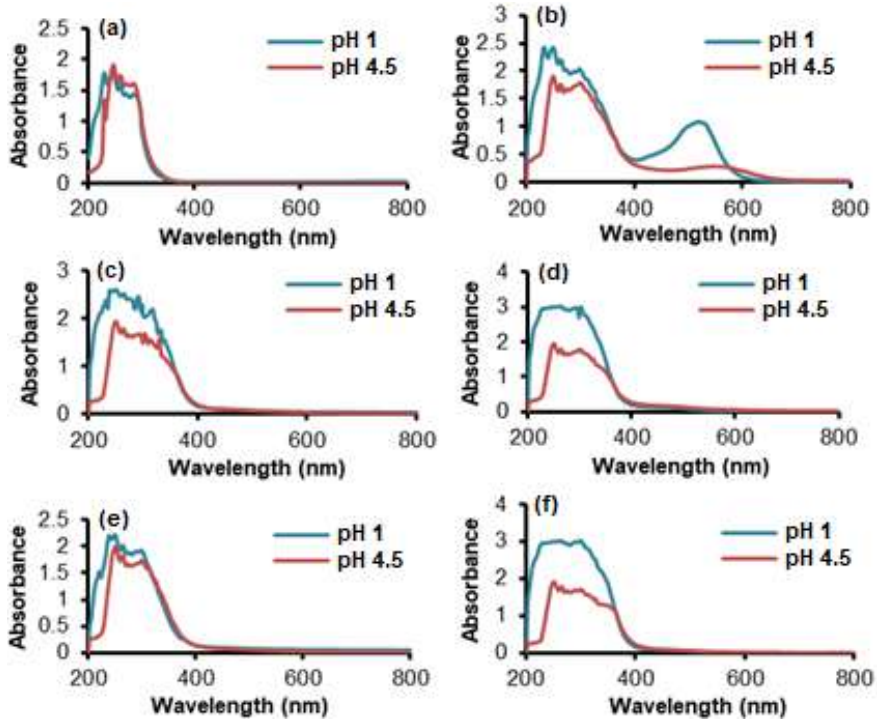

Fig 2. Anthocyanin profiles from UV-Vis spectrophotometry of (a) WREJms, (b) BREJwj, (c) RRCJcm, (d) RREJbl, (e) RRCJin and (f) RREJas

position at 451 nm at pH 1, while at pH 4.5, the peak position was at 466 nm. It indicates that the absorbance shift to a longer wavelength region (bathochromic). Anthocyanins are categorized as flavonoids due to flavylium ions in the heterocyclic C ring. Anthocyanins are ionic; as a result, they are more stable in low pH (< 3) solutions. At pH 4–5, flavylium cations and quinoidal anions are moderately formed to reduce anthocyanin pigments [30]. The spectra characteristic of anthocyanins is shown by two peaks; the first peak at 240–280 nm is assigned as the absorption of ring A, while the second peak at 450–560 nm shows the absorption of ring B [31].

Red rice contains phytochemicals such as phenolics, flavonoids, leucoanthocyanidins, anthocyanidins, tannins, quinones, and anthraquinones as antioxidants properties [18]. Anthocyanins are water-soluble and most organic solvents, but they are insoluble in non-polar organic solvents. Furthermore, alkaline or neutral solutions can decrease anthocyanins' stability [30]. In this study, RREJas red rice showed the highest total anthocyanin of 10.87 mg/g among red rice (Fig. 3). Previous research related to anthocyanins in rice showed that the total anthocyanin

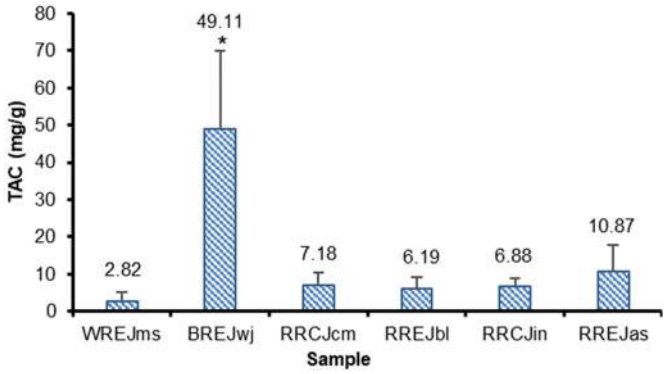

Fig 3. The total anthocyanin content (TAC) of pigmented rice. Error bars show standard deviation from triplicate. An asterisk (*) indicate the results test statistically significant ($p < 0.001$)

content in Sri Lanka red rice (SRI3) was 0.33 mg/100 g [7], whereas higher than RREJas red rice. Anthocyanins are modified by hydroxylation, methylation, glycosylation, and acylation, which control their color and stability. Modifications occurs at C3' (R1), C4' (R2), C5' (R3), C3 (R4), C5 (R5), and C7 (R6). The increase in the number of hydroxyl (-OH) groups in the B-ring will provide blue color in anthocyanins. Meanwhile,

increased methylation generates redness in anthocyanins. B-ring methylation causes anthocyanins to be easily oxidized and destabilizes [13].

Based on the TLC analysis, two spots were found in RREJbl red rice, RREJas, and BREJwj black rice. In RRCJcm and RRCJin, one spot was found, while white rice did not show any spots in visible light. Identifying separation TLC of the bioactive compound can be quantified based on the retention factor (Rf) value. The more polar compound has a smaller Rf value and vice versa. Molecules with OH or NH_2 groups are polar and more able to form hydrogen-silica matrix group (Si–OH) bonds. Thus, the compounds are more difficult to move upwards. Simultaneously, non-polar molecules have fewer interactions with the matrix and tend to be more soluble in the eluent to move upwards faster [32].

This study showed that RREJbl and RREJas showed a similarity of Rf value. Likewise, RRCJcm and RRCJin revealed the presence of anthocyanin (Fig. 4(a)). BREJwj was assumed to contain peonidin-3-*O*-glucoside and pelargonidin-3-*O*-glucoside [33,34]. A previous study [34] stated that the separation of TLC of anthocyanin compounds in berries showed an Rf value of 0.80, which corresponds to the pelargonidin-3-*O*-glucoside compound. A previous study revealed that rice bran extract's dark spots showed phenolic compounds, and blue fluorescent indicates the presence of flavonoids [12].

Characterization of flavonoids with TLC analysis of Bay leaves (*Eugenia polyantha*) showed the intense blue fluorescent in 366 nm with an Rf value of 0.26 indicating flavanols, and Rf of 0.44 and 0.77 represented flavones [35]. Hence, we predict that all rice may contain phenolic acid and flavonoid compounds (Fig. 4(b-c)). However, BREJwj showed the highest intensity. RREJbl red rice has a higher density than black rice and white rice (Fig. 5(a-b)). Thin-layer chromatography (TLC) analysis between black rice (*O. sativa* L.) from East Java, Central Java, and West Java showed that spot intensity and density were not significantly different from red rice and white rice [18].

FRAP Activity of Pigmented Rice Extracts

RREJas red rice showed the highest antioxidant activity with an IC_{50} value of 6.65 µg/mL, closest to ascorbic acid with an IC_{50} of 5.21 µg/mL (Fig. 6). The smaller IC_{50} value shows a higher antioxidant activity. The antioxidant activities from the highest to the lowest

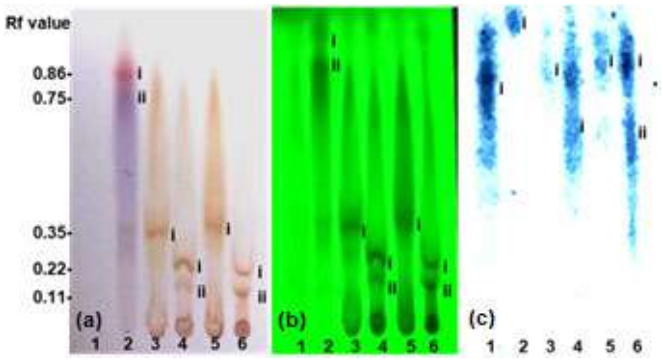

Fig 4. Anthocyanin profile based on thin layer chromatography (TLC) visualization under (a) visible light, (b) UV 254 nm, (c) UV 366 nm

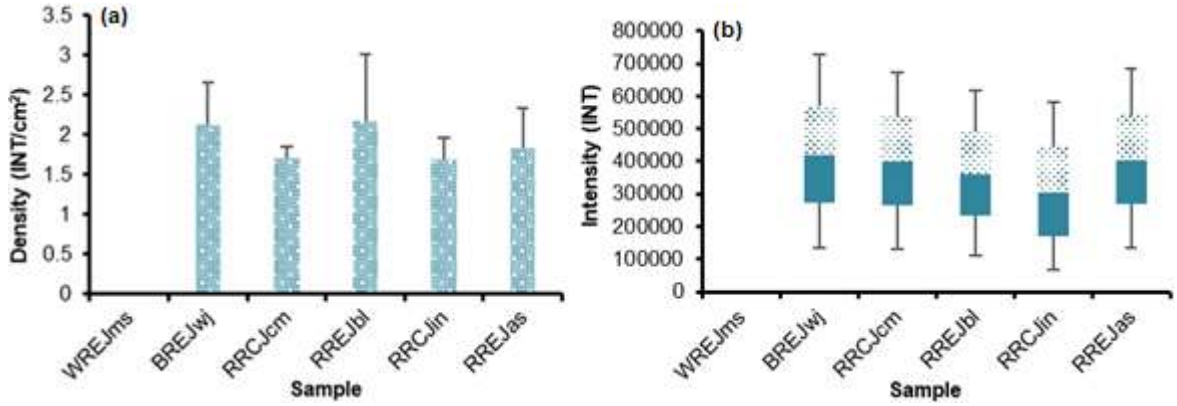

Fig 5. Density and intensity of red rice anthocyanin profiles based on TLC analysis. (a) density of each spot and (b) intensity. 1= WREJms. 2 = BREJwj. 3 = RRCJcm. 4 = RREJbl. 5 = RRCJin. 6 = RREJas

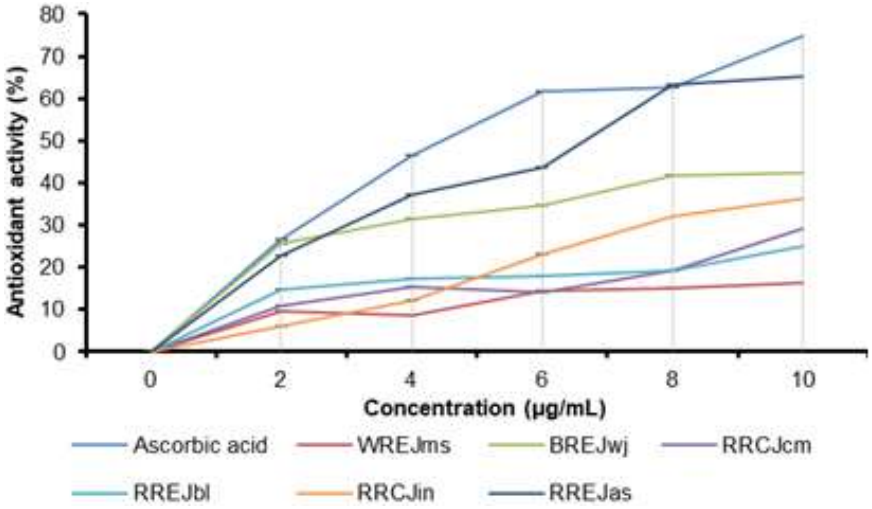

Fig 6. Antioxidant activity of pigmented rice anthocyanins in inhibiting Ferric-reducing/antioxidant power (FRAP) as free radicals. Error bars show the standard deviation from triplicates experiment

were RREJas, BREJwj, RRCJin, RRCJcm, RREJbl, and WREJms, with IC_{50} of 6.65, 12.87, 12.97, 21.78, 34.00, and 43.02 µg/mL, respectively (Table 2). Antioxidant activity of red rice anthocyanin extracts may have correlated with its structure, namely the number of hydroxyl groups in the pyran ring [B] and hydrogen donor or acceptor [16]. Furthermore, the presence of proanthocyanidin, phenolic, and flavonoid compounds is presumed to affect antioxidant activity in red rice. A previous study has shown that the antioxidant activity of red rice bran is higher than black and white rice bran in various free radical inhibition tests, which correlates positively with phenolic and flavonoid content. The dominant phenolic compounds found in red rice bran include ferulic, vanillic, and p-coumaric acids [36].

Inhibition of α-Amylase Enzyme

The α-amylase enzyme inhibition was performed to determine the anti-diabetic activity. This study used pigmented rice extracts to assess the activity of inhibiting the α-amylase enzyme with the acarbose synthetic drug as a positive control. RREJas had the highest percentage of α-amylase inhibition closes to BREJwj and acarbose with an IC_{50} of 144.46 µg/mL (Fig. 7 and Table 2). Therefore, our study indicated that RREJas red rice might have the potential as anti-diabetic. Polarity and the glucose group of anthocyanin affected to inhibit the α-amylase enzyme activity. A previous study showed that cyanidin-3-*O*-rutinoside is the most potent α-amylase inhibitor between cyanidin and cyanidin-3-*O*-glucoside [37]. Acarbose is known as an

Table 2. IC_{50} value of pigmented rice anthocyanins as FRAP and α-amylase inhibitor

No	Antioxidant activity		Antidiabetic activity	
	Sample	IC_{50} (µg/mL)	Sample	IC_{50} (µg/mL)
1	Ascorbic acid	5.21	Acarbose	16.53
2	WREJms	43.02	WREJms	198.22
3	BREJwj	12.87	BREJwj	109.03
4	RRCJcm	21.78	RRCJcm	172.58
5	RREJbl	34.00	RREJbl	183.73
6	RRCJin	12.97	RRCJin	172.20
7	RREJas	6.65	RREJas	144.46

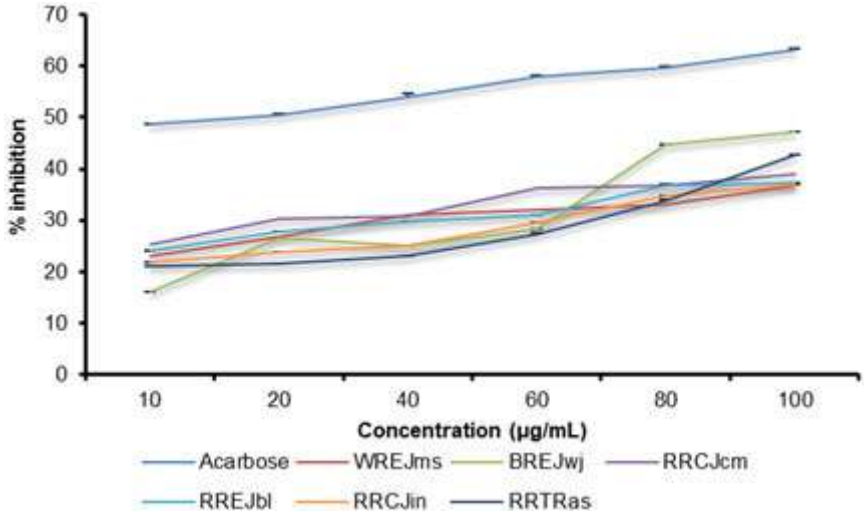

Fig 7. In vitro inhibition of α-amylase enzyme against pigmented rice anthocyanins

anti-diabetic drug that works by inhibiting digestive enzymes. Acarbose was found to bind to the catalytic site of α-amylase and bind to the residues of ASP197, GLU233, and ASP300. In silico studies related to anthocyanins on enzyme inhibition found that cyanidin-3-glucoside was most effective at inhibiting the α-amylase enzyme than cyanidin-3-rutinoside, cyanidin-3.5-glucoside, and peonidin-3-glucoside. However, the four anthocyanins were able to bind to the side chain of α-amylase at the same residue as the drug acarbose, namely the residue of GLU233 [38].

■ CONCLUSION

The present study revealed that carbohydrate, protein, lipid, water, and ash level in pigmented rice have different values. RREJbl red rice shows the lowest carbohydrate level. The RRCJcm red rice was rich in essential and non-essential amino acids. Thus, red rice is good for health-promoting properties. Spectra and TLC characteristics demonstrate the presence of anthocyanin in red rice. Total anthocyanin content in RREJas red rice was 10.87 mg/g, higher than white rice. Moreover, RREJas had high biological function activities as antioxidant and anti-diabetic through α-amylase inhibition. In the future, further research is needed to establish the anthocyanin compound of red rice in Indonesia by HPLC or LC/MS analysis and its health benefit.

■ ACKNOWLEDGMENTS

This research is funded by Professor Grants Brawijaya University 2019-2020 No. 08/UN10.F09/PN/2020 and the DIKTI (Directorate General of Higher Education) Grant for Magister Program 2020 No. 037/SP2H/LT/DRPM/2020.

■ AUTHOR CONTRIBUTIONS

Ayu Tri Agustin contributes to conception and design, acquisition of data, analysis, and interpretation of data, drafting the article, final approval of the version to be published. Anna Safitri contributes to the acquisition of data, drafting the article. Fatchiyah Fatchiyah contributes to conception and design, analysis and interpretation of data, drafting the article, critically revising the article for important intellectual content, final approval of the version to be published.

■ REFERENCES

[1] Rathna Priya, T.S., Eliazer Nelson, A.R.L., Kavitha, R., and Antony, U., 2019, Nutritional and functional properties of coloured rice varieties of South India: A review, *J. Ethn. Foods*, 6 (1), 11.

[2] Thushara, P.A.N., Godakumbura, P.I., and Prashantha, M.A.B., 2019, Importance, health benefits and bioactivities of Sri Lankan traditional rice (*Oryza sativa* L.) varieties: A review, *Int. J.*

Agric. Environ. Biores., 4 (3), 119–128.

[3] Wang, W., Li, Y., Dang, P., Zhao, S., Lai, D., and Zhou, L., 2018, Rice secondary metabolites: structures, roles, biosynthesis, and metabolic regulation, *Molecules*, 23 (12), 3098.

[4] Raghuvanshi, R.S., Dutta, A., Tewari, G., and Suri, S., 2017, Qualitative characteristics of red rice and white rice procured from local market of Uttarakhand: A comparative study, *J. Rice Res.*, 10 (1), 49–53.

[5] Saragih, B., Naibaho, N.M., and Saragih, B., 2019, Nutritional, functional properties, glycemic index and glycemic load of indigenous rice from North and East Borneo, *Food Res.*, 3 (5), 537–545.

[6] Ghasemzadeh, A., Karbalaii, M.T., Jaafar, H.Z.E., and Rahmat, A., 2018, Phytochemical constituents, antioxidant activity, and antiproliferative properties of black, red, and brown rice bran, *Chem. Cent. J.*, 12 (1), 17.

[7] Sompong, R., Siebenhandl-Ehn, S., Linsberger-Martin, G., and Berghofer, E., 2011, Physicochemical and antioxidative properties of red and black rice varieties from Thailand, China and Sri Lanka, *Food Chem.*, 124 (1), 132–140.

[8] Thitipramote, N., Pradmeeteekul, P., Nimkamnerd, J., Chaiwut, P., Pintathong, P., and Thitilerdecha, N., 2016, Bioactive compounds and antioxidant activities of red (Brown Red Jasmine) and black (Kam Leum Pua) native pigmented rice, *Int. Food Res. J.*, 23 (1), 410–414.

[9] Anggraeni, V.J., Ramdanawati, L., and Ayuantika, W., 2019, Optimization of total anthocyanin extraction from brown rice (*Oryza nivara*), *J. Phys.: Conf. Ser.*, 1338, 012006.

[10] Wahyuningsih, S., Wulandari, L., Wartono, M.W., Munawaroh, H., and Ramelan, A.H., 2017, The effect of pH and color stability of anthocyanin on food colorant, *IOP Conf. Ser.: Mater. Sci. Eng.*, 193, 012047.

[11] Dyankova, S., and Doneva, M., 2016, Extraction and characterization of anthocyanin colorants from plant sources, *AST*, 8 (1), 85–89.

[12] Rukmana, R.M., Soesilo, N.P., Rumiyati, R., and Pratiwi, R., 2017, The effect of ethanolic extract of black and white rice bran (*Oryza sativa* L.) on cancer cells, *Indones. J. Biotechnol.*, 21 (1), 63–69.

[13] Wu, H.Y., Yang, K.M., and Chiang, P.Y., 2018, Roselle anthocyanins: antioxidant properties and stability to heat and pH, *Molecules*, 23 (6), 1357.

[14] Ali, H.M., Almagribi, W., and Al-Rashidi, M.N., 2016, Antiradical and reductant activities of anthocyanidins and anthocyanins, structure-activity relationship and synthesis, *Food Chem.*, 194, 1275–1282.

[15] Agustin, A.T., Safitri, A., and Fatchiyah, F., 2020, An in silico approach reveals the potential function of cyanidin-3-O-glucoside of red rice in inhibiting the advanced glycation end products (AGES)-receptor (RAGE) signaling pathway, *Acta Inform. Med.,* 28 (3), 170–179.

[16] Sari, D.R.T., Cairns, J.R.K., Safitri, A., and Fatchiyah, F., 2019, Virtual prediction of the delphinidin-3-O-glucoside and peonidin-3-O-glucoside as anti-inflammatory of TNF-α signaling, *Acta Inform. Med.*, 27 (3), 152–157.

[17] Rahayu, W.M., Astuti, M., and Marsono, Y., 2019, Improved hypoglycemic effect of anthocyanin extract combination from red rice and black soybean, *J. Phys.: Conf. Ser.*, 1146, 012015.

[18] Fatchiyah, F., Sari, D.R.T., Safitri, A., and Cairns, J.R.K., 2020, Phytochemical compound and nutritional value in black rice from Java Island, Indonesia, *Syst. Rev. Pharm.*, 11 (7), 414–421.

[19] Boue, S.M., Daigle, K.W., Chen, M.H., Cao, H., and Heiman, M.L., 2016, Antidiabetic potential of purple and red rice (*Oryza sativa* L.) bran extracts, *J. Agric. Food Chem.*, 64 (26), 5345–5353.

[20] Khalil-Moghaddam, S., Ebrahim-Habibi, A., Pasalar, P., Yaghmaei, P., and Hayati-Roodbari, N., 2012, Reflection on design and testing of pancreatic alpha-amylase inhibitors: An in silico comparison between rat and rabbit enzyme models, *Daru, J. Pharm. Sci.*, 20 (1), 77.

[21] Cirak, C., and Radusiene, J., 2019, Factors affecting the variation of bioactive compounds in *Hypericum* species, *Biol. Futura*, 70 (3), 198–209.

[22] Sadimantara, M.S.A., Asranudin, Holilah, Sadimantara, F.N., and Asyik, N., 2019, Physicochemical and antioxidant properties of red

rice varieties of Wakawondu and Wangkariri from North Buton, Indonesia, *Int. J. Sci. Technol. Res.*, 8 (8), 1623–1627.

[23] Kurnianingsih, N., Ratnawati, R., Fatchiyah, F., Barlianto, W., Ali, M.M., Safitri, A., and Suyanto, E., 2019, The difference of amino acid profiling from two morphological purple sweet potatoes from Kawi Mountain cultivars, East Java, Indonesia, *J. Phys.: Conf. Ser.*, 1374, 012017.

[24] Dini, C., Zaro, M.J., Rolny, N., Caputo, M., Boido, E., Dellacassa, E., and Viña, S.Z., 2020, Characterization and stability analysis of anthocyanins from *Pachyrhizus ahipa* (Wedd) Parodi roots, *Food Biosci.*, 34, 100534.

[25] Laokuldilok, T., Shoemaker, C.F., Jongkaewwattana, S., and Tulyathan, V., 2011, Antioxidants and antioxidant activity of several pigmented rice brans, *J. Agric. Food Chem.*, 59 (1), 193–199.

[26] Kazeem, M.I., Ogunbiyi, J.V., and Ashafa, A.O.T., 2013, *In vitro* studies on the inhibition of α-amylase and α-glucosidase by leaf extracts of *Picralima nitida* (Stapf), *Trop. J. Pharm. Res.*, 12 (5), 719–725.

[27] Thaidi, N.I.A., Jusoh, H.M., Ghazali, A.B., Susanti, D., and Haron, N., 2020, The effect of bioactive polyphenols from *Anacardium occidentale* Linn. leaves on α-amylase and dipeptidyl peptidase IV activities, *Indones. J. Chem.*, 20 (5), 1010–1017.

[28] Kulasinghe, A., Samarasinghe, G., Wimalasiri, S., Silva, R., and Madhujith, T., 2019, Macronutrient and Mineral Composition of Selected Traditional Rice Varieties in Sri Lanka, *Proceedings of the International Conference on Food Quality, Safety and Security (FOOD QualSS 2018)*, Colombo, Sri Lanka, 24-25 October 2018.

[29] Wu, G., 2014, Dietary requirements of synthesizable amino acids by animals: A paradigm shift in protein nutrition, *J. Anim. Sci. Biotechnol.*, 5 (1), 34.

[30] Khoo, H.E., Azlan, A., Tang, S.T., and Lim, S.M., 2017, Anthocyanidins and anthocyanins: colored pigments as food, pharmaceutical ingredients, and the potential health benefits, *Food Nutr. Res.*, 61 (1), 1361779.

[31] Kumar, S., and Pandey, A.K., 2013, Chemistry and biological activities of flavonoids: An overview, *Sci. World J.*, 2013, 162750.

[32] Namir, H., Hadžić, R., Malešević, I., Jurčević, M., and Starčević, D., 2019, Application of thin layer chromatography for qualitative analysis of gunpowder in purpose of life prediction of ammunition, *Int. J. Biosens. Bioelectron.*, 5 (1), 4–12.

[33] Cretu, G.C., and Morlock, G.E., 2014, Analysis of anthocyanins in powdered berry extracts by planar chromatography linked with bioassay and mass spectrometry, *Food Chem.*, 146, 104–112.

[34] Filip, M., Vlassa, M., Copaciu, F., and Coman, V., 2012, Identification of anthocyanins and anthocyanidins from berry fruits by chromatographic and spectroscopic techniques to establish the juice authenticity from market, *JPC J. Planar Chromatogr. - Mod. TLC*, 25 (6), 534–541.

[35] Syarifah, A.L., Retnowati, R., and Soebiantoro, S., 2019, Characterization of secondary metabolites profile of flavonoid from salam leaves (*Eugenia polyantha*) using TLC and UV spectrophotometry, *Pharm. Sci. Res.*, 6 (3), 155–163.

[36] Jun, H.I., Song, G.S., Yang, E.I., Youn, Y., and Kim, Y.S., 2012, Antioxidant activities and phenolic compounds of pigmented rice bran extracts, *J. Food Sci.*, 77 (7), C759–C764.

[37] Akkarachiyasit, S., Yibchok-Anun, S., Wacharasindhu, S., and Adisakwattana, S., 2011, *In vitro* inhibitory effects of cyandin-3-rutinoside on pancreatic α-amylase and its combined effect with acarbose, *Molecules*, 16 (3), 2075–2083.

[38] Sui, X., Zhang, Y., and Zhou, W., 2016, *In vitro* and *in silico* studies of the inhibition activity of anthocyanins against porcine pancreatic α-amylase, *J. Funct. Foods*, 21, 50–57.

Synthesis and Characterization of CaO Limestone from Lintau Buo Supported by TiO_2 as a Heterogeneous Catalyst in the Production of Biodiesel

Vivi Sisca[1,2], Aju Deska[1], Syukri[1], Zilfa[1], and Novesar Jamarun[1*]

[1]*Department of Chemistry, University of Andalas, Limau Manis, Padang 25163, West Sumatera, Indonesia*

[2]*Department of Biology Education, Institute of Education YPM Bangko, Jendral Sudirman St. 2, Meranging, Jambi 37313, Indonesia*

* ***Corresponding author:***

tel: +62-751-71671
email: novesarjamarun@sci.unand.ac.id

Received: March 13, 2021
Accepted: June 16, 2021

DOI: 10.22146/ijc.64675

Abstract: *Biodiesel constitutes an alternative to diesel fuel, developing a base catalyst in cost efficiency and reducing the impact on the environment due to toxic waste and excessive chemicals. This study employed a mixture of an oxide catalyst, CaO/TiO_2, which was ably synthesized as a heterogeneous catalyst to convert waste frying oil (WFO) into biodiesel. Heterogeneous catalysts have been characterized by XRD, FT-IR, TEM, SEM-EDX, and BET to identify their crystal type, morphology, composition, and surface area. Catalytic activity was affected by the amount, oil/methanol ratio, reaction temperature, and duration. A 94% biodiesel yield was achieved by optimizing the following reaction parameters: 5wt.%, 6:1 methanol: oil, 65 °C, for 4 h. The addition of TiO_2 to CaO improves the catalyst stability and transforms the reactants into products. The structure and characteristics of TiO_2 maintained stability and supported CaO well. Its repeated biodiesel fuel production demonstrated the catalyst stability from WFO throughout the transesterification reaction.*

Keywords: *CaO/TiO_2; heterogeneous catalyst; WFO; transesterification; biodiesel*

■ INTRODUCTION

The global energy demand continues to increase with the rapidly growing population, transportation needs, and industries that use fuel in carrying out activities. However, environmental damage due to excessive fuel use is a significant concern for developed and developing countries. Among the solutions offered is producing an environmentally-friendly energy fuel such as biodiesel. It is a better alternative fuel than others since it has similar characteristics to diesel fuel produced by the mining industry. Well-known to be highly biodegradable and non-toxic and contributes to low carbon dioxide (CO_2) emissions into the environment [1]. Biodiesel production typically uses homogeneous and heterogeneous catalysts through transesterification reactions [1-2]. The advantages of heterogeneous catalysts are that they are environmentally friendly, reduce waste problems, are easily separable from glycerol, have higher activity and selectivity, and are reusable in transesterification reactions [3-4]. Therefore, over the past decade, heterogeneous catalysts have become an essential subject in biodiesel production applications, such as using alkaline materials as solid catalysts [5-6].

Based on the related literature, metal oxides are often applied in biodiesel production at transesterification reaction of triglycerides to biodiesel [7-8]. CaO is a cheap and abundant [9] heterogeneous base catalyst with a significant quantity and efficiency in biodiesel applications [10]. However, the main problem is that CaO is unstable due to leaching during the transesterification process, which interferes with the catalytic activity [11]. Therefore, current research concentrating on applying various catalytic aids to overcome this problem has increased [12-13]. The solution is to modify CaO to stabilize the catalyst in repeated use, such as modification with TiO_2.

TiO_2 is among the catalytic supports heavily investigated based on several benefits such as its high porosity, better structural power, solid molecular

structure, reliable thermal properties, and non-toxicity [14]. Additionally, TiO_2 possesses a small crystal size and high adsorption power [15]. Due to the advantages mentioned earlier, numerous studies on the application of TiO_2 with other metal modifications have been carried out. For example, lithium was impregnated with TiO_2 catalyst for biodiesel production with a product yield of 98% [16]. De and Boxi [17] investigated Cu impregnated TiO_2 to produce biodiesel, achieving 90.93% at 45 °C and methanol to oil ratio of 20:1 for 45 min. Mohammad et al. suggested the modification of TiO_2 with CaO by the Ti ion substitution process in the Ca lattice. The Ti(IV) ion has a higher valence than the Ca(II) ion, resulting in defects and stable catalytic results [1]. Consequently, TiO_2 is reliable in modifying CaO, allowing the catalytic activity to be more consistent than the CaO-only method. Thus, the search for heterogeneous catalysts can produce satisfying products with short reaction times, lower temperature and pressure, selling points, and high-quality measurement standards in biodiesel manufacturing [18-19].

This study aims to develop heterogeneous catalysts in the transesterification process by exploring CaO from limestone supported by TiO_2. The CaO/TiO_2 catalyst modification process was employed to synthesize biodiesel from WFO by examining the effect of methanol/oil ratio, catalyst weight, and temperature as test parameters. Additionally, the repeated use of catalysts has been investigated to solve production costs for manufacturing biodiesel. Furthermore, the characterization of the catalyst is to determine the characteristics of the material properties.

■ EXPERIMENTAL SECTION

Materials

Waste Frying oil (WFO) was obtained from traders who sell fried foods in Indonesia's Padang area. The limestone was obtained from the Lintau Buo area of West Sumatra, Indonesia. TiO_2, CH_3OH, and n-hexane were obtained from Merck, Indonesia. Most of the chemicals were received without further purification.

Instrumentation

Evaluation of catalyst crystallography was carried out using a PANalytical Expert Pro X-ray diffractometer (XRD) diffractometer equipped with Cu-Kα radiation. The elemental compositions were analyzed using X-ray Spectroscopy (EDX) combined with SEM. The FTIR spectrum was analyzed by utilizing a Bruker Tensor 27 in the wavelength of 4000–500 cm^{-1} to determine the catalyst's functional groups. The BET technique was employed to assess the surface area (SA) and pore distribution with N_2 adsorption at 77 K using Quantachrome's Autosorb 1C. Catalyst surface morphology was then examined using (TEM) and scanning electron microscopy (SEM), JEOL energy scattering (JSM-6290LV). Gas Chromatography-Mass Spectroscopy (GC-MS) of FAAEs was performed on the Bruker GC-45 X applying the Scion MS system.

Procedure

Catalyst preparation

Preparation of CaO. A total of 10 g of sieved limestone with 90 µm was prepared, washed with water, and allowed to dry for 3 h at 105 °C. The sample was then crushed and calcined at 900 °C for 5 h to produce CaO.

Preparation of CaO/TiO_2. In designing the catalyst, the composition of CaO dopants on the TiO_2 support matrix is crucial. Therefore, CaO and TiO_2 were varied (0.25:1, 0.5:1, 0.75:1, 1:1, and 1.25:1 mol/mol). The CaO/TiO_2 catalyst was prepared by the wet impregnation method [20]. CaO was mixed with 100 mL of distilled water to dilute the solution before adding TiO_2. The solution was then stirred for 4 h at 50 °C and dried for 2 h at 100 °C. Next, it was calcined for 5 h in a furnace at 600 °C. Finally, the sample was cooled and stored in a desiccator. A catalyst is used in the transesterification reaction to study the catalytic activity. The CaO/TiO_2 (1:1 mol/mol ratio) with the most optimal activity was used as a catalyst for further process.

Catalytic activity test

The catalytic activity was determined by using a catalyst in the transesterification reaction. An investigation was carried out inside a 500 mL three-neck flask outfitted with a condenser and magnetic stirrer. In the initial stage, 5 wt.% catalyst was filled into a flask. After that, methanol and WFO were mixed at a ratio of

6:1(methanol:oil) at a speed of 850 rpm, at 65 °C for 4 h. After the reaction is complete, transfer to a separatory funnel to separate the product from the glycerol. To see the parameters that affect the catalytic activity carried out under the following conditions and variables: the amount of catalyst (1, 3, 5, 7 wt.%), methanol:oil ratio (3:1, 6:1, 9:1, 12:1), reaction temperature (55, 60, 65, and 70 °C), reaction time (2, 4, 6, and 8 h), and stability (1, 2, 3, 4). Each product obtained was analyzed using GC-MS to determine the amount of methyl ester compound. The following equation is used:

$$\text{Yield of biodiesel } (\%) = \frac{\text{weight of biodiesel}}{\text{weight of oil}} \times 100\% \quad [21]$$

■ RESULTS AND DISCUSSION

XRD Analysis

In this study, characterization was carried out on CaO/TiO_2 1:1 catalyst at optimal reaction conditions. XRD analysis determines the crystallinity of fresh and used CaO/TiO_2 catalyst, as depicted in Fig. 1. Phase identification of the X-ray diffraction pattern was carried out using Highscore Plus software, using the search match method, and refinement was performed using the Rietveld method. The CaO/TiO_2 catalyst demonstrated peaks of CaO at 2θ = 32.43, 37.62, 54.24, 64.65, and 67.90°; and peaks of $Ca(OH)_2$ at 2θ = 18.07, 28.72, 34.15, 47.21, 50.89, 54.45, 62.72, and 64.39°. TiO_2 anatase is confirmed by the diffraction at 2θ = 25.32, 36.99, 37.86, 38.59, 48.05, 53.96, 55.079, 62.736 and 75.12°. The presence of CaO peaks is the result of limestone calcination [22]. When exposed to air and hydrated, peaks of $CaCO_3$ and $Ca(OH)_2$ appear [23-24]. The diffraction of CaO/TiO_2 is a combination of the peak of TiO_2 and CaO [25-26]. In addition, $CaTiO_3$ peaks were observed at 2θ = 32.88, 33.12, 33.29, 47.49, 47.59, 58.86, 59.38, and 69.50°, which were formed due to the interaction between CaO and TiO_2 on the catalyst surface [27]. The XRD results also follow SEM and TEM analysis, showing that the CaO catalyst was successfully supported using TiO_2 to improve catalyst activity. After being used for the reaction, XRD results of CaO/TiO_2 showed peaks of $Ca(OH)_2$ at 2θ = 18.09, 34.15, 47.21, and 50.89°. Characteristic of $CaCO_3$ was observed at 2θ = 29.37, 35.95, 39.39, 43.14, 47.48, 48.48°,

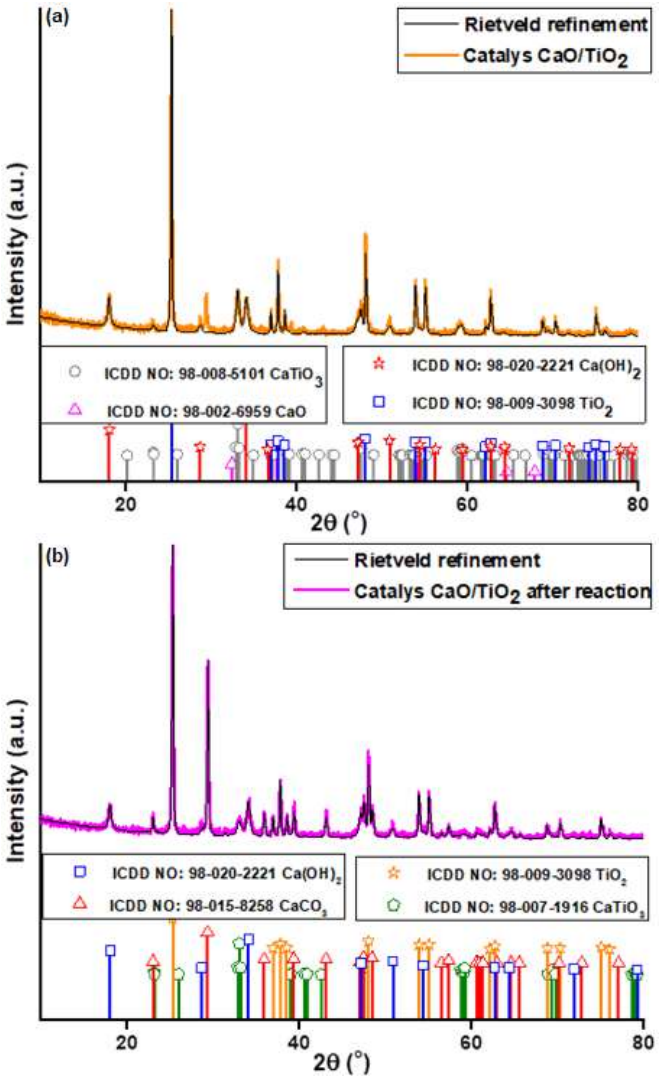

Fig 1. XRD pattern of CaO/TiO_2 (a) before and (b) after transesterification

while the TiO_2 was at 2θ = 25.32, 37.85, 48.05, 53.96, 55.08, and 75.12°. The presence of $CaTiO_3$ can be confirmed from the diffraction at 2θ = 32.86, 33.06, 33.23, 47.43, 47.48, 59.27, and 69.37°. The XRD pattern of before and after used in a transesterification were different since the interaction between the catalyst and WFO affects the active site and causing the changes in the catalytic activity.

FTIR Analysis

FTIR analysis was carried out to determine the functional groups of CaO/TiO_2 catalysts before and after use (shown in Fig. 2). The FTIR spectrum of the catalysts

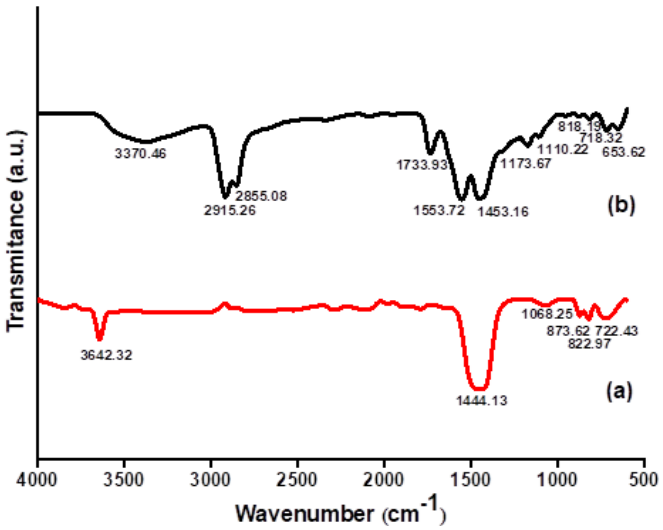

Fig 2. FTIR spectra of CaO/TiO_2 (a) before and (b) after transesterification

before used has two sharp and broad peaks at the wavenumber of 3642 cm^{-1}, associated with the -OH vibration [7]. Identical CaO bonds are observed at the wavenumbers of 1444.13 cm^{-1} and 873.62 cm^{-1} [26-28]. An absorption at 722.43 cm^{-1} is associated with the vibration of the Ti–O bond [29-30]. The new phase of $CaTiO_3$ is found at a wavenumber of 1068.25 cm^{-1} [13]. For the used sample, the catalyst showed a peak at a wavenumber of 3370.46 cm^{-1}, which was associated with –OH vibrations [31]. Wavenumbers of 2855.08 cm^{-1} and 2915.26 cm^{-1} were attributable to the stretching vibration of the C-H bond. The strain characteristic of the carbonate ion C=O was observed at 1733.93 cm^{-1} [16], while absorption at 1553.72 cm^{-1} was associated with the $-CH_2$ groups [32]. A new phase of $CaTiO_3$ observed at 1110.22 cm^{-1} and 718.32 cm^{-1} was related to Ti–O vibrations [7,33]. The existence of C–H and $-CH_2$ stretching vibrations suggesting the presence of organic compounds on the catalyst, as can be seen in the morphological analysis.

Morphological Analysis with SEM and TEM

The morphology of the CaO/TiO_2 catalyst before and after the reaction analyzed using SEM and TEM are shown in Fig. 3. Analysis of CaO/TiO_2 using TEM (Fig. 3(a)) and SEM (Fig. 3(b)) shows agglomeration in various particle shapes. It was seen on the TEM image that the refined grains were scattered on the spherical particles. This phenomenon indicates that the sample consists of two mixed oxides. According to EDX results,

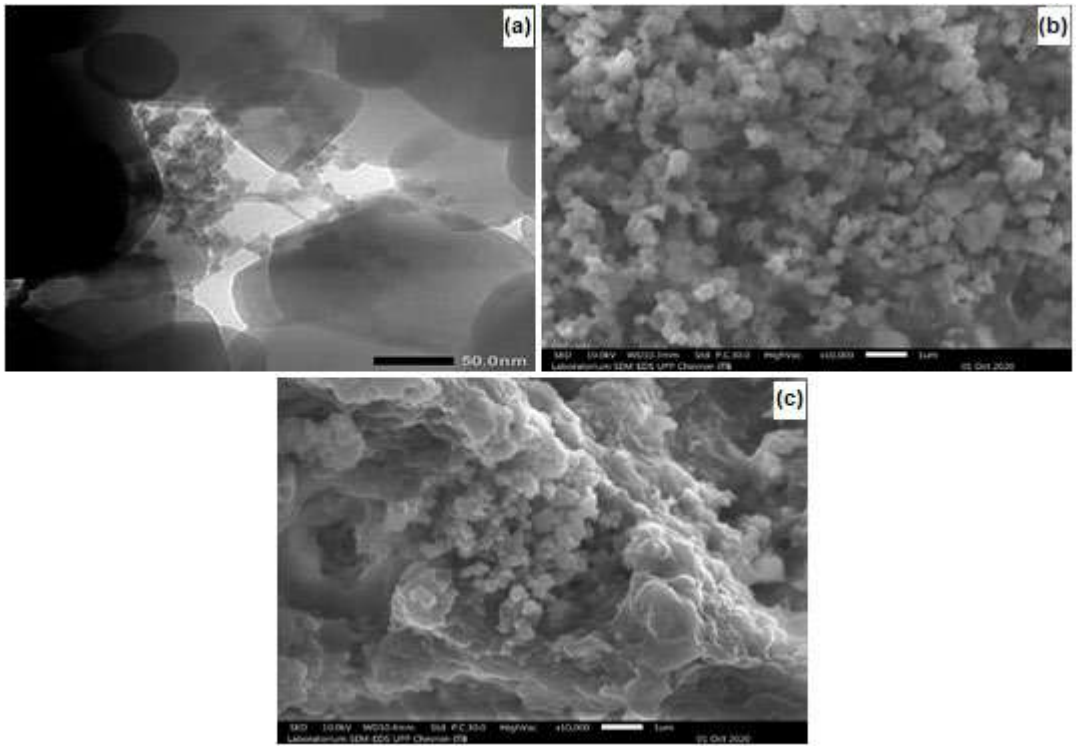

Fig 3. (a) TEM image of CaO/TiO_2 and SEM images of CaO/TiO_2 (b) before and (c) after a reaction

the catalyst consists of Ca, and Ti confirmed that CaO is dispersed in the TiO_2 support matrix. The results of the analysis are in agreement with those in Ref. [33]. CaO combined with TiO_2 causes an increase in catalyst stability, primarily due to the interaction between the two metal oxides, as evidenced by the presence of $CaTiO_3$ on XRD. TiO_2 support can maintain the catalytic activity of CaO, which can avoid leaching in the reaction medium [34]. After transesterification, the morphology of the catalyst shows that the sample had agglomeration and accumulation of glycerol on the active surface. It is assumed that the adsorption of fatty acids or glycerol in the pores inhibits further transesterification between the reactants and the active site of the pores [35].

EDX Analysis

EDX was used to determine the CaO/TiO_2 catalyst components before and after use, as shown in Fig. 4. The EDX results show that Ca and Ti elements were the components of the CaO/TiO_2 catalyst. Meanwhile, the catalyst was used also contains the same elements. However, there was a change in composition, namely, a decrease in the amount of Ca and Ti on the catalyst's surface. Therefore, this case produces fewer CaO particles [12]. The availability of Ca and Ti indicates that the catalyst has good catalytic activity in converting reactants into products due to the cooperation between the dopant and the support matrix.

Catalyst Surface Area

The surface area directly affects the catalytic activity. Higher catalytic activity is gained from a larger surface area [1]. The surface area of CaO/TiO_2 of 136 m^2/g, and this larger surface area was associated with the addition of TiO_2 (Table 1). A high interaction of TiO_2 with CaO provides an increase in the surface area of the catalyst, which reduces the surface diffusion of CaO. Aside from that, it results in sintering and a stable crystalline structure of CaO/TiO_2 [36]. After the catalyst was used, the surface area was enhanced to 252 m^2/g. Increasing the surface area can maintain the catalytic activity upon reuse [19].

Comparison of Biodiesel Yield Using CaO and TiO_2 Catalyst

The catalytic test for the CaO catalyst obtained a Fatty Acid Methyl Ester (FAME) yield of 86%, compared to the 61% yield by TiO_2 catalyst (carried out in our previous study) in (Fig. 5). This indicates that the difference in the amount of product is probably affected by the strength of the catalyst interacting with the surface. However, CaO can only be used twice with the highest yield. The 3rd and 4th repetitions experienced decreased activity and the number of FAME products [37]. Therefore, we are interested in improving the catalytic activity of CaO with the support of TiO_2.

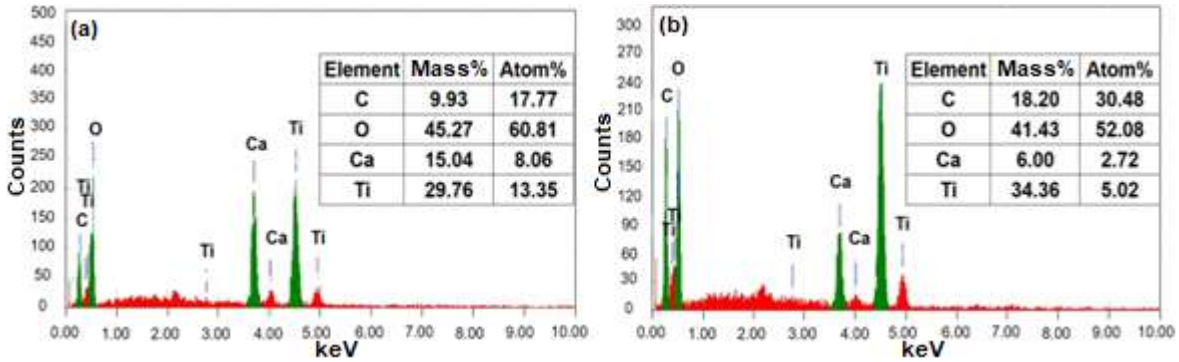

Fig 4. EDX analysis of CaO/TiO_2 (a) before and (b) after a reaction

Table 1. The surface area of CaO/TiO_2 before and after reaction

Catalyst	Surface area (m^2/g)	Pore volume (cc/g)	Pore size (Å)
CaO/TiO_2	136	0.389	20.27
CaO/TiO_2 after reaction	252	0.520	15.85

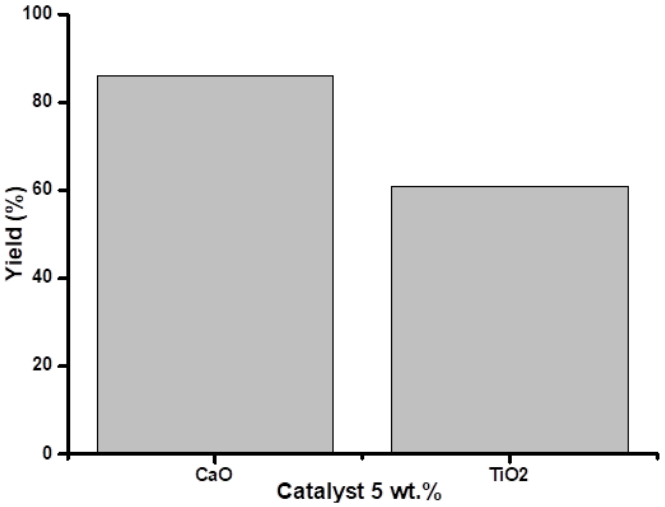

Fig 5. Yield product of biodiesel using (a) CaO and (b) TiO_2

Catalytic Activity Test

Effect of CaO/TiO₂ ratio

The transesterification reaction with different total weight ratios is shown in Fig. 6. This demonstrates the catalytic performance of a mixture of CaO/TiO_2 oxides with various Ca/Ti mol ratios. The FAME increases by increasing the CaO/TiO_2 ratio up to 1:1. However, it starts to decrease by increasing the ratio, possibly due to the destruction of the TiO_2 lattice structure at higher CaO concentrations because of the lattice mismatch, which inevitably causes structural instability within the material [38]. The changes in the material structure and catalytic properties were also disrupted, directly affecting biodiesel yield [17]. These results indicate that the optimum Ca/Ti ratio obtained is 1:1 at 94%. In other words, the Ca addition is the reason for obtaining the maximum amount of product.

Effect amount of catalyst

The impact of loading CaO/TiO_2 on biodiesel yield was investigated by assorting the catalyst weight 1, 3, 5, and 7 wt.%. The use of catalysts up to 5 wt.% gradually increased biodiesel production and achieved a maximum of 94%. However, the increase in yield is insignificant after attaining the optimum result. The addition of a catalyst can further reduce the biodiesel yield, primarily owing to the decreasing quantity of active sites that could swift the reaction rate [39]. In addition, the catalyst was used excessively, causing the reactants and their products to be absorbed by the catalyst powder. This results in aggregation and thus reducing the total active sites [40]. According to Wen et al. [19], the maximum yield was 85.3% within the following reaction conditions: methanol/oil 50:1, 10 wt.%, and 433 K. Meanwhile, Mguni et al. [25] reported that the maximum biodiesel yield was 84% under the reaction conditions: 225 °C, 1 h, methanol/oil 18:1, and 5 wt.% (Fig. 7).

Effect of methanol:oil molar ratio

The ratio of methanol:oil is an essential parameter

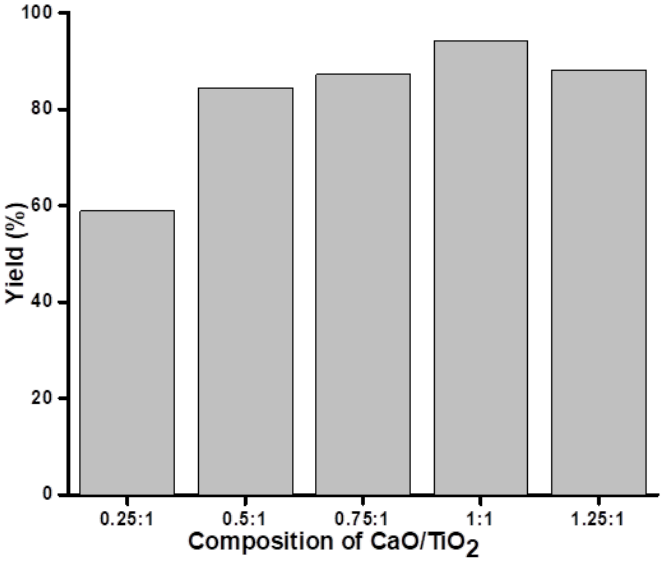

Fig 6. Effect of CaO/TiO_2 ratio on biodiesel yield

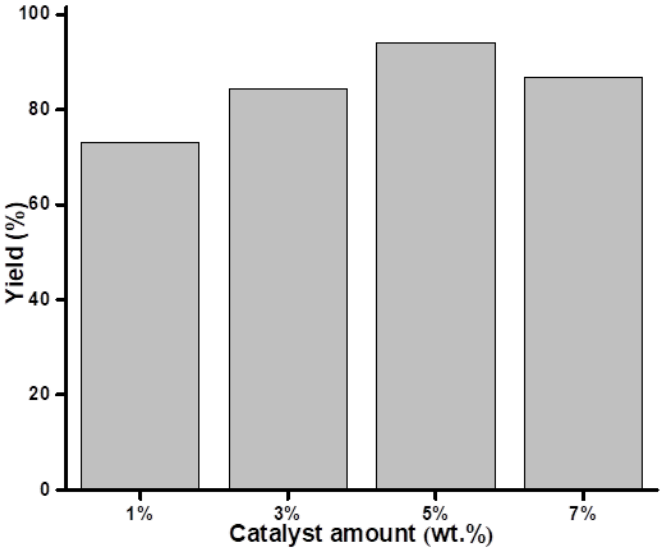

Fig 7. Effect of CaO/TiO_2 catalyst ratio on biodiesel yield

in transesterification to obtain the maximum biodiesel yield. Transesterification is a reversible reaction, and excessive methanol is intended to shift the equilibrium forward to obtain the optimal results [41]. In determining the optimal ratio of methanol:oil, the reactions implemented with different rates, 3:1, 6:1, 9:1, and 12:1. The yield of FAME products increases with a ratio up to 6:1. Nonetheless, a drop in the result was noticed when the ratio exceeded 6:1. This is because excessive alcohol consumption complicates the heating and elimination processes. To improve transesterification, the molar ratio of methanol:oil is retained [18]. Therefore, 6:1 was considered the optimal ratio for biodiesel yield. The results were not significantly different from Madhuvilakku and Piraman [18], which reported that the optimum conversion was 92.2% in 200 mg at 60 °C for 5 h with methanol:oil ratio of 6:1. Therefore, the ratio of 6:1 was considered the optimal ratio for biodiesel yield. The results were not significantly different from Suprapto et al. [42]; the optimum conversion was 56.13% in 1% of catalyst at 60 °C for 2 h, with methanol:oil ratio of 1:1 (Fig. 8).

Effect of reaction temperature

The reaction temperature has a crucial impact on the transesterification reaction. Transesterification was performed at 55, 60, 65, and 70 °C. The biodiesel yield improves with an increase in the temperature up to 65 °C, leading to a reduction. At a low temperature, the reaction is not totally done before, resulting in a low biodiesel yield. A moderate temperature of 65 °C can affect the reaction by increasing the kinetic energy, leading to a higher product [43]. At relatively high reaction temperatures, FAME with a low yield was acquired because the evaporation of methanol is in the vicinity of a similar temperature. During the reaction, methanol was lost and inhibited the transesterification [44]. Consequently, T = 65 °C was considered as the optimal temperature for biodiesel yield. The results obtained were similar to those of Mohammad et al. [1] mentioned that the optimum result was 93.33% in the following conditions: calcination at 600 °C, 0.5%, palm oil:methanol ratio of 3:5, reaction at 65 °C, 150 min, and ± 500 rpm. In the experiment by Moradi et al. [45], the optimum yield was 98.5% by using methanol:oil ratio of 16:1, 6 wt.%, at 60 °C, for 8 h (Fig. 9).

Effect of reaction time

Time is among the crucial variables for the reaction to obtain product selectivity. Therefore, the biodiesel production process was conducted at various durations to optimize the reaction's completion time. The procedure was repeated for 2, 4, 6, and 8 h. The interaction was slow for the first 2 h because there was insufficient time to increase the mixing and dispersion of the catalyst and methanol in WFO [46]. However, within

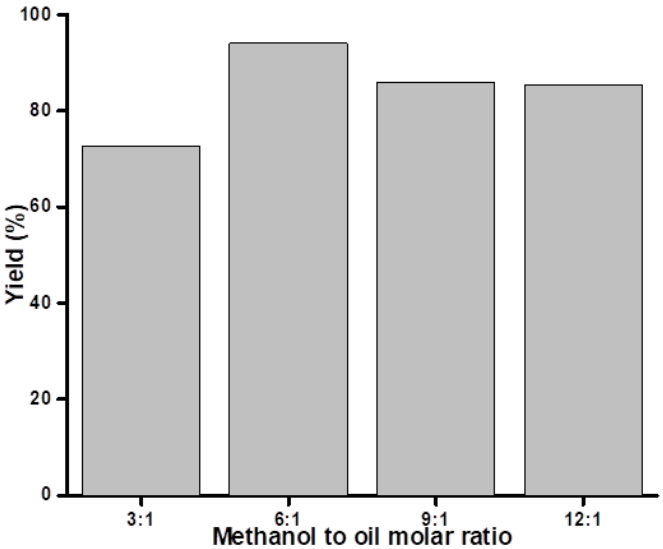

Fig 8. Effect of methanol/oil ratio on biodiesel yield

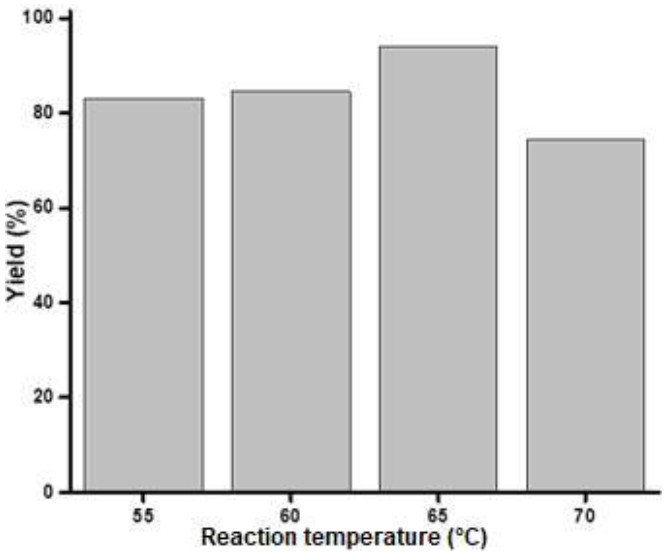

Fig 9. Effect of reaction temperature on biodiesel yield

4 h, the interaction between the reactants and products could increase the reaction rate. The amount of product tends to decrease when it exceeded the optimum time, as shown in Fig. 10. This could be explained by the possibility of a reversible reaction [46-47]. It is in line with the results by Sithole et al. [48], reporting that the optimum result of 100% was achieved using 20 wt.% catalysts and methanol:oil molar ratio of 18:1. Wong et al. [35] also obtained the optimum biodiesel yield of 95% using a catalyst weight of 5 wt.% and methanol:oil molar ratio of 12:1, at 65 °C, for 4 h.

Stability of Catalyst

Among the benefits of heterogeneous catalysts is that the former could be recycled during various reaction cycles. Therefore, catalyst stability is a prominent test in developing heterogeneous catalysts for transesterification, especially when there is a loss of active elements due to catalyst leaching, such as most previously reported solid catalysts [48]. Stability studies were conducted under optimal reaction conditions after each reaction process, namely, separating the catalyst, washing with methanol and n-hexane, and drying for reuse. Interestingly, this catalyst could be utilized repeatedly, as shown by the FAME results in Fig. 11. This catalyst was stable enough to be applied in biodiesel production. However, the fourth usage inflicts a decrease in the count of products, although the change was insignificant. One of the factors causing a decrease in selectivity was the damage to the surface of the active catalyst caused by the replacement of Ca ions [19], blockage of the active site by adsorbed products (such as monoglycerides, diglycerides, and glycerides), as well as moisture and CO_2 contamination in the air during the filtration process, triggering a decrease in catalytic activity [49]. Fig. 11 shows that the mixed oxide CaO/TiO_2 has a high probability of being used in large-scale biodiesel processes since reuse is a potential solution to overcome large waste generation and relatively low costs. Salinas et al. showed four reaction cycles, with no deactivation of the active species on the catalyst or leaching observed. A mean conversion of 81 ± 6% was achieved after four cycles using the same catalyst [50]. A study by Wen et al. reported that the FAME yield decreased from 92.3% to 81.2% as repeated

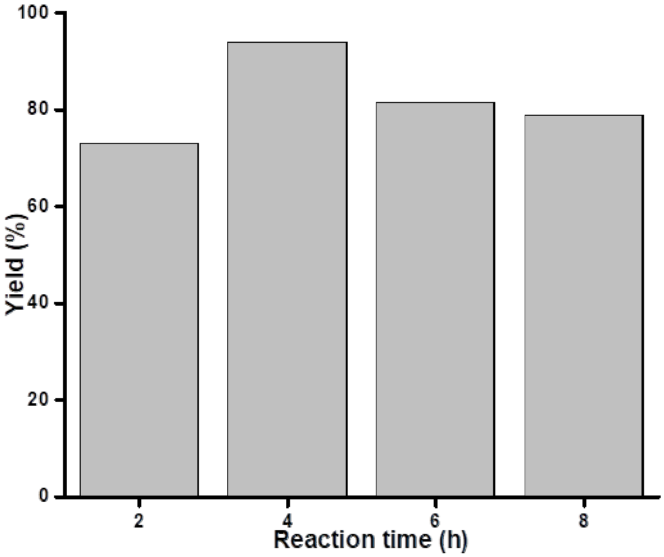

Fig 10. Effect of reaction time on biodiesel yield

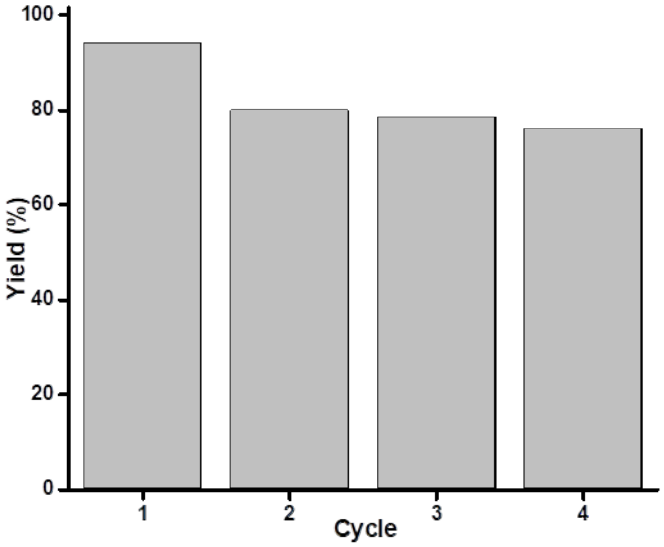

Fig 11. The differences in the amount of biodiesel and variations in reuse (1, 2, 3, and 4 cycles)

1–4 times [19], pointing out that this catalyst was stable for biodiesel production (Fig. 11.).

■ CONCLUSION

Waste Frying Oil (WFO) is a promising raw material for biodiesel production cheaper than conventional vegetable oils. Additionally, WFO is environmentally friendly to use. CaO supported by TiO_2 can increase biodiesel yield since the TiO_2 catalyst is superior. The morphological analysis demonstrated that showed CaO particles were scattered on the surface of

TiO_2, which indicated mixed metal oxides interactions so that the surface of the active site was damaged. It is indicated by its low intensity and the formation of a new phase of $CaTiO_3$ in the XRD pattern, increasing stability and maintaining catalytic activity. The maximum biodiesel yield of 94% was obtained under 5 wt.% catalyst conditions and a 6:1 methanol:oil ratio, with a reaction temperature of 65 °C in 4 h. The high yield of biodiesel shows suitable good catalytic properties to be used for use in biodiesel production from WFO.

■ AUTHOR CONTRIBUTIONS

VS collected the experimental data, VS and AD drafted the manuscript, and SY, ZF, NJ developed the idea and corrected the manuscript. All authors read and approved the final manuscript.

■ REFERENCES

[1] Mohamad, M., Ngadi, N., Wong, S., Yahya, N.Y., Inuwa, I.M., and Lani, N.S., 2018, Synthesis and characterization of CaO-TiO_2 for transesterification of vegetable palm oil, *Int. J. Eng. Trans. B*, 31 (8), 1326–1333.

[2] Solis, J.L., Berkemar, A.L., Alejo, L., and Kiros, Y., 2017, Biodiesel from rapeseed oil (*Brassica napus*) by supported Li_2O and MgO, *Int. J. Energy Environ. Eng.*, 8 (1), 9–23.

[3] Jafarmadar, S., and Pashae, J., 2013, Experimental study of the effect of castor oil biodiesel fuel on performance and emissions of turbocharged DI diesel, *Int. J. Eng. Trans. B*, 26 (8), 905–912.

[4] Hosseini, S.E., and Wahid, M.A., 2012, Necessity of biodiesel utilization as a source of renewable energy in Malaysia, *Renewable Sustainable Energy Rev.*, 16 (8), 5732–5740.

[5] Atabani, A.E., Silitonga, A.S., Badruddin, I.A., Mahlia, T.M.I., Masjuki, H.H., and Mekhilef, S., 2012, A comprehensive review on biodiesel as an alternative energy resource and its characteristics, *Renewable Sustainable Energy Rev.*, 16 (4), 2070–2093.

[6] Agrawal, S., Singh, B., Frómeta, A.E.N., and Sharma, Y.C., 2012, Commercial- and whitewashing-grade limestone as a heterogeneous catalyst for synthesis of fatty acid methyl esters from used frying oil (UFO), *Biomass Convers. Biorefinery*, 2 (4), 297–304.

[7] Mguni, L.L., Mukenga, M., Jalama, K., and Meijboom, R., 2013, Effect of calcination temperature and MgO crystallite size on MgO/TiO_2 catalyst system for soybean oil transesterification, *Catal. Commun.*, 34, 52–57.

[8] Ajala, E.O., Ajala, M.A., Odetoye, T.E., Aderibigbe, F.A., Osanyinpeju, H.O., and Ayanshola, M.A., 2020, Thermal modification of chicken eggshell as heterogeneous catalyst for palm kernel biodiesel production in an optimization process, *Biomass Convers. Biorefinery*, 10 (1), 1–17.

[9] Yahya, N.Y., and Ngadi, N., 2016, Effect of Calcination temperature on catalyst surface area of Ca supported TiO_2 by sol-gel method for biodiesel production, *Appl. Mech. Mater.*, 818, 219–222.

[10] Kouzu, M., and Hidaka, J., 2012, Transesterification of vegetable oil into biodiesel catalyzed by CaO: A review, *Fuel*, 93, 1–12.

[11] Boey, P.L., Maniam, G.P., and Hamid, S.A., 2011, Performance of calcium oxide as a heterogeneous catalyst in biodiesel production: A review, *Chem. Eng. J.*, 168 (1), 15–22.

[12] Ho, W.W.S., Ng, H.K., Gan, S., and Tan, S.H., 2014, Evaluation of palm oil mill fly ash supported calcium oxide as a heterogeneous base catalyst in biodiesel synthesis from crude palm oil, *Energy Convers. Manage.*, 88, 1167–1178.

[13] Lani, N.S., Ngadi, N., Yahya, N.Y., and Rahman, R.A., 2017, Synthesis, characterization and performance of silica impregnated calcium oxide as heterogeneous catalyst in biodiesel production, *J. Cleaner Prod.*, 146, 116–124.

[14] Yahya, N.Y., Ngadi, N., Wong, S., and Hassan, O., 2018, Transesterification of used cooking oil (UCO) catalyzed by mesoporous calcium titanate: Kinetic and thermodynamic studies, *Energy Convers. Manage.*, 164, 210–218.

[15] Nassar, M.Y., Ali, E.I., and Zakaria, E.S., 2017, Tunable auto-combustion preparation of TiO_2

nanostructures as efficient adsorbents for the removal of an anionic textile dye, *RSC Adv.*, 7 (13), 8034–8050.

[16] Galván-Ruiz, M., Hernández, J., Baños, L., Noriega-Montes, J., and Rodríguez-García, M.E., 2009, Characterization of calcium carbonate, calcium oxide, and calcium hydroxide as starting point to the improvement of lime for their use in construction, *J. Mater. Civ. Eng.*, 21 (11), 694–698.

[17] De, A., and Boxi, S.S., 2020, Application of Cu impregnated TiO_2 as a heterogeneous nanocatalyst for the production of biodiesel from palm oil, *Fuel*, 265, 117019.

[18] Madhuvilakku, R., and Piraman, S., 2013, Biodiesel synthesis by TiO_2-ZnO mixed oxide nanocatalyst catalyzed palm oil transesterification process, *Bioresour. Technol.*, 150, 55–59.

[19] Wen, Z., Yu, X., Tu, S.T., Yan, J., and Dahlquist, E., 2010, Biodiesel production from waste cooking oil catalyzed by TiO_2-MgO mixed oxides, *Bioresour. Technol.*, 101 (24), 9570–9576.

[20] Mohamad, M., Ngadi, N., Wong, S.L., Jusoh, M., and Yahya, N.Y., 2017, Prediction of biodiesel yield during transesterification process using response surface methodology, *Fuel*, 190, 104–112.

[21] Siregar, A.G.A., Manurung, R., and Taslim, T., 2021, Synthesis and characterization of sodium silicate produced from corncobs as a heterogeneous catalyst in biodiesel production, *Indones. J. Chem.*, 21 (1), 88–96.

[22] Farooq, M., Ramli, A., Naeem, A., Mahmood, T., Ahmad, S., Humayun, M., and Islam, M.G.U., 2018, Biodiesel production from date seed oil (*Phoenix dactylifera* L.) via egg shell derived heterogeneous catalyst, *Chem. Eng. Res. Des.*, 132, 644–651.

[23] Ngamcharussrivichai, C., Nunthasanti, P., Tanachai, S., and Bunyakiat, K., 2010, Biodiesel production through transesterification over natural calciums, *Fuel Process. Technol.*, 91 (11), 1409–1415.

[24] Margaretha, Y.Y., Prastyo, H.S., Ayucitra, A., and Ismadji, S., 2012, Calcium oxide from pomacea sp. shell as a catalyst for biodiesel production, *Int. J. Energy Environ. Eng.*, 3 (1), 33.

[25] Mguni, L., Meijboom, R., and Jalama, K., 2012, Biodiesel production over nano-MgO supported on titania, *World Acad. Sci. Eng. Technol.*, 60 (4), 380–384.

[26] Aghilinategh, M., Barati, M., and Hamadanian, M., 2019, Supercritical methanol for one put biodiesel production from Chlorella vulgaris microalgae in the presence of CaO/TiO_2 nano-photocatalyst and subcritical water, *Biomass Bioenergy*, 123, 34–40.

[27] Putra, M.D., Ristianingsih, Y., Jelita, R., Irawan, C., and Nata, I.F., 2017, Potential waste from palm empty fruit bunches and eggshells as a heterogeneous catalyst for biodiesel production, *RSC Adv.*, 7 (87), 55547–55554.

[28] Safaei-Ghomi, J., Ghasemzadeh, M.A., and Mehrabi, M., 2013, Calcium oxide nanoparticles catalyzed one-step multicomponent synthesis of highly substituted pyridines in aqueous ethanol media, *Sci. Iran.*, 20 (3), 549–554.

[29] Lopez, T., Sanchez, E., Bosch, P., Meas, Y., and Gomez, R., 1992, FTIR and UV-Vis (diffuse reflectance) spectroscopic characterization of TiO_2 sol-gel, *Mater. Chem. Phys.*, 32 (2), 141–152.

[30] Nolan, N.T., Seery, M.K., and Pillai, S.C., 2009, Spectroscopic investigation of the anatase-to-rutile transformation of sol-gel-synthesized TiO_2 photocatalysts, *J. Phys. Chem. C*, 113 (36), 16151–16157.

[31] Zoccal, J.V.M., Arouca, F.D.O., and Gonçalves, J.A.S., 2010, Synthesis and characterization of TiO_2 nanoparticles by the method Pechini, *Mater. Sci. Forum*, 660-661, 385–390.

[32] Gardy, J., Hassanpour, A., Lai, X., Ahmed, M.H., and Rehan, M., 2017, Biodiesel production from used cooking oil using a novel surface functionalised TiO_2 nano-catalyst, *Appl. Catal., B*, 207, 297–310.

[33] Mi, G., Murakami, Y., Shindo, D., and Saito, F., 1999, Microstructural investigation of $CaTiO_3$ formed mechanochemically by dry grinding of a CaO-TiO_2 mixture, *Powder Technol.*, 104 (1), 75–79.

[34] Xie, W., and Zhao, L., 2013, Production of biodiesel by transesterification of soybean oil using calcium

supported tin oxides as heterogeneous catalysts, *Energy Convers. Manage.*, 76, 55–62.

[35] Wong, Y.C., Tan, Y.P., Taufiq-Yap, Y.H., Ramli, I., and Tee, H.S., 2015, Biodiesel production via transesterification of palm oil by using CaO-CeO_2 mixed oxide catalysts, *Fuel*, 162, 288–293.

[36] Wan Omar, W.N.N., and Amin, N.A.S., 2011, Biodiesel production from waste cooking oil over alkaline modified zirconia catalyst, *Fuel Process. Technol.*, 92 (12), 2397–2405.

[37] Sisca, V., and Jamarun, N., 2019, Biodiesel production from waste cooking oil using catalyst calcium oxide derived of limestone Lintau Buo, *Arch. Pharm. Pract.*, 11 (3), 8–14.

[38] Boxi, S.S., and Paria, S., 2014, Effect of silver doping on TiO_2, CdS, and ZnS nanoparticles for the photocatalytic degradation of metronidazole under visible light, *RSC Adv.*, 4 (71), 37752–37760.

[39] Mohamad, M., and Ngadi, N., 2014, Effect of TiO_2 mixed CaO catalyst in palm oil transesterification, *Appl. Mech. Mater.*, 695, 319–322.

[40] Wang, Y.G., Nie, X.A., and Liu, Z.X., 2014, Biodiesel synthesis from *Styrax tonkinensis* catalyzed by $S_2O_8^{2-}$ /ZrO_2-TiO_2-Fe_3O_4, *Appl. Mech. Mater.*, 521, 621–625.

[41] Kaur, M., and Ali, A., 2011, Lithium ion impregnated calcium oxide as nanocatalyst for the biodiesel production from karanja and jatropha oils, *Renewable Energy*, 36 (11), 2866–2871.

[42] Suprapto, Fauziah, T.R., Sangi, M.S., Oetami, T.P., Qoniah, I., and Prasetyoko, D., 2016, Calcium oxide from limestone as solid base catalyst in transesterification of *Reutealis trisperma* oil, *Indones. J. Chem.*, 16 (2), 208–213.

[43] Hayyan, A., Alam, M.Z., Mirghani, M.E.S., Kabbashi, N.A., Hakimi, N.I.N.M., Siran, Y.M., and Tahiruddin, S., 2010, Sludge palm oil as a renewable raw material for biodiesel production by two-step processes, *Bioresour. Technol.*, 101 (20), 7804–7811.

[44] Patil, P.D., Gude, V.G., and Deng, S., 2009, Biodiesel production from jatropha curcas, waste cooking, and *Camelina sativa* oils, *Ind. Eng. Chem. Res.*, 48 (24), 10850–10856.

[45] Moradi, G., Mohadesi, M., and Hojabri, Z., 2014, Biodiesel production by CaO/SiO_2 catalyst synthesized by the sol-gel process, *React. Kinet. Mech. Catal.*, 113 (1), 169–186.

[46] Boro, J., Thakur, A.J., and Deka, D., 2011, Solid oxide derived from waste shells of *Turbonilla striatula* as a renewable catalyst for biodiesel production, *Fuel Process. Technol.*, 92 (10), 2061–2067.

[47] Alsharifi, M., Znad, H., Hena, S., and Ang, M., 2017, Biodiesel production from canola oil using novel Li/TiO_2 as a heterogeneous catalyst prepared via impregnation method, *Renewable Energy*, 114, 1077–1089.

[48] Sithole, T., Jalama, K., and Meijboom, R., 2014, Biodiesel production from waste vegetable oils over MgO/ZrO_2 catalyst, *Proceedings of the World Congress on Engineerings-WCE 2014*, Vol II, July 2-4, London, U.K.

[49] Sudsakorn, K., Saiwuttikul, S., Palitsakun, S., Seubsai, A., and Limtrakul, J., 2017, Biodiesel production from jatropha curcas oil using strontium-doped CaO/MgO catalyst, *J. Environ. Chem. Eng.*, 5 (3), 2845–2852.

[50] Salinas, D., Araya, P., and Guerrero, S., 2012, Study of potassium-supported TiO_2 catalysts for the production of biodiesel, *Appl. Catal., B*, 117-118, 260–267.

Green Synthesis of Silver Nanoparticles using *Lantana camara* Fresh Leaf Extract for Qualitative Detection of Hg^{2+}, Cu^{2+}, Pb^{2+}, and Mn^{2+} in Aqueous Solution

Henry Fonda Aritonang*, Talita Kojong, Harry Koleangan, and Audy Denny Wuntu

Physical Chemistry Division, Faculty of Mathematics and Natural Sciences, Sam Ratulangi University, Jl. Kampus Unsrat Kleak, Manado 95115, Indonesia

** Corresponding author:*

tel: +62-431-827560
email: henryaritonang@unsrat.ac.id

Received: March 25, 2021
Accepted: June 22, 2021

DOI: 10.22146/ijc.64902

Abstract: *This research was focused on the discovery of new environmentally friendly sensors based on nanoscale materials whose main purpose was to detect the presence of heavy metals in aqueous solutions. The environmentally friendly extracellular biosynthetic technique was applied to produce silver nanoparticles (AgNps). The reducing agents used were distilled water and ethanol extract obtained from fresh leaves of* Lantana camara. *The silver-containing extracts (Ag-extract) were then used to detect the presence of Hg^{2+}, Cu^{2+}, Pb^{2+}, and Mn^{2+} in aqueous solutions by the colorimetric method using UV-visible spectroscopy. The colloidal synthesis of AgNPs was then monitored by the same method. The spectrum obtained showed peaks between 430 and 450 nm according to the Plasmon absorbance of AgNP. AgNPs' size and shape were characterized using the Transmission Electron Microscopy (TEM) technique, which showed the average size varies from 1.6 to 25 nm. The colorimetric data showed that Ag-extract, both of distilled water or ethanol solvents, was the best for detecting the presence of Hg^{2+} followed by Mn^{2+}. On the other hand, Ag-extract in distilled water cannot detect Cu^{2+}, Pb^{2+}, and Mn^{2+} ions, while almost all Ag-extracts in ethanol solvents could identify the presence of these metals.*

Keywords: *green synthesis; silver nanoparticles;* Lantana camara *fresh leaf extract; qualitative detection; heavy metal ions*

■ INTRODUCTION

Heavy metals in natural waters are usually present in small amounts, although many of them are toxic even at very low concentrations. Arsenic (As), lead (Pb), cadmium (Cd), copper (Cu), nickel (Ni), mercury (Hg), chromium (Cr), manganese (Mn), cobalt (Co), zinc (Zn), and selenium (Se) are among them [1-2]. Therefore, monitoring water quality is very important to evaluate water conditions.

Some of the most recent analytical methods commonly used to detect heavy metal ions are inductively coupled plasma-optical emission spectroscopy (ICP-OES) [3], inductively coupled plasma mass spectrometry (ICP-MS) [4], atomic absorption spectrometer (AAS) [5], cyclic voltammetry [6], graphite furnace atomic absorption spectrometer (GFAAS) [7] and X-ray fluorescence spectrometry [8]. The advantages of using these methods are that they have relatively wide application, high sensitivity, high selectivity, and can be used to measure a relatively large number of elements. These techniques, however, require expensive types of equipment, complex analytical steps, and highly trained technicians [9-10]. Nanotechnology can be an alternative tool to replace these methods [11-12].

Nanoparticles have been widely used in various fields, such as surface plasmon resonance (SPR) [9] based on chemical sensors using colorimetry. This method is most commonly used in metal determination because it is relatively easy and readable for the human eye. Silver nanoparticles (AgNPs) are one of the best plasmonics that has been used in SPR-based nanosensors to detect various analytes, including metal ions, such as Hg^{2+}, Pb^{2+}, Co^{2+}, Cd^{2+}, and Cu^{2+} [13]. In addition, AgNPs can also be used to enhance their role as metal ion sensors. The functionalization of AgNPs with guanine has been used as a Ba^{2+} ion sensor [14].

Likewise, Mn^{2+} and Cd^{2+} metal ions can be detected in water samples by functional AgNPs with sulfoanthranilic dithiocarbamate acid [15]. Timolol forms aggregate with AgNPs so that it can be detected in drug samples [16]. In addition, AgNPs can be used by two compounds at once, namely 6-mercaptonicotinic acid and melamine, which can detect Cr^{3+} and Ba^{2+} ions [17], citrate and melamine, which act as ligands that can detect the presence of Cr^{3+} and Hg^{2+} ions in water samples [18], and trisodium citrate and L-cysteine which are used to detect Co^{2+} [19]. The development of chemical sensing procedures has been carried out by Amirjani and Fatmehsari [20] using the iPhone 4s camera to detect ammonia content in water samples.

Methods that have been used to produce AgNPs include chemical methods [21], electrochemistry [22], radiation [23], photochemical methods [24], Langmuir-Blodgett [25], and phytochemicals-based approaches [26]. The use of chemical methods involves toxic chemicals, such as reducing agents and capping agents that are not safe for the environment. Therefore, some researchers used green synthesis as an alternative method for synthesizing nanoparticles using microorganisms [27], enzymes [28], bacterial cellulose [29-30], and plant extracts [31-34].

Some green synthesis using plant extracts such as *Actinidia deliciosa* [16], *Impatiens balsamina* [31], *Lantana camara* L (*L. camara*) [31,35], *Astragalus tribuloides* [36], *Caralluma tuberculata* [37], *Tragopogon collinus* [38], and *Muntingia calabura* [39], have been reported. The extracts act as reducing and stabilizing agents [40].

In the manufacture of *Lantana camara* extract, water solvent was more widely used [31,35,41-42], and only a few studies reported the use of alcohol [35,43] or petroleum ether [44] solvents. However, the AgNPs produced were only tested for their antibacterial activity. In addition, information concerning the application of plant extracts containing AgNPs applied to detect the presence of heavy metals in aqueous solutions is still very limited, especially extracts produced from different solvents, namely water and ethanol.

Therefore, this study was aimed to synthesize AgNP by utilizing fresh leaf extracts from *L. camara,* which is extracted using distilled water and ethanol solvents. Furthermore, extracts from each solvent containing AgNPs were used to detect the presence of heavy metals in aqueous solutions.

■ EXPERIMENTAL SECTION

Materials

All reagents used were analytic grade and without further purification. Ethanol, silver nitrate ($AgNO_3$), mercury(II) chloride ($HgCl_2$), copper(II) chloride dihydrate ($CuCl_2{\cdot}2H_2O$), lead (II) nitrate ($Pb(NO_3)_2$), and manganese(II) sulfate monohydrate ($MnSO_4{\cdot}H_2O$) were all purchased from Sigma-Aldrich in Indonesia with a purity of at least 99.5%. Fresh leaves of *L. camara* (Fig. 1) were harvested from around Sam Ratulangi University, Indonesia. Milli-Q water was used to prepare all aqueous solutions used in the experiment.

Instrumentation

The instruments used were UV-Visible Spectrophotometer (Shimadzu UV-1800) and TEM (JEOL HT-7700).

Procedure

The following procedure was used to obtain an aqueous extract of *L. camara* leaves. First, the leaves were thoroughly washed with distilled water and cut into small pieces. After that, 2.5 g of cut leaves were added to 25 mL of distilled water (W) in a 100 mL beaker and heated at 70 °C for 1.5 h. It was then allowed to cool and was filtered with Whatman No. 40 filter paper. The extract (W-extract) was consequently used as fresh material for the next step. A similar procedure, which was used for the preparation of the ethanol extract of *L. camara* leaves (E-extract). Both extracts (from those of water and ethanol) were then used to synthesize AgNPs.

Aqueous $AgNO_3$ solutions, with concentrations of 1, 2, 3, 4, and 5 mM, were placed in Erlenmeyer flasks. Each solution was then placed in a 100 mL beaker containing an aqueous extract of *L. camara* with a ratio of $AgNO_3$ solution:extract = 17:1 (v/v) (18 mL). After

that, the beaker is covered with aluminum foil. All mixtures were then stirred at 1500 rpm at 70 °C for 1 h. Subsequently, they were stored in a refrigerator for analysis with a UV-vis spectrophotometer to characterize the AgNPs and TEM to analyze the size of AgNPs. The same process was applied to the ethanol extracts from *L. camara* leaves. Each colloid produced from the two solvents was then labeled as W1, W2, W3, W4, W5, and E1, E2, E3, E4, and E5.

The colorimetric method, which utilizes AgNPs contained in extracts (Ag-extracts), has been widely used to detect heavy metals in aqueous solutions. In this study, heavy metal solutions were prepared using 1000 ppm Hg^{2+}, Cu^{2+}, Pb^{2+}, and Mn^{2+}, and 1 mL of each solution was added to 3 mL of Ag-extract. The color change of the solution was then observed and characterized by a UV-vis spectrophotometer in the range of 350–650 nm. All solutions in this experiment ($AgNO_3$, Ag-extract, and Ag-extract-heavy metals) were characterized using the same method. Analysis of the size distribution of the AgNPs was carried out using the TEM (JEOL HT-7700) method, which was operated with a voltage acceleration of 120 kV. AgNPs' size was analyzed using ImageJ software for each TEM image. The histograms of the size distribution are established by the Origin software.

■ RESULTS AND DISCUSSION

Profile of *L. camara* Fresh Leaf Extract

The same color, light brown, was observed for *L. camara* fresh leaf extracts from both solvents. However, after heating, the color became different, where the W-extract was dark brown while the E-extract was dark green (Fig. 1). It suggests that different solvents can dissolve different components of secondary metabolites found in each sample.

Synthesis of AgNPs

Similar to the initial extract, the color of the extract after the addition of the $AgNO_3$ solution was also changed, and the difference was quite significant, as shown in Fig. 2. The W-extract colors were darker than the E-extract colors.

In Fig. 2, it appears that each precursor concentration produced a different color. The higher the concentration of the Ag precursor, the brighter the color of the solution. The comparison of the leaf extracts colors from the two solvents showed that the W-extract solution was darker than the E-extract solution. These results also indicated that there were differences in the number of secondary metabolites found in each solution [45]. The difference in extract color before and after adding $AgNO_3$ solution also showed that Ag^+ was reduced. AgNP formation from Ag^+ ions started from chemical reactions in the presence of phytochemical compounds (flavonoids, terpenoids, steroids) found in *L. camara* leaves as reducing and stabilizing agents. Furthermore, the Ag^+ ion could interact with the –OH group, which was oxidized into the –CHO and –COOH

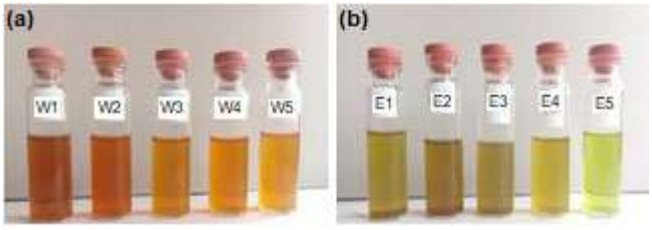

Fig 2. The color profile of Ag-extract at each concentration using (a) W and (b) E solvents

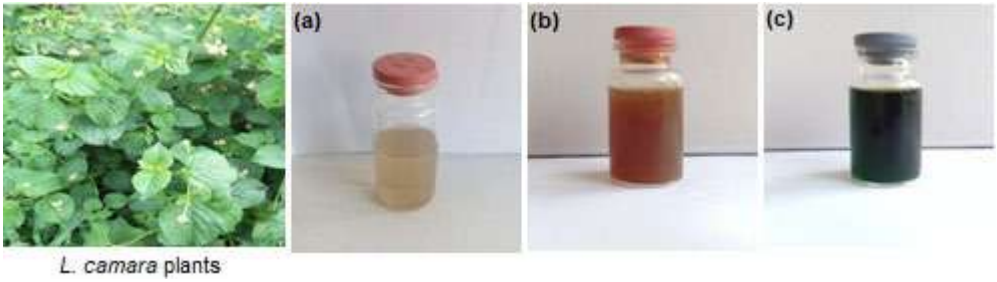

Fig 1. The color of fresh leaf extract from *L. camara*, (a) before and after heating with (b) W and (c) E solvents

groups and which were then reduced the Ag^+ ions into AgNPs. In this case, the COOH group functions as a stabilizer for AgNPs [43].

Analysis of AgNPs with UV-Vis Spectrophotometer

The Ag-extract solution was analyzed using a UV-Vis spectrophotometer to determine the characteristics of AgNPs based on the wavelength peak spectrum. The UV-Vis spectra of AgNPs in each solvent are in the range of 430 to 450 nm, as shown in Fig. 3. This range of maximum absorption peaks is similar to that reported by previous studies [20] and the broadening of peaks indicates that the particles were polydisperse. By careful observation, the absorption peak was around 440–430 nm, and the absorption location characteristic of the AgNPs peak was shifted towards a longer wavelength.

The UV-Vis spectrum in Fig. 3 shows that the Ag^+ ion was reduced to Ag^0, which is confirmed by the absorbance peak, which occurs around 430–440 nm [46]. The higher the concentration of Ag, the higher the absorbance value. Thus, it seems that E solvent was able to dissolve chlorophyll from fresh *L. camara* leaf extract, which emerges in the spectrum of 620–680 nm (Fig. 3(b)).

Surface morphology of AgNPs

The morphology, size, and surface shape of the biosynthesized AgNPs are visualized by TEM images. In the TEM image, as shown in Fig. 4(a, c, e, and g), nanoparticles generally show typical spherical and ellipsoidal morphology. The size distribution of biosynthesized nanoparticles was analyzed by ImageJ software. Based on the particle size distribution curve (Fig. 4(b, d), the average size of AgNPs at W1 and W5

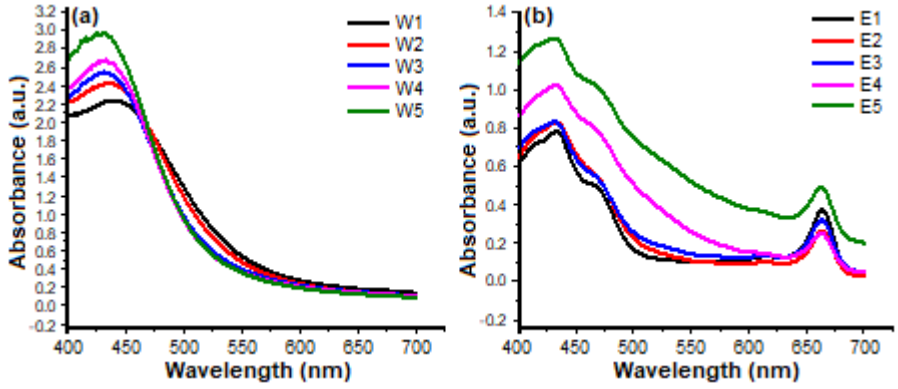

Fig 3. The UV-Vis spectrum of Ag-extract in (a) W and (b) E solvents, respectively

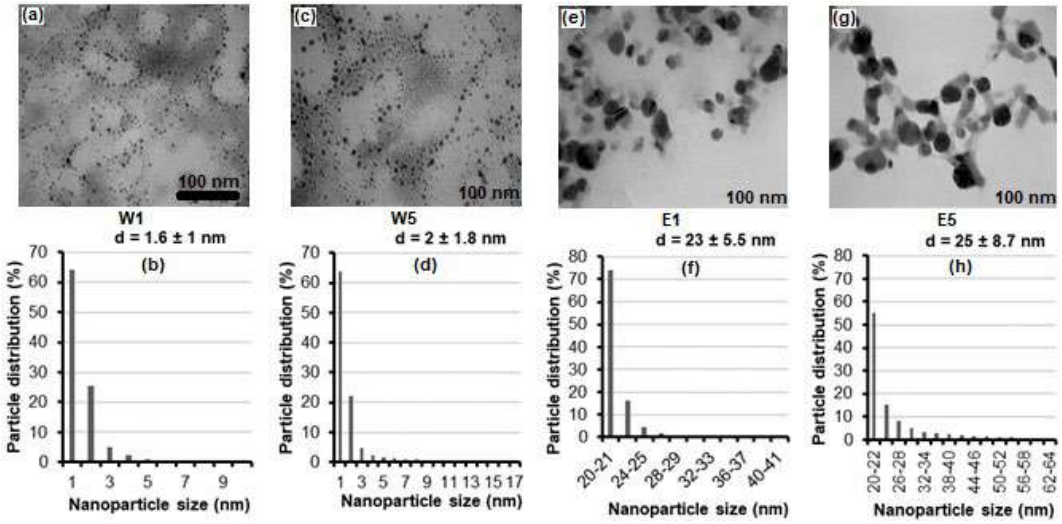

Fig 4. TEM image (**a, c, e, g**) and size distribution (b, d, f, h) of AgNPs produced from W1 (a, b), W5 (c, d), E1 (e, f), and E5 (g, h), respectively

were 1.6 ± 1 and 2 ± 1.8 nm, respectively. Meanwhile, those of AgNPs in E1 and E5 were 23 ± 5.5 and 25 ± 8.7 nm, respectively (Fig. 4(f) and 4(h)).

The TEM image (Fig. 4) reveals the presence of several organic layers surrounding the AgNP surface. In particular, most of the particles in TEM images do not physically in contact with each other but appear to be separated by organic layers. Therefore, the TEM image clearly shows the AgNPs layer with the organic layers. Organic layers (including alkaloids, phenolic compounds, terpenoids, enzymes, co-enzymes, proteins, sugars, etc.) facilitated the reduction of Ag^+ ions and also stabilized the surface of the resulting AgNP [47-49]. Correlation between the TEM image and the color of the extract solution (Fig. 1) was clearly related to the color concentration of the solution. The color of the E extract solution is relatively more concentrated than the color of the W extract solution. The difference in the concentration of this solution shows that E solvent dissolved more organic matter contained in *L. camara* leaves than the W solvent did (including chlorophyll in Fig. 3(b)). Therefore, the organic layer shown in the TEM image produced from the E solvent is more clearly seen than those produced from the W solvent.

Heavy Metal Ions Sensing Studies

Test results of the colorimetric detection tests for heavy metals are presented in Fig. 5. The color change was observed in all of the Ag-extract solutions containing heavy metals. This was due to different sensitivities, such as the Ag-extract solution, which contains Hg^{2+} and Pb^{2+} ions, respectively, in the W and E solvents, the rate of the color change of the solution also varies over time.

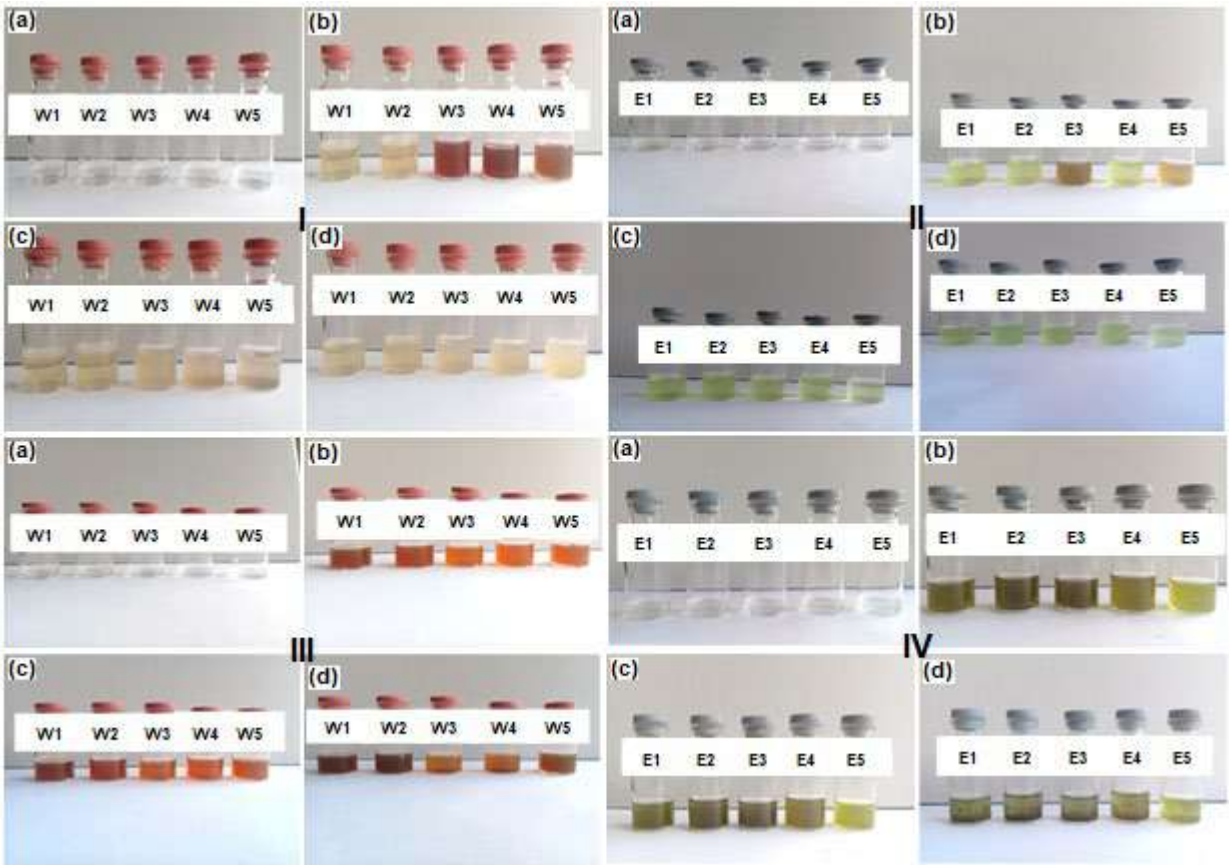

Fig 5. Discoloration of Ag-extract solution containing Hg^{2+} (**I**, **II**) and Pb^{2+} (**III**, **IV**) ions in each of the distilled water, W (**I**, **III**) and ethanol solvent, E (**II**, **IV**): (**a**) pure $AgNO_3$ solutions, (**b**) at the time of addition of heavy metal solutions, (**c**) after 15 min, and (**d**) after 24 h of adding heavy metal solutions

Table 1 Variation in AgNP size and the presence of heavy metal ions in the rate of change of Ag-extract absorption intensity for each colloid of W1-W5 and E1-E5.

Colloids	Average particle size (nm)	Detection of heavy metal ions				General explanation
		Hg^{2+}	Cu^{2+}	Pb^{2+}	Mn^{2+}	
W1	1.6	+	+	-	-	**Hg^{2+}**: absorption intensity was decreased, and the peak of the Ag spectrum was disappeared (very fast, W1 and W2 = 30 sec; W3, W4, and W5 = 30 min). **Cu^{2+}**: absorption intensity was decreased when the addition of the heavy metal solution was left up to 15 min, but it still showed a peak in the Ag spectrum and only W3 that had no peak. After 24 h of immersion, the peak of the Ag spectrum disappeared. **Pb^{2+}** and **Mn^{2+}**: generally, absorption intensity was decreased to 24 h immersion but still had a peak in the Ag spectrum.
W2	1.6	+	+	-	-	
W3	1.7	+	+	-	-	
W4	1.8	+	+	-	-	
W5	2	+	+	-	-	
E1	23	+	+	+	+	**Hg^{2+}**: absorption intensity was decreased, and the peak of the Ag spectrum was disappeared (very fast, W1 and W2 = 30 sec; W3, W4, and W5 = 30 min). **Cu^{2+}**: in general, the intensity of absorption was increased when compared to the absence of Cu ions, but the peak of the Ag spectrum was disappeared when a heavy metal solution was added for up to 24 h. **Pb^{2+}**: at the beginning of adding a heavy metal solution, all absorption intensities were increased the peak of the Ag spectrum was not observed. After 15 min and 24 h, the absorption intensity was dropped, and the peak of the Ag spectrum was not observed. **Mn^{2+}**: intensity of absorption was decreased up to 24 h of immersion, and the peak of the Ag spectrum was not observed.

It was observed that the Ag-extract solution changed color immediately after the addition of aqueous Hg^{2+}. The color difference was quite significant compared to that without Hg^{2+} ions, where W1 and W2 showed light brown color while W3, W4, and W5 showed brown color. After being left for 15 min, all solutions had the same color as W1 and W2, even after 24 h of immersion (Fig. 5**I**). The same result was shown by Ag-extract (E), where the color changed immediately after the addition of the Hg solution. In this case, E1, E2, and E4 are light green, while E3 and E5 are brown. A different result was shown by Amirjani and Haghshenas [13], where the color of the solution changed from blue to purple due to the formation of silver nano triangles functionalized by citrate. However, after 15 min, the color of the solution became the same. They all turned light green, even after being left for 24 h (Fig. 5**II**). Similar results were obtained by other researchers for the interaction of metal ions with green synthesized AgNPs [50-51]. Damir et al. [52] also reported that the *L. camara* leaf extract containing AgNPs changed color from brown to transparent after the addition of a Hg^{2+} ion solution, but no color change was observed with the addition of Zn^{2+}, Cr^{3+}, Cd^{2+}, Fe^{2+}, and Pb^{2+} ions. A similar result was also observed by Alzahrani [12], who reported that the onion extract solution containing AgNPs became transparent after the addition of Hg^{2+} ion solution, whereas the addition of Zn^{2+}, Co^{2+}, Cd^{2+}, Cu^{2+}, Ni^{2+}, and Mn^{2+} ions did not change the color.

Different results were observed for Ag-extracts, which were added with Pb(II) (Fig. 5**III**, **IV**). Visually, the color of the Ag-extract at the time of Pb addition and after 15 minutes showed a relatively similar brown. W1 and W2 are relatively darker than W3, W4, and W5. After 24 h, the five extracts became darker than before. On the other hand, in E solvent, it was noted that the extract color at the time of the Pb addition and after 15 min was relatively the same, namely light green E5. After 24 h, the colors of the five extracts were relatively similar and lighter than before.

The decreased color intensity of the solution could be explained as follows. Initially, the stabilizing agents derived from leaf extracts surrounded AgNPs to produce nano-sized particles, and no agglomeration occurred. The addition of Ag-extract to the heavy metal solutions caused these heavy metal ions to be directly adsorbed and attached to the surface of AgNPs. As a result, the stabilizing agents from the extract were removed from the AgNP's surface. Over time, this adsorption causes more heavy metal ions to surround the AgNPs surface, and more stabilizing agents are removed from the AgNPs surface. The increase in heavy metal ions surrounding the surface of AgNPs caused aggregation, which in turn caused the color intensity of the solution to decrease [50-51,53]. Color changes observed after Ag-extracts containing heavy metal ions were analyzed using a UV-vis spectrophotometer and are presented in Fig. 6.

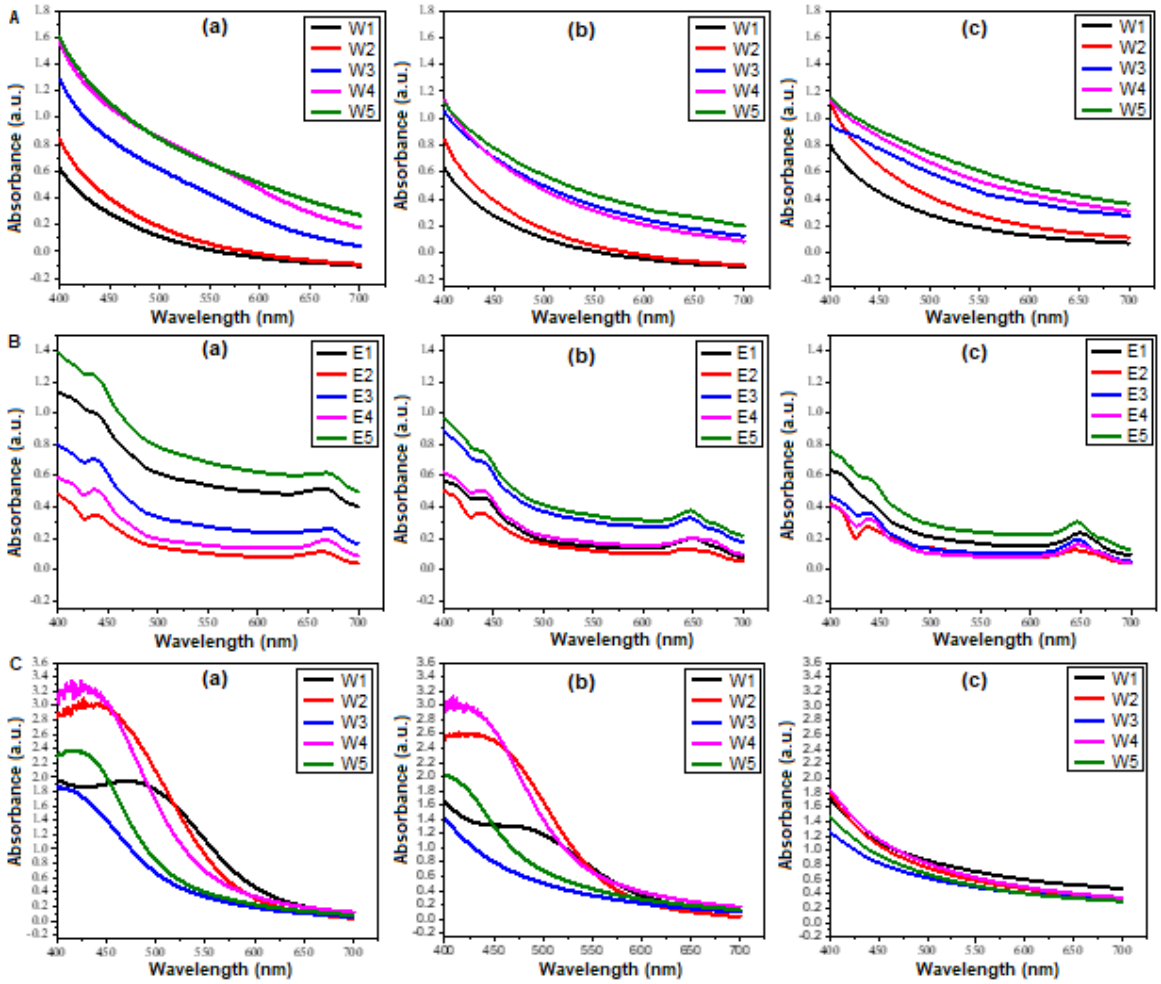

Fig 6. The UV-Vis absorption spectrum of AgNPs in extract solutions containing Hg^{2+} (**A**, **B**), Cu^{2+} (**C**, **D**), Pb^{2+} (**E**, **F**), and Mn^{2+} (**G**, **H**) ions in each distilled water, W (**A**, **C**, **E**, **G**) and ethanol, E (**B**, **D**, **F**, **H**) solvent: (a) at the time of heavy metal solutions addition, (b) after 15 min, and (c) after 24 h of heavy metal solutions addition

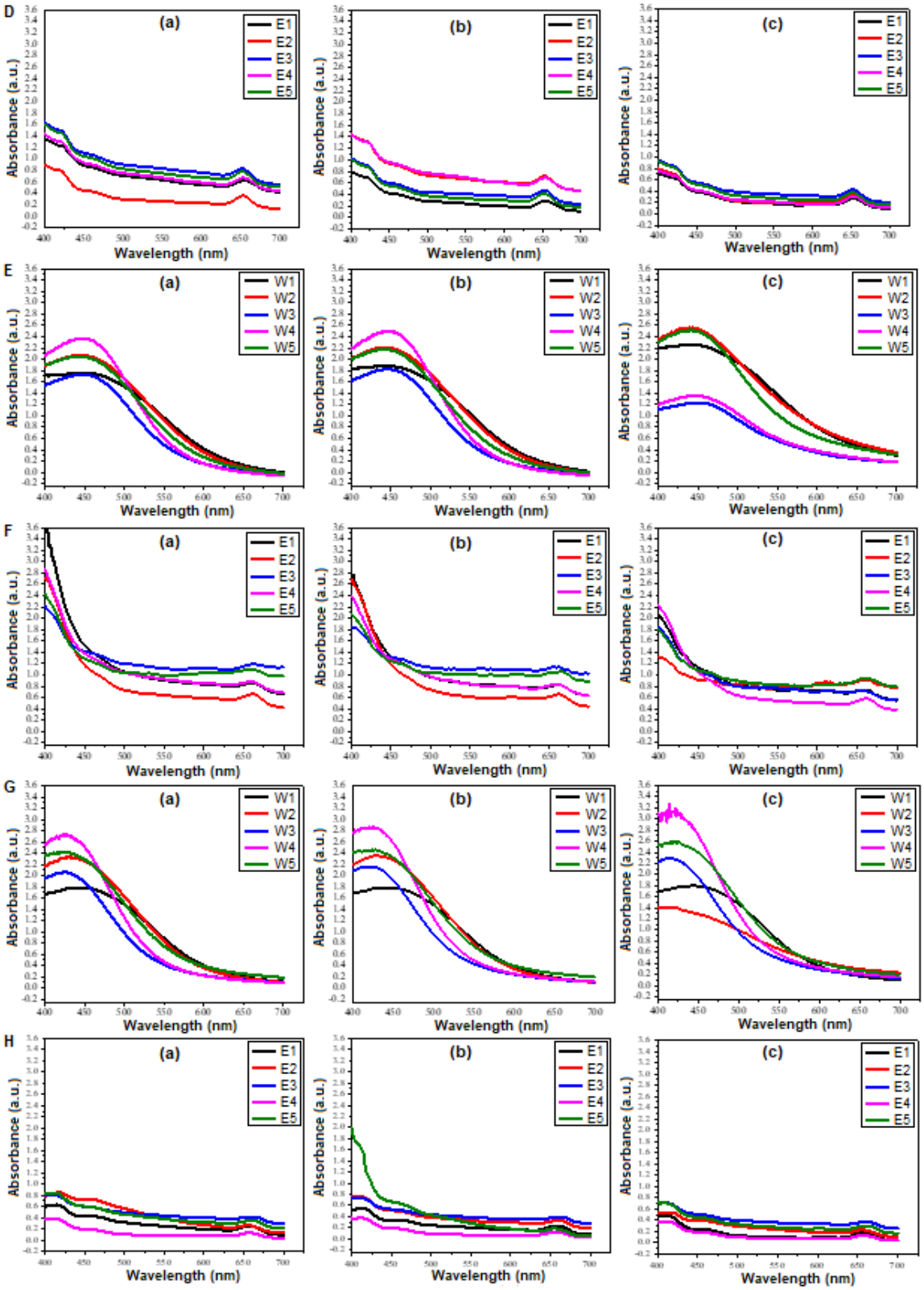

Fig 6. The UV-Vis absorption spectrum of AgNPs in extract solutions containing Hg^{2+} (**A**, **B**), Cu^{2+} (**C**, **D**), Pb^{2+} (**E**, **F**), and Mn^{2+} (**G**, **H**) ions in each distilled water, W (**A**, **C**, **E**, **G**) and ethanol, E (**B**, **D**, **F**, **H**) solvent: (a) at the time of heavy metal solutions addition, (b) after 15 min, and (c) after 24 h of heavy metal solutions addition (*Continued*)

Based on the UV-vis spectrum, it was revealed that the peak spectrum of AgNPs containing Hg^{2+} ions was missing. In addition, the absorption intensity of the solution was also relatively reduced compared to those without Hg^{2+} ions. The decrease was quite consistent from W1 to W5. This could be related to the intensity of AgNPs without Hg^{2+} ions, where the concentration of Ag at W1 is lower than W2 and so on. It was reasonable because the average size of AgNPs on W1 was relatively smaller than on W2 and so on, so Hg^{2+} ions covered the larger surface area of AgNPs and caused the absorption intensity to decrease faster. The opposite result was shown by W2 and so on because it had a relatively larger AgNPs size. Ag-extract from distilled water containing Hg^{2+} ions experienced the fastest color change, namely W1 and W2 at 30 sec while W3, W4, W5 at 30 min. This decrease in color intensity is shown in Fig. 5A and 5B. This indicated that Ag-extract could be used to detect the presence of Hg^{2+} ions in aqueous solutions ("+" sign in Table 1).

Different observations were produced by the UV-Vis AgNPs absorption spectrum after the addition of Pb solution. In general, the peak intensity of the AgNPs spectrum containing Pb^{2+} ions was decreased, but this decrease did not eliminate the peak of the AgNPs spectrum ("-" sign in Table 1). The same result was also shown by other heavy metal ions, namely Cu and Mn but with different reduction rates. The time required for these three heavy metal ions to be adsorbed on the AgNPs surface was relatively longer, which was different from that shown by the Hg^{2+} ion with the order of $Hg^{2+} > Mn^{2+} > Cu^{2+} > Pb^{2+}$ (Table 1). Unlike Hg^{2+} ions, these three ions did not show a direct relationship between AgNPs size and the decreased absorption intensity. Despite its relatively smaller particle size, it did not show a greater decrease in absorption. This information indicated that the Ag-extract from *L. camara* using W solvent was very sensitive in detecting the presence of Hg^{2+} ions in an aqueous solution. Therefore, this method is selective enough to detect the presence of metal ions in a water sample.

The results of this study indicated that the analytical performance of this method could detect biomolecular interactions directly without labeling. In addition, it was relatively easy to use and sensitive in detecting and identifying biomolecules so that different biochemical interactions could be monitored [54].

■ CONCLUSION

An eco-friendly and cost-effective protocol for the synthesis of AgNPs by utilizing renewable natural resources of *L. camara* fresh leaves was proposed. The results showed that the extracts produced using water and ethanol solvents could be used as reducing agents and capping agents to produce AgNPs. Ag-extract could be used as a sensor to detect the presence of Hg^{2+}, Cu^{2+}, Pb^{2+}, and Mn^{2+} in aqueous solutions. However, water solvent is more sensitive in detecting Hg^{2+} and Cu^{2+}. The order of sensitivity of the Ag-extract sensor in detecting the presence of heavy metal ions in an aqueous solution was $Hg^{2+} > Mn^{2+} > Cu^{2+} > Pb^{2+}$.

■ ACKNOWLEDGMENTS

The author would like to thank Sam Ratulangi University for its financial support through the RTUU research scheme from PNBP funds with contract number 901/UN12.13/LT/2018.

■ AUTHOR CONTRIBUTIONS

Conceptualization of the presented idea, H.F.A. (Henry F. Aritonang); methodology, H.F.A. and T.K (Talita Kojong); fabricated the sample and data curation, H.F.A. and T.K., and H.K. (Harry Koleangan); writing–original draft preparation, H.F.A., T.K., H.K., and A.D.W. (Audy D. Wuntu); writing–review and editing, H.F.A., T.K., H.K., A.D.W. All authors have read and agreed to the published version of the manuscript.

■ REFERENCES

[1] Briffa, J., Sinagra, E., and Blundell, R., 2020, Heavy metal pollution in the environment and their toxicological effects on humans, *Heliyon*, 6 (9), e04691.

[2] Ali, H., Khan, E., and Ilahi, I., 2019, Environmental chemistry and ecotoxicology of hazardous heavy metals: Environmental persistence, toxicity, and bioaccumulation, *J. Chem.*, 2019, 6730305.

[3] Massadeh, A.M., El-Rjoob, A.W.O., and Gharaibeh, S.A., 2020, Analysis of selected heavy metals in tap

water by inductively coupled plasma-optical emission spectrometry after pre-concentration using Chelex-100 ion exchange resin, *Water Air Soil Pollut.*, 231 (5), 243.

[4] Da Le, N., Hoang, T.T.H., Phung, V.P., Nguyen, T.L., Duong, T.T., Dinh, L.M., Pham, T.M.H., Phung, T.X.B., Nguyen, T.D., Duong, T.N., Le, T.M.H., Le, P.T., and Le, T.P.Q., 2021, Trace metal element analysis in some seafood in the coastal zone of the Red River (Ba Lat Estuary, Vietnam) by green sample preparation and inductively coupled plasma-mass spectrometry (ICP-MS), *J. Anal. Methods Chem.*, 2021, 6649362.

[5] Adugna, E., Hymete, A., Birhanu, G., and Ashenef, A., 2020, Determination of some heavy metals in honey from different regions of Ethiopia, *Cogent Food Agric.*, 6 (1), 1764182.

[6] Raicopol, M.D., Pandele, A.M., Dascălu, C., Vasile, E., Hanganu, A., Vasile, G.G., Bugean, I.G., Pirvu, C., Stanciu, G., and Buica, G.O., 2020, Improving the voltammetric determination of Hg(II): A comparison between ligand-modified glassy carbon and electrochemically reduced graphene oxide electrodes, *Sensors*, 20 (23), 6799.

[7] López-García, I., Marín-Hernández, J.J., and Hernández-Córdoba, M., 2020, Speciation of chromium in waters using dispersive micro-solid phase extraction with magnetic ferrite and graphite furnace atomic absorption spectrometry, *Sci Rep.*, 10 (1), 5268.

[8] Zhang, H., Antonangelo, J., and Penn, C., 2021, Development of a rapid field testing method for metals in horizontal directional drilling residuals with XRF sensor, *Sci Rep.*, 11 (1), 3901.

[9] Senila, M., Cadar, O., Senila, L., Böringer, S., Seaudeau-Pirouley, K., Ruiu, A., and Lacroix-Desmazes, P., 2020, Performance parameters of inductively coupled plasma optical emission spectrometry and graphite furnace atomic absorption spectrometry techniques for Pd and Pt determination in automotive catalysts, *Materials*, 13 (22), 5136.

[10] Feng, X., Zhang, H., and Yu, P., 2020, X-ray fluorescence application in food, feed, and agricultural science: A critical review, *Crit. Rev. Food Sci. Nutr.*, 0 (0), 1–11.

[11] Singh, C., Kumar, J., Kumar, P., Chauhan, B.S., Tiwari, K.N., Mishra, S.K., Srikrishna, S., Saini, R., Nath, G., and Singh, J., 2019, Green synthesis of silver nanoparticles using aqueous leaf extract of *Premna integrifolia* (L.) rich in polyphenols and evaluation of their antioxidant, antibacterial and cytotoxic activity, *Biotechnol. Biotechnol. Equip.*, 33 (1), 359–371.

[12] Alzahrani, E., 2020, Colorimetric detection based on localized surface plasmon resonance optical characteristics for sensing of mercury using green-synthesized silver nanoparticles, *J. Anal. Methods Chem.*, 2020, 6026312.

[13] Amirjani, A., and Haghshenas, D.F., 2018, Ag nanostructures as the surface plasmon resonance (SPR)-based sensors: A mechanistic study with an emphasis on heavy metallic ions detection, *Sens. Actuators, B*, 273, 1768–1779.

[14] Patel, K., Bhamore, J.R., Park, T.J., and Kailasa, S.K., 2018, Selective and sensitive colorimetric recognition of Ba^{2+} ion using guanine-functionalized silver nanoparticles, *ChemistrySelect*, 3 (36), 10182–10187.

[15] Mehta, V.N., Rohit, J.V., and Kailasa, S.K., 2016, Functionalization of silver nanoparticles with 5-sulfoanthranilic acid dithiocarbamate for selective colorimetric detection of Mn^{2+} and Cd^{2+} ions, *New J. Chem.*, 40, 4566–4574.

[16] Amirjani, A., Bagheri, M., Heydari, M., and Hesaraki, S., 2016. Colorimetric determination of Timolol concentration based on localized surface plasmon resonance of silver nanoparticles, *Nanotechnology*, 27 (37), 375503.

[17] Modi, R.P., Mehta, V.N., and Kailasa S.K., 2014, Bifunctionalization of silver nanoparticles with 6-mercaptonicotinic acid and melamine for simultaneous colorimetric sensing of Cr^{3+} and Ba^{2+} ions, *Sens. Actuators, B*, 195, 562–571.

[18] Kailasa, S.K., Chandel, M., Mehta, V.N., and Park, T.J., 2018, Influence of ligand chemistry on silver nanoparticles for colorimetric detection of Cr^{3+} and Hg^{2+} ions, *Spectrochim. Acta, Part A*, 195, 120–127.

[19] Koochak, N.N., Rahbarimehr, E., Amirjani, A., and Haghshenas, D.F., 2021, Detection of cobalt ion based on surface plasmon resonance of L-cysteine functionalized silver nanotriangles, *Plasmonics*, 16 (2), 315–322.

[20] Amirjani, A., and Fatmehsari, D.H., 2018, Colorimetric detection of ammonia using smartphones based on localized surface plasmon resonance of silver nanoparticles, *Talanta*, 176, 242–246.

[21] Awad, M.A., Hendi, A.A., Ortashi, K.M.O., Alotaibi, R.A., and Sharafeldin, M.S., 2016, Characterization of silver nanoparticles prepared by wet chemical method and their antibacterial and cytotoxicity activities, *Trop. J. Pharm. Res.*, 15 (4), 679–685.

[22] Islam, T., Hasan, M.M., Awal, A., Nurunnabi, Md., and Ahammad, A.J.S., 2020, Metal nanoparticles for electrochemical sensing: Progress and challenges in the clinical transition of point-of-care testing, *Molecules*, 25 (24), 5787-5842.

[23] Salleh, M.S.N., Ali, R.R., Shameli, K., Hamzah, M.Y., and Chan, J.Z., 2020, Silver nanoparticles on pullulan derived via gamma irradiation method: a preliminary analysis, *IOP Conf. Ser.: Mater. Sci. Eng.*, 808, 012030.

[24] Moglia, I., Santiago, M., Soler, M., and Olivera-Nappa, A., 2020, Silver nanoparticle synthesis in human ferritin by photochemical reduction, *J. Inorg. Biochem.*, 206, 111016.

[25] Saha, S., Ghosh, M., Dutta, B., and Chowdhury, J., 2016, Self-assembly of silver nanocolloids in the Langmuir–Blodgett film of stearic acid: Evidence of an efficient SERS sensing platform, *J. Raman Spectrosc.*, 47, 168–176.

[26] Afreen, A., Ahmed, R., Mehboob, S., Tariq, M., Alghamdi, H.A., Zahid, A.A., Ali, I., Malik, K., and Hasan, A., 2020, Phytochemical-assisted biosynthesis of silver nanoparticles from *Ajuga bracteosa* for biomedical applications, *Mater. Res. Express*, 7(7) 075404

[27] Bahrulolum, H., Nooraei, S., Javanshir, N., Tarrahimofrad, H., Mirbagheri, V.S., Easton, A.J., and Ahmadian, G., 2021, Green synthesis of metal nanoparticles using microorganisms and their application in the agrifood sector, *J. Nanobiotechnol.*, 19 (1), 86.

[28] Mondal, A.H., Yadav, D., Mitra, S., and Mukhopadhyay, K., 2020, Biosynthesis of silver nanoparticles using culture supernatant of *Shewanella* sp. ARY1 and their antibacterial activity, *Int. J. Nanomed.*, 15, 8295–8310.

[29] Aritonang, H.F., Onggo, D., Ciptati, C., and Radiman, C.L., 2015, Insertion of platinum particles in bacterial cellulose membranes from $PtCl_4$ and H_2PtCl_6 precursors, *Macromol. Symp.*, 353 (1), 55–61.

[30] Aritonang, H.F., Kamea, O.E., Koleangan, H., and Wuntu, A.D., 2020, Biotemplated synthesis of Ag-ZnO nanoparticles/bacterial cellulose nanocomposites for photocatalysis application, *Polym.-Plast. Technol. Mater.*, 59 (12), 1292–1299.

[31] Aritonang, H.F., Koleangan, H., and Wuntu, A.D., 2019, Synthesis of silver nanoparticles using aqueous extract of medicinal plants' (*Impatiens balsamina* and *Lantana camara*) fresh leaves and analysis of antimicrobial activity, *Int. J. Microbiol.*, 2019, 8642303.

[32] Jadoun, S., Arif, R., Jangid, N.K., and Meena, R.K., 2020, Green synthesis of nanoparticles using plant extracts: A review, *Environ. Chem. Lett.*, 19 (1), 355–374.

[33] Castillo-Henríquez, L., Alfaro-Aguilar, K., Ugalde-Álvarez, J., Vega-Fernández, L., Montes de Oca-Vásquez, G., and Vega-Baudrit, J.R., 2020, Green synthesis of gold and silver nanoparticles from plant extracts and their possible applications as antimicrobial agents in the agricultural area, *Nanomaterials*, 10 (9), 1763–1786.

[34] Vanlalveni, C., Lallianrawna, S., Biswas, A., Selvaraj, M., Changmai, B., and Rokhum, S.L., 2021, Green synthesis of silver nanoparticles using plant extracts and their antimicrobial activities: A review of recent literature, *RSC Adv.*, 11 (5), 2804–2837.

[35] Ajitha, B., Reddy, Y.A.K., Shameer, S., Rajesh, K.M., Suneetha, Y., and Reddy, P.S., 2015, *Lantana camara* leaf extract mediated silver nanoparticles: Antibacterial, green catalyst, *J. Photochem. Photobiol., B*, 149, 84–92.

[36] Sharifi-Rad, M., Pohl, P., Epifano, F., and Álvarez-Suarez, J.M., 2020, Green synthesis of silver nanoparticles using *Astragalus tribuloides* Delile. root extract: Characterization, antioxidant, antibacterial, and anti-inflammatory activities, *Nanomaterials*, 10 (12), 2383.

[37] Zarei, Z., Razmjoue, D., and Karimi, J., 2020, Green synthesis of silver nanoparticles from *Caralluma tuberculata* extract and its antibacterial activity, *J. Inorg. Organomet. Polym. Mater.*, 30 (11), 4606–4614.

[38] Seifipour, R., Nozari, M., and Pishkar, L., 2020, Green synthesis of silver nanoparticles using *Tragopogon collinus* leaf extract and study of their antibacterial effects, *J. Inorg. Organomet. Polym. Mater.*, 30 (8), 2926–2936.

[39] Ahmad, M.A., Salmiati, S., Marpongahtun, M., Salim, M.R., Lolo, J.A., and Syafiuddin, A., 2020, Green synthesis of silver nanoparticles using *Muntingia calabura* leaf extract and evaluation of antibacterial activities, *Biointerface Res. Appl. Chem.*, 10 (5), 6253–6261.

[40] Mikhailova, E.O., 2020, Silver nanoparticles: Mechanism of action and probable bio-application, *J. Funct. Biomater.*, 11 (4), 84.

[41] Sangule, O.T., 2020, Green synthesis of silver nanoparticles from leaf extract of *Lantana camara*, characterization and antimicrobial activity, *Int. J. Recent Sci. Res.*, 11 (4), 38297–38300.

[42] Palei, N.N., Ramu, S., Vijaya, V., Thamizhvanan, K., and Balaji, A., 2020, Green synthesis of silver nanoparticles using leaf extract of *Lantana camara* and its antimicrobial activity, *Int. J. Green Pharm.*, 14 (2), 155–161.

[43] Kumar, B., Smita, K., and Cumbal, L., 2016, Biosynthesis of silver nanoparticles using *Lantana camara* flower extract and its application, *J. Sol-Gel Sci. Technol.*, 78 (2), 285–292.

[44] Shriniwas, P.P., and Subhash, T.K., 2017, Antioxidant, antibacterial and cytotoxic potential of silver nanoparticles synthesized using terpenes rich extract of *Lantana camara* L. leaves, *Biochem. Biophys. Rep.*, 10, 76–81.

[45] Dubey, D., and Pandhy, R.N., 2013, Antibacterial activity of *Lantana camara* L. against multidrug resistant pathogens from ICU patients of a teaching hospital, *J. Herb. Med.*, 3 (2), 65–75.

[46] Ajitha, B., Reddy, Y.A.K., and Reddy, P.S., 2015, Green synthesis and characterization of silver nanoparticles using *Lantana camara* leaf extract, *Mater. Sci. Eng., C*, 49, 373–381.

[47] Shaik, M.R., Khan, M., Kuniyil, M., Al-Warthan, A., Alkhathlan, H.Z., Siddiqui, M.R.H., Shaik, J.P., Ahmed, A., Mahmood, A., Khan, M., and Adil, S.F., 2018, Plant-extract-assisted green synthesis of silver nanoparticles using *Origanum vulgare* L. extract and their microbicidal activities, *Sustainability*, 10 (4), 913.

[48] Mittal, A.K., Chisti, Y., and Banerjee, U.C., 2013, Synthesis of metallic nanoparticles using plant extracts, *Biotechnol. Adv.*, 31 (2), 346–356.

[49] Jha, A.K., Prasad, K., Prasad, K., and Kulkarni, A.R., 2009, Plant system: Nature's nanofactory, *Colloids Surf., B*, 73 (2), 219–223.

[50] Maiti, S., Barman, G., and Laha, J.K., 2016, Detection of heavy metals (Cu^{+2}, Hg^{+2}) by biosynthesized silver nanoparticles, *Appl. Nanosci.*, 6 (4), 529–538.

[51] Karthiga, D., and Anthony, S.P., 2013, Selective colorimetric sensing of toxic metal cations by green synthesized silver nanoparticles over a wide pH range, *RSC Adv.*, 3 (37), 16765–16774.

[52] Demir, D., Bölgen, N., and Vaseashta, A., 2018, "Green Synthesis of Silver Nanoparticles Using *Lantana camara* Leaf Extract and Their Use as Mercury(II) Ion Sensor" in *Advanced Nanotechnologies for Detection and Defence against CBRN Agents. NATO Science for Peace and Security Series B: Physics and Biophysics*, Eds. Petkov, P., Tsiulyanu, D., Popov, C., and Kulisch, W., Springer, Dordrecht, 427–433.

[53] Ihsan, M., Niaz, A., Rahim, A., Zaman, M.I., Arain, M.B., Sirajuddin, Sharif, T., and Najeeb, M., 2015, Biologically synthesized silver nanoparticle-based colorimetric sensor for the selective detection of Zn^{2+}, *RSC Adv.*, 5 (111), 91158–91165.

[54] Daghestani, H.N., and Day, B.W., 2010, Theory and applications of surface plasmon resonance, resonant mirror, resonant waveguide grating, and dual polarization interferometry biosensors, *Sensors*, 10 (11), 9630–9646.

Ground State Energies of Helium-Like Ions Using a Simple Parameter-Free Matrix Method

Redi Kristian Pingak[1*], Atika Ahab[1], and Utama Alan Deta[2]

[1]*Department of Physics, Universitas Nusa Cendana, Jl. Adisucipto Penfui, Kupang 85001, Nusa Tenggara Timur, Indonesia*

[2]*Department of Physics, Universitas Negeri Surabaya, Jl. Ketintang Gd C3 Lt 1, Surabaya 60231, Indonesia*

* ***Corresponding author:***

tel: +62-82147618836
email: rpingak@staf.undana.ac.id

Received: May 6, 2021
Accepted: June 7, 2021

DOI: 10.22146/ijc.65737

Abstract: *This study aims to use hydrogenic orbitals within an analytic and numeric parameter-free truncated-matrix method to solve the projected Schrödinger equation of some helium-like ions ($3 \leq Z \leq 10$). We also derived a new analytical expression of the ion ground state energies, which was simple and accurate and improved the accuracy of the analytic calculation, numerically using Mathematica. The standard matrix method was applied, where the wave function of the ions was expanded in a finite number of eigenvectors comprising hydrogenic orbitals. The Hamiltonian of the systems was calculated using the wave function and diagonalized to obtain their ground state energies. The results showed that a simple analytic expression of the ground state energies of He-like ions was successfully derived. Although the analytic expression was derived without involving any variational parameter, it was reasonably accurate with a 0.12% error for Ne^{8+} ion., The accuracy of the analytic energies was also numerically improved to 0.10% error for Ne^{8+} ion from this method. The results clearly showed that the energies obtained using this method were more accurate than the hydrogenic perturbation theory and the uncertainty principle-variational approach. In addition, for $Z > 4$, our results were more accurate than those from the geometrical model.*

Keywords: *helium-like ions; ground state energies; parameter-free matrix method; hydrogenic orbital approximation; projected Schrödinger equation*

■ INTRODUCTION

Theoretical calculations of energies of two-electron systems such as helium and helium-like ions have been attractive since the discovery of quantum mechanics [1] because these systems are the most simple many-body systems, and therefore, traditionally used as a testing ground for various methods in theoretical quantum calculations [2]. In addition, highly accurate experimental data for such systems are available, which can be used as a reference to evaluate the accuracy of theoretical calculations.

A large number of theoretical studies have been conducted to calculate the energies of helium-like ions accurately. The methods used in the studies ranged from the most sophisticated to the simplest ones. Some relatively new advanced calculations were quantum electrodynamics calculations [2-3], explicitly correlated basis sets derived from regularized Krylov sequences [4-6] and discrete variational-perturbation approach based on explicitly correlated wave functions [7-8]. Furthermore, some highly accurate calculations on the energies of the ions using various methods were recently reported, including the application of the free iterative complement interaction method [9-10], Non-Relativistic QED (NRQED) [11], and Quantum Mechanics of Coulumb Charge (QMCC) [12]. Older sophisticated calculations include the work of Pekeris, who applied the iteration method with the use of perimetric coordinates in the wave function expansion [13]. In general, up to thousands of variational parameters were used in most sophisticated calculations to produce highly accurate energies of helium-like ions [14]. However, these methods mostly involved tedious analytical calculations and or expensive numerical

calculations, mainly due to many parameters in their calculations. Moreover, wavefunctions obtained from such methods are often computationally prohibitive to be used in calculating cross-sections of many physical processes such as double ionization of atoms by ion [14]. Therefore, finding simpler wavefunctions with a low number of parameters is essential for studying those physical processes.

In addition to the methods mentioned above, several relatively more straightforward methods have also been developed recently by reducing the number of variational parameters. For instance, Liverts and Barnea [15] performed numerical calculations, which only used three parameters as inputs in their Mathematica code. Some analytical calculations using trial wave functions with a minimum number of parameters were also developed [16]. The final form of the proposed wavefunction can be written as a parameter-free function. However, the calculations to obtain its final form still involved optimizing a parameter in the initially proposed wavefunction. A numerical calculation using the variational method was also applied in [17]. Moreover, a parameter-free-like method using a simple geometrical model was developed by Gomez [18] to calculate the energies of helium-like ions. In this geometrical model, there was only a single parameter used in the calculations, but errors were still relatively large, especially for ions with large Z.

The simplest possible method to calculate the energies of helium-like ions is to use the hydrogenic orbital approximation. In this method, two-electron wave functions of the ions are written as the Hartree product of two hydrogenic orbitals. In this approach, correlated wave functions, which often make theoretical calculations more complicated, are neglected, and no variational parameter is needed [19]. However, the ground state energy results have relatively large errors, especially for the ions with relatively small atomic number Z, which indicates a large discrepancy between results obtained from the simplest methods with those from the most accurate ones. Hence, finding a simple yet accurate method to calculate energies of two-electron atoms such as helium-like ions remains a significant challenge.

To increase the accuracy of the hydrogenic standard perturbation theory, a simple numerical calculation using the hydrogenic orbital approximation in the framework of a matrix calculation was introduced by Masse and Walker [20]. In their work, a numerical calculation using a Mathematica code containing only seven lines was applied to calculate the three lowest energies of the helium atom with reasonable accuracy. Although the method did not require any parameter in the calculation, it managed to significantly reduce errors obtained from the standard 1^{st} order perturbation theory. Furthermore, a simple analytical matrix method, based on the work of [20], was developed in our previous work [21] to obtain accurate analytical energies of the helium atom. The numerical and analytical matrix approach applied in the two studies performed well for helium and yielded much more accurate energies than those from the 1^{st} order standard hydrogenic perturbation theory. This method was also applied recently in our previous study to obtain the first excited state energies of some helium-like ions with reasonable accuracy [22].

To the best of our knowledge, the parameter-free matrix method has not been used to calculate the ground state energies of helium-like ions. Also, since the method has proven accuracy when used with the helium atom [20-21], it should perform better if applied to other two-electron systems such as helium-like ions with larger atomic numbers than the helium atom.

The purpose of the present study was to extend the parameter-free matrix method to obtain accurate ground state energies of light helium-like ions ($3 \leq Z \leq 10$) with analytic and numeric calculations. The Mathematica code of Masse and Walker [20] and the analytic matrix method [21] were used for the numerical and analytical calculations, respectively. In this work, only *s*-orbitals were included in the wave functions to avoid long calculations. To demonstrate the ease of the method, a simple analytic expression for energies of any helium-like ion, which only depends on the atomic number Z, was derived in this work. This analytical expression can then be used as an easy-to-use equation to calculate the energies of helium-like ions. With this

parameter-free and straightforward method, this work aims not to better highly advanced variational calculation methods but to produce more accurate ground state energies of helium-like ions than other simple approaches in the literature, with much less algebra and minimum computational time. Hartree atomic units were used throughout this work.

■ COMPUTATIONAL METHODS

The parameter-free matrix method solved the projected Schrödinger equation in a finite subspace. The Hamiltonian was in the form of a finite square matrix, and the wave functions were in the form of a column vector. The Hamiltonian matrix elements were calculated after the wave function was defined to solve the energy eigenvalue equation. In this work, the two-electron wave function of the ions was written as a linear combination of basis states formed from the Hartree product of two hydrogenic orbitals. Once the Hamiltonian matrix elements were found, the last step was to solve the secular equation to obtain energy eigenvalues of the ions. The ground state energy was the smallest among the energy eigenvalues obtained. The formulations needed to perform those calculations are presented below. The non-relativistic time-independent Schrödinger equation projected into a finite subspace for two-electron atoms (ions) with a fixed nucleus is

$$\hat{H}\left|\Psi\right\rangle = E\left|\Psi\right\rangle \tag{1}$$

or explicitly as

$$\left(-\frac{\nabla_1^2}{2}-\frac{\nabla_2^2}{2}-\frac{Z}{r_1}-\frac{Z}{r_2}+\frac{1}{r_{12}}\right)\left|\Psi\right\rangle = E\left|\Psi\right\rangle \tag{2}$$

where r_1 and r_2 are the nuclear-electron distance of electron 1 and electron 2, respectively, r_{12} is the electron-electron distance, and Z is the atomic number of the ions. In the orbital approximation, the wavefunction in Eq. (2) can be written as a linear combination of the Hartree product of hydrogenic orbitals as

$$\left|\Psi\right\rangle = \sum_{i=1}^{n} c_i \left|\Phi_i\right\rangle = \sum_{i=2}^{n} c_{11}\left|\phi_1\phi_1\right\rangle + c_{1i}\left|\phi_1\phi_i\right\rangle + c_{i1}\left|\phi_i\phi_1\right\rangle \tag{3}$$

where φ_1 is the hydrogenic orbital of an electron in the ground state and φ_i is that of the other electron, which can be in any state of the helium-like ions. The number of terms in the expansion depends on the number of basis states one wants to use in the calculation. Elements of the Hamiltonian matrix is determined using Eq. (4)

$$H_{pq} = \left\langle \Phi_p \left| H \right| \Phi_q \right\rangle \tag{4}$$

substituting the explicit form of Hamiltonian in Eq. (2) into Eq. (4) yielded

$$H_{pq} = \left(-\frac{Z^2}{2n_1^2}-\frac{Z^2}{2n_2^2}\right)\delta_{pq} + \left\langle \Phi_p \left| \frac{1}{r_{12}} \right| \Phi_q \right\rangle \tag{5}$$

where the first two terms in Eq. (5) are the two hydrogenic one-electron solutions of the non-relativistic Schrödinger equation. The electron-electron interaction potential in Eq. (5) can be determined using Eq. (6)

$$V = \frac{1}{r_{12}} = \sum_{lm} \frac{4\pi}{2l+1} \frac{r_<^l}{r_>^{l+1}} (-1)^m Y_l^{-m}(\Omega_1) Y_l^m(\Omega_2)$$

$$V = \begin{cases} \dfrac{1}{r_1}, & \text{if } r_2 < r_1 \\ \dfrac{1}{r_2}, & \text{if } r_1 < r_2 \end{cases} \tag{6}$$

Each hydrogenic orbital $|\varphi_i\rangle$ used in the basis states $|\Phi_p\rangle$ is the product of the radial function and the spherical harmonics. Since only s-orbitals were used in this article, the orbital can then be written as

$$\left|\phi_{n00}(r,\theta,\phi)\right\rangle = \left|R_{n0}(r) Y_0^0\right\rangle \tag{7}$$

where the well-known hydrogenic radial function for s-orbitals can be written in terms of Laguerre polynomials as

$$R_{n0}(r_i) = \left\{\frac{Z(n-1)!}{n^2(n)!}\right\}^{\frac{1}{2}} \left(\frac{2Z}{n}\right) e^{-\frac{Zr_i}{n}} L_{n-1}^1\left(\frac{2Zr_i}{n}\right) \tag{8}$$

Substituting Eq. (7) and (8) into Eq. (5) and integrating it over all space yields

$$H_{pq} = \left(-\frac{Z^2}{2n_1^2}-\frac{Z^2}{2n_2^2}\right)\delta_{pq} + \left(Y_0^0\right)^4 \iint R_{n_1 0}(r_1) R_{n_2 0}(r_2) \frac{1}{r_{12}} R_{n_3 0}(r_1) R_{n_4 0}(r_2) d^3r_1 d^3r_2 \tag{9}$$

Since the angular part of the integrations canceled $(Y_0^0)^4$, Eq. (9) becomes

$$H_{pq} = \left(-\frac{Z^2}{2n_1^2}-\frac{Z^2}{2n_2^2}\right)\delta_{pq} + \iint r_1^2 R_{n_1 0}(r_1) R_{n_2 0}(r_2) \frac{1}{r_{12}} r_2^2 R_{n_3 0}(r_1) R_{n_4 0}(r_2) dr_1 dr_2 \tag{10}$$

By substituting Eq. (8) into Eq. (10), r_1^2 and r_2^2 can be

absorbed into the radial functions, and therefore, Eq. (10) has a simpler form as

$$H_{pq} = \left(-\frac{Z^2}{2n_1^{\,2}} - \frac{Z^2}{2n_2^{\,2}} \right)\delta_{pq} + \iint P_{n_1 0}(r_1) P_{n_2 0}(r_2) \frac{1}{r_{12}} P_{n_3 0}(r_1) P_{n_4 0}(r_2) dr_1 dr_2 \quad (11)$$

As a consequence, a modified radial function $P_{n0}(r_i)$ has to be defined as

$$P_{n0}(r_i) \equiv \left\{ \frac{Z(n-1)!}{n^2 (n)!} \right\}^{\frac{1}{2}} \left(\frac{2Zr_i}{n} \right) e^{-\frac{Zr_i}{n}} L^1_{n-1}\left(\frac{2Zr_i}{n} \right) \quad (12)$$

where i =1,2. Eq. (11) was the expression used to analytically and numerically calculate elements of the Hamiltonian matrix in this article.

After the Hamiltonian matrix was obtained, the secular equation, see Eq. (13), was simply solved to obtain all energy eigenvalues (assuming the Hamiltonian matrix is of size j × j).

$$\det \begin{bmatrix} H_{11}-E & H_{12} & \ldots & H_{1j} \\ H_{21} & H_{22}-E & \ldots & H_{2j} \\ \ldots & \ldots & \ldots & \ldots \\ H_{j1} & H_{j2} & \ldots & H_{jj}-E \end{bmatrix} = 0 \quad (13)$$

Solutions to Eq. (13) contain j energy eigenvalues, and the lowest energy corresponds the ground state energy of the He-like ions. In this work, Eq. (11) and (13) were solved both analytically and numerically.

■ RESULTS AND DISCUSSION

Analytic Expression for the Ground State Energies of He-Like Ions and Analytical Results

In this section, an analytic expression for the He-like ion energies was derived using the free-parameter matrix method with three basis states. First, Eq. (3) was used to determine the two-electron wavefunction expanded in three basis states consisting of hydrogenic s-orbitals, as shown in Eq. (14)

$$|\Psi\rangle = c_{11}|1s1s\rangle + c_{12}|1s2s\rangle + c_{21}|2s1s\rangle \quad (14)$$

Then, the Hamiltonian was in the form of a 3 × 3 matrix, whose nine components were determined using Eq. (11). To determine H_{11}, one had

$$H_{11} = -Z^2 + \langle P_{10}P_{10}|\frac{1}{r_{12}}|P_{10}P_{10}\rangle \quad (15)$$

P_{10} was simply determined using Eq. (12), which was then substituted into Eq. (15) to obtain (in integral form)

$$H_{11} = -Z^2 + 2^4 Z^6 \iint r_1^{\,2} e^{-2Zr_1} \frac{1}{r_{12}} r_2^{\,2} e^{-2Zr_2} dr_1 dr_2 \quad (16)$$

To evaluate the integral in Eq. (16), one could rewrite it as

$$H_{11} = -Z^2 + 2^4 Z^6 \int_0^\infty r_1^{\,2} e^{-2Zr_1} (I_2) dr_1 \quad (17)$$

where I_2 had been defined to be

$$I_2 \equiv \int_0^\infty \frac{1}{r_{12}} r_2^{\,2} e^{-2Zr_2} dr_2 \quad (18)$$

using Eq. (6) and detail procedures in [21], one obtained

$$I_2 = \frac{1}{4Z^3 r_1} \left\{ (-Zr_1 - 1) e^{-2Zr_1} + 1 \right\} \quad (19)$$

substituting Eq. (19) back into Eq. (17) yielded

$$H_{11} = -Z^2 + 4Z^3 \int_0^\infty \left\{ \left(-Zr_1^{\,2} - r_1 \right) e^{-4Zr_1} + r_1 e^{-2Zr_1} \right\} dr_1 \quad (20)$$

Similarly, other elements of the Hamiltonian matrix were obtained using the same procedures involved in obtaining H_{11}. The other elements could be easily proven to be equal to Eq. (21), Eq. (22) and Eq. (23).

$$H_{12} = H_{21} = H_{13} = H_{31} = \sqrt{2} Z^3 \int_0^\infty \left\{ \begin{matrix} \left(\frac{Z^2}{2} r_1^{\,3} - \frac{Z}{2} r_1^{\,2} - r_1 \right) e^{-7Zr_1/2} + \\ \left(-\frac{Z}{2} r_1^{\,2} + r_1 \right) e^{-3Zr_1/2} \end{matrix} \right\} dr_1 \quad (21)$$

$$H_{23} = H_{32} = \frac{2Z^4}{3^3} \int_0^\infty \left(-3Z^2 r_1^{\,4} + 4Zr_1^{\,3} + 4r_1^{\,2} \right) e^{-3Zr_1} dr_1 \quad (22)$$

$$H_{22} = H_{33} = \frac{-5Z^2}{8} + \frac{Z^3}{2} \int_0^\infty \left\{ \begin{matrix} \left(-\frac{Z^3}{4} r_1^{\,4} + \frac{3Z^2}{4} r_1^{\,3} - r_1 \right) e^{-3Zr_1} + \\ \left(\frac{Z^2}{4} r_1^{\,3} - Zr_1^{\,2} + r_1 \right) e^{-Zr_1} \end{matrix} \right\} dr_1 \quad (23)$$

Eq. (20) to Eq. (23) were then evaluated to obtain all elements of the Hamiltonian matrix, as shown in Eq. (24). All are in Hartree atomic units.

$$H = \begin{bmatrix} -Z\left(Z - \frac{5}{8}\right) & \sqrt{2}\left(\frac{4096}{64827}Z\right) & \sqrt{2}\left(\frac{4096}{64827}Z\right) \\ \sqrt{2}\left(\frac{4096}{64827}Z\right) & -Z\left(\frac{5}{8}Z - \frac{17}{81}\right) & \frac{16}{729}Z \\ \sqrt{2}\left(\frac{4096}{64827}Z\right) & \frac{16}{729}Z & -Z\left(\frac{5}{8}Z - \frac{17}{81}\right) \end{bmatrix} \quad (24)$$

Finally, to calculate the ground state energies of He-like ions, the secular equation in Eq. (13) was then solved as shown in Eq. (25)

$$\det\begin{bmatrix} -Z\left(Z-\frac{5}{8}\right)-E & \sqrt{2}\left(\frac{4096}{64827}Z\right) & \sqrt{2}\left(\frac{4096}{64827}Z\right) \\ \sqrt{2}\left(\frac{4096}{64827}Z\right) & -Z\left(\frac{5}{8}Z-\frac{17}{81}\right)-E & \frac{16}{729}Z \\ \sqrt{2}\left(\frac{4096}{64827}Z\right) & \frac{16}{729}Z & -Z\left(\frac{5}{8}Z-\frac{17}{81}\right)-E \end{bmatrix}=0 \quad (25)$$

Eq. (25) is a very simple expression for energies of helium-like ions because it only depends on the atomic number Z of the ions. In that equation, an otherwise complicated calculation to solve the Schrödinger equation has been reduced into a simple calculation of the determinant of a 3 × 3 matrix. The calculation of the ground state energies of any He-like ion was done by substituting the atomic number Z of the ions into Eq. (25). The equation was then solved analytically to obtain three energy eigenvalues of the ions, with the lowest energy was the ground state energy. The obtained ground state energies for helium-like ions ($3 \le Z \le 10$) are shown in Table 1.

Numerical Calculation of the Ground State Energies of Helium-like Ions

As the number of basis state increases, energies are expected to be more accurate because more physical information is included in the wavefunction. It was proven to be valid in the study of the helium atom [21]. It would also make the analytical calculation very inefficient to perform for more than three basis states. Therefore, a numerical calculation using a simple Mathematica code was used here to perform the calculation.

It is important to state the meaning of analytical and numerical terms used in this article. Analytical calculation refers to the calculation by hand involving only 3 basis states and 3 × 3 Hamiltonian matrix. Meanwhile, numerical calculation refers to a calculation involving more than 3 basis states, i.e., Hamiltonian of size greater than 3 × 3. In addition, the numerical calculation was performed using a Mathematica code involving a matrix of size 25 ×25. Here, 25 basis states were used, which can be written as

$$|\Psi\rangle = \sum_{n=2}^{13} c_{11}|1s1s\rangle + c_{1n}|1sns\rangle + c_{n1}|ns1s\rangle \quad (26)$$

and therefore, the Hamiltonian was a 25 × 25 matrix, as shown below

$$H=\begin{bmatrix} H_{1,1} & H_{1,2} & \ldots & H_{1,25} \\ H_{2,1} & H_{2,2} & \ldots & H_{2,25} \\ \ldots & \ldots & \ldots & \ldots \\ H_{25,1} & H_{25,2} & \ldots & H_{25,25} \end{bmatrix} \quad (27)$$

and the corresponding secular equation was

$$\det\begin{bmatrix} H_{1,1}-E & H_{1,2} & \ldots & H_{1,25} \\ H_{2,1} & H_{2,2}-E & \ldots & H_{2,25} \\ \ldots & \ldots & \ldots & \ldots \\ H_{25,1} & H_{25,2} & \ldots & H_{25,25}-E \end{bmatrix}=0 \quad (28)$$

The calculations of all matrix elements in Eq. (27) using Eq. (11) and the solutions to the secular equation in Eq. (28) were performed using a Mathematica code modified from [20].

All the numerical energies are presented in Table 1 along with energies obtained from other simple approaches available in the literature, such as the geometrical model (GM) [18], the hydrogenic 1st order perturbation theory (SPT) [19], and the uncertainty principle-variational approach (UPV) [23]. The exact ground state energies of the ions were taken from [13] and were used to calculate the percentage errors, as shown in Table 1. Corresponding experimental values for the respective atoms were adapted from [24] and also shown in Table 1.

Comparisons with Ground State Energies using other Simple Methods

From Table 1, it is clear that our method yielded reasonably accurate ground state energies of helium-like ions. The least accurate result of our method was obtained for the He atom [19], with percentage errors of 2.51% and 2.02%, respectively, from our analytical and numerical calculations. Although this result for the He atom was less accurate compared to the geometrical model [18] (0.32% error), it was still more accurate than the results of the first-order perturbation theory [19] (5.28% error) and uncertainty principle-variational approach [23] (2.60% error). The most accurate results in this article were obtained for the ground state energy

Table 1. Ground state energies of helium atom and light he-like ions from our analytical calculation (AC), our numerical calculation (NC), the geometrical model (GM) [18], standard first-order perturbation theory (SPT) [19] and the uncertainty principle-variational approach (UPV) [23]. Energies are in atomic units

Atom/ Ion	AC (% error)	NC (% error)	SPT (% error)	GM (% error)	UPV (% error)	Exact [13]	Experiment [24]
He	-2.8304[‡] (2.51%)	-2.8446[‡] (2.02%)	-2.7500 (5.28%)	-2.9128 (0.32%)	-2.8279 (2.60%)	-2.9034	-2.90338
Li^+	-7.1886 (1.25%)	-7.2053 (1.02%)	-7.1250 (2.16%)	-7.3249 (0.62%)	-7.1880 (1.26%)	-7.2799	-7.2790
Be^{2+}	-13.5570 (0.72%)	-13.5740 (0.60%)	-13.5000 (1.18%)	-13.7373 (0.60%)	-13.5486 (0.78%)	-13.6556	-13.6574
B^{3+}	-21.9285 (0.47%)	-21.9455 (0.39%)	-21.8750 (0.75%)	-22.1477 (0.53%)	-21.9083 (0.56%)	-22.0310	-22.0360
C^{4+}	-32.3014 (0.32%)	-32.3183 (0.27%)	-32.2500 (0.52%)	-32.5573 (0.47%)	-32.2672 (0.43%)	-32.4062	-32.4174
N^{5+}	-44.6749 (0.24%)	-44.6918 (0.20%)	-44.6250 (0.39%)	-44.9661 (0.41%)	-44.6252 (0.35%)	-44.7814	-44.8035
O^{6+}	-59.0489 (0.18%)	-59.0657 (0.15%)	-59.0000 (0.31%)	-59.3751 (0.37%)	-58.9824 (0.29%)	-59.1566	-59.1958
F^{7+}	-75.4231 (0.14%)	-75.4398 (0.12%)	-75.3750 (0.25%)	-75.7833 (0.33%)	-75.3388 (0.26%)	-75.5317	-75.5441
Ne^{8+}	-93.7975 (0.12%)	-93.8142 (0.10%)	-93.7500 (0.21%)	- (-)	-93.6943 (0.23%)	-93.9068	-94.0086

[‡]energies were taken from our previous calculation in [21]

of Ne^{8+}, with errors reaching as small as 0.12% from our analytical calculations and 0.10% from our numerical calculations, which are more accurate than standard perturbation theory, uncertainty principle-variational approach, and the geometrical model. The comparisons of the percentage errors of our analytical (AC) and numerical energies (NC) with other relatively simple calculations are shown in Fig. 1.

It should be noted that although our model generated more accurate energies than the geometrical model for Z > 4, the geometrical model was much more accurate than ours for Z = 2 and Z = 3. In particular, % errors from our numeric calculation were about 6.3 times larger than that from the geometrical model for the helium atom and approximately 1.6 times larger for the Li^+ ion. This strongly indicates that a general conclusion about whether our model or the geometrical model was more accurate in calculating ground state energies of two-electron systems can not be drawn. On the other hand, our model was more accurate than the standard perturbation theory calculated in [19] and the uncertainty principle variational calculation presented in [23].

Fig. 1 clearly shows the numerical results are more accurate than the analytical ones, especially for small Z. The accuracy is the result of the 25 basis states used in the numeric calculation, compared to only three basis states in the analytic one. For larger atomic number, the differences between the two become less obvious. It indicates that adding the number of basis states does not significantly impact the accuracy of our calculations for ions with a relatively large atomic number. The discussion on this is presented in the following section.

As shown in Fig. 1, the results indicate that errors from our analytical and numerical calculations for all ions were much smaller than those from standard perturbation theory [19] and the uncertainty principle-variational approach [23]. In particular, for ions with a small atomic number such as Li^+ and Be^{2+}, calculation using the standard perturbation theory gives errors of

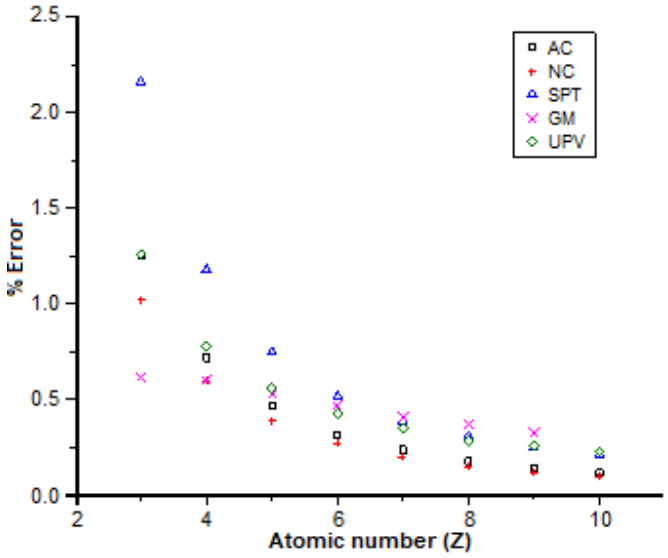

Fig 1. Percentage errors of our calculation (AC and NC) are compared with those from standard perturbation theory (SPT) [19], the geometrical model (GM) [18], and the uncertainty principle-variational approach (UPV) [23] as a function of atomic number Z ($3 \leq Z \leq 10$)

about 2.16% and 1.18%, respectively. Errors from our method for the respective ions are 1.25% and 0.72% (analytic) and 1.02% and 0.60% (numeric). These results indicate that our method significantly reduces errors obtained from standard perturbation theory for He-like ions, especially for ions with relatively small atomic number Z. Errors from our numeric energies for all ions are also much lower than errors found in [23]. Although our analytic calculation for Li^+ ion has approximately the same error as in [23], as atomic number increases, error from our calculations becomes much smaller than that from their calculations. Furthermore, comparisons to the geometrical model [18] show that for Li^+ (Z = 3), our energy calculation is less accurate. For Be^{2+} (Z = 4), the error from our numerical calculation is the same as that from the geometrical model. For Z > 4 (B^{3+} through F^{7+}), all our analytical and numerical energies are much better than those from the geometrical model. It also indicates that as nuclear charge increases, our approach becomes much more powerful than the geometrical model.

It should be noted that the accuracy of our results (which did not use any variational parameter) is, of course, not to be compared with the accuracy of calculations using several or even hundreds to thousands of variational parameters such as the work of [3,25-29] which reproduced experimental values and exact values of Pekeris [13]. As stated in the introduction, our simple calculation in this paper was only intended to demonstrate that using the hydrogenic orbitals without correlation function in a simple matrix calculation could be more accurate than some other simple methods in the literature.

Percentage Errors as a Function of Atomic Number Z

Table 1 also shows that the percentage errors decrease as the atomic number of the ions increases. The results were reliable because as the atomic number increases, electrostatic interaction between nuclei and electrons becomes more dominant compared to mutual interaction between the two electrons [19]. Most recently, Rahman et al. [30] calculated the electron-electron repulsion energies and Coulomb ionic energies of the He atom and some He-like ions (Li^+ and Be^{2+}) and found that as atomic number increases, the increase in the ionic energies of the ions was much more significant than that in the electron-electron repulsion energies. They found that the ionic energies of He, Li^+ and Be^{2+} were -6.7533 a.u., -16.1275 a.u., and -29.5020 a.u., respectively, while the repulsion energies of the respective ions were 0.9458 a.u., 1.5677 a.u., and 2.1909 a.u. It is clear from these results that the increase in the repulsion energies was much less than the increase in the ionic energies as Z increases. This was caused by the fact that electrons are more localized near higher Z ions [30]. Therefore, the fact that our approximation does not include electron correlation function in the wavefunction has led to lower percentage errors in ground state energies for ions with larger atomic numbers has already been anticipated.

To further clarify this, the probability amplitudes for each state used in the wave function expansion in our analytic and numerical calculation were calculated and presented in Table 2.

There is a very clear indication from Table 2 that the largest contribution to the ground state energy of the

Table 2. Amplitudes $c_{1i} = c_{i1}$ of the states used in the wavefunction expansion $|n_1,l_1,m_{l1};n_2,l_2,m_{l2}\rangle$ of our analytical and numerical calculations

Analytical Calculation								
State	Li^+	Be^{2+}	B^{3+}	C^{4+}	N^{5+}	O^{6+}	F^{7+}	Ne^{8+}
$\|1,0,0; 1,0,0\rangle$	-0.9862	-0.9937	-0.9964	-0.9977	-0.9984	-0.9988	-0.9991	-0.9993
$\|1,0,0; 2,0,0\rangle$	0.1170	0.0792	0.0597	0.0478	0.0398	0.0342	0.0299	0.0266
$\|2,0,0; 1,0,0\rangle$	0.1170	0.0792	0.0597	0.0478	0.0398	0.0342	0.0299	0.0266
Numerical Calculation								
State	Li^+	Be^{2+}	B^{3+}	C^{4+}	N^{5+}	O^{6+}	F^{7+}	Ne^{8+}
$\|1,0,0; 1,0,0\rangle$	0.9847	0.9927	0.9957	0.9972	0.9980	0.9985	0.9989	0.9991
$\|1,0,0; 2,0,0\rangle$	-0.1101	-0.0760	-0.0578	-0.0466	-0.0390	-0.0336	-0.0294	-0.0262
$\|2,0,0; 1,0,0\rangle$	-0.1101	-0.0760	-0.0578	-0.0466	-0.0390	-0.0336	-0.0294	-0.0262
$\|1,0,0; 3,0,0\rangle$	-0.0415	-0.0296	-0.0229	-0.0186	-0.0157	-0.0136	-0.0119	-0.0107
$\|3,0,0; 1,0,0\rangle$	-0.0415	-0.0296	-0.0229	-0.0186	-0.0157	-0.0136	-0.0119	-0.0107
$\|1,0,0; 4,0,0\rangle$	-0.0243	-0.0174	-0.0135	-0.0110	-0.0093	-0.0080	-0.0071	-0.0063
$\|4,0,0; 1,0,0\rangle$	-0.0243	-0.0174	-0.0135	-0.0110	-0.0093	-0.0080	-0.0071	-0.0063
$\|1,0,0; 5,0,0\rangle$	-0.0167	-0.0120	-0.0093	-0.0076	-0.0064	-0.0055	-0.0049	-0.0043
$\|5,0,0; 1,0,0\rangle$	-0.0167	-0.0120	-0.0093	-0.0076	-0.0064	-0.0055	-0.0049	-0.0043
$\|1,0,0; 6,0,0\rangle$	-0.0124	-0.0089	-0.0069	-0.0056	-0.0048	-0.0041	-0.0036	-0.0032
$\|6,0,0; 1,0,0\rangle$	-0.0124	-0.0089	-0.0069	-0.0056	-0.0048	-0.0041	-0.0036	-0.0032
$\|1,0,0; 7,0,0\rangle$	-0.0098	-0.0070	-0.0054	-0.0044	-0.0037	-0.0032	-0.0028	-0.0025
$\|7,0,0; 1,0,0\rangle$	-0.0098	-0.0070	-0.0054	-0.0044	-0.0037	-0.0032	-0.0028	-0.0025
$\|1,0,0; 8,0,0\rangle$	-0.0079	-0.0057	-0.0044	-0.0036	-0.0030	-0.0026	-0.0023	-0.0021
$\|8,0,0; 1,0,0\rangle$	-0.0079	-0.0057	-0.0044	-0.0036	-0.0030	-0.0026	-0.0023	-0.0021
$\|1,0,0; 9,0,0\rangle$	-0.0066	-0.0047	-0.0037	-0.0030	-0.0025	-0.0022	-0.0019	-0.0017
$\|9,0,0; 1,0,0\rangle$	-0.0066	-0.0047	-0.0037	-0.0030	-0.0025	-0.0022	-0.0019	-0.0017
$\|1,0,0; 10,0,0\rangle$	-0.0057	-0.0040	-0.0031	-0.0026	-0.0022	-0.0019	-0.0016	-0.0015
$\|10,0,0; 1,0,0\rangle$	-0.0057	-0.0040	-0.0031	-0.0026	-0.0022	-0.0019	-0.0016	-0.0015
$\|1,0,0; 11,0,0\rangle$	-0.0049	-0.0035	-0.0027	-0.0022	-0.0019	-0.0016	-0.0014	-0.0013
$\|11,0,0; 1,0,0\rangle$	-0.0049	-0.0035	-0.0027	-0.0022	-0.0019	-0.0016	-0.0014	-0.0013
$\|1,0,0; 12,0,0\rangle$	-0.0043	-0.0031	-0.0024	-0.0019	-0.0016	-0.0014	-0.0012	-0.0011
$\|12,0,0; 1,0,0\rangle$	-0.0043	-0.0031	-0.0024	-0.0019	-0.0016	-0.0014	-0.0012	-0.0011
$\|1,0,0; 13,0,0\rangle$	-0.0038	-0.0027	-0.0021	-0.0017	-0.0014	-0.0012	-0.0011	-0.0010
$\|13,0,0; 1,0,0\rangle$	-0.0038	-0.0027	-0.0021	-0.0017	-0.0014	-0.0012	-0.0011	-0.0010

ions came from the $|1,0,0; 1,0,0\rangle$ state, i.e. when the two electrons are in the ground state of the ions. This can be seen from the probability amplitude values (c_{11}^2) for the $|1,0,0; 1,0,0\rangle$ state which reached about 97.26% and 96.96% from our analytic and numeric calculations, respectively, for Li^+ ion. A similar calculation was performed by [31], who found that the largest contribution to the ground state energy of the He atom was from $|1,0,0; 1,0,0\rangle$ state (about 93%). Hutchinson et al. [31] found that the remaining contribution to the ground state energy of the He atom came from the higher l bound states as well as the unbound states of the atom. This is also in agreement with our results, as shown in Table 2. The importance of including hydrogenic unbound states and the bound states in the wavefunction was also discussed in [32-33], which also showed that reasonably accurate ground state energies of two-electron atoms could be generated by the matrix mechanics utilizing hydrogenic matrix mechanics. These studies supported the reasonably accurate results obtained in this article for he-like ions.

Meanwhile, Table 2 also indicated that the contribution from higher states was much smaller compared to the |1,0,0; 1,0,0⟩ with the lowest one came from the |1,0,0; 2,0,0⟩ state (c_{12}^2 = 1.37%) for the analytic calculation and $c_{1,13}^2 = 1.44 \times 10^{-3}$% for the|1,0,0; 13,0,0⟩ state from the numeric calculation for Li^+ ion. Furthermore, it is clear from Table 2 that as the atomic number Z of the ions increases, the contribution of |1,0,0; 1,0,0⟩ state to the ground state energies of the ions also increases while at the same time the contribution of the higher states decreases. For instance, the contribution was about 96.96% for Li^+ ion (Z = 3), which increased and reached about 99.82% for Ne^{8+} ion (Z = 10). A similar finding was also reported by Tapilin [24,34], who used configuration weight function and showed that in all cases considered, the |1,0,0; 1,0,0⟩ configuration was an increasing function. He also showed that the growth of the |1,0,0; 1,0,0⟩ configuration slowed down with increasing nuclear charge Z and tended to be constant. This is in agreement with our results shown in Table 2 and Fig. 2. This also explains why energies from our calculation for larger Z ions were more accurate than those for lower Z ions, as shown in Table 1 and Fig. 1. This finding is visualized in Fig. 2, where probability amplitudes of the states used in the wave function expansion were plotted as a function of atomic number Z for analytic calculation (Fig. 2(a)) and numeric calculation (Fig. 2(b)).

Fig. 2 demonstrates that contribution from the |1,0,0; 1,0,0⟩ state when using 3 basis states in our analytical calculation was approximately the same as that when using 25 basis states for a particular ion. There was a slight increase in the probability amplitudes of the state, but since the probability amplitudes almost reached 100%, further addition of hydrogenic s-bound states in the wave function using approximation here would not significantly improve the accuracy of our calculation. The use of correlation function involving variational parameters should therefore be included to significantly improve the results of our calculations, which has been performed using various method and widely reported in the literature. Including the correlation function and variational parameters would improve the accuracy. However, at the same time, the difficulty levels of the calculations increase, which was out of the scope of the present research. Calculation of electron correlation in He and He-like ions can be found, for example, in [35], which used the Laguerre-based wave function to obtain the fully correlated wave function and the Hartree-Fock wave function. A similar calculation on the He atom using a modified Hylleraas trial function containing two linear parameters was also reported recently by Purwaningsih et al. [36].

Table 2 also clearly indicates that as the nuclear charge Z increased, the contribution from higher n states

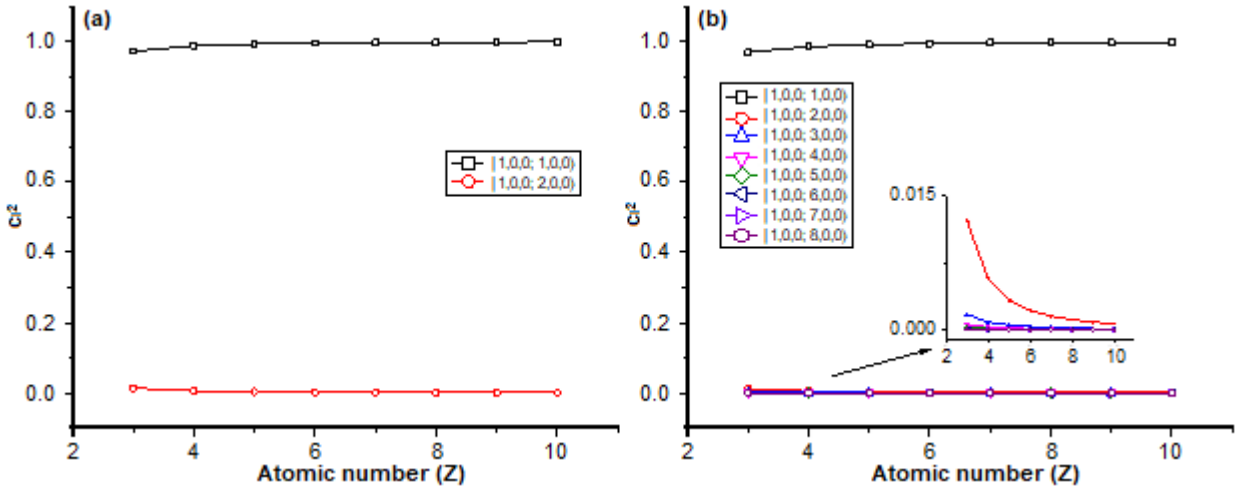

Fig 2. Probability amplitudes c_{1i}^2 of states used in the wave function was plotted against the ion atomic number Z for the analytic calculation (a) and numeric calculation (b). Since |1,0,0; n,0,0⟩ and |n,0,0; 1,0,0⟩ states were equivalent, only |1,0,0; n,0,0⟩ states were shown

to the ground state energies of the ions decreased. This was expected because the same number of basis states were used in our calculation, meaning that the larger the contribution from the ground state configuration $|1,0,0; 1,0,0\rangle$ for a particular ion should lead to the smaller contribution from the higher n-state configuration $|1,0,0; n,0,0\rangle$. The probability amplitudes continued to decrease for larger n for a particular ion for a particular matrix size.

Comments on the Accuracy and Limitations of Our Method and Further Improvement

The fact that our matrix method based on hydrogenic orbitals could generate reasonably accurate results with errors not larger than 1.02% for helium-like ions with $Z \geq 3$ was expected since many studies have shown that the use of (modified) hydrogenic wave functions could produce accurate results. For instance, studies by [20] and our previous work [21-22] showed that the reasonably accurate ground state energy of the He atom and the first excited state energy of some light He-like ions could be obtained using this method. In addition, the use of $|1,0,0; n,0,0\rangle$ states, i.e. one electron was kept at the ground states, and the other one in a particular excited state n was used by Hall and Siegel [37], who applied the shooting method to obtain accurate excited state energies of the He atom in coordinate space. This type of state configuration was also used as a pseudo-two-body problem by Gueribah et al. [38], who used the experimental energies to determine the local equivalent potential of the He atom using the Heisenberg model. Moreover, was applied by Herschbach et al. [39] applied the scaling dimension technique to obtain accurate ground state energies of two-electron atoms based on the dimensional dependence of a hydrogen atom. In their study, zeroth-order hydrogenic wave function was used to evaluate the expectation values of the electron-electron repulsion in the two-electron atoms. Finally, Rahman et al. [40] used the linear combination of hydrogenic wave functions to obtain accurate energy levels of hydrogenic ions by means of an iteration technique. Their method was also extended to many-body problems and proven to be accurate for the calculation of the helium-like ions, especially the hydrogen anion.

Since the results from our simple matrix calculation were reasonably accurate, the matrix method can be extended to study the chemical and physical properties of other systems. This was already done in some recent studies, such as in [41-43]. However, since we only used s-states $|1,0,0; n,0,0\rangle$ in our wave function, results in this article could be improved by including higher bound l-states $|1,0,0; n,l,m_l\rangle$ and continuum states. This would be our next focus on this topic. In addition, since no variational parameter and correlation function were involved in our calculation, results from our calculation were expected to have larger errors than those from other calculations involving variational parameters and correlation function. However, we have successfully shown that for ions with $Z > 4$, our parameter-free matrix results were more accurate than the geometrical model [18], which used one variational parameter in the model to calculate the ground state energy of the ions.

■ CONCLUSION

A parameter-free matrix method based on hydrogenic orbital approximations has been successfully applied in the present study to accurately calculate the ground state energies of helium-like ions from Li^+ to Ne^{8+}. A new and very simple analytic expression for the ground state energy of any helium-like ion was derived and has been proven to be reasonably accurate. A simple numerical calculation was also applied to improve the accuracy of analytical energies. Despite being simple, our results for all ions are much more accurate than some other simple methods available in the literature, such as the standard hydrogenic perturbation theory and the uncertainty principle-variational approach. In addition, our results are also more accurate than the geometrical model for $Z > 4$ (B^{3+} through F^{7+}). Therefore, our method can be introduced as an alternative and reasonably accurate method to obtain ground state energies of two-electron atoms with less algebra and inexpensive computer calculations.

■ ACKNOWLEDGMENTS

The authors thank Prof. Thad G. Walker and Dr. Robert Masse for the permission to modify their Mathematica code to perform the numerical calculation in this article. We also thank Prof. Christopher T.

Chantler for his comments on our manuscript. This research was a part of research funded by PNBP Research-grant 2021 No. 41/UN15.15.2.PPK/SPP/FST/IV/2021 of The Faculty of Science and Engineering, University of Nusa Cendana.

■ AUTHOR CONTRIBUTIONS

RKP wrote the original draft of the manuscript and performed the calculation. RKP, AA, and UAD analyzed and interpreted the results as well as revised the manuscript. All authors agreed to the final version of this manuscript.

■ REFERENCES

[1] Paterson, D., Chantler, C.T., Hudson, L.T., Serpa, F.F., Gillaspy, J.D., and Takacs, E., 2001, Absolute Test of Quantum Electrodynamics for Helium-Like Vanadium" in *The Hydrogen Atom, Lecture Notes in Physics Vol 570*, Eds. Karshenboim, S.G., Bassani, F., Pavone, F., Inguscio, M., Hansch, T., (eds.), Springer, Berlin, Heidelberg, 699–713.

[2] Yerokhin, V.A., and Pachucki, K., 2010, Theoretical energies of low-lying states of light helium-like ions, *Phys. Rev. A*, 81 (2), 022507.

[3] Tupitsyn, I.I., Bezborodov, S.V., Malyshev, A.V., Mironova, D.V., and Shabaev, V.M., 2020, Calculations of relativistic, correlation, nuclear, and quantum-electrodynamics corrections to energy and ionization potential of the ground state of helium-like ions, *Opt. Spectrosc.*, 128 (1), 21–31.

[4] Cioslowski, J., and Prątnicki, F., 2020, Uniform description of the helium isoelectronic series down to the critical nuclear charge with explicitly correlated basis sets derived from regularized Krylov sequences, *J. Chem. Phys.*, 153 (22), 224106.

[5] Cioslowski, J., and Prątnicki, F., 2019, Natural amplitudes of the ground state of the helium atom: Benchmark calculations and their relevance to the issue of unoccupied natural orbitals in the H_2 molecule, *J. Chem. Phys.*, 150 (7), 074111.

[6] Cioslowski, J., and Prątnicki, F., 2018, Simpler is often better: Computational efficiency of explicitly correlated two-electron basis sets generated by the regularized Krylov sequences of Nakatsuji, *J. Chem. Phys.*, 149 (18), 184107.

[7] Stoyanov, Z.K., Pavlov, R., Mihailov, L.M., Velchev, Ch.J., Mutafchieva, Y.D., Tonev, D., and Chamel, N., 2016, Nuclear induces effects and mass correlations in low and multiply charged helium-like ions, *J. Phys. Conf. Ser.*, 724, 012048.

[8] Velchev, C.J., Pavlov, R., Tonev, D., Stoyanov, Z.K., Mihailov, L.M., Mutafchieva, Y.D., and Van Neck, D., 2017, "Effects of Isotope Characteristics on the Electron System Ground State Energy of Helium-Like Ions" in *Quantum Systems in Physics, Chemistry, and Biology. Progress in Theoretical Chemistry and Physics Vol 30*, Eds. Tadjer, A., Pavlov, R., Maruani, J., Brändas, E., Delgado-Barrio, G., Springer, Cham, 283–300.

[9] Nakashima, H., and Nakatsuji, H., 2007, Solving the Schrödinger equation for helium atom and its isoelectronic ions with the free iterative complement interaction (ICI) method, *J. Chem. Phys.*, 127 (22), 224104.

[10] Nakashima, H., and Nakatsuji, H., 2008, Solving the electron-nuclear Schrödinger equation of helium atom and its isoelectronic ions with the free-iterative-complement interaction method, *J. Chem. Phys.*, 128 (15), 154107.

[11] Turbiner, A.V., Vieyra, J.C.L., and Olivares-Pilòn, H., 2019, Few-electron atomic ions in non-relativistic QED: The ground state, *Ann. Phys.*, 409, 167908.

[12] Turbiner, A.V., Vieyra, J.C.L., del Valle, J.C., and Nader, D.J., 2020, Ultra-compact accurate wave functions for He-like and Li-like iso-electronic sequences and variational calculus: I. Ground state, *Int. J. Quantum Chem.*, 121 (8), e26586.

[13] Pekeris, C.L., 1958, Ground states of two-electron atoms, *Phys. Rev.*, 112 (5), 1649–1658.

[14] Rodriguez, K.V., Gasaneo, G., and Mitnik, D.M., 2007, Accurate and simple wavefunctions for the helium isoelectronic sequence with correct cusp conditions, *J. Phys. B: At., Mol. Opt. Phys.*, 40 (19), 3923–3939.

[15] Liverts, E.Z., and Barnea, N., 2011, S-States of helium-like ions, *Comput. Phys. Commun.*, 182 (9), 1790–1795.

[16] Ancarani, L.U., Rodriguez, K.V., and Gasaneo, G., 2007, A simple parameter-free wavefunction for the ground state of two-electron atoms, *J. Phys. B: At. Mol. Opt. Phys.*, 40 (13), 2695–2702.

[17] Utomo, Y.R., Maruto, G., Utomo, A.B.S., Nurwantoro, P., and Sholihun, S., 2020, Numerical calculation of energy eigen-values of the hydrogen negative ion in the $2p^2$ configuration by using the variational method, *J. Fis. Indones.,* 24 (1), 30–32.

[18] Gomez, R.W., 1992, Ground and excited energy levels of helium-like atoms using a simple geometrical model, *Eur. J. Phys*., 13 (3), 135–138.

[19] Bransden, B.H., and Joachain, C.J., 2000, *Quantum Mechanics*, 2nd Ed., Prentice Hall, Hoboken, US.

[20] Massé, R., and Walker, T.G., 2015, Accurate energies of the He atom with undergraduate quantum mechanics, *Am. J. Phys*., 83 (8), 730–732.

[21] Pingak, R.K., Kolmate, R., and Bernandus., 2019, A simple matrix approach to determination of the helium atom energies, *JPFA*, 9 (1), 10–21.

[22] Pingak, R.K., and Deta, U.A., 2020, A simple numerical matrix method for accurate triplet-1s2s $^3S_1$ energy levels of some light helium-like ions, *J. Phys. Conf. Ser*., 1491, 012035.

[23] Harbola, V., 2011, Using uncertainty principle to find the ground-state energy of the helium and a helium-like Hookean atom, *Eur. J. Phys.*, 32 (6), 1607–1615.

[24] Tapilin, V.M., 2019, Solving the Schrodinger equation for helium-like ions with the method of configuration weight functions, *J. Struct. Chem.*, 60 (1), 1–6.

[25] King, A.W., Baskerville, A.L., and Cox, H., 2018, Hartree-Fock implementation using a Laguerre-based wave function for the ground state and correlation energies of two-electron atoms, *Philos. Trans. R. Soc., A*, 376 (2115), 20170153.

[26] Aznabaev, D.T., Bekbaev, A.K., Ishmukhamedov, I.S., and Korobov, V.I., 2015, Energy levels of a helium atom, *Phys. Part. Nucl. Lett.*, 12 (5), 689–694.

[27] Chen, Y.H., and Chao, S.D., 2017, Kinetic energy partition method applied to ground state helium-like atoms, *J. Chem. Phys.*, 146 (12), 124120.

[28] Aznabaev, D.T., Bekbaev, A.K., and Korobov, V.I., 2018, Nonrelativistic energy levels of helium atoms, *Phys. Rev. A*, 98, 012510.

[29] Yerokhin, V.A., Patkóš, V., Puchalski, M., and Pachucki, K., 2020, QED calculation of ionization energies of 1*snd* states in helium, *Phys. Rev. A*, 102, 012807.

[30] Rahman, F.U., Sarwono, Y.P., and Zhang, R.Q., 2021, Solution of two-electron Schrodinger equations using a residual minimization method and one-dimensional basis functions, *AIP Adv.*, 11 (2), 025228.

[31] Hutchinson, J., Baker, M., and Marsiglio, F., 2013, The spectral decomposition of the helium atom two-electron configuration in terms of hydrogenic orbitals, *Eur. J. Phys.*, 34, 111–128.

[32] Di Rocco, H.O., 2013, Comment on 'The spectral decomposition of the helium atom two-electron configuration in terms of hydrogenic orbitals', *Eur. J. Phys.*, 34 (2), L43.

[33] Forestell, L., and Marsiglio, F., 2015, The importance of basis states: An example using the hydrogen basis, *Can. J. Phys.*, 93 (10), 1009–1014.

[34] Tapilin, V.M., 2019, A new method of solving the many-body Schrodinger equation, *J. Struct. Chem.*, 58, 1–8.

[35] Baskerville, A.L., King, A.W., and Cox, H., 2019, Electron correlation in Li^+, He, H^- and the critical nuclear charge system Z_C: Energies, densities and Coulumb holes, *R. Soc. Open Sci.*, 6 (1), 181357.

[36] Purwaningsih, S., Nurwantoro, P., and Hermanto, A., 2019, Calculation of ground state energy of helium using Hylleraas trial function expansion, *Int. J. Eng. Res. Sci. Technol.*, 12 (8), 1178–1182.

[37] Hall, S., and Siegel, P.B., 2015, Calculating helium atomic excited states in coordinate space, *Am. J. Phys.*, 83 (12), 1028–1038.

[38] Gueribah, S., Ighezou, E.Z., Lombard, R.J., and Ngo, H., 2011, The Heisenberg model of the He atom revisited, *Few-Body Syst.*, 51, 59–67.

[39] Herschbach, D.R., Loeser, J.G., and Virgo, W.L., 2017, Exploring unorthodox dimensions for two-electron atoms, *J. Phys. Chem. A,* 121 (33), 6336–6340.

[40] Rahman, F.U., Zhao, R., Sarwono, Y.P., and Zhang, R.Q., 2018, A scheme of numerical solution for three-dimensional isoelectronic series of hydrogen atom using one-dimensional basis functions, *Int. J. Quantum Chem.*, 118 (19), e25694.

[41] Le Vot, F., Meléndez, J.J., and Yuste, S.B., 2016, Numerical matrix method for quantum periodic potentials, *Am. J. Phys.*, 84 (6), 426–433.

[42] Pavelich, R.L., and Marsiglio, F., 2015, The Kronig-Penney model extended to arbitrary potentials via numerical matrix mechanics, *Am. J. Phys.*, 83 (9), 773–781.

[43] Jugdutt, B.A., and Marsiglio, F., 2013, Solving for three-dimensional central potentials using numerical matrix methods, *Am. J. Phys.*, 81 (5), 343–350.

Short Communication:

Bioactive Secondary Metabolites from the Mangrove Endophytic Fungi *Nigrospora oryzae*

Antonius Rolling Basa Ola[1,2*], Titus Lapailaka[1], Hermania Em Wogo[1], Julinda Bendalina Dengga Henuk[3], Agnes Simamora[3], Lince Mukkun[3], Peter Proksch[4], and Chong Dat Pham[5]

[1]*Department of Chemistry, Faculty of Science and Engineering, Universitas Nusa Cendana, Jl. Adisucipto, Penfui-Kupang 85118, NTT, Indonesia*

[2]*Laboratorium Riset Terpadu (Biosains), Universitas Nusa Cendana, Kupang, NTT, Indonesia*

[3]*Agro Technology Department, Faculty of Agriculture, Universitas Nusa Cendana, Kupang, NTT, Indonesia*

[4]*Institute of Pharmaceutical Biology and Biotechnology, Heinrich Heine Universität, Universitätsstrasse 1, 40225 Düsseldorf, Germany*

[5]*Department of Cancer Systems Imaging, University of Texas MD Anderson Cancer Center, 1881 East Road, Houston, TX-77054, USA*

* ***Corresponding author:***

tel: +62-81285759981
email: antonius.ola@staf.undana.ac.id

Received: January 13, 2021
Accepted: March 23, 2021

DOI: 10.22146/ijc.63129

Abstract: *Mangrove forest has a distinctive habitat adapting with marine and terrestrial environment. Chemical investigation of the extract from mangrove endophytic fungi* Nigrospora oryzae *had resulted in the isolation of sterigmatocystin (**1**) and pestalopyrone (**2**). The structure of sterigmatocystin (**1**) and pestalopyrone (**2**) were elucidated using mass, UV and NMR spectrometers together with the comparison with the literature data. The study also showed that sterigmatocystin displayed moderate cytotoxicity but it could be further developed as antiviral and antibacterial agent based on the SAR information reported from its analogue and derivatives.*

Keywords: Nigrospora oryzae*; mangrove; sterigmatocystin; pestalopyrone*

■ INTRODUCTION

Endophytic fungi have been known as a rich source of valuable metabolites with various biological properties including antibacterial [1], cytotoxic [2] and anti-fungal activities [2-5]. Recent advances have also shown that the most important and valuable drugs from plants have been also produced by the endophytic fungi. For example, paclitaxel known as natural product from the plant *Taxus brevolia* has been widely found in endophytic fungi. At least 20 species of endophytic fungi have been reported to produce paclitaxel [6]. In addition, the metabolites of the Madagascar plant of periwinkle (*Catharanthus roseus*), namely vincristine and vinblastine, were also reported to be produced by the endophytic fungi *Talaromyces radicus* [7] and *Fusarium oxysporum* [8].

The production of the bioactive metabolites of endophytic fungi was influenced by some factors especially their habitat of growing. Mangrove habitat is distinctive one due to their adaptation to terrestrial and marine environments. With this extreme condition, mangrove-associated-endophytic fungi produced various bioactive molecules for their adaptation against abiotic and biotic stress [9-10]. In this work, we reported the isolation and structural elucidation of cytotoxic metabolites from the mangrove endophytic fungi *Nigrospora oryzae* grown on solid rice media.

■ EXPERIMENTAL SECTION

Materials

Materials used in this study were silica gel 60 M

(230–400 mesh), which was obtained from Macherey-Nagel GmbH & Co. KG, Dueren (Germany), TLC plates (silica gel 60 F-254) was obtained from Merck KGaA, Darmstadt, Germany and Sephadex LH-20 was ordered from Sigma. All solvents were freshly distilled including *n*-hexane, dichloromethane, ethyl acetate and methanol. Methanol for HPLC was purchased from Merck.

Instrumentation

The 1D and 2D NMR spectra were recorded on a Bruker ARX 500 NMR spectrometer. Chemical shifts of NMR spectra were analyzed by referencing to the residual solvent peak at (ppm) δ_H 7.26 ($CDCl_3$) and δ_H 3.31 (CD_3OD) for ^1H, and δ_C 77.0 ($CDCl_3$) and 49.2 (CD_3OD) for ^{13}C, respectively. Mass spectra were analyzed with a LCMS HP1100 Agilent Finnigan LCQ Deca XP Thermoquest, while HPLC data was recorded by a Dionex P580 system with routine detection at 235, 254, 280, and 340 nm. TLC was performed on pre coated silica gel plates with solvent system using EtOAc/MeOH/H_2O (30:5:4) and CH_2Cl_2/MeOH (9:1). The monitoring was undertaken by spraying the plates with anisaldehyde reagent or with detection at 254 and 366 nm.

Procedure

Isolation and identification of endophytic fungi

The isolation and identification of endophytic fungi from the leaves of mangrove *Avicennia marina* was undertaken according to the previously published protocol [11-12]. Briefly: After surface sterilization by immersing the leaves in 70% ethanol (50 mL), fresh healthy leaves were cut into small segment (0.5 cm × 0.5 cm) and then put onto the surface of malt extract agar containing the antibiotic chloramphenicol to inhibit the growth of bacteria. The composition of media for isolation followed the procedure described earlier [11] including malt extract and agar (15 g/L for each) together with the addition of chloroamphenicol (0.2 g/L) dissolved in distilled water and maintained at pH 7.4–7.8 by adding 10% NaOH or 36.5% HCl dropwise. After two days incubation at room temperature, the fungal strain grew out from the tissue of leaves. The pure strain of *Nigrospora oryzae* was isolated from the mixed culture and periodically check for its purity and identified using internal transcribed spacer (ITS) DNA with specific fungal primer pairs following the published protocol earlier [11-12].

Extraction and isolation

The pure strain of *Nigrospora oryzae* was grown in 1 L of Erlenmeyer flask. Rice (100 g) and distilled water (110 mL) were added to the Erlenmeyer and sterilized with autoclave. The fungus was cut into several pieces and then added into the Erlenmeyer flask containing the solid rice media. The fermentation was carried out for 3 weeks. The culture was extracted with ethyl acetate. The crude extract (800 mg) was fractionated with Sephadex LH-20 using the mixture of dichloromethane and methanol (1:1). Fraction III (35 mg) was further separated and purified with semi-preparative HPLC to afford compound **1** (5 mg) and **2** (1 mg).

Sterigmatocystin (1). White amorphous powder; ^1H-NMR ($CDCl_3$, 500 MHz): δ = 13.2 (s, 1H), 7.51 (t, *J* = 8.4 Hz, 1H), 6.85 (d, *J* = 7.3 Hz, 1H), 6.84 (dd, *J* = 1.0, 7.25 Hz, 1H), 6.77 (dd, *J* = 1.0, 8.4 Hz, 1H), 6.50 (dd, *J* = 2.9, 2.0 Hz, 1H), 6.45 (s, 1H), 5.46 (t, *J* = 2.65 Hz, 1H), 4.82 (ddd, *J* = 2.0, 4.4, 7.1 Hz, 1H), 4.0 (s, 3H). ^{13}C-NMR ($CDCl_3$, 125 MHz): δ = 181.2, 164.6, 163.3, 162.1, 155.3, 154.2, 145.4, 135.9, 113.1, 111.9, 108.2, 106.9, 105.9, 105.8, 102.6, 90.8, 56.8, 47.8; UV λ_{max} (PDA) 247.6 and 326.5 nm; ESIMS *m/z* 325.3 $[M+H]^+$, 670.9 $(2M+Na)^+$.

Pestalopyrone (2). Amorphous powder; ^1H-NMR (MeOD, 500 MHz): δ = 6.63 (qq, *J* = 0.96, 7.1 Hz, 1H), 6.12 (d, *J* = 2.1 Hz, 1H), 5.56 (d, *J* = 2.1 Hz, 1H), 3.86 (s, 3H), 1.86 (d, *J* = 7.2 Hz, 3H), 1.84 (s, 3H). ^{13}C-NMR (MeOD, 125 MHz): δ = 174.1, 166.9, 162.7, 131.0, 128.3, 98.9, 88.8, 56.9, 14.3, 12.0; UV λ_{max} (PDA) 226 and 310 nm; ESIMS *m/z* 181.0 $[M+H]^+$and at *m/z* 382.7 $(2M+Na)^+$.

Cell proliferation assay

Cytotoxicity was assessed against the murine lymphoma (L5178Y) cell line using a microplate 3-(4,5-dimethylthiazole-2-yl)-2,5-diphenyltetrazoliumbromide (MTT) assay as previously described [11,13]. The cells were seeded on 96-well plates with 10^4 cells per well and allowed to attach for 24 h and then treated with 10 μg/mL of the tested compound for 24 h. For the assay, the culture

medium was made to contain 0.7 mg/mL of 3-(4,5-dimethylthiazol-2-yl)-2,5-diphenyltetrazolium bromide (MTT). After two hours of incubation at 37 °C, the cells were lysed with a mixture of 95% isopropanol/5% formic acid. The concentration of reduced MTT as a marker for cell viability was measured using a Wallac Victor2 multilabel counter at 560 nm. Cells incubated only with vehicle control (DMSO) were considered 100% viable. The isolated compounds were bioassay-guided using L5178Y cancer cell line. Kahalalide F isolated from Indian sacoglossan mollusk *Elysia grandifolia* [14] was used as positive control with IC_{50} value of 4.3 µM.

■ RESULTS AND DISCUSSION

Fungal strain isolated from the leaves of mangrove of *Avecenia marina* was massively produced with rice media and subsequently extracted using ethyl acetate. The chromatographic separation using combination of Sephadex LH-20 together with semi-preparative HPLC afforded compounds **1** and **2**. Compound **1** was obtained as an amorphous powder. The UV spectrum showed absorption at 247.6 and 326.5 nm (Fig. 1(a)). The mass spectral data showed molecular ion peak at 325.3 $(M+H)^+$ and at 670.9 $(2M+Na)^+$ indicating that compound **1** has the molecular mass of 324.3 g/mol. The melting point of compound **1** was not measured due to the limited quantity of **1** obtained in this work.

The ^{1}H-NMR spectrum of **1** showed signals of a methoxy group at δ 4.00 (s), an intramolecular hydrogen bond of aromatic OH proton at δ 13.2 (s), one ABX system which the signals observed at δ 6.77 (dd, J = 1.0, 8.4 Hz, H7), 7.51 (t, J = 8.4 Hz, H8) and 6.84 (dd, J = 1.0, 7.25 Hz, H9), one aromatic signal at δ 6.44 (s, H-5), two olefinic proton signals at δ 6.50 (dd, J = 2.9, 2.0 Hz, H1) and δ 5.46 (t, J = 2.65 Hz, H2) together with two methyne signals resonating at δ 4.82 (ddd, J = 2.0, 4.4, 7.1 Hz, H3) and δ 6.85 (d, J = 7.3 Hz, H4). Analysis of ^{1}H–^{1}H COSY revealed the presence of two spin system. The aromatic signal at δ 6.84 ppm (H9) had correlation with the signal δ 7.51 ppm (H8) which in turn showing correlation with δ 6.77 ppm (H7). Another spin system was observed from the correlation of signal at δ 6.50 ppm (H1) and δ 5.46 ppm (H2) which further have correlation with signal δ 4.82 ppm (H3). The latter signal was then connected with another methyne proton at δ 6.83 ppm (H4). The position of methoxy group was assigned to C17 based on the HMBC correlation from methoxy proton signal at δ 4.00 ppm (H18) to C17 at δ_c 163.5 ppm. This was then supported from the HMBC correlation of H5 (δ_H 6.44 ppm) to C17 (δ_c 163.5 ppm) as well (Fig. 2(a)). The NMR data of compound **1** (Table 1) was very similar to those reported for sterigmatocystin [15-16]. The UV λ_{max} observed here was also in agreement with those reported for sterigmatocystin type of metabolites which normally observed at 248 and 322 nm [17]. Therefore, compound **1** was identified as sterigmatocystin (Fig. 2(a)).

Compound **2** was isolated as amorphous powder having maximum wavelength at 226 and 310 nm which was characteristic to pyrone moiety (Fig. 1(b)). The molecular mas of compound **2** was determined as 180.0 g/mol based on the mass spectral data showing the molecular ion peak at m/z of 181.0 $(M+H)^+$ and at *m/z* of 382.7 $(2M+Na)^+$ in positive mode. Due to the limited quantity of the material, the melting point of compound **2** was not measured. The ^{1}H-NMR spectrum revealed the aromatic signals at δ 6.12 ppm (d, J = 2.1 Hz, H5) and at δ 5.56 ppm (d, J = 2.1 Hz, H3) and one olefinic signal

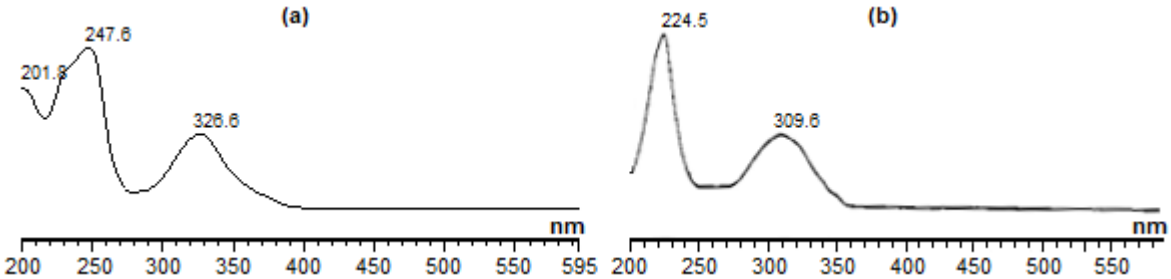

Fig 1. UV spectra of compound **1** (a) and compound **2** (b)

Table 1. NMR data of compound **1** ($CDCl_3$) and **2** (MeOD)

No	^{1}H-NMR (δ_H in ppm, multiplicities, *J* in Hz)				^{13}C-NMR (δ_C in ppm)			
	1 ($CDCl_3$)	Ref ($CDCl_3$) [15]	**2** (CD_3OD)	Ref (CD_3OD) [18]	**1** ($CDCl_3$)	Ref ($CDCl_3$) [16]	**2** (MeOD)	Ref (CD_3OD) [18]
1	6.50, dd, *J* = 2.9, 2.0	[15]6.50, dd, *J* = 2.8, 1.6			145.4	145.5		
2	5.46, t, *J* = 2.65	5.45, t, *J* = 2.6			102.6	102.7	166.9	166.9
3	4.82, ddd, *J* = 2.0, 4.4, 7.1	[15]4.81, dt, *J* = 2.2, 7.1	5.56, d, *J* = 2.1	6.12, d, *J* = 1.0*	47.8	48.2	88.8	98.8 [20]
4	6.85, d, *J* = 7.3	6.84, m			113.1	113.4	174.1	174.1
5	6.45, s	6.44, s	6.12, d, *J* = 2.1	5.55, d, *J* = 1.0*	90.8	90.7	98.9	88.5 [20]
6					162.1	162.5	162.7	162.6
7	6.77, dd, *J* = 1.0, 8.4	6.76, dd, *J* = 1.15, 8.55			111.9	111.4	128.3	128.3
8	7.51, t, *J* = 8.4	7.50, t, *J* = 8.3	6.63, qq, *J* = 0.96, 7.1	6.63, qq, *J* = 1.2, 7.2	135.9	135.9	131.0	131.0
9	6.84, dd, *J* = 1.0, 7.25	6.84, m	1.86, d, *J* = 7.2	1.85, d, *J* = 7.5	105.9	106.1	14.3	12.0
10			1.84, s	1.87, d, *J* = 1.0	155.3	155.1	12.0	14.3
11					108.2	109.1		
12					181.2	181.6		
13					105.8	106.1		
14					154.2	154.2		
15					106.9	106.7		
16					164.6	164.7		
17					163.3	163.5		
6-OH	13.2, s							
11-OCH3	4.00, s	4.00, s	3.86, s	3.70, s	56.8	57.0	56.9	56.9

*Reversed in the report Oleinikova et al. [15]; Lee et al. [18]

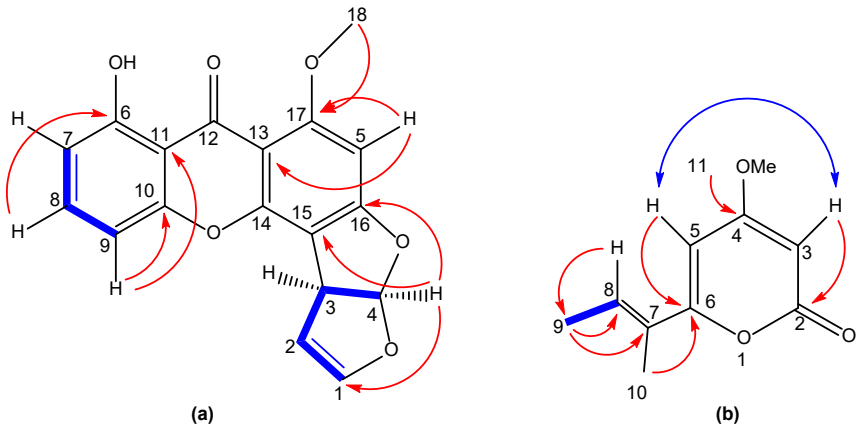

Fig 2. COSY and Key HMBC Corelations of **(a)** Sterigmatocystin **1** and (**b**) Pestalopyrone **2** (Blue for COSY and Red for HMBC correlations)

at δ 6.63 ppm (qq, *J* = 0.96, 7.1 Hz, H8) together with signals from two methyl attached to the double bond at δ 1.86 (d, *J* = 7.2 Hz, H9) and 1.84 (s, H10) ppm. The COSY spectra showed the presence of two spin systems. The

methyl signal at δ 1.86 ppm (H9) showed correlation with olefinic signal at δ 6.63 ppm (H8). The weak *meta* coupling correlation was observed from the aromatic signals at δ 6.12 (H5) and 5.56 (H3) ppm. In addition, the ^{13}C-NMR showed the presence of four quaternary carbons resonating at δ 174.1 (C4), 167.1 (C2), 162.8 (C6) and δ 128.5 (C7) ppm. The position of the quaternary carbons was assigned by the HMBC correlations. Moreover, the HMBC correlation from the methoxy signal at δ 3.86 ppm to the carbon resonating at 174.1 ppm (C4) confirmed the position of methoxy group at C4 (Fig. 2(b)). The ^{1}H-NMR spectrum was in a good agreement with the data reported for pestalopyrone [18-19]. The structure was also confirmed by comparison with the ^{13}C-NMR data which has been previously reported by Lee et al. [18].

Sterigmatocystin **1** was evaluated for the cytotoxic property against L5178Y murine cell line. Sterigmatocystin **1** was able to inhibit the growth of the cell line by 64% at the concentration of 10 μg/mL. The moderate cytotoxic activity of sterigmatocystin **1** and its derivatives have been earlier reported [20-21]. Pestalopyrone **2** was not tested due the limited quantity of the material. Pestalopyrone had been reported to be phytotoxic against hazelnut [22]. However, recent finding suggested that pestalopyrone based structures such as pestalopyrones A-D had no cytotoxic and antibacterial properties [23]. Pestalopyrone was also found inactive against dengue virus [24].

Although sterigmatocystin did not have strong cytotoxic activity, several derivatives of sterigmatocystin including 5-methoxydihydrosterigmatocystin showed potent antibacterial activity [17]. Sterigmatocystin was also reported to have antiparasitic property against *Trypanosoma cruzi* [25]. Moreover, sterigmatocystin derivatives, sterigmatocystins A–C, showed specific antiviral activity [26]. Therefore, sterigmatocystin would be further developed in the direction of antibacterial and antiviral activity based on this valuable SAR (structure activity relationship) information. Moreover, this study confirmed that the endophytic fungi are still potential and valuable sources of bioactive secondary metabolites [27-28].

■ CONCLUSION

Chemical investigation of the extract from the mangrove associated fungus *Nigrospora oryzae* resulted in the isolation of sterigmatocystin and pestalopyrone. Sterigmatocystin showed moderate cytotoxic activity against murine cancer cell line. Comparison of bioactivity between sterigmatocystin and its analogues (derivatives) suggested that sterigmatocystin could be developed as antiviral and antibacterial agents.

■ REFERENCES

[1] Bara, R., Zerfass, I., Aly, A.H., Goldbach-Gecke, H., Raghavan, V., Sass, P., Mándi, A., Wray, V., Polavarapu, P.L., Pretsch, A., Lin, W.H., Kurtán, T., Debbab, A., Brőtz-Oesterhelt, H., and Proksch, P., 2013, Atropisomeric dihydroanthracenones as inhibitors of multiresistant *Staphylococcus aureus*, *J. Med.Chem.*, 56 (8), 3257–3272.

[2] Uzma, F., Mohan, C.D., Hashem, A., Konappa, N.M., Rangappa, S., Kamath, P.V., Singh, B.P., Mudili, V., Gupta, V.K., Siddaiah, C.N., Chowdappa, S., Alqarawi, A.A., and Abd_Allah, E.F., 2018, Endophytic fungi–Alternative sources of cytotoxic compounds: A review, *Front. Pharmacol.*, 9, 309.

[3] Bara, R., Aly, A.H., Pretsch, A., and Wray, V., 2013, Antibiotically active metabolites from *Talaromyces wortmannii*, an endophyte of *Aloe vera*, *J. Antibiot*, 66 (8), 491–493.

[4] Ola, A.R.B., Metboki, G., Lay, C.S., Sugi, Y., De Rozari, P., Darmakusuma, D., and Hakim, E.H., 2019, Single Production of kojic acid by *Aspergillus flavus* and the revision of flufuran, *Molecules*, 24 (22), 4200.

[5] Ola, A.R.B., Tawo, B.D., Belli, H.L.L., Proksch, P., Tommy, D., and Hakim, E.H., 2018, A new antibacterial polyketide from the endophytic fungi *Aspergillus fumigatiaffinis*, *Nat. Prod. Commun.*, 13 (12), 1573–1574.

[6] Ola, A.R.B., 2020, Production of valuable chemical compounds isolated from plants by endophytic fungi, *IOP Conf. Ser.: Mater. Sci. Eng.*, 823, 012045.

[7] Palem, P.P.C., Kuriakose, G.C., and Jayabaskaran, C., 2015, An endophytic fungus, *Talaromyces radicus*, isolated from *Catharanthus roseus*, produces vincristine and vinblastine, which induce apoptotic cell death, *PLoS One,* 10 (12), e0144476.

[8] Kumar, A., Patil, D., Rajamohanan, P.R., and Ahmad, A., 2013, Isolation, purification and characterization of vinblastine and vincristine from endophytic fungus *Fusarium oxysporum* isolated from *Catharanthus roseus*, *PLoS One*, 8 (9), e71805.

[9] Handayani D., Wahyuningsih, T., Rustini, Artasasta, M.A., Putra, A.E., and Proksch, P., 2020, Bioactive compound from the mangrove plant endophytic fungus *Diaporthe amygdali* SgKB4, *Rasayan J. Chem.*, 13 (1), 327–332.

[10] Ola, A.R.B., Soa, C.A.P., Da Cunha, T., Sugi, Y., Belli, L.L.H., and Lalel, H.J.D., 2020, Antimicrobial metabolite from the endophytic fungi *Aspergillus flavus* isolated from *Sonneratia alba*, a mangrove plant of Timor-Indonesia, *Rasayan J. Chem.*, 13 (1), 377–381.

[11] Kjer, J., Wray, V., Edraba-Ebel, R., Ebel, R., Pretsch, A., Lin, W., and Proksch, P., 2009, Xanalteric acids I and II and related phenolic compounds from an endophytic *Alternaria sp.* isolated from the mangrove plant *Sonneratia alba*, *J. Nat. Prod.*, 72 (11), 2053–2057.

[12] Ola, A.R.B., Aly, A.H., Lin, W., Wray, V., and Debbab, A., 2014, Structural revision and absolute configuration of lateritin, *Tetrahedron Lett.*, 55 (45), 6184–6187.

[13] Chen, H., Daletos, G., Okoye, F., Lai, D., Dai, H., and Proksch, P., 2015, A new cytotoxic cytochalasin from the endophytic fungus *Trichoderma harzianum*, *Nat. Prod. Commun.*, 10 (4), 585–587.

[14] Ashour, M., Edrada, R., Ebel, R., Wray, V., Wätjen, W., Padmakumar, K., and Proksch, P., 2006, Kahalalide derivatives from the Indian sacoglossan mollusk *Elysia grandifolia*, *J. Nat. Prod.*, 69 (11), 1547–1553.

[15] Oleinikova, G.K., Denisenko, V.A., Slinkina, N.N., and Afiyatullov, S.S., 2012, Secondary metabolites of the marine fungus *Aspergillus ustus* KMM 4640, *Chem. Nat. Compd.*, 48 (3), 467–469.

[16] Song, X., Luo, M., Huang, H., and Lu, L., 2017, Secondary metabolites of the marine fungus *Aspergillus versicolor* SCSIO 05772, *Chem. Nat. Compd.*, 53 (2), 354–355.

[17] Song, F., Ren, B., Chen, C., Yu, Ke., Liu, X., Zhang, Y., Yang, N., He, H., Liu, X., Dai, H., and Zhang, L., 2014, Three new sterigmatocystin analogues from marine-derived fungus *Aspergillus versicolor* MF359, *Appl. Microbiol. Biotechnol.*, 98 (8), 3753–3758.

[18] Lee, J.C., Yang, X., Schwartz, M., Strobel, G., and Clardy, J., 1995, The relationship between an endangered North American tree and an endophytic fungus, *Chem. Biol.*, 2 (11), 721–727.

[19] Venkatasubbaiah, P., and Van Dyke C.G., 1991, Phytotoxins produced by *Pestalotiopsis oenotherae*, a pathogen of evening primrose, *Phytochemistry*, 30 (5), 1471–1474.

[20] Bradner, W.T., Bush, J.A., Myllymaki, R.W., Nettleton, D.E., and O'Herron, F.A., 1975, Fermentation, isolation, and antitumor activity of sterigmatocystins, *Antimicrob. Agents Chemother.*, 8 (2), 159–163.

[21] Cai, S., Zhu, T.J., Du, L., Zhao, B., Li, D., and Gu, Q., 2011, Sterigmatocystins from the deep-sea-derived fungus *Aspergillus versicolor*, *J. Antibiot.*, 64 (2), 193–196.

[22] Evidente, A., Zonno, M.C., Andolfi, A., Troise, C., Cimmino, A., and Vurro, M., 2012, Phytotoxic α-pyrones produced by *Pestalotiopsis guepinii*, the causal agent of hazelnut twig blight*, J. Antibiot.*, 65 (4), 203–206.

[23] Feng, L., Han, J., Wang, J., Zhang, A.X., Miao, Y.Y., Tan, N.H., and Wang Z., 2020, Pestalopyrones A–D, four tricyclic pyrone derivatives from the endophytic fungus *Pestalotiopsis neglecta* S3, *Phytochemistry*, 179, 112505.

[24] Wang, J., Peng, Q., Yao, X., Liu, Y., and Zhou, X., 2020, New pestallic acids and diphenylketone derivatives from the marine alga-derived

endophytic fungus *Pestalotiopsis neglecta* SCSIO41403, *J. Antibiot.*, 73 (8), 585–588.

[25] Almeida, C., Ortega, H., Higginbotham, S., Spadafora, C., Arnold, A.E., Coley, P.D., Kursar, T.A., Gerwick, W.H., and Cubilla-Rios, L., 2014, Chemical and bioactive natural products from *Microthyriaceae* sp., an endophytic fungus from a tropical grass, *Lett. Appl. Microbiol.*, 59 (1), 58–64.

[26] Han, X., Tang, X., Luo, X., Sun, C., Liu, K., Zhang, Y., Li, P., and Li, G., 2020, Isolation and identification of three new sterigmatocystin derivatives from the fungus *Aspergillus versicolor* guided by molecular networking approach, *Chem. Biodivers.*, 17 (6), 2000208.

[27] Akone, S.H., Pham, C.D., Chen, H., Ola, A.R.B., Ntie-Kang, F., and Proksch, P., 2019, Epigenetic modification, co-culture and genomic methods for natural product discovery, *Phys. Sci. Rev.*, 4 (4), 0118.

[28] Newman, D.J., and Cragg, G.M., 2015, Endophytic and epiphytic microbes as "sources" of bioactive agents, *Front. Chem.,* 3, 34.

Review:

The Origin, Physicochemical Properties, and Removal Technology of Metallic Porphyrins from Crude Oils

Jumina[1*], Yehezkiel Steven Kurniawan[1,2], Dwi Siswanta[1], Bambang Purwono[1], Abdul Karim Zulkarnain[3], Agustinus Winarno[4], Joko Waluyo[5], and Johan Syafri Mahathir Ahmad[6]

[1]*Department of Chemistry, Faculty of Mathematics and Natural Sciences, Universitas Gadjah Mada, Sekip Utara, Yogyakarta 55281, Indonesia*

[2]*Ma Chung Research Center for Photosynthetic Pigments, Universitas Ma Chung, Malang 65151, Indonesia*

[3]*Department of Pharmaceutical Technology, Faculty of Pharmacy, Universitas Gadjah Mada, Sekip Utara, Yogyakarta 55281, Indonesia*

[4]*Department of Mechanical Engineering, Vocational College, Universitas Gadjah Mada, Sekip Utara, Yogyakarta 55281, Indonesia*

[5]*Department of Mechanical and Industrial Engineering, Faculty of Engineering, Universitas Gadjah Mada, Jl. Grafika No. 2 UGM Campus, Yogyakarta 55281, Indonesia*

[6]*Department of Civil and Environmental Engineering, Faculty of Engineering, Universitas Gadjah Mada, Jl. Grafika No. 2 UGM Campus, Yogyakarta 55281, Indonesia*

* ***Corresponding author:***

tel: +62-2745-45188
email: jumina@ugm.ac.id

Received: December 24, 2020
Accepted: March 29, 2021

DOI: 10.22146/ijc.62521

Abstract: *Crude oil is an indispensable energy feedstock for daily activities, although some amounts of metallic porphyrins components with undesired characteristics have been identified. These constituents are assumed to originate from the geochemical process of chlorophyll and heme derivatives. In addition, their chemical structures have been thoroughly characterized using spectroscopy techniques, while several analytical methods were adopted in the detection and concentration quantification in the crude oils. The metallic porphyrins have several demerits, including the deactivation of used catalysts, contamination of the treated petrochemical products, and corrosion of the industrial equipment. Also, the removal process is considered challenging due to the strong interaction with the asphaltene fraction of crude oil. This review article, therefore, provides brief information on the origin, physicochemical properties, and possible removal technology of metallic porphyrins from crude oil samples. Besides, a better understanding of chemistry contributes a useful insight towards the development and establishment of better futuristic processing technology.*

Keywords: *crude oil; metallic porphyrin; origin; property; removal*

■ INTRODUCTION

Despite the extensive research on renewable energy, crude oil remains an indispensable energy feedstock [1-4]. This is attributed to the limited amount of industrial processes implicated in serious demerits, including expensive upfront cost, geographic mal-distribution, natural intermittent supply, and others. In contrast, crude oil-based chemical materials are well established worldwide. Therefore, some industries prefer maintaining fossil-based technological systems against establishing new and high-cost technologies [5].

Crude oil is generally defined as a fuel liquid produced through long-time geological activities involving high temperature and pressure in oil reservoirs associated with sedimentary rocks and

situated beneath earth's surface piles [6]. This natural resource comprises light and heavy hydrocarbon fractions with other impurities, including oxygenated-, nitrogenated-, and sulphated-compounds, alongside trace metals [7]. The respective compound composition varies appreciably across the reservoirs, and crude oil also contains paraffin (alkanes), naphthenes (cycloalkanes), as well as aromatic compounds [8]. In addition, some components have been separated through a fractionation distillation process for commercial applications, and further actions in the form of thermal cracking, catalytic reforming, isomerization, and hydrodealkylation processes are possibly required to attain the product market requirement [9]. Therefore, impurity elimination is pivotal to obtain products with high-purity [10].

The oxygenated-, nitrogenated- and sulphated-compounds present are easily removed through the absorption and hydrocracking processes [11]. However, trace metal removal is difficult in a simple process, due to the high solubility and the poisonous impact of catalysis techniques [12]. Furthermore, the amount present was reportedly dominated by metallic porphyrins [6], and special attention is attributed to these constituents over the past several years. This is due to the high poison potential and ability to deactivate catalysts used during petrochemical processes [11]. Hence, further information on the intrinsic chemical nature is required. This review article involves the assessment of data on the metallic porphyrin's origin, its chemical structure, and physicochemical properties. Also, the removal process from crude oils is briefly discussed to provide chemists and engineers working on crude oil processing with essential knowledge.

■ ORIGIN OF METALLIC PORPHYRINS

Treibs [13] firstly discovered metallic porphyrins as "molecular fossils" from crude oil samples in 1934, and further investigations have gained significant interest. This has been identified as the predominant trace metal, and Table 1 lists others present in Venezuelan crude oil, comprising vanadium and nickel at 440–617 and 70–94 mg L^{-1}, respectively, which is 600 times higher than the others [6]. Conversely, vanadium (160 mg L^{-1}) and nickel (80 mg L^{-1}) metals in the lithosphere are not as abundant as iron (50,000 mg L^{-1}) and calcium (40,000 mg L^{-1}). Therefore, some extensive studies were conducted to evaluate the reason for the much higher concentration of vanadyl-porphyrins or nickel-porphyrins in crude oil compared to others.

Furimsky [6] attributed the abundant quantity of vanadium and nickel to the intrinsic high reducibility of the mineral form. This property impacts greater stability on metallic species and ensures the formation of tighter bonds to the core porphyrin framework. This hypothesis suggests all metallic species are generated from the reduction of corresponding metallic oxides by hydrogen gas (Eq. (1)).

$$M_xO_y(s) + yH_2(g) \rightarrow xM(s) + yH_2O(g) \quad (1)$$

The reduction reaction of V_2O_5 to V species is not spontaneous (ΔG_{300K} = +33.4 kJ mol^{-1}) while V_2O_5 to vanadyl (V=O) species is highly favorable (ΔG_{300K} = -8.3 kJ mol^{-1}). Similarly, the reduction of NiO to Ni species is also spontaneous (ΔG_{300K} = -4.0 kJ mol^{-1}), while FeO, CaO, or CuO are considered as unfavorable, due to the positive Gibbs energy produced, at +5.4, +227, and +24.2 kJ mol^{-1}, respectively [6]. Therefore, Furimsky stipulated the significance of much higher vanadyl and nickel metal concentrations in metallic porphyrins, compared to iron, calcium, and copper metals in crude oils.

Treibs [13] proposed plausible evolution reactions required to form metallic porphyrins in crude oil. This includes the production from chlorophyll compounds in plants and heme compounds in animals [14], as shown in Fig. 1. Furthermore, the chlorophylls from plants are

Table 1. Trace metal composition in the Venezuelan crude oil sample [6]

Metals	Concentration (mg L^{-1})
Fe	4.0–7.5
Ca	11–57
Mg	1.0–10
V	440–617
Ni	70–94
Cu	2.0–17
Mo	3.0–22
Cd	1.0–5.0
Zn	1.0–12

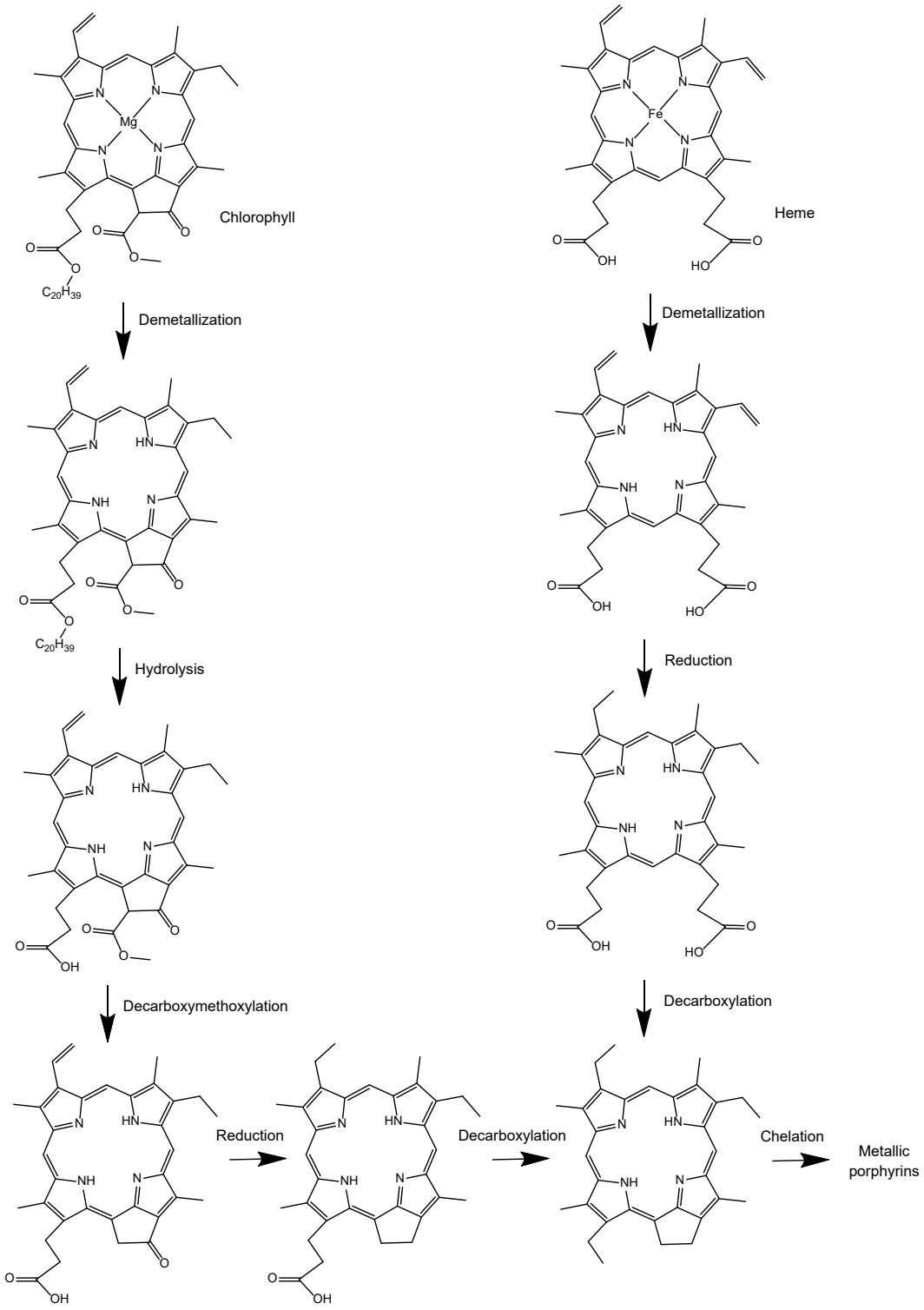

Fig 1. Schematic evolution reactions of chlorophyll and heme compounds to form metallic porphyrins

determined to engage in demetallization reactions and consequently release Mg^{2+} ions. These Mg^{2+}-free porphyrins then engage in hydrolysis, decarbomethoxylation, reduction, and decarboxylation reactions to produce the "free" ligand. The high reducibility of vanadyl and nickel facilitates the

chelation required in the formation of stable metal complexes. Moreover, heme compounds are converted to Fe^{2+}-free porphyrins through a demetallization reaction and further treated with reduction and decarboxylation processes. The vanadyl and nickel species were finally complexed with the porphyrin ligand to form metallic porphyrins [14].

Castillo and Vargas [15] performed further studies by investigating the occlusion characteristics of metallic porphyrins during asphaltene aggregation. Consequently, either vanadyl- or nickel-porphyrin was predominant in the asphaltene fraction of crude oil [16]. Therefore, the combination phenomenon and the respective physicochemical properties were evaluated using UV-Vis spectroscopy. The asphaltene aggregation degree was examined at 350 nm, while the metallic porphyrin electronic properties were evaluated based on the Soret signal at 400–410 nm. Furthermore, the results obtained showed the trapping of more than 50% metallic porphyrins on the aggregate, which occurred during the colloidal asphaltene formation process, through strong acid-base interactions, hydrophobic inclusion, and π-π stacking intermolecular forces, based on UV-Vis data [17]. Tynan and Yen [18] reported free energy of about 60 kJ mol^{-1} generated through the combined interactions of asphaltene-vanadyl porphyrin aggregation, which is much stronger than hydrogen bonds (10–40 kJ mol^{-1}). This trapping process is considered irreversible, due to these strong connections formed, and further increases the difficulties of removing metallic porphyrins from asphaltene [15].

■ STRUCTURE OF METALLIC PORPHYRINS

The metallic porphyrins structure of vanadium and nickel have previously been studied to provide a better insight into the chemistry field. Initially, the structures were investigated through UV-Vis spectroscopy, by observing the conjugated moiety. Moreover, the electronic absorptions were predominantly investigated through the π-π* transition, as n-π* transition is unavailable, due to the discrepancy in the symmetry of the n orbital (on symmetry plane) and π* orbital (on anti-symmetry plane).

These metallic porphyrins produced high-intensity Soret signals at about 400 nm, and also around 500–600 nm, corresponding to α- and β- bands from peripheral substituents in the framework [19]. Fig. 2 shows the labelling of α-, β-, α*-, β*- and meso substituents, and the high signal intensity prompts researchers to use UV-Vis spectroscopy during quantification assessment. However, the concentrations calculated from the UV-Vis spectrum produced showed the absence of approximately half the total quantity, in contrast with the value measured through atomic absorption spectroscopy (AAS) [6]. These reports were observed in crude oil samples obtained from Europe, Russian, and others [20-21]. Therefore, metallic non-porphyrin species were assumed to be present, although none was ever discovered and verified to this day [22].

Through technological development over the years, further chemical analysis using mass spectrometry and X-ray spectroscopy have confirmed the non-existence of metallic non-porphyrins in crude oils [22]. Therefore, false calculation obtained with UV-Vis spectroscopy was attributed to the postulation stipulating the presence of only one species [6]. This possibility was neglected in previous assessments, owing to variations in electronic structures, and the instigating the consequent dissimilarity in spectra. Moreover, metallic porphyrins have also been identified in the form of alkyl-, oxygenated-, nitrogenated-, and sulfur-containing porphyrins [22].

Fig. 3 shows some examples of metallic porphyrin structures discovered, while Table 2 demonstrate the Soret-, α-, and β-bands of specific vanadyl forms. Berezin [23] introduced the concept of "Mutual Atomic Effect",

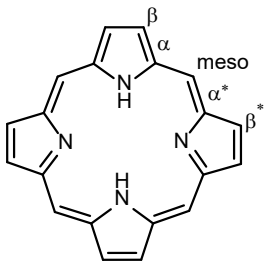

Fig 2. Peripheral substituents location on the porphyrin framework

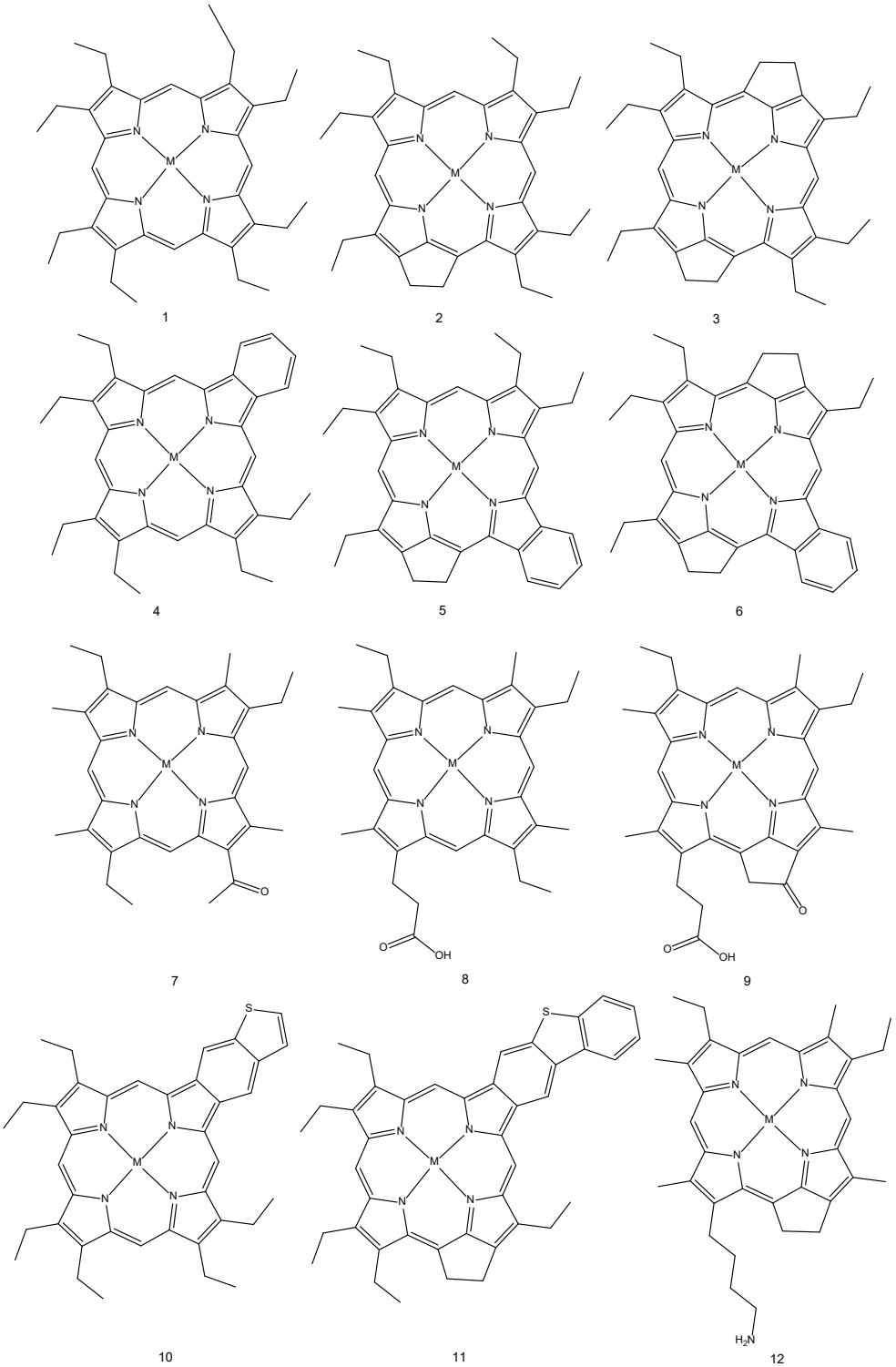

Fig 3. The example of the discovered metallic porphyrins (M = Ni or VO)

which describes the influence of different peripheral substitution on the electronic distribution and light absorption magnitude, as observed in Fig. 2. This phenomenon instigates a spectral shift and/or higher/lower extinction coefficient [23]. The dissimilarity in the Soret-, α- or β-band of each vanadyl-porphyrin caused

Table 2. Absorption signals of vanadyl-porphyrin derivatives on the UV-Vis spectrum [28]

Vanadyl-porphyrins	Wavelength (nm)		
	Soret band	α-band	β-band
Unmodified	399	559	524
ETIO	407	571	533
DPEP	411	573	533
Benzo-substituted	414	579	545
Octaethyl-substituted	407	571	533

*Dichloromethane was used as the solvent

the inevitable miss-calculations observed with UV-Vis spectroscopy. In addition, Foster and Cantu [24-25] also reported on the variations in extinction coefficients amongst one another. This was detected with the values for etioporphyrin (ETIO) determined to be four times higher than deoxophylloertythroetioporphyrin (DPEP) derivatives [20]. Moreover, other possible factors implicated in the underestimated calculation comprise the multiple π-π stacking interactions in asphaltene-metallic porphyrin aggregations. The presence of polycyclic aromatic hydrocarbons potentially influenced poor measurement precision, and consequently interfered with signal intensity, as observed using UV-Vis spectroscopy [26].

Yakubov et al. [27] reported on the UV-Vis spectra modifications observed with porphyrins, after the demetallization reaction. Subsequently, the free porphyrins provided four Q-signals in the visible regions after the removal of central metal ions (either Ni^{2+} or VO^{2+}). These were usually noted as I, II, III, and IV signals [10], and the order is numbered from the longer to shorter wavelength, at 620, 565, 535, and 500 nm, respectively. Also, the signals attributed for the conformation and nature of peripheral substitutions possibly existed in six different conformations, including saddle, ruffle, dome, wave on the x-axis, wave on the y-axis, and propeller forms, as shown in Fig. 4 [22].

The limitations of metallic porphyrins characterization through UV-Vis instigated the use of mass spectrometry and Fourier-transform ion cyclotron resonance mass spectrometry. This technique elucidated the correct structure [19,28-30], and about 370 variants were consequently reported. In addition, the vanadyl-porphyrin alone were classified into 6 categories, including

1. $C_nH_{2n-y}N_4VO$ ($35 < n < 60$; $39 < y < 46$)
2. $C_nH_{2n-y}N_4VO_2$ ($26 < n < 47$; $29 < y < 39$)
3. $C_nH_{2n-y}N_4VO_3$ ($26 < n < 34$; $29 < y < 39$)
4. $C_nH_{2n-y}N_4VO_4$ ($27 < n < 37$; $31 < y < 37$)
5. $C_nH_{2n-y}N_4VSO$ ($34 < n < 56$; $37 < y < 47$)
6. $C_nH_{2n-y}N_5VO$ ($28 < n < 43$; $26 < y < 36$)

Fig. 3 shows the structures of alkyl-, sulfur-containing and oxygenated-porphyrins, where M denotes either VO^{2+} or Ni^{2+}. Particularly, M at VO^{2+} yields compound **1**–**6**, which are collectively classified as alkyl porphyrins class 1 ($C_nH_{2n-y}N_4VO$ with $35 < n < 60$ and $39 < y < 46$). In addition, compounds **1**, **2**, and **3** were infamous as ETIO, DPEP, and Di-DPEP (dicyclic-deoxophylloerythroetioporphyrins), while **4**, **5**, and **6** comprise rhodo-ETIO (rhodo-etioporphyrins), rhodo-DPEP (rhodo-deoxophylloerythroetioporphyrins), and rhodo-Di-DPEP (rhodo-dicylic-deoxophylloerythroetio porphyrins), respectively. Moreover, **7**, **8**, and **9** are oxygenated-porphyrin derivatives, with **7** belonging to class 2 ($C_nH_{2n-y}N_4VO_2$ having $26 < n < 47$ and $29 < y < 39$), resulting from the one extra oxygen atom present in the form of a ketone group. Conversely, compound **8** is categorized in class 3 ($C_nH_{2n-y}N_4VO_3$ with $26 < n < 34$ and $29 < y < 39$), due to the two extra oxygen atoms in the form of carboxylic acid. The compound **9** is grouped in class 4 ($C_nH_{2n-y}N_4VO_4$ with $27 < n < 37$ and $31 < y < 37$) because of the additional three oxygen atoms, while

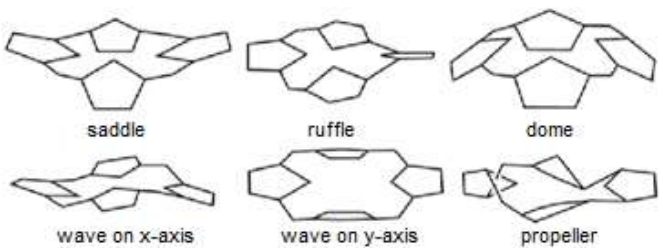

Fig 4. Conformation of metallic porphyrins

10 and **11** represent sulfur-containing porphyrins ($C_nH_{2n-y}N_4VSO$ with $34 < n < 56$ and $37 < y < 47$), and **12** denotes a nitrogen-containing class ($C_nH_{2n-y}N_5VO$ with $28 < n < 43$ and $26 < y < 36$).

The metallic porphyrin derivatives have been thoroughly investigated through theoretical and experimental researches. The Density Functional Theory (DFT) computational method has been applied to evaluate the electronic structure of vanadyl-porphyrins present in the crude oil. Furthermore, tests using the varied porphyrin substituent showed the influence of alkyl chains on the solubility of metallic variants in an oily environment. The results also predicted the development of higher reactivity following an increase in the substituent quantity. This output consequently becomes more poisonous after applying catalysts in hydrodemetallization and hydrodesulfurization processes [16].

Garcia-Montoto et al. [9] predicted the three steps of the poisoning mechanism. First is the coke formation from metallic porphyrins on the catalyst surface, which is a rapid reaction with first-order reaction halftime of about a hundred hours. Second, the metallic porphyrins slowly cover the entire surface to ensure gradual activity deactivation. Third, the yields tend to create pore plugging, then facilitate access restriction to the catalyst active site, and consequently prompt a drastic termination of activity [9].

In addition, the product also demonstrated some other disadvantages, in the crude oil. These include influencing the physicochemical properties of petrochemicals, contaminating the desired output, and corroding metallic equipment during the process [6]. Therefore, porphyrin detection and quantification are crucial to select a suitable removal technique.

■ DETECTION AND QUANTIFICATION OF METALLIC PORPHYRINS IN CRUDE OILS

Prior to the detection and quantification processes, several analytical methods have contemporarily been developed to isolate the metallic porphyrins in crude oil samples [31]. This approach is pivotal due to the existence of trace concentration (less than 1.0 g L^{-1}) in the investigated entity [6]. The matrix crude oil samples tend to vary across sources, and further enhances the difficulty towards establishing a direct and standard detection as well as quantification [26]. Besides, there are a total of three well-known analytical isolation techniques, including Saturate, Aromatic, Resin and Asphaltene (SARA), Soxhlet extraction, and vacuum sublimation method, as shown in Fig. 5 [16].

Particularly, SARA has been identified as the most used approach, resulting from the good ability to separate asphaltene fractions from others, including the saturated, aromatic, and resin fractions [32-34]. This technique is initiated by dissolving the crude oil in dichloromethane solvent, followed by the addition of alumina material, and drying through flowing nitrogen gas [35]. The residue is packed as the stationary phase of the chromatography column and subsequently eluted stepwise using *n*-hexane:cyclohexane 1:1 v/v, *n*-hexane:toluene 7:3 v/v, carbon tetrachloride:chloroform 7:3 v/v, and acetonitrile:methanol 1:1 v/v to respectively obtain the saturated (A1), aromatic (A2), resin (A3), and asphaltene (A4) fractions of crude oil. Preconcentration of metallic porphyrins using the SARA method has been reported for Venezuela crude oil, Russia Tatarstan crude oil, Kuwait crude oil, Athabasca oil sand, Utah oil sand, China Qingchuan gilsonite oil, Texas shale oil, heavy Eurasian oil, and light East Asian oil [16,36-37].

Marquez et al. [16] adopted the SARA technique while isolating metallic porphyrins from Venezuela crude oil (Table 3) to give concentrated vanadium and nickel-porphyrins in resin and asphaltene fractions. Compared to other methods, SARA technology gives satisfying preconcentration of metallic porphyrins which are commonly found only in resin and asphaltene fractions. Zheng et al. [36] also reported a successful preconcentration of metallic porphyrins at 120–550, 50–800, 240–640, 21–170, 366–3888, and 257–270 mg kg^{-1} from Russia Tatarstan crude oil, Kuwait crude oil, Athabasca oil sand, Utah oil sand, China Qingchuan gilsonite oil, and Texas shale oil samples, respectively, which is remarkable. However, the SARA technique is time-consuming and expensive due to a complicated chromatographic solvent composition for each fraction.

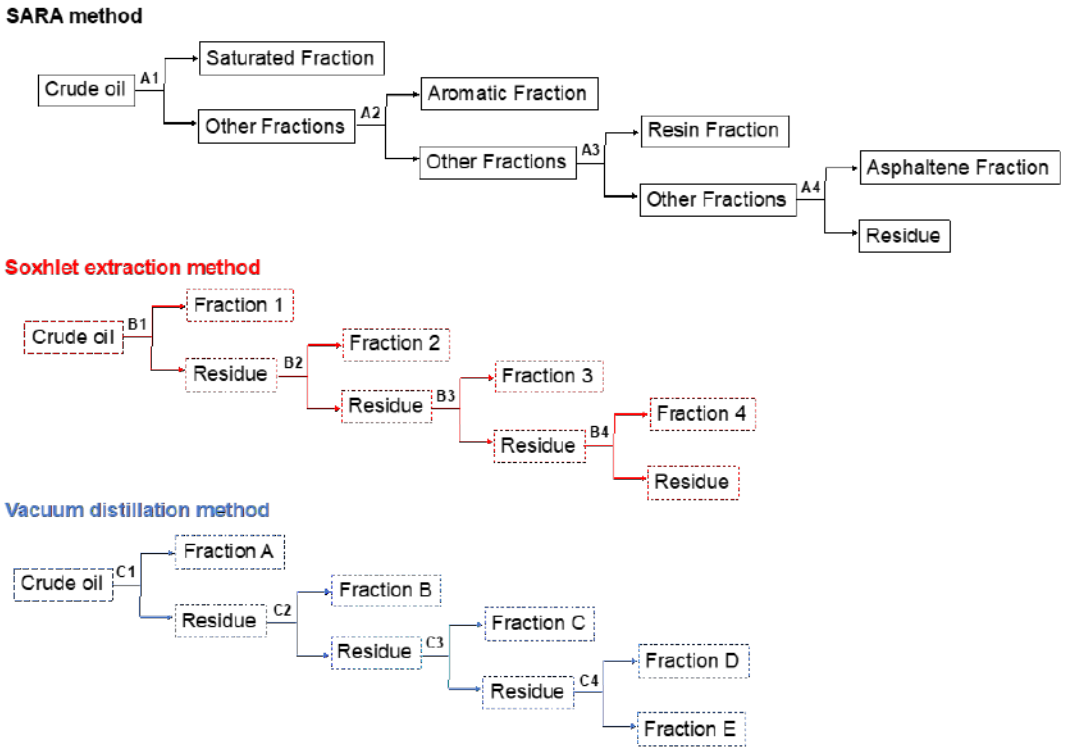

Fig. 5. Isolation of metallic porphyrins from crude oil using SARA, Soxhlet extraction, and vacuum distillation methods

Table 3. The physicochemical properties of the obtained fractions of crude oils for metallic porphyrins from Venezuelan crude oil [16]

Fraction	Color	Yield (%)	Vanadium content (mg kg^{-1})	Nickel content (mg kg^{-1})
SARA method				
Saturated fraction	Pale yellow	21	0	0
Aromatic fraction	Yellow	6	0	0
Resin fraction	Black	36	900	80
Asphaltene fraction	Red wine	15	1,100	100
Soxhlet extraction method				
Fraction 1	Red wine	8	120	2
Fraction 2	Orange	29	75	2
Fraction 3	Brown dark	49	950	26
Fraction 4	Colorless	11	1,060	39
Vacuum sublimation method				
Fraction A	Light yellow	12	5	34
Fraction B	Orange	15	104	14
Fraction C	Dark red	19	226	7
Fraction D	Red	23	178	6
Fraction E	Black	29	514	50

Conversely, Soxhlet extraction method is distinguished as a low-cost and faster isolation method. This process is initiated by mixing the crude oil and alumina material in dichloromethane as the solvent, followed by covering the residue in a Soxhlet extractor with cellulose filter paper. The extraction process required four consecutively used solvents, including acetonitrile, methanol, *n*-heptane, and benzene to obtain

fractions 1, 2, 3, and 4, respectively. Table 3 shows the existence of metallic porphyrins in all yields from Venezuela crude oil, especially fraction 4, which however contained a lesser amount in contrast with the asphaltene fraction generated through SARA [16]. Additionally, the Soxhlet extraction method employs carcinogenic benzene as the solvent which has been banned for a green and safety process [38]. Kumolo et al. [39] identified the metallic porphyrins in Duri crude oil using the Soxhlet extraction method and it was found that both vanadium and nickel-porphyrins were found in *n*-heptane and aromatic solvents demonstrating low efficiency of the Soxhlet extraction method.

The vacuum distillation method required heating the desired sample under vacuum conditions to ensure crude oil fraction sublimation. Therefore, yields from the asphaltene fraction in SARA served as the feedstock, after drying with flowing nitrogen gas and placing in the vacuum distillation apparatus. Nikolaychuk et al. [40] reported that vacuum distillation required a high temperature (350–1300 K) depending on the origin of crude oil. Usage of high temperature on the vacuum distillation method was reported for the undesired thermal cracking of crude oil, which is unfavorable [41]. For the Venezuela crude oil samples, the vacuum condition was set at 1.3×10^{-5} atm, a heating temperature from 353 to 513 K, which was gradually increased, and the products were obtained at respective levels (Table 3). The obtained fractions from the vacuum distillation method include fraction A (collected at 363–393 K), fraction B (collected at 403–433 K), fraction C (collected at 443–473 K), fraction D (collected at 483–523 K), and fraction E (residue). Table 3 identified this technique as the least useful ascribed to poor preconcentration ability as well as narrow suitability for only volatile compounds [16]. Therefore, the vacuum distillation technique is the most expensive due to the usage of vacuum technology.

Numerous analytical approaches have been adopted during metallic porphyrin detection and quantification [26]. These include gel permeation chromatography, Ultraviolet-Visible (UV-Vis) spectroscopy, inductively coupled plasma-mass spectrometry (ICP-MS), and electron paramagnetic resonance. However, UV-Vis spectroscopy is known to be the simplest with extensive application [31], as observed with the concentration of vanadyl-porphyrins, estimated using the Eq. (2) as follow;

$$\text{Conc. of vanadyl-porphirins (mg kg}^{-1}) = \frac{1.87 \text{ h V}}{\text{m l}} \qquad (2)$$

where h denotes the height of α-band at 570–580 nm, V represents the sample volume (dilution factor), m is the crude oil sample mass, and l signifies the cuvette thickness [27].

Reliability of up to 15% was determined during vanadyl-porphyrin direct quantification using UV-Vis spectroscopy [42]. This analysis technique has low applicability due to the presence of various metallic porphyrins in the sample. Furthermore, the consequent aggregation with the asphaltene fractions lowers the collective absorbance in contrast with the free form [31].

Conversely, gel permeation chromatography reportedly provides metallic porphyrin measurements with better validity [43]. Garcia-Montoto et al. [9] reported a successful quantification using this technique, alongside the addition of HR4 styrene-divinylbenzene as well as 0.5% v/v isopropanol in benzene as the stationary and mobile phase, respectively. Subsequently, the metallic porphyrin yields were separated based on molecule size and concentration before the standard calibration curve is calculated [9]. The preparation and purification processes were technically difficult because of the inability to directly inject crude oil into the apparatus [44]. Moreover, a different porphyrin ligand structure demonstrates varied retention time, which subsequently increases the analysis complexity. Furthermore, some metallic porphyrins tend to be adsorbed on the stationary phase and consequently poison the column used [45].

Electron paramagnetic resonance is potentially adopted in vanadyl-porphyrins. This is due to the presence of one unpaired electron in the 3d orbital of V^{4+} ions [46], which easily resonates in the static magnetic field. In addition, the measurement technique is assumed valid enough because quantification is centered on vanadium atoms and not the porphyrin frameworks as observed with UV-Vis spectroscopy. The precision with this method is remarkable at up to 99.9% [47].

Tynan and Yen [18] reported on the tendency to effectively use electron paramagnetic resonance in the detection of both non-aggregated and aggregated vanadyl-porphyrins. However, the only limitation was impacted by the inability to distinguish the different porphyrin framework types attached to vanadium atoms.

The total intrinsic metallic content was determined through ICP-MS analysis [26]. This required first ashing the crude oil sample for 12 h at 823 K. Therefore, the output was digested using a mixture of concentrated nitric acid (75% wt/v): hydrogen peroxide (30% v/v): concentrated hydrochloric acid (36% wt/v) 4:1:1 v/v/v for 24 h. Subsequently, the solution derived was diluted with distilled water before subjecting to the ICP-MS measurement for the quantification of ^{51}V and ^{60}Ni. This assessment procedure was analyzed for precision and the results showed similarity with the electron paramagnetic resonance method because measurements were based on the metal elements.

■ REMOVAL OF METALLIC PORPHYRINS FROM CRUDE OILS

Currently, there are numbers of separation techniques established to ensure metallic porphyrin removal from crude oils [31]. These include solvent extraction, chelation with chemical agents, supercritical water extraction, and hydrodemetallization processes [12]. Solvent extraction is a well-known technique for metallic porphyrins removal from crude oil because of its convenient operation condition. Particularly, the solvent extraction technique is aimed at releasing the metal ions from the metallic porphyrins complex, and polar solvents in the form of *N*,*N*-dimethylformamide, acetonitrile, *iso*-propanol, and methanol have frequently been applied [48]. Moreover, a small amount of sulfonic or sulfuric acid is sometimes added to ensure the protonation of nitrogen atoms present in porphyrin and to further weaken the metal-porphyrin bonds. This removal technique is, unfortunately, suitable for only crude oil with low resin-asphaltene fraction. Also, the high viscosity instils difficulty for the diffusion process to reach an equilibrium state, and the porphyrin removal process ultimately becomes also time-consuming [31]. As an example, the removal of vanadium-porphyrins from heavy oil using solvent extraction technique only gave 45% removal at 303 K [49]. Therefore, larger solvent quantity and energy are required to improve feasibility, which is unfavorable.

The principle of metal chelation with chemical agents involves the use of suitable chemical agents characterized by a higher complexation tendency towards vanadium and nickel, followed by the possible release from the porphyrin framework [50-51]. A study by Mokhtari and Pourabdollah [52] showed the vanadyl-porphyrin extraction process, using calix[4]arene, a nano-basket dicarboxylic acid. This compound and its derivatives demonstrate outstanding discrimination capacity in line with metal ions, due to the strong complexation energy resulting from electrostatic interactions and size exclusions [53-58]. Remarkably, about 96% of the vanadium is reportedly removed over a 90 min operation period [52]. Shang et al. [59] reported a shorter removal time for vanadium- and nickel-porphyrins by 85 and 83%, respectively, while using a sulfonyl acid chemical in a microwave electric field set at 600 Watts for 3 min. The high removal percentage was attributed to the porphyrin framework deformation observed during microwave irradiation, and further facilitates the demetallization reaction [60].

Supercritical extraction is advanced technology using supercritical fluid as the extracting solvent at above critical temperature and pressure. Mandal et al. [61] investigated the supercritical water extraction of nickel and vanadium from heavy oils, under conditions operated at 22.1 MPa, 763 K, and without a catalyst. Therefore, about 80% of the metallic porphyrins were respectively removed. Based on kinetic and thermodynamic studies, hydroxyl and hydrogen radicals were proposed to play a pivotal role in the demetallization process. The attachment to vanadium and nickel occurs in the hydride and hydroxyl forms, and consequently weaken the metal-porphyrin bonds. Conversely, these radicals also attacked porphyrin rings, and therefore instigates conformational changes, as well as weakens the chelating capacity towards both vanadyl and nickel ions [62]. However, supercritical extraction technology is not economically feasible due to its requirement for high temperature and

pressure.

In addition, several demetallization procedures have been exploited over the past several years, including the oxidative [63], bio- [64-65], electrolytic [66], ultrasonic [67], and photo-demetallation [68]. These have however been recognized as ineffective resulting from the intrinsic tendency to change the crude oil physicochemical properties, which is unfavorable. Oxidative demetallation of crude oil was studied by Gould [63], however, a significant change in the physicochemical properties of crude oil happened. Bio-demetallation offers up to 55% of vanadyl-porphyrins [64] and 11% of nickel-porphyrins [65] demetallization percentage from crude oil after 24 h process at 328 K due to metabolic inhibition of microorganism in the presence of a large amount of vanadyl-porphyrins. The tolerance level of microorganisms for bio-demetallation is very low, around 20 mg kg^{-1} vanadyl-porphyrins in crude oil making bio-demetallation technology is not applicable for commercial process.

Electrolytic-demetallation was reported for Orinoco Belt crude oil with 73% demetallization percentage at 0.01 A cm^{-2} current density, however, this technology is energy-consuming [66]. Ultrasonic-demetallation was reported for crude oil at 423 K in 1-methyl naphthalene solvent yielding 35% demetallation percentage, however, a heavy part of crude oil was decoagulated and depolymerized into maltene fraction [67]. Meanwhile, a photo-demetallation process in a liquid-liquid extraction reactor was reported for metallic porphyrins removal from crude oil under ultraviolet irradiation for 10 h. This technology exhibits high demetallation percentages, i.e. 75 and 96% for commercial light oil and light gas oil. Unfortunately, some aromatic parts of crude oil were also decomposed thus the physicochemical properties of the crude oil were changed [68].

Comparably, hydrodemetallization processes are highly selective targets for metallic porphyrins which could be applied for a wide coverage of crude oil samples [69]. Despite the propensity to hydrogenate the hydrocarbon parts, the products obtained remain significantly satisfying [70]. The demetallation percentage is around 60-90% using metal oxides in the aluminium oxide or sodium aluminium silicate as the catalyst materials in the hydrodemetallization process. As an example, as much as 71% demetallation percentage was achieved for Lago crude oil using hydrodemetalation process at 739 K using 3.5% CoO and 10% MoO_3 catalyst at Al_2O_3 support. On the other hand, vanadyl- and nickel-porphyrins were successfully removed in 85 and 68%, respectively, from European crude oil at 683 K [71-72]. Unfortunately, some of the drawbacks experienced during hydrodemetallization include large heat and hydrogen gas consumption, which leads to an elevated operational cost. Furthermore, it is possible to gradually deposit vanadium or nickel metals on the used catalyst, and consequently lower catalyst activity by increasing operation time [12].

Lee et al. [73] successfully converted the vanadyl-porphyrins present in the asphaltene fractions of crude oil to vanadium(III) sulfide (V_2S_3) before the potential application as a hydrocracking catalyst. Therefore, the cracking phase ensued at 693 K and 11.0 MPa H_2 to obtain middle distillates, naphtha, gas, vacuum gas oils, and coke fractions in 30% yield. The strategy devised in this study is significantly useful while the asphaltene fraction during a suitable recycling process. This outcome is attributed to the activity of vanadium as a catalyst material. Langeslay et al. [74] also acknowledged the moderate catalytic activity of vanadium sulfide during the hydrodesulfurization of thiophene, hydrodenitrogenation, and hydrogenation of pyridine and toluene, respectively. This technology significantly influences the removal of metallic porphyrins from crude oils and the consequent utility as active catalyst materials during petrochemical processing.

■ CONCLUSION

The metallic porphyrins present in crude oil samples originate from evolution reactions involving chlorophyll and heme compounds. In addition, isolation and purification processes were followed by characterization using UV-Vis spectroscopy and Fourier transform ion cyclotron resonance mass spectrometry. The results showed a propensity to distinguish alkyl-, oxygen-, nitrogen-, and sulfur-containing porphyrins. Also, a total of six vanadyl classes have been discovered,

including $C_nH_{2n-y}N_4VO$, $C_nH_{2n-y}N_4VO_2$, $C_nH_{2n-y}N_4VO_3$, $C_nH_{2n-y}N_4VO_4$, $C_nH_{2n-y}N_4VSO$, and $C_nH_{2n-y}N_5VO$ types. The several analytical methods established to detect and quantify metallic porphyrins comprise gel permeation chromatography, UV-Vis spectroscopy, ICP-MS analysis, and electron paramagnetic resonance. Moreover, the porphyrin presence is undesirable, as observed with the negative effects on the petrochemical's physicochemical properties, used catalyst deactivation, contamination of desired products, and the corrosion of metal equipment during processing. Therefore, it is essential to remove the metallic porphyrins through solvent extraction, supercritical water extraction, chelation with chemical agents, or hydrodemetallization processes. Each removal technology has its own advantages and disadvantages. Solvent extraction is the most applied technology today, however, this technique is only suitable for crude oil with a low resin-asphaltene amount. Hydrodemetallization offers a promising way due to its wide application and high selectivity, however, hydrodemetallization is inevitably high-cost technology. Further research and development for these technologies still open to establishing an efficient technology for the removal of metallic porphyrins from crude oil.

■ ACKNOWLEDGMENTS

The financial support from RISPRO LPDP Kemenkeu RI under contract number PRJ-48/LPDP/2020 for budget year 2020-2022 is deeply acknowledged. Technical and material supports from PT. Pertamina (Persero) are also greatly appreciated.

■ REFERENCES

[1] Wahyuningsih, T.D., and Kurniawan, Y.S., 2017, Green synthesis of some novel dioxolane compounds from Indonesian essential oils as potential biogrease, *AIP Conf. Proc.*, 1823, 020081.

[2] Jumina, Yasodhara, Y., Triono, S., Kurniawan, Y.S., Priastomo, Y., Chawla, H.M., and Kumar, N., 2020, Preparation and evaluation of a-cellulose based new heterogeneous catalyst for production of biodiesel, *J. Appl. Polym. Sci.*, 138 (2), 49658.

[3] Lang, K., and Auer, B.R., 2020, The economic and financial properties of crude oil: A review, *North Am. J. Econ. Finance*, 52, 100914.

[4] Wahyuningsih, T.D., and Kurniawan, Y.S., 2020, Synthesis of dioxo-dioxane and dioxo-dioxepane ethyl oleate derivatives as bio-lubricant base stocks, *Indones. J. Chem.*, 20 (3), 503–509.

[5] Ederington, L.H., Fernando, C.S., Hoelscher, S.A., Lee, T.K., and Linn, S.C., 2019, A review of the evidence on the relation between crude oil prices and petroleum product prices, *J. Commod. Mark.*, 13, 1–15.

[6] Furimsky, E., 2016, On exclusivity of vanadium and nickel porphyrins in crude oil, *Energy Fuels*, 30 (11), 9978–9980.

[7] Munoz, G., Gunessee, B.K., Bégué, D., Bouyssiere, B., Baraille, I., Vallverdu, G., and Silva, H.S., 2019, Redox activity of nickel and vanadium porphyrins: A possible mechanism behind petroleum genesis and maturation?, *RSV Adv.*, 9 (17), 9509–9516.

[8] Corma, A., Corresa, E., Mathieu, Y., Sauvanaud, L., Al-Bogami, S., Al-Ghrami, M.S., and Bourane, A., 2017, Crude oil to chemicals: Light olefins from crude oil, *Catal. Sci. Technol.*, 7, 12–46.

[9] Garcia-Montoto, V.G., Verdier, S., Maroun, Z., Egeberg, R., Tiedje, J.L., Sandersen, S., Zeuthen, P., and Bouyssiere, B., 2020, Understanding the removal of V, Ni and S in crude oil atmospheric residue hydrodemetallization and hydrodesulfurization, *Fuel Process. Technol.*, 201, 106341.

[10] Liu, T., Lu, J., Zhao, X., Zhou, Y., Wei, Q., Xu, C., Zhang, Y., Ding, S., Zhang, T., Tao, X., Ju, L., and Shi, Q., 2015, Distribution of vanadium compounds in petroleum vacuum residuum and their transformations in hydrodemetallization, *Energy Fuels*, 29 (4), 2089–2096.

[11] Argyle, M.D., and Bartholomew, C.H., 2015, Heterogeneous catalyst deactivation and regeneration: A review, *Catalysts*, 5 (1), 145–269.

[12] Jenifer, A.C., Sharon, P., Prakash, A., and Sande, P.C., 2015, A review of the unconventional methods used for the demetallization of petroleum fractions

over the past decade, *Energy Fuels*, 29 (12), 7743–7752.

[13] Treibs, A., 1934, Chlorophyll and haemin derivatives in bituminous rock, petroleum, mineral waxes and asphalts, *Justus Liebigs Ann. Chem.*, 510 (1), 42–62.

[14] Treibs, A., 1936, Chlorophyll and hemin derivatives in organic materials, *Angew. Chem.*, 49 (38), 682–686.

[15] Castillo, J., and Vargas, V., 2016, Metal porphyrin occlusion: Adsorption during asphaltene aggregation, *Pet. Sci. Technol.*, 34 (10) 873–879.

[16] Espinosa, M., Pacheco, U.S., Leyte, F., and Ocampo, R., 2014, Separation and identification of porphyrin biomarkers from a heavy crude oil Zaap-1 offshore well, Sonda de Campeche, Mexico, *J. Porphyr. Phtalocyanines*, 18 (7), 542–551.

[17] Silva, H.S., Alfarra, A., Vallverdu, G., Begue, D., Bouyssiere, B., and Baraille, I., 2019, Asphaltene aggregation studied by molecular dynamic simulations: Role of the molecular architecture and solvents on the supramolecular or colloidal behavior, *Petrol. Sci.*, 16, 669–684.

[18] Tynan, E.C., and Yen, T.F., 1969, Association of vanadium chelates in petroleum asphaltenes as studied by ESR, *Fuel*, 43, 191–208.

[19] Liu, H., Mu, J., Wang, Z., Ji, S., Shi, Q., Guo, A., Chen, K., and Lu, J., 2015, Characterization of vanadyl and nickel porphyrins enriched from heavy residues by positive-ion electrospray ionization FT-ICR mass spectrometry, *Energy Fuels*, 29 (8), 4803–4813.

[20] Glebovskaya, E., and Volkenshtein, M., 1948, Spectra of porphyrins in petroleums and bitumens, *J. Gen. Chem.*, 18, 1440.

[21] Skinner, D.A., 1952, Chemical state of vanadium in Santa Maria Valley crude oil, *Ind. Eng. Chem.*, 44 (5), 1159–1165.

[22] Qian, K., Fredriksen, T.R., Mennito, A.S., Zhang, Y., Harper, M.R., Merchant, S., Kushnerick, J.D., Rytting, B.M., and Kilpatrick, P.K., 2019, Evidence of naturally-occurring vanadyl porphyrins containing multiple S and O atoms, *Fuel*, 239, 1258-1264.

[23] Berezin, B.D.J., 1999, Mutual atomic effect in porphyrin molecules and its manifestation in their structure and electronic absorption spectra, *J. Appl. Spectrosc.*, 66 (4), 521–527.

[24] Foster, N.S., Day, J.W., Filby, R.H., Alford, A., and Rogers, D., 2002, The role of Na-montmorillonite in the evolution of copper, nickel, and vanadyl geoporphyrins during diagenesis, *Org. Geochem.*, 33 (8), 907–919.

[25] Cantú, R., Stencel, J.R., Czernuszewicz, R.S., Jaffé, P.R., and Lash, T.D., 2000, Surfactant-enhanced partitioning of nickel and vanadyl deoxophylloerythroetioporphyrins from crude oil into water and their analysis using surface-enhanced resonance Raman spectroscopy, *Environ. Sci. Technol.*, 34, 192–198.

[26] Sugiyama, I., and Williams-Jones, A.E., 2018, An approach to determining nickel, vanadium and other metal concentrations in crude oil, *Anal. Chim. Acta*, 1002, 18–25.

[27] Yakubov, M.R., Milordov, D.V., Yakubova, S.G., Borisov, D.N., Gryaznov, P.I., and Usmanova, G.S., 2015, Sulfuric acid assisted extraction and fractionation of porphyrins from heavy petroleum residuals with a high content of vanadium and nickel, *Pet. Sci. Technol.*, 33 (9), 992–998.

[28] Banda-Cruz, E.E., Padron-Ortega, S.I., Gallardo-Rivas, N.V., Rivera-Armenta, J.L., Paramo-Garcia, U., Zavala, N.P.D., and Mendoza-Martinez, A.M., 2016, Crude oil UV spectroscopy and light scattering characterization, *Petrol. Sci. Technol.*, 34 (8), 732–738.

[29] Zhang, Y., Schulz, F., Rytting, B.M., Walters, C.C., Kaiser, K., Metz, J.N., Harper, M.R., Merchant, S.S., Mennito, A.S., Qian, K., Kushnerick, J.D., Kilpatrick, P.K., and Gross, L., 2019, Elucidating the geometric substitution of petroporphyrins by spectroscopic analysis and atomic force microscopy molecular imaging, *Energy Fuels*, 33 (7), 6088–6097.

[30] Gao, Y.Y., Shen, B.X., and Liu, J.C., 2012, The structure identification of vanadium porphyrins in Venezuela crude oil, *Energ. Sources Part A*, 34, 2260–2267.

[31] Milordov, D.V., Usmanova, G.S., Yakubov, M.R., Yakubova, S.G., and Romanov, G.V, 2013, Comparative analysis of extractive methods of porphyrin separation from heavy oil asphaltenes,

Chem. Technol. Fuels Oils, 49 (3), 232–238.

[32] Munawar, Aditiawati, P., and Astuti, D.I., 2012, Sequential isolation of saturated, aromatic, resinic, and asphaltic fractions degrading bacteria from oil contaminated soil in South Sumatera, *Makara J. Sci.*, 16 (1), 58–64.

[33] Ashoori, S., Sharifi, M., Masoumi, M., and Salehi, M.M., 2017, The relationship between SARA fractions and crude oil stability, *Egypt. J. Pet.*, 26 (1), 209–213.

[34] Musin, L.I., Foss, L.E., Shabalin, K.V., Nagornova, O.A., Borisova, Y.Y., Borisov, D.N., and Yakubov, M.R., 2020, Simple methods for the separation of various subfractions from coal and petroleum asphaltenes, *Energy Fuels*, 34 (6), 6523–6543.

[35] Rakhmatullin, I., Efimov, S., Tyurin, V., Gafurov, M., Al-Muntaser, A., Varfolomeev, M., and Klochkov, V., 2020, Qualitative and quantitative analysis of heavy crude oil samples and their SARA fractions with ^{13}C nuclear magnetic resonance, *Processes*, 8 (8), 995.

[36] Zheng, F., Shi, Q., Vallverdu, G.S., Giusti, P., and Bouyssiere, B., 2020, Fractionation and characterization of petroleum asphaltene: Focus on metalopetroleomis, *Processes*, 8 (11), 1504.

[37] Farmani, Z., and Schrader, W., 2019, A detailed look at the saturate fractions of different crude oils using direct analysis by ultrahigh resolution mass spectrometry (UHRMS), *Energies*, 12 (18), 3455.

[38] Kurniawan, Y.S., Priyangga, K.T.A., Krisbiantoro, P.A., and Imawan, A.C., 2021, Green chemistry influences in organic synthesis: A review, *J. Multidiscip. Appl. Nat. Sci.*, 1, 1-12.

[39] Kumolo, S.T., Yulizar, Y., Haerudin, H., Kurniawaty, I., and Apriandanu, D.O.B., 2019, Identification of metal porphyrins in Duri crude oil, *IOP Conf. Ser.: Mater. Sci. Eng.*, 496, 012038.

[40] Nikolaychuk, E., Veli, A., Stratiev, D., Shishkova, I., Burilkova, A., Tamahkyarova, E., Mitkova, M., and Yordanov, D., 2018, Physical vacuum distillation and high temperature simulated distillation of residual oils from different origin, *Int. J. Oil, Gas Coal Technol.*, 17 (2), 208–221.

[41] Elayane, J., Bchitou, R., and Bouhaouss, A., 2017, Study of the thermal cracking during the vacuum distillation of atmospheric residue of crude oil, *Sci. Stud. Cercet. Stiint.: Chim. Ing. Chim., Biotehnol., Ind. Aliment. (Univ. Bacau)*, 18 (1), 61–71.

[42] Zhao, X., Liu, Y., Xu, C., Yan, Y., Zhang, Y., Zhao, S., Chung, K., Gray, M.R., and Shi, Q., 2013, Separation and characterization of vanadyl porphyrins in Venezuela Orinoco heavy crude oil, *Energy Fuels*, 27 (6), 2874–2882.

[43] Maryutina, T.A., and Timerbaev, A.R., 2017, Metal speciation analysis of petroleum: Myth or reality?, *Anal. Chim. Acta*, 991, 1–8.

[44] Putman, J.C., Rowland, S.M., Corilo, Y.E., and McKenna, A.M., 2014, Chromatographic enrichment and subsequent separation of nickel and vanadyl porphyrins from natural seeps and molecular characterization by positive electrospray ionization FT-ICR mass spectrometry, *Anal. Chem.*, 86 (21), 10708–10715.

[45] Mironov, N.A., Sinyashin, K.O., Abilova, G.R., Tazeeva, E.G., Milordov, D.V., Yakubova, S.G., Borisov, D.N., Gryaznov, P.I., Borisova, Y.Y., and Yakubov, M.R., 2017, Chromatographic isolation of vanadyl porphyrins from heavy oil resins, *Russ. Chem. Bull.*, 66 (8), 1450–1455.

[46] Biktagirov, T.B., Gafurov, M.R., Volodin, M.A., Mamin, G.V., Rodionov, A.A., Izotov, V.V., Vakhin, A.V., Isakov, D.R., and Orlinskii, S.B., 2014, Electron paramagnetic resonance study of rotational mobility of vanadyl porphyrin complexes in crude oil asphaltenes: Probing the effect of thermal treatment of heavy oils, *Energy Fuels*, 28 (10), 6683–6687.

[47] Gafurov, M.R., Volodin, M.A., Rodionov, A.A., Sorokina, A.T., Dolomatov, M.Y., Petrov, A.V., Vakhin, A.V., Mamin, G.V., and Orlinskii, S.B., 2018, EPR study of spectra transformations of the intrinsic vanadyl-porphyrin complexes in heavy crude oils with temperature to probe the asphaltenes' aggregation, *J. Petrol. Sci. Eng.*, 166, 363–368.

[48] Yakubov, M.R., Milordov, D.V., Yakubova, S.G., Borisov, D.N., Gryaznov, P.I., Mironov, N.A., Abilova, G.R., Borisova, Y.Y., and Tazeeva, E.G., 2016, Features of the composition of vanadyl porphyrins in the crude extract of asphaltenes of heavy oil with high vanadium content, *Pet. Sci. Technol.*, 34 (2), 177–183.

[49] Salleh, N.F., Ishak, N., Ruslan, M.S.H., Mandal, P.C., and Yusup, S., 2018, Fundamental studies on extraction of vanadyl oxide tetraphenyl porphyrin (VO TPP) presence in heavy oil model using toluene assisted ionic liquids, *IOP Conf. Ser.: Mater. Sci. Eng.*, 458, 012069.

[50] Tahoun, M., Gee, C.T., McCoy, V.E., Sander, P.M., and Muller, C.E., 2021, Chemistry porphyrins in fossil plants and animals, *RSC Adv.*, 11, 7552–7563.

[51] Xili, C., Minghuan, S., and Bengao, L., 2010, Effect and mechanism research of removing nickel and vanadium porphyrins from model oil by chemical agent, *Pet. Process. Petrochem.*, 41 (9), 19–22.

[52] Mokhtari, B., and Pourabdollah, K., 2012, Extraction of vanadyl porphyrins in crude oil by inclusion dispersive liquid-liquid microextraction and nano-basket of calixarene, *J. Inclusion Phenom. Macrocyclic Chem.*, 74 (1), 183–189.

[53] Kurniawan, Y.S., Sathuluri, R.R., Iwasaki, W., Morisada, S., Kawakita, H., Ohto, K., Miyazaki, M., and Jumina, 2018, Microfluidic reactor for Pb(II) ion extraction and removal with amide derivative of calix[4]arene supported by spectroscopic studies, *Microchem. J.*, 142, 377–384.

[54] Sathuluri, R.R., Kurniawan, Y.S., Kim, J.Y., Maeki, M., Iwasaki, W., Morisada, S., Kawakita, H., Miyazaki, M., and Ohto, K., 2018, Droplet-based microreactor system for stepwise recovery of precious metal ions from real metal waste with calix[4]arene derivatives, *Sep. Sci. Technol.*, 53 (8), 1261–1272.

[55] Kurniawan, Y.S., Sathuluri, R.R., Ohto, K., Iwasaki, W., Kawakita, H., Morisada, S., Miyazaki, M., and Jumina, 2019, A rapid and efficient lithium-ion recovery from seawater with tripropyl-monoacetic acid calix[4]arene derivative employing droplet-based microfluidic reactor system, *Sep. Purif. Technol.*, 211, 925–934.

[56] Murphy, P., Dalgarno, S.J., and Paterson, M.J., 2016, Transition metal complexes of calix[4]arene: Theoretical investigations into small guest binding within the host cavity, *J. Phys. Chem. A*, 120 (5), 824–839.

[57] Kurniawan, Y.S., Ryu, M., Sathuluri, R.R., Iwasaki, W., Morisada, S., Kawakita, H., Ohto, K., Maeki, M., Miyazaki, M., and Jumina, 2019, Separation of Pb(II) ion with tetraacetic acid derivative of calix[4]arene by using droplet-based microreactor system, *Indones. J. Chem.*, 19 (2), 368–375.

[58] Jumina, Priastomo, Y., Setiawan, H.R., Mutmainah, Kurniawan, Y.S., and Ohto, K., 2020, Simultaneous removal of lead(II), chromium(III), and copper(II) heavy metal ions through an adsorption process using C-phenylcalix[4]pyrogallolarene material, *J. Environ. Chem. Eng.*, 8 (4), 103971.

[59] Shang, H., Liu, Y., Shi, J.C., Shi, Q., and Zhang, W.H., 2016, Microwave-assisted nickel and vanadium removal from crude oil, *Fuel Process. Technol.*, 142, 250–257.

[60] Li, Y., Shang, H., Zhang, Q., Elabyouki, M., and Zhang, W., 2020, Theoretical study of the structure and properties of Ni/V porphyrins under microwave electric field: A DFT study, *Fuel*, 278, 118305.

[61] Mandal, P.C., Goto, M., and Sasaki, M., 2014, Removal of nickel and vanadium from heavy oils using supercritical water, *J. Jpn. Pet. Inst.*, 57 (1), 18–28.

[62] Mandal, P.C., Wahyudiono, Sasaki, M., and Goto, M., 2012, Non-catalytic vanadium removal from vanadyl etioporphyrin (VO-EP) using a mixed solvent of supercritical water and toluene: A kinetic study, *Fuel*, 92 (1), 288–294.

[63] Gould, K.A., 1980, Oxidative demetallization of petroleum asphaltenes and residua, *Fuel*, 59 (10), 733–736.

[64] Salehizadeh, H., Mousavi, M., Hatamipour, S., and Kermanshahi, K., 2007, Microbial demetallization of crude oil using *Aspergillus* sp.: Vanadium oxide

octaethyl porphyrin (VOOEP) as a model of metallic porphyrins, *Iran. J. Biotechnol.*, 5 (4), 226–231.

[65] Dedeles, G.R., Abe, A., Saito, K., Asano, K., Saito, K., Yokota, A., and Tomita, F., 2000, Microbial demetallization of crude oil: Nickel protoporphyrin disodium as a model organo-metallic substrate, *J. Biosci. Bioeng.*, 90 (5), 515–521.

[66] Ovalles, C., Rojas, I., Acevedo, S., Escobar, G., Jorge, G., Gutierrez, L.B., Rincon, A., and Scharifker, B., 1996, Upgrading of Orinoco Belt crude oil and its fractions by an electrochemical system in the presence of protonating agents, *Fuel Process. Technol.*, 48 (2), 159–172.

[67] Sakanishi, K., Yamashita, N., Whitehurst, D.D., and Mochida, I., 1998, Depolymerization and demetallation treatments of asphaltene in vacuum residue, *Catal. Today*, 43 (3-4), 241–247.

[68] Reyes, D.J.K., de Montellano, A.G.S.O., Tzab, R.A.T., Oskam, G., and Gil, J.J.A., 2014, Effects of UV-Vis irradiation on vanadium etioporphyrins extracted from crude oil and the role of nanostructured titania, *Int. J. Photoenergy*, 2014, 401239.

[69] Nguyen, M.T., Nguyen, D.L.T., Xia, C., Nguyen, T.B., Shokouhimehr, M., Sana, S.S., Grace, A.N., Aghbashlo, M., Tabatabaei, M., Sonne, C., Kim, S.Y., Lam, S.S., and Le, Q.V., 2021, Recent advances in asphaltene transformation in heavy oil hydroprocessing: Progress, challenges, and future perspectives, *Fuel Process. Technol.*, 213, 106681.

[70] Kohli, K., Prajapati, R., Maity, S.K., Sau, M., and Sharma, B.K., 2019, Deactivation of a hydrotreating catalyst during hydroprocessing of synthetic crude by metal bearing compounds, *Fuel*, 243, 579–589.

[71] Ongarbayev, Y., Oteuli, S., Tileuberdi, Y., Maldybaev, G., and Nurzhanova, S., 2019, Demetallization and desulfurization of heavy oil residues by adsorbents, *Pet. Sci. Technol.*, 37 (9), 1045–1052.

[72] Magomedov, R.N., Popova, A.Z., Maryutina, T.A., Kadiev, K.M., and Khadzhiev, S.N., 2015, Current status and prospects of demetallization of heavy petroleum feedstock (Review), *Petrol. Chem.*, 55, 423–443.

[73] Lee, D., Kim, K.D., and Lee, Y.K., 2020, Conversion of V-porphyrin in asphaltenes into V_2S_3 as an active catalyst for slurry phase hydrocracking of vacuum residue, *Fuel*, 263, 116620.

[74] Langeslay, R.R., Kaphan, D.M., Marshall, C.L., Stair, P.C., Sattelberger, A.P., and Delferro, M., 2019, Catalytic applications of vanadium: A mechanistic perspective, *Chem. Rev.*, 119 (4), 2128–2191.

Review:

Various Adsorbents for Removal of Rhodamine B Dye: A Review

Zainab Mohammad Saigl

Department of Chemistry, Faculty of Science, King Abdulaziz University, P.O. Box 80203, Jeddah 21589, Saudi Arabia

* ***Corresponding author:***

tel: +966-12-6952000 ext. 26546
email: zsaigl@kau.edu.sa

Received: January 5, 2021
Accepted: May 10, 2021

DOI: 10.22146/ijc.62863

Abstract: *Lately, there has been an increase in dye manufacturing, resulting in increased environmental pollution. Recent studies show a wide availability of usage adsorbents, including banana peels, potatoes, algae, etc. Food and Drug Administration prohibited the use of Rhodamine B (RhB) for its toxicity and harmful effects. Therefore, this study presents a wide range of non-conventional low-cost alternative adsorbents to remove RhB dye from wastewater. It has been observed that the mechanism of the dye adsorption is focused on kinetics, isotherm, and thermodynamics models, which depend on the chemical nature of the materials and various physicochemical experimental conditions such as solution pH, initial dye concentration, adsorbent dosage, and temperature of the system. The kinetic data of adsorption of RhB dye usually follow the pseudo-first-order and pseudo-second-order kinetic models. Several studies revealed that Langmuir and Freundlich adsorption isotherm models are frequently used to evaluate the adsorption capacity of the adsorbents. Furthermore, thermodynamic examination showed that RhB adsorption was endothermic and unconstrained in nature. Thus, both photocatalytic degradation and adsorption methods offer good potential to remove RhB dye from industrial effluents. The work is in progress to evaluate the possibility of using other modified waste biomass for industrial pollution control.*

Keywords: *Rhodamine B dye; pseudo-second-order; thermodynamic; isotherm; agricultural wastes*

■ INTRODUCTION

Generally, water can be utilized as an excellent solvent, metabolite, and living environment. Unfortunately, due to the high technology required for industrial societies, several environmental problems appeared and negatively impacted the atmosphere. Over time, population growth, rapid industrialization, and urbanization represent big challenges, particularly the water resources in developing countries contaminated by organic and inorganic compounds such as chiral pollutants and heavy metals [1]. Thus, there are many research articles interested in this global problem [2-3]. As a result, water pollution by new emerging pollutants is becoming a subject of global anxiety, with hazardous environmental consequences [4].

Rhodamine B (RhB) dye is a synthetic dye widely used as a coloring in textiles and food products [5-7]. It is a bright red organic fluorescent pigment used as a coloring agent in various industries such as textiles, paper, paint, etc. Its high solubility in water and its low-cost nature makes it a commonly used pigment in various industries. Colors are characterized by complex chemical structures; subsequently, they are non-biodegradable [8]. RhB dye, likes other dyes, stable to light, heat, oxidation, and is not biologically degradable [9]. Some studies suggest that RhB dye is considered as carcinogenic and mutagenic origin in animals and humans. It causes biological issues such as skin, respiratory inflammation, hemolysis, degenerative changes in the liver, and kidneys, etc. [5-6,10-11]. It is known as water tracer fluorescent as it is used as a tracker inside the water to evaluate the flow rate and direction of the water flow [9,12].

This dye belongs to the xanthine family and is commonly used in the biological, analytical, and optical

Table 1. General properties of Rhodamine B

Common name	Rhodamine B
Chemical name	[9-(2-carboxyphenyl)-6-diethylamino-3-xanthenylidene]-diethylammonium chloride
Chemical formula	$C_{28}H_{31}ClN_2O_3$
Molecular weight	479.017 g/mol
Adsorption maximum	545 nm
Class	Triphenylmethane
Appearance	Basic Violet 10; Brilliant Pink B
Molecular structure	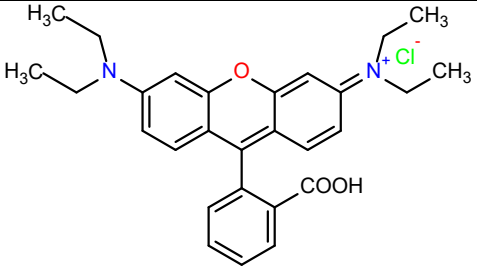

sciences [13]. Among its uses is that it is frequently used in the manufacture of paper, textile and leather dyeing, and fluorescent cell dyeing, and it is also found in wastewater [14-15]. Expanding release of a significant overabundance of dyes by color fabricating and material business leads to extreme environmental issues. RhB dye is broadly utilized for coloring, and their release in water bodies give antagonistic impacts on human and creature [16]. Now the rapid growth of industrialization and unplanned urbanization is causing severe environmental problems, especially for groundwater containing RhB stains, which is one of them. As a result, many studies and research conducted by scientists have reached the adsorption of RhB in many fields [17-18]. Therefore, the utilize of RhB dye as a colorant in foodstuffs was denied. In general, synthetic dyes are used to manufacture various types of paper, textiles, tanning leather, plastics, food processing, and rubber. Subsequently, when it is discharged into water, it is considered a dangerous source of contamination due to its intractable nature [19]. However, many merchants continue to utilize RhB as a food additive, imperiling the prosperity of clients. In this way, the advancement of a simple method for the assurance of RhB in numerous samples is fundamental [20].

Metal ions are the most toxic pollutants in the environment, non-biodegradable and highly toxic leading to carcinogenesis [21]. Removal of organic and inorganic pollutants from aqueous solutions mainly includes chemical, biological, and physical approaches. Various methods, including chemical precipitation, ion exchange, membrane separation, and adsorption, can handle these contaminants. While chemical precipitation is the most common technique, it does not appear to meet the requirements of the strict effluent standard. Therefore, adsorption is favored for the removal of pollutants from all different water treatment systems. It has many advantages over other separation methods, including high solid-phase stability and reusability, ease of separation, reduced costs due to low reagent use, and no need for toxic organic solvents [1]. Therefore, great attention has been oriented towards using various adsorbents such as nanoparticles, carbon nanotubes, graphene, and composite nanomaterials to separate organic and inorganic pollutants [4,22-25]. Moreover, the removal method using biomass has been increased because they are simple, eco-friendly, and cheap [10]. The residual biomass was turned into adsorbent materials after chemical activation with acids or chemical reagents, allowing the development of a large pore in the activated materials [26].

The current review shows the progress in the adsorption process using different adsorbents for removal of RhB dye to overcome the limitations that result from other techniques due to their complications. This would give the readers a broad insight into several possible modifications of adsorbents used for the

effective separation of RhB dye. In addition, kinetic data, thermodynamic examination, and isotherm models of adsorption of RhB dye are frequently used to evaluate the adsorption capacity of the adsorbents. Thus, the present study aimed to determine the optimum conditions for removing RhB from an aqueous solution.

Current Treatment Technology for Color Removal of Dyes

As a type of xanthene color, RhB is produced by phenols and phthalic anhydride, and it is widely used in materials [27]. Extracting the dye from waste clothing is a great inspiration for most researchers worldwide [28]. These techniques include electrostatic deposition, coagulation, air stripping, membrane filtration, catalytic carbon absorption, electrochemical oxidation, wet oxidation, biological oxidation, and chemical oxidation techniques [29]. Chemical oxidation technologies are usually classified into conventional chemical oxidation and advanced oxidation processes [29].

Chemical treatment

There are several different technologies for the adsorption of RhB dye, including chemical oxidation, ion exchange, chemical precipitation, and photocatalytic degradation, etc. Although, according to its versatility, adsorption is considered a worldwide recommended water treatment technology [18].

(i) Conventional chemical methods such as microemulsion, co-chemical precipitation system, chemical hydrothermal procedure, thermal dissolving process, and the mechanical chemical process often used in dyes lysis are expensive. The adsorption process is beneficial and popular among all methods because it is low cost, highly effective, and easy to operate [6,30].

(ii) Chemical agents for treating dye wastewater involve adding ozonation, ion exchange, and reducing agents. Hence, the improvement of cost-effective techniques is of most extreme significance in treating wastewaters that contain dye [31]. By previous experiments on the adsorption of RhB, we can differently research several chemical approaches. Nanometer-wide metal oxides such as TiO_2, MnO_2, CeO_2, MgO, Al_2O_3, Fe_2O_3, etc., are classified as suitable photocatalysts for wastewater treatment [6]. The preparation of carbon nanomaterials (NPCs) using the template method has also become increasingly important in recent years.

In general, the materials have a broad surface, porous sizes, good chemical, and thermal stability. Therefore, they are very promising absorbents for wastewater treatment. Also, industrial carbon has been labeled and used as an adsorbent to remove RhB from water [32]. Over the past few years, due to their extraordinarily high surface area, metal-organic frameworks (MOFs) have emerged as a promising alternative adsorbent for dye wastewater treatment due to their large surface area and good chemical tenability [11,33]. Since organic coloring is complicated to extract because it is hard to decompose, there are many methods for removing the dyes from environmental matrices. A photocatalytic method is a modern way to convert organic coloring to CO_2 and H_2O as final products. Ag_3PO_4/Bi_2WO_6 nanocomposites and $Co_{1-x}Cu_xFe_2O_4$ ($0 \leq x \leq 0.5$) nanoparticles have been synthesized for photolysis of RhB dye under visible irradiation [34-35]. Different types of adsorbents have been used to adsorb RhB dye from aqueous solutions. Synthesizing MgO-supported Fe-Co-Mn nanoparticles (MgO-FCM-NPs) are used as an adsorbent to extract RhB dye. Various techniques were used to test MgO-FCM-NPs, such as scanning electron microscopy (SEM), vibration sample magnetization (VSM), X-ray diffraction (XRD), and Fourier-transform infrared spectroscopy (FTIR) [36].

Physical methods

There has been comprehensive research into traditional physical treatment methods such as adsorption, filtration, electrolysis, and reverse osmosis for RhB dye adsorption. Adsorption technology continues to be sustainable, effective, and the safest strategy to resolve the challenges of the alarming rise in urbanization and industrialization [21,37-40]. Activated carbon (AC) is known for its superior surface areas and microporous structures that contribute to the higher capacity of adsorption of RhB dye [17,41-43]. Membrane separation, for its simple operation process,

small space occupancy, and low energy consumption, is considered a promising technology for dye wastewater [9]. Many studies have concentrated on advanced electrochemical oxidation processes (EAOPs), such as the electro-Fenton (EF) method. Moreover, an assortment of combined strategies was created, counting the coupling of EAOPs with photocatalysis, adsorption, nano-filtration, ultrasounds and microwaves, and the application of microbial fuel cells [27,44]. Numerous ponders were centered on electrochemical progressed oxidation forms (EAOPs) like electro-Fenton (EF) prepare. EF prepare might overcome these issues by the in situ electrochemical eras of H_2O_2 in the cathode [27].

Since the residual pigments in the wastewater are characterized by strong color, high organic content, and stable chemical structure due to azo functional groups. There are several different ways to extract dye from wastewater. Therefore, the use of electrochemical processes as an innovative option is for extracting dyes from colored effluents. The material of the anode has been shown to play a vital role in the electrolysis of organic contaminants for the removal of dye from the effluent. The dimensionally stable anode (DSA) is made of a base metal titanium coated with thin conductive ruthenium or iridium oxide. DSA anode achieves performance with high chemical stability even at high current densities, has a longer life, is commercially available, and at low cost [45]. Semiconductor photocatalysts have gotten expanding attention owing to their application in natural contamination treatment [46].

Biological treatment

Biological studies are an example of many critical biological methods for the adsorption and treatment of RhB dye from wastewater. Physical adsorption by degradation is commonly used in the treatment of effluents [41]. The biological water treatment methods have been less successful because most synthetic dyes are stable to heat and light. Also, many dyes are biologically not degradable because of their complex polymeric structure. In general, the dyes chosen by industries have good stability and fastness [47].

Several tons of dyes are gradually being dumped into wastewater. Discharge of wastewater rich in untreated or partially treated dyes into the natural environment is a major concern due to their respiratory infections and allergic reactions. Among these dyes, RhB [48] is broadly utilized in material passing on and in research facilities as a biological recolor [49]. The biological aerated filter (BAF) has played an important role in treating wastewater to extract RhB dye for many years. However, multiple adsorbents with an adsorption potential have been used to separate RhB dye [41].

Different Adsorbents for the Removal of RhB Dye

A wide range of solid raw agricultural residues has been discovered for the adsorption of RhB dye, such as pine and grapefruit peel, canola peel, peanut husk, pistachio nuts, and red peelings. Abundance in nature is one of the most important factors to consider before investigating various raw agricultural solid waste as low-cost absorbents. Banana, potato, and cucumber are among the agricultural products that are widely grown internationally, and their peels were examined on farmland for treating wastewater from dyes. However, their structure and surface chemistry effect on their ability to absorb the anionic and cationic dyes has been studied [37].

Studies recommend that adsorbents are promising approaches to treating colored effluents, including residual agricultural and industrial materials such as activated carbon from the wood residue, sawdust, and rice husks. Also, the previous studies referred that adsorption using biological materials such as microalgae is excellent removal of pigments. For example, the microalgae species Chlorella pyrenoids belonging to the Chlorophyta division have been used as an important bio-absorbent for removing RhB [13].

The effectiveness of this process was tested by using magnetite/carbon nanocomposite as a sorbent to extract anionic and cationic dyes from wastewater. As far as organic contaminants are concerned, pigments have a high potential to alter the environment due to their high color and optical emission. They also cause changes in biological cycles that primarily impact photosynthesis processes [28]. Subsequently, it is essential to minimize their concentration in wastewater to a more

secure constrain [49]. Therefore, there is an urgent need for various adsorbents to quickly remove toxic pollutants from the environment, efficiently and affordable.

Organic adsorbents

Agricultural wastes. Researchers have used various biomass-based adsorbents to remove different dyes during the last ten years, including RhB dye from aquatic environments [50–51]. Several agricultural wastes and biomasses include *Artocarpus odoratissimus*, coffee beans, banana, orange, lignocellulosic, pomegranate, potato, and cucumber peels [50-56].

Artocarpus odoratissimus, locally known as Tarp in Brunei Darussalam, has been used to remove RhB from aqueous solutions. The skin and core are discarded as wastes. Therefore, they can utilize as adsorbents to reduce the waste disposal problems while converting the wastes into useful adsorbents to clean up wastewater. It has been successfully used as an adsorbent to remove RhB dye from an aqueous solution [57]. Banana peels as an adsorbent have many advantages for removing various toxins from water due to their cost-effective, plentiful, and high carbon and the disposal of banana peels. Banana is one of the most eaten fruits in the world. However, many banana peels are wasted every year despite numerous uses, and their disposal poses a serious issue. Therefore, recent research focuses on the adsorption of RhB dye to the prepared, environmentally friendly green banana peel powder [48].

Moreover, a systematic comparison of potato and cucumber peels' surface and structural properties as effective natural adsorbents was performed in some research to remove both ionic and cationic dyes such as RhB dye from the aqueous solutions [37]. In addition, coffee beans are widely produced and used exceeding 150 million of 60 kg bags which means plenty of waste coffee ground. The carbonized coffee grounds can be used for adsorption, soil remediation, and removing dangerous organic and inorganic compounds from aqueous or wastewater. Furthermore, the coffee ground powder is efficiently used as a zero-cost adsorbent for adsorption and subsequent removal of RhB dye from aqueous solutions [58].

Besides, adsorption is the favored strategy for treating color wastewater which depends on the choice of adsorbents and the adsorption capacities. The reason for choosing *Casuarina equisetifolia* cone (CEC) could be a sort of nonluminous plant, where the root depended on microscopic organisms, Frankie spp. Furthermore, CEC is found in nature in abundance, so it has a small economic value. Moreover, CEC can be effectively prepared into powder for adsorption due to its brittleness. It contains lignocellulosic fabric, which is one of the materials known to be included in the adsorption of poisons. Thus, choosing CEC as an adsorbent to evacuate poison may be an economical choice [59].

Carbon materials. Recently, considerable numbers of adsorbents have been used in removing different dyes, including RhB dye. Among those adsorbents, activated carbon exhibited several advantages. High surface area, porosity, and chemical properties are all responsible for its higher adsorption capacity in wastewater treatment with organic dye molecules [60-61]. Most carbon adsorbents are generated from fruit peels, sugar, beans, and zeolites [62-65]. White sugar undergoing the acid dehydration method was used to prepare a highly porous carbon. The carbon then gets activated in a nitrogen environment, which gives the activated sugar-based carbon (ASC). The ASC was characterized using some classical characterization techniques such as X-ray diffraction (XRD), Brumaire-Emmett-Teller (BET), and Fourier Transform Infrared (FTIR). The obtained result reveals that the pore parameters of the ASC were considered adequate for adsorption.

The obtained findings reveal that the pore parameters of the ASC were considered adequate for adsorption; for instance, 1144.77 m^2/g, 0.53 cm^3/g, and 2.17 nm were recorded for surface area, the volume, and size of the pore, individually. Furthermore, ASC was used to remove RhB dye, and the results showed maximum adsorption efficiency of about 98.28% and an adsorption capacity of 123.46 mg/g within 12 min contact time. RhB adsorption onto ASC followed Langmuir isotherm and pseudo-second-order models. It was found to be regenerated up to 7-times, and the data related to the equilibrium and kinetic., respectively [17].

Also known as the African locust bean, a dicotyledonous angiosperm belonging to the family

Fabaceae is *Parkia biglobosa*. It is classified under spermatophytes, i.e., vascular plants usually referred to in the beginning as locust beans. They are pink and, when fully grown, turn dark brown. On average, they are 30–40 cm long, with some reaching lengths of about 45 cm. A novel adsorbent for RhB dye removal uses activated carbon prepared from the locust bean pod. The goal was to turn locus bean pod biomass waste into AC by preparing a superior functionalized adsorbent to remove RhB dye from the aqueous solutions. The kinetic, isothermal, and thermodynamic parameters regulating the adsorption mechanism have also been examined [41].

In addition, zeolites from Brazilian coal fiery remains have been utilized as a successful low-cost adsorbent in numerous applications. Zeolites have lasting negative charges in their precious stone structures, which empower them to be adjusted by cationic surfactants, such as hexadecyltrimethylammonium [51]. Furthermore, the alteration of the zeolitic fabric improves the expulsion of natural and anionic poisons from effluents [65].

Besides, researchers are paying attention nowadays to biochar carbon materials to remove organic dyes from wastewater. This is due to their inexpensive cost and stability, and sustainability [66-68]. Moreover, the carbon-rich plantain peel (PP) is approximately 30 percent of the plantain fruit. Salts such as sodium chloride and zinc chloride activated PP biochar using ferric nitrate, as well as acids and bases, can be used as chemical activating agents. PP is a waste without any economic value and is generally friendly environmental. For the removal of RhB from wastewater, prepared activated biochar has been used [69]. Moreover, the preparation of biochar from bamboo shoot shell (BSS) hydrothermal carbonization to obtain hydrocar, followed by a treatment for high-temperature carbonization, has been reported to evaluate biochar's ability to remove RhB dye from wastewater. The main component of BSS is very similar to other types of woody biomass containing cellulose, hemicellulose, and lignin, an ideal raw material for carbon material production [42].

Likewise, agricultural waste cassava slag was used to develop cassava slag biochar by hydrothermal technique carbonization process. The structural properties, adsorption performance, and mechanism were comprehensively investigated with multiple tools, such as Scanning Electron Microscopy (SEM), Leica microscope, Brunauer-Emmett-Teller (BET), batch adsorption experiments, Fourier-transform infrared (FTIR), and X-ray photoelectron spectroscopy (XPS). The results from the experiment showed that the cassava slag biochar could remove 96% of RhB from an aqueous solution, with a maximum adsorption amount of 105.3 mg/g. The good adsorption efficiency of RhB could be due to intermolecular hydrogen bonding and electrostatic interaction. In addition, for different colors, the cassava slag biochar has indicated an excellent adsorption efficiency and was economically practical in engineering applications, suggesting a great potential in functional operations [70].

Inorganic adsorbents

Inorganic adsorbents such as zeolites, clays, and perlite are natural, low-cost, abundant, and sustainable materials used in the adsorption process to remove dyes [51,71]. Zeolites naturally occur as porous aluminosilicates consisting of different structures linked together by a shared oxygen atom. The use of zeolite as an adsorbent is available in various types. The 3A zeolite was assessed as a promising adsorbent for the removal of RhB samples from wastewater. Taguchi configuration of the experiment is a multivariate optimization method used to optimize effective parameters. It is a very successful approach and has some benefits over conventional univariate optimization strategies, such as minimizing experimental costs and reducing practical research time [72]. As a synthetic zeolite, beta zeolite is one of the most widely used molecular sieves, particularly in adsorption due to many important characteristics, such as large pores, high Si/Al ratio, and three-dimensional pore networks. Therefore, adsorption materials based on graphene oxide/Beta zeolite composite materials and their adsorption performance for RhB have been studied [73].

Clays are fine-grained minerals, there are around 30 different types of clays, but most “natural” clays are mixtures of these different types. They have a high special surface area and a high potential of cation

exchange potential [74]. Therefore, they have been widely used as sorbents to remove various forms of pollutants. Clay can remove up to 70% of the wastewater. Modified Moroccan natural clay with cetyltrimethylammonium bromide has been investigated for RhB dye removal [49,75]. The quests showed that clay minerals are effective absorbents for removing cationic dyes such as RhB dye from water [7].

In addition to that, expanded perlite has been used to treat wastewater from RhB. It has also been studied applying pseudo-first-order, pseudo-second-order, and intra-part-diffusion models. The results showed that the sorption mechanism was better fitted with a pseudo-second-order model. To describe the phenomenon of adsorption, adsorption isotherms models, e.g., Langmuir, Freundlich, and Temkin, and thermodynamic studies were applied. In addition, the UV spectrophotometric technique is used for the determination of RhB. The results have shown that expanded perlite is a suitable adsorbent for removing RhB from aqueous solutions. The quantity removed was depended on the initial concentration, contact time, solution temperature, and pH of the solution [9]. Besides, paper industries produce a large amount of sludge every year, which can be used as an adsorbent to remove dyes. Therefore, it can be considered a promising, eco-friendly adsorbent with low-cost production to remove dyes from wastewater in a short time. Response surface optimization of RhB dye removal using paper industry waste as adsorbent has been investigated [76].

Moreover, SiO_2/TiO_2 particles were synthesized and coated with white Portland cement paste on the surface, with RhB degradation tests examining the photocatalytic efficiencies of treated pastes before and after an accelerated weathering process. Via investigations of its pozzolanic reactions with the major components of cement concrete, bonding, and its mechanisms on hardened cement-based materials were studied [30]. Also, a typical Zr-MOF(bpy) material has nitrogen atoms that can form hydrogen bonds with the carboxyl groups found on RhB dye to be removed. The addition of ZnO nanoparticles to Zr-MOF(bpy) during growth Zr-MOF(bpy) synthesis aided its gelation and created the gel-like ZnO/Zr-MOF(bpy) nanocomposite. This addition enhanced RhB dye adsorption appropriately [77].

Similarly, synthesized $ZnFe_2O_4$ nanocomposite was used as an adsorbent to remove RhB, characterized by SEM**,** BET, and FTIR**.** The parameter effects that were studied are initial RhB concentration (5–25 mg L^{-1}), pH (3.4–11.1), and temperature (20–60 °C). At equilibrium, the adsorption capacity increased from 5.02 to 9.83 mg g^{-1}, with the increasing amount of initial concentration of RhB from 5 to 25 mg L^{-1} at pH 7.0 and 20 °C. The experimental results showed that at a solution pH of 4.4 and the adsorption capacity obtained was 6.02 mg g^{-1}, and the maximum Rhodamine B removal could be achieved. Among the pseudo-first-order kinetic, the pseudo-second-order, and the intraparticle diffusion models, it was best fitted using a pseudo-second-order kinetic model. The adsorption of RhB onto ZnFe-NC was also analyzed using both Langmuir and Freundlich isotherm model. In addition, various thermodynamic parameters, such as standard Gibbs free energy (ΔG°), enthalpy (ΔH°), and entropy (ΔS°), have also been calculated [78].

Cobalt ferrite is cubic inverse spinel and occupied a prominent place in photocatalysis, with characteristic behavior and a narrow bandgap range of 1.1–2.3 eV. The characteristic feature of cobalt ferrite is high coercivity, moderate saturation, large magnetocrystalline anisotropy, and large magnetostrictive coefficient at room temperature. The microwave combustion method is one of the most effective and feasible methods for preparing copper-doped cobalt ferrite nanoparticles. They focused on preparing copper doped cobalt ferrite nanoparticles by microwave combustion method employing L-arginine as fuel and studying the structural, morphological, optical, vibrational, and magnetic properties of $Co_{1-x}Cu_xFe_2O_4$ ($0 \le x \le 0.5$) nanoparticles by various characterization techniques. The prepared materials were employed for the photocatalytic degradation of RhB under visible light irradiation and a suitable degradation mechanism is proposed [34].

Likewise, recent researches describe the synthesis of magnetic Fe_2O_3 and $Fe_2O_3/g\text{-}C_3N_4$ monoliths prepared by implementing the nano casting and vacuum

impregnation methods, individually. For examining the magnetic potentiality of the monoliths, vibrating sample magnetometer (VSM) analysis was used. The monoliths have great significance in wastewater treatment applications because of their nature to easily separate. The toxic dye, i.e., RhB, has been removed photo catalytically from the aqueous medium using the synthesized monoliths. Fe_2O_3/g-C_3N_4 monolith degradation efficiency was 94.7% in 140 min at pH ~7 under visible light. This was assigned because the monoliths, along with the efficient charge separation efficiency, exhibited a porous nature, which increases their catalytic activity. Moreover, the monolithic catalysts showed excellent stability and reusability over several studies of degradation processes [79].

Moreover, L-Serine (L-Ser) capped magnetite nanoparticles (Fe_3O_4 NPs) is a green one-pot synthesis. It has potential application for the adsorption of RhB dye from an aqueous solution. Due to their high surface area to volume ratio, nanostructured materials can easily functionalize their surface by different molecules for efficient adsorption. Moreover, its unique structural, electrical, optical, and magnetic properties can provide outstanding opportunities for the adsorption of dyes. The study of facile green synthesis of L-Ser capped Fe_3O_4 NPs via a coprecipitation of Fe_3C and Fe_2C salts in the presence of L-Ser as a capping agent. The as-synthesized L-Ser capped Fe_3O_4 NPs were characterized by using UV-Visible Spectrophotometry [47]. Furthermore, recent research found that uranyl-organic frameworks are good candidates for removing such chemical pollutants. Part of the uranyl-organic frameworks, heterometallic uranyl-based (such as Ni–U, Ag–U) photocatalysts, have excellent photocatalytic activities for degradation of RhB under UV/visible light irradiation [80].

Additionally, impregnation of TiO_2 and bentonite followed by microwave irradiation processes is the way for preparing bentonite–TiO_2 composites, characterized by XRD, FTIR, and SEM. Liquid phase adsorption of RhB was used to study the adsorption and photocatalytic capabilities of the composites. The adsorption and photocatalytic degradation experiments were conducted in the presence or absence of UV light irradiation [81]. Also, Cu_2O/rGO nanocomposites would have Cu_2O nanoparticles distributed evenly on reduced graphene oxide (rGO). It was fabricated by a facile in-situ wet-reduced method. The crystalline and photoluminescence structures of Cu_2O/rGO nanocomposites have been analyzed and characterized. Comparing Cu_2O/rGO nanocomposites with the pure Cu_2O nanoparticles, the corresponding removal percentage of RhB achieved more than 95% showing good photocatalytic activity of the Cu_2O/rGO nanocomposites. A mechanism for photocatalytic of the Cu_2O/GO nanocomposites activity could be ascribed to the enhanced adsorption intensity and effective charge carriers separation by rGO [82].

Recently, and due to economic concerns, functionalized polymeric resins have become an alternative to activated carbon and other absorbents. Characterizing polymeric resins is done by their high surface area, moderate swelling, and narrow pore size distribution. Improving the adsorption of resins can be done by modification using the interaction between adsorbate and adsorbent. Mainly, for it is comparatively lower in cost than activated carbon and serves several advantages as a matrix, styrene-divinylbenzene cross-linked copolymer was used to prepare ion-exchange resins. Additionally, the polystyrene-based matrix can provide excellent chemical and physical stability together with resistance to degradation by oxidation or hydrolysis.

Moreover, solvent impregnated resins (SIR) are synergistic properties of both ion exchange and solvent extraction. SIR is defined as a liquid complexing agent distributed homogenously in a solid polymeric medium. The removal with SIR processes happens when a solute is extracted from the aqueous phase into the pores of the resin in an organic phase. As a result, the resin reduces the entrainment and irreversible emulsification during solvent extraction as it acts as a carrier of the solvent [83]. Therefore, the removal of RhB dye from water using a solvent impregnated polymeric Dowex 5WX8 resin has been achieved [83]. The tables below summarize the analytical features of experimental, thermodynamic, isothermal, and kinetic parameters of adsorption from 2016 to 2020.

Table 2. Analytical features of experimental and thermodynamic parameters of adsorption RhB by different techniques during 2016

Adsorbent	Experimental Parameters							Thermodynamic			Ref.
	Q_{max} (mg/g)	pH	T (°C)	Co (mg/L)	T (min)	AD (g/L)	Model	ΔG° (kJ/mol)	ΔH° (kJ/mol)	ΔS° (J/mol K)	
Casuarina equisetifolia Cone Powder	49.5	2	25	50	30	0.05	L, F, and S	-0.1	14.19	51.16	[59]
Raphia hookerie fruit epicarp	666.6	3	26	100	50	2	L, F, T, and DR	-3.1	11.74	49.23	[8]
Azolla pinnata	199.7	3.6	65	20-600	30	2	L, F, DR, T	-0.6	23.3	80.4	[84]
Casuarina equisetifolia needles	82.34	4.4	25	50	180	0.04	L, F, and DR	-2.2	20.1	75	[85]
Bi_2O_3-bentonite nanocomposite	69	3	400	20	80	1	L and F	NA	NA	NA	[16]
Aleurites Moluccana Waste Seeds	117	6	25	300	60	0.05	L, F, S, and R-B	5.0	-12.9	-57.12	[86]
Surfactant-modified zeolite	0.388	8	45	20	40	0.5	L, F, T, and D-R	-24	NA	NA	[65]

Q_{max}: Maximum adsorption of RhB adsorbed per unit mass of adsorbent after equilibrium (mg g^{-1}), T (°C): Temperature, Co: Initial Concentration (mg L^{-1}), T (min): Equilibrium Contact Time, AD: Adsorbent dosage (g L^{-1}), ΔG°: Standard Gibbs free energy (kJ mol^{-1}), ΔH°: Standard enthalpy (kJ mol^{-1}), ΔS°: Standard entropy (J mol^{-1} K^{-1}), L: Langmuir isotherm model, F: Freundlich Isotherm model and DR: Dubinin-Radushkevich. NA: Not Achieved

Table 3. Analytical features of isothermal and kinetic parameters of adsorption RhB by different techniques during 2016

Adsorbent	Isotherm							Kinetic parameter						Ref.
	Langmuir				Freundlich			Pseudo-first order			Pseudo-second order			
	q_m (mg/g)	k_L (L/mg)	R^2	R_L	K_F	n	R^2	K_1 (min^{-1})	q_e (mg/g)	R^2	K_2 (g/min mg)	q_e (mg/g)	R^2	
Casuarina equisetifolia Cone Powder	49.5	0.033	0.993	0.057	4.087	2.21	0.900	0.018	8.22	0.919	0.004	11.5	0.985	[59]
Raphia hookerie fruit epicarp	666.6	0.01	0.9876	0.19	10.55	1.29	0.9969	0.038	25.2	0.984	0.0033	47.1	0.9820	[8]
Azolla pinnata	72.2	0.001	0.986	0.085	4.3	2.1	0.925	0.001	18.4	0.977	0.0020	31.5	0.995	[84]
Casuarina equisetifolia needles	82.34	0.02	0.99	0.11	3.73	1.90	0.950	7.2	0.09	0.801	0.040	7.2	0.999	[85]
Bi_2O_3-bentonite nanocomposite	31.25	0.727	0.892	0.0643	12.62	0.49	0.944	0.07	NA	NA	0.004	NA	NA	[16]
Aleurites Moluccana waste seeds	101	0.003	0.996	NA	2.8	0.4	0.962	0.06	21.2	0.866	0.004	23.6	0.949	[86]
Surfactant-modified zeolite	2.03	0.041	0.067	NA	0.110	1.38	0.900	0.004	0.01	0.219	1.02	0.23	0.990	[65]

q_m: Monolayer maximum adsorption capacity of RhB per unit mass of sorbent (mg g^{-1}) and K_L: Langmuir constant related to the binding energy of RhB sorption (L mg^{-1}), R_L: indicates the dimensionless separation factor, K_F: adsorption capacity of the sorbent (L g^{-1}), n: gives an indication of how favorable the adsorption process in terms of surface heterogeneity and affinity for the adsorbate, q_e: Equilibrium quantity of adsorbate per unit mass of the sorbent (mg g^{-1}), K_1: First-order kinetic model (min^{-1}), K_2: Second-order kinetic model (g (mg $min)^{-1}$), and R^2: Correlation factor and NA: Not achieved

Table 4. Analytical features of experimental and thermodynamic parameters of adsorption RhB by different techniques during 2017

Adsorbents	Experimental parameters							Thermodynamics			Ref.
	Q_{max} (mg/g)	pH	T (K)	C° (mg/L)	T (min)	AD (g/L)	Model	ΔG° (kJ/mol)	ΔH° (kJ/mol)	ΔS° (J/mol K)	
Coal-based carbon membrane with an electric field	NA	4	NA	100	480	NA	NA	NA	NA	NA	[9]
Natural Moroccan Clay	83.95	2-12	298	20	270	0.01	F, L, Te	8.016	12.887	0.0701	[75]
Modified Moroccan Clay	90.10	2-12	298	20	270	0.01	F, L, Te	9.355	26.214	0.1193	[75]

Table 4. Analytical features of experimental and thermodynamic parameters of adsorption RhB by different techniques during 2017 (*Continued*)

Adsorbents	Experimental parameters							Thermodynamics			Ref.
	Q_{max} (mg/g)	pH	T (K)	C° (mg/L)	T (min)	AD (g/L)	Model	ΔG° (kJ/mol)	ΔH° (kJ/mol)	ΔS° (J/mol K)	
Coal-based carbon membrane with an electric field	NA	4	NA	100	480	NA	NA	NA	NA	NA	[9]
Natural Moroccan Clay	83.95	2-12	298	20	270	0.01	F, L, Te	8.016	12.887	0.0701	[75]
Modified Moroccan Clay	90.10	2-12	298	20	270	0.01	F, L, Te	9.355	26.214	0.1193	[75]
$Co_{1-x}Cu_xFe_2O_4$ ($0 \le x \le 0.5$) nanoparticles	NA	2	298	6	330	0.31	K_1, K_2	NA	NA	NA	[34]
L-Serine capped magnetite nanoparticles	6.82	7.4	300	10	60	2.18	K_2, F, L	-1.165	41.75	0.145	[47]
Artocarpus odoratissimus peel	131	4.15	358	0–1000	210	210	L	NA	11.32	46.31	[57]
Coffee ground	3.02 and 1.661	2	292	15	180	50	K_1, K_2, F, L	2.420	52.185	170.429	[58]
Paper waste	75	4.4	308	75	60	0.5–2.5	K_2, L	-11.94	11.70	0.0768	[76]
Graphene oxide/Beta zeolite	64.47	6.5	330	0.1179	60	2.5	F, L	NA	NA	NA	[73]
Uranyl coordination polymer	10	2.7	293	40–100	270	0.157	L	NA	NA	NA	[80]
$ZnFe_2O_4$ nanocomposite	9.83	7	293	25	1440	12.1	K_1, K_2, L, F	-0.42	6.60	24	[78]
Bentonite-titanium dioxide composites	NA	8	343	200	120	10.84	F, L	NA	14.56	NA	[81]
Zinc oxide loaded activated carbon (ZnO-AC)	128.2	7	313	50	140	50	K_1, K_2, F, L	-11.0819	28.043	57.192	[5]

Q_{max}: Maximum adsorption of RhB adsorbed per unit mass of adsorbent after equilibrium (mg g^{-1}), T (°C): Temperature, Co: Initial Concentration (mg L^{-1}), T(min): Equilibrium Contact Time, A.D: Adsorbent dosage (g L^{-1}), ΔG°: Standard Gibbs free energy (kJ mol^{-1}), ΔH°: Standard enthalpy (kJ mol^{-1}), ΔS°: Standard entropy (J mol^{-1} K^{-1}), L: Langmuir isotherm model, F: Freundlich Isotherm model and DR: Dubinin-Radushkevich. NA: Not Achieved

Table 5. Analytical features of isothermal and kinetic parameters of adsorption RhB by different techniques during 2017

Adsorbents	Kinetic parameters						Isotherm parameters						Ref.
	pseudo-first order			pseudo-second order			Langmuir			Freundlich			
	q_e (mg/g)	K_1 (min^{-1})	R^2	q_e (mg/g)	K_2 (g min^{-1} mg^{-1})	R^2	q_m (mg/g)	K_L (L/g)	R^2	K_F	n	R^2	
Natural Moroccan Clay	4.362	0.01	0.688	84.03	0.05	0.999	68.4	-1.678	0.999	107	-4.79	0.996	[75]
Modified Moroccan Clay	3.526	0.07	0.9469	90.09	0.05	0.999	90.1	0.03	0.999	98.3	-7.88	0.996	[75]
$Co_{1-x}Cu_xFe_2O_4$ ($0 \le x \le 0.5$) nanoparticles	NA	0.657	0.980	NA	0.86	0.958	NA	NA	NA	NA	NA	NA	[34]
L-Ser capped Fe_3O_4 NPs	6.11	0.01	0.9756	7.940	0.01	0.991	7.19	0.03–0.08	0.991	7.19	0.03–0.08	0.999	[47]
Artocarpus odoratissimus peel	NA	NA	NA	NA	NA	NA	130	0.02	0.986	NA	NA	NA	[57]
Coffee ground	4.018	37.9	0.999	4.018	6.56	0.999	5.25	4.364	0.958	1.19	2.06	0.884	[58]
Paper waste	NA	NA	NA	3.74	0.69	1	6.71	0.01	0.996	NA	NA	NA	[76]
Graphene oxide/Beta zeolite	NA	NA	NA	NA	NA	NA	27.9	0.080	0.992	2.53	1.83	0.879	[73]
Uranyl coordination polymer	NA	NA	NA	NA	NA	NA	205	NA	0.991	NA	NA	NA	[80]
$ZnFe_2O_4$ nanocomposite	3.38	0.05	0.9861	10.10	0.04	0.999	12.1	0.19	0.994	3.03	2.66	0.972	[78]
Bentonite-titanium dioxide composites	NA	NA	NA	NA	NA	NA	0.25	1523	0.995	0.12	5.62	0.988	[81]
Zinc oxide loaded activated carbon (ZnO-AC)	76.37	0.05	0.876	120.5	0.02	0.999	128	6.50	0.997	88	7.35	0.735	[5]

q_m: Monolayer maximum adsorption capacity of RhB per unit mass of sorbent (mg g^{-1}) and K_L: Langmuir constant related to the binding energy of RhB sorption (L mg^{-1}), R_L: indicates the dimensionless separation factor, K_F: adsorption capacity of the sorbent (L g^{-1}), n: gives an indication of how favorable the adsorption process in terms of surface heterogeneity and affinity for the adsorbate, q_e: Equilibrium quantity of adsorbate per unit mass of the sorbent (mg g^{-1}), K_1: First-order kinetic model (min^{-1}), K_2: Second-order kinetic model (g $(mg\ min)^{-1}$), and R^2: Correlation factor and NA: Not achieved

Table 6. Analytical features of experimental and thermodynamic parameters of adsorption RhB by different techniques during 2018

Adsorbents	Experimental parameters							Thermodynamics			Ref.
	Q_{max} (mg/g)	pH	T (K)	C° (mg/L)	T (min)	AD (g/L)	Model	ΔG° (kJ/mol)	ΔH° (kJ/mol)	ΔS° (J/mol.K)	
Banana peel	211.9	6	383	100	30	0.1	F-L K_1–K_2	NP	NP	NP	[37]
Cucumber peel	179.9	6	383	100	30	0.1	F-L K_1–K_2	NP	NP	NP	[37]
Potato peel	107.4	6	383	100	30	0.1	F-L K_1–K_2	NP	NP	NP	[37]
Banana peel powder	NP	4	304–333	100	60	0.04–0.5	L-F-T	NP	NP	NP	[48]
Chlorella pyrenoidosa	63.14	8	298	100	120	0.1	L-F-K_1–K_2-E-Te-S	NP	NP	NP	[13]
Clay minerals	24	2–12	295	NP	20	NP	L-K_2	-14.6	3.7	0.06	[7]
Electrochemical decolorization	NP	6.5	298	50	90	NP	K_1	NP	NP	NP	[45]
Ability of 3A zeolite in removal of RhB	NP	9	NP	20	40	0.5	NP	NP	NP	NP	[73]
Ag_3PO4/Bi_2WO_6 nanocomposites	NP	0.71	353	NP	30	2.5	NP	NP	NP	NP	[35]
Iron-doped mesoporous silica	NP	3	308	10	180	1	NP	NP	NP	NP	[44]
Iron oxide/carbon nanocomposites	93.35	6.5	298	100	60	1	L-F, K_1–K_2	NP	NP	NP	[28]

Q_{max}: Maximum adsorption of RhB adsorbed per unit mass of adsorbent after equilibrium (mg g^{-1}), T (°C): Temperature, Co: Initial Concentration (mg L^{-1}), T (min): Equilibrium Contact Time, A.D: Adsorbent dosage (g L^{-1}), ΔG°: Standard Gibbs free energy (kJ mol^{-1}), ΔH°: Standard enthalpy (kJ mol^{-1}), ΔS°: Standard entropy (J mol^{-1} K^{-1}) and L: Langmuir isotherm model, F: Freundlich Isotherm model and DR: Dubinin-Radushkevich. NA: Not Achieved

Table 7. Analytical features of isothermal and kinetic parameters of adsorption RhB by different techniques during 2018

Adsorbents	Kinetic Parameters						Isothermal Parameters					Ref.
	Pseudo-first order kinetic			Pseudo-second order kinetic			Langmuir		Freundlich			
	q_e (mg/g)	K_1 (min^{-1})	R^2	q_e (mg/g)	K_2 (g mg^{-1} min^{-1})	R^2	q_m (mg/g)	K_L (L/mg)	R^2	K_F	n	R^2	
Banana peel	97	23.58	0.9919	99.9	5.14	0.9992	211.9	0.288–0.013	0.999	35.76	0.4752	0.836	[37]
Cucumber peel	78.5	24.85	0.9009	76.5	21.79	0.9998	107.4	0.459–0.027	0.999	5.44	0.7928	0.80	[37]
Potato peel	84	49.31	0.9944	85.6	16.97	0.9995	179.9	0.172–0.053	0.993	14.94	0.4338	0.853	[37]
Banana peel powder	NP	NP	NP	NP	NP	NP	1.6572	0.0658	0.9740	NP	NP	NP	[48]
Chlorella pyrenoidosa	24.75	0.284	0.9799	25.54	NP	NP	NP	0.0070	0.9905	NP	NP	NP	[13]
Iron oxide/carbon nanocomposites	72.79	23.21	0.990	102.27	0.65	0.9985	131.80	0.19	0.9398	34.41	3.06	0.8454	[28]
Direct carbonization of Zn/Co zeolitic imidazolate	89.8	0.0963	0.8935	101.8	9.1×10^{-1}	0.9991	119.9	0.18	0.9991	61.1	7.50	0.9458	[32]
Polyamide grafted heavy metals	4.1	0.033	0.8979	1.5	1.157	0.9968	19.9	1.04	0.9946	2.88	2.12	0.9873	[19]
Novel biopolymer silicalite-1	2.2	0.012	0.97	4.5	0.034	0.99	45	0.034	0.97	3.4	1.61	0.99	[10]
Microporous nanohybrids of carbon xerogels	NP	NP	NP	NP	NP	NP	50	0.008	0.995	8.50	2.43	0.946	[87]

q_m: Monolayer maximum adsorption capacity of RhB per unit mass of sorbent (mg g^{-1}) and K_L: Langmuir constant related to the binding energy of RhB sorption (Lmg^{-1}), R_L: indicates the dimensionless separation factor, K_F: adsorption capacity of the sorbent (L g^{-1}), n: gives an indication of how favorable the adsorption process in terms of surface heterogeneity and affinity for the adsorbate, q_e: Equilibrium quantity of adsorbate per unit mass of the sorbent (mg g^{-1}), K_1: First-order kinetic model (min^{-1}), K_2: Second-order kinetic model (g (mg min)$^{-1}$), and R^2: Correlation factor and NA: Not achieved

Table 8. Analytical features of experimental and thermodynamic parameters of adsorption RhB by different techniques during 2019

Adsorbent	Experimental Parameters							Thermodynamic			Ref.
	Q_{max} (mg/g)	pH	T (C°)	C° (mg/L)	T (min)	AD (g/L)	Model	ΔG° (kJ/mol)	ΔH° (kJ/mol)	ΔS° (J/mol K)	
Acid activated locust bean	454.5	6.8	30	1000	120	0.1	L,F,K_1	-26.35	58.779	208.95	[88]
Hybrid ion- exchanger	1.23	2.9>	50	10	180	5	L,F,K_2	1.69	NA	NA	[18]

Table 8. Analytical features of experimental and thermodynamic parameters of adsorption RhB by different techniques during 2019 (*Continued*)

Adsorbent	Experimental Parameters						Thermodynamic				Ref.
	Q_{max} (mg/g)	pH	T (C°)	C° (mg/L)	T (min)	AD (g/L)	Model	ΔG° (kJ/mol)	ΔH° (kJ/mol)	ΔS° (J/mol K)	
MgO nanoparticles	2462.5	7	25	10	60	0.04	L,F	−12.06	9.440	72.00	[36]
Activated sugar-based carbon (ASC)	123.46	2–11	15–45	50	12	0.08	L,F,K_2	NA	NA	NA	[17]
Zeolitic imidazolate frameworks (ZIF)	85.0	10<	30	20–200	1440	2.1	L,F	NA	NA	NA	[41]
Organo-vermiculites (organo-Vts)	528	2	25	50–1000	90	0.05	L,F	−20.8	−5.21	52.79	[89]

Q_{max}: Maximum adsorption of RhB adsorbed per unit mass of adsorbent after equilibrium (mg g^{-1}), T (°C): Temperature, Co: Initial Concentration (mg L^{-1}), T (min): Equilibrium Contact Time, A.D: Adsorbent dosage (g L^{-1}), ΔG°: Standard Gibbs free energy (kJ mol^{-1}), ΔH°: Standard enthalpy (kJ mol^{-1}), ΔS°: Standard entropy (J mol^{-1} K^{-1}), L: Langmuir isotherm model, F: Freundlich Isotherm model and DR: Dubinin-Radushkevich. NA: Not Achieved

Table 9. Analytical features of isothermal and kinetic parameters of adsorption RhB by different techniques during 2019

Adsorbent	Isothermal							Kinetic parameter						Ref.
	Langmuir				Freundlich			Pseudo-first order			Pseudo-second order			
	q_m (mg/g)	K_L (L/mg)	R^2	R_L	K_F	n	R^2	K_1 (min^{-1})	q_e (mg/g)	R^2	K_2	q_e (mg/g)	R^2	
Acid activated locust bean	455	4.66	0.9991	0.6	80	0.4	0.9966	0.03	73	0.9865	0.1	909	0.9941	[88]
Hybrid ion- exchanger	1.23	0.97	0.992	0	1.2	1.2	0.986	0.01	51	0.854	0.3	69.4	0.992	[18]
MgO nanoparticle	2791	0.07	0.9991	0	18	1.2	0.9993	3.92	0.9	0.9823	0.2	95.4	0.9992	[36]
Activated sugar-based carbon (ASC)	123	0.72	0.9796	0.2	50	2.7	0.6416	0.39	61	0.9679	0.7	71.9	0.9982	[17]
Zeolitic imidazolate frameworks (ZIF)	85	0.01	0.9970	NA	0.9	3.9	0.8048	0.01	21	0.8377	0.2	73	0.9989	[41]

q_m: Monolayer maximum adsorption capacity of RhB per unit mass of sorbent (mg g^{-1}) and K_L: Langmuir constant related to the binding energy of RhB sorption (L mg^{-1}), R_L: indicates the dimensionless separation factor, K_F: adsorption capacity of the sorbent (L g^{-1}), n: gives an indication of how favorable the adsorption process in terms of surface heterogeneity and affinity for the adsorbate, q_e: Equilibrium quantity of adsorbate per unit mass of the sorbent (mg g^{-1}), K_1: First-order kinetic model (min^{-1}), K_2: Second-order kinetic model (g (mg $min)^{-1}$), and R^2: Correlation factor and NA: Not achieved

Table 10. Analytical features of experimental and thermodynamic parameters of adsorption RhB by different techniques during 2020

Adsorbent	Experimental Parameters						Thermodynamic				Ref.
	Q_{max} (mg/g)	pH	T (°C)	C° (mg/L)	T (min)	AD (g/L)	Model	ΔG° (kJ/mol)	ΔH° (kJ/mol)	ΔS° (J/mol K)	
Cassava slag biochar (HCS)	105.3	4.99	35	500	1–720	0.1	L, F, DR, T	-8.116	222.5	1.192	[70]
Dowex 5WX8 Resin	43.47	2.8	25	50	12	0.08	L and F	NA	NA	NA	[83]
Three-dimensional layered double hydroxide	49.6	NA	150	60	30	0.05	L and F	NA	NA	NA	[90]
SiO_2/TiO_2 composite powders	625	3.2	25	75–300	8.6	NA	L and F	NA	-14.75	-40.43	[30]
CdO nanomaterial	NA	6	35	10–100	80	0.1	L, F, T	-79.55	NA	NA	[91]
Ni-graphene hybrid composites (NGC25b)	963	NA	70	120	15	NA	L and F	NA	NA	NA	[74]
Grass-Waste	54	6.6	35	100	400	0.1	L and F	-0.23	20.28	0.07	[49]

Q_{max}: Maximum adsorption of RhB adsorbed per unit mass of adsorbent after equilibrium (mg g^{-1}), T (°C): Temperature, Co: Initial Concentration (mg L^{-1}), T (min): Equilibrium Contact Time, A.D: Adsorbent dosage (g L^{-1}), ΔG°: Standard Gibbs free energy (kJ mol^{-1}), ΔH°: Standard enthalpy (kJ mol^{-1}), ΔS°: Standard entropy (J mol^{-1} K^{-1}), L: Langmuir isotherm model, F: Freundlich Isotherm model and DR: Dubinin-Radushkevich. NA: Not Achieved

Table 11. Analytical features of isothermal and kinetic parameters of RhB adsorption by different techniques during 2020

Adsorbent	Isothermal							Kinetic parameter						Ref.
	Langmuir				Freundlich			Pseudo-first order			Pseudo-second order			
	q_m (mg/g)	K_L (L/mg)	R^2	R_L	K_F	n	R^2	K_1 (min^{-1})	q_e (mg/g)	R^2	K_2 (g/min mg)	q_e (mg/g)	R^2	
Cassava slag biochar (HCS)	105.3	0.51	0.973	NA	12.9	2.3	0.989	0.038	5.09	0.923	0.01	24.1	0.99	[70]
Dowex 5WX8 Resin	43.4	0.01	0.990	0.2	NA	<1	0.087	NA	NA	NA	NA	NA	NA	[83]
Three-dimensional layered double hydroxide	52.63	0.3	0.930	NA	18.6	3.8	0.982	0.7	25.9	0.9872	0.08	50.8	0.999	[90]
SiO_2/TiO_2 composite powders	NA	NA	NA	NA	NA	NA	NA	NA	NA	NA	NA	NA	NA	[30]
CdO nanomaterial	361.01	0.68	0.994	NA	1.63	0.8	0.989	0.006	4.008	0.906	0.01	3.5	0.9907	[91]
Ni-graphene hybrid composites (NGC25b)	963.04	NA	0.957	NA	NA	NA	NA	NA	NA	0.9989	NA	NA	NA	[74]

q_m: Monolayer maximum adsorption capacity of RhB per unit mass of sorbent (mg g^{-1}) and K_L: Langmuir constant related to the binding energy of RhB sorption (L mg^{-1}), R_L: indicates the dimensionless separation factor, K_F: adsorption capacity of the sorbent (L g^{-1}), n: gives an indication of how favorable the adsorption process in terms of surface heterogeneity and affinity for the adsorbate, q_e: Equilibrium quantity of adsorbate per unit mass of the sorbent (mg g^{-1}), K_1: First-order kinetic model (min^{-1}), K_2: Second-order kinetic model (g (mg min)$^{-1}$), and R^2: Correlation factor and NA: Not achieved

Modern Techniques for the Removal of RhB Dye

In general, most of the toxic material composition in the textile industry effluents and the challenging conditions of breaking down the bonding of few dyes used in textiles, usage of conventional techniques needs a flavor of modern technological support. The modern enabling techniques for water quality monitoring utilize smart sensors interfaced with modern controllers and interconnected using wireless standards to monitor water quality. Several examples of widely used sensors are smart [92], optical [93], and wireless [51] sensors.

■ CONCLUSION

This review covers recent information and future applications of RhB dye adsorption. The results showed that kinetic data of adsorption of RhB dye usually follow the pseudo-first-order and pseudo-second-order kinetic models. It has also been revealed that Langmuir and Freundlich adsorption isotherm models are frequently used to evaluate the adsorption capacity of the adsorbents. Furthermore, thermodynamic examination showed that RhB adsorption was endothermic and unconstrained in nature. Therefore, both photocatalytic degradation and adsorption methods offer good potential to remove RhB dye from industrial effluents. The present review indicated that the adsorption technique using natural adsorbents such as different fruit peels and rice husk was beneficial and cost-effective for better removal of RhB dye. The work is in progress to evaluate the possibility of using other modified waste biomass for industrial pollution control.

■ REFERENCES

[1] Ali, I., Gupta, V.K., and Aboul-Enein, H.Y., 2005, Metal ion speciation and capillary electrophoresis: application in the new millennium, *Electrophoresis*, 26 (21), 3988–4002.

[2] Basheer, A.A., 2018, Chemical chiral pollution: Impact on the society and science and need of the regulations in the 21st century, *Chirality*, 30 (4), 402–406.

[3] Basheer, A.A., and Ali, I., 2018, Stereoselective uptake and degradation of (±)-*o,p*-DDD pesticide stereomers in water-sediment system, *Chirality*, 30 (9), 1088–1095.

[4] Basheer, A.A., 2018, New generation nano-adsorbents for the removal of emerging contaminants in water, *J. Mol. Liq.*, 261, 583–593.

[5] Li, Y., Yan, X., Hu, X., Feng, R., and Zhou, M., 2019, Trace pyrolyzed ZIF-67 loaded activated carbon pellets for enhanced adsorption and catalytic degradation of Rhodamine B in water, *Chem. Eng. J.*, 375, 122003.

[6] Nekouei Marnani, N., and Shahbazi, A., 2019, A novel environmental-friendly nanobiocomposite synthesis by EDTA and chitosan functionalized magnetic graphene oxide for high removal of

Rhodamine B: Adsorption mechanism and separation property, *Chemosphere*, 218, 715–725.

[7] Li, Z., Potter, N., Rasmussen, J., Weng, J., and Lv, G., 2018, Removal of rhodamine 6G with different types of clay minerals, *Chemosphere*, 202, 127–135.

[8] Inyinbor, A.A., Adekola, F.A., and Olatunji, G.A., 2016, Kinetics, isotherms and thermodynamic modeling of liquid phase adsorption of Rhodamine B dye onto *Raphia hookerie* fruit epicarp, *Water Resour. Ind.*, 15, 14–27.

[9] Tao, P., Xu, Y., Song, C., Yin, Y., Yang, Z., Wen, S., Wang, S., Liu, H., Li, S., Li, C., Wang, T., and Shao, M., 2017, A novel strategy for the removal of Rhodamine B (RhB) dye from wastewater by coal-based carbon membranes coupled with the electric field, *Sep. Purif. Technol.,* 179, 175–183.

[10] Sabarish, R., and Unnikrishnan, G., 2018, Novel biopolymer templated hierarchical silicalite-1 as an adsorbent for the removal of Rhodamine B, *J. Mol. Liq.*, 272, 919–929.

[11] Ghasemi, E., and Kaykhaii, M., 2016, Application of Micro-cloud point extraction for spectrophotometric determination of Malachite green, Crystal violet and Rhodamine B in aqueous samples, *Spectrochim. Acta, Part A*, 164, 93–97.

[12] Bethi, B., Manasa, V., Srinija, K., and Sonawane, S.H., 2018, Intensification of Rhodamine-B dye removal using hydrodynamic cavitation coupled with hydrogel adsorption, *Chem. Eng. Process.*, 134, 51–57.

[13] da Rosa, A.L.D., Carissimi, E., Dotto, G.L., Sander, H., and Feris, L.A., 2018, Biosorption of Rhodamine B dye from dyeing stones effluents using the green microalgae *Chlorella pyrenoidosa*, *J. Cleaner Prod.*, 198, 1302–1310.

[14] Yu, Y., Wang, C., Luo, L., Wang, J., and Meng, J., 2018, An environment-friendly route to synthesize pyramid-like g-C_3N_4 arrays for efficient degradation of Rhodamine B under visible-light irradiation, *Chem. Eng. J.*, 334, 1869–1877.

[15] Pascariu, P., Airinei, A., Olaru, N., Olaru, L., and Nica, V., 2016, Photocatalytic degradation of Rhodamine B dye using ZnO-SnO_2 electrospun ceramic nanofibers, *Ceram. Int.*, 42 (6), 6775–6781.

[16] Patil, S.P., Bethi, B., Sonawane, G.H., Shrivastava, V.S., and Sonawane, S., 2016, Efficient adsorption and photocatalytic degradation of Rhodamine B dye over Bi_2O_3-bentonite nanocomposites: A kinetic study, *J. Ind. Eng. Chem.*, 34, 356–363.

[17] Xiao, W., Garba, Z.N., Sun, S., Lawan, I., Wang, L., Lin, M., and Yuan, Z., 2020, Preparation and evaluation of an effective activated carbon from white sugar for the adsorption of Rhodamine B dye, *J. Cleaner Prod.*, 253, 119989.

[18] Saruchi, and Kumar, V., 2019, Adsorption kinetics and isotherms for the removal of Rhodamine B dye and Pb^{+2} ions from aqueous solutions by a hybrid ion-exchanger, *Arabian J. Chem.*, 12 (3), 316–329.

[19] Saleh, T.A., and Ali, I., 2018, Synthesis of polyamide grafted carbon microspheres for removal of Rhodamine B dye and heavy metals, *J. Environ. Chem. Eng.*, 6 (4), 5361–5368.

[20] Chen, J., and Zhu, X., 2016, Magnetic solid phase extraction using ionic liquid-coated core-shell magnetic nanoparticles followed by high-performance liquid chromatography for determination of Rhodamine B in food samples, *Food Chem.*, 200, 10–15.

[21] Ali, I., Burakov, A.E., Melezhik, A.V., Babkin, A.V, Burakova, I.V, Neskomornaya, E.A., Galunin, E.V., Tkachev, A.G., and Kuznetsov, D.V., 2019, Removal of copper(II) and zinc(II) ions in water on a newly synthesized polyhydroquinone/graphene nanocomposite material: kinetics, thermodynamics and mechanism, *ChemistrySelect*, 4 (43), 12708–12718.

[22] Ali, I., Alharbi, O.M.L., Alothman, Z.A., Al-Mohaimeed, A.M., and Alwarthan, A., 2019, Modeling of fenuron pesticide adsorption on CNTs for mechanistic insight and removal in water, *Environ. Res.*, 170, 389–397.

[23] Burakova, E.A., Dyachkova, T.P., Rukhov, A.V, Tugolukov, E.N., Galunin, E.V., Tkachev, A.G., Basheer, A.A., and Ali, I., 2018, Novel and economic method of carbon nanotubes synthesis on a nickel magnesium oxide catalyst using microwave radiation, *J. Mol. Liq.*, 253, 340–346.

[24] Ali, I., 2018, Microwave assisted economic synthesis of multi walled carbon nanotubes for arsenic species removal in water: Batch and column operations, *J. Mol. Liq.*, 271, 677–685.

[25] Ali, I., and Aboul-Enein, H.Y., 2002, Speciation of metal ions by capillary electrophoresis, *Crit. Rev. Anal. Chem.*, 32 (4), 337–350.

[26] Ali, I., Alharbi, O.M.L., Alothman, Z.A., and Alwarthan, A., 2018, Facile and eco-friendly synthesis of functionalized iron nanoparticles for cyanazine removal in water, *Colloids Surf., B*, 171, 606–613.

[27] Tian, J., Olajuyin, A.M., Mu, T., Yang, M., and Xing, J., 2016, Efficient degradation of rhodamine B using modified graphite felt gas diffusion electrode by electro-Fenton process, *Environ. Sci. Pollut. Res.*, 23 (12), 11574–11583.

[28] Ianoş, R., Păcurariu, C., Muntean, S.G., Muntean, E., Nistor, M.A., and Nižňanský, D., 2018, Combustion synthesis of iron oxide/carbon nanocomposites, efficient adsorbents for anionic and cationic dyes removal from wastewaters, *J. Alloys Compd.*, 741, 1235–1246.

[29] Tariq, M., Muhammad, M., Khan, J., Raziq, A., Uddin, M.K., Niaz, A., Ahmed, S.S., and Rahim, A., 2020, Removal of Rhodamine B dye from aqueous solutions using photo-Fenton processes and novel Ni-Cu@MWCNTs photocatalyst, *J. Mol. Liq.*, 312, 113399.

[30] Wang, D., Hou, P., Stephan, D., Huang, S., Zhang, L., Yang, P., and Cheng, X., 2020, SiO_2/TiO_2 composite powders deposited on cement-based materials: Rhodamine B removal and the bonding mechanism, *Constr. Build. Mater.*, 241, 118124.

[31] Kumar, V., Singh, M., Behera, K., and Pandey, S., 2020, Ionic liquid induced removal of Rhodamine B from water, *J. Mol. Liq.*, 319, 114195.

[32] Zhang, J., Yan, X., Hu, X., Feng, R., and Zhou, M., 2018, Direct carbonization of Zn/Co zeolitic imidazolate frameworks for efficient adsorption of Rhodamine B, *Chem. Eng. J.*, 347, 640–647.

[33] Oyekanmi, A.A., Ahmad, A., Hossain, K., and Rafatullah, M., 2019, Statistical optimization for adsorption of Rhodamine B dye from aqueous solutions, *J. Mol. Liq.*, 281, 48–58.

[34] Sundararajan, M., and Kennedy, L.J., 2017, Photocatalytic removal of Rhodamine B under irradiation of visible light using $Co_{1-x}CuxFe_2O_4$ ($0 \leq x \leq 0.5$) nanoparticles, *J. Environ. Chem. Eng.*, 5 (4), 4075–4092.

[35] Jonjana, S., Phuruangrat, A., Thongtem, T., Kuntalue, B., and Thongtem, S., 2018, Decolorization of Rhodamine B photocatalyzed by Ag_3PO_4/Bi_2WO_6 nanocomposites under visible radiation, *Mater. Lett.*, 218, 146–149.

[36] Rahdar, S., Rahdar, A., Zafar, M.N., Shafqat, S.S., and Ahmadi, S., 2019, Synthesis and characterization of MgO supported Fe-Co-Mn nanoparticles with exceptionally high adsorption capacity for Rhodamine B dye, *J. Mater. Res. Technol.*, 8 (5), 3800–3810.

[37] Stavrinou, A., Aggelopoulos, C.A., and Tsakiroglou, C.D., 2018, Exploring the adsorption mechanisms of cationic and anionic dyes onto agricultural waste peels of banana, cucumber and potato: Adsorption kinetics and equilibrium isotherms as a tool, *J. Environ. Chem. Eng.*, 6 (6), 6958–6970.

[38] Al-Shaalan, N.H., Ali, I., Alothman, Z.A., Al-Wahaibi, L.H., and Alabdulmonem, H., 2019, High performance removal and simulation studies of diuron pesticide in water on MWCNTs, *J. Mol. Liq.*, 289, 111039.

[39] Ali, I., Alharbi, O.M.L., Al-Othman, Z.A., Alwarthan, A., and Al-Mohaimeed, A.M., 2019, Preparation of a carboxymethylcellulose-iron composite for uptake of atorvastatin in water, *Int. J. Biol. Macromol.*, 132, 244–253.

[40] Ali, I., Alharbi, O.M.L., Al-Othman, Z.A., and Badjah, A.Y., 2018, Kinetics, thermodynamics, and modeling of amido black dye photodegradation in water using Co/TiO_2 nanoparticles, *Photochem. Photobiol.*, 94 (5), 935–941.

[41] Zhang, J., Hu, X., Yan, X., Feng, R., Zhou, M., and Xue, J., 2019, Enhanced adsorption of Rhodamine B by magnetic nitrogen-doped porous carbon

prepared from bimetallic ZIFs, *Colloids Surf., A*, 575, 10–17.

[42] Waheed, A., Mansha, M., Kazi, I.W., and Ullah, N., 2019, Synthesis of a novel 3,5-diacrylamidobenzoic acid based hyper-cross-linked resin for the efficient adsorption of Congo Red and Rhodamine B, *J. Hazard. Mater.*, 369, 528–538.

[43] Yao, H., Wang, X., Gao, J., Gao, C., Zhao, R., Zhai, X., Wu, Y., Hao, C., Yang, J., Mei, S., and Qiu, H., 2019, Hydrothermal synthesis of flower-like Cu_2MoS_4/g-C_3N_4 composite and its adsorption performances for Rhodamine B, *Mater. Chem. Phys.*, 223, 648–658.

[44] Jinisha, R., Gandhimathi, R., Ramesh, S.T., Nidheesh, P.V., and Velmathi, S., 2018, Removal of Rhodamine B dye from aqueous solution by electro-Fenton process using iron-doped mesoporous silica as a heterogeneous catalyst, *Chemosphere*, 200, 446–454.

[45] Baddouh, A., Bessegato, G.G., Rguiti, M.M., El Ibrahimi, B., Bazzi, L., Hilali, M., and Zanoni, M.V.B., 2018, Electrochemical decolorization of Rhodamine B dye: Influence of anode material, chloride concentration and current density, *J. Environ. Chem. Eng.*, 6 (2), 2041–2047.

[46] Li, D., Li, J., and Tang, J., 2016, Mercury oxide as an efficient photocatalyst for degradation of Rhodamine B dye under visible-light irradiation, *Solid State Sci.*, 61 (3), 201–206.

[47] Belachew, N., Rama Devi, D., and Basavaiah, K., 2017, Green synthesis and characterisation of L-Serine capped magnetite nanoparticles for removal of Rhodamine B from contaminated water, *J. Exp. Nanosci.*, 12 (1), 114–128.

[48] Singh, S., Parveen, N., and Gupta, H., 2018, Adsorptive decontamination of Rhodamine-B from water using banana peel powder: A biosorbent, *Environ. Technol. Innovation*, 12, 189–195.

[49] Zahir, A., Aslam, Z., Aslam, U., Abdullah, A., Ali, R., and Bello, M.M., 2020, *Paspalum notatum* grass-waste-based adsorbent for Rhodamine B removal from polluted water, *Chem. Biochem. Eng. Q.*, 34 (2), 93–104.

[50] Berradi, M., Hsissou, R., Khudhair, M., Assouag, M., Cherkaoui, O., El Bachiri, A., and El Harfi, A., 2019, Textile finishing dyes and their impact on aquatic environs, *Heliyon*, 5 (11), e02711.

[51] Imam, S., and Babamale, H., 2020, A short review on the removal of Rhodamine B dye using agricultural waste-based adsorbents, *Asian J. Chem. Sci.*, 7 (1), 25-37.

[52] Shahzadi, A., Nosheen, S., Kiran, S., Riaz, S., Mughal, T.A., and Shahid, L., 2020, Plant waste utilization as ecofriendly sorbents for removal of reactive dyes from wastewater, *Pak. J. Sci.*, 72 (2), 119.

[53] Alwared, A.I., Al-Musawi, T.J., Muhaisn, L.F., and Mohammed, A.A., 2020, The biosorption of reactive red dye onto orange peel waste: A study on the isotherm and kinetic processes and sensitivity analysis using the artificial neural network approach, *Environ. Sci. Pollut. Res.*, 28 (3), 2848–2859.

[54] Stavrinou, A., Aggelopoulos, C.A., and Tsakiroglou, C.D., 2020, A methodology to estimate the sorption parameters from batch and column tests: The case study of methylene blue sorption onto banana peels, *Processes*, 8 (11), 1467.

[55] Nayak, A.K., and Pal, A., 2020, Statistical modeling and performance evaluation of biosorptive removal of Nile blue A by lignocellulosic agricultural waste under the application of high-strength dye concentrations, *J. Environ. Chem. Eng.*, 8 (2), 103677.

[56] Saigl, Z.M., and Ahmed, A.M., 2021, Separation of Rhodamine B dye from aqueous media using natural pomegranate peels, *Indones. J. Chem.*, 21 (1), 212–224.

[57] Lim, L.B.L., Priyantha, N., Fang, X.Y., and Mohamad Zaidi, N.A.H., 2017, *Artocarpusodoratissimus* peel as a potential adsorbent in environmental remediation to remove toxic Rhodamine B dye, *J. Mater. Environ. Sci.*, 8 (2), 494–502.

[58] Shen, K., and Gondal, M.A., 2017, Removal of hazardous Rhodamine dye from water by adsorption onto exhausted coffee ground, *J. Saudi Chem. Soc.*, 21 (Suppl. 1), S120–S127.

[59] Dahri, M.K., Kooh, M.R.R., and Lim, L.B.L., 2016, Remediation of Rhodamine B dye from aqueous solution using *Casuarina equisetifolia* cone powder as a low-cost adsorbent, *Adv. Phys. Chem.*, 2016, 9497378.

[60] Garba, Z.N., and Rahim, A.A., 2016, Evaluation of optimal activated carbon from an agricultural waste for the removal of para-chlorophenol and 2,4-dichlorophenol, *Process Saf. Environ. Prot.*, 102, 54–63.

[61] Al-Saadi, A.A., Saleh, T.A., and Gupta, V.K., 2013, Spectroscopic and computational evaluation of cadmium adsorption using activated carbon produced from rubber tires, *J. Mol. Liq.*, 188, 136–142.

[62] Nasrullah, A., Saad, B., Bhat, A.H., Khan, A.S., Danish, M., Isa, M.H., and Naeem, A., 2019, Mangosteen peel waste as a sustainable precursor for high surface area mesoporous activated carbon: Characterization and application for methylene blue removal, *J. Cleaner Prod.*, 211, 1190–1200.

[63] Senthilkumar, T., Chattopadhyay, S.K., and Miranda, L.R., 2017, Optimization of activated carbon preparation from pomegranate peel (*Punica granatum* peel) using RSM, *Chem. Eng. Commun.*, 204 (2), 238–248.

[64] Xiao, W., Garba, Z.N., Sun, S., Lawan, I., Wang, L., Lin, M., and Yuan, Z., 2020, Preparation and evaluation of an effective activated carbon from white sugar for the adsorption of Rhodamine B dye, *J. Cleaner Prod.*, 253, 119989.

[65] Alcântara, R.R., Muniz, R.O.R., and Fungaro, D.A., 2016, Full factorial experimental design analysis of Rhodamine B removal from water using organozeolite from coal bottom ash, *Int. J. Energy Environ.*, 7 (5), 357–374.

[66] Dai, L., Zhu, W., He, L., Tan, F., Zhu, N., Zhou, Q., He, M., and Hu, G., 2018, Calcium-rich biochar from crab shell: An unexpected super adsorbent for dye removal, *Bioresour. Technol.*, 267, 510–516.

[67] Sewu, D.D., Boakye, P., and Woo, S.H., 2017, Highly efficient adsorption of cationic dye by biochar produced with Korean cabbage waste, *Bioresour. Technol.*, 224, 206–213.

[68] Jin, L., Zhao, X., Qian, X., and Dong, M., 2018, Nickel nanoparticles encapsulated in porous carbon and carbon nanotube hybrids from bimetallic metal-organic-frameworks for highly efficient adsorption of dyes, *J. Colloid Interface Sci.*, 509, 245–253.

[69] Adekola, F.A., Ayodele, S.B., and Inyinbor, A.A., 2019, Activated biochar prepared from plantain peels: Characterization and Rhodamine B adsorption data set, *Chem. Data Collect.*, 19, 100170.

[70] Wu, J., Yang, J., Huang, G., Xu, C., and Lin, B., 2020, Hydrothermal carbonization synthesis of cassava slag biochar with excellent adsorption performance for Rhodamine B, *J. Cleaner Prod.*, 251, 119717.

[71] Esvandi, Z., Foroutan, R., Peighambardoust, S.J., Akbari, A., and Ramavandi, B., 2020, Uptake of anionic and cationic dyes from water using natural clay and clay/starch/$MnFe_2O_4$ magnetic nanocomposite, *Surf. Interfaces*, 21, 100754.

[72] Rahmani, M., Kaykhaii, M., and Sasani, M., 2018, Application of Taguchi L16 design method for comparative study of ability of 3A zeolite in removal of Rhodamine B and Malachite green from environmental water samples, *Spectrochim. Acta, Part A*, 188, 164–169.

[73] Cheng, Z.L., Li, Y.X., and Liu, Z., 2017, Novel adsorption materials based on graphene oxide/Beta zeolite composite materials and their adsorption performance for rhodamine B, *J. Alloys Compd.*, 708, 255–263.

[74] Tao, X., Wang, S., and Li, Z., 2020, Ultrasound-assisted bottom-up synthesis of Ni-graphene hybrid composites and their excellent Rhodamine B removal properties, *J. Environ. Manage.*, 255, 109834.

[75] Damiyine, B., Guenbour, A., and Boussen, R., 2017, Rhodamine B adsorption on natural and modified Moroccan clay with cetyltrimethylammonium bromide: Kinetics, equilibrium and thermodynamics, *J. Mater. Environ. Sci.*, 8 (3), 860–871.

[76] Thakur, A., and Kaur, H., 2017, Response surface optimization of Rhodamine B dye removal using

paper industry waste as adsorbent, *Int. J. Ind. Chem.*, 8 (2), 175–186.

[77] Cui, W., Kang, X., Zhang, X., and Cui, X., 2019, Gel-like ZnO/Zr-MOF(bpy) nanocomposite for highly efficient adsorption of Rhodamine B dye from aqueous solution, *J. Phys. Chem. Solids*, 134, 165–175.

[78] Konicki, W., Siber, D., and Narkiewicz, U., 2017, Removal of Rhodamine B from aqueous solution by $ZnFe_2O_4$ nanocomposite with magnetic separation performance, *Pol. J. Chem. Technol.*, 19 (4), 65–74.

[79] Singh, J., and Basu, S., 2020, Synthesis of mesoporous magnetic Fe_2O_3/g-C_3N_4 monoliths for Rhodamine B removal, *Microporous Mesoporous Mater.*, 303, 110299.

[80] Ren, Y.N., Xu, W., Zhou, L.X., and Zheng, Y.Q., 2017, Efficient tetracycline adsorption and photocatalytic degradation of rhodamine B by uranyl coordination polymer, *J. Solid State Chem.*, 251, 105–112.

[81] Laysandra, L., Sari, M.W.M.K., Soetaredjo, F.E., Foe, K., Putro, J.N., Kurniawan, A., Ju, Y.H., and Ismadji, S., 2017, Adsorption and photocatalytic performance of bentonite-titanium dioxide composites for methylene blue and rhodamine B decoloration, *Heliyon*, 3 (12), e00488.

[82] Huang, H., Zhang, J., Jiang, L., and Zang, Z., 2017, Preparation of cubic Cu_2O nanoparticles wrapped by reduced graphene oxide for the efficient removal of rhodamine B, *J. Alloys Compd.*, 718, 112–115.

[83] Khan, M.A., Momina, Siddiqui, M.R., Otero, M., Alshareef, S.A., and Rafatullah, M., 2020, Removal of Rhodamine B from water using a solvent impregnated polymeric Dowex 5WX8 resin: Statistical optimization and batch adsorption studies, *Polymers*, 12 (2), 1–12.

[84] Kooh, M.R.R., Lim, L.B.L., Lim, L.H., and Dahri, M.K., 2016, Separation of toxic rhodamine B from aqueous solution using an efficient low-cost material, *Azolla pinnata*, by adsorption method, *Environ. Monit. Assess.*, 188 (2), 1–15.

[85] Parthasarathy, P., and Narayanan, S.K., 2014, Determination of kinetic parameters of biomass samples using thermogravimetric analysis, *Environ. Prog. Sustainable Energy*, 33 (1), 256–266.

[86] Postai, D.L., Demarchi, C.A., Zanatta, F., Melo, D.C.C., and Rodrigues, C.A., 2016, Adsorption of Rhodamine B and methylene blue dyes using waste of seeds of *Aleurites Moluccana*, a low cost adsorbent, *Alexandria Eng. J.*, 55 (2), 1713–1723.

[87] Shouman, M.A., and Fathy, N.A., 2018, Microporous nanohybrids of carbon xerogels and multi-walled carbon nanotubes for removal of Rhodamine B dye, *J. Water Process Eng.*, 23, 165–173.

[88] Bello, O.S., Adegoke, K.A., Sarumi, O.O., and Lameed, O.S., 2019, Functionalized locust bean pod (*Parkia biglobosa*) activated carbon for Rhodamine B dye removal, *Heliyon*, 5 (8), e02323.

[89] Wang, J., Gao, M., Shen, T., Yu, M., Xiang, Y., and Liu, J., 2019, Insights into the efficient adsorption of rhodamine B on tunable organo-vermiculites, *J. Hazard. Mater.*, 366, 501–511.

[90] Zhu, Z., Xiang, M., Li, P., Shan, L., and Zhang, P., 2020, Surfactant-modified three-dimensional layered double hydroxide for the removal of methyl orange and Rhodamine B: Extended investigations in binary dye systems, *J. Solid State Chem.*, 288, 121448.

[91] Geetha Malini, P.S., Durgadevi, P., Senthil Kumar, N., and Rani, S., 2020, Synthesis and characterisation of CdO nanoparticles: An efficient nanomaterial for the removal of Rhodamine B, *Mater. Today: Proc.*, In Press, Corrected Proof.

[92] Saharan, P., Sharma, A.K., Kumar, V., and Kaushal, I., 2019, Multifunctional CNT supported metal doped MnO_2 composite for adsorptive removal of anionic dye and thiourea sensing, *Mater. Chem. Phys.*, 221, 239–249.

[93] Skarga-Bandurova, I., Krytska, Y., Shorokhov, M., Suvorin, O., Barbaruk, L., and Ozheredova, M., 2019, Towards development IoT-based water quality monitoring system, *The 7th International Conference on Future Internet of Things and Cloud Workshops (FiCloudW 2019)*, Institute of Electrical and Electronics Engineers Inc., 140–145.

NOTE:

Comparing the Chemical Characteristics of Pectin Isolated from Various Indonesian Fruit Peels

Siti Susanti[1*], Anang Mohamad Legowo[1], Nurwantoro[1], Silviana[2], and Fahmi Arifan[3]

[1]*Food Technology Division, Department of Agriculture, Faculty of Animal and Agricultural Sciences, Diponegoro University, Jl. Prof. Soedarto SH, Tembalang, Semarang 50275, Central Java, Indonesia*

[2]*Department of Chemical Engineering, Faculty of Engineering, Diponegoro University, Jl. Prof. Soedarto SH, Tembalang, Semarang 50275, Central Java, Indonesia*

[3]*Diploma Program of Chemical Engineering, Faculty of Vocational School, Diponegoro University, Jl. Prof. Soedarto SH, Tembalang, Semarang 50275, Central Java, Indonesia*

** **Corresponding author:***

email: sitisusanti@live.undip.ac.id

Received: September 16, 2020
Accepted: February 9, 2021

DOI: 10.22146/ijc.59799

Abstract: *The Indonesian pectin manufacturing industry is underdeveloped, and pectin is imported to meet its increasing demand; we attempted to isolate pectins from various fruit peels, such as orange peel (OP), papaya peel (PP), mango peel (MP), watermelon peel (WP), and chayote peel (CP) and investigated their chemical characteristics (equivalent weight of the extracted pectins and their moisture, ash, methoxyl, and galacturonic acid (GA) contents). Acid extraction, purification, precipitation, and drying processes were used to process the isolated pectins. We examined their chemical properties for conformance to quality standards advised by the International Pectin Producers Association (IPPA). The moisture (except OP pectin) and ash contents (except PP pectin) of the extracted pectins were within the limit set by IPPA. However, the equivalent weight (W eq) of any of the isolated pectins did not satisfy IPPA standards. The methoxyl contents of the pectins isolated from OP, WP, and CP satisfied IPPA standards. High methoxyl pectins were isolated from PP and MP. The galacturonic acid contents of the isolated pectins were higher than the acceptable limit of the GA level. Thus, OP, PP, MP, WP, and CP are potential sources of pectin.*

Keywords: *natural source; chemical; pectin; fruit peels*

■ INTRODUCTION

Pectin is a polysaccharide and a functional ingredient utilized in the food and pharmaceutical industries. Natural pectin can be isolated from the cell walls of different plant parts [1]. The fruit peel, which is considered a waste product in the food and fruit-based industries, is also a source of natural pectin [2].

Pectin is used as a stabilizer in food and has emerged as an important ingredient used in the food industry. The last decade has seen a growing interest in Indonesian culinary. This has resulted in a gradual increase in the demand for pectin [3]. Unfortunately, pectin is still imported into Indonesia as the pectin manufacturing industry in Indonesia is still undeveloped. However, a huge amount of waste that can be potential sources of pectin is generated each year by the fruit industries present in the country [3]. The utilization of fruit peels as sources of pectin is still in its nascent stage.

The peels of various indigenous fruits (such as banana, durian, grapefruit, and papaya peels) can be potential sources of natural pectin [4]. Various extraction and isolation methods for obtaining pectin have been reported. The isolation methods employed can potentially influence the yield and chemical characteristics of pectin.

This study outlined the procedure to isolate pectin from various fruit peels (mango, orange, papaya,

watermelon, and chayote) using the following reported protocols of extraction and studied the characteristics of the isolated pectins. It also investigated whether the quality of the isolated pectin samples adheres to the quality standards advised by the International Pectin Producers Association (IPPA) [5]. Herein, we present scientific data that can be potentially utilized for developing the pectin manufacturing industry by using indigenous fruit peels as sources of natural pectin. The use of fruit peels as sources of natural pectin can utilize the waste generated from fruit-based food industries. Thus, optimal waste management can be achieved, leading to environmental preservation.

■ EXPERIMENTAL SECTION

Materials

Orange peel (OP), papaya peel (PP), mango peel (MP), watermelon peel (WP), and chayote peel (CP) were used as the pectin sources. The fruit peels were collected from fruit-based food industries in different parts of Semarang City, Central Java Province, Indonesia. The chemicals used in this study were hydrochloric acid (HCl), phenolphthalein, 96% ethanol, sodium hydroxide (NaOH), and distilled water.

Instrumentation

Dry fruit peels were powdered by using an electric metal grinder (Nima, Japan). Extraction equipment series such as ring stand clamp (Thomas® Scientific, USA), laboratory glass thermometer (NFS 200 Celsius degree, R-TEK, India), portable magnetic stirrer (Z693448-1EA, Merck), heating mantle (E103, MTOPs, Korea), and three-neck distilling flask (500 mL, PYREX®, USA) were used for pectin extraction.

Procedure

The fruit peels were washed to remove all traces of dirt. After that, the fruit peels were sun-dried to obtain dry matter with an average moisture content of 8.64% and then powdered.

Pectin isolation

Pectin was isolated from various fruit peel powders following a previously reported protocol [6] that was slightly modified. The peel powder (50 g) was suspended in distilled water (250 mL). Subsequently, HCl (1 N, 0.5 mL) was added to the solution, and the suspension was heated at 80 °C for 120 min. The mixture (pH = 2.8) was filtered through two layers of cheesecloth. Following this, the filtrate was coagulated using 96% ethanol (filtrate: ethanol ratio was 1:1 by volume), and the mixture was stirred continuously for 15 min. Subsequently, the isolated pectin was washed with ethanol (5 mL). The pectin was dried in an oven at 40 °C for 8 h, ground, and then sifted to obtain fine powdered pectin.

Determination of chemical characteristic of pectin

The chemical characteristics of the isolated pectins (obtained from OP, PP, MP, WP, and CP) were analyzed. The equivalent weights (W eq) of the pectins and the moisture, ash, galacturonic acid (GA), and methoxyl contents were determined. Six different samples of each pectin were used for testing each of these parameters. The moisture and ash contents of pectins were determined by the following protocols outlined [7]. W eq of the pectins and the methoxyl and GA contents were determined following the process established by Ranganna [8].

Statistical analysis

All data were statistically tested using the analysis of variance technique. Following this, Duncan multiple range tests (significance level: 5%) were conducted to analyze the obtained data [9].

■ RESULTS AND DISCUSSION

Generally, the fruit peel is not utilized to its full extent and is often discarded as a waste product that causes environmental problems (especially water pollution). Cell walls that form the fruit peel tissue contain pectin, which is a form of fiber [10]. Therefore, fruit peels can be potentially used as a natural source of pectin. Several researchers have successfully isolated pectin from fruit peels [6,11–13]. Some researchers from Indonesia have also successfully isolated pectin from fruit peels [14–16]. Although various methods have been reported for pectin extraction, almost all extraction methods require the use of an acid solution. The acid of

interest used in our studies is hydrochloric acid (HCl, 1 N), which is a strong acid and ensures efficient pectin extraction (compared with other acids such as acetic acid). The lower the pH, the faster the rate of degradation of the extracted material. The extraction process runs smoothly when the hydrolytic molecules are quickly released from the galacturonic acid chains [16].

We used pectin isolated from OP, PP, MP, WP, and CP for the studies. To ensure that the fruit peel contained sufficient pectin, preliminary research (involving the alcohol test) was conducted with the peel samples [17]. The fruits were squeezed to obtain the fruit liquid. Following this, four tablespoons of ingredients were added to one spoonful of the juice. High pectin content is indicated by the formation of thick clots in the mixture. The formation of fewer clots with a liquid-like consistency indicates low pectin content.

Peels of ripe fruits were used as sources of pectin because they contain sufficient quantities of pectin that can be used for analyzing the properties of pectin. Ripe fruits contain protopectin that can be easily broken down by fruit ripening hormones. The extent of conversion of protopectin to pectin (and finally to pectic acid) increases as the fruit ripens. Pectic acid is highly soluble in fruit liquid [10]. Therefore, the amount of pectin in the peel of ripe fruit is more than that present in the peel of raw fruit.

The extraction methods affect the characteristics of pectin. The chemical properties of pectin affect the physical characteristics and quality of pectin. The quality standards advised by IPPA are commonly used as references for evaluating the quality of pectin. We studied the chemical characteristics of pectin obtained from OP, PP, MP, WP, and CP.

Moisture Content of Pectin

The moisture content of food products is an important determinant of the durability of food products because it is related to the microbial activity in stored products. Food products with low moisture content are relatively more stable and have a longer shelf-life than food products with high moisture content. As shown in Fig. 1, the moisture content of pectin extracted from OP was the maximum (15.03%). Pectins extracted from other fruit peels exhibited a lower moisture content ($p \leq 0.05$). It was assumed that an inefficient drying process was responsible for the retention of water in the pectin sample isolated from OP, resulting in the high moisture content of the sample [18]. We observed that the pectin sample (especially the sample extracted from OP) could not be effectively dried by heating it at 40 °C for 8 h. The optimum drying temperature for drying the pectin extracted from OP (moisture content < 12%) was found to be 50 °C. The sample should be heated at 50 °C for 6 h for efficient drying [18]. According to IPPA guidelines, the acceptable moisture level in pectin is ≤ 12%. Thus, the moisture contents of pectin extracted from PP, MP, WP, and CP were within the permissible limit of moisture content [5].

Ash Content of Pectin

Ash is the inorganic residue obtained from the combustion of organic matter. The ash content can be used to estimate the mineral content of the material as well as to determine the purity of pectin. The higher the ash content, the lower the pectin purity. Fig. 2 reveals that the ash contents of pectin, extracted from the fruit peels, were within ($p \leq 05$) the IPPA-recommended upper limit of ash content (≤ 10%). However, the ash content of pectin extracted from PP was significantly higher than the acceptable limit of ash content (12.06%, $p \leq 0.05$). Thus, OP, MP, WP, and CP are the potential

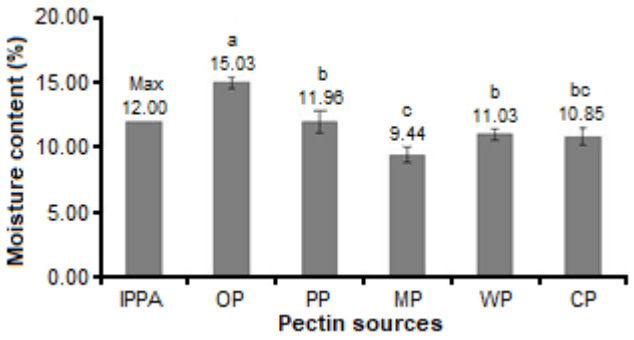

Fig 1. Moisture content (%) of pectin isolated from various fruit peels such as OP, PP, MP, WP, and CP. The data are expressed as mean ± STDEV. The standards advised by IPPA are taken as reference. The letters above each bar graph represent the significant differences between the groups

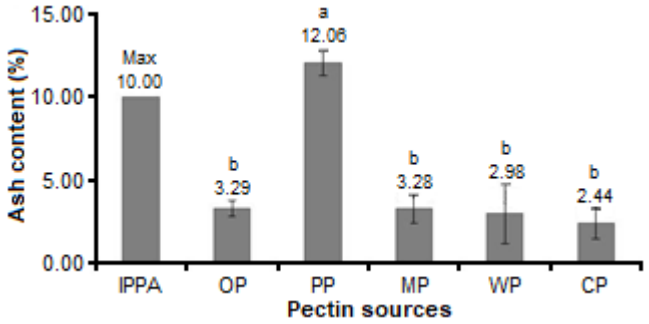

Fig 2. Ash content (%) of pectin isolated from various fruit peels such as OP, PP, MP, WP, and CP. The data are expressed as the mean ± STDEV. The standard laid down by IPPA is taken as the reference. The letters above each bar graph represent the significant differences between the groups

sources of natural pectin because they can potentially produce pure pectin.

The raw materials used and the extraction and isolation methods employed for pectin extraction determined the ash content of pectin. The amount and composition of the minerals present in the raw materials can potentially influence the purity of pectin [16]. The ash content increased as the extraction time increased. The ash content in pectin extracted from PP was found to be the maximum when the extraction time was 120 min (Fig. 2). Thus, the extraction time for obtaining pectin from PP should be such that high-quality pectin (in terms of purity) can be obtained. Although an extraction time of 120 min afforded the maximum amount of pectin, the optimal extraction time was found to be in the range of 60–90 min. Highly pure pectin with low ash content was obtained under this optimum extraction condition [14,19].

Equivalent Weight (W eq) of Pectin

The high and low pectin levels caused by the presence of free GA groups in the molecular chain of pectin can be estimated from the W eq values [17]. Fig. 3 shows that the W eq of the isolated pectins was significantly higher than the IPPA-recommended acceptable maximum limit of W eq (≤ 800 mg). The W eq of CP pectin ($p \leq 0.05$) was the highest (9,394 mg). Different W eq was observed for different pectin samples because fruit peels of different fruits were used as the raw materials. The extraction method used for obtaining the pectin samples and the titration process used for analyzing the samples can potentially affect the W eq of the pectins [13]. The pectin chains are depolymerized (forming pectic acids) when the extraction time is significantly long (120 min). It also leads to an increase in the number of unesterified GA groups.

Methoxyl Content of Pectin

The methoxyl contents of pectins are a determinant of the gel-forming abilities of pectins [20]. Based on the methoxyl content, pectin is divided into two groups: high methoxyl pectin (HMP, > 7.12%) and low methoxyl pectin (LMP, 2.50–7.12%). The methoxyl levels in pectins extracted from OP, WP, and CP were lower than the IPPA prescribed maximum acceptable level. Hence, they were categorized as LMPs. The calculated methoxyl levels in pectins extracted from PP and MP were higher than the IPPA-recommended maximum permissible level of methoxyl content. Hence, they were categorized as HMPs (Fig. 4). The higher the amount of methoxyl in pectin, the greater the ability of pectin to thicken a medium.

Ga Content of Pectin

The purity of pectin can be determined by its GA content [17]. The purity of pectin increases as the GA content increases. This is caused by a decrease inorganic content. The GA contents of pectin extracted from different fruit peels were greater than the acceptable limit

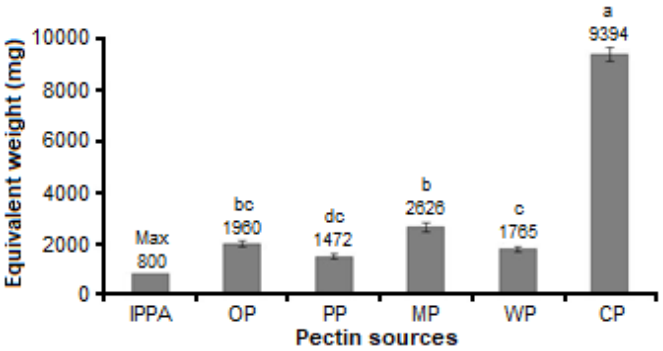

Fig 3. Equivalent weight (mg) of pectin isolated from various fruit peels such as OP, PP, MP, WP, and CP. The data are expressed as the mean ± STDEV. The standard laid down by IPPA is taken as the reference. The letters above each bar graph represent the significant differences between the groups

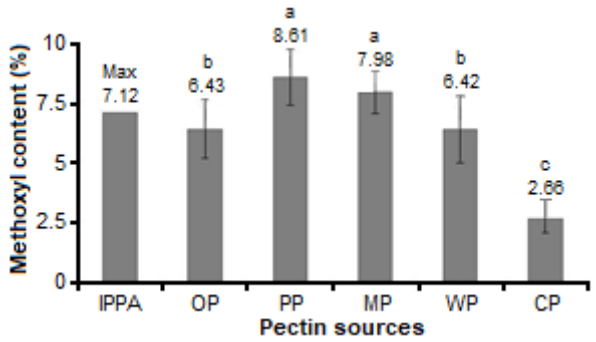

Fig 4. Methoxyl content (%) of pectin isolated from various fruit peels such as OP, PP, MP, WP, and CP. The data are expressed as the mean ± STDEV. The standard laid down by IPPA is taken as the reference. The letters above each bar graph represent the significant differences between the groups

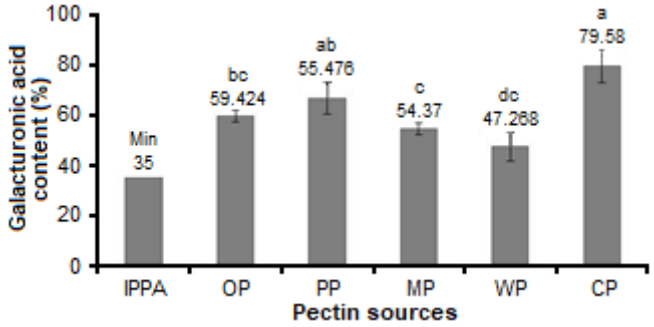

Fig 5. GA content (%) of pectin isolated from various fruit peels such as OP, PP, MP, WP, and CP. The data are expressed as the mean ± STDEV. The standard laid down by IPPA is taken as the reference. The letters above each bar graph represent the significant differences between the groups

of GA content (set by IPPA). The maximum amount of GA was found in CP pectin (Fig. 5). Thus, OP, PP, MP, WP, and CP can potentially produce high-quality pectin.

■ CONCLUSION

Pectins were extracted from the peels of orange, papaya, mango, watermelon, and chayote, and they exhibited different chemical characteristics. These different chemical characteristics can be attributed to the extraction methods used to isolate the pectins and the type of raw materials used as the pectin source. All the fruit peels used for carrying out the studies can be potentially used as alternative sources of pectin. However, the chemical characteristics of the extracted pectins do not strictly adhere to the quality standards advised by IPPA. Thus, different extraction methods and alternate pectin sources should be continuously explored to achieve the indigenous production of high-quality pectin.

■ REFERENCES

[1] Buchanan, B.B., Gruissem, W., and Jones, R.L., 2015, *Biochemistry and Molecular Biology of Plants*, 2nd Ed., John Wiley and Sons, New York, USA.

[2] Sundarraj, A.A., and Ranganathan, T.V., 2017, A review - Pectin from agro and industrial waste, *Int. J. Appl. Environ. Sci.*, 12 (10), 1777–1801.

[3] Naqash, F., Masoodi, F.A., Rather, S.A., Wani, S.M., and Gani, A., 2017, Emerging concepts in the nutraceutical and functional properties of pectin, *Carbohydr. Polym.*, 168, 227–239.

[4] Petkowicz, C.L.O., Vriesmann, L.C., and Williams, P.A., 2017, Pectins from food waste: Extraction, characterization and properties of watermelon rind pectin, *Food Hydrocolloids*, 65, 57–67.

[5] International Pectin Producers Association (IPPA), 2014, *Pectin Commercial Production and Pectin in Organic Food Products*, https://ippa.info.

[6] Hamidon, N.H., and Zaidel, D.N.A., 2017, Effect of extraction conditions on pectin yield extracted from sweet potato peels residues using hydrochloric acid, *Chem. Eng. Trans.*, 56, 979–984.

[7] Grassino, A.N., Barba, F.J., Brnčić, M., Lorenzo, J.M., Lucini, L., and Brnčić, Z.R., 2018, Analytical tools used for the identification and quantification of pectin extracted from plant food matrices, wastes and by-products: A review, *Food Chem.*, 266, 47–55.

[8] Ranganna, S., 1995, Handbook of Analysis and Quality Control for Fruit and Vegetable Products, Tata McGraw-Hill Publishing Company Limited, New Delhi, India.

[9] Elmore, J.G., Wild, D.M.G., Nelson, H.D., and Katz, D.L., 2020, *Jekel's Epidemiology, Biostatistics and Preventive Medicine and Public Health*, 5th Ed., Elsevier Health Sciences, London.

[10] Lara-Espinoza, C., Carvajal-Millán, E., Balandrán-Quintana, R., López-Franco, Y., and Rascón-Chu,

A., 2018, Pectin and pectin-based composite materials: beyond food texture, *Molecules*, 23 (4), 942.

[11] Akili, M.S., Ahmad, U., and Suyatma, N.E., 2012, Karakteristik edible film dari pectin hasil ekstraksi kulit pisang, *JTEP*, 26 (1), 39–46.

[12] Guo, X., Han, D., Xi, H., Rao, L., Liao, X., Hu, X., and Wu, J., 2012, Extraction of pectin from navel orange peel assisted by ultra-high pressure, microwave or traditional heating: A comparison, *Carbohydr. Polym.*, 88 (2), 441–448.

[13] Freitas, C.M.P., Sousa, R.C.S., Dias, M.M.S., and Coimbra, J.S.R., 2020, Extraction of pectin from passion fruit peel, *Food Eng. Rev.*, 12 (4), 460–472.

[14] Djenar, N.S., and Suryadi, J., 2020, Microwave power and pH regulating solution effect on characteristics of pectin from sukun peel (*Artocarpus altilis*) using Microwave Assisted Extraction (MAE), *Proceedings of the International Seminar of Science and Applied Technology (ISSAT 2020)*, Politeknik Negeri Bandung, Bandung, 24-25 November 2020.

[15] Hasanah, U., Setyowati, M., Edwarsyah, Efendi, R., Safitri, E., Idroes, R., Heng, L.Y., and Sani, N.D., 2018, Isolation of pectin from coffee pulp Arabica Gayo for the development of matrices membrane, *IOP Conf. Ser.: Mater. Sci. Eng.*, 523, 012014.

[16] Raji, Z., Khodaiyan, F., Rezaei, K., Kiani, H., Schultz, M, and Zanganeh, S., 2020, The influence of particle size and acid type on pectin extraction, *IJFAS*, 9 (1), 1–4.

[17] Paasikallio, T., Huuskonen, A., and Wiebe, M.G., 2017, Scaling up and scaling down the production of galactaric acid from pectin using *Trichoderma reesei*, *Microb. Cell Fact.*, 16 (1), 119.

[18] Hosseini, S.S., Khodaiyan, F., and Yarmand, M.S., 2016, Optimization of microwave assisted extraction of pectin from sour orange peel and its physicochemical properties, *Carbohydr. Polym.*, 140, 59–65.

[19] Su, D.L., Li, P.J., Quek, S.Y., Huang, Z.Q., Yuan, Y.J., Li, G.Y., and Shan, Y., 2019, Efficient extraction and characterization of pectin from orange peel by a combined surfactant and microwave assisted process, *Food Chem.*, 286, 1–7.

[20] Xie, F., Gu, B.J., Saunders, S.R., and Ganjyal, G.M., 2021, High methoxyl pectin enhances the expansion characteristics of the cornstarch relative to the low methoxyl pectin, *Food Hydrocolloids*, 110, 106131.